NOTE TO USER

This reproduction is the best copy available.

UMI®

Discriminating Lithology in Arctic Environments from Earth Orbit: An Evaluation of Satellite Imagery and Classification Algorithms

by

David William Leverington

A Thesis
Submitted to the Faculty of
Graduate Studies in Partial Fulfilment of
the Requirements for the Degree of

DOCTOR OF PHILOSOPHY

Department of Geological Sciences
The University of Manitoba
Winnipeg, Manitoba

©2001

National Library of Canada
Acquisitions and Bibliographic Services
395 Wellington Street
Ottawa ON K1A 0N4
Canada

Bibliothèque nationale du Canada
Acquisitions et services bibliographiques
395, rue Wellington
Ottawa ON K1A 0N4
Canada

Your file Votre référence

Our file Notre référence

The author has granted a non-exclusive licence allowing the National Library of Canada to reproduce, loan, distribute or sell copies of this thesis in microform, paper or electronic formats.

The author retains ownership of the copyright in this thesis. Neither the thesis nor substantial extracts from it may be printed or otherwise reproduced without the author's permission.

L'auteur a accordé une licence non exclusive permettant à la Bibliothèque nationale du Canada de reproduire, prêter, distribuer ou vendre des copies de cette thèse sous la forme de microfiche/film, de reproduction sur papier ou sur format électronique.

L'auteur conserve la propriété du droit d'auteur qui protège cette thèse. Ni la thèse ni des extraits substantiels de celle-ci ne doivent être imprimés ou autrement reproduits sans son autorisation.

0-612-62651-2

Canada

THE UNIVERSITY OF MANITOBA

FACULTY OF GRADUATE STUDIES

*****

COPYRIGHT PERMISSION PAGE

Discriminating Lithology in Arctic Environments from Earth Orbit:

An Evaluation of Satellite Imagery and Classification Algorithms

BY

David William Leverington

A Thesis/Practicum submitted to the Faculty of Graduate Studies of The University of Manitoba in partial fulfillment of the requirements of the degree of Doctor of Philosophy

DAVID WILLIAM LEVERINGTON © 2001

Permission has been granted to the Library of The University of Manitoba to lend or sell copies of this thesis/practicum, to the National Library of Canada to microfilm this thesis/practicum and to lend or sell copies of the film, and to Dissertations Abstracts International to publish an abstract of this thesis/practicum.

The author reserves other publication rights, and neither this thesis/practicum nor extensive extracts from it may be printed or otherwise reproduced without the author's written permission.

Abstract

Empirical investigations of classification algorithms for lithological discrimination were performed for field areas on Melville Island, Nunavut, and in the Cape Smith Belt of northern Québec. These investigations suggest that a neural network classifier (a majority-vote consensus algorithm that combines the classification results of ten feedforward backpropagation neural networks) is capable of consistently producing results that approximate those produced by the best individual neural network execution, and that are equal or superior to those generated by the maximum likelihood and evidential reasoning classifiers. The majority-vote consensus routine serves to eliminate the effect of the natural variability among individual neural network classification results, by producing strong results without necessitating the manual evaluation and ranking of all individual neural network classifications.

Two sets of evidential-reasoning classification results were generated based on two different measures of initial evidence: 1) the proportions of training data that contain the image values being classified; and 2) output activations generated by multiple neural network classifications. Evidential-reasoning results produced using the first measure were generally poor, while those produced using the second were frequently comparable to those of the majority-vote neural network consensus algorithm.

Empirical investigations of the use of feedforward backpropagation neural networks in the classification of satellite images suggest that: 1) differences in weight initializations between otherwise identical classifications are not sufficient for the generation of sets of error-independent results for use with consensus algorithms; 2) classifications of satellite images are not characterized by over-generalization; 3) the addition of random noise to input vectors during training is not a useful means for supplementing sparse training datasets; 4) commonly applied guidelines for the definition of network topologies are valid; and 5) the absolute and relative magnitudes of output activations may be used as measures of classification confidence.

Evaluations of Landsat TM, Radarsat, and IKONOS images, conducted for the Melville Island and Cape Smith Belt regions, demonstrate that: 1) Radarsat images are useful for the discrimination of lithological classes characterized by good correlations with geomorphology and surface roughness, and 2) IKONOS images are good sources of high-resolution information regarding geomorphology, land cover, and lithological units with distinctive weathering characteristics.

Acknowledgements

I would like to thank my advisor, Dr. Wooil Moon, for his guidance and support over the past five years. I would also like to thank the thesis committee members [Dr. Jim Teller, Dr. Don Hall, and Dr. George Tabisz (University of Manitoba); Dr. Ed Cloutis (University of Winnipeg); and Dr. Jón Benediktsson (University of Iceland)] for their helpful comments on the thesis at various stages in its development. The faculty, staff, and graduate students of the Department of Geological Sciences were very supportive during my stay here in Winnipeg; in particular, I would like to thank Dr. Jim Teller, Dr. Norman Halden, Dr. George Clark, and Dr. Lorne Ayres for their advice, assistance, and encouragement.

My studies at the University of Manitoba were supported in part by postgraduate scholarships from the Natural Sciences and Engineering Research Council of Canada (NSERC) and the Faculty of Graduate Studies, University of Manitoba.

I am very grateful to Ian Fieldhouse for his enthusiastic assistance in the course of both arctic field seasons. Financial support for the field components of this study was provided in part by grants from the Northern Scientific Training Program (Department of Indian and Northern Affairs, Government of Canada) and the Geological Society of America. An NSERC Operating Grant to Dr. Wooil Moon was used to cover additional field and research costs. I thank the Nunavut Research Institute for granting a research licence to conduct field work on Melville Island, Nunavut. Falconbridge Ltd. kindly provided logistical assistance for the northern Québec field season; I am especially grateful for the assistance provided by Terry Mallinson (Donaldson Exploration Camp, Raglan Mine), and Patti Tirschmann (Falconbridge Prairies Headquarters, Winnipeg). Helpful advice regarding field work was provided by Dr. Chris Harrison [Institute of Sedimentary and Petroleum Geology, Geological Survey of Canada (GSC)] and Dr. Marc St-Onge (Continental Geoscience Division, GSC).

Landsat and Radarsat satellite images used in this research were provided through a grant from the Canada Centre for Remote Sensing (Government of Canada). Moss and algae samples were kindly identified by Dr. Michele Piercey-Normore (Department of Botany, University of Manitoba). Lichen samples were identified by Pak Yau Wong (Canadian Museum of Nature). Assistance with the documentation and interpretation of Québec thin sections was kindly provided by Dr. Al Turnock (Geological Sciences, University of Manitoba). Sergio Mejia (Geological Sciences, University of Manitoba) was very helpful in providing computer hardware and software support, facilitating the preparation of the thesis manuscript.

I am very grateful to Lisa Tam for her friendship during my time here in Winnipeg. I would like to express my deepest appreciation to my parents, William and Mary, and my siblings, Michael and Colleen, for their love and support through the years.

Table of Contents

Abstract i

Acknowledgements ii

Table of Contents iii

List of Figures viii

List of Tables xiv

1 INTRODUCTION 1
- 1.1 Introduction 1
- 1.2 Thesis Objectives 4
- 1.3 Thesis Outline 6

2 IMAGING OF EARTH FROM ORBITAL PLATFORMS 8
- 2.1 Introduction 8
- 2.2 The Electromagnetic Spectrum 8
- 2.3 Optical and Radar Remote Sensing 10
  - 2.3.1 Imaging in the Visible and Infrared 10
    - 2.3.1.1 Reflection and Emission Spectra of Rocks 11
    - 2.3.1.2 Viewing and Illumination Geometry, Grain Size, and Mixing State 16
  - 2.3.2 Synthetic Aperture Radar (SAR) 19
    - 2.3.2.1 Speckle 26
    - 2.3.2.2 Radar Brightness 27
    - 2.3.2.3 Layover and Foreshortening 30
    - 2.3.2.4 Lithological Discrimination 32
- 2.4 Sensors and Images 35
  - 2.4.1 Landsat TM Imagery 36
  - 2.4.2 Radarsat-1 Imagery 40
  - 2.4.3 IKONOS Imagery 43
- 2.5 Basic Image Processing Concepts 45
  - 2.5.1 Image Arithmetic and RGB Colour Composites 46
  - 2.5.2 The Intensity-Hue-Saturation Transform 48
  - 2.5.3 Unsupervised Classification 50
  - 2.5.4 Supervised Classification 51

2.5.4.1 Evaluating Classification Results 52
2.5.5 Spectral Mixture Modelling 55
2.6 Chapter Summary 55

3 ALGORITHMS FOR IMAGE CLASSIFICATION 58
3.1 Introduction 58
3.2 The Gaussian Maximum Likelihood Algorithm 58
3.3 The Evidential Reasoning Algorithm 61
3.3.1 Evidence Generation and Combination 62
3.3.2 Evidence Interpolation and Extrapolation 66
3.3.3 Evidential Reasoning Software Description 71
3.4 The Feedforward Backpropagation Neural Network Algorithm 71
3.4.1 Neural Network Basics 72
3.4.2 McCulloch-Pitts Networks 75
3.4.3 Perceptrons 77
3.4.4 The Delta Rule 81
3.4.4.1 Batch and On-Line Learning 88
3.4.4.2 A Simple Delta Rule Example 92
3.4.5 Multi-Layer Networks and Backpropagation 96
3.4.5.1 Network Terminology 97
3.4.5.2 The Sigma Function 97
3.4.5.3 The Backpropagation Algorithm 100
3.4.5.4 Bias 102
3.4.5.5 Network Topology 103
3.4.5.6 Initialization of Network Weights 108
3.4.5.7 Momentum 109
3.4.5.8 Over-Generalization and Training With Noise 111
3.4.5.9 Combining Neural Network Results 113
3.4.6 Neural Network Software Description 115
3.5 Chapter Summary 116

4 STUDY AREAS 118
4.1 Introduction 118
4.2 The Melville Island Study Area 118
4.2.1 Regional Geological and Tectonic Framework 118
4.2.1.1 Canadian Shield 121
4.2.1.2 Arctic Platform 121
4.2.1.3 Innuitian Tectonic Province 121
4.2.2 The Bedrock Geology of Eastern Melville Island 126
4.2.2.1 Southeastern Melville Island 128
4.2.3 The Surface State of Geological Materials on Melville Island . . 129
4.2.4 Glacial Deposits on Melville Island 130
4.2.5 The Vegetation of Melville Island 132

4.2.6 The Climate of Melville Island 134
4.2.7 The Melville Island Field Area 135
4.2.7.1 Geology and Vegetation of the Melville Island Field Area 137
4.2.7.2 Melville Island Field Sites 140
4.2.8 Melville Island Satellite Images 144
4.3 The Cape Smith Belt Study Area 146
4.3.1 Geological Overview 146
4.3.2 The Québec-Baffin Segment of the Trans-Hudson Orogen 149
4.3.3 The Geology of the Cape Smith Belt and Surrounding Region 150
4.3.4 The Surface State of Geological Materials in the Cape Smith Belt Region 159
4.3.5 Glacial Deposits in the Cape Smith Belt Region 159
4.3.6 The Vegetation of the Cape Smith Belt Region 160
4.3.7 The Climate of the Cape Smith Belt Region 160
4.3.8 Cape Smith Belt Field Area 161
4.3.8.1 Geology and Vegetation of the Cape Smith Belt Field Area 163
4.3.8.2 Cape Smith Belt Field Sites 164
4.3.9 Cape Smith Belt Satellite Images 170
4.4 Chapter Summary 173

5 EVALUATION OF THREE CLASSIFICATION ALGORITHMS FOR LITHOLOGICAL DISCRIMINATION 175
5.1 Introduction 175
5.2 Methodology 176
5.2.1 Construction of Training and Test Databases 177
5.2.1.1 Melville Island Training and Test Database 177
5.2.1.2 Cape Smith Belt Training and Test Database 181
5.2.2 Classification Methodology 181
5.2.2.1 Algorithm Parameters 186
5.3 Results 189
5.3.1 Melville Island Field Area 189
5.3.1.1 Evidential Reasoning 193
5.3.1.2 Maximum Likelihood 202
5.3.1.3 Neural Network 207
5.3.1.4 Evaluation of the Melville-Island Field Area Classified Databases 221
5.3.2 Cape Smith Belt Field Area 228
5.3.2.1 Evidential Reasoning 230
5.3.2.2 Maximum Likelihood 234
5.3.2.3 Neural Network 234
5.3.2.4 Evaluation of the Cape Smith Belt Field Area Classified

Databases 240
5.4 Failure of the Evidential Reasoning Algorithm 243
5.5 Operational Considerations 244
5.5.1 Maximum Likelihood Algorithm 248
5.5.2 Evidential Reasoning Algorithm 248
5.5.3 Neural Network Algorithm 249
5.6 Chapter Summary 250

6 EMPIRICAL NEURAL NETWORK INVESTIGATIONS REGARDING NETWORK TOPOLOGY AND THE USE OF NOISE DURING TRAINING 252
6.1 Introduction 252
6.2 Noise 252
6.2.1 Methodology 253
6.2.1.1 Training and Test Databases 253
6.2.1.2 Classification Methodology 253
6.2.2 Results 254
6.3 Network Topology 257
6.3.1 Methodology 260
6.3.1.1 Training and Test Databases 260
6.3.1.2 Classification Methodology 261
6.3.2 Results 261
6.4 Chapter Summary 268

7 EMPIRICAL NEURAL NETWORK INVESTIGATIONS REGARDING EVIDENTIAL-REASONING CONSENSUS AND THE GENERATION OF CONFIDENCE IMAGES 269
7.1 Introduction 269
7.2 Evidential Reasoning Consensus 270
7.2.1 Methodology 273
7.2.2 Results 273
7.2.2.1 Implications for the Evidential Reasoning Algorithm . . 277
7.3 Confidence Images 277
7.3.1 Methodology 279
7.3.2 Results 279
7.4 Chapter Summary 285

8 A VISUAL EVALUATION OF RADARSAT, LANDSAT TM, AND IKONOS IMAGERY FOR DISCRIMINATING LITHOLOGY 288
8.1 Introduction 288
8.2 Methodology 289
8.3 Results 291
8.3.1 Tingmisut Lake Region (Melville Island) 291
8.3.1.1 Landsat TM Image 294

8.3.1.2 Radarsat Image 299
8.3.1.3 IKONOS Images 322
8.3.1.4 Evaluation of Satellite Imagery at Three Zones Within the Tingmisut Lake Region 326
8.3.2 Weatherall Bay Region (Melville Island) 347
8.3.2.1 Landsat TM Image 356
8.3.2.2 Radarsat Image 363
8.3.3 Lac Watts Region (Cape Smith Belt) 369
8.3.3.1 Landsat TM Image 372
8.3.3.2 Radarsat Image 379
8.4 Chapter Summary and Discussion 392

9 SUMMARY AND CONCLUSIONS 397
9.1 Introduction 397
9.2 Ground-Truth Databases 397
9.3 Empirical Evaluations of Classifiers 398
9.4 Over-Generalization and Artificial Noise in Neural Network Classifications 401
9.5 Network Topology in Neural Network Classifications 402
9.6 Confidence Images Generated From Output-Layer Activations 403
9.7 Visual Evaluation of TM, Radarsat, and IKONOS Imagery 403
9.8 Research Implications 405
9.9 Recommendations for Future Research 408

REFERENCES 411

APPENDIX A: Descriptions of Melville Island Field Sites 443

APPENDIX B: Descriptions of Cape Smith Belt Field Sites 487

APPENDIX C: List of Original Programs 516

APPENDIX D: Evidential Reasoning Source Code 523

APPENDIX E: Evidential Reasoning Source Code (Consensus Version) 530

APPENDIX F: Neural Network Source Code (Learning Module) 537

APPENDIX G: Neural Network Source Code (Classification Module) 548

List of Figures

Figure 2.1 The electromagnetic spectrum 9
Figure 2.2 Spectral reflectance curves for vegetation, soil, and water 12
Figure 2.3 Spectral reflectance curves for four rock types 14
Figure 2.4 Spectral emission curves for four rock types 15
Figure 2.5 Geometry of a simple radar system 21
Figure 2.6 Resolution of a simple radar system, plotted against ground distance from the sensor 23
Figure 2.7 Schematic illustration of the concept of SAR 25
Figure 2.8 The effect of terrain relief and depression angle on geometric distortion in radar images 31
Figure 2.9 Spatial and spectral resolutions of selected optical sensors 37
Figure 3.1 Gaussian parameterization of training data for three classes. 60
Figure 3.2 Illustration of the orthogonal sum. 64
Figure 3.3 Interpolation and extrapolation of training data for three classes 67
Figure 3.4 Interpolation and extrapolation of a bi-modal histogram distribution. 69
Figure 3.5 A typical feedforward neural network. 73
Figure 3.6 Schematic comparison between a biological neuron and an artificial neuron 74
Figure 3.7 McCulloch-Pitts networks 76
Figure 3.8 An example of a perceptron 79
Figure 3.9 A network capable of implementing the Delta Rule 82
Figure 3.10 Schematic representation of an error function 84
Figure 3.11 Three-dimensional depiction of an actual error surface 89
Figure 3.12 Two-dimensional depiction of the error surface given in Figure 3.11, shown with the training path iteratively taken by weight values during training . 90
Figure 3.13 Learning curves produced by networks using non-random (fixed-order) and random submission of training data 93
Figure 3.14 Graphs of the sigma function, the derivative of the sigma function, and the threshold function 99
Figure 3.15 Biases 104
Figure 3.16 Three of an infinite number of possible network topologies that could be used to relate two inputs to two outputs 105
Figure 3.17 Learning curves for the exclusive-OR (XOR) problem 107
Figure 3.18 Learning curves produced using three different momentum settings 110
Figure 4.1 Locations of the two study areas 119
Figure 4.2 Geological provinces of the Canadian High Arctic 120
Figure 4.3 Geology of Melville Island 127
Figure 4.4 Geology of the Melville Island Field Area 136
Figure 4.5 Photographs of the Melville Island Field Area 139
Figure 4.6 Areal extents of Figures 4.7 and 4.8 141
Figure 4.7 Site locations in the northwestern part of the Melville Island Field Area . . 142

Figure 4.8 Site locations in the southeastern part of the Melville Island Field Area . . 143
Figure 4.9 Landsat TM images for eastern Melville Island 145
Figure 4.10 Radarsat images for eastern Melville Island 147
Figure 4.11 Archean Provinces of the Canadian Shield 148
Figure 4.12 Geological map of the Cape Smith Belt 151
Figure 4.13 Geology of the Cape Smith Belt Field Area 162
Figure 4.14 Photographs of the Cape Smith Belt Field Area 165
Figure 4.15 Areal extents of Figures 4.16 to 4.18 166
Figure 4.16 Site locations in the central part of the Cape Smith Belt Field Area 167
Figure 4.17 Site locations in the eastern part of the Cape Smith Belt Field Area 168
Figure 4.18 Site locations in the northern and southeastern parts of the Cape Smith Belt Field Area 169
Figure 4.19 TM images for central Cape Smith Belt and surrounding regions 171
Figure 4.20 Radarsat images for central Cape Smith Belt and regions to the north . . 172
Figure 5.1 Classes used in the *A* to *E* Series of classifications 182
Figure 5.2 Sets of classifications performed for the Melville Island (*B* to *E* Series) and Cape Smith Belt (*A* Series) Field Areas 187
Figure 5.3 Classified image of the Melville Island Field Area produced by the evidential reasoning algorithm (*B* Series, Execution #6) 198
Figure 5.4 Classified image of the Melville Island Field Area produced by the evidential reasoning algorithm (*C* Series, Execution #1) 199
Figure 5.5 Classified image of the Melville Island Field Area produced by the evidential reasoning algorithm (*D* Series, Execution #2) 200
Figure 5.6 Classified image of the Melville Island Field Area produced by the evidential reasoning algorithm (*E* Series, Execution #6) 201
Figure 5.7 Classified image of the Melville Island Field Area produced by the maximum likelihood algorithm (*B* Series, Execution #1) 208
Figure 5.8 Classified image of the Melville Island Field Area produced by the maximum likelihood algorithm (*C* Series, Execution #1) 209
Figure 5.9 Classified image of the Melville Island Field Area produced by the maximum likelihood algorithm (*D* Series, Execution #1) 210
Figure 5.10 Classified image of the Melville Island Field Area produced by the maximum likelihood algorithm (*E* Series, Execution #1) 211
Figure 5.11 The complexity of class histograms increases from Series *B* to Series *E* . 214
Figure 5.12 Box plots showing the considerable variation in individual overall classification results produced by the neural network classifier for the Melville Island Field Area 215
Figure 5.13 Classified image of the Melville Island Field Area produced by the consensus neural network algorithm (*B* Series, Execution #1) 222
Figure 5.14 Classified image of the Melville Island Field Area produced by the consensus neural network algorithm (*C* Series, Execution #6) 223
Figure 5.15 Classified image of the Melville Island Field Area produced by the consensus neural network algorithm (*D* Series, Execution #1) 224

Figure 5.16 Classified image of the Melville Island Field Area produced by the consensus neural network algorithm (*E* Series, Execution #6) 225
Figure 5.17 Classified image of the Cape Smith Belt Field Area produced by the evidential reasoning algorithm (*A* Series, Execution #6) 233
Figure 5.18 Classified image of the Cape Smith Belt Field Area produced by the maximum likelihood algorithm (*A* Series, Execution #6) 236
Figure 5.19 Box plots showing the considerable variation in individual overall classification results produced by the neural network classifier for the Cape Smith Belt Field Area 238
Figure 5.20 Classified image of the Cape Smith Belt Field Area produced by the consensus neural network algorithm (*A* Series, Execution #6) 241
Figure 5.21 Histograms of original ("raw") training data for the *E1* Series of tests . . 245
Figure 5.22 Histograms of interpolated and extrapolated training data for the *E1* Series 246
Figure 5.23 Histograms of interpolated and extrapolated training data for the *E1* Series 247
Figure 6.1 Learning curves for non-jitter and jitter training (±4) 255
Figure 6.2 Changes in network topology performed for one- and two-hidden-layer tests 262
Figure 6.3 Plot of changes in consensus results, and corresponding changes in average tss error after 20,000 iterations, with changing number of nodes in a network with one hidden layer. *D1* training and test database 263
Figure 6.4 Plot of changes in consensus results, and corresponding changes in average tss error after 20,000 iterations, with changing number of nodes in a network with one hidden layer. *A1* training and test database 264
Figure 6.5 Plot of changes in consensus results, and corresponding changes in average tss error after 20,000 iterations, with changing number of nodes in a network with two hidden layers. *D1* training and test database 265
Figure 6.6 Plot of changes in consensus results, and corresponding changes in average tss error after 20,000 iterations, with changing number of nodes in a network with two hidden layers. *A1* training and test database 266
Figure 7.1 Differences between the majority-vote and evidential reasoning consensus methods tested in this research 272
Figure 7.2 Box-plots showing the association between neural network classification success and highest output activations 280
Figure 7.3 Box-plots showing the association between correct and incorrect *C6* neural network classifications and differences between highest next-highest output activations 281
Figure 7.4 An image that gives the greatest output activations for the *C6N1* neural network execution 283
Figure 7.5 An image that gives the difference between highest and next-highest output activations for the *C6N1* neural network execution 284
Figure 8.1 Locations of the three regions used to evaluate the visual content of

satellite images 290
Figure 8.2 Bedrock geology of the Tingmisut Lake region 292
Figure 8.3 Mosaic of aerial photographs of the Tingmisut Lake region 293
Figure 8.4 TM colour composite (channels 321:RGB; true colour) for the Tingmisut Lake region 295
Figure 8.5 TM colour composite (channels 543:RGB) for the Tingmisut Lake region 296
Figure 8.6 TM colour composite (channels 754:RGB) for the Tingmisut Lake region 297
Figure 8.7 Radarsat image of the Tingmisut Lake region 300
Figure 8.8 View of the immediate Tingmisut Lake area, showing the extent of ice, snow, and water five days before acquisition of the Radarsat image 302
Figure 8.9 Photographs of the west ("a") and east ("b") flanks of the central portion of the gabbro dike 304
Figure 8.10 Photograph of the south slope of the Tingmisut Inlier dolostone unit . . . 306
Figure 8.11 Photographs of talus material of the south slope of the Tingmisut Inlier dolostone unit 307
Figure 8.12 Photographs of dolostone materials at a location on the summit of the Tingmisut Inlier 308
Figure 8.13 Photographs of small Canyon Fiord Formation materials 309
Figure 8.14 Photographs of large Canyon Fiord Formation materials 311
Figure 8.15 Photographs of large Great Bear Cape Formation materials 312
Figure 8.16 Photographs of small Great Bear Cape Formation materials 313
Figure 8.17 Photographs of vegetated Great Bear Cape Formation materials 314
Figure 8.18 Photographs of large Sabine Bay Formation materials 315
Figure 8.19 Photographs of small Sabine Bay Formation materials 316
Figure 8.20 Photographs of Assistance Formation materials 317
Figure 8.21 Photographs of Degerböls Formation materials 319
Figure 8.22 Photographs of Trold Fiord Formation materials 320
Figure 8.23 Photographs of Bjorn Formation materials 321
Figure 8.24 Panchromatic IKONOS image of the Tingmisut Lake region 323
Figure 8.25 IKONOS colour composite (multispectral channels 321:RGB; true colour) for the Tingmisut Lake region 324
Figure 8.26 IKONOS colour composite (multispectral channels 432:RGB; colour infrared) for the Tingmisut Lake region 325
Figure 8.27 Aerial photograph of the north zone of the Tingmisut Lake region 327
Figure 8.28 Ground photograph of the north zone of the Tingmisut Lake region 328
Figure 8.29 TM colour composite (channels 543:RGB) for the north zone of the Tingmisut Lake region 330
Figure 8.30 Radarsat image of the north zone of the Tingmisut Lake region 331
Figure 8.31 Panchromatic IKONOS image of the north zone of the Tingmisut Lake region 332
Figure 8.32 Aerial photograph of the north zone of the Tingmisut Lake region: detail

. 333
Figure 8.33 Panchromatic IKONOS image of the north zone of the Tingmisut Lake region: detail 334
Figure 8.34 IKONOS colour composite (multispectral channels 432:RGB; colour infrared) for the north zone of the Tingmisut Lake region 335
Figure 8.35 Aerial photograph of the central zone of the Tingmisut Lake region 336
Figure 8.36 Ground photograph of the central zone of the Tingmisut Lake region . . . 337
Figure 8.37 TM colour composite (channels 543:RGB) for the central zone of the Tingmisut Lake region 339
Figure 8.38 Radarsat image of the central zone of the Tingmisut Lake region 340
Figure 8.39 Panchromatic IKONOS image of the central zone of the Tingmisut Lake region 341
Figure 8.40 Aerial photograph of the central zone of the Tingmisut Lake region: detail 342
Figure 8.41 Panchromatic IKONOS image of the central zone of the Tingmisut Lake region: detail 343
Figure 8.42 IKONOS colour composite (multispectral channels 321:RGB; true colour) for the central zone of the Tingmisut Lake region 344
Figure 8.43 Aerial photograph of the south zone of the Tingmisut Lake region 345
Figure 8.44 Ground photograph of the southern zone of the Tingmisut Lake region . 346
Figure 8.45 TM colour composite (channels 543:RGB) for the south zone of the Tingmisut Lake region 348
Figure 8.46 Radarsat image of the south zone of the Tingmisut Lake region 349
Figure 8.47 Panchromatic IKONOS image of the south zone of the Tingmisut Lake region 350
Figure 8.48 Aerial photograph of the south zone of the Tingmisut Lake region: detail 351
Figure 8.49 Panchromatic IKONOS image of the south zone of the Tingmisut Lake region: detail 352
Figure 8.50 IKONOS colour composite (multispectral channels 432:RGB; colour infrared) for the south zone of the Tingmisut Lake region 353
Figure 8.51 Bedrock geology of the Weatherall Bay region 354
Figure 8.52 TM colour composite (channels 321:RGB; true colour) for the Weatherall Bay region 359
Figure 8.53 TM colour composite (channels 543:RGB) for the Weatherall Bay region 360
Figure 8.54 TM colour composite (channels 754:RGB) for the Weatherall Bay region 361
Figure 8.55 Radarsat image of the Weatherall Bay region 364
Figure 8.56 Ground view of the western exposure of the Blue Fiord Formation 367
Figure 8.57 Photographs of the western exposure of the Blue Fiord Formation 368
Figure 8.58 Bedrock geology of the Lac Watts region 371
Figure 8.59 TM colour composite (channels 321:RGB; true colour) for the Lac Watts

region 373
Figure 8.60 TM colour composite (channels 543:RGB) for the Lac Watts region . . . 374
Figure 8.61 TM colour composite (754:RGB) for the Lac Watts region 375
Figure 8.62 TM colour composite (channels 543:RGB) for the north zone of the Lac Watts region 376
Figure 8.63 TM colour composite (channels 543:RGB) for the south zone of the Lac Watts zone 377
Figure 8.64 Radarsat image of the Lac Watts region 380
Figure 8.65 Radarsat image of the north zone of the Lac Watts region 381
Figure 8.66 Radarsat image of the south zone of the Lac Watts region 382
Figure 8.67 Photographs of an area of complete grass and moss cover, on Spartan Group pelite 384
Figure 8.68 Photographs of peridotite materials of the Watts Group 386
Figure 8.69 Photographs of materials of a tonalite intrusion 387
Figure 8.70 Photographs of basalt of the Chukotat Group 388
Figure 8.71 Photographs of basalt / gabbro of the Watts Group 389
Figure 8.72 Photographs of basalts of the Watts Group 390
Figure 8.73 Photographs of pelite of the Spartan Group 391

List of Tables

Table 2.1 Basic characteristics of Landsat TM images 38
Table 2.2 Radarsat beam modes 41
Table 2.3 Standard-beam incidence angles for the Radarsat sensor 43
Table 2.4 Basic characteristics of IKONOS images 45
Table 2.5 Example of an error matrix 54
Table 3.1 Inputs and outputs to be related in the example discussed in Section 3.4.4.2 92
Table 4.1 Bedrock units of the Melville Island Field Area 138
Table 4.2 Tectonostratigraphic units in the eastern Cape Smith Belt and surrounding region 155
Table 4.3 Bedrock units of the Cape Smith Belt Field Area 163
Table 5.1 Classes used as the basis for TM classifications of the Melville Island Field Area 179
Table 5.2 Classes used in the four series (*B*, *C*, *D*, and *E*) of TM classifications of the Melville Island Field Area 183
Table 5.3 Classes used in TM classifications of the Cape Smith Belt Field Area 184
Table 5.4 Summary of Melville Island classification results 190
Table 5.5 Summary of Melville Island classification results, expressed as Kappa coefficients 191
Table 5.6 Ranking system used to categorize classes in terms of the ability of the algorithm and TM imagery to discriminate them 192
Table 5.7 Summary of the magnitude of errors of omission and commission for all evidential reasoning classifications of the Melville Island Field Area 194
Table 5.8 Summary of ability of evidential reasoning and TM imagery combination to discriminate the surface-cover classes in the Melville Island Field Area (*B* Series) 195
Table 5.9 Summary of ability of evidential reasoning and TM imagery combo to discriminate the surface-cover classes in the Melville Island Field Area (*C* Series) 196
Table 5.10 Summary of ability of evidential reasoning and TM imagery combo to discriminate the surface-cover classes in the Melville Island Field Area (*D* Series) 197
Table 5.11 Summary of ability of evidential reasoning and TM imagery combo to discriminate the surface-cover classes in the Melville Island Field Area (*E* Series) 197
Table 5.12 Summary of the magnitude of errors of omission and commission for all maximum likelihood classifications of the Melville Island Field Area 203
Table 5.13 Summary of ability of maximum likelihood and TM imagery combination to discriminate the surface-cover classes in the Melville Island Field Area (*B* Series) 204
Table 5.14 Summary of ability of maximum likelihood and TM imagery combo to

discriminate the surface-cover classes in the Melville Island Field Area (*C* Series) 205
Table 5.15 Summary of ability of maximum likelihood and TM imagery combo to discriminate the surface-cover classes in the Melville Island Field Area (*D* Series) 206
Table 5.16 Summary of ability of maximum likelihood and TM imagery combo to discriminate the surface-cover classes in the Melville Island Field Area (*E* Series) 206
Table 5.17 Differences between the proportions of test pixels correctly classified for the consensus neural network and the corresponding maximum likelihood executions: Melville Island Field Area 213
Table 5.18 Differences between Kappa values for the consensus neural network and the corresponding maximum likelihood executions: Melville Island Field Area 213
Table 5.19 Summary of the magnitude of errors of omission and commission for all consensus neural network classifications of the Melville Island Field Area . . . 217
Table 5.20 Summary of ability of the consensus neural network and TM imagery combination to discriminate the surface-cover classes in the Melville Island Field Area (*B* Series) 218
Table 5.21 Summary of ability of neural-network and TM imagery combo to discriminate the surface-cover classes in the Melville Island Field Area (*C* Series) 219
Table 5.22 Summary of ability of neural-network and TM imagery combo to discriminate the surface-cover classes in the Melville Island Field Area (*D* Series) 220
Table 5.23 Summary of ability of neural-network and TM imagery combo to discriminate the surface-cover classes in the Melville Island Field Area (*E* Series) 220
Table 5.24 Summary of Cape Smith Belt classification results 229
Table 5.25 Summary of Melville Island classification results, expressed as Kappa ("KHAT") values 229
Table 5.26 Summary of the magnitude of errors of omission and commission for all classifications of the Cape Smith Belt Field Area 231
Table 5.27 Summary of ability of evidential reasoning and TM imagery combo to discriminate the surface-cover classes in the Cape Smith Belt Field Area (*A* Series) 232
Table 5.28 Summary of ability of maximum likelihood and TM imagery combo to discriminate the surface-cover classes in the Cape Smith Belt Field Area (*A* Series) 235
Table 5.29 Summary of ability of neural network and TM imagery combo to discriminate the surface-cover classes in the Cape Smith Belt Field Area (*A* Series) 239
Table 6.1 Comparison of the *D* Series overall results (percentage of test pixels correctly classified for Melville Island Field Area) for 1) no jitter (2000-8000

iterations), 2) no jitter (20,000 iterations), and 3) ±4 jitter (20,000 iterations) classifications 256
Table 6.2 Comparison of the *A* Series overall results (percentage of test pixels correctly classified for Cape Smith Belt Field Area) for 1) no jitter (2000-8000 iterations), 2) no jitter (20,000 iterations), and 3) ±4 jitter (20,000 iterations) classifications 256
Table 6.3 Summary of the magnitude of errors of omission and commission for *D* Series non-jitter and jitter classifications of the Melville Island Field Area . . 258
Table 6.4 Summary of the magnitude of errors of omission and commission for *A* Series non-jitter and jitter classifications of the Cape Smith Belt Field Area . 259
Table 7.1 Summary of evidential-reasoning consensus results for all Series of the Melville Island Field Area 275
Table 7.2 Summary of evidential-reasoning consensus results for all Series of the Melville Island Field Area, expressed as Kappa coefficients 275
Table 7.3 Summary of evidential reasoning consensus results for the *A* Series of the Cape Smith Belt Field Area 276
Table 7.4 Summary of evidential reasoning consensus results for the *A* Series of the Cape Smith Belt Field Area, expressed as Kappa coefficients 276
Table 8.1 Exposed bedrock units of the Weatherall Bay region 357

1 INTRODUCTION

1.1 Introduction

Geological maps provide basic information on the spatial distribution of rock units, and place bedrock and surficial materials in their proper geological context. Such maps, however, are generally not useful sources of high-resolution information on the distribution of individual rock types exposed at the surface. With recent and expected advances in remote-sensing technology, satellite imaging is in the process of becoming a viable means for the generation of high-resolution regional-scale digital databases of surface lithology, particularly for arctic and arid regions where vegetation cover is sparse. These geological databases could ultimately be of considerable value to the earth science community, including field, exploration, and environmental scientists. These databases could especially benefit researchers whose studies involve isolated regions where extensive field campaigns would be expensive and logistically difficult.

There are two primary methods by which information about the compositions of surface materials can be derived from satellite imagery: 1) visual analysis of raw or processed imagery; and 2) generation of class-specific information using specialized computer algorithms. As long as additional information on the nature of relevant surface materials is available (preferably collected through *in situ* field work), there is potential for both of these methods to be used to discriminate lithological classes from satellite images. Visual analysis involves the use of basic spectral information along with visual cues such as size, shape, pattern, and context to discriminate lithological units. Visual analysis is a technique that is particularly well suited for use with radar (e.g., the Radarsat-1 system) and high-resolution

optical imagery (e.g., the recently-launched IKONOS system), since both of these image types provide visual geomorphological information that can sometimes be related to lithological classes. Much research is currently focussed on the use of such image types for the visual discrimination of lithological classes and other geological features (e.g., Paradella *et al.*, 1998; Simms and Bell, 1998; Rivard *et al.*, 1999; Sharma *et al.*, 1999).

The alternative (and complementary) means for deriving geological information from satellite images involves the use of specialized algorithms to infer information about the nature and distribution of materials exposed at the surface. Among the most commonly used such algorithms are those which perform supervised classification, clustering, and spectral mixture modelling. Because these algorithms are capable of using large numbers of images to infer information over large areas at pixel resolutions, and because the trend in remote sensing instrumentation is toward greatly increased spectral and spatial resolutions, the importance of these algorithms is expected to increase in the future. Inferences regarding surface cover, derived from large amounts of remote sensing data and made for hundreds of thousands of individual pixel locations, are difficult or impossible to make through visual inspection alone.

There are numerous supervised-classification algorithms available for use in image classifications. The maximum likelihood classifier is the most commonly used classification algorithm in the field of remote sensing (Richards, 1993), and is applicable toward problems involving class-specific training data that can be modelled using multivariate normal distributions. The evidential reasoning and neural network classification algorithms have been shown in past research to be potential alternatives to the maximum likelihood classifier, on

the basis that these algorithms do not parameterize training data using such restrictive models as the normal distribution (e.g., Peddle *et al.*, 1994; Peddle, 1995). The evidential reasoning and neural network classifiers may be especially well suited for classifications involving lithological classes (which are often characterized by spatial variations in vegetation cover and weathering characteristics), since these algorithms have greater capacity for dealing with classes whose spectral characteristics are variable or complex.

The utility of the evidential reasoning and neural network algorithms in the classification of satellite imagery and other geographic databases has been demonstrated in numerous empirical studies (e.g., Peddle, 1995; Leverington and Duguay, 1996a; Tian *et al.*, 1999). There nevertheless remain a number of important issues that need to be addressed regarding the use of these algorithms. For example, with regard to the evidential reasoning algorithm, although the method for the combination of evidence using orthogonal summation is well established, methods for generating initial measures of evidence are not (Moon, 1990, 1993). Peddle's (1991, 1995) evidence algorithm, which calculates evidence as a function of the proportions of class training data that contain the image values being classified, has shown promise (e.g., Peddle, 1995; Leverington and Duguay, 1996a) but, if it is to be validated as a general algorithm applicable for use with a wide range of image and class types, needs to be further tested using a greater variety of classification datasets (including those involving a variety of lithological classes).

With regard to the use of feedforward backpropagation neural networks (the most commonly applied neural network algorithm for classification problems), there are many issues that need to be resolved. For example: 1) there remain uncertainties regarding the most

appropriate network topologies to be used for particular classifications; 2) it is unclear if overgeneralization, the progressive incorporation during training of features of the training dataset that are not characteristic of the data as a whole, is typical of classifications involving satellite imagery; 3) it is uncertain if the addition of artificial noise to input vectors during training is a useful means to prevent overgeneralization and to extrapolate from sparse training datasets; 4) the variability in classification success between individual image classifications performed by feedforward backpropagation neural networks (caused by variations in weight initializations) is a shortcoming of the neural network algorithm that needs to be addressed, since it can hinder the utility of neural networks by necessitating the generation and evaluation of multiple results in order to produce an acceptable result; and 5) consensus algorithms, which combine multiple sets of neural network results to produce new results, have the potential to address not only the variability in classification success noted above, but also have the potential to produce final results that are superior to all neural network results used as input (e.g., Rugova, 1994; Benediktsson *et al.*, 1997a); such possibilities need to be empirically tested with real-world datasets.

1.2 Thesis Objectives

With a view toward the advancement of both algorithmic and visual techniques for the extraction of lithological information from satellite images, the objectives of this thesis are to: 1) evaluate maximum likelihood, evidential reasoning, and neural network algorithms in the classification of satellite imagery for lithological discrimination; 2) evaluate two consensus algorithms [majority vote and orthogonal summation] for the combination of individual neural

network results [for the purpose of elimination of the effects of variation caused by variation in weight initializations, and possibly for improvement of neural network results beyond those produced by individual neural network executions]; 3) investigate the occurrence of over-generalization in neural network classifications of satellite imagery, and to investigate the use of artificial noise [jitter] to improve classification results and prevent over-generalization; 4) investigate the use of neural-network output activations in the estimation of classification confidence, and in the generation of "confidence images"; and 5) evaluate Landsat TM, Radarsat, and IKONOS images as sources of lithological information.

Two northern study areas were used as a basis for the evaluation of classification algorithms and satellite imagery: one located on eastern Melville Island, Nunavut, and the other in the north-central portion of the Cape Smith Belt of Québec. The Melville Island Study Area is characterized by the widespread exposure of Paleozoic clastic and carbonate sequences of the Sverdrup Basin and Franklinian Mobile Belt. The Cape Smith Belt Study Area is characterized by the widespread exposure of mafic and ultramafic thrust sheets of the Cape Smith Belt, an Early Proterozoic greenstone belt. The Melville Island and Cape Smith Belt study areas were chosen for use in this research because of the generally good exposure of geological materials within their boundaries, the complementary lithological characteristics of the two study areas, and because relatively high-resolution geological maps (at 1:250,000 and 1:50,000 scale, respectively) of the study areas were available for use in guiding various aspects of the study.

1.3 Thesis Outline

This document consists of nine chapters and seven appendices. Background information regarding general remote sensing image types and processing methods is given in Chapter 2. Detailed descriptions of the maximum likelihood, evidential reasoning, and neural network classification algorithms are given in Chapter 3. Background information on the regional and local geology of the two northern study areas is given in Chapter 4, along with a description of field work conducted at the study areas, and an overview of Landsat TM and Radarsat satellite images available to this study. Results involving empirical tests of the maximum likelihood, evidential reasoning, and majority-vote consensus neural network algorithms for discriminating lithology at the two study areas from Landsat TM images are presented and discussed in Chapter 5. Chapter 6 presents investigations into the occurrence of over-generalization during neural network training, as well as the use of artificial noise during training to improve neural network classification results. Chapter 6 also discusses and investigates the validity of accepted "rules of thumb" for the definition of neural network topologies in the classification of satellite imagery. Investigations regarding the use of the evidential reasoning algorithm as a consensus algorithm for combining neural network output-layer activations are given in Chapter 7, along with investigations into the use of output activations for neural network output-layer activations as measures of evidence to be input to the evidential reasoning algorithm are presented. Chapter 8 presents a visual evaluation of Landsat TM, Radarsat, and IKONOS imagery for lithological discrimination at the two northern study areas. Chapter 9 presents a summary of all research findings. Appendices A and B summarize field descriptions of all field sites. Appendix C lists and describes all key

computer programs written for this research. Appendices D to G give source code for the most important computer programs used here.

2 IMAGING OF EARTH FROM ORBITAL PLATFORMS

2.1 Introduction

This chapter provides an overview of basic remote sensing topics and concepts relevant to this research. The electromagnetic spectrum is briefly introduced, along with an elementary description of its use in both optical and radar remote sensing for lithological discrimination. The characteristics and utility of Landsat Thematic Mapper, Radarsat, and IKONOS imagery are documented. Finally, basic methods for the derivation of lithological information from satellite imagery are summarized, with emphasis on those methods that were used in this study. Descriptions of the classification algorithms used in this research are treated separately in Chapter 3.

2.2 The Electromagnetic Spectrum

Remote sensing involves the identification and investigation of materials through the measurement of reflected or emitted electromagnetic radiation. An overview of the electromagnetic spectrum is given in Figure 2.1. The range of the electromagnetic spectrum to which human eyes are sensitive (i.e., the *visible* portion of the spectrum) extends from about 0.4 μm to 0.7 μm. Within the visible range, the sensation described by most people as "blue" is produced by the interaction of the eye with radiation in the ~0.4 to 0.5 μm range; "green" is associated with radiation in the ~0.5 to 0.6 μm range, and "red" is associated with radiation in the ~0.6 to 0.7 μm range. Toward shorter wavelengths from the visible range are the ultraviolet, the x-ray, and the gamma-ray ranges. Toward longer wavelengths from the visible range are the infrared and the microwave ranges (Figure 2.1).

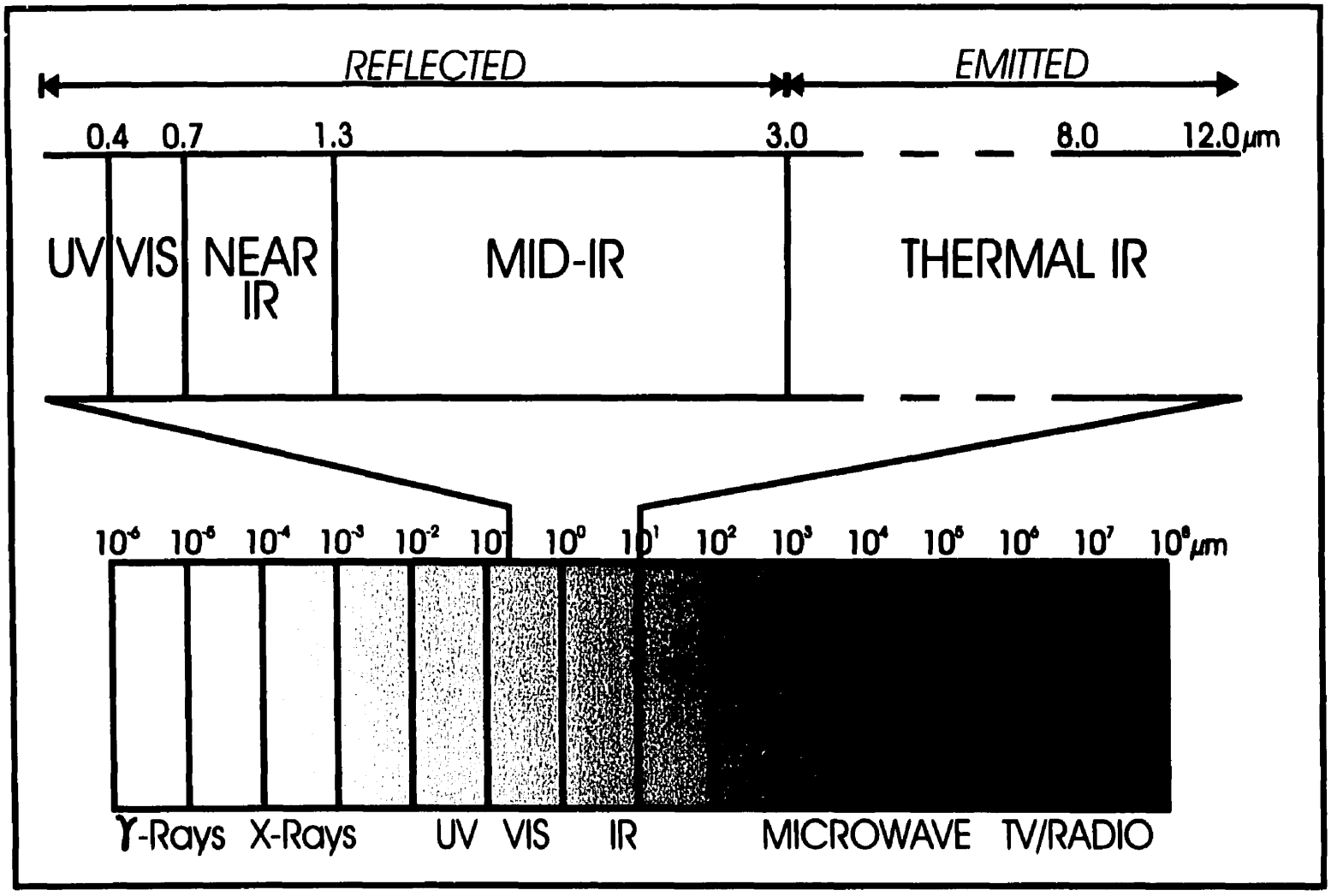

Figure 2.1 The electromagnetic spectrum [modified after EOSAT (1988) and Lillesand and Kiefer (1994)].

The infrared range of the spectrum is often subdivided differently by different workers. For the purposes of this report, the portion of the electromagnetic spectrum between 0.7 and 25 μm is subdivided into three main ranges (Lillesand and Kiefer, 1994) (Figure 2.1): 1) the *near-infrared* range (0.7 to 1.3 μm), 2) the *mid-infrared* range (1.3 μm to 3.0 μm), and 3) the *thermal-infrared* range (3.0 to 25 μm).

2.3 Optical and Radar Remote Sensing

Remote sensing of the Earth's surface is most often conducted in the visible, infrared, and microwave portions of the electromagnetic spectrum.

2.3.1 Imaging in the Visible and Infrared

When imaging the Earth's surface, radiation measured in the visible to near-infrared range is typically reflected solar radiation, while radiation measured in the thermal-infrared range is almost entirely produced by thermal emission from earth materials. Spectral response curves, in which amounts of reflected or emitted electromagnetic radiation are plotted against wavelength, are commonly used to describe the spectral properties of materials. Each type of material is associated with particular spectral features (e.g., spectral troughs or peaks) that together comprise the material's *spectral signature*. For visible to mid-infrared wavelengths, reflection spectra are most commonly used to characterize materials (where trough features in reflectance spectra indicate absorption of energy over the associated wavelengths). At thermal-infrared wavelengths, emission spectra (or transmission spectra used as a proxy for emission spectra) are commonly used to characterize earth materials.

2.3.1.1 Reflection and Emission Spectra of Rocks

Materials reflect and emit electromagnetic radiation as a function of their physical and chemical properties. Reflectance spectra are given in Figure 2.2 for three general material types: water, green vegetation, and dry soil. Because these three material types reflect light in different ways at different wavelengths, they can be distinguished from each other over an area of interest by imaging the area at several properly-chosen wavelengths (e.g., locations where green vegetation is prevalent may be recognized by their relatively low reflectance at about 0.6 μm, and their high reflectance at about 0.8 μm; locations where water is prevalent may be recognized by their low reflectance in the visible range, and their extremely low reflectance at longer wavelengths).

Reflection and emission spectra are also known for individual mineral types. Absorption features in mineral reflectance spectra in the range from 0.4 to 1.0 μm are generally associated with electronic transitions (mainly those related to crystal field effects and charge transfer) caused by the presence of transition metals (e.g., Ti, V, Fe, Mn, Cu, Ni, Cr, Zn), while absorption features in the range from 1 to 3 μm are generally associated with vibrational transitions caused by the presence of common anionic constituents (e.g., carbonates, hydroxyls, and phosphates) (Kendall, 1966; Hunt, 1980; Mathews, 1986; Gupta, 1991; Burns, 1993; Drury, 1993; Gaffey *et al.*, 1993; Salisbury, 1993). The greatest potential for the discrimination of different lithologies using reflected light is within the range from about 0.7 to 3 μm, since variation between spectra is greatest in this range (Drury, 1993; Schetselaar, 1994; Galvao and Vitorello, 1995).

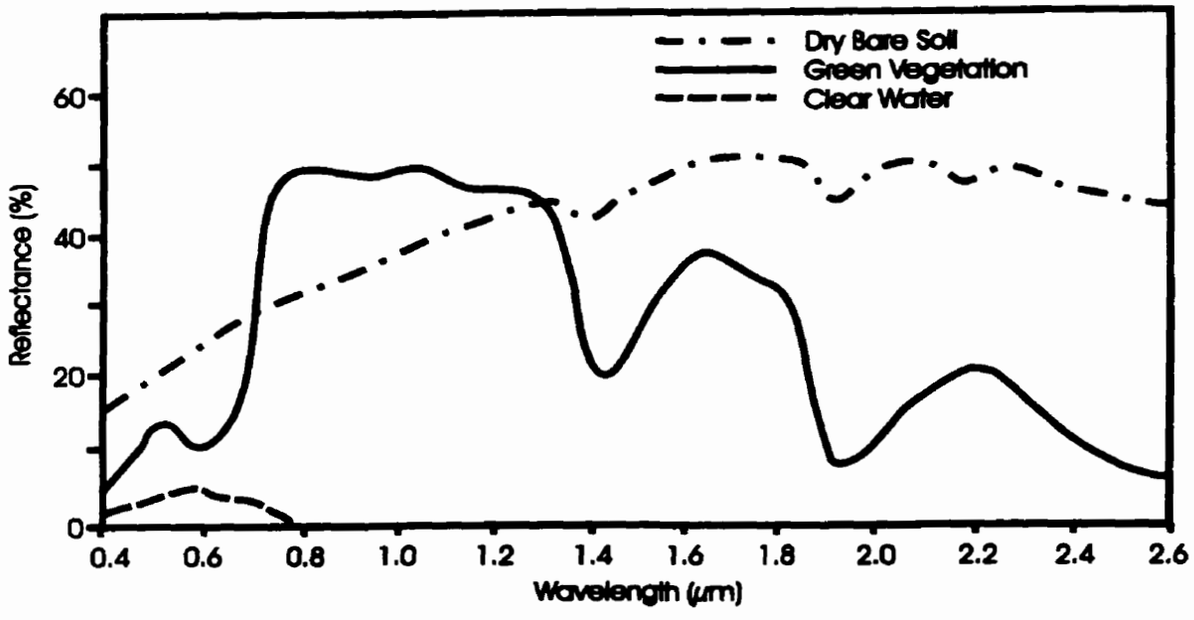

Figure 2.2 Spectral reflectance curves for vegetation, soil, and water (after Lillesand and Kiefer, 1994).

The thermal emission spectra of minerals are mainly influenced by vibrational transitions caused by the presence of silicates, carbonates, oxides, phosphates, sulphates, nitrates, nitrites, and hydroxyls (Gupta, 1991; Salisbury and D'Aria, 1992). Because emission spectra can vary considerably between individual mineral types, the thermal portion of the spectrum has considerable potential for future use in the discrimination of minerals through remote sensing techniques (Kahle and Alley, 1992; Drury, 1993; Gaffey *et al.*, 1993; Kahle *et al.*, 1993; Rivard *et al.*, 1993).

Because rocks are aggregates of minerals, and thus are compositionally more complex and variable materials, defining representative lithological spectral curves can be problematic (Gupta, 1991). Nevertheless, the spectral characteristics of individual rock types can be broadly described (Figures 2.3 and 2.4). As with the general land-cover classes discussed above, different rock types may potentially be distinguished from each other in an area of interest by imaging the area at well-chosen wavelengths, although the spectral differences between certain lithologies can be so subtle as to necessitate the use of imagery with high spectral resolution (50 to 100 nm) if they are to be resolved (Cloutis, 1995a).

Variation in the spectral properties of samples within a single lithological class can be significant. Such variation is typically related to differences in the proportions of component minerals (and associated impurities), differences in the degree of surface weathering, and differences in the nature of vegetative or other cover (e.g., Klein and Hurlbut, 1985; Ager and Milton, 1987; Birnie *et al.*, 1989; Arvidson *et al.*, 1993; Macias, 1995; Cloutis, 1995b; Cloutis, 1997). Weathering products commonly dominate rock spectra, even when the depth

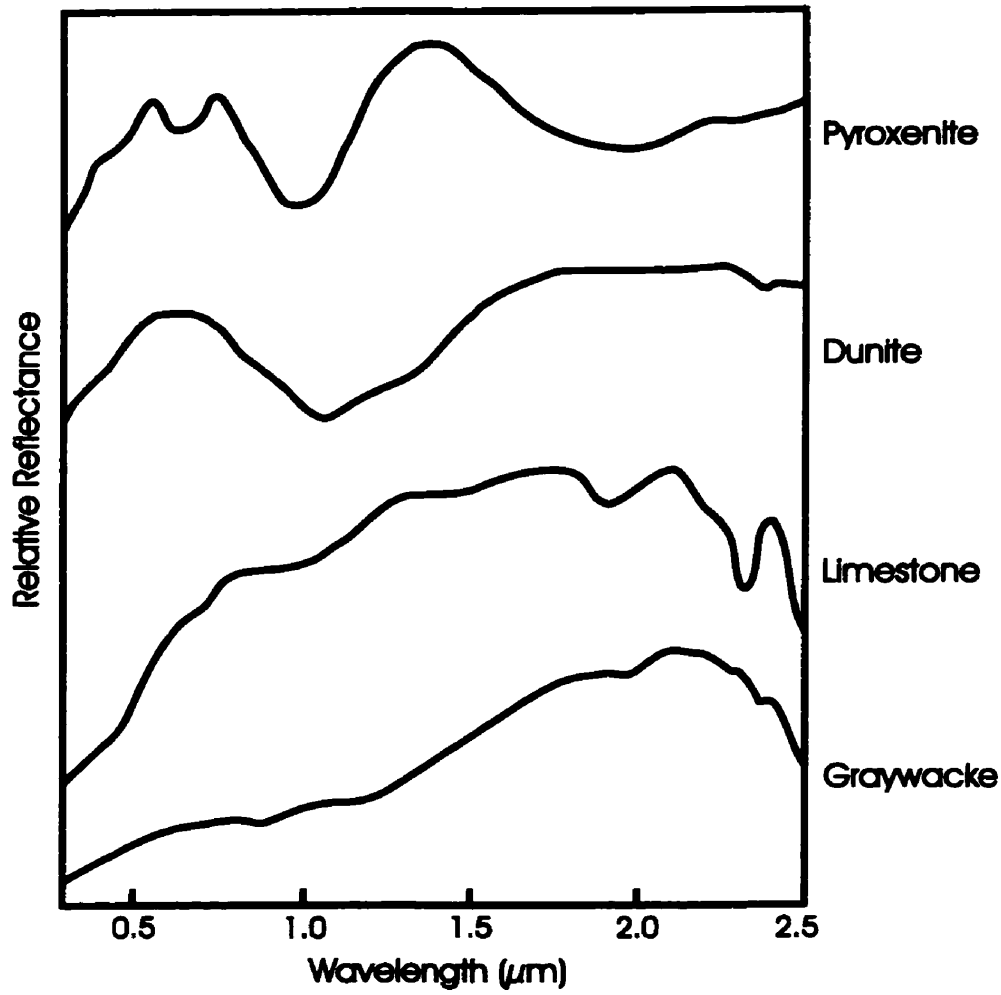

Figure 2.3 Spectral reflectance curves for four rock types (after Salisbury and Hunt, 1974). Curves are offset for clarity.

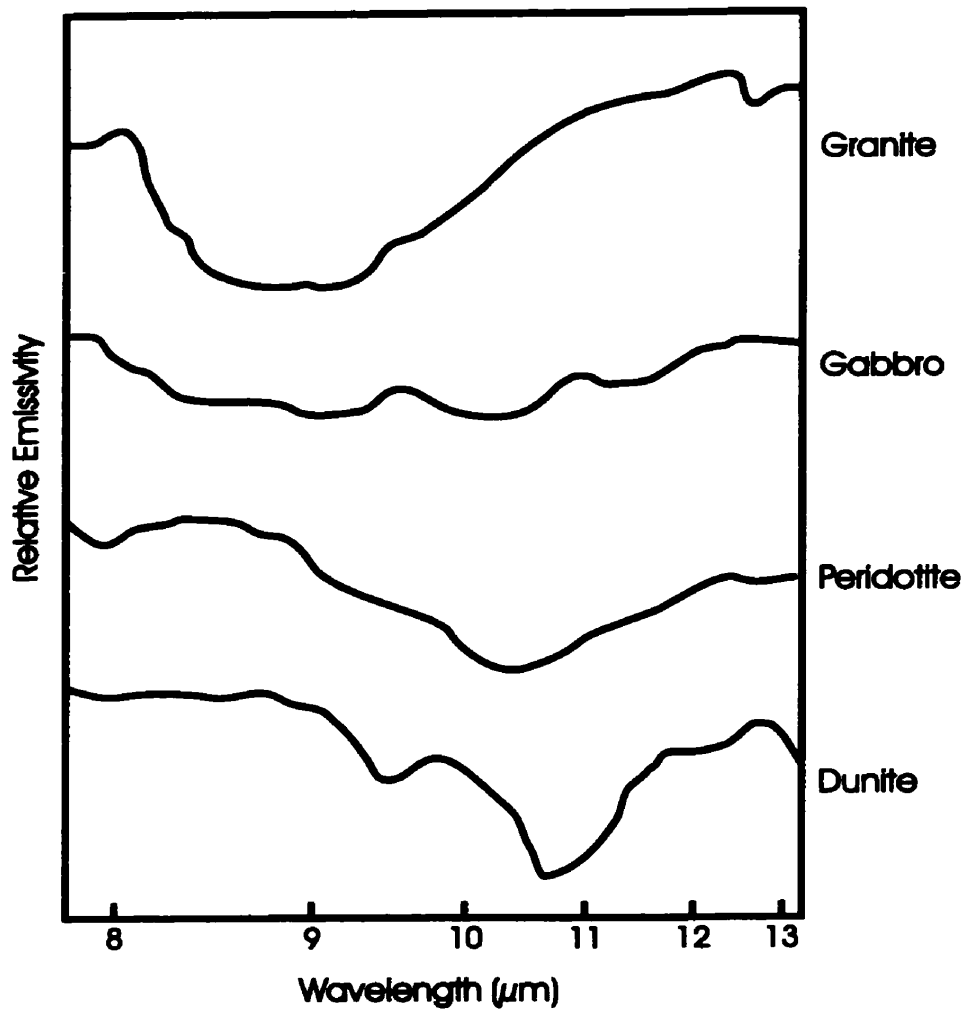

Figure 2.4 Spectral emission curves for four rock types (after Vickers and Lyon, 1967). Curves are offset for clarity.

of weathering is less than several hundred micrometers, adding features to spectra that may be inconsistent with the underlying, more pristine mineralogy (Birnie *et al.*, 1989; Cloutis, 1992; Cloutis, 1995a). Thus, the subtle spectral differences between some lithologies, and the variability in spectral properties within individual lithological classes caused by variations in physical and chemical properties, can make the successful discrimination of lithology by optical remote sensing methods difficult, particularly when the spectral and spatial resolutions of employed remote sensing instruments are poor.

2.3.1.2 Viewing and Illumination Geometry, Grain Size, and Mixing State

As noted above, variations in the spectral properties of geological materials are in large part a function of variations in: 1) mineralogy; 2) weathering characteristics; and 3) vegetation or other cover. Several other factors that can be important influences on the spectral or overall brightness properties of surficial materials include: 1) viewing and illumination geometry; 2) grain size; and 3) mixing state. These factors, all of which can be related to or influenced by rock mineralogy and weathering characteristics, are outlined below.

1) Viewing and Illumination Geometry: There are numerous kinds of *reflectance*, each of which can be defined by the geometrical properties of the light source and the detector (Hapke, 1993). The degree of collimation (i.e., the degree to which the associated light rays are parallel) of the source and of the detector may be described using the following terms: *directional* (i.e., a highly-collimated source or detector), *conical*, or *hemispherical* (i.e., a perfectly diffuse source or detector); the appropriate terms for the source and detector

may be specified as adjectives when referring to reflectance, with the adjective describing the source specified before that of the detector. Thus, the *directional-hemispherical reflectance* is the total fraction of light scattered into the upward hemisphere by a surface illuminated from above by a highly collimated source (Hapke, 1993). Strictly speaking, all measured reflectances are *conical-conical* (also referred to as *biconical*), since perfect collimation and diffuseness cannot be achieved. In practice, however, direct sunlight can usually be treated as collimated (and thus *directional*), and light scattered by clouds on an overcast day can be treated as diffuse (and thus *hemispherical*) (Hapke, 1993). A photosensitive detector on an aircraft or spacecraft essentially measures *directional-directional* (also referred to as *bidirectional*) reflectance of the ground or clouds.

Although the overall brightness of spectral data of rocks and soil can change as a function of illumination and viewing geometry (due mainly to changes in the amount of shadow in the field-of-view of the detector), the overall shape of the spectral signature of rocks and soil tends to be invariant with varying illumination and viewing geometries (ASD, 2001). The manner in which changing illumination and viewing geometry affects overall brightness is related largely to the morphology of surface materials and terrain features.

2) Grain Size: The amount of light scattered and absorbed by a single grain is dependent in part on its overall size. In general, light is absorbed as it propagates through a grain, and light is scattered when it interacts with grain surfaces and internal imperfections (Hapke, 1993; Clark, 1999). Greater amounts of absorption of light are generally associated with larger grains, which have greater internal paths where photons can be absorbed. Smaller grains have proportionally more surface reflections compared to internal photon length paths.

At visible to mid-infrared wavelengths, multiple scattering is often dominant in geological materials, and reflectance increases as grain size decreases (Clark, 1999). The overall shape of the spectral signature of geological materials tends to be invariant with varying grain sizes (Clark, 1999).

3) Mixing State: At virtually all scales of viewing, the materials of the universe may be considered complex mixtures of materials. There are generally considered to be four types of mixtures (Clark, 1999). The first type of mixture is a *linear mixture* (also known as an *areal* or *checkerboard mixture*), and involves materials that are optically separated so that there is no multiple scattering between components. For a linear mixture (e.g., a flat bedrock surface covered in places by patches of low green vegetation), the combined signal received at a detector is a linear sum of the products of each surface component's spectrum with its corresponding fractional area.

The second type of mixture is an *intimate mixture*, which occurs when different materials are in intimate contact in a scattering surface (e.g., the mineral grains in a rock or soil). In contrast to a linear mixture, the detected signal of an intimate mixture is often a highly non-linear combination of the end-member spectra. Darker materials tend to dominate intimate mixtures because photons can be readily absorbed when they encounter a dark grain; photons have such a high probability of encountering a dark grain in a mixture of light and dark grains that a small percentage of dark grains can reduce reflectance considerably (Clark, 1999).

The third type of mixture is a *coating*. This type of mixture occurs when one material

coats a different material. The coating material can influence reflectance properties by acting as a scattering and transmitting layer whose optical thickness varies with material properties and wavelength (Clark, 1999).

The fourth type of mixture is a *molecular mixture*. This type of mixture occurs when mixtures occur on a molecular level, as with two liquids, or a solid and a liquid mixed together (Clark, 1999). Examples of molecular mixtures can include gasoline spilled onto a soil, or the interlayer water in the clay mineral, montmorillonite.

2.3.2 Synthetic Aperture Radar (SAR)

The microwave portion of the electromagnetic spectrum ranges between wavelengths of about 1 mm and 1 m. Two different classes of remote-sensing imaging systems are used at these wavelengths: 1) *passive* systems, and 2) *active* systems. A passive microwave device measures microwave radiation emitted by materials mainly as a function of their internal energy; such sensors are commonly used for mapping sea ice (e.g., Cavalieri and Gloersen, 1984) and for measuring atmospheric constituents such as water vapour (e.g., Miao *et al.*, 2000). An active microwave device, by comparison, is itself a source of microwave radiation that is directed toward objects of interest, which subsequently reflect a proportion of this radiation back to the device. Active microwave systems thus provide their own illumination and consequently can operate under all lighting conditions, day or night. Because microwaves with appropriately-chosen wavelengths can penetrate the atmosphere under almost all conditions (including haze, snow, cloud, smoke, and rain) without significant attenuation,

sensors that use microwaves can generate imagery in a more timely and reliable manner compared to optical sensors. A passive microwave system is known as a *microwave scanning radiometer*, while an active microwave system is known as a *radar* (Lowe, 1980).

Radar is an acronym of *radio detection and ranging* [strictly speaking, the acronym should be "midar", since modern radar systems differ from earlier systems in their use of microwave energy rather than radio energy (Avery and Berlin, 1992)]. Radar sensors developed for remote sensing purposes are usually mounted on airborne or satellite platforms in *side-looking* configurations in relation to the flight line of the platform (Figure 2.5). Such radar systems operate by directing discrete pulses of high-energy microwave radiation toward surfaces of interest, over extremely short time periods. After each pulse, and before the next pulse is transmitted, the energy of microwave radiation reflected off of the surface and back toward the sensor is measured, along with the time elapsed since the emission of the pulse (Drury, 1993). The measurement of the time elapsed since the emission of a particular radiation pulse allows the distance to the surface to be measured, since radiation velocity is known. This distance from the radar to the surface is called the *slant range*, which may be used to calculate the horizontal distance between the sensor and the surface (the *ground range*). The angle that the slant range forms with the horizontal is called the *depression angle*; the complement of this angle is called the *look angle* (Figure 2.5).

The radar antenna illuminates a narrow strip oriented perpendicularly to the track of the platform; the movement of the platform along its path allows successive areas to be imaged, and thus provides sufficient data for the generation of an image. The width of the

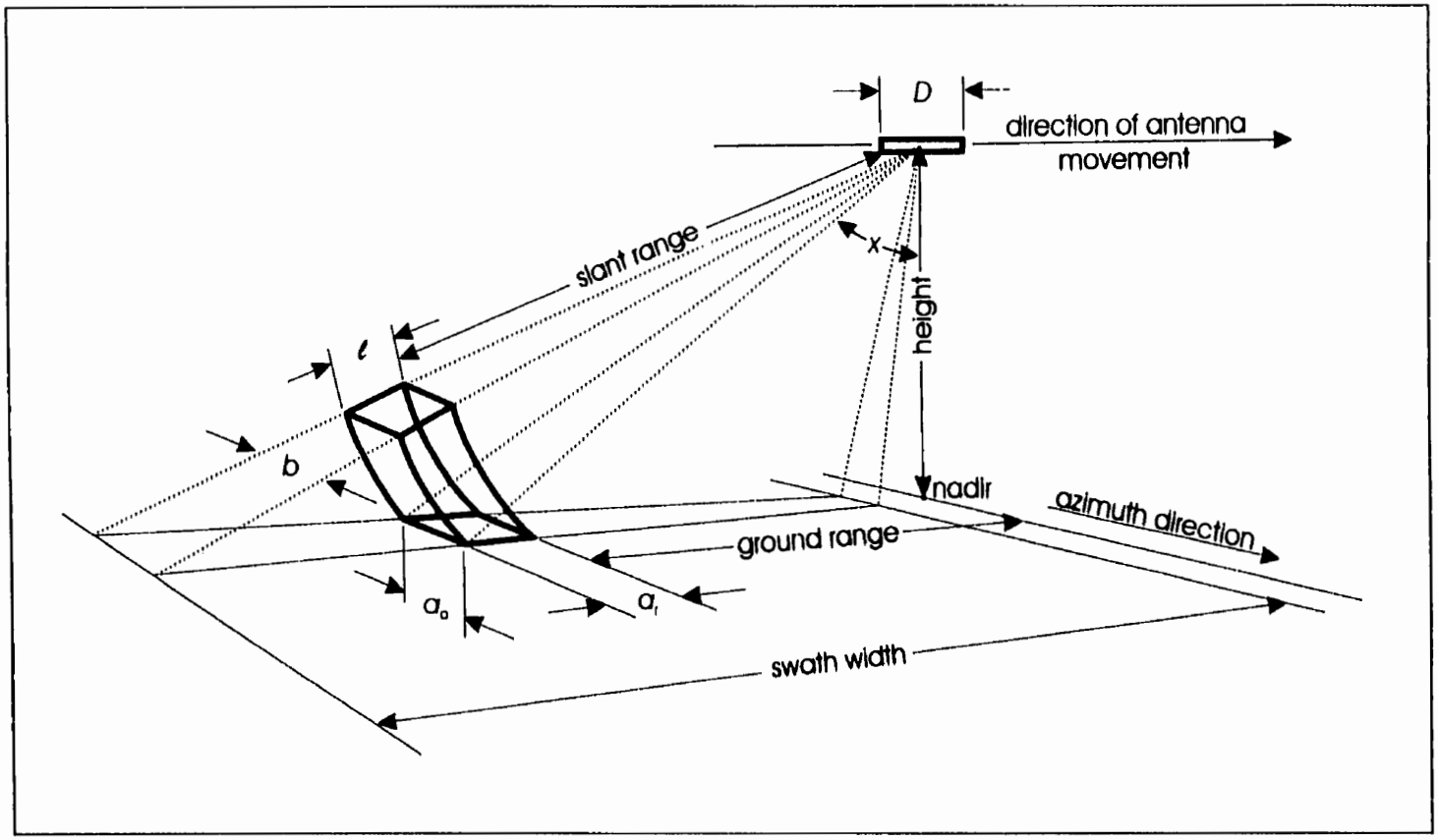

Figure 2.5 Geometry of a simple radar system, where b is beam width, D is length of the antenna, ℓ is length of the radar pulse, a_a is azimuth resolution, a_r is ground-range resolution, and x is the look angle (which is equal to 90° minus the depression angle) (modified after Ulaby *et al.*, 1981). The radar pulse is shown in bold.

radar beam, or *beam width*, is directly proportional to the wavelength of the transmitted pulses, and inversely proportional to the length of the antenna. The beam width of a simple radar system increases with increasing range (Ulaby *et al.*, 1981) (Figure 2.5).

Slant-range resolution is equal to half the pulse length for all distances from the sensor. The corresponding ground-range resolution is given by:

$$a_r = l / (2 \cos \theta) \qquad \textit{where} \qquad l = c\,\tau \tag{2.1}$$

where a_r is the ground-range resolution, l is the pulse length, θ is the depression angle, c is the speed of light, and τ is the pulse duration (Ulaby *et al.*, 1981; Leberl, 1990) (Figure 2.5). Thus, ground-range resolution degrades with decreasing distance from the radar (this is a consequence of the inverse relation between depression angle and ground-range distance from the sensor, and is the reason why remote sensing radar systems do not image directly below the sensor). Azimuth resolution is given by the beam width, which varies with distance from the sensor:

$$a_a = r\,\gamma \qquad \textit{where} \qquad \gamma \sim \lambda / D \tag{2.2}$$

where a_a is azimuth resolution, r is the slant range, γ is the vertex angle of the radar beam (in radians), λ is the radiation wavelength, and D is the length of the antenna (Leberl, 1990) (Figure 2.5). Thus, azimuth resolution degrades with increasing distance from a simple radar system, since the pulse beam width increases with distance. Overall, the resolution in an image produced using a simple radar system will degrade with distance from the sensor, since the lowering of ground-range resolution with distance from the sensor gradually flattens out

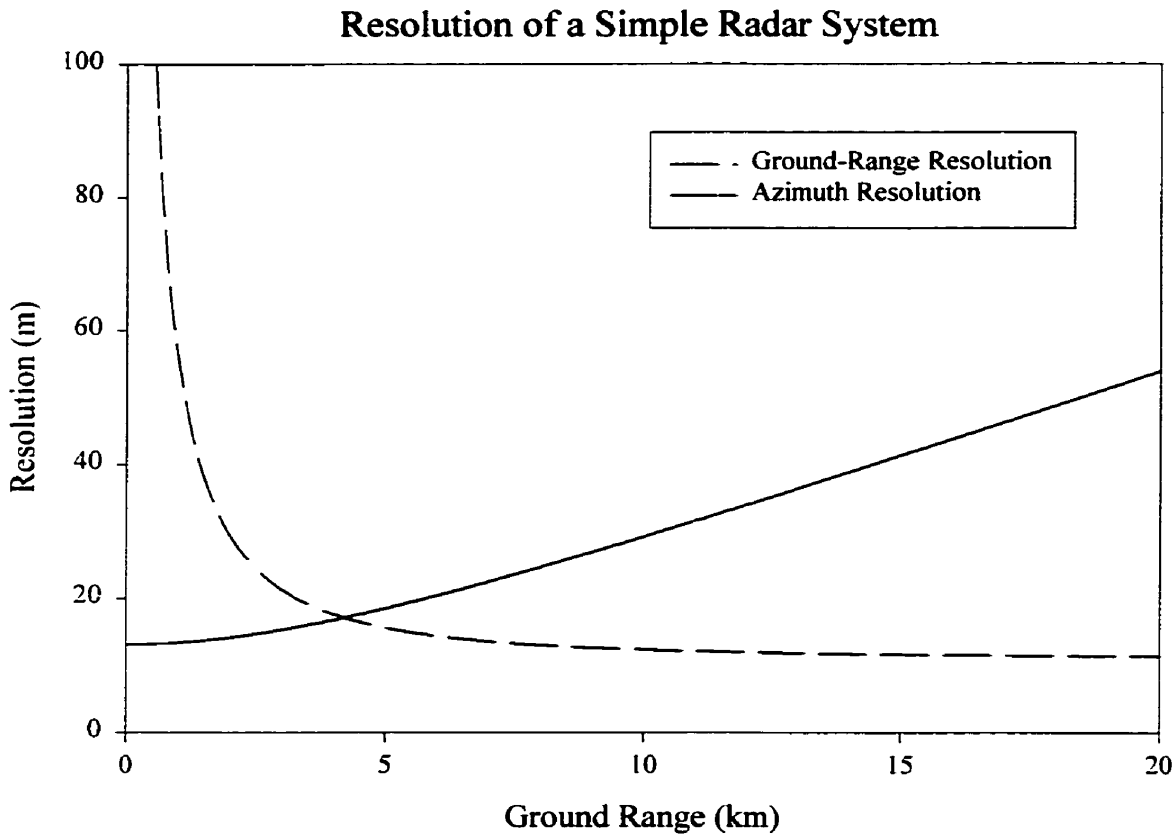

Figure 2.6 Resolution of a simple radar system, plotted against ground distance from the sensor (after Leberl, 1990). In this example, flying height is 5 km, pulse length is 22 m, and the vertex angle (which defines beam width) is 0.15°.

while the degradation of azimuth resolution continues even at large distances from the sensor (Figure 2.6) (Leberl, 1990).

The overall degradation of resolution with increasing distance from the radar can cause the spatial resolution of imagery produced by a simple radar system to be very poor, especially if the system is to be operated from orbit. A simple radar system's spatial resolution can be increased by increasing the length of the radar antenna, which will decrease the radar beam width (Equation 2.2). In practice, however, the length of antenna necessary for high-resolution imaging from high altitudes or from orbit would simply be too large to operate. The solution to this problem involves the replacement of the simple radar system described above (known as a *real-aperture* system) with a *synthetic-aperture radar (SAR)* system, which simulates the use of a very long antenna using properties of the radar waves themselves.

The SAR concept is based on the idea that a very long antenna can be synthesized by recording radar data at successive radar positions as the system moves through space; through specialized processing techniques, these positions can later be treated as though they were individual antenna elements of a single linear antenna array (Ulaby *et al.*, 1982) (Figure 2.7). This synthesis is possible because electromagnetic waves emitted by radar systems are coherent, meaning they are generated in phase and have a uniform wavelength. A SAR system illuminates a surface area such that only a narrow strip as wide as the antenna is perfectly in line at any particular time; radiation returned from other illuminated parts of the surface (immediately behind and in front of the narrow strip) will be subject to a Doppler shift (Drury, 1993). Although these shifts are very small, they can be detected electronically if the

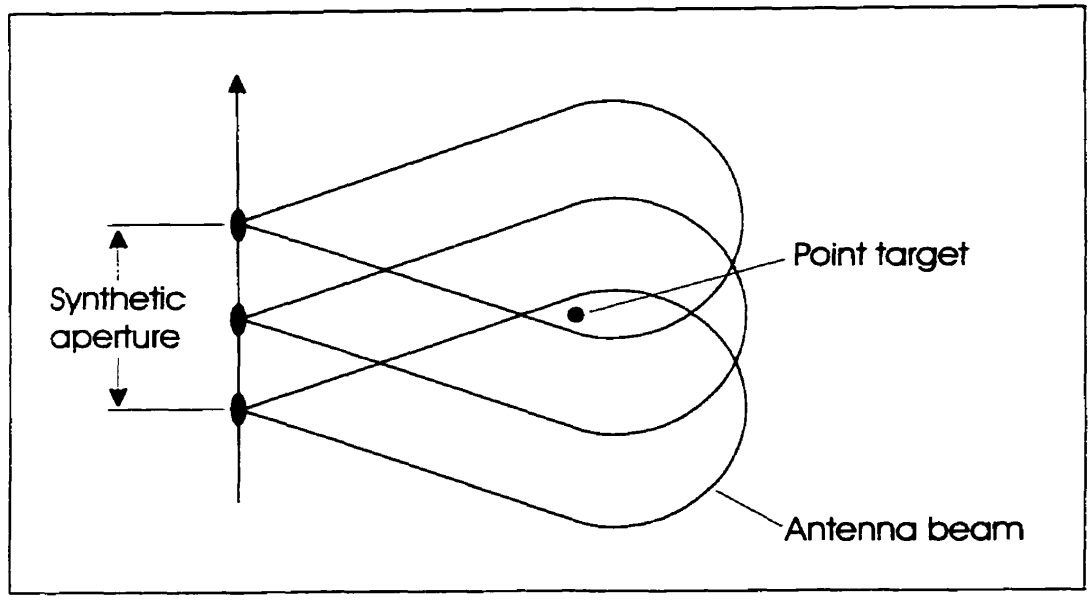

Figure 2.7 Schematic illustration of the concept of SAR, which involves synthesizing a large antenna through the forward motion of a real antenna along a flight path (after Richards, 1993). This view from above shows the illumination of a point target from several locations using a real antenna. Later processing can synthesize an antenna whose length can be as large as the distance travelled by the antenna during illumination of the point target.

radiation is coherent (Avery and Berlin, 1992; Drury, 1993). Sophisticated computer algorithms use measured Doppler shifts to simulate the use of a very long antenna, so that resolution in the azimuth direction becomes independent of distance from the sensor:

$$a_a = D / 2 \tag{2.3}$$

where a_a is azimuth resolution and D is the along-track length of the antenna. Thus, the azimuth resolution of a SAR depends only on the size of the real antenna (Ulaby *et al.*, 1981). Mathematical summaries of SAR theory are given by e.g., Ulaby *et al.*(1982), and Leberl (1990).

2.3.2.1 Speckle

An individual pixel location contains many individual reflectors (including e.g., rocks and leaves) whose collective radar reflections interact to produce the overall reflectance associated with the pixel. The coherent nature of radar waves causes random constructive and destructive interference of microwave radiation reflected off of individual reflectors, resulting in random bright and dark pixels on radar imagery (Lillesand and Kiefer, 1994). This can be problematic when radar images are used for applications such as lithological discrimination, since it increases the range of radar backscatter values associated with individual surface classes (Section 2.3.2.4). An important technique used to reduce (but not eliminate) the amount of speckle in radar images is called *multiple-look processing*. Multiple-look processing involves the averaging of several independent images of the same area, each produced using different portions of the synthetic aperture. The number of images averaged

in this technique is called the *number of looks*, and the amount of speckle in the final image varies inversely to the square root of this value (Lillesand and Kiefer, 1994). The size of the resolution cell of the final image is directly proportional to the number of looks (Lillesand and Kiefer, 1994). Speckle may also be reduced using filters (e.g., Gebhardt *et al.*, 1995).

2.3.2.2 Radar Brightness

The strength of SAR backscatter is primarily a function of the physical roughness and electrical properties of ground materials. This contrasts with optical remote sensing, in which relative strengths of measured radiation are directly related to the chemistry of materials (Section 2.3.1) (Abdelsalam *et al.*, 2000). Most practical knowledge of the manner in which different earth materials reflect microwave radiation has been derived from empirical observations (Lillesand and Kiefer, 1994).

The radar brightness recorded for a particular location in a SAR image is mainly a function of three physical factors: 1) topography and slope, 2) surface roughness, and 3) the complex dielectric constant. These factors, along with wavelength and polarization effects, are summarized below:

1) Topography: Radar images typically have a three-dimensional, side-lighted appearance, since the radar system is an active, side-looking system. Local variations in surface slope cause differences in the *local incidence angle* (the angle between the incident radar beam at the surface and the normal to the ground at the point of incidence). These variations result in relatively strong microwave reflections being produced by slopes facing the radar, and relatively weak reflections, or no reflections, being produced by slopes facing

away from the radar (Lillesand and Kiefer, 1994). Dark regions that correspond to areas of no microwave illumination due to terrain effects are said to be characterized by *radar shadow*.

2) Surface Roughness: A useful measure of surface roughness is given by the *Rayleigh criterion*, which states that surfaces may be regarded as rough if the root-mean-square height of surface variations exceeds one-eighth of the microwave wavelength divided by the cosine of the local incidence angle (Lillesand and Kiefer, 1994). A rough surface by this definition will act as a *diffuse reflector* (reflecting in all directions in a relatively uniform manner), while a smooth surface will act as a *specular reflector* (i.e., reflections will be mirror-like). Rough surfaces will thus return a relatively high signal (with a relatively large proportion of incident radiation reflected back toward the sensor), while smooth surfaces will return in very low signals (with most radiation being reflected away from the sensor) (Lillesand and Kiefer, 1994). A special type of surface geometry in which two smooth surfaces cause a double reflection back toward the sensor is known as a *corner reflector*. Corner reflectors, commonly associated with, e.g., buildings and boulder fields, can produce particularly high radar returns, saturating the values of individual pixels in a radar image.

3) Complex Dielectric Constant (ϵ): The *complex dielectric constant* is a measure of the proportion of microwave radiation that is reflected by a material and that which penetrates the material (Drury, 1993). Because the dielectric constants of most earth materials are very similar in the absence of water, ranging in value from ~3 to 8 at microwave wavelengths, radar is considered to be relatively insensitive to the electrical properties of most surface materials in their dry state (Avery and Berlin, 1992). Those materials that are characterized by very high dielectric constants, such as water (ϵ= ~80) and metals, are those

that are excellent reflectors (poor absorbers) of microwave energy (Drury, 1993). Although water has a very high dielectric constant, bodies of water with relatively calm, flat surfaces are typically associated with very low radar backscatter since their surfaces act as specular reflectors (e.g., Lowman, 1994).

Variations in the dielectric constant of most earth materials are mainly caused by variations in moisture content For example, plants are excellent radar reflectors in part because of the high moisture content of their leaves (e.g., Fung and Ulaby, 1978). Similarly, water-saturated soils are good radar reflectors (Ulaby *et al.*, 1983; Dobson and Ulaby, 1986; Pultz *et al.*, 1990). Sands in hyper-arid environments, meanwhile, are very poor radar reflectors, and microwaves with wavelengths of about 3 to 60 cm can typically penetrate these sands to depths of about 0.5 to 6 m (Schaber *et al.*, 1986; McCauley *et al.*, 1986; Schaber, 1999, Schaber and Breed, 1999; Schaber *et al.*, 1997; Robinson *et al.*, 1999).

4) Wavelength and Polarization effects: In general, longer wavelengths are associated with greater penetration into a material. For example, C-band ($\lambda \approx 3.75$-7.5 cm) radiation is typically scattered along the surface of a dense vegetative canopy whereas a significant proportion of L-band ($\lambda \approx 15$-30 cm) or P-band ($\lambda \approx 30$-100 cm) radiation can penetrate such a canopy, reaching the ground surface (Costa *et al.*, 1998; Schaber, 1999; Schaber and Breed, 1999). Thus, long-wavelength microwaves can be used to image surface features in areas where optical devices may be of comparatively little value. In arid environments, microwaves with longer wavelengths can penetrate loose dry sands to greater depths than those with shorter wavelengths (Schaber *et al.*, 1986; McCauley *et al.*, 1986; Schaber, 1999; Schaber and Breed, 1999; Schaber *et al.*, 1997; Robinson *et al.*, 1999).

The electrical and magnetic fields of electromagnetic radiation transmitted by radar systems oscillates either in a horizontally (H) or vertically (V) polarized plane in relation to the long axis of the antenna. When a polarized electromagnetic pulse strikes the ground, it is depolarized (rotated) to some degree, such that the pulse oscillates in several planes (Avery and Berlin, 1992). Depolarization is a function of several terrain parameters, including surface geometry and roughness (Avery and Berlin, 1992). Radar systems selectively measure returned microwave radiation on the basis of polarization, either horizontal or vertical. A common radar design involves horizontal transmission and horizontal reception (designated *HH*), but several other systems may be employed (i.e., HV; VV; VH). Strong microwave returns measured by like-polarized systems (HH or VV) are often associated with simple reflections off surface scatterers that are oriented in the same direction as the polarization of incident radiation. Significant depolarization of microwave radiation, in contrast, is often associated with multiple reflections (*volume scattering*) related to, e.g., scattering within a vegetation canopy or off dry alluvium (Blanchard and Rouse, 1980; Evans *et al.*, 1986). The complex nature of the interaction of radar signals with surface features can make it difficult to predict whether a like-polarized or cross-polarized system will provide higher information content for a particular application (Lillesand and Kiefer, 1994).

2.3.2.3 Layover and Foreshortening

The side-viewing geometry of radar systems can cause significant geometric distortions in radar images. Particularly problematic and common distortions include those associated with relief displacement, including *layover* and *foreshortening* (Figure 2.8).

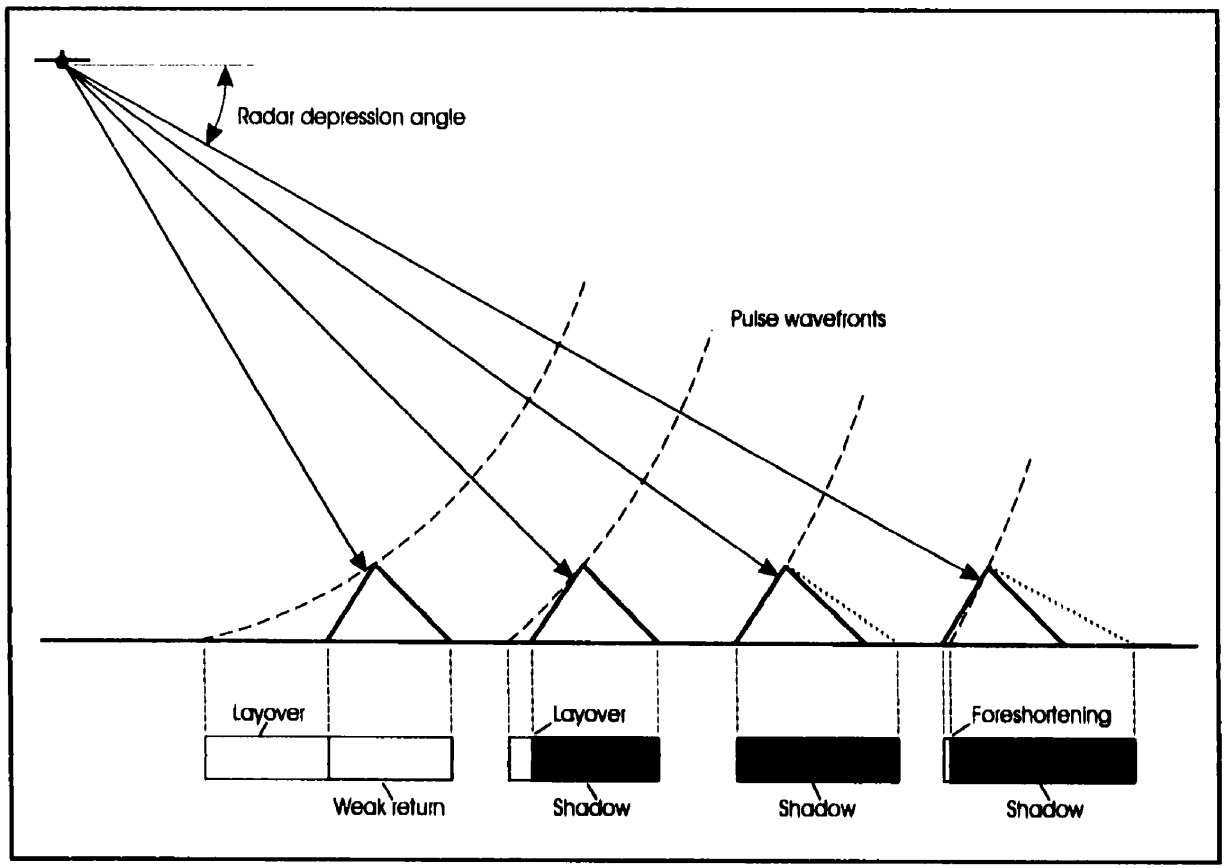

Figure 2.8 The effect of terrain relief and depression angle on geometric distortion in radar images (after Lillesand and Kiefer, 1994).

Layover, or the horizontal displacement of the peak of a topographic feature such that its ground range is less than that of the feature's base, results when the top of a topographic feature is closer to the radar platform than the bottom of the feature (i.e., layover results when the foreslope of the feature is more steep than the pulse wavefront) (Figure 2.8). Foreshortening is a less extreme example of layover, in which a symmetric topographic feature is depicted in radar imagery to be leaning toward the radar (but unlike the layover case, the peak of the feature has a greater ground range than the base of the feature) (i.e., foreshortening occurs when the foreslope of the feature is less steep than the microwave pulse wavefront) (Avery and Berlin, 1992) (Figure 2.8). Both foreshortening and layover are always conspicuous in radar images of high-relief terrain. It is interesting to note that the direction of relief displacement of layover and foreshortening distortions is reversed from that of optical imaging (that is, while positive topographic features lean toward the nadir in radar imagery, they lean away from the nadir in optical imagery) (Lillesand and Kiefer, 1994).

2.3.2.4 Lithological Discrimination

SAR data is useful for the detection and mapping of topographic and structural features exposed at the Earth's surface, as long as the direction of imaging (the *look direction*) is generally perpendicular to the trend of topographic and structural features (Lowman, 1994; Moon *et al.*, 1994). For example, radar is applicable toward the mapping of lineaments in shield and other terrains; this lineament information, which can sometimes be related to, e.g., regional foliation trends and the geometric properties of ductile shear zones, may then be used in the interpretation of tectonic and geological models (Graham and

Grant, 1991; Lowman *et al.*, 1992; Kusky *et al.*, 1993; Lowman, 1994; Rivard *et al.*, 1994; McGregor *et al.*, 1994; Rivard *et al.*, 1999; Sharma *et al.*, 1999). Radar imagery may also be applied toward mapping surficial deposits associated with glacial landforms and geomorphic terrain classes (e.g., Graham and Grant, 1991, 1994; Kenny *et al.*, 1994; Simms and Bell, 1998).

Individual lithologies can be mapped using radar imagery if the contacts between lithologies are marked by structural features (e.g., faults, unconformities, inhomogeneities in weathering) (e.g., Lowman, 1991). Furthermore, radar images may be used to discriminate well-exposed lithological units on the basis of their local geometric properties, as long as these properties are correlated with lithology in a useful and consistent manner [recall that, although radar backscatter is not directly related to the chemistry of ground materials (as optical data is), radar is capable of discriminating surfaces characterized by different measures of roughness, topography, and water distribution that may be correlated with lithology (Section 2.3.2.1)] (Abdelsalam *et al.*, 2000). For example, Budkewitsch *et al.*(1996) found that Radarsat C-band (λ = 5.3 cm) SAR imagery can be used to visually differentiate carbonate units from clastic lithologies on Bathurst Island, Nunavut; the carbonate units in this region are associated with strong radar backscatter relative to surrounding sedimentary lithologies, as a consequence of their surface roughness. Similarly, Fielding *et al.* (1986) found that ignimbrite sheets of the Puna / Altiplano of the Andean Cordillera are associated with strong backscatter in SIR-B [Shuttle Imaging Radar L-band (λ = 23.5 cm) SAR] radar imagery, while surrounding materials (including Paleozoic to Cenozoic sedimentary rocks, and younger andesitic stratovolcanoes) are associated with lower radar backscatter due to

their relatively smooth and well-rounded geometries. Numerous other studies have found that SAR imagery can be used to visually discriminate well-exposed lithological units on the basis of lithological correlations with surface roughness and topography (e.g., Daily *et al.*,1978; Evans *et al.*, 1986; Singhroy *et al.*, 1992; Smith *et al.*, 1999). Even in regions extensively covered by vegetation, radar has been found to be useful for visually mapping lithology in regions where topography and lithology are correlated (i.e., where there are erosional contrasts between different lithologies) (e.g., Singhroy *et al.*, 1993; Rivard *et al.*, 1999).

Despite the successes noted above, surface-roughness characteristics of different lithological classes are often not sufficiently different or consistent to allow lithological classes to be reliably differentiated using SAR imagery (e.g., Smith *et al.*, 1999; McGregor *et al.*, 1999). Lithological discrimination using SAR imagery is further impeded by factors such as speckle, radar shadow, layover and foreshortening effects, and backscatter variations caused by local topography (Sections 2.3.2.2 and 2.3.2.3). Thus, it is not unusual for SAR imagery to be found to be generally inferior to optical imagery (including aerial photographs and satellite images) for deriving lithological (e.g., Evans, 1988; Dall *et al.*, 1995; McGregor *et al.*, 1999).

Lowman (1994) summarizes that the main advantage of radar imagery for geological study is in its ability to show subtle topographic features with high spatial resolution over large areas. Further, radar imagery provides information on surface roughness and texture, and provides a good synoptic overview that reveals the continuity of both structure and morphology (Mustard, 1994; Rivard *et al.*, 1999). The surface-roughness and texture information provided by radar imagery complements the chemical information provided by

aerial photography and digital remote sensing in the visible and infrared (Graham and Grant, 1991; Kruse, 1992; Lowman, 1994; Metternicht and Zinck, 1998), and provides especially significant geological insight when integrated with both optical and geophysical data (Paradella *et al.*, 1998; Madon *et al.*, 1999; McGregor *et al.*, 1999; Rivard *et al.*, 1999). Although radar can sometimes provide information on the distribution of lithologies on the basis of correlations with roughness, backscatter properties often vary considerably within and between lithological classes, making lithological discrimination on the basis of roughness very difficult (Rudant *et al.*, 1994; Schetselaar, 1994; McGregor *et al.*, 1999). Because of radar features such as speckle, much more information can be derived from radar imagery through visual analysis than through per-pixel classification (Rudant *et al.*, 1994; Costa *et al.*, 1998; Adam *et al.*, 1998; Shimabukuro *et al.*, 1998), particularly when data for only a single radar wavelength and polarization are available (Ferrazzoli *et al.*, 1999; Haack *et al.*, 2000).

2.4 Sensors and Images

Three different types of satellite imagery were used in this research: 1) Landsat Thematic Mapper (TM) images, 2) Radarsat images, and 3) IKONOS images. The Landsat TM sensor is a well-established optical instrument that images in seven broad spectral ranges in the visible and infrared. The Radarsat sensor is an advanced C-band synthetic aperture radar (SAR) system. The IKONOS sensor is the first orbiting high-resolution (1 m pixel spacing) optical sensor available for common use.

2.4.1 Landsat TM Imagery

A total of 6 Landsat platforms were successfully launched between 1972 and 1999. Landsat-5, which produced the Landsat images used in this research, was launched in 1984 into a circular, sun-synchronous, near-polar orbit with an elevation of 705 km above the earth's surface. The orbit inclination is 98.2° with respect to the equator. The platform crosses the equator on the north-to-south portion of each orbit at 9:45 a.m. local solar time. Each orbit takes ~99 minutes, and the satellite has a 16-day repeat cycle (233 revolutions) (Lillesand and Kiefer, 1994).

The Landsat Thematic Mapper (TM) sensor, which has been the main remote sensing instrument of all Landsat platforms since Landsat-4 (1982), is an across-track scanner that images the Earth's surface in seven spectral channels, covering relatively wide spectral ranges in the visible and infrared ranges (Figure 2.9; Table 2.1). The total field of view of the sensor is 15.4°, and the swath width of TM imagery is 185 km. Pixel size is 30 m x 30 m for all spectral channels except the thermal channel, which has a pixel size of 120 x 120 m. TM data has an 8-bit radiometric resolution (256 levels of brightness).

Because the initial intent of the Landsat program was to provide a means to map general land cover classes and to monitor world agriculture (Drury, 1993), the spectral ranges selected for use in the Landsat series are not ideal for geological applications. Only Band 7, which provides data for the range 2.08 and 2.35 μm, was added for geological study (specifically, for mapping hydrothermal alteration based on the hydroxyl spectral features that are characteristic of this range) (Lillesand and Kiefer, 1994).

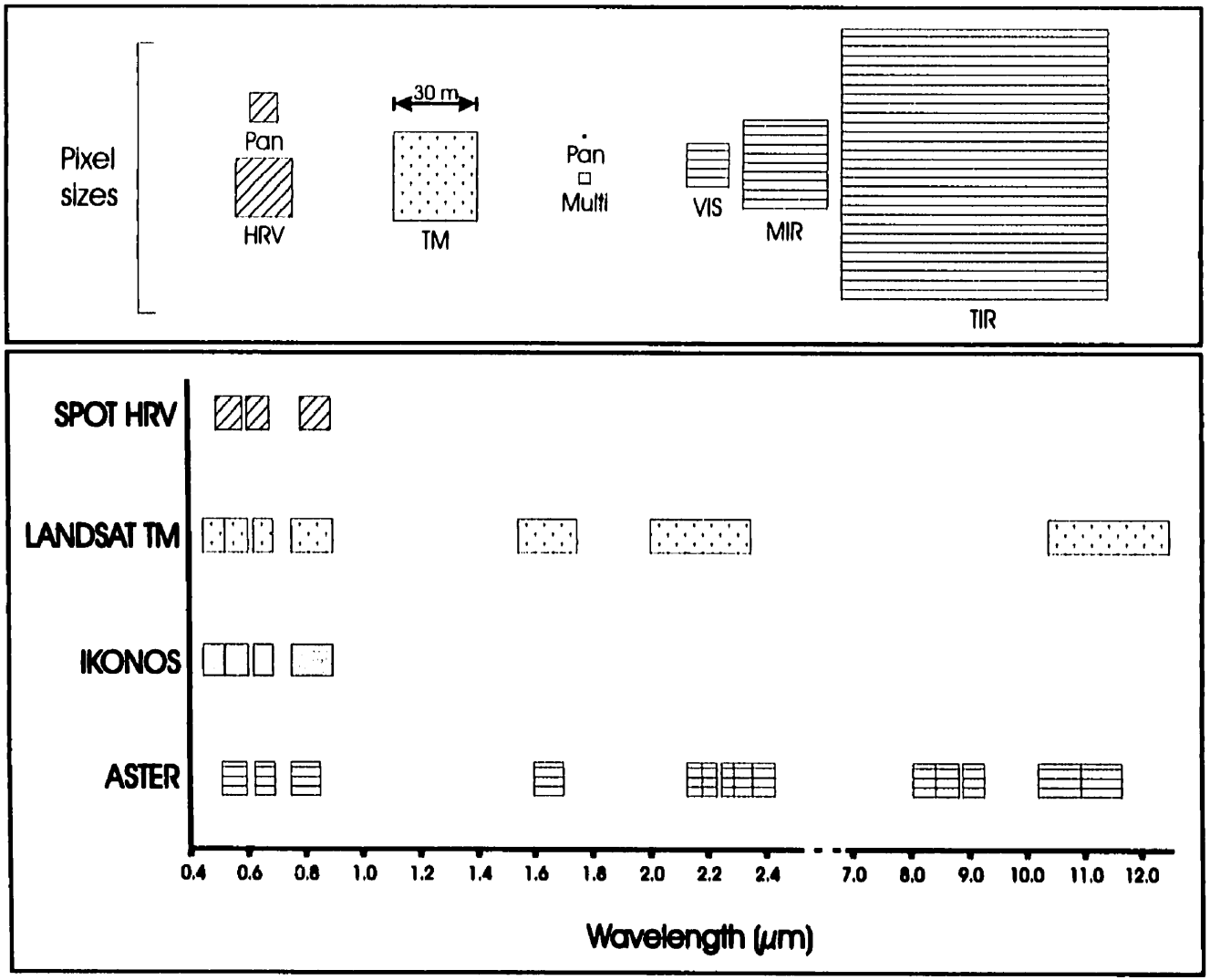

Figure 2.9 Spatial and spectral resolutions of selected optical sensors. Sensor names and designations: *Pan* - Panchromatic; *HRV* - High Resolution Visible; *TM* - Thematic Mapper; *Multi* - Multispectral; *VIS* - visible; *MIR* - mid-infrared; *TIR* - thermal infrared.

Despite its limitations, the TM sensor produces data with a spectral resolution that is superior to that of all other optical image types generated from Earth orbit [aside from those produced by the experimental ASTER (Fujisada, 1998; Abrams, 2000) and MODIS (Barnes *et al.*, 1998; Justice *et al.*, 1998) sensors, which have just become operational as of this writing] (e.g., Glackin, 1998; Kaufman *et al.*, 1998). The most recent Landsat system has been equipped with a modified TM system (the Extended Thematic Mapper, or *ETM+*), providing an additional 60 m resolution thermal channel, a 15 m resolution panchromatic channel, and advanced calibration equipment.

Table 2.1 Basic characteristics of Landsat TM images. Channel number 7 is not listed in proper order because it was the last to be added to the TM sensor.

Channel Number	Wavelength Range (μm)	Spectral Region	Pixel Size (m)
1	0.45-0.52	visible (blue)	30 x 30
2	0.52-0.60	visible (green)	30 x 30
3	0.63-0.69	visible (red)	30 x 30
4	0.76-0.90	near-infrared	30 x 30
5	1.55-1.75	mid-infrared	30 x 30
7	2.08-2.35	mid-infrared	30 x 30
6	10.4-12.5	thermal infrared	120 x 120

Landsat Thematic Mapper imagery has been widely used to discriminate general land-cover classes since its introduction in 1982. Thematic Mapper imagery is useful for differentiating and mapping a wide variety of vegetation classes (e.g., Horler and Ahern, 1986; Pilon and Wiart, 1990; Franklin and Wilson, 1991; Beaubien, 1994; Lunetta and

Balogh, 1999; Pinder *et al.*, 1999; Sohn *et al.*, 1999; Lymburner *et al.*, 2000; Koutsias and Karteris, 2000; Mukai and Hasegawa, 2000; Puhr and Donoghue, 2000), urbanization features (e.g., Khorram *et al.*, 1987; Chavez and Bowell, 1988; Wang and Liu, 1994), snow and ice classes (e.g., Dozier, 1984, 1989; Hall *et al.*, 1987; Duguay, 1993; Bronge and Bronge, 1999), clouds (e.g., Cahalan and Snider, 1989), and features related to water turbidity and pollution (e.g., Gibbons *et al.*, 1989; Jensen *et al.*, 1989; Abuzar and Al-Ghunaim, 1993).

Landsat TM imagery has been found to be useful for a variety of geological applications. Along with being a valuable information source for applications as diverse as studying geological structure (e.g., Johnson and Harrison, 1989; Lowman *et al.*, 1992; Qari, 1992; El Rakaiby and Shalaby, 1992; McGregor *et al.*, 1999) and monitoring volcanic activity (e.g., Rothery *et al.*, 1988; Francis and De Silva, 1989; Urai, 2000), Landsat TM imagery can be a useful tool for discriminating surface lithology. As with the use of all optical imagery, the application of TM for lithological discrimination is mainly limited to areas where rock exposure is not greatly restricted by vegetation or overburden cover (Drury, 1986; Harding and Forrest, 1989) [although in some cases useful information can be generated for heavily forested regions (Kettles *et al.*, 2000); also, the methods of geobotanical analysis have had limited success in relating bedrock properties to the spectral properties of overlying vegetation (e.g., Bell *et al.*, 1991; Bélanger, 1991; Warner *et al.*, 1991; Paradella and Vitorello, 1995)]. Even where rock exposure is good, the utility of Landsat TM imagery for discriminating and mapping lithology has been found to be variable, depending on the lithological, weathering, topographic, and vegetational characteristics of the area of interest

(Birnie *et al.*, 1989; Arvidson *et al.*, 1994; Ricchetti, 2000).

Landsat TM imagery has been used with mixed success to map igneous and metamorphic units (e.g., Rowan *et al.*, 1987; Abrams *et al.*, 1988; Harding *et al.*, 1989; Pontual, 1989; Spatz and Taranik, 1989; Qari, 1992; Mustard, 1994; Abdelhamid and Rabba, 1994; Glikson and Creasey, 1995; Macias, 1995; El Rakaiby, 1995; Van der Meer *et al.*, 1995), as well as clastic, carbonate, and evaporitic lithologies (e.g., Evans, 1988; Sgavetti *et al.*, 1995; Ernst and Paylor, 1996; Riaza *et al.*, 2000). TM imagery has also been used to map the distribution of glacial till (e.g., Schau *et al.*, 1993; Giugni *et al.*, 1998), and geomorphic land-cover classes (e.g., Quarmby *et al.*, 1989; Franklin, 1991). In general, because the potential for the discrimination of different lithologies is greatest in the near-, mid-, and thermal-infrared ranges of the spectrum, TM bands 3, 4, 5, and 7 have been found to have the greatest value for lithological discrimination (Spatz and Taranik, 1989; Drury, 1993; Schetselaar, 1994); band 6, the TM thermal band, is unfortunately much too broad to take advantage of the considerable potential for lithological discrimination in the thermal range.

2.4.2 Radarsat-1 Imagery

Radarsat-1 imagery is produced by a synthetic aperture radar (SAR) operating at 5.3 GHz (C-band, wavelength = 5.6 cm), using HH polarization. The spacecraft was launched in 1995 into a circular, sun-synchronous, near-polar orbit with an elevation of 798 km above the earth's surface. The platform crosses the equator in a southerly direction at dawn and a northerly direction at dusk. The orbit is inclined 98.6 degrees relative to the equator. The spacecraft operates at an altitude of 798 km. Each orbit takes about 101 minutes, and the

orbit repeat cycle is 24 days (343 revolutions) (Parashar *et al.*, 1993).

The Radarsat-1 system is a cooperative venture between the Canadian government, several provincial governments, and the government of the United States. The Radarsat program was initiated by the Canadian federal government to facilitate both northern nautical logistics and the assertion of sovereignty over Canada's arctic water bodies. Radar sensors are ideal for monitoring ice cover and nautical activities in the arctic, since they are capable of imaging under any lighting conditions and through atmospheric haze and cloud (Parashar *et al.*, 1993) (see Section 2.3.2).

The Radarsat-1 SAR system has a unique capability to direct and shape its radar beam over a 45-500 km range, with varying surface resolution. A total of 35 beam modes are available, each corresponding to a particular spatial resolution, swath width, and range of incidence angles (Table 2.2) (Luscombe *et al.*, 1993).

Table 2.2 Radarsat beam modes (Luscombe *et al.*, 1993).

Radarsat Mode	Incidence Angle (degrees)	Resolution (m)	Swath Width (km)
Standard (7 modes - see Table 2.3)	20-49	28 x 25	100
Wide Swath	20-39	28 x 35	150
Fine Resolution (5 modes)	37-48	10 x 9	45
Extended Coverage (low incidence)	10-23	26 x 43	170
Extended Coverage (high incidence)	49-59	20 x 28	75
ScanSAR (narrow)	20-39 / 31-46	50 x 50 / 50 x 50	300
ScanSAR (wide)	20-49	100 x 100	500

Radarsat-1 imagery has been successfully used for a variety of applications, including forestry (e.g., Kux *et al.*, 1998; Malcolm *et al.*, 1998; Shimabukuro *et al.*, 1998), agriculture (e.g., McNairn *et al.*, 1998), sea ice monitoring (e.g., Ramsay *et al.*, 1998), flood mapping (e.g., Adam *et al.*, 1998; Zhou *et al.*, 2000), and measurement of coastal erosion (e.g., Singhroy, 1996; Barbosa *et al.*, 1999).

Radarsat-1 imagery has also been found to be useful in geological studies, including the characterization of impact landforms (e.g., Smith *et al.*, 1999), the detection and mapping in arid regions of ancient fluvial features buried under thin covers of sand (e.g., Robinson *et al.*, 1999), the derivation of structural information in shield terrains (e.g., McGregor *et al.*, 1999; Rivard *et al.*, 1999; Sharma *et al.*, 1999; Lepage *et al.*, 2000), and the mapping of glacial deposits (e.g., Simms and Bell, 1998). For well-exposed regions, discrimination of lithology by visual means is possible with Radarsat-1 imagery on the basis of lithology-related contrasts in surface roughness and moisture (e.g., Budkewitsch *et al.*, 1996; Smith *et al.*, 1999), although as with all radar types, caution must be exercised in such an application, since SAR backscatter properties from different sources may be quite similar, making lithological relations to SAR backscatter unreliable (McGregor *et al.*, 1999; Arkin *et al.*, 1999).

Radarsat-1 viewing geometry influences the effects of terrain and surface roughness, and thus is an important consideration in geological studies. Singhroy and Saint-Jean (1999) have summarized the general incidence-angle parameters that are preferable for mapping surficial geology. In general, small (10 to 25°) and moderate (25 to 59°) incidence angles (where incidence angle refers to the angle from the vertical to the radar beam) are recommended when imaging low relief areas [the smaller incidence angles will provide

maximum relief enhancement (Singhroy and Saint-Jean, 1999; Rivard *et al.*, 1999), while the larger incidence angles will increase terrain textural contrasts]. Incidence angles between about 20 and 35° are recommended for moderate-relief environments; incidence angles between about 35 and 59° are recommended for high relief environments, to reduce geometric distortion (and thus provide more information on slope features) and shadow effects (Singhroy and Saint-Jean, 1999). The Radarsat sensor has seven different standard-beam modes, each corresponding to a different range of incidence angles (Table 2.3). Although the standard beam modes have been found to be useful, greater amounts of structural information can be provided by the higher-resolution fine beam modes (McGregor *et al.*, 1999).

Table 2.3 Standard-beam incidence angles for the Radarsat sensor (Luscombe *et al.*, 1993). Values given in degrees.

Beam Number	Incidence Angle (near)	Incidence Angle (far)
1	20.0	27.4
2	24.2	31.2
3	30.4	36.9
4	33.6	39.6
5	36.5	42.2
6	41.4	46.5
7	44.9	49.4

2.4.3 IKONOS Imagery

The IKONOS satellite was launched on September 24, 1999, into a circular, sun-synchronous, near-polar orbit with an elevation of 681 km above the earth's surface. The

orbit inclination is 98.1° with respect to the equator. The platform crosses the equator on the north-to-south portion of each orbit at 10:30 a.m. local solar time. Each orbit takes ~98 minutes, and the satellite has a 14-day repeat cycle.

The IKONOS satellite is owned and operated by Space Imaging, a privately held company in the United States. The IKONOS imaging system is an along-track (pushbroom) scanner that images the Earth's surface in four multispectral channels covering spectral ranges identical to those of the first four Landsat TM channels (Figure 2.9; Table 2.4). The IKONOS system also has a panchromatic channel that images in the visible and near-infrared (Table 2.4). The total field of view of the sensor is 0.93°, and nominal swath width of IKONOS imagery is 11 km at nadir. Because the sensor can image over a range of incidence angles (e.g., Zhou and Li, 2000), revisit time is only 1-3 days. Nominal pixel size is 4 m x 4 m for the multispectral channels and 1 m x 1 m for the panchromatic channel (at <26° off nadir). IKONOS data has an 11-bit radiometric resolution (up to 2048 levels of brightness). IKONOS imagery first became available to consumers in 2000, and has a spatial resolution that is superior to that of all other commercial image types generated from orbit.

Like those of the Landsat TM sensor, the spectral ranges selected for use in the IKONOS satellite are not ideal for geological applications. Nevertheless, as the first commercial high-resolution imaging satellite, IKONOS represents an important advance in the field of remote sensing. Despite their spectral limitations, images generated by the IKONOS sensor are expected to be widely used in a variety of fields, including geology and geological engineering.

Table 2.4 Basic characteristics of IKONOS images. Note that the four multispectral channels have identical spectral characteristics to the first four channels of the Landsat TM sensor.

Channel Number	Wavelength Range (μm)	Spectral Region	Pixel Size (m)
Multispectral - 1	0.45-0.52	visible (blue)	4 x 4
Multispectral - 2	0.52-0.60	visible (green)	4 x 4
Multispectral - 3	0.63-0.69	visible (red)	4 x 4
Multispectral - 4	0.76-0.90	near-infrared	4 x 4
Panchromatic	0.45-0.90	visible to near-infrared	1 x 1

2.5 Basic Image Processing Concepts

This section briefly summarizes the basic concepts behind the following image processing procedures: image arithmetic, RGB (red-green-blue) colour compositing, the intensity-hue-saturation transform, and image classification. The purpose of all of these procedures is to combine multiple digital images to produce one or more new images that provide new information. The combination of multiple images to produce a new image is sometimes called *data fusion*, although this term is usually used in a more restrictive sense to describe the combination of images produced by different sensors (e.g., Wald, 1999). Although single images can often be used by themselves to extract useful geological information (e.g., Schau *et al.*, 1993), a greater amount of information can often be generated when several sources of information are analysed together. The act of combining images and datasets can help workers visualize relations between complimentary datasets, and thus can result in a more comprehensive interpretation of available datasets (Evans, 1988; McGregor *et al.*, 1999; Rivard *et al.*, 1999).

None of the above procedures can be used to combine images unless the images are already referenced to a common reference system and have common pixel dimensions. Images produced at the same time and by the same sensor are usually already in this state when delivered to the end user. Images produced by different sensors, or images produced by the same sensor but at different times, instead require conversion to a common reference system and pixel size using the procedures of *georeferencing* and *resampling* (for details see Richards, 1993, pp.56-63). These procedures are simple in concept but in practice can be difficult to apply in a satisfactory manner, since relative spatial offsets of only a few pixels can degrade the results of an image combination procedure. *Orthorectification* may be used to correcting geometric distortions in satellite imagery caused by variations in topography. Issues related to georeferencing errors in the processing of single- and multi-source imagery are discussed by Richards (1993) and Ehlers (1997).

2.5.1 Image Arithmetic and RGB Colour Composites

Two (or more) digital data sources can be combined using simple image arithmetic. For example, two images can be summed, subtracted, multiplied, or ratioed (or some combination of these or other functions can be performed), generating an output image that contains digital information that is a function of that contained in both input images. Whether or not the output image will contain useful information depends on the nature of the two sources being combined, as well as the nature of the combination algorithm. For example, the normalized ratio of TM channels 4 and 3, known as a Normalized Difference Vegetation Index (NDVI) can be calculated using the following equation:

$$\text{Normalized Ratio} = (\textit{Channel 4} - \textit{Channel3}) / (\textit{Channel 4} + \textit{Channel 3}) \qquad (2.4)$$

where *Channel 4* represents an image scanned in the near-infrared, and *Channel 3* represents an image scanned in the red portion of the electromagnetic spectrum (Table 2.1). This image ratio produces useful information on relative amounts of vegetative cover, since vegetation has a relatively high near-infrared reflectance and relatively low visible reflectance (Figure 2.2). By the normalized ratio, healthy green vegetation is characterized in the output image by high values, while clouds, water, and snow are typically associated with negative values because of their greater relative reflectance in the visible range of the spectrum. The ratio of other TM bands would not produce as much, if any, vegetative information, and would be considered a less useful combination of data if vegetative information is the goal.

Two or three data sources can be combined for visual analysis simply by assigning each source to a unique additive primary colour (red, green, or blue) and combining the colours using appropriate mixing algorithms. Thus, for example, by assigning TM channel 3 to red, TM channel 4 to green, and TM channel 5 to blue, the overall digital information content of the three images can be visualized by the generation of a combined RGB (red-green-blue) image. This RGB technique is said to produce a *composite* image from the three source images; the colour of any given pixel in a colour-composite RGB image is a function of the absolute and relative values of the three source images. RGB compositing is not only useful for visualizing combined image datasets produced by a single sensor, but it can also be used to fuse data generated by different sensors. For example, Costa *et al.* (1998) used RGB compositing techniques to combine JERS-1 (L-band) radar data with that produced by the

Radarsat-1 sensor (beam modes *S1* and *S7*), to better visualize the distribution of land-cover classes in a floodplain habitat. Lynne and Taylor (1986) used RGB compositing to fuse a SIR-B radar image with Landsat images for the mapping of regional geological structures and sedimentary lithological units in central Australia. The full information content of an RGB image can only be recognized with an intuitive understanding of how primary colours mix (Madon *et al.*, 1999).

The arithmetic and RGB composite methods can be used together when more than three data sources must be combined for visual analysis. The studies of, e.g., Glikson and Creasey (1995) and Macias (1995) showed that useful lithological information can be derived by combining arithmetically-combined TM images using the RGB composite technique. The RGB fusion of three images produced by arithmetic combination resulted in the generation of final images that were useful in the mapping of igneous and metamorphic lithologies, when interpreted with reference to ground-truth information. Other examples of the successful combination of imagery using image arithmetic and RGB compositing techniques are given by El Rakaiby (1995), Abdelhamid and Rabba (1994), and Van der Meer *et al.* (1995). Examples of the use of the results of principle components analysis and decorrelation stretching (Richards, 1993) as inputs to the RGB colour compositing procedure for visualizing geological information in digital images are given by, e.g., Lynne and Taylor (1986), Abrams *et al.* (1988), Pontual (1989), Qari (1992), and Ernst and Paylor (1996).

2.5.2 The Intensity-Hue-Saturation Transform

The RGB (red, green, and blue) primary colour system is only one of many colour

systems that may be used to visualize digital images. The *intensity-saturation-hue* (IHS) colour system is based on the three parameters of intensity, saturation, and hue. *Intensity* is a measure of the total energy or brightness of an object (analogous to "albedo"), *hue* is a measure of the average wavelength of colour present (e.g., blue, green, yellow, and orange are four hues), and *saturation* can be thought of as a measure of the purity of the colour (i.e., the width about the average wavelength of the spectral region in which much of the light is reflected from an object; if light of only a "single" wavelength is reflected, then the light is "spectrally pure", or "completely saturated") (Gillespie, 1980, pp. 203-205; Harris, 1994).

A common fusion technique that employs the IHS colour system involves: 1) the combination of three images using the RGB composite method described above (these images are typically optical images), 2) the conversion of the RGB database to the IHS format (i.e., the conversion from three primary-colour images to three equivalent images representing intensity, hue, and saturation), 3) the replacement of the intensity image by a fourth image (often a radar image or geophysical dataset), and 4) the conversion of the augmented IHS database back to RGB format for final display (e.g., Rheault *et al.*, 1991; Harris *et al.*, 1994; Mustard, 1994; Saint-Jean *et al.*, 1995; Paradella *et al.*, 1998). The value of the technique is that the general colour relations evident in the RGB database are generally preserved but are augmented somewhat with regard to colour intensity by the values in the fourth image. Madon *et al.* (1999) compared the IHS transform with image arithmetic and RGB fusion methods using airborne radar and magnetics data, and found that the IHS transform produced a superior product. A description of the mathematical foundations of the IHS transform may be found in Gillespie (1980). The IHS transform is widely supported by remote-sensing

software packages.

2.5.3 Unsupervised Classification

Image classification involves the conversion of a (frequently) multi-channel image database into a single-channel thematic map in which image values represent a "decision assigning a pixel to a group" (Gillespie, 1980, p. 188). Unsupervised classification involves the use of statistical clustering techniques (e.g., Richards, 1993, pp. 229-243) to segment pixel locations in terms of unknown classes, based on similarities in spectral characteristics. The clustering (i.e., grouping) of pixels in multispectral space involves quantifying the similarity between pixel values using some kind of similarity measure. The most frequently encountered clustering algorithms are based on calculation of Euclidean distance (or a variation on this kind of measure), using some kind of quality indicator (e.g., the sum of squared error, which computes the commulative distance of each pattern from its cluster centre for each cluster individually, and then sums these measures over all clusters) to fine-tune clustering operations to some pre-specified level (Richards, 1993, p.230). Once clustered, pixel locations are assigned symbols (e.g., colours) which denote membership to particular spectral classes; this produces a map of surface cover for the area of interest. The analyst is responsible for determining the appropriate labels of classes generated in the clustering procedure, based on information about real-world materials exposed at the surface in the area of interest. Clustering operations are termed "unsupervised" because the analyst does not participate directly in the grouping of image data.

2.5.4 Supervised Classification

The application of the maximum likelihood, evidential reasoning, and feedforward backpropagation neural network algorithms (i.e., three of the algorithms examined in this research - see Chapter 3) in image classification involves the methodology of *supervised classification*. In supervised classification, the desire of the image analyst is to derive a classified image based on 1) a database of relevant source imagery, and 2) a collection of representative ground-truth information.

In supervised classification, data corresponding to a proportion of ground-truth locations (pixels) are submitted to the classifier as *training locations* or *training pixels*, such that each class is represented by a selection of pixels whose associated database values collectively characterize the class. Classification of the entire image is performed based on the numerical properties of this training data. That is, the *class label* (or simply the *label*) that is assigned to any given pixel location within a database during classification will be based on a comparison between the numerical properties of that location and the numerical properties in the training data set that correspond to each of the classes represented in the study.

In geological study, image classification is most often used for the classification of optical imagery (e.g., Evans, 1988; Abarca-Hernández and Chica-Olmo, 1999; Thakur and Dikshit, 1997), although it is sometimes used to fuse optical imagery with radar imagery (e.g., Evans, 1988; Haack *et al.*, 2000). Visual analysis of radar imagery is usually preferable to the use of per-pixel image classification algorithms, due to factors such as radar speckle (Rudant *et al.*, 1994; Costa *et al.*, 1998; Shimabukuro *et al.*, 1998).

Although image classification can be a useful and much less subjective alternative to techniques that depend on visual analysis (Schetselaar, 1994), some workers contend that interpretation accuracy associated with visual analysis can be superior to that of classification since the image interpreter can use additional visual cues such as size, shape, pattern, and context, which are often not taken into account in per-pixel classification (Costa *et al.*, 1998). Rivard (1996) suggests that classification techniques (as well as other complex computer-based techniques) are inferior to less sophisticated visual image analysis methods, and that classification techniques in fact act as an barrier to the wider use of remote sensing, since they are more publicized and more fashionable but require expensive machines, software, and expertise if they are to be used.

2.5.4.1 Evaluating Classification Results

The success of a classification can be determined qualitatively by visual comparison between the classified image and known information regarding the spatial distribution of particular classes. A quantitative estimate of general classification success is typically made to supplement the qualitative evaluation, by comparing predicted class labels with known class labels for specific locations in the database whose properties are known from field data or other information. The locations (pixels) used in this process are called *test locations* or *test pixels*. Usually, test pixels are separate and distinct from the pixels used to train the classifier. The use of a proportion of a ground-truth database for training a classifier and the remainder of the database for evaluating classification results is called *cross-validation*.

In the simplest quantitative evaluations of classified imagery, the percentage of test

pixels classified correctly are examined for each land-cover class, as well as for the test-pixel database as a whole (thus, for example, the results of the classification of test pixels using this simple evaluation scheme might be compiled as follows: Class A: 67%, Class B: 89%, Class C: 78%, All Test Pixels: 82%). Such an evaluation does not provide a great deal of information on the nature of classification errors, but provides information on overall classification success.

More revealing analyses of classification results can be made by constructing a *confusion matrix* from the results of test-pixel classifications (e.g., Richards, 1993; Lillesand and Kiefer, 1994). A confusion matrix (sometimes called an *error matrix* or *contingency table*) is constructed by defining a table whose columns are assigned to groups of pixels that are known belong to particular surface-cover classes, and whose rows are assigned to predicted surface-cover classes (Table 2.5). All non-diagonal elements of the confusion matrix represent errors of omission and commission, and thus provide information on which classes have been confused with each other (e.g., Richards, 1993).

Classification results are commonly also given in the form of the Kappa (*KHAT*) statistic, which is a measure of the percentage of test pixels correctly classified beyond that expected by chance alone (e.g., Lillesand and Kiefer, 1994; Kalkhan *et al.*, 1997). The Kappa statistic is computed using the following:

$$\kappa = \frac{N\sum_{i=1}^{r} x_{ii} - \sum_{i=1}^{r} (x_{i+} \cdot x_{+i})}{N^2 - \sum_{i=1}^{r} (x_{i+} \cdot x_{+i})} \qquad (2.5)$$

Table 2.5 Example of an error matrix, based on three hypothetical classes and calculated using a database of 49 test pixels. All test pixels known to belong to "Class A" are placed in the column labelled "Known Class A"; pixels in this column are tabulated by row, depending on which class they were assigned during classification. The test pixels known to belong to the remaining classes are compiled in the same manner. Non-diagonal elements in the matrix provide specific information on errors of omission and commission; total proportional error within a column is termed "total error of omission" (E.Omission), and total proportional error within a row is termed "total error of commission" (E.Commission) (e.g., Richards, 1993; Lillesand and Kiefer, 1994).

	Known Class A	Known Class B	Known Class C	Total	E.Commission
Predicted A	10	4	0	14	0.2857
Predicted B	5	20	0	25	0.2500
Predicted C	0	1	9	10	0.1000
Total	15	25	9	49	
E.Omission	0.3333	0.2500	0.0000		0.7959

where r is the number of rows in the matrix, x_{ii} is the number of observations in row i and column i (on the major diagonal), x_{i+} is the total of observations in row i (shown as marginal total to right of the matrix), x_{+i} is the total of observations in column i (shown as marginal total at bottom of the matrix), and N is the total number of observations included in the matrix (Bishop *et al.*, 1975).

If the agreement is perfect between predicted and actual test-pixel classes, the Kappa value will be 1. The Kappa value will be zero if the observed agreement equals chance agreement (Cohen, 1960). Positive Kappa values between 0 and 1 occur from greater than chance agreement, and negative Kappa values occur from less than chance agreement (Skidmore and Turner, 1989).

2.5.5 Spectral Mixture Modelling

The spectral mixture modelling technique is an alternative to supervised classification that, although not tested in this research, is widely used in geological remote sensing (e.g., Mustard and Pieters, 1987; Gillespie *et al.*, 1990; Gillespie, 1992; Adams *et al.*, 1993; Mustard, 1994; Brown *et al.*, 2000). The spectral mixture modelling technique recognizes that the image values associated with individual pixel locations are a function of the reflectance properties of the different sub-classes of material present within those pixels (that is, the reflectance properties of, e.g., a "grassland" pixel are a function of the spectral properties of the different materials present within the geographic bounds of that pixel, including, e.g., green vegetation, water, rocks, and soil). Whereas supervised classification produces a single classified image based on pre-defined pixel-scale classes, the spectral mixture modelling technique produces a *fraction image* for each of a set of pre-defined *spectral end members*. The fraction image for a given spectral end member provides information on the proportion of the area of each pixel that is associated that end member. Fraction images are generated from input images using specialized algorithms that make assumptions regarding the manner in which end-member spectra are mixed (e.g., linear versus non-linear mixing). Although the method has several practical weaknesses (e.g., if there are M images available, only $M+1$ spectral end members may be defined), it remains a viable and promising alternative to the method of supervised classification.

2.6 Chapter Summary

Terrestrial remote sensing is most often conducted in the visible, infrared, and

microwave portions of the spectrum. Optical (visible and infrared) remote sensing may be used to discriminate between different lithologies based on their differences in surface chemistry. In practice, spectral differences between rock types can be subtle, necessitating the use of remote sensing imagery with very high spectral resolution if lithologies are to be separated. Lithological discrimination using optical imagery is often complicated by factors such as vegetation cover and chemical weathering. Radar imagery can be acquired under all lighting conditions, and under virtually all atmospheric conditions. Radar imagery, which is sensitive to topographic, surface roughness, and moisture parameters, may be used to map lithology in cases in which there is a good correlation between these parameters and lithology.

The Landsat TM imaging system is an across-track scanner that images the Earth's surface in seven broad channels in the visible and infrared. TM imagery has been widely used by the remote sensing community for over 15 years, and remains a standard against which new types of optical imagery may be measured. Radarsat SAR imagery is produced by a single C-band sensor with HH polarization. Although developed for mapping ice in the Canadian Arctic, Radarsat imagery is currently used for a variety of purposes, including the mapping of lithology and geological structure. The IKONOS imaging system is an along-track scanner that images the Earth's surface using four multispectral channels in the visible and near-infrared. The IKONOS system can also image the Earth's surface using a panchromatic channel that images in the visible to near-infrared. IKONOS imagery first became available to consumers in 2000, and has a spatial resolution (4 m multispectral; 1 m panchromatic) that is superior to that of all other commercial image types generated from orbit.

There are numerous techniques which may be used to combine satellite images to produce new information. Methods such as image arithmetic, RGB compositing, and the IHS transform are typically used to combine images for visual analysis. Techniques such as image classification and spectral mixture modelling may be used to map the spatial distribution of individual classes and spectral end-members, respectively.

3 ALGORITHMS FOR IMAGE CLASSIFICATION

3.1 Introduction

This chapter focuses on the maximum likelihood, evidential reasoning, and neural network classification algorithms (Sections 3.2, 3.3, and 3.4, respectively), which were tested in this study with regard to their utility in lithological discrimination (Chapters 5 and 6). Although none of these three algorithms is new to the remote sensing field, only the maximum likelihood classifier is widely used for image classification (although the use of various supervised and unsupervised neural network classifiers is becoming increasingly common). The utility of the evidential reasoning and neural network algorithms in image classification for lithological discrimination is promising but not yet clear. Complicating the use of these algorithms are the numerous parameters that must be set prior to classification. As a result, there is much experimentation to be done to determine exactly how these algorithms should be used in practice. Further, there are opportunities for the improvement in the methodologies used in the employment of these algorithms, and for changes in the nature of the algorithms themselves for optimized performance.

3.2 The Gaussian Maximum Likelihood Algorithm

The maximum likelihood classifier is the most commonly used supervised classification algorithm in the remote sensing field (Richards, 1993). The algorithm is based on the assignment of conditional probabilities to each class involved in a classification. In the classification of a pixel location, the assigned class is that which is associated with the highest probability. In the most commonly employed version of the classifier, probability distributions

are parameterized from training data using multivariate normal models [i.e., the model for a particular class is defined entirely by the mean vector and the covariance matrix of the training data - see Richards (1993, pp. 182-186)]. An example of the parameterization of frequency histograms by univariate normal models is given in Figure 3.1.

The multivariate maximum likelihood algorithm (which, as used in this research, assumes equal prior probabilities and uses a Gaussian distribution function) is given as:

$$\boldsymbol{x} \in \omega_i \text{ if } g_i(\boldsymbol{x}) > g_j(\boldsymbol{x}) \text{ for all } j \neq i \tag{3.1a}$$

where

$$g_i(\boldsymbol{x}) = -\ln|\Sigma_i| - (\boldsymbol{x}-\boldsymbol{m}_i)^t \, \Sigma_i^{-1} (\boldsymbol{x}-\boldsymbol{m}_i) \tag{3.1b}$$

where ln is the natural logarithm, $\mathbf{x}$ is the position of the pixel in question, $\mathbf{m}$ is the mean vector of the data in class ω_i, and Σ_i is the covariance matrix of the data in class ω_i (Richards, 1993, pp.184 and 319; Bishop, 1995a, pp.34-39).

When training data can be approximately parameterized using normal models, the Gaussian maximum likelihood classifier (hereafter refered to simply as the "maximum likelihood classifier") will often produce very good results. However, the results of classifications can be poor when training-data frequency histograms are characterized by relatively complex (e.g., distinctly non-Gaussian) distributions (e.g., Peddle, 1995; Voudouri-Maniati, 1997). Spatial variations in vegetation cover or in the weathering state of rocks can potentially cause individual geological classes to be characterized by complex frequency

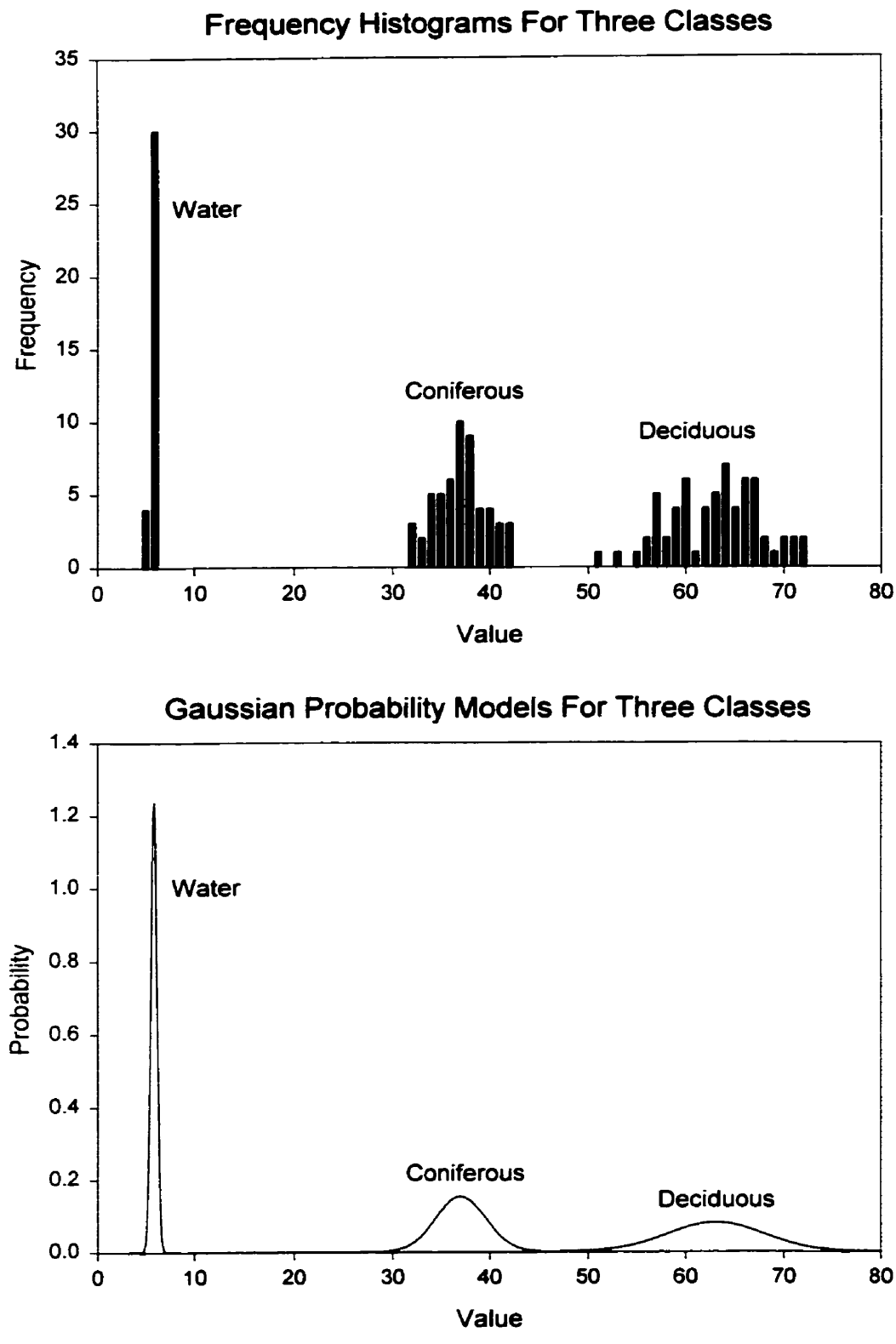

Figure 3.1 Gaussian parameterization of training data for three classes (water, coniferous vegetation, and deciduous vegetation).

histograms, sometimes necessitating the subdivision of a class into subclasses whose frequency distributions can be more closely modelled by Gaussian distributions. Because the evidential reasoning and neural network algorithms do not parameterize training-data histograms with simple unimodal functions, they are potentially useful alternatives to the maximum likelihood classifier for the classification of satellite imagery (e.g., Peddle, 1995).

3.3 The Evidential Reasoning Algorithm

The mathematical theory of evidence was first outlined by Shafer (1976), based on the Rule of Combination formulated by Dempster (1967). The evidential reasoning algorithm as applied to the classification of remote sensing imagery is based upon the derivation of a *mass of evidence* for a given set of all-encompassing class propositions, for a given source. The combination of evidence from more than one source is performed through the employment of *Dempster's orthogonal sum* (Section 3.3.1). The evidential reasoning algorithm does not make statistical assumptions of probability distributions as the maximum likelihood classifier does (Section 3.2). Rather, the algorithm treats signature data in such a way that the main features of relatively complex frequency histograms can be faithfully modelled. All information types (nominal, ordinal, interval, and ratio) are valid for use as classification sources (Peddle, 1991, 1995), and thus evidential reasoning can handle both satellite imagery (ratio and continuous data) values and values corresponding to such discrete and thematic sources as land cover and surface geology (nominal and discontinuous data). Evidential reasoning's flexible capabilities for handling thematic data and complex signature distributions makes it a useful algorithm for classification and data fusion (e.g., Moon, 1990, 1993; Wang

and Civco, 1994), and a potential alternative to the commonly-used maximum likelihood algorithm (Peddle, 1991, 1993, 1995; Peddle *et al.*, 1994; Leverington and Duguay, 1996a; Duguay and Peddle, 1996).

3.3.1 Evidence Generation and Combination

Although the method for orthogonal summation of evidence is well established, methods for generating initial evidence measures are not. Moon (1990,1993) has noted that methods commonly available for evidence generation are sometimes subjective. Peddle (1991, 1995) has responded to this situation by developing a simple method for evidence generation that is both intuitive and that can be universally applied. This method was used to produce the results presented in Chapter 5, and is described as follows: When only a single source is involved, evidence for a particular class proposition is simply given as the proportion of the total signature data corresponding to that class that has a value equal to the test pixel value. If the total of all individual class proportions does not exceed 1, the difference between the total and 1 is allocated to the set of all possible classes (θ). The mass allocated to θ may be thought of as being associated with uncertainty. If the total of the class proportions exceeds 1, the proportions are normalized to unity and the set of all possible classes (θ) is allocated zero evidence. In the language of evidential reasoning, the sum of evidential mass assigned to a particular class proposition is called the *support*, while one-minus the total support of any contradictory class propositions is called *plausibility* (Richards, 1993). In a single-source evidential reasoning classification, the class label whose associated evidence is greatest is assigned to the pixel in question [this kind of rule is sometimes referred to as a

"maximum support decision rule" (Richards, 1993); although such a rule is a natural choice for classification purposes, a rule that compares not only support but also plausibility could also be employed (e.g., Lee *et al.*, 1987)].

A simple illustration of the practical generation of evidence from signature data can be helpful in understanding evidential reasoning as applied in this project. Imagine that a test pixel is associated with a value of 27 in a classification based on a single source (e.g., a single satellite image channel). Now imagine that the classifier must decide which of three hypothetical classes this pixel likely belongs to: class *A*, *B*., or *C*. The classifier must base this decision on a comparison between the pixel value and the signature values associated with each class. The proportion of class *A*'s signature data that equals 27 might be 4%, while *B* and *C*'s proportions might be 0.2% and 19%, respectively. In this hypothetical case, a class labelling of *C* would be made, since *C* has the highest evidential mass assigned to it (Leverington, 1995). In classifications involving two or more sources, evidence is first compiled for each source individually in the manner given above. Evidence is then combined source by source through the application of Dempster's orthogonal sum, which is both a commutative and associative procedure and thus can be applied in any order (Richards, 1993).

The manner in which the orthogonal sum is used to combine evidence is depicted in Figure 3.2. The orthogonal sum is visualized by first constructing a unit square. This square is divided vertically in proportion to the evidential mass distribution of one source, and horizontally in proportion to the mass distribution of the other source. A number of rectangles are formed as a result of this division of the unit square, and the areas of these rectangles are used to determine the evidential mass associated with any particular class (or

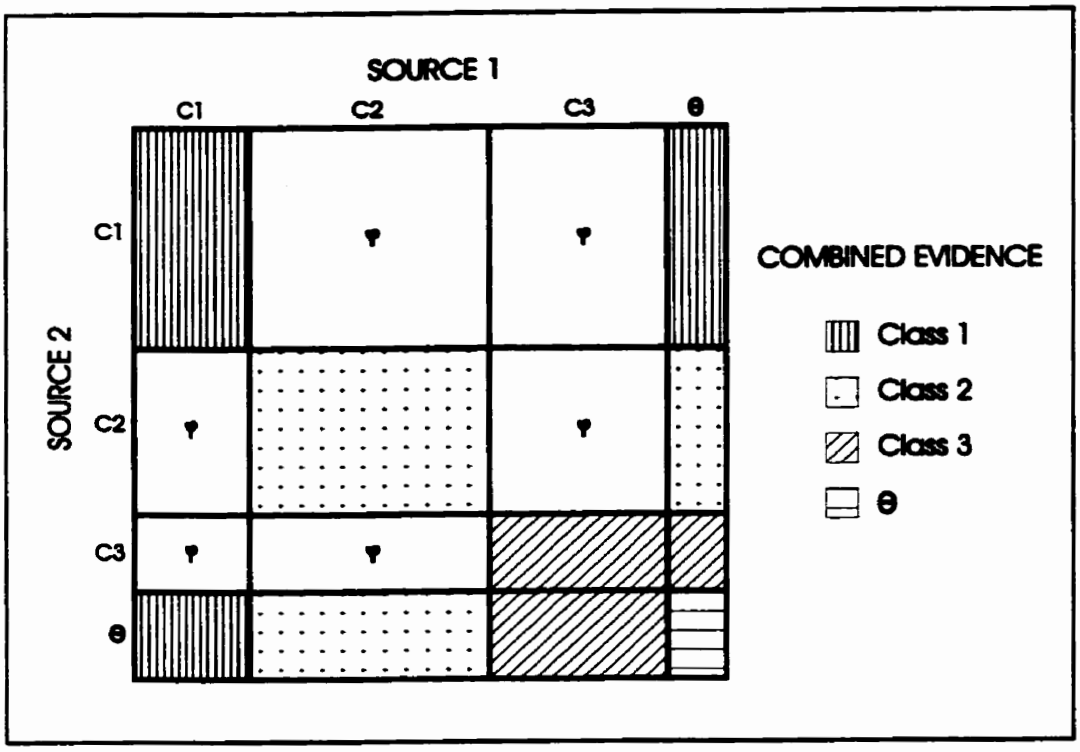

Figure 3.2 Illustration of the orthogonal sum. The orthogonal sum is used for merging evidence from two data sources (after Richards, 1993).

with uncertainty, θ). The evidential mass (i.e., the proportion of the area of the unit square) that is assigned to any given class is equal to the sum of three rectangles: the rectangle formed by the product of each source's mass associated with the class, and the two rectangles formed by the product of one source's mass associated with the class and the mass associated with the other source's uncertainty (θ) (see Figure 3.2). The remaining uncertainty after the combination of evidence from both sources is equal to the area of the rectangle formed from the product of masses attributed to uncertainty (θ) in both sources. Evidence values for each source and for θ are normalized by dividing evidence values by the sum of the areas of all rectangles that are not contradictory (Richards, 1993). The areas of all rectangles that are contradictory are not considered in the calculation of evidence, and are designated as φ in Figure 3.2 (with φ representing the *null set*).

The decision rule used for evidential reasoning classifications executed in this research is very simple: the class which is assigned the maximum evidence after orthogonal summation of all sources is the class label assigned to the pixel location being classified (this is the "maximum support decision rule" noted above for the single-source case).

The decision rule and geometric description for the application of the orthogonal sum (as given above) can also be expressed algebraically. Given pixel position **x**, and classes A_n, the decision rule for two sources is given as follows:

$$\mathbf{x} \in A_n \text{ if } m(A_n) > m(A_p) \text{ for all } p \neq n \qquad (3.2a)$$

The orthogonal sum equation to determine the new mass m^1 assigned to the n^{th} labelling proposition of A can be written as:

$$m^1(A_n) = K^{-1} \sum m_1(A_i)\, m_2(A_j) \qquad (3.2b)$$

$$A_i \cap A_j = A_n$$

$$K = 1 - \sum m_1(A_i)\, m_2(A_j) \qquad (3.2c)$$

$$A_i \cap A_j = \varphi$$

where m_1 and m_2 represent two mass distributions, and φ is the null set (Richards 1993).

Equation 3.2 simply states that pixel **x** is a member of class A_n if the evidence for that proposition is greater than the evidence for any other class proposition. Equation 3.2b states that, in the application of the orthogonal sum, the new mass (m^1) assigned to a particular class proposition equals the product of a normalizing factor (1 over a normalizing value K) with the sum of all relevant products produced in the multiplication of the two mass distributions (where "relevant" means those products that involve class A_n in both A_i and A_j; note that evidence attributed to uncertainty (θ) also involves class A_n, and is included in consideration here). Equation 3.2c describes the normalizing value (K) as being 1 minus the sum of all non-constructive products (i.e., the products assigned to the null set, φ, in Figure 3.2). Equation 3.2c is equivalent to summing all constructive products; the value produced by this equation is used in Equation 3.2b to normalize evidence.

3.3.2 Evidence Interpolation and Extrapolation

Training data belonging to a continuous data type (such as satellite imagery) cannot normally be input to the evidential reasoning algorithm directly. Rather, this type of training data must first be interpolated and extrapolated using an *evidence propagation function* (Peddle, 1991, 1995). Failure to perform this step may result in poor results (especially when

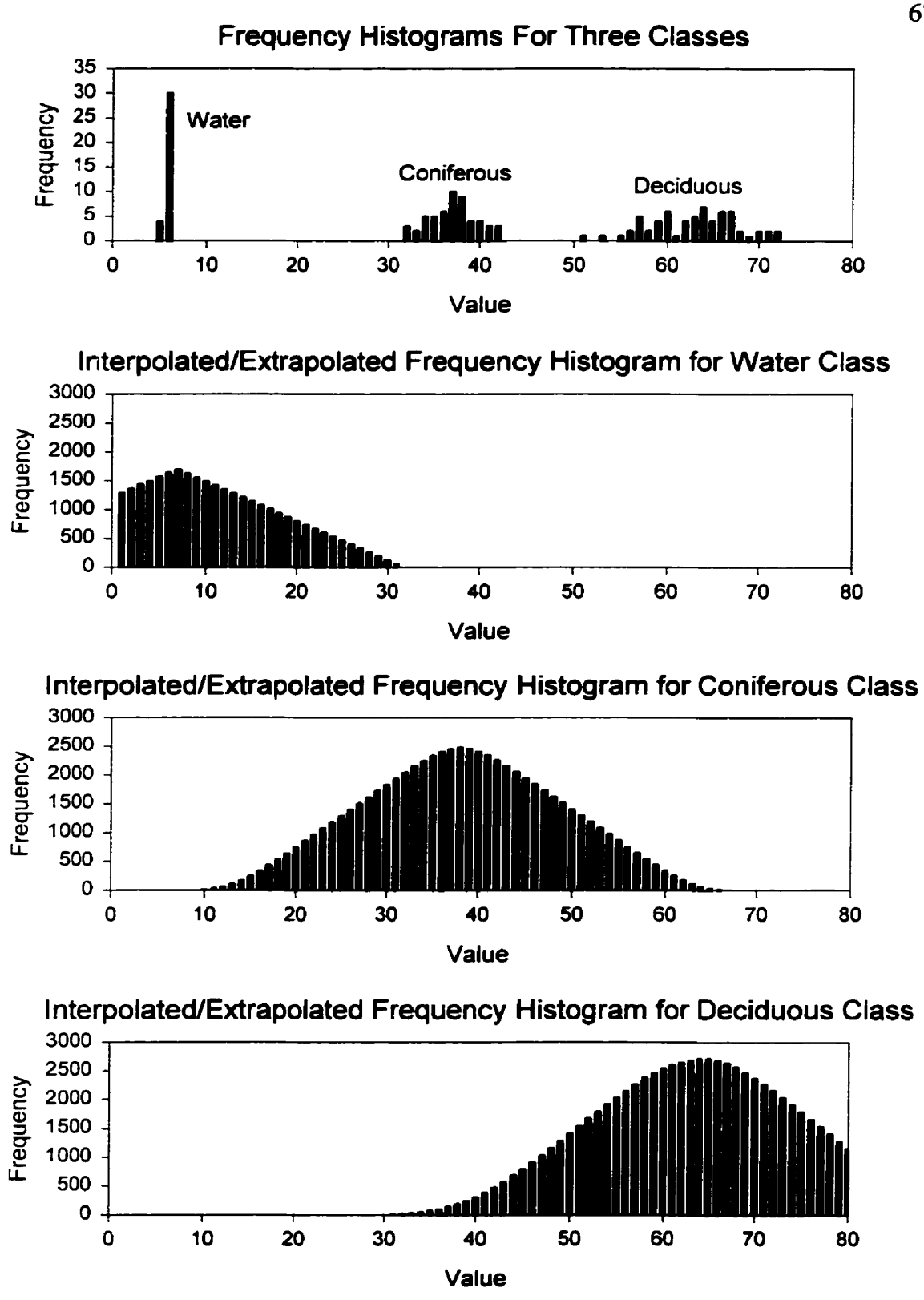

Figure 3.3 Interpolation and extrapolation of training data for three classes.

training databases are small) since the evidence for all values not represented in the original training data will otherwise be zero (given that their frequency of occurrence in the original training data sets is zero). The use of an evidence propagation function allows values proximal to original training values to be represented (Figure 3.3).

A simple evidence propagation function that uses linear decay has been found to be effective for evidence propagation (Peddle, 1991, 1995), although a wide range of functions could conceivably be useful in this regard. The general method of evidence propagation involves the definition of a *bin* that moves across all values represented in the training data set, extrapolating evidence from a central bin value to the surrounding bin values. The bin size must necessarily be an odd number, as it must be symmetrically centred upon a single data value. The bin moves across all values represented in the data set, adding to the frequency distribution of proximal values according to a predefined equation. Thus, for example, a bin with size 51 might be defined; such a bin will extrapolate the evidence of the central bin value to the 25 values on either side of the central bin value. When such a bin has moved across all possible values in a frequency histogram, all non-zero frequencies will have been extrapolated, producing a new training histogram (Figure 3.3). This method of extrapolation and interpolation of training data is more flexible than that used by the maximum likelihood algorithm to parameterize training data, since evidence propagation does not constrain the resulting data to fit to a simple unimodal function (Figure 3.4).

The specific evidence propagation function used in this project is summarized as follows: the frequency of occurrence of a given central data value i is first multiplied by a value (termed here the "extrapolation factor") equal to the chosen bin size, and then added

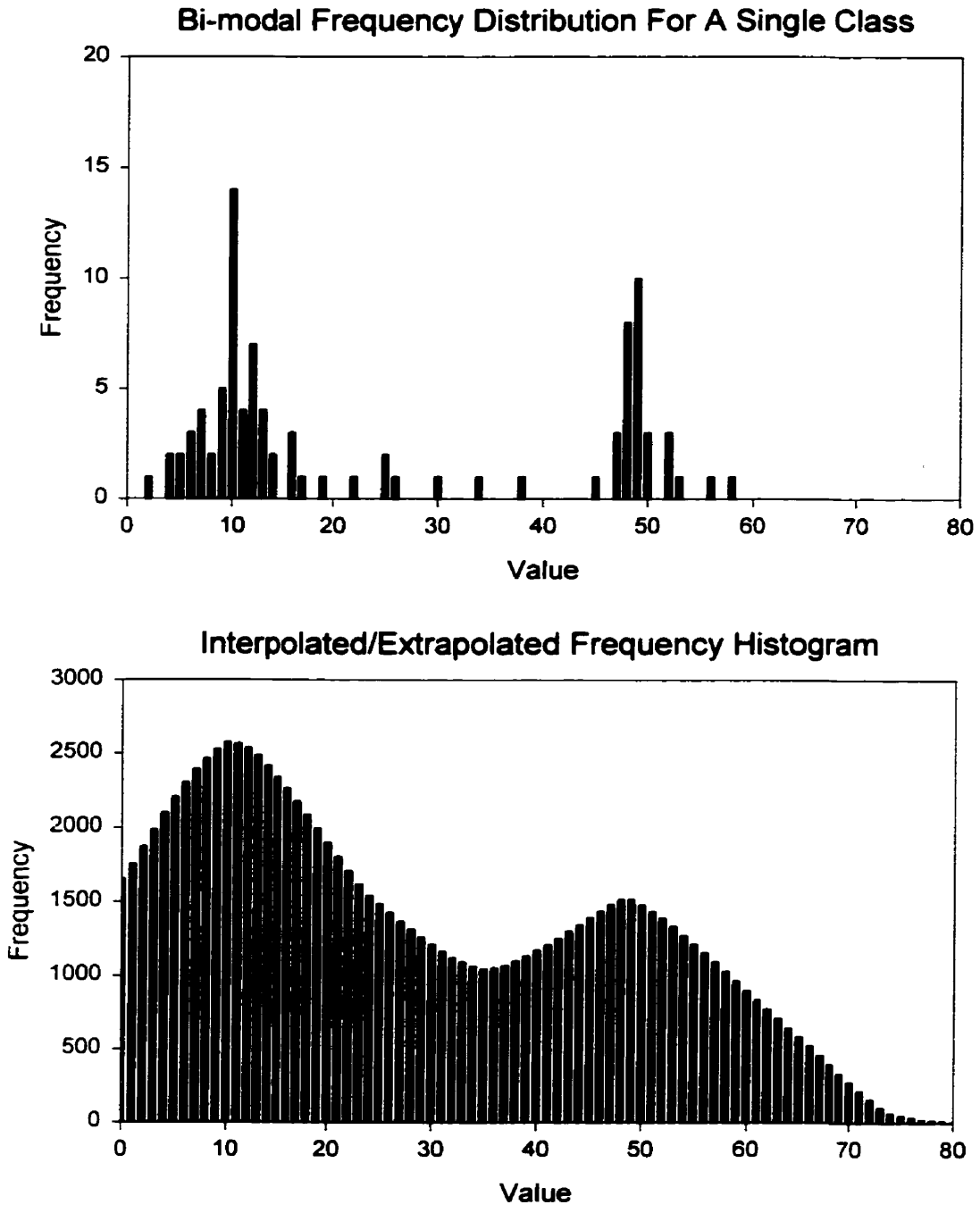

Figure 3.4 Interpolation and extrapolation of a bi-modal histogram distribution.

to the original frequency of occurrence of i. The extrapolation factor is then decremented by 2, multiplied by i, and added to the frequency of the adjacent values (i+1 and i-1); this operation is performed for all values within the bin, with the extrapolation factor gradually decreasing with increasing distance from the centre of the bin. A bin size of 51 ensures a sufficient level of evidence propagation for the treatment of continuous data sources such as those associated with satellite imagery. Peddle (1995) has found that large bins generally produce favourable classification results, and that a maximum bin size applicable to a given problem may not exist.

The generalized equation for the extrapolation process, for a given class, is given below. For training sample value i, with frequency of occurrence (of the central value) a, and bin size b, the signature frequency for value j belonging to class c is given as:

$$freq^{l}(j) = freq(j) + a\,(b\text{-}2(|i\text{-}j|)) \qquad (3.3)$$

where $freq$ designates the frequency of occurrence of a particular value j, $freq^{l}$ designates the new frequency of occurrence of j as a result of evidence propagation from value i, and where $|i\text{-}j| < b/2$ (i.e., where j lies within the bin) (Peddle, 1991). The frequencies of occurrence given in the unmodified signature data file are not changed until all modifications to all values are calculated (i.e., new frequencies are calculated based only on the original signature data).

When sources characterized by discrete data values (e.g., land cover classes) are used, evidence propagation should normally not be performed, since there is not necessarily any relation between adjacent values (i.e., the extrapolation of frequency values from one thematic class to adjacent thematic classes will in most cases be meaningless).

3.3.3 Evidential Reasoning Software Description

The evidential reasoning software is composed of one main program (*ER129FX.C*), and several smaller programs for histogram display and for the extrapolation and interpolation of signature files (Appendix C). All programs were written by the author in *C* based on the principles outlined by Richards (1993) and Peddle (1991, 1995), and are modified versions of the software used by Leverington and Duguay (1996a). The bin size employed in the software is 51, and the decision rule is based on maximum support.

3.4 The Feedforward Backpropagation Neural Network Algorithm

Although the long-term goal of the neural-network community remains the design of autonomous machine intelligence, the main modern application of neural networks is in the field of pattern recognition (Holmström *et al.*, 1997; Joshi *et al.*, 1997). In the sub-field of data classification, neural-network methods have been found to be useful alternatives to statistical techniques such as those which involve regression analysis or probability density estimation (Holmström *et al.*, 1997). The potential utility of neural networks in the classification of multisource satellite-imagery databases has been recognized for over a decade, and today neural networks are an established (though still relatively new) tool in the field of remote sensing. Although some practical drawbacks are associated with neural networks (e.g., relatively long training times), evidence of their strength in image classification continues to accumulate (e.g., Lee *et al.*, 1990; Benediktsson *et al.*, 1990; Bischof *et al.*, 1992; Heermann and Khazenie, 1992; An and Chung, 1994; Key, 1994; Peddle *et al.*, 1994; Chen *et al.*, 1995; Foody *et al.*, 1995; Gopal and Woodcock, 1996; Leverington and Duguay

1996a, 1996b, 1997; Bruzzone *et al.*, 1999; Jiminez *et al.*, 1999; Tian *et al.*, 1999; Zhou, 1999; Del Frate *et al.*, 2000).

3.4.1 Neural Network Basics

Neural networks are members of a family of computational architectures inspired by biological brains (McClelland *et al.*, 1986; Rich and Knight, 1991; Winston, 1991; Luger and Stubblefield, 1993). Such architectures are commonly called *connectionist* systems, being composed of interconnected and interacting components called *nodes* or *neurons* (these terms are considered synonyms in connectionist terminology, and are used interchangeably in this document). Neural networks are characterized by a lack of explicit representation of knowledge; there are no symbols or values that directly correspond to classes of interest. Rather, knowledge is implicitly represented in the patterns of interactions between network components (Lugar and Stubblefield, 1993). A graphical depiction of a typical feedforward neural network is given in Figure 3.5. The term "feedforward" indicates that the network has links that extend in only one direction. There are no backward links in a feedforward network; all links proceed from input nodes toward output nodes.

Individual nodes in a neural network emulate biological neurons by taking input data and performing simple operations on the data, selectively passing the results on to other neurons (Figure 3.6). The output of each node is called its *activation* (the terms *node values* and *activations* are used interchangeably here). *Weight values* are associated with each vector and node in the network, and these values constrain how input data (e.g., satellite image values) are related to output data (e.g., land-cover classes). Weight values associated

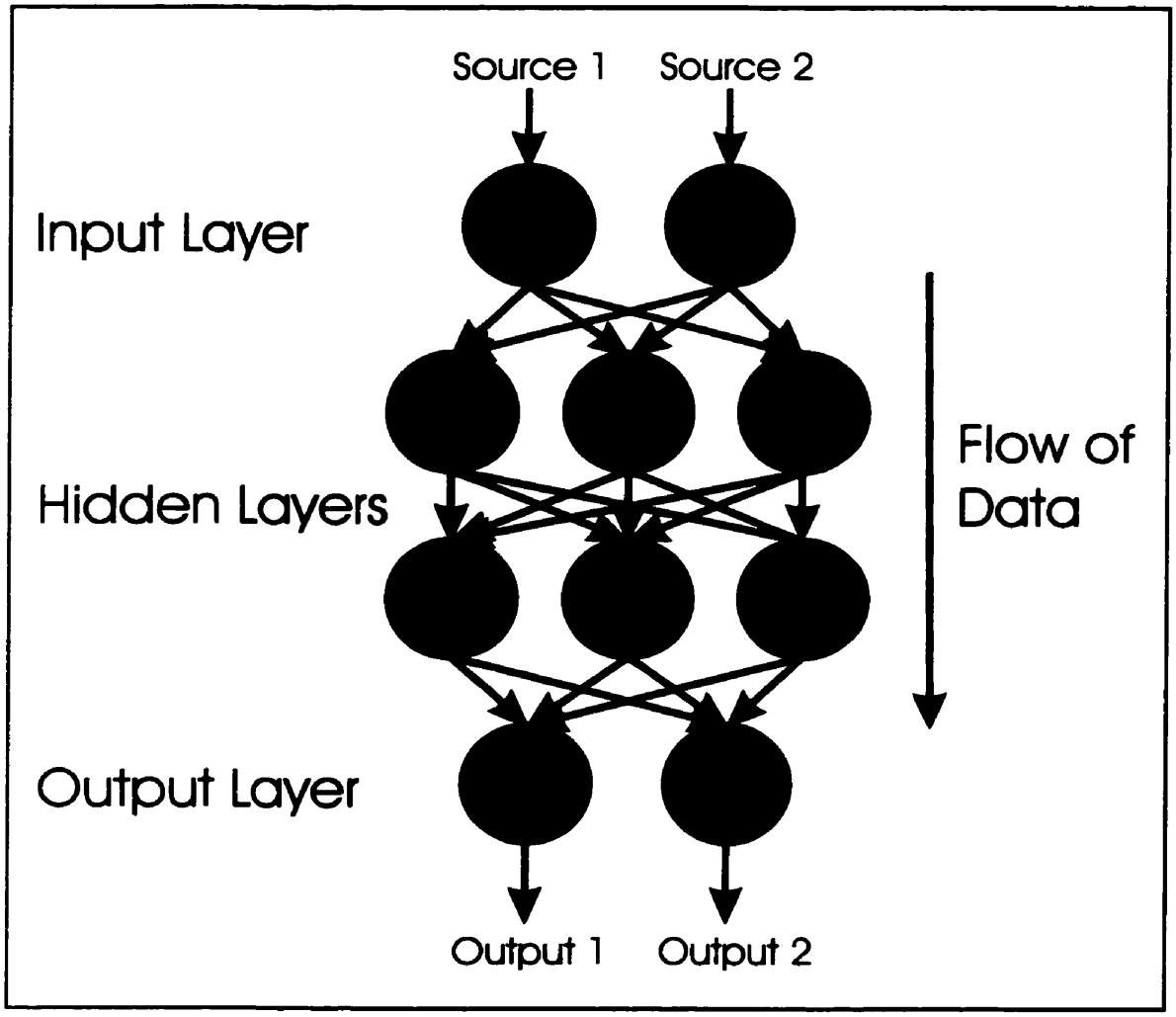

Figure 3.5 A typical feedforward neural network.

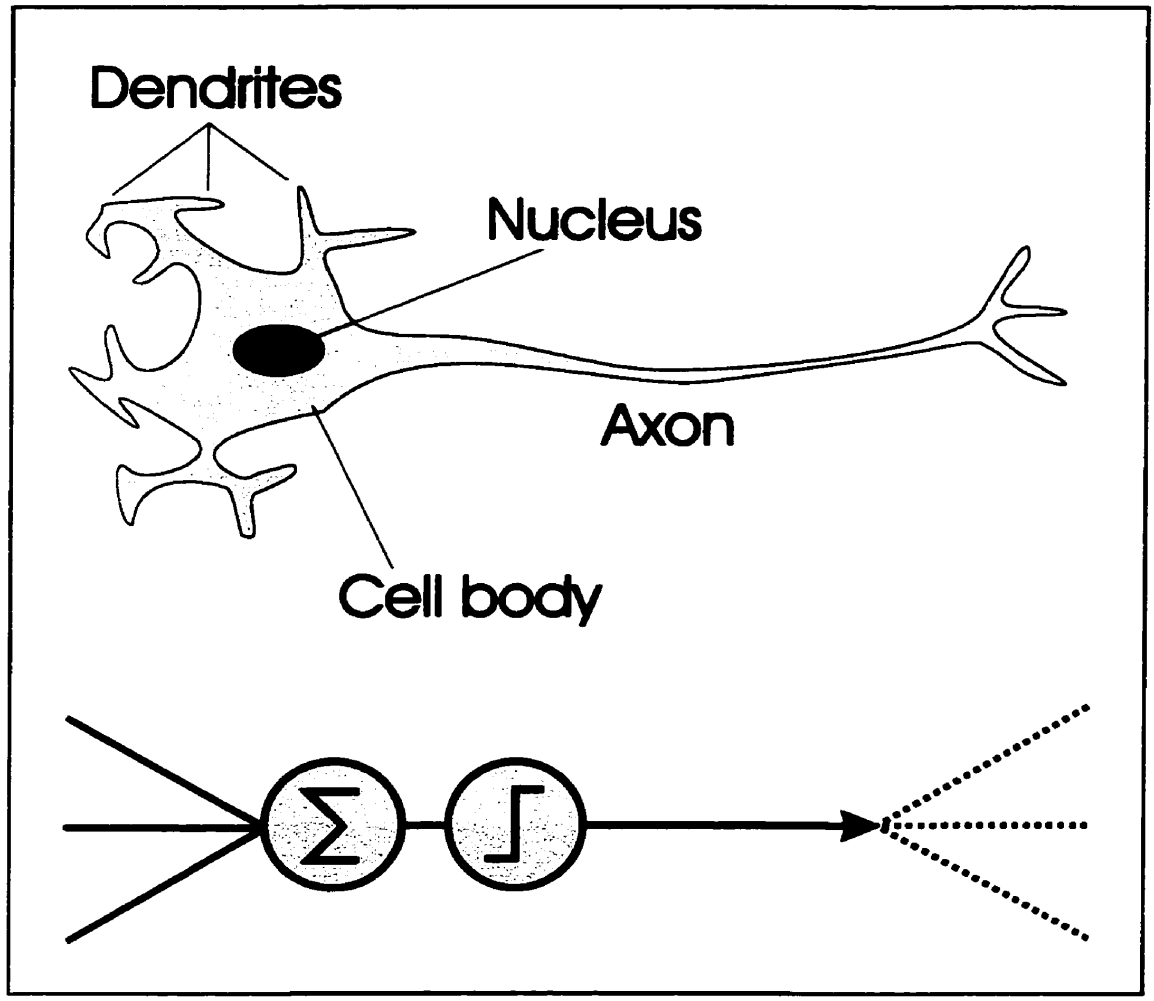

Figure 3.6 Schematic comparison between a biological neuron and an artificial neuron (after Winston, 1991; Rich and Knight, 1991). For the biological neuron, electrical signals from other neurons are conveyed to the cell body by dendrites; resultant electrical signals are sent along the axon to be distributed to other neurons. The operation of the artificial neuron is analogous to (though much simpler than) the operation of the biological neuron; activations from other neurons are summed at the neuron and passed through an activation function, after which the value is sent to other neurons.

with individual nodes are also known as *biases*. Weight values are determined by the iterative flow of training data through the network (i.e., weight values are established during a *training phase* in which the network learns how to identify particular classes by their typical input data characteristics). A more formal description of the foundations of multi-layer, feedforward, backpropagation neural networks is given in Section 3.4.5.

Once trained, the neural network can be applied toward the classification of new data. Classifications are performed by trained networks through 1) the activation of network input nodes by relevant data sources [these data sources must directly match those used in the training of the network], 2) the forward flow of this data through the network, and 3) the ultimate activation of the output nodes. The pattern of activation of the network's output nodes determines the outcome of each pixel's classification.

Useful summaries of neural network principles are given by Rumelhart *et al.* (1986), McClelland and Rumelhart (1988), Rich and Knight (1991), Winston (1991), Anzai (1992), Lugar and Stubblefield (1993), Gallant (1993), and Richards (1993). The remainder of this background section draws heavily on these summaries. A brief historical account of the development of connectionist theories is given in Gallant (1993).

3.4.2 McCulloch-Pitts Networks

Neural computing began with the development of the McCulloch-Pitts network in the 1940's (McCulloch and Pitts, 1943; Luger and Stubblefield, 1993). These simple connectionist networks, shown in Figure 3.7, are stand-alone "decision machines" that take a set of inputs, multiply these inputs by associated *weights*, and output a value based on the

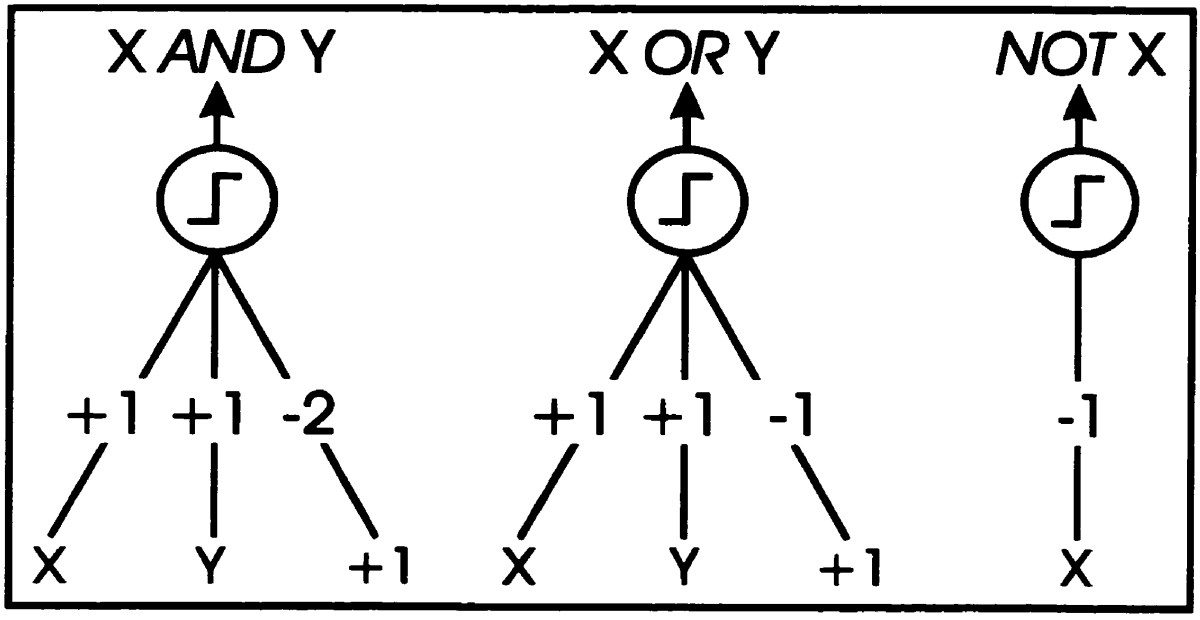

Figure 3.7 McCulloch-Pitts networks (after Luger and Stubblefield, 1993).

sum of these products. Input values (also known as input *activations*) are thus related to output values (output *activations*) by simple mathematical operations involving weights associated with network links.

McCulloch-Pitts networks are strictly binary; they take as input and produce as output only 0's or 1's. These 0's and 1's can be thought of as excitatory or inhibitory entities, respectively (Luger and Stubblefield, 1993). If the sum of the products of the inputs and their respective weights is greater than or equal to 0, the output node returns a 1 (otherwise, a 0 is returned). The value of 0 is thus a *threshold* that must be exceeded or equalled if the output of the system is to be 1. The above rule, which governs the manner in which an output node maps input values to output values, is known as an *activation function* (meaning that this function is used to determine the activation of the output node).

McCulloch-Pitts networks can be constructed to compute logical functions such as those depicted in Figure 3.4 (for example, in the "X AND Y" case, no combination of inputs can produce a sum of products that is greater than or equal to 0, except the combination X=Y=1). McCulloch-Pitts networks do not *learn*, and thus the weight values must be determined in advance using other mathematical or heuristic means. Nevertheless, these networks did much to inspire further research into connectionist models during the 1950's (Luger and Stubblefield, 1993).

3.4.3 Perceptrons

The development of a connectionist system capable of limited learning occurred in the late 1950's, when Rosenblatt created a system known as a *perceptron* (see Rosenblatt, 1962;

Luger and Stubblefield, 1993). Again, this system consists of binary activations (inputs and outputs) (see Figure 3.8). In common with the McCulloch-Pitts neuron described above, the perceptron's binary output is determined by summing the products of inputs and their respective weight values. In the perceptron implementation, a variable threshold value is used (whereas in the McCulloch-Pitts network, this threshold is fixed at 0): if the linear sum of the input/weight products is greater than a threshold value (θ), the output of the system is 1 (otherwise, a 0 is returned). The output unit is thus said to be, like the perceptron output unit, a *linear threshold unit*. To summarize, the perceptron "classifies" input values as either 1 or 0, according to the following rule, referred to as the *activation function*:

PERCEPTRON OUTPUT = 1 if (sum of products of inputs and weights) > θ (3.4)
(otherwise, PERCEPTRON OUTPUT = 0)

The perceptron is trained (i.e., the weights and threshold values are calculated) based on an *iterative training phase* involving training data. Training data is composed of a list of input values and their associated desired output values. In the training phase, the inputs and related outputs of the training data are repeatedly submitted to the perceptron. The perceptron calculates an output value for each set of input values. If the output of a particular training case is labelled 1 when it should be labelled 0, the threshold value (θ) is increased by 1, and all weight values associated with inputs of 1 are decreased by 1. The opposite is performed if the output of a training case is labelled 0 when it should be labelled 1. No changes are made to the threshold value or weights if a particular training case is correctly classified. This set of training rules is summarized as:

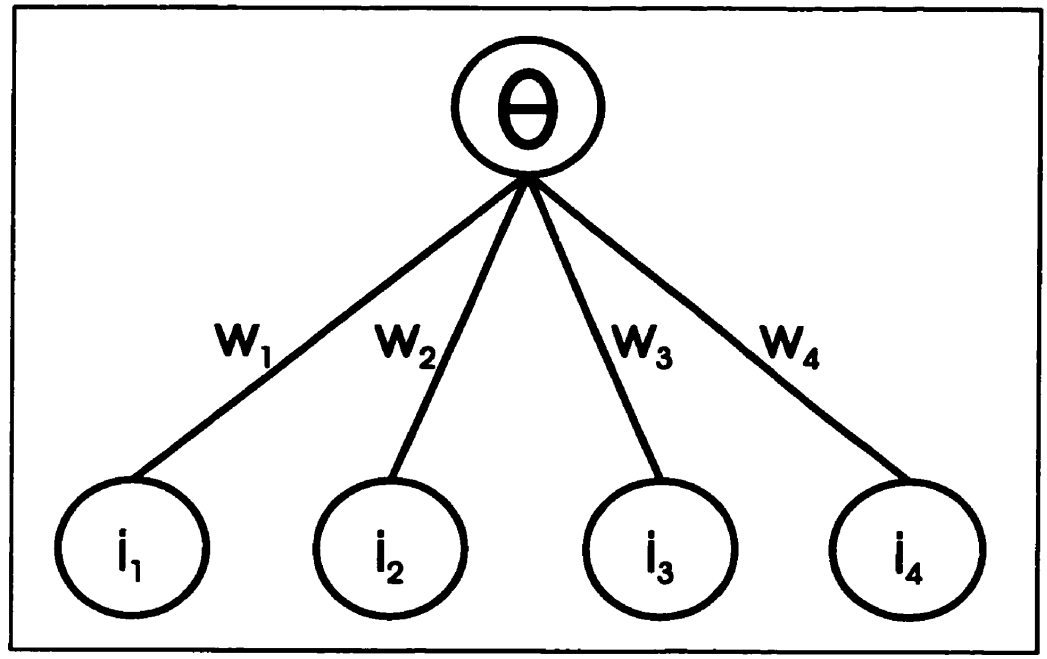

Figure 3.8 An example of a perceptron. The system consists of binary activations. Weights are identified by *w*'s, and inputs are identified by *i*'s. A variable threshold value (θ) is used at the output node.

If OUTPUT is correct, then no changes are made to the threshold or weights (3.5a)

If OUTPUT = 1, but *should* be 0 (3.5b)
then $\{\theta = \theta + 1\}$
and $\{weight_x = weight_x - 1, \text{ if } input_x = 1\}$

If OUTPUT = 0, but *should* be 1 (3.5c)
then $\{\theta = \theta - 1\}$
and $\{weight_x = weight_x + 1, \text{ if } input_x = 1\}$

where the subscript x refers to a particular input-node and weight pair. The effect of the above training rules is to make it less likely that a particular error will be made in subsequent training iterations. For example, in equation (3.5b), increasing the threshold value serves to make it less likely that the same sum of products will exceed the threshold in later training iterations, and thus makes it less likely that an output value of 1 will be produced when the same inputs are presented. Also, by modifying only those weights that are associated with input values of 1, only those weights that could have contributed to the error are changed (weights associated with input values of 0 are not considered to have contributed to error).

Once the network is trained, it can be used to classify new data sets whose input/output associations are similar to those that characterize the training data set. Thus, through an iterative training stage in which the weights and threshold gradually migrate to useful values (i.e., values that minimize or eliminate error), the perceptron can be said to "learn" how to solve simple problems.

3.4.4 The Delta Rule

The development of the perceptron was a large step toward the goal of creating useful connectionist networks capable of learning complex relations between inputs and outputs. In the late 1950's, the connectionist community understood that what was needed for the further development of connectionist models was a mathematically-derived (and thus potentially more flexible and powerful) rule for learning. By the early 1960's, the Delta Rule [also known as the Widrow and Hoff learning rule or the least mean square (LMS) rule] was invented (Widrow and Hoff, 1960). This rule is similar to the perceptron learning rule above (McClelland and Rumelhart, 1988), but is also characterized by a mathematical utility and elegance missing in the perceptron and other early learning rules.

The Delta Rule uses the difference between target activation (i.e., target output values) and obtained activation to drive learning. For reasons discussed below, the use of a threshold activation function (as used in both the McCulloch-Pitts network and the perceptron) is dropped; instead, a linear sum of products is used to calculate the activation of the output neuron (alternative activation functions can also be applied - see Section 3.4.5.2). Thus, the activation function in this case is called a *linear activation function*, in which the output node's activation is simply equal to the sum of the network's respective input/weight products. The strengths of network's connections (i.e., the values of the weights) are adjusted to reduce the difference between target and actual output activation (i.e., error). A graphical depiction of a simple two-layer network capable of employing the Delta Rule is given in Figure 3.9. Note that such a network is not limited to having only one output node.

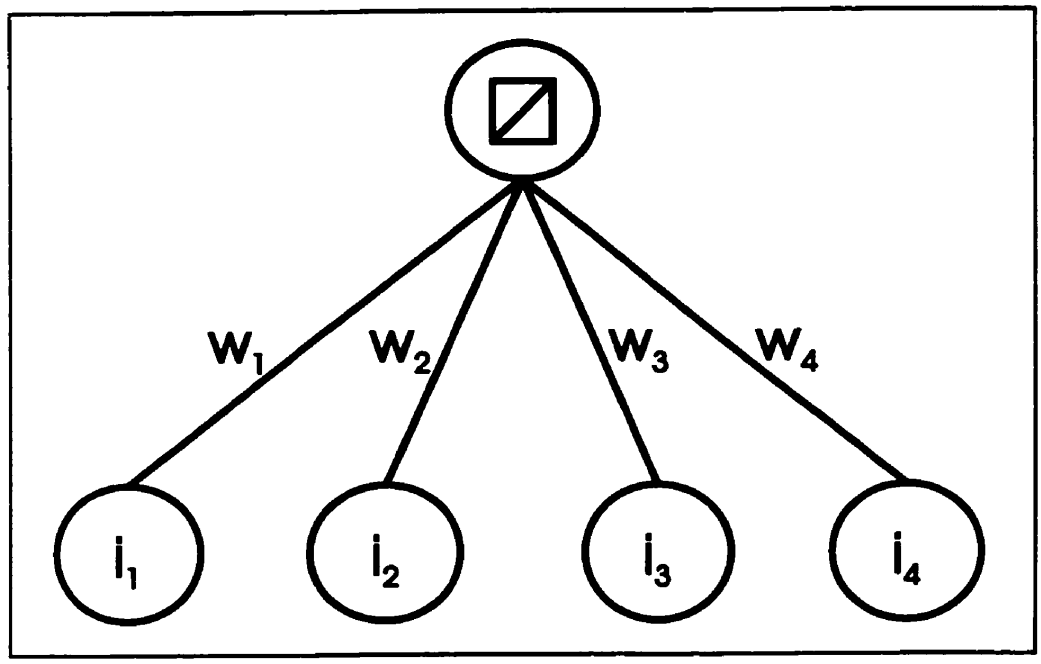

Figure 3.9 A network capable of implementing the Delta Rule. Non-binary values may be used. Weights are identified by *w*'s, and inputs are identified by *i*'s. A simple linear sum of products (⊠) is used as the activation function at the output node of the network shown here.

During forward propagation through a network, the output (activation) of a given node is a function of its inputs. The inputs to a node, which are simply the products of the output of preceding nodes with their associated weights, are summed and then passed through an activation function before being sent out from the node. Thus, we have the following:

$$S_j = \sum_i w_{ij} a_i \qquad 3.6a$$

and

$$a_j = f(S_j) \qquad 3.6b$$

where S_j is the sum of all relevant products of weights and outputs from the previous layer i, w_{ij} represents the relevant weights connecting layer i with layer j, a represents the activations of the nodes in the previous layer i, a_j is the activation of the node at hand, and f is the activation function.

For any given set of input data and weights, there will be an associated magnitude of error, which is measured by an *error function* (also known as a *cost function*) (Figure 3.10) (e.g., Oh, 1997; Yam and Chow, 1997). The Delta Rule employs the error function for what is known as *gradient descent learning*, which involves the modification of weights along the most direct path in weight-space to minimize error; change applied to a given weight is proportional to the negative of the derivative of the error with respect to that weight (McClelland and Rumelhart 1988, pp.126-130). The error function is commonly given as the sum of the squares of the differences between all target and actual node activations for the

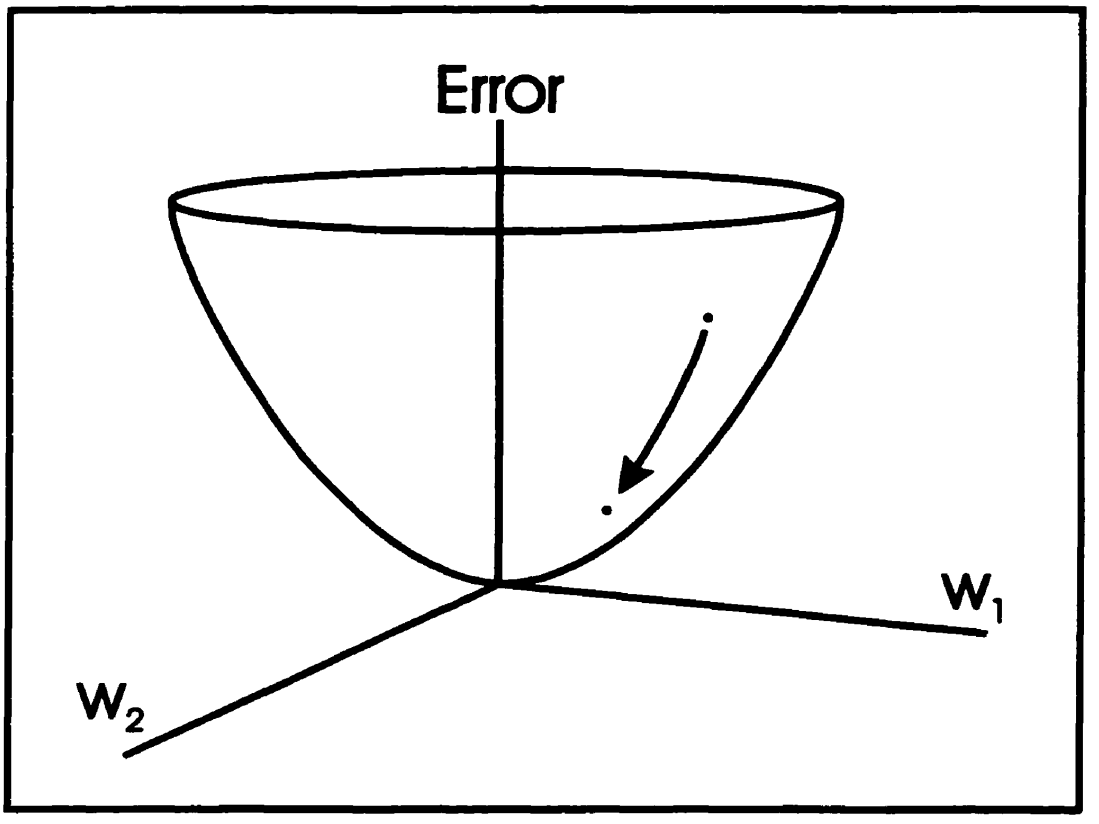

Figure 3.10 Schematic representation of an error function for a network containing only two weights (w_1 and w_2) (after Lugar and Stubblefield, 1993). Any given combination of weights will be associated with a particular measure of error. The Delta Rule uses gradient descent learning to iteratively change network weights to minimize error (i.e., to locate the global minimum in the error surface).

output layer. For a particular *training pattern* (i.e., training case), error is thus given by:

$$E_p = \frac{1}{2}\sum_n (t_{j_n} - a_{j_n})^2 \tag{3.7a}$$

where E_p is total error over the training pattern, ½ is a value applied to simplify the function's derivative, n represents all output nodes for a given training pattern, t_j sub n represents the target value for node n in output layer j, and a_j sub n represents the actual activation for the same node. This particular error measure is attractive because its derivative, whose value is needed in the employment of the Delta Rule, is easily calculated.

Error over an entire set of training patterns (i.e., over one *iteration*, or *epoch*) is calculated by summing all E_p:

$$E = \sum_p E_p = \frac{1}{2}\sum_p \sum_n (t_{j_n} - a_{j_n})^2 \tag{3.7b}$$

where E is total error, and p represents all training patterns. An equivalent term for E in Equation 3.7b is *sum-of-squares error*. A normalized version of Equation 3.7b is given by the *mean squared error* (MSE) equation:

$$MSE = \frac{1}{2PN}\sum_p \sum_n (t_{j_n} - a_{j_n})^2 \tag{3.7c}$$

where P and N are the total number of training patterns and output nodes, respectively. It is the error of Equations 3.7b and 3.7c that gradient descent attempts to minimize (in fact, this

is not strictly true if weights are changed after each input pattern is submitted to the network; see Section 3.4.4.1 below; see also Rumelhart *et al.*, 1986: v1, p.324; Reed and Marks, 1999: pp. 57-62). Error over a given training pattern is commonly expressed in terms of the *total sum of squares* ("tss") error, which is simply equal to the sum of all squared errors over all output nodes and all training patterns. As noted in Section 3.4.6, the network used in this project was programmed to minimize the sum-of-squares error (Equation 3.7b), and expresses error from iteration to iteration in terms of tss error.

The negative of the derivative of the error function is required in order to perform gradient descent learning. The derivative of Equation 3.7a (which measures error for a given pattern p), with respect to a particular weight w_{ij} sub x, is given by the chain rule as:

$$\frac{\delta E_p}{\delta w_{ij_x}} = \frac{\delta E_p}{\delta a_{j_z}} \frac{\delta a_{j_z}}{\delta w_{ij_x}} \tag{3.8a}$$

where a_j sub z is the activation of the node in the output layer that corresponds to the weight w_{ij} sub x (note: subscripts refer to particular layers of nodes or weights, and the "sub-subscripts" simply refer to individual weights and nodes within these layers). It follows that

$$\frac{\delta E_p}{\delta a_{j_z}} = (2)(\frac{1}{2})(t_{j_z} - a_{j_z})(-1) = -(t_{j_z} - a_{j_z}) \tag{3.8b}$$

and

$$\frac{\delta a_{j_z}}{\delta w_{ij_x}} = \frac{\delta}{\delta w_{ij_x}} \sum_n (w_{ij_n} a_{i_n}) = \frac{\delta}{\delta w_{ij_x}} (w_{ij_0} a_{i_0} + w_{ij_1} a_{1_1} \ldots w_{ij_n} a_{i_n}) = a_{i_x} \tag{3.8c}$$

Thus, the derivative of the error over an individual training pattern is given by the product of the derivatives of Equation 3.8a:

$$\frac{\delta E_p}{\delta w_{ij_x}} = -(t_{j_z} - a_{j_z})(a_{i_x}) \tag{3.8d}$$

Because gradient descent learning requires that any change in a particular weight be proportional to the negative of the derivative of the error, the change in a given weight must be proportional to the *negative* of equation 3.8d. Replacing the difference between the target and actual activation of the relevant output node by δ, and introducing a learning rate ϵ, Equation 3.8d can be re-written in the final form of the delta rule:

$$\Delta w_{ij_x} = -\epsilon \frac{\delta E}{\delta w_{ij}} = \epsilon \delta a_{i_x} \tag{3.8e}$$

The reasoning behind the use of a linear activation function here instead of a threshold activation function can now be justified: the threshold activation function that characterizes both the McColloch and Pitts network and the perceptron is not differentiable at the transition between the activations of 0 and 1 (slope = ∞), and its derivative is 0 over the remainder of the function. As such, the threshold activation function cannot be used in gradient descent learning. In contrast, a linear activation function (or any other function that is differentiable) allows the derivative of the error to be calculated.

Equation 3.8e is the Delta Rule in its simplest form (McClelland and Rumelhart, 1988). From Equation 3.8e it can be seen that the change in any particular weight is equal

to the products of 1) the learning rate [ϵ], 2) the difference between the target and actual activation of the output node [δ], and 3) the activation of the input node associated with the weight in question. A higher value for ϵ will necessarily result in a greater magnitude of change. Because each weight update can reduce error only slightly, many iterations are required in order to satisfactorily minimize error (Reed and Marks, 1999).

An actual example of the iterative change in neural network weight values as a function of an error surface is given in Figures 3.11 and 3.12; these figures were produced from data generated by a modified version of the neural network program written for this research (Section 3.4.6). Figure 3.11 is a three-dimensional depiction of the error surface associated with a particular mathematical problem. Figure 3.12 shows the two-dimensional version of this error surface, along with the path that weight values took during training. Note that weight values changed such that the path defined by weight values followed the local gradient of the error surface.

3.4.4.1 Batch and On-Line Learning

Weights can be updated in two primary ways: *batch* training, and *on-line* (also called *sequential* or *pattern-based*) training. In batch mode, the value of $\delta E_p/\delta w_{ij}$ is calculated after each pattern is submitted to the network, and the total derivative $\delta E/\delta w_{ij}$ is calculated at the end of a given iteration by summing the individual pattern derivatives. Only after this value is calculated are the weights updated. As long as the learning rate ϵ is small, batch mode approximates gradient descent (Reed and Marks, 1999).

On-line mode (also called "pattern-mode learning") involves updating the values of

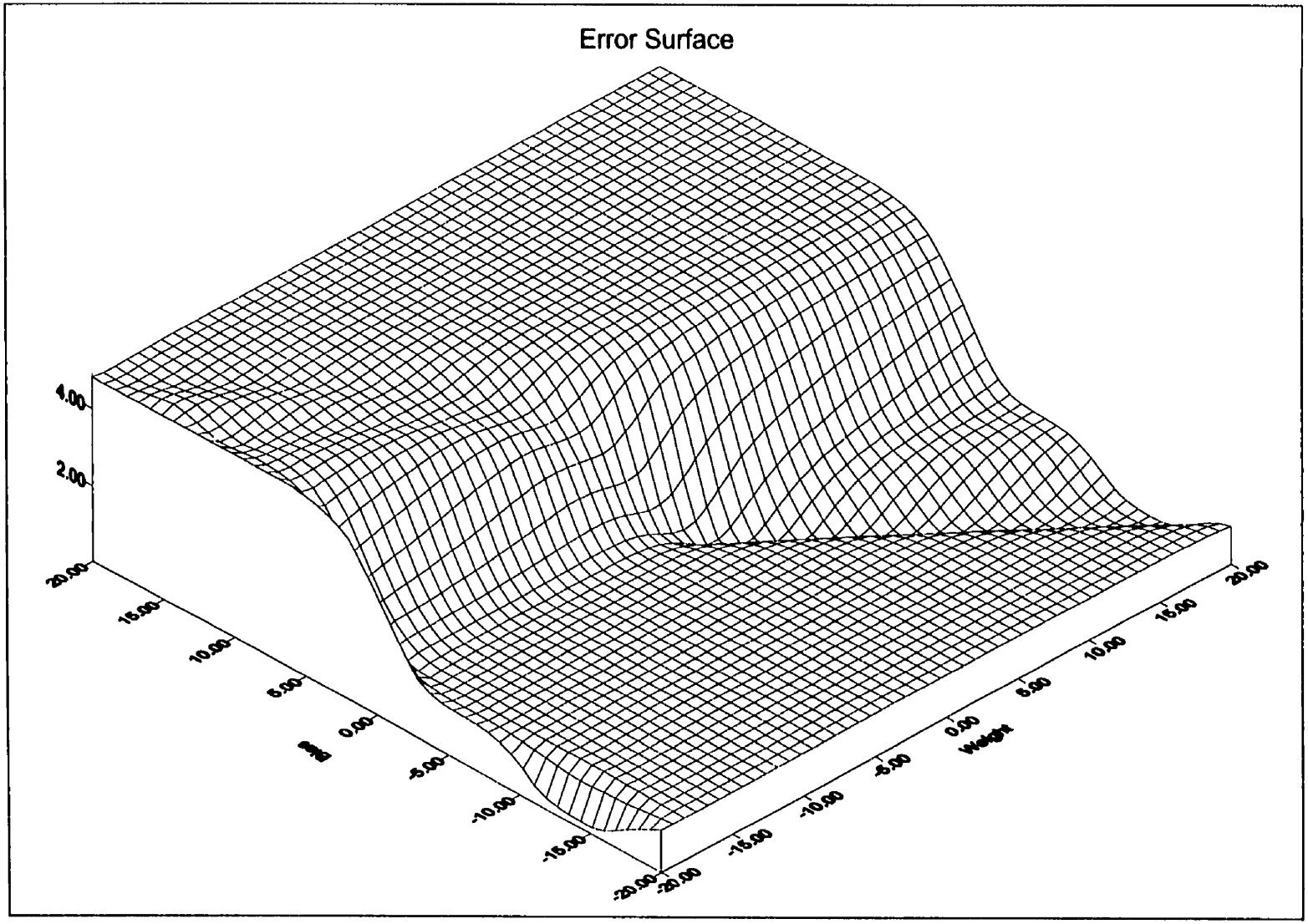

Figure 3.11 Three-dimensional depiction of an actual error surface, generated by a modified version of the neural network program written for this research (Section 3.4.6). The simple network used in this case has only two weights: *weight* and *bias*.

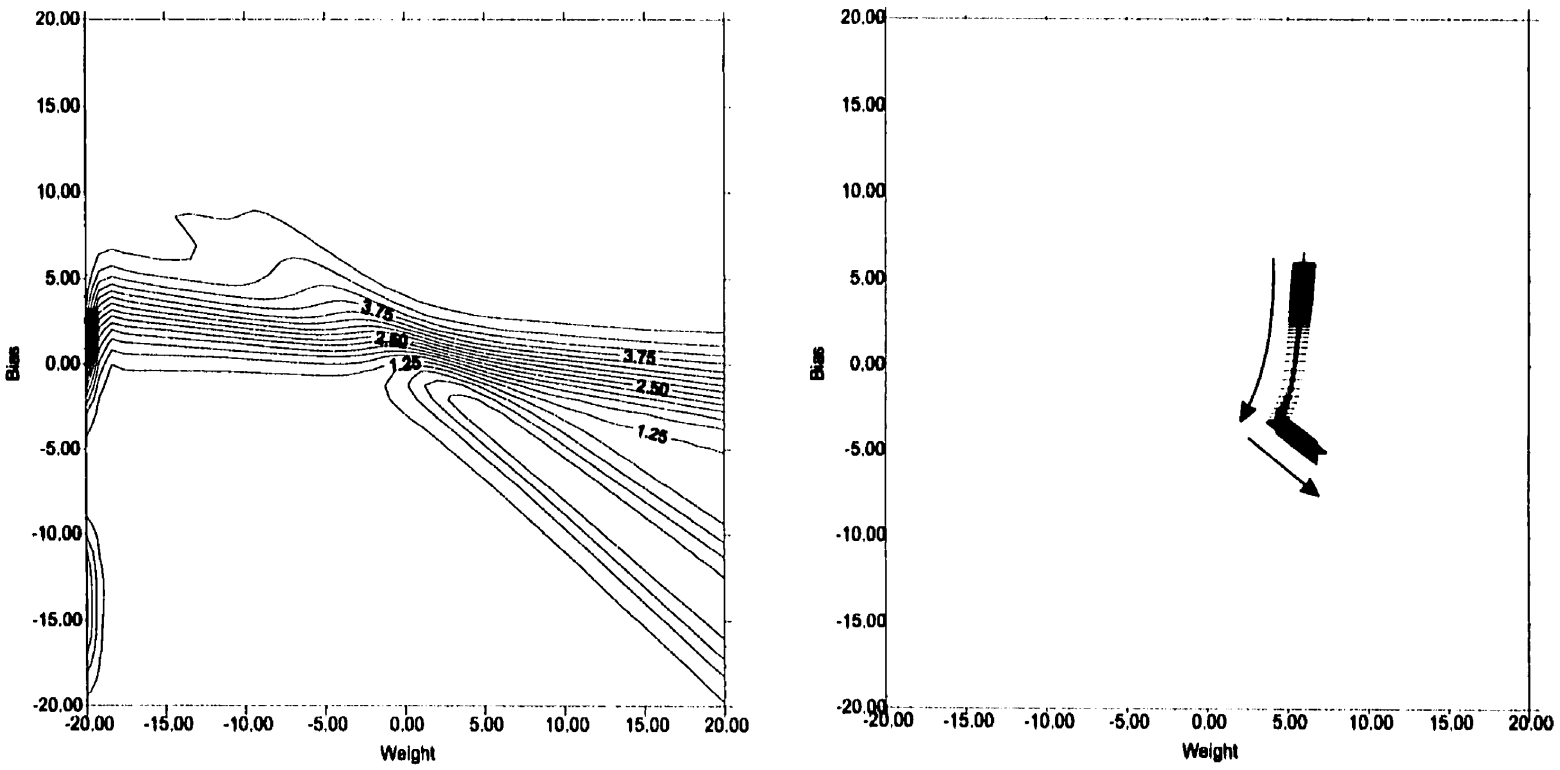

Figure 3.12 Two-dimensional depiction of the error surface given in Figure 3.11, with the training path taken by weight values (starting at weight values [+6, +6]). Note that the path followed the local gradient of the error surface.

weights after each training pattern is submitted to the network (note that the term can be misleading: on-line mode does *not* involve training during the normal feedforward operation of the network; it involves off-line training just like batch mode). As noted earlier, on-line learning does not involve true gradient descent, since the sum of all pattern derivatives over a given iteration is never determined for a particular set of weights; weights are instead changed slightly after each pattern, causing the pattern derivatives to be evaluated with respect to slightly different weight values.

On-line mode is not a simple approximation of the gradient descent method, since although single-pattern derivatives as a group sum to the gradient, each derivative has a random deviation that does not have to be small (Reed and Marks, 1999: p.59). Although error usually decreases after most weight changes, there may be derivatives that cause the error to increase as well. Unless learning rates are very small, the weight vector tends to jump about the $E(\mathrm{w})$ surface, mostly moving downhill, but sometimes jumping uphill; the magnitudes of the jumps are proportional to the learning rate ϵ (Reed and Marks, 1999).

Cyclic, fixed orders of training patterns are generally avoided in on-line learning, since convergence can be limited if weights converge to a limit cycle (Reed and Marks 1999: p.61). Also, if large numbers of patterns are in a training dataset, an ordered presentation of the training cases to the network can cause weights/error to move very erratically over the error surface (with any given series of an individual class' training patterns potentially causing the network to move in weight-space in a direction that is very different from the overall desired direction). Thus, training patterns are usually submitted at random in on-line learning. A comparison between the learning curves produced by networks using non-random and

random submission of training data is given in Figure 3.13. Note that the network using non-random submission produced an extremely erratic learning curve, compared to the relatively smooth learning curve produced by the network using random submission.

The on-line mode has an advantage over batch mode, in that the more erratic path that the weight values travel in is more likely to bounce out of local minima; pure gradient descent offers no chance to escape a local minimum. Further, the on-line mode is superior to batch mode if there is a high degree of redundancy in the training data, since, when using a large training dataset, the network will simply update weights more often in a given iteration, while a batch-mode network will simply take longer to evaluate a given iteration (Bishop, 1995a, p.264). An advantage of batch mode is that it can settle on a stable set of weight values, without wandering about this set.

3.4.4.2 A Simple Delta Rule Example

A simple example of the employment of the Delta Rule, based on a discussion given in McClelland and Rumelhart (1988), is as follows: imagine that the following inputs and outputs are related as in Table 3.1. Imagine further that is the desire of a worker is to train

Table 3.1 Inputs and outputs to be related in the example discussed in Section 3.4.4.2.

	INPUTS				OUTPUTS
Network Node #	0	1	2	3	4
Activations:	+1	-1	+1	-1	+1
	+1	+1	+1	+1	+1
	+1	+1	+1	-1	-1
	+1	-1	-1	+1	-1

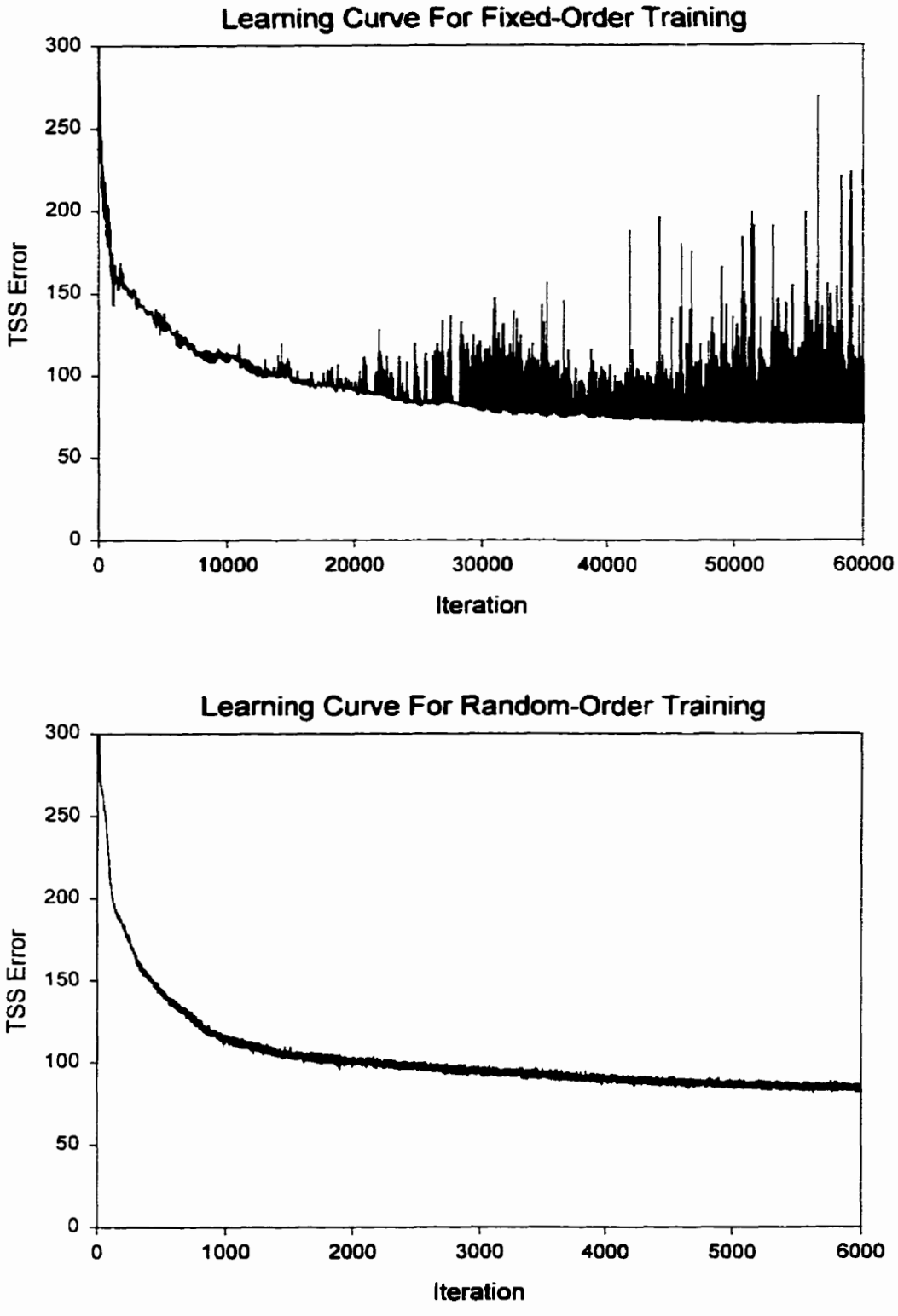

Figure 3.13 Learning curves produced by networks using non-random (fixed-order) and random submission of training data. Learning curve data were generated by the neural network program written for this research (Section 3.4.6).

a network to be able to correctly label each of the four input cases in this table. This problem will require a network with four input nodes and one output node. All 4 weights associated with each input node are initially set to 0, and an arbitrary learning rate (ϵ) of 0.25 is used in this example.

During the training phase, each training case is presented to the network individually, and weights are modified according to the Delta Rule. For example, when the first training case is presented to the network, the sum of products equals 0. Because the desired output for this particular training case is 1, the error equals 1-0 = 1. Using equation (3.8e), the changes in the four weights are respectively calculated to be {0.25, -0.25, 0.25, -0.25}. Since the weights are initially set to {0, 0, 0, 0}, they become {0.25, -0.25, 0.25, -0.25} after this first training case.

Presentation of the second set of training inputs causes the network to calculate a sum of products of 0, again. Thus, the changes in the four weights in this case are calculated to be {0.25, 0.25, 0.25, 0.25), and, once the changes are added to the previously-determined weights, the new weight values become {0.5, 0, 0.5, 0}. After presentation of the third and fourth training cases, the weight values become {0, -0.5, 0, 0.5} and {-0.5, 0, 0.5, 0}, respectively. At the end of this training *iteration*, the total sum of squared errors = $1^2 + 1^2 + (-2)^2 + (-2)^2 = 10$.

After this first iteration, it is not clear that the weights are changing in a manner that will reduce network error. In fact, with the last set of weights given above, the network would only produce a correct output value for the last training case; the first three would be classified incorrectly. However, with repeated presentation of the same training data to the

network (ie. with multiple iterations of training), it becomes clear that the network's weights do indeed evolve to reduce classification error: error is eliminated altogether by the twentieth iteration. The network has learned to classify all training cases correctly, and is now ready to be used on new data whose relations between inputs and desired outputs generally match those of the training data.

The Delta Rule will find a set of weights that solves a network learning problem, provided such a set of weights exists. The required condition for this set of weights existing is that all solutions must be a linear function of the inputs. As was presented by Minsky and Papert (1969), this condition does not hold for many simple problems (e.g., the exclusive-OR function, in which an output of 1 must be produced when either of two inputs are 1, but an output of 0 must be produced with neither or both of the inputs are 1; see McClelland and Rumelhart 1988, pp. 145-152). Minsky and Papert recognized that a *multi-layer network* could convert an "unsolvable" problem to a "solvable" problem (note: a multi-layer network consists of one or more intermediate layers placed between the input and output layers; this accepted terminology can be somewhat confusing and contradictory, in that the term "layer" in "multi-layer" refers to a row of weights, whereas the term "layer" in general neural-network usage usually means a row of nodes; see Section 3.4.5.1 and, e.g., Vemuri, 1992, p.42). Minsky and Papert also recognized that the use of a linear activation function (such as that used in the Delta Rule example above, where network output is equal to the sum of the input/weight products) would not allow the benefits of having a multi-layer network to be realized, since a multi-layer network with linear activation functions is functionally equivalent to a simple input-output network using linear activation functions. That is, linear

systems cannot compute more in multiple layers than they can in a single layer (McClelland and Rumelhart, 1988).

Based on the above considerations, the questions at the time became 1) what kind of activation function should be used in a multi-layer network, and 2) how can intermediate layers in a multi-layer network be "taught"? The original application of the Delta Rule involved only an input layer and an output layer. It was generally believed that no general learning rule for larger, multi-layer networks, could be formulated. As a result of this view, research on connectionist networks for applications in artificial intelligence was dramatically reduced in the 1970's (McClelland and Rumelhart, 1988; Joshi *et al.*, 1997).

3.4.5 Multi-Layer Networks and Backpropagation

Eventually, despite the apprehensions of earlier workers, a powerful algorithm for apportioning error responsibility through a multi-layer network was formulated in the form of the *backpropagation* algorithm (Rumelhart *et al.*, 1986). The backpropagation algorithm employs the Delta Rule, calculating error at output units in a manner analogous to that used in the example of Section 3.4.4.2, while error at neurons in the layer directly preceding the output layer is a function of the errors on all units that use its output. The effects of error in the output node(s) are propagated backward through the network after each training case. The essential idea of backpropagation is to combine a non-linear multi-layer perceptron-like system capable of making decisions with the objective error function of the Delta Rule (McClelland and Rumelhart, 1988).

3.4.5.1 Network Terminology

A multi-layer, feedforward, backpropagation neural network is composed of 1) an input layer of nodes, 2) one or more intermediate (*hidden*) layers of nodes, and 3) an output layer of nodes (Figure 3.5). The output layer can consist of one or more nodes, depending on the problem at hand. In most classification applications, there will either be a single output node (the value of which will identify a predicted class), or the same number of nodes in the output layer as there are classes (under this latter scheme, the predicted class for a given set of input data will correspond to that class associated with the output node with the highest activation).

As noted in Section 3.4.4.2, it is important to recognize that the term "multi-layer" is often used to refer to multiple layers of *weights*. This contrasts with the usual meaning of "layer", which refers to a row of nodes (Vemuri, 1992). For clarity, it is often best to describe a particular network by its number of layers, and the number of nodes in each layer (e.g., a "4-3-5" network has an input layer with 4 nodes, a hidden layer with 3 nodes, and an output layer with 5 nodes).

3.4.5.2 The Sigma Function

The use of a smooth, non-linear activation function is essential for use in a multi-layer network employing gradient-descent learning. An activation function commonly used in backpropagation networks is the *sigma* (or *sigmoid*) function:

$$a_{j_m} = \frac{1}{(1+e^{-S_{j_m}})} \qquad \textit{where } S_{j_m} = \sum_{x=0}^{n} w_{ij_x} a_{i_x} \tag{3.9}$$

where a_j sub m is the activation of a particular "receiving" node m in layer j, S_j is the sum of the products of the activations of all relevant "emitting" nodes (i.e., the nodes in the preceding layer i) by their respective weights, and w_{ij} is the set of all weights between layers i and j that are associated with vectors that feed into node m of layer j. This function maps all sums into [0,1] (Figure 3.14) (an alternate version of the function maps activations into [-1, 1]; e.g., Gallant 1993, pp. 222-223). If the sum of the products is 0, the sigma function returns 0.5. As the sum gets larger the sigma function returns values closer to 1, while the function returns values closer to 0 as the sum gets increasingly negative. The derivative of the sigma function with respect to S_j sub m is conveniently simple, and is given by Gallant (1993, p.213) as:

$$\frac{d}{d(S_{j_m})}(1+e^{-S_{j_m}})^{-1} = -1(1+e^{-S_{j_m}})^{-2}e^{-S_{j_m}}(-1) = \frac{1}{1+e^{-S_{j_m}}}\left(1-\frac{1}{1+e^{-S_{j_m}}}\right) = a_{j_m}(1-a_{j_m}) \quad (3.10)$$

The sigma function applies to all nodes in the network, except the input nodes, whose values are assigned input values. The sigma function superficially compares to the threshold function (which is used in the perceptron) as shown in Figure 3.14. Note that the derivative of the sigma function reaches its maximum at 0.5, and approaches its minimum with values approaching 0 or 1. Thus, the greatest change in weights will occur with values near 0.5, while the least change will occur with values near 0 or 1. McClelland and Rumelhart (1988) recognize that it is these features of the equation (i.e., the shape of the function) that contribute to the stability of learning in the network; weights are changed most for units whose values are near their midrange, and thus for those units that are not yet committed to being either "on" or "off".

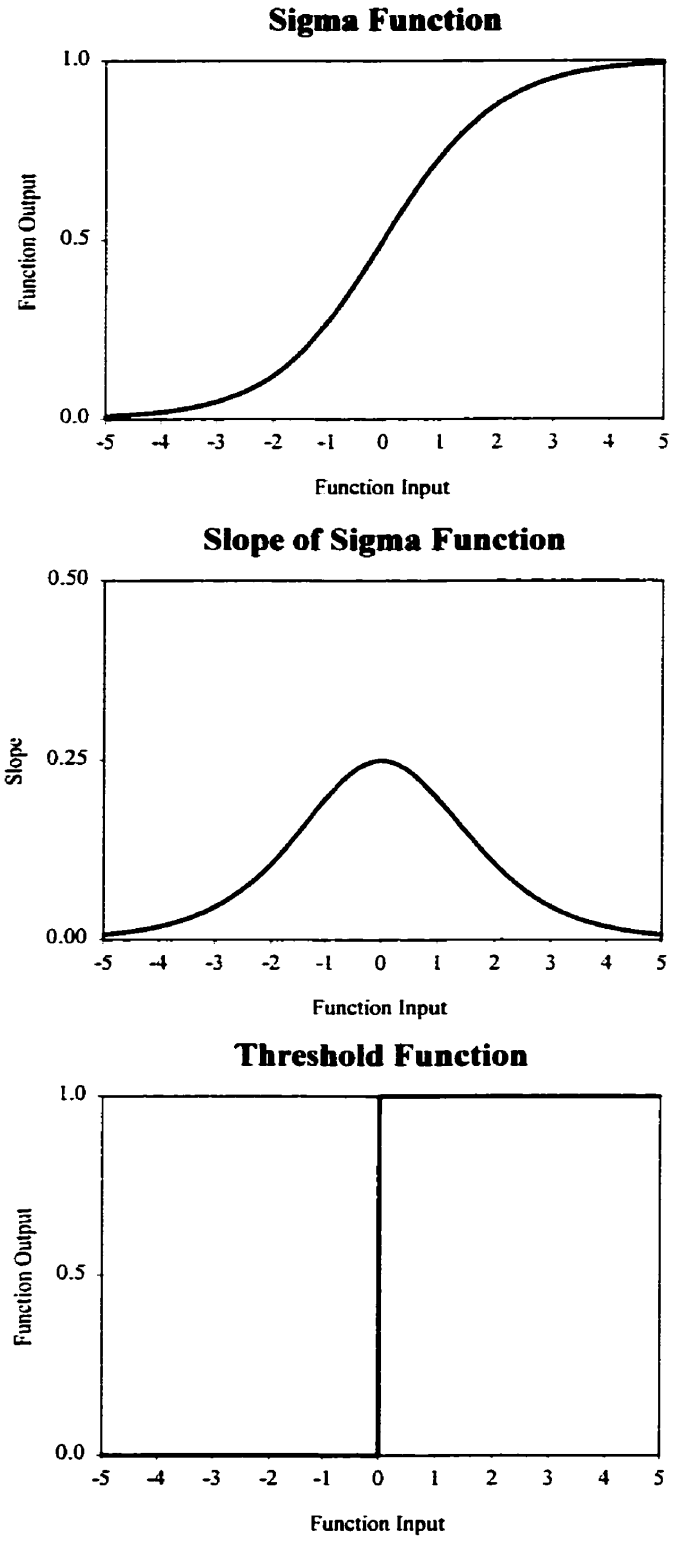

Figure 3.14 Graphs of the sigma function, its derivative, and the threshold function. The sigma function approximates the threshold function, but, because it is differentiable, can be used with the Delta Rule to drive learning in a neural network.

3.4.5.3 The Backpropagation Algorithm

In the employment of the backpropagation algorithm, each iteration of training involves the following steps: 1) a particular case of training data is fed through the network in a forward direction, producing results at the output layer, 2) error is calculated at the output nodes based on known target information, and the necessary changes to the weights that lead into the output layer are determined based upon this error calculation, 3) the changes to the weights that lead to the preceding network layers are determined as a function of the properties of the neurons to which they directly connect (weight changes are calculated, layer by layer, as a function of the errors determined for all subsequent layers, working backward toward the input layer) until all necessary weight changes are calculated for the entire network. The calculated weight changes are then implemented throughout the network, the next iteration begins, and the entire procedure is repeated using the next training pattern.

In the case of a neural network with hidden layers, the backpropagation algorithm is given by the following three equations (modified after Gallant, 1993), where i is the "emitting" or "preceding" layer of nodes, j is the "receiving" or "subsequent" layer of nodes, k is the layer of nodes that follows j (if such a layer exists for the case at hand), ij is the layer of weights between node layers i and j, jk is the layer of weights between node layers j and k, weights are specified by w, node activations are specified by a, delta values for nodes are specified by δ, subscripts refer to particular layers of nodes (i, j, k) or weights (ij, jk), "sub-subscripts" refer to individual weights and nodes in their respective layers, and ϵ is the learning rate:

$$\Delta w_{ij_m} = \epsilon \delta_{j_p} a_{i_q} \tag{3.11a}$$

$$\textit{where } \delta_{j_p} = a_{j_p}(1-a_{j_p})(t_{j_p}-a_{j_p}) \textit{ if output node} \tag{3.11b}$$

$$\textit{where } \delta_{j_p} = a_{j_p}(1-a_{j_p})\sum_{x=0}^{n} \delta_{k_x} w_{jk_x} \textit{ if intermediate node} \tag{3.11c}$$

Being based on the generalized Delta Rule, it is not surprising that Equation (3.11a) has the same form as Equation (3.8e). Equation (3.11a) states that the change in a given weight *m* located between layers *i* and *j* is equal to the products of: 1) the learning rate [ϵ]; 2) the delta value for node *p* in layer *j* [where node *p* is the node to which the vector associated with weight *m* leads]; and 3) the activation of node *q* in layer *i* [where node *q* is the node from which the vector associated with weight *m* leads]. In practice, the learning rate (ϵ) is typically given a value of 0.1 or less; higher values may provide faster convergence on a solution, but may also increase instability and may lead to a failure to converge (Gallant, 1993). The delta value for node *p* in layer *j* in Equation (3.11a) is given either by Equation (3.11b) or by Equation (3.11c), depending on the whether or not the node is in an output or intermediate layer.

Equation (3.11b) gives the delta value for node *p* of layer *j* if node *p* is an output node. Together, Equations (3.11a) and (3.11b) were derived through exactly the same procedure as Equation 3.8e, with the understanding that a sigma activation function is used

here instead of a simple linear activation function (use of a different activation function will typically change the value of δ). Both sets of equations were determined by finding the derivative of the respective error functions with respect to any particular weight.

Equation (3.11c) gives the delta value for node p of layer *j* if node *p* is an intermediate node (i.e., if node *p* is in a hidden layer). This equation states that the delta value of a given node of interest is a function of the activation at that node (a_j sub *p*), as well as the sum of the products of the delta values of relevant nodes in the subsequent layer with the weights associated with the vectors that connect the nodes. Details on the derivation of equation (3.11c), which applies to intermediate nodes, are given in Richards (1993, pp.215-219) and Reed and Marks (1999, pp.53-55). Proof that the backpropagation algorithm actually performs a gradient descent to minimize error is given by e.g Gallant (1993, pp.217-219).

3.4.5.4 Bias

Equations (3.11a), (3.11b), and (3.11c) describe the main implementation of the backpropagation algorithm for multi-layer, feedforward neural networks. It should be noted, however, that most implementations of this algorithm employ an additional class of weights known as *biases*. Biases are values that are added to the sums calculated at each node (except input nodes) during the feedforward phase. That is, the bias associated with a particular node is added to the term S_j in Equation (3.6a), prior to the use of the activation function at that same node. The negative of a bias is sometimes called a ***threshold*** (Bishop, 1995a).

For simplicity, biases are commonly visualized simply as values associated with each

node in the intermediate and output layers of a network, but in practice are treated in exactly the same manner as other weights, with all biases simply being weights associated with vectors that lead from a single node whose location is *outside* of the main network and whose activation is always 1 (Figure 3.15). The change in a bias for a given training iteration is calculated like that for any other weight [using Equations (3.11a), (3.11b), and (3.11c)], with the understanding that a_i sub m in Equation (3.11a) will always be equal to 1 for all biases in the network.

The use of biases in a neural network increases the capacity of the network to solve problems by allowing the hyperplanes that separate individual classes to be offset for superior positioning. More specific discussions on the utility of biases in neural networks are given by, e.g., Gallant (1993, pp.65-66), Bishop (1995a, p.78), and Reed and Marks (1999, pp.15-17).

3.4.5.5 Network Topology

The precise network topology required to solve a particular problem usually cannot be determined (Figure 3.16; Richards, 1993; Castellano *et al.*, 1997; Tamura and Tateishi, 1997; Reed and Marks, 1999), although research efforts continue in this regard (e.g., Kůrková, 1992; Amirikian and Nishimura, 1994; Wang *et al.*, 1994). This is a critical problem in the neural-network field, since a network that is too small or too large for the problem at hand may produce poor results. This is analogous to the problem of curve fitting using polynomials: a polynomial with too few coefficients cannot evaluate a function of interest, while a polynomial with too many coefficients will fit the noise in the data and

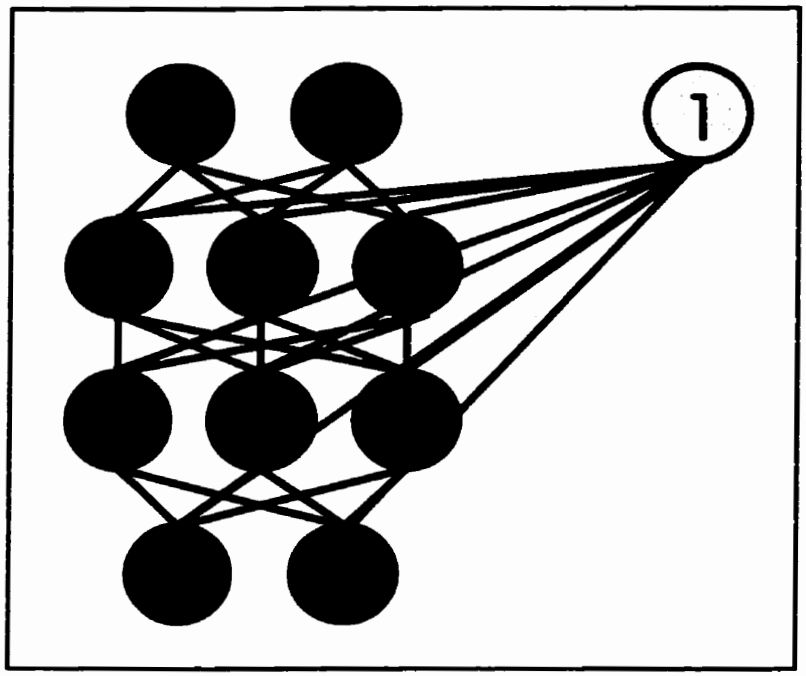

Figure 3.15 Biases are weights associated with vectors that lead from a single node whose location is outside of the main network and whose activation is always 1.

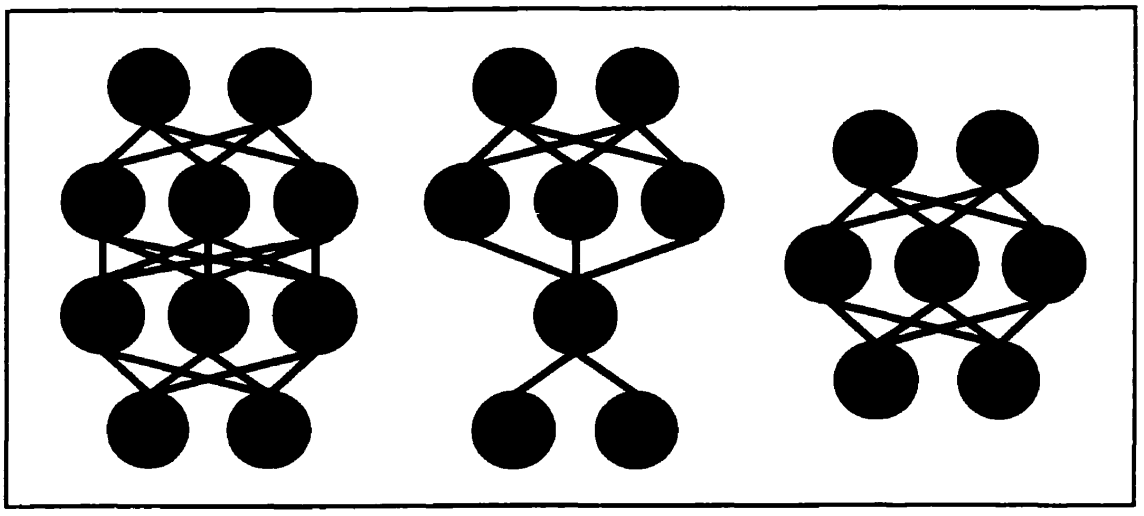

Figure 3.16 Three of an infinite number of possible network topologies that could be used to relate two inputs to two outputs.

produce a poor representation of the function (Kwok and Yeung, 1997a; see also Bishop, 1995a, pp.9-15; Reed and Marks, 1999, p.42).

General "rules of thumb" regarding network topology are commonly used. At least one intermediate layer is always used; as noted in Section 3.4.4.2, even simple problems such as the exclusive-OR problem cannot be solved without intermediate layers (Figure 3.17). Many applications of the backpropagation algorithm involve the use of networks consisting of only one intermediate layer of nodes, although the use of two intermediate layers can generate superior results for certain problems in which higher order functions are involved (Gallant, 1993; Reed and Marks, 1999, p.38). The number of nodes used in each intermediate layer is typically between the number of nodes used for the input and output layers (e.g., Richards, 1993). Ultimately, the only method that can be confidently used to determine the appropriate number of layers in a network for a given problem is trial and error (Gallant, 1993), and, as noted above, the utility of a particular network topology is in part a function of the number and representativeness of available training samples.

An experimental means for determining an appropriate topology for solving a particular problem involves the training of a larger-than-necessary network, and the subsequent removal of unnecessary weights and nodes during training (e.g., Sietsma and Dow, 1991; Reed, 1993; Castellano *et al.*, 1997). This approach, called *pruning*, requires advance knowledge of how large a network should start at, but such upper bounds may not be difficult to estimate (Huang and Huang, 1991; Sartori and Antsaklis, 1991). An alternative means for determining appropriate network topology involves algorithms which start with a small network and build it larger; such algorithms are known as *constructive* algorithms (e.g.,

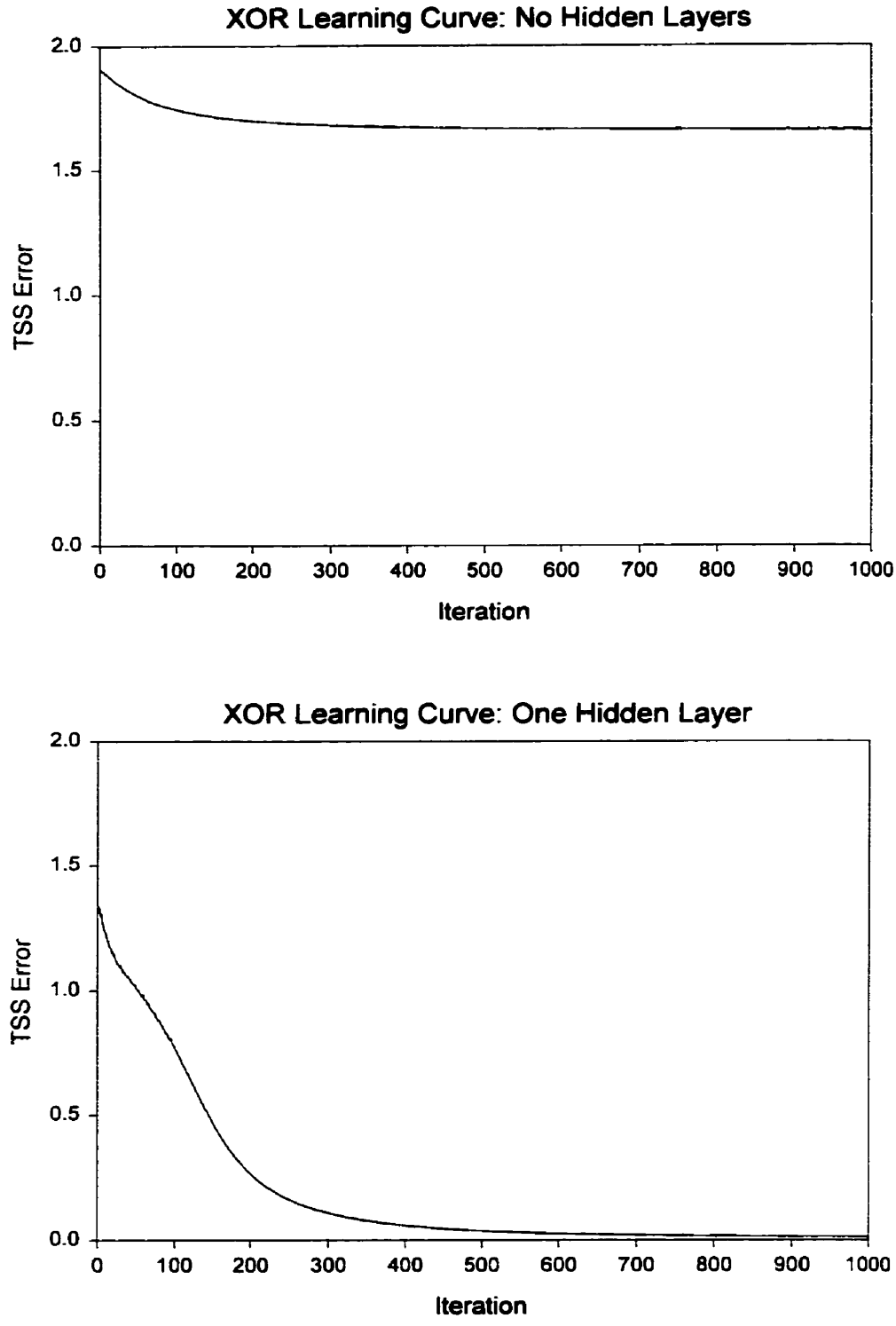

Figure 3.17 Learning curves for the exclusive-OR (XOR) problem. A neural network with no hidden layers cannot solve the XOR problem (top curve), but a neural network with a single hidden layer can solve the problem with a relatively small number of iterations (bottom curve). Learning curve data were generated by the neural network program written for this research (Section 3.4.6).

Hirose *et al.*, 1991; Bartlett, 1994; Kwok and Yeung, 1997b; Parekh *et al.*, 2000). Additionally, much neural network research remains focussed on the use of *evolutionary* and *genetic* algorithms, based on simplified principles of biological evolution, to determine network topology, weights, and overall network behaviour (e.g., Odri *et al*, 1993; Angeline *et al.*, 1994; Maniezzo, 1994; Smalz and Conrad, 1994; Yao and Liu, 1997; Fogel, 2000).

A complication to the issue of network topology is the Hughes phenomenon (Hughes, 1968; Landgrebe, 1978; Shahshahani and Landgrebe, 1994), which arises when the dimensionality of a problem (which is related to, e.g., the number of sources and network weights used) is high relative to the number of representative training samples available. The Hughes phenomenon can reduce the utility of classification results, and thus can effectively place upper limits on, e.g., network sizes.

3.4.5.6 Initialization of Network Weights

Although the ideal initial values for weights (i.e., those that will maximize the effectiveness and speed with which a neural network learns) cannot yet be determined theoretically (Thimm and Fiesler, 1997), it is general practice to assign randomly-generated positive and negative quantities as the initial weight values. Such a random distribution can help minimize the chances of the network becoming stuck in local minima (Gallant, 1993). Typically, values are selected from a range $[-a,+a]$ where $0.1 < a < 2$ (Reed and Marks, 1999, p.57). The reason for using random initial weights is to break symmetry, while the reason for using small initial weights is to avoid immediate saturation of the activation function (Reed and Marks, 1999, p.97). Further discussions regarding the benefits of the use of small initial

weights are given by Reed and Marks (1999, p.116 and p.120).

3.4.5.7 Momentum

The speed of convergence of a network can be improved by increasing the learning rate ϵ. Unfortunately, increasing ϵ will usually result in increasing network instability, with weight values oscillating erratically as they converge on a solution. Instead of changing ϵ, most standard backpropagation algorithms employ a *momentum* term in order to speed convergence while avoiding instability. The momentum term is added to Equation 3.11a, and is equal to the product of some fraction $0 \leq \alpha \leq 1$ by the change in weight that occurred in the previous weight change. By adding fractions of previous weight changes, weight changes can be kept on a faster and more even path (Gallant, 1993).

Figure 3.18 shows three learning curves, each generated using a different momentum setting. The data used to produce these learning curves was generated by the neural network program written for this research (Section 3.4.6). The first learning curve was generated with momentum set to zero (that is, no momentum). The second learning curve was generated using momentum on all non-bias weights (here termed *half-momentum*); note that although the learning curve is characterized by greater iteration-to-iteration variation in tss error, the network using half-momentum converged to a better solution (lower tss error) using a smaller number of iterations, compared with the network using zero momentum. The third learning curve applied momentum to all weights, included biases (here termed *full-momentum*); the network using full-momentum did not learn as quickly or as successfully as the network using half-momentum, and the iteration-to-iteration variation in tss error was greatly increased. All

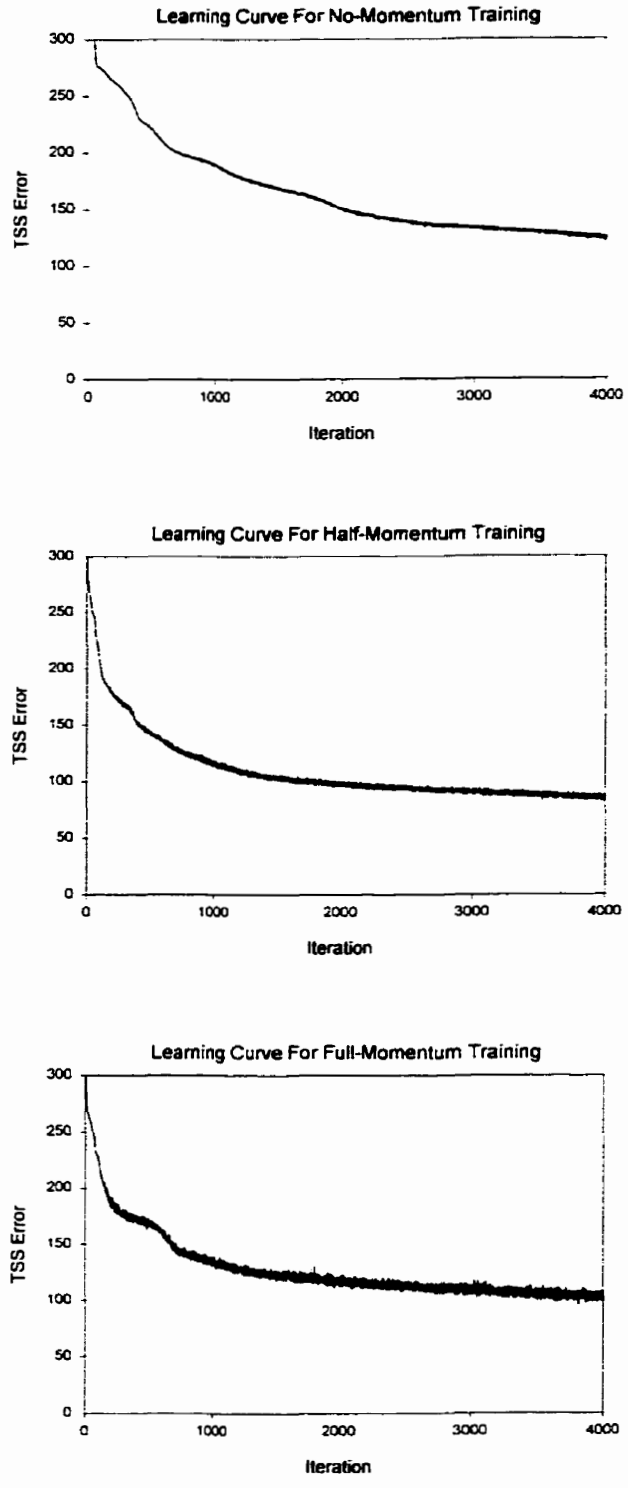

Figure 3.18 Learning curves produced using three different momentum settings. Learning curve data were generated by the neural network program written for this research (Section 3.4.6).

neural network executions used in the research presented in Chapters 5 and 6 used half-momentum.

The value for α is typically set to 0.9, with the learning rate α set to 0.1 (see Reed and Marks, 1999: Figure 6.1). A useful discussion of considerations relevant to the choice of both learning rate ϵ and momentum α is given by Reed and Marks (1999, pp.74-77 and 87-90).

3.4.5.8 Over-Generalization and Training With Noise

The purpose of training a feedforward backpropagation network is to modify weight values iteratively such that the weights, over time, converge on a solution that relates inputs to outputs in a manner that is useful to the user. It is normally desirable in training for a network to be able to *generalize* basic relations between inputs and outputs based on training data that do not consist of all possible inputs and outputs for a given problem. A difficulty that can arise in the training of a neural network involves the adaptation of weight values so closely to training data that the utility of the network in processing new data is diminished; this problem is called *over-generalization* (or *over-training*) (e.g., Bishop, 1995a; Reed and Marks, 1999; Karystinos and Pados, 2000). In over-generalization, the network has ceased to be able to relate general ranges of values to classes, and instead relates input values to classes in a manner that is contrary to the more general relation that is desired. While early stages of learning generally result in the successful evaluation of the main features of the underlying function that properly maps inputs to outputs, later stages of learning may incorporate features of the training dataset that are uncharacteristic of the data as a whole (e.g., due to the use of incomplete or noisy training data) (Reed and Marks, 1999). Measured

error in such a situation will continually be decreasing during training, but the generalization capabilities of the network will also be decreasing (as the network modifies weights to suit peculiarities of the training data being used).

One approach used to prevent over-generalization is the termination of training before over-generalization can occur (Reed and Marks, 1999). That is, for a given network, training data, and learning algorithm, there may be an optimal amount of training that produces the best generalization. While potentially effective, this solution is often not useful, since algorithms that provide information on approximately when to stop training are not necessarily dependable; such algorithms may, for example, be fooled into the premature termination of training by factors such as, e.g., local minima in the error surface. A premature halt to training will result in a network that is not trained to its highest potential, while a late halt to training can result in a network whose operation is characterized by over-generalization (Reed and Marks, 1999).

Another solution that is sometimes used to help combat over-generalization is the use of jitter (i.e., the addition of a small amount of artificial noise to training data while a network is being trained) (e.g., Sietsma and Dow, 1991; Holmström and Koistinen, 1992; Bishop, 1995a, pp.346-349; Bishop, 1995b; Reed and Marks, 1999, pp.277-289). This is performed by adding a random vector to each training pattern each time it is submitted to the network. The addition of noise to training data allows values that are proximal to true training values to be taken into account during training; as such, the use of jitter may be thought of as a means of extrapolating training data to proximal values. The use of jitter helps to fill out otherwise sparse training datasets by relating a greater variety of input values (and

combinations of input values) to output classes, allowing the network's weights to converge on a solution that relates general ranges of values to class labels, rather than relating specific values to class labels (and thus potentially avoiding over-generalization).

3.4.5.9 Combining Neural Network Results

The random initialization of network weights prior to each execution of the neural network training algorithm often causes final classification results to vary from execution to execution, even when all other factors (e.g., training data, learning rate, momentum, network topology) are kept constant. In practice, the variation in results can be very large in the classification of satellite imagery (e.g., Chapter 5; see also, e.g., Leverington and Duguay, 1997). Thus, in order to generate the best possible neural network result, multiple neural network classifications must typically be generated; these classifications must then be individually evaluated so that the most useful individual set of results can be selected.

Alternative means of utilizing a number of sets of neural network results are available, some of which offer the potential for generating final classification results that are superior to those produced by any of the individual neural networks used. For example, multiple neural network results can be combined using a simple consensus rule: for a given pixel, the class label with the largest number of network "votes" is that which is assigned (that is, the results of the individual neural-network executions are combined through a simple majority vote) (Hansen and Salamon, 1990). The reasoning behind such a consensus rule is that a consensus of numerous neural networks should be less fallible than any of the individual networks, each of which will have generated results with different error attributes as a

consequence of differing weight initializations (Hansen and Salamon, 1990). In the investigations discussed in Chapter 5, majority-vote consensus results were generated and based on a combination of ten equally-weighted neural-network results.

The above consensus rule is a simple predecessor of other consensus algorithms designed to improve the classification results of neural networks (e.g., Benediktsson and Swain, 1992; Battiti and Colla, 1994; Rogova, 1994; Benediktsson *et al.*, 1997a, 1997b, 1997c; Ji and Ma, 1997; Benediktsson and Kanellopoulos, 1999; Gutta *et al.*, 2000; Khotanzad *et al.*, 2000). The consensus algorithm of Rugova (1994), for example, involves the combination of neural network output activations using orthogonal summation (a version of this particular algorithm is empirically evaluated in Chapter 7). Neural networks themselves can be used to combine the results of other neural network executions. This approach is attractive, since neural networks approximate posterior probabilities at output nodes (see discussion in Section 7.1) and no scaling of input data for the combining neural network is required (Benediktsson *et al.*, 1997b, 1997c).

For all types of consensus algorithms, results can be significantly and consistently superior to all individual results used as input only if individual results are generally error-independent (Hansen and Salamon, 1990; Rugova, 1994). Error independence may be a property of output data if, e.g., there are many possible output classes with complex decision boundaries, or if the various networks have different input features, architectures, initializations, or learning algorithms (Battati and Colla, 1994).

3.4.6 Neural Network Software Description

The general feedforward backpropagation algorithm described in Section 3.4.5 [and which is fully described in Rumelhart *et al.* (1986), McClelland and Rumelhart (1988), Gallant (1993), Richards (1993), Bishop (1995a), and Reed and Marks (1999)] was used as the basis for the creation of neural network software for this project. The software was written in *C* by the author, and was designed specifically for image processing purposes (although with minor modifications it could be applied to non-classification problems). The neural network software is made up of two main programs: 1) a training module, and 2) a feedforward classification module. Additional modules were written for majority-vote and evidential-reasoning consensus operations (Section 3.4.5.9). Several other programs used for data conversion and file management were also written for this research (all neural network programs used in this research are summarized in Appendix C).

The neural network implemented here is a standard feedforward network that uses backpropagation to calculate derivatives of training error and to adjust weights to minimize error. The error function used by the network is the sum-of-squares error. The sigma nonlinearity in [0.0,1.0] is used as the activation function for all hidden and output nodes. Default settings for the learning rate (ϵ) and momentum (α) are 0.1 and 0.9, respectively. Initial weights are uniformly distributed in [-0.5,+0.5]. The network is configured for classification, and thus utilizes an output layer in which a unique node is assigned to each class; for a given input pattern, the "winning class" is the class whose output node has the highest activation. During training, target activations for "correct" and "incorrect" nodes are 0.9 and 0.1, respectively. The network is configured to learn in on-line mode, rather than

batch mode.

3.5 Chapter Summary

The maximum likelihood classifier, the most commonly used supervised classification algorithm in the remote sensing field, classifies pixels based on the assignment of conditional probabilities to each class. Probability distributions are parameterized from training data using multivariate normal models. The evidential reasoning and maximum likelihood classifiers are not constrained by unimodal models of training data, and thus are potential alternatives to the maximum likelihood algorithm, particularly in cases in which the histograms describing training data deviate significantly from generally Gaussian distributions.

The evidential reasoning algorithm is based upon the derivation of a mass of evidence for a given set of all-encompassing class propositions, for a given source. The combination of evidence from more than one source is performed through the employment of Dempster's orthogonal sum. The evidential reasoning algorithm as used in this research treats signature data in such a way that the main features of relatively complex frequency histograms can be faithfully modelled. Recent studies have shown that the evidential reasoning algorithm has considerable potential as an algorithm for image classification..

Neural networks are composed of interconnected and interacting components called nodes (neurons). Individual nodes in a neural network emulate biological neurons by taking input data and performing simple operations on the data, selectively passing the results on to other neurons via connecting vectors. Weight values are associated with each vector and node in the network, and these values constrain how input data (e.g., satellite image values)

are related to output data (e.g., land-cover classes). Weight values are established during a training phase in which the network learns how to identify particular classes by their typical input data characteristics. Once trained, a neural network can be applied toward the classification of new data. Neural networks are unique in that they are characterized by a lack of explicit representation of knowledge; there are no symbols or values that directly correspond to classes of interest. Rather, knowledge is implicitly represented in the patterns of interactions between network components. Research continues to demonstrate the potential of neural networks (including the type used in this research: the feedforward backpropagation neural network) for image classification.

4 STUDY AREAS

4.1 Introduction

This chapter provides an overview of the geology, vegetation, and climate of the two study areas used in this research: 1) eastern Melville Island, Nunavut, and 2) central Cape Smith Belt, northern Québec (Figure 4.1). The geology of the Melville Island Study Area consists mainly of sedimentary lithologies, including sandstones, shales, mudstones, carbonates, and evaporites. The geology of the Cape Smith Belt Study Area consists of a wide variety of metamorphosed sedimentary and igneous rocks, including tonalite, peridotite, gabbro, pyroxenite, and pelite. Relief is generally subdued at both study areas (varying by less than ~200 m), and exposure of geological materials is good.

4.2 The Melville Island Study Area

This section presents the regional geological and tectonic framework for the Canadian Arctic Islands, followed by a summary of the geology of the eastern part of Melville Island. The portion of the island visited and sampled in the summer of 1998 (i.e., the Melville Island Field Area) is described in detail.

4.2.1 Regional Geological and Tectonic Framework

There are three first-order elements of the modern tectonic framework of the Canadian Arctic Islands: 1) Canadian Shield, 2) Arctic Platform, and 3) Innuitian Tectonic Province (Trettin, 1991a); each of these elements is briefly described below. The geological provinces of the Canadian High Arctic are given in Figure 4.2.

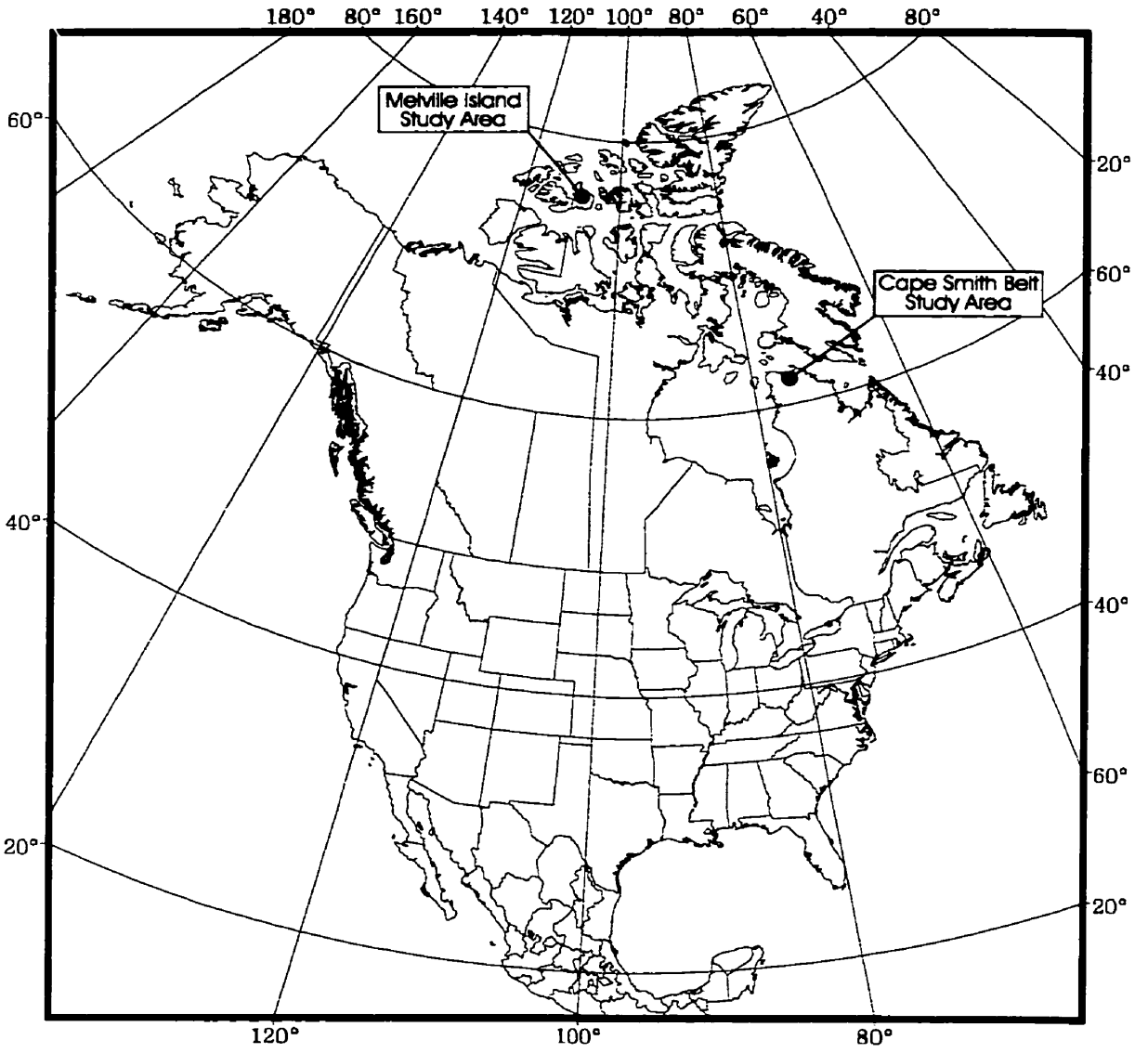

Figure 4.1 Map of North America showing the locations of the two study areas (eastern Melville Island, Nunavut, and Cape Smith Belt of northern Québec).

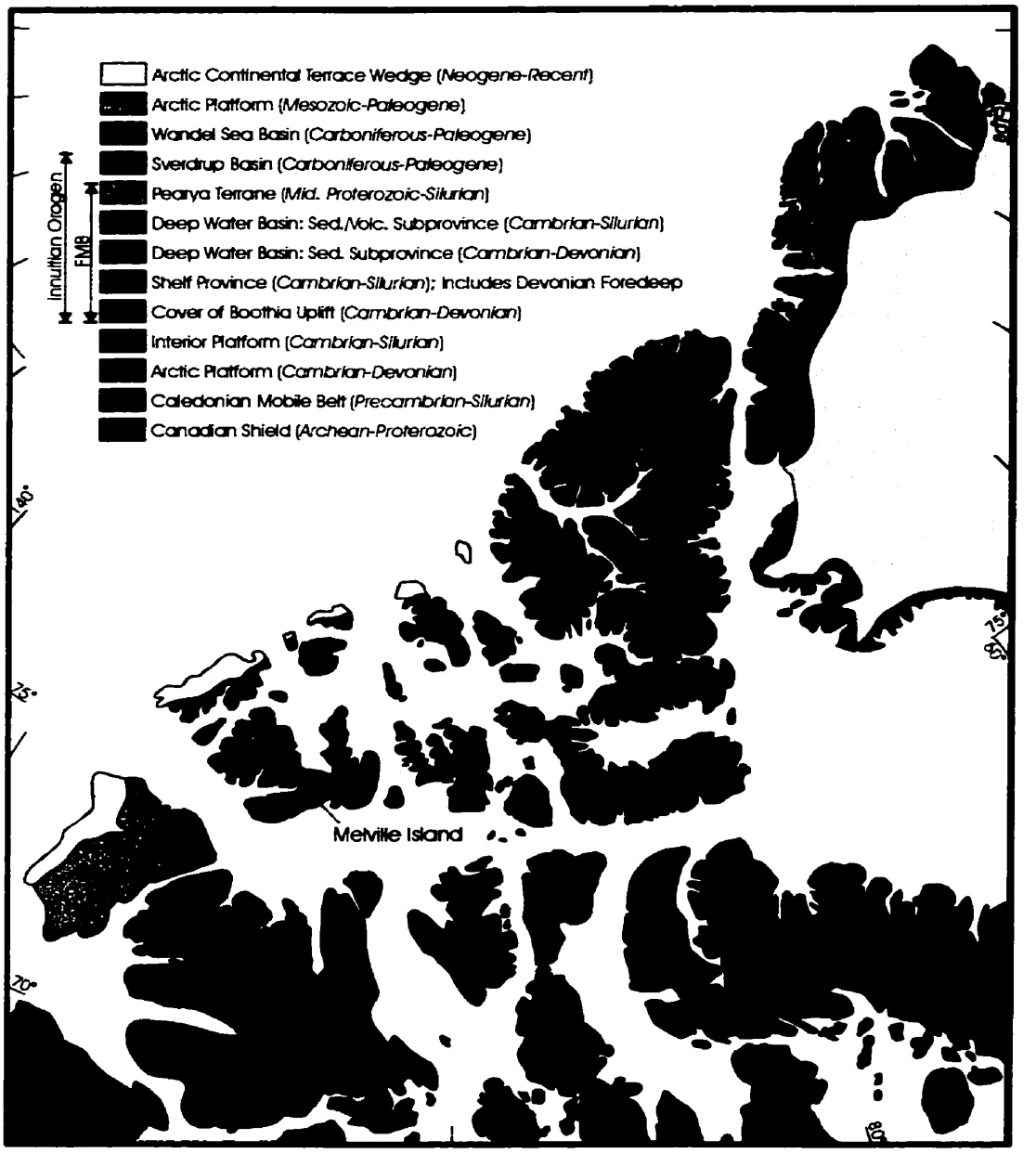

Figure 4.2 Geological provinces of the Canadian High Arctic (after Trettin, 1987, and Harrison, 1994). The Franklinean Mobile Belt is designated *FMB*.

4.2.1.1 Canadian Shield

The Canadian Shield borders the Arctic Platform on the southeast, and also extends into the Arctic Platform as inliers and salients (Figure 4.2). The Canadian Shield is composed of a metamorphic-plutonic basement and unconformably overlying sedimentary and volcanic successions that are only slightly deformed (Frisch and Trettin, 1991). The Canadian Shield extends under the Arctic Platform, as well as under the Franklinian Mobile Belt of the Innuitian Tectonic Province, but its northern limit in the subsurface has not been identified (Trettin, 1989).

4.2.1.2 Arctic Platform

The term "Arctic Platform" is a structural designation, and represents those Phanerozoic successions in the northern portion of the North American continent that have not been folded or faulted on a regional scale. The sedimentary rocks of the Arctic Platform can be divided stratigraphically into a lower-middle Paleozoic succession (mainly of shallow marine origin) and a Mesozoic-Paleogene succession (Trettin, 1991a). In the south and southeast, in the vicinity of Melville Island, the Arctic Platform is part of a broad region underlain by relatively undeformed Cambrian through Devonian strata that unconformably overlie the variably metamorphosed sedimentary and volcanic succession of the Canadian Shield (Harrison, 1994a).

4.2.1.3 Innuitian Tectonic Province

The Innuitian Tectonic Province (syn. Innuitian Province) is related to the *Innuitian*

Orogenic System (syn. Innuitian Orogen), which was introduced by Fortier *et al.*(1954) to describe the "complex assemblage of mountain structures extending from the Beaufort Sea across the Princess Elizabeth Islands and which continues through north Greenland" (Trettin, 1991a). The concept of the Innuitian Tectonic Province encompasses the entire geological history of the Innuitian Orogen, including related patterns of subsidence and deposition (the use of the term Innuitian Orogen, by comparison, is more restrictive and more useful for regional mapping purposes, since it does not include units such as the undeformed Cretaceous to Holocene Arctic Continental Terrace Wedge, and does include in the subsurface the entire Precambrian succession, including the crystalline basement) (Trettin, 1991a). The Innuitian Tectonic Province is characterized by its location on the northern margin of the North American craton, and by westerly to southwesterly structural and depositional trends (Trettin, 1991a). Its southeastern and southern limit corresponds to the limit of Phanerozoic folding or thrust faulting (thus this is a structural, rather than stratigraphic boundary), whereas its northwestern limit is given by the boundary between continental and Mesozoic-Tertiary oceanic crust (Trettin 1991a).

The Innuitian Tectonic Province is described by Trettin (1991a) as being composed of four major stratigraphic successions which have been labelled according to the tectonic setting in which they were deposited: 1) a concealed upper Middle and Upper Proterozoic succession, known only from cratonward equivalents in the northernmost part of the Canadian Shield, 2) the uppermost Proterozoic to Upper Devonian succession of the *Franklinian Mobile Belt*, 3) the Carboniferous to Neogene successions of the *Sverdrup Basin* and of part of the Wandel Sea Basin, and 4) the Lower Cretaceous to Recent Arctic Continental Terrace

Wedge.

The **Franklinian Mobile Belt** is a mid-Paleozoic orogen that contains shelf marginal and basinal sediments, and foreland-type siliciclastic rocks that are age equivalent to those that compose the Arctic Platform (Harrison, 1994a). The Franklinian Mobile Belt was formed by plate convergence of an unknown landmass with North America in the Silurian and Devonian periods (Patchett *et al.*, 1999). On Melville Island and elsewhere, the Arctic Platform is transitional into the Franklinian Mobile Belt of the Innuitian Tectonic Province. The Parry Islands Fold Belt of Melville and Bathurst Islands, along with the Central Ellesmere Fold Belt of the eastern arctic, are among the *foreland deformed regions* of the Franklinian Mobile Belt (Harrison, 1994a). The *internal zone* of this fold belt includes deformed lower Paleozoic basinal shale, and clastic and carbonate facies of the Hazen and Canrobert Hills fold belts (exposed on northern Ellesmere Island and western Melville Island, respectively) (Harrison, 1994a). The *northern zone* of the Franklinian Mobile Belt includes the volcanic and clastic terranes represented in the Clements Markham and Northern Heiberg fold belts (exposed on northern Ellesmere Island and Axel Heiberg Island, respectively). The northern limit of the Franklinian Mobile Belt is given by the faulted contact between the Clements Markham Fold Belt and the Pearya Terrane (which has been interpreted by Trettin (1987) to be an exotic continental fragment - an accreted terrane - with Grenvillian and Caledonian affinities) (Harrison, 1994a). In the vicinity of Melville Island, most of the internal zone and certain portions of the foreland zone are covered by Carboniferous through Paleocene strata of the Sverdrup Basin (Harrison, 1994a).

The record of the Franklinian Mobile Belt begins in the mid-Early Cambrian. The

Lower Cambrian to Upper Silurian or Lower Devonian successions were deposited in two major provinces: 1) a southern or southeastern shelf, and 2) a northern deep water basin (Higgins *et al.*, 1991; Trettin *et al.*, 1991). The ***shelf province*** (syn. **Franklinian Shelf**) consists of all strata of Early Cambrian (or older) to Early Devonian age lying between the slope of the deep water basin and the limit of mid-Paleozoic folding or thrust faulting (Trettin, 1991a). The record of the shelf province is mainly composed of carbonate sediments, although craton-derived clastic sediments and evaporites are also included (Trettin, 1991a). The deposits of the shelf province thicken toward the shelf edge, where thicknesses of more than 9 km are reached. The ***deep water basin*** of the Franklinian Mobile Belt is mainly characterized by sediment gravity flow deposits, graptolitic mudrock, and radiolarian chert. The deep water basin can be divided into two parts: a southeastern part, and a northwestern part (Trettin *et al.*, 1991). The southeastern part of the basin (called the ***sedimentary subprovince***, and exposed from northeastern Greenland to northwestern Melville Island) is composed of sediments of Early Cambrian to Early Devonian age. The northwestern part of the basin (called the ***sedimentary-volcanic subprovince***, and exposed only in northern Ellesmere Island and Axel Heiberg Island) contains arc-type volcanic deposits and associated shallow marine carbonates in addition to the predominant deep water sediments of Early Cambrian to early Late Silurian age (Trettin *et al.*, 1991).

The strata of the shelf province (Franklinian Shelf) are conformably overlain by a ***clastic wedge*** which was deposited in a syntectonic foreland basin during the Ellesmerian Orogeny, a southerly-directed deformation that ultimately folded these materials in the latest Devonian or Early Carboniferous (Trettin, 1991a; Harrison, 1995). Preserved deposits of the

clastic wedge are up to 5 km thick, and range in age from early Middle to latest Devonian; up to 6 km of latest Devonian and Early Carboniferous age clastic sediments are believed to have been removed by erosion (Embry, 1991). Middle to Upper Devonian clastic sediments are widely preserved, and are particularly widespread in the western Arctic, occurring over much of Bathurst, Melville, Prince Patrick, and Banks islands (Embry, 1991). The clastic wedge is mainly composed of sediments of shallow-marine and non-marine origin, although turbidites and submarine slope deposits of early Middle Devonian age occur in the western part of the wedge. The provenance of basin sediments includes the northern parts of the Franklinian mobile belt, the Caledonides, and the Canadian Shield (Trettin, 1991a).

The Melville Island geological units that were folded during the Ellesmerian orogeny are part of a 470 km salt-based fold belt that extends from eastern Bathurst Island to central Melville Island (Harrison, 1995). Typical regional-scale folds of this belt have wavelengths of 12 to 17 km, axial planes that dip 80 to 90° north or south, and axial plunge variation that is 0 to 6° (Harrison, 1995). The near-horizontal basal detachment of the fold belt is at a depth of about 5 km, below a lower ductile layer of Middle Ordovician evaporites (Harrison, 1995).

As noted above, the **Sverdrup Basin** overlies the central and northwestern parts of the Franklinian mobile belt (with angular unconformity). The axial region of the Sverdrup Basin contains as much as 3 km of Paleozoic strata, 9 km of Mesozoic strata, and locally more than 3 km of syntectonic clastic sediments of latest Cretaceous and Tertiary age (Trettin, 1991a). Late Paleozoic deposition in the basin was characterized by carbonate, evaporite, and clastic sediments, whereas Mesozoic and Tertiary deposition was dominated by clastic sediments, apart from some impure carbonates of Middle Triassic age; based on

paleomagnetic studies, the shift from carbonate to clastic lithologies in the Sverdrup Basin has been ascribed to drift into more northerly latitudes (Davies and Nassichuk, 1991; Trettin, 1991a). Local and regional uplift, as well as eustatic falls in sea level, produced numerous disconformities in the stratigraphic succession (Trettin, 1991a).

The tectonic history of the Sverdrup Basin can be divided into five partly overlapping phases: 1) initial rifting, locally accompanied by deformation (late Early Carboniferous to Early Permian), 2) thermal subsidence (Late Permian to earliest Cretaceous), 3) renewed rifting at the present continental margin (Middle Jurassic to Early Cretaceous or later), 4) thermal subsidence (Late Cretaceous), and 5) deformation and syntectonic deposition (latest Cretaceous to early Oligocene) (Trettin, 1991a; Embry, 1991; Davies and Nassichuk, 1991). Differential loading, extension, or compression caused the flow of Carboniferous evaporites through much of Triassic to Neogene time (Trettin, 1991a).

4.2.2 The Bedrock Geology of Eastern Melville Island

A variety of sedimentary lithologies are well exposed over much of Melville Island, N.W.T (Figures 4.2 and 4.3). Three sedimentary successions dominate the geology of the island: 1) late Precambrian to Late Devonian infill of the Franklinian Mobile Belt; 2) Carboniferous to Tertiary infill of the Sverdrup Basin, sitting with angular unconformity on the Franklinian rocks; and 3) late Cenozoic semi-consolidated sand and gravel, unconformably overlying the Franklinian and Sverdrup rocks (Tozer and Thorsteinsson, 1964; Goodbody and Christie, 1994). Arctic Platform deposits are exposed over the southwestern extent of Melville Island. Folded Franklinian Mobile Belt deposits are exposed over much of central

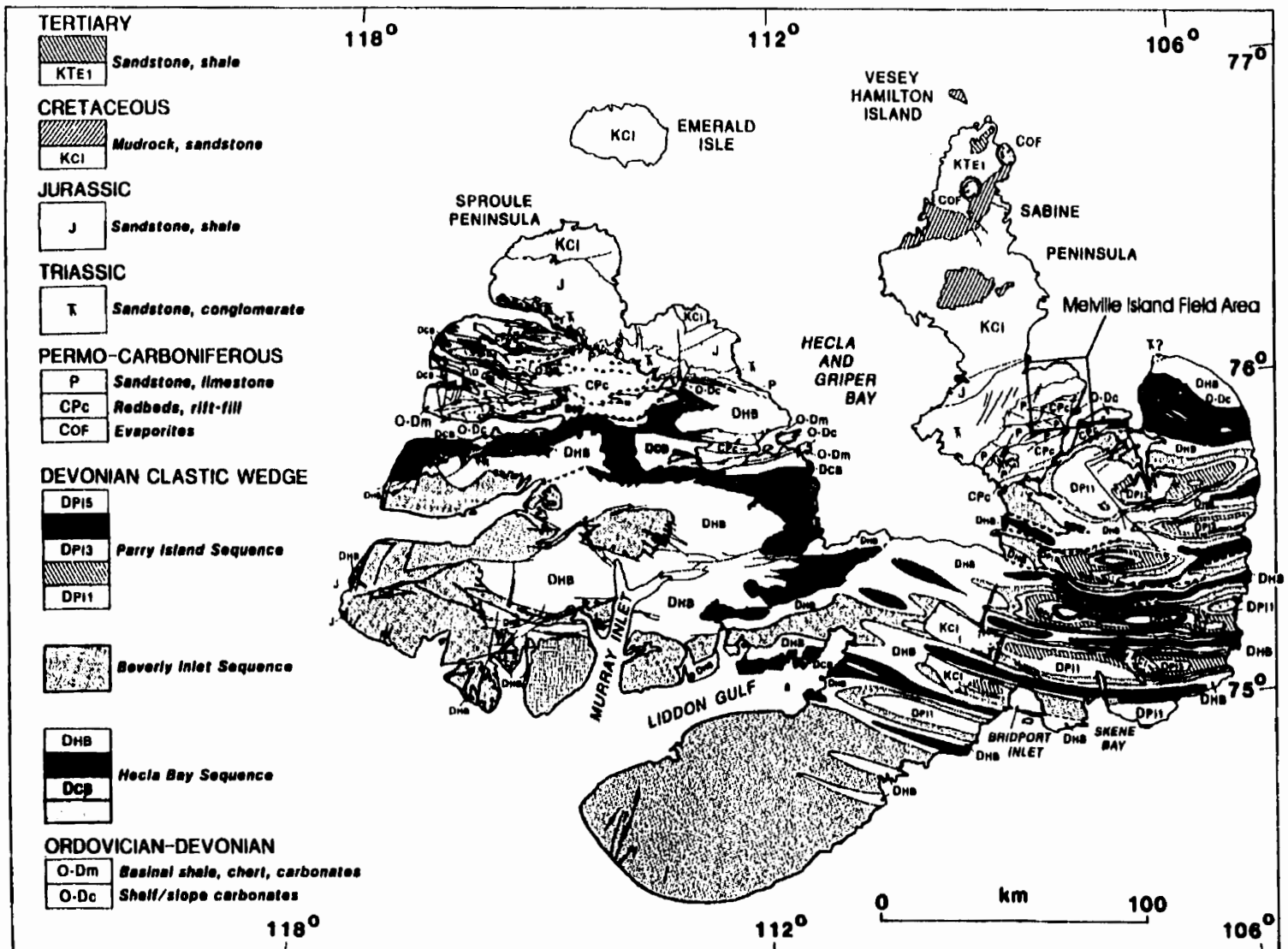

Figure 4.3 Geological map of Melville Island (Harrison, 1994a). The outline of the Melville Island Field Area is given.

Melville Island, while the Sverdrup Basin deposits are exposed over the northern portion of the island (Figures 4.2 and 4.3).

4.2.2.1 Southeastern Melville Island

In the eastern portion of Melville Island, **Franklinian deposits** lying in open folds are exposed at the surface in the region south of Weatherall Bay. As noted in Section 4.2.1.3, the Franklinian deposits were deformed during the latest Devonian or Early Carboniferous Ellesmerian Orogeny (Tozer and Thorsteinsson, 1964, Harrison *et al.*, 1991; Trettin, 1991b). These rocks, which were deposited after a transition from a carbonate sedimentary regime to a clastic-dominated sedimentary regime in the early Middle Devonian, are composed mainly of sandstones, shales, siltstones, and minor coal of the Hecla Bay, Beverly Inlet, and Parry Island clastic sequences (Embry, 1991, Goodbody and Christie, 1994, Harrison, 1994b) (Figure 4.3). Fold axes trend east-west in southern Melville Island.

4.2.2.2 Northeastern Melville Island

Ordovician-Devonian carbonate outcrops, which represent surface exposures of the Blue Fiord Formation and are associated with the **Towson Point Carbonate Platform Facies** (Harrison, 1995), are located both south and east of Weatherall Bay (Figure 4.3). Internal seismic patterns have been interpreted by Harrison (1995) to indicate the Blue Fiord Formation is composed of 1) extensive shelf carbonates, 2) shelf-edge carbonate buildups and proximal fore-reef facies carbonate debris aprons, and 3) lower slope to base-of-slope and rise facies layered carbonates and mudrocks.

Horizontal and gently north-dipping Sverdrup strata characterize much of the surface geology of **Sabine Peninsula** (Goodbody and Christie, 1994) (Figure 4.3). These rocks, deposited in the Sverdrup Basin [the subsidence of which commenced in the Namurian, continuing to the Late Cretaceous (Davies and Nassichuk, 1991)], are composed mainly of sandstone, shale, mudstone, and conglomerate, although limestone and calcareous lithologies are also present (Harrison, 1995).

Anhydrite and gypsum are exposed at the northern tip of Sabine Peninsula, in the form of two **piercement diapirs** of the Otto Fiord Formation (Barrow Dome and Colquhoun Dome; each feature is ~ 6 km across) (Figure 4.3). Also characteristic of the diapirs are tectonic rafts of more competent sediments including limestone, dolostone, calcareous mudrock, and minor black shale; bedded salt (halite) is probable in the subsurface below the carbonate and sulphate cap rock (Harrison, 1995). These Pennsylvanian evaporitic rocks are also associated with localized native-sulfur deposits, and are intruded by gabbro dykes, sills, and irregular masses (Tozer and Thorsteinsson, 1964, Harrison, 1995). The apparent radiometric ages for the intrusive igneous rocks on Sabine Peninsula are 123-152 Ma, by K/Ar (Harrison, 1995). The stratigraphic roots of the diapirs are at greater depths than the depths that have been imaged by seismic profiles (Harrison, 1995).

4.2.3 The Surface State of Geological Materials on Melville Island

Weathered and frost-shattered felsenmeer, in the form of fine sand to coarse rubble, is the most common surficial material on Melville Island (Hodgson *et al.*, 1984). Because much of this weathered rock has remained essentially in place, and because soil development

in the region is primitive (Edlund, 1986; Edlund, 1994), the main structural and lithological features of the bedrock of Melville Island are clearly visible in optical satellite imagery (Harrison *et al.*, 1985; Harrison, 1994a).

Bedrock outcrops are scattered throughout Melville Island, although the thickness of stratigraphic sections can be limited. Good outcrops are typically found in upland areas where bedrock has been folded or tilted. For example, on southern Sabine Peninsula, good bedrock outcrops are found in incised river valleys or on hog-back ridges and cuestas (Harrison, 1995).

4.2.4 Glacial Deposits on Melville Island

At its maximum during the late Wisconsinan, the Laurentide Ice Sheet extended from the Arctic mainland of Canada across Victoria, Prince of Wales, and Somerset islands to the southernmost extents of Melville and Bathurst Islands (Bryson *et al.*, 1969; Dyke *et al.*, 1982; Dyke, 1984; Hodgson *et al.*, 1984; Dyke, 1987; Dyke and Prest, 1987, Sharpe, 1992). The maximum extent of glacial ice in the Queen Elizabeth Islands during the late Wisconsinan remains uncertain (e.g., Mayewski *et al.*, 1981; Dyke 1984; England, 1998; Dyke, 1999; England, 1999; Wolfe and King, 1999). Most of Melville Island is believed to lie north and west of the limits of late-Wisconsinan glaciation (Hodgson *et al.*, 1984; Hodgson, 1989).

Principal glacial deposits on Melville Island, which include till and ice-contact gravels, are found in the central and southwestern region of the island on Dundas Peninsula (Tozer and Thorsteinsson, 1964; Hodgson *et al.*, 1984). Four units of till have been identified here (Hodgson *et al.*, 1984; Hodgson and Vincent, 1984). One of these units (the Winter Harbour

Till) is believed to have been deposited by the northern extent of the Laurentide Ice Sheet during the late-Wisconsinan, while the other units predate this unit and may have been deposited during an earlier glacial advance (Hodgson *et al.*, 1984; Hodgson, 1989).

Related to the late-Wisconsinan glaciation are elevated flights of beach ridges that ring the coastal regions of Melville Island, demonstrating that all coastal areas were submerged during at least one marine transgression (McLaren and Barnett, 1978; Hodgson *et al.*, 1984; Harrison, 1995). Such beach deposits record postglacial emergence of at least 55 to 90 m in west and central Melville Island, and more than 100 m in parts of eastern Melville Island (McLaren and Barnett, 1978; Hodgson *et al.*, 1984). Some of the formerly submerged areas cannot be distinguished from weathered rock at higher elevations, because of either 1) absence of marine reworking, or 2) later erosion of marine deposits (Hodgson *et al.*, 1984). The area of post-glacial marine overlap on eastern Melville Island is extensive, including much of Sabine Peninsula, and the shoreline of the island east of Weatherall Bay (McLaren and Barnett, 1978).

Erratics of sedimentary, plutonic, and metamorphic rocks are widely scattered over Melville Island, providing evidence for at least one complete and extensive glaciation of Melville Island that is presumed to have occurred during Early or Middle Pleistocene time (Tozer and Thorsteinsson, 1964; McLaren and Barnett, 1978; Harrison, 1995).

Record of glaciation of Melville Island by local ice caps is present on Melville Island, in the form of ice-marginal channels and small related watercourses (Tozer and Thorsteinsson, 1964; Hodgson *et al.*, 1984). There are several modern glaciers distributed on western Melville Island (e.g., Harrison, 1995).

4.2.5 The Vegetation of Melville Island

The Queen Elizabeth Islands represent "the extreme arctic ecosystem, where most plants are at or near their physiological limits of tolerance" (Edlund and Alt, 1989, p.3). Much of Melville Island is sparsely vegetated, reflecting both the harsh climate, and the poor development of soils on the island (Edlund 1986, Edlund 1994). Although there are regions of "exceptional diversity and abundance", a significant proportion of the island's surface area is either extremely impoverished (having a total vascular flora of less than 10 species) or is unvegetated [having only moss- and lichen-based (cryptogamic) communities, or no vegetation cover at all] (Edlund, 1994, p.247).

Of the thirteen vegetation communities recognized on Melville Island, the *barrens communities* (communities that form less than 20% surface cover, and which typically occur on well drained deposits) are the most common type of vascular-plant communities (Edlund, 1994). The *tundra communities* (communities that form nearly continuously vegetated terrain with an extensive cryptogamic ground cover) are mainly restricted to moderately to imperfectly drained soils on mid- to lower slopes where there has been a persistent snow cover in winter (Edlund 1994, p.251). Less extensive than the barrens and tundra communities are the *wetland (meadow) communities*, which are commonly found below the marine limit in fine sands and silts. *Cryptogamic communities* are found mainly on the coarse, neutral-to-weakly-acidic deposits of the Hecla Bay, Griper Bay, Parry Island, and Beverly Inlet formations (Edlund, 1994). Areas which are characterized by materials that are highly acidic or basic, contain no available nutrients, or are physically unstable, are typically unvegetated (e.g., the Kanguk Shale on Sabine Peninsula, whose weathering products have

a pH of 3.0) (Edlund, 1994, p.249).

The barrens and tundra communities are mainly dominated by *Dryas integrifolia* and *Salix arctica* (prostrate shrubs: "arctic avens" and "arctic willow", respectively), and by *Saxifraga oppositifolia* and *Luzula* (herbaceous species: "purple saxifrage" and "wood-rushes", respectively) (Edlund, 1994). Wetland communities are dominated by species such as grasses, cotton grasses, sedges, and woodrushes (Edlund, 1994).

As noted above, there are correlations between vegetation and bedrock lithology on Melville Island (Tozer and Thorsteinsson, 1964; Edlund, 1986; Edlund, 1994). Soil development in the region is primitive, and thus vascular plants root directly into soils that have similar physical and chemical properties to weathered bedrock (Edlund, 1986; Edlund and Alt, 1989). The correlation of vegetation distribution with lithology is based on such factors as the particle size, pH, weathering rate, and drainage of weathering products. For example, *Saxifraga oppostifolia* and *Dryas integrifolia* are calcifilous (calcium-loving) species that are commonly found on well-drained, weakly to moderately alkaline soils; *Luzula* and other grass-like plants are associated with weakly acidic to neutral soils; *Salix arctica* is associated with acidic sediments; boulder- and cobble-sized materials, which mantle large areas on Melville Island, are typically too coarse to support vascular plant communities; cryptogamic communities are found on coarse acidic rocks but typically cannot establish themselves on coarse carbonate rocks, since the rate of weathering of such alkaline materials is often too rapid for the establishment of even crustose lichen communities (Edlund 1986; Edlund and Alt, 1989; Edlund, 1994).

The specific vegetation communities present in the region of interest (northwest of the

West Arm of Weatherall Bay) include: 1) purple saxifrage barrens, 2) purple saxifrage tundra, 3) dryas-salix tundra, 4) luzula barrens, and 5) unvegetated areas (Edlund, 1994, p.248). Descriptions of the dominant vegetative species noted in the Melville Island Field Area during this project's 1998 field season are given in Section 4.2.7.1.

4.2.6 The Climate of Melville Island

Melville Island belongs to the Western Parry Channel sub-region of the Northwestern climate region of the Canadian Arctic Islands (Maxwell, 1980, 1981, 1982). Climatic conditions in this region are similar to those of the Arctic Ocean, which lies to the northwest. Except in the area located south and southeast of Melville Island, the region's channels are dominated by multi-year ice in both summer and winter. Mean January temperatures in the region are approximately -34°C, while mean July temperatures are approximately 4°C. Winter is prolonged, with the period of sub-zero mean daily temperatures extending approximately from August 20 to June 15. The annual mean temperature for the east-coast locale of Rae Point, the only location for which climatic data is available on Melville Island, is -17.9°C.

The Canadian Arctic Islands are classified as "polar desert" because of the low annual precipitation amounts among these islands (Maxwell, 1980). The annual precipitation in the Northwestern climate region is approximately 100 to 125 mm, with 30-35% falling as liquid precipitation (Maxwell, 1981). In general, the largest monthly precipitation values in the Canadian Arctic Islands occur in July and August (Maxwell, 1980). The depth of winter snow cover in the Canadian Arctic Islands is variable, averaging 30 cm inland; large portions of the islands accumulate relatively little winter snowcover (McKay, 1990).

Melville Island lies in the zone of continuous permafrost (ACGR, 1988). The amount of water lost from the surface of Melville Island is thus not as great as might be expected, since ice-rich cryotic ground acts as a barrier to water flow below the base of the active layer (the active layer, the upper layer of ground subject to annual freezing and thawing, is typically only 10 to 100 cm deep) (Maxwell, 1980; Edlund and Alt, 1989). The summer moisture regime of surface materials varies with topographic position and proximity to a source of moisture; lower slopes and valley bottoms typically remain moist throughout the summer, while hilltops characterized by thin winter snow cover may be very dry (Edlund and Alt, 1989).

4.2.7 The Melville Island Field Area

The author and one field assistant (Ian Fieldhouse) were transported by Twin Otter from Resolute Bay, Cornwallis Island, to an unprepared landing strip located southeast of Tingmisut Lake, Melville Island, on July 8, 1998 (Figure 4.4). The base camp used for the duration of the field period was established at this drop-off location. Over a period of 24 days, ground-truth reconnaissance of a ~20 x 20 km region located immediately west and north of the West Arm of Weatherall Bay was conducted; this region is referred to in this document as the Melville Island *Field Area*, to differentiate it from the *study area*, which encompasses all of eastern Melville Island. Departure from Melville Island to Resolute Bay occurred on August 1, 1998. The Melville Island Field Area was, along with the Cape Smith Belt Field Area (Section 4.3.8), used as the basis for the evaluation of classification algorithms and TM imagery presented in Chapters 5, 6, and 7. A portion of the Melville

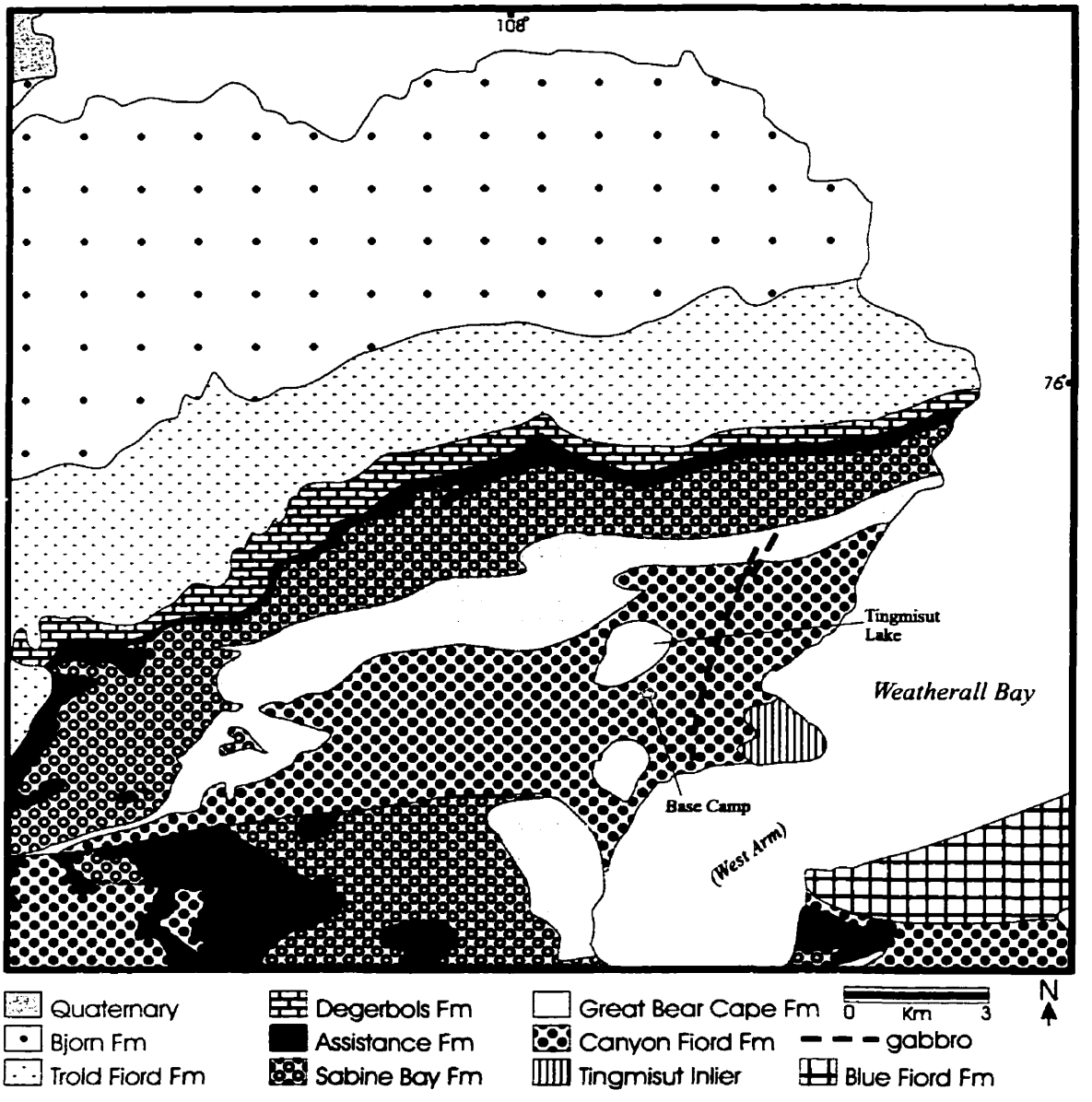

Figure 4.4 Geology of the Melville Island Field Area (after Harrison, 1995). Bedrock units are described in Table 4.1.

Island Field area was used to evaluate TM, Radarsat, and IKONOS imagery in Chapter 8.

4.2.7.1 Geology and Vegetation of the Melville Island Field Area

Geological materials exposed at the surface are mainly late-Paleozoic clastic and carbonate sequences of the Sverdrup Basin (Trettin, 1991a; Goodbody and Christie, 1994; Harrison, 1995). Also exposed in the study area are Ordovician and Silurian carbonates of the shelf province of the Franklinian Mobile Belt (Higgins *et al.*, 1991; Trettin, 1991a; Harrison, 1994a; Patchett *et al.*, 1999), and a Cretaceous gabbro dike (Harrison, 1995) (Figure 4.4). Brief descriptions of geological units are given in Table 4.1.

North-dipping cuesta landforms dominate the low-relief terrain; elevations in the region range from 0 to about 200 m above sea level. Notable ridge-forming sedimentary units include the Great Bear Cape Formation (limestone), the Degerböls Formation (limestone; Figure 4.5a), and the Bjorn Formation (sandstone). The near-vertical gabbro intrusion forms a distinct ridge that is oriented at high angle to the strike of the sedimentary formations (Figure 4.5b).

Weathered and frost-shattered felsenmeer, in the form of fine sand to coarse rubble, is the most common surficial material in the study area (Hodgson *et al.*, 1984). The locations of large bedrock outcrops are mainly restricted to the vicinities of incised river valleys or on hog-back ridges and cuestas (Harrison, 1995). Quaternary landforms such as till accumulations and ice-contact gravels are not present in the study area since most of Melville Island lies north and west of the apparent limits of the late Wisconsinan glaciation (Tozer and

Table 4.1 Bedrock units of the Melville Island Field Area (Harrison, 1994b; Harrison, 1995).

FORMATION / UNIT	DESCRIPTION AND INTERPRETATION
Unnamed Gabbro Unit (Cretaceous)	Near-vertical gabbro intrusion; ~123 Ma (Balkwill and Fox, 1982).
Bjorne Formation (Triassic)	Sandstone, variably carbonaceous and pebbly, weathers orange, grey-green, buff, and red; conglomerate; minor shale; fluvial and deltaic.
Trold Fiord Formation (Permian)	Sandstone, peloidal and glauconitic, green and red weathering, variably calcareous; minor pebbly bioclastic limestone; spiculitic chert; marine.
Degerböls Formation (Permian)	Limestone, bioclastic, common brachiopods, crinoids, and bryozoans; unrestricted shallow marine.
Assistance Formation (Permian)	Sandstone, grey to grey-green, variably glauconitic, quartzose, and carbonaceous; siltstone; fossiliferous ironstone; transgressive marine.
Sabine Bay Formation (Permian)	Sandstone, quartzose, cherty, and variably pebbly and carbonaceous; chert-pebble conglomerate; siltstone; minor coal; fluvial and marginal marine.
Great Bear Cape Formation (Permian)	Limestone, fossiliferous, variably pebbly and arenaceous; calcareous sandstone; unrestricted shallow water marine.
Canyon Fiord Formation (Carb.-Perm.)	Red-bed sandstone, variably pebbly and calcareous; chert-pebble conglomerate; oligomictic conglomerate and breccia; minor limestone; fluvial and shallow water marine.
Tingmisut Inlier (Beverly Inlet Fm) (Silurian)	Dolostone
Blue Fiord Formation (Ordovician)	Limestone, light brown, dark brown, and light gray; dolostone; subtidal and intertidal.

Thorsteinsson, 1964; Hodgson *et al.*, 1984). Although elevated flights of beach ridges ring many coastal regions of Melville Island (McLaren and Barnett, 1978; Hodgson *et al.*, 1984; Harrison, 1995), such beach deposits are not conspicuous in the field area itself.

The vegetative cover of most of the study area is sparse, and consists mainly of "*Saxifraga oppositifolia* barrens" [cover is generally <10%, and drainage is good; significant varieties include *Saxifraga oppositifolia* ("purple saxifrage"), *Salix arctica* ("arctic willow"), and the lichens *Thamnolia subuliformis* and *Lecidea lapicida*]. Less extensive in the study area are various cryptogamic communities (consisting only of lichen cover), and "*Saxifraga oppositifolia* tundra" [cover is nearly continuous and includes an extensive cryptogamic

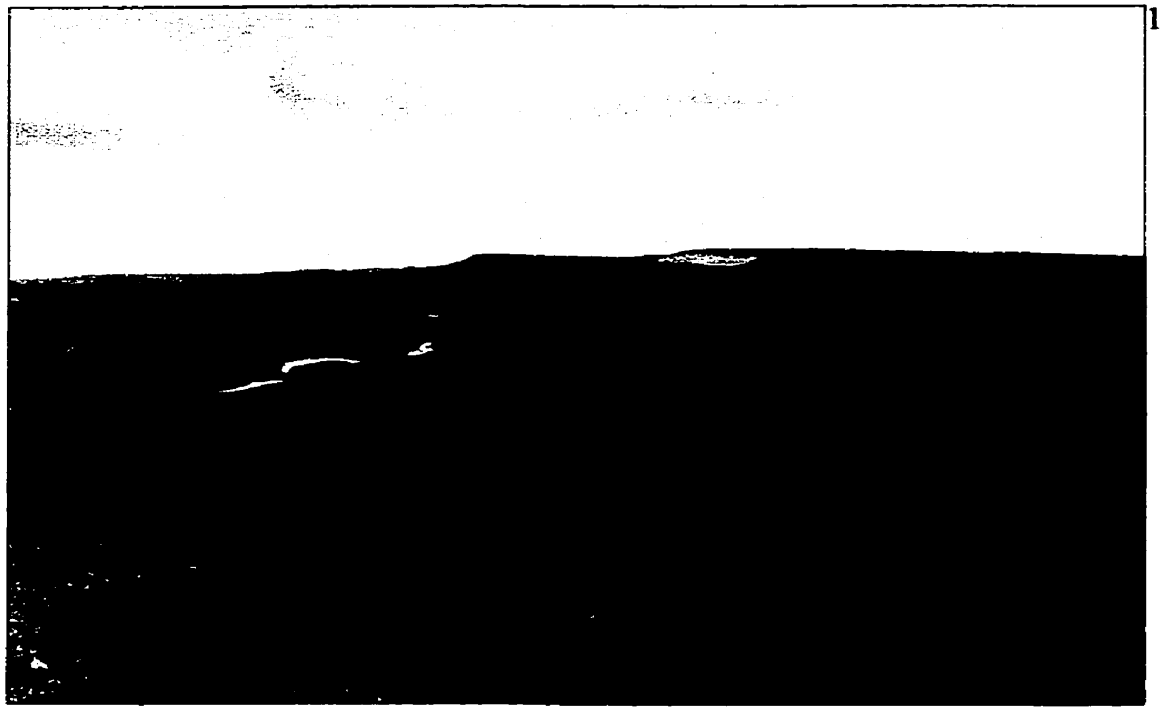

a

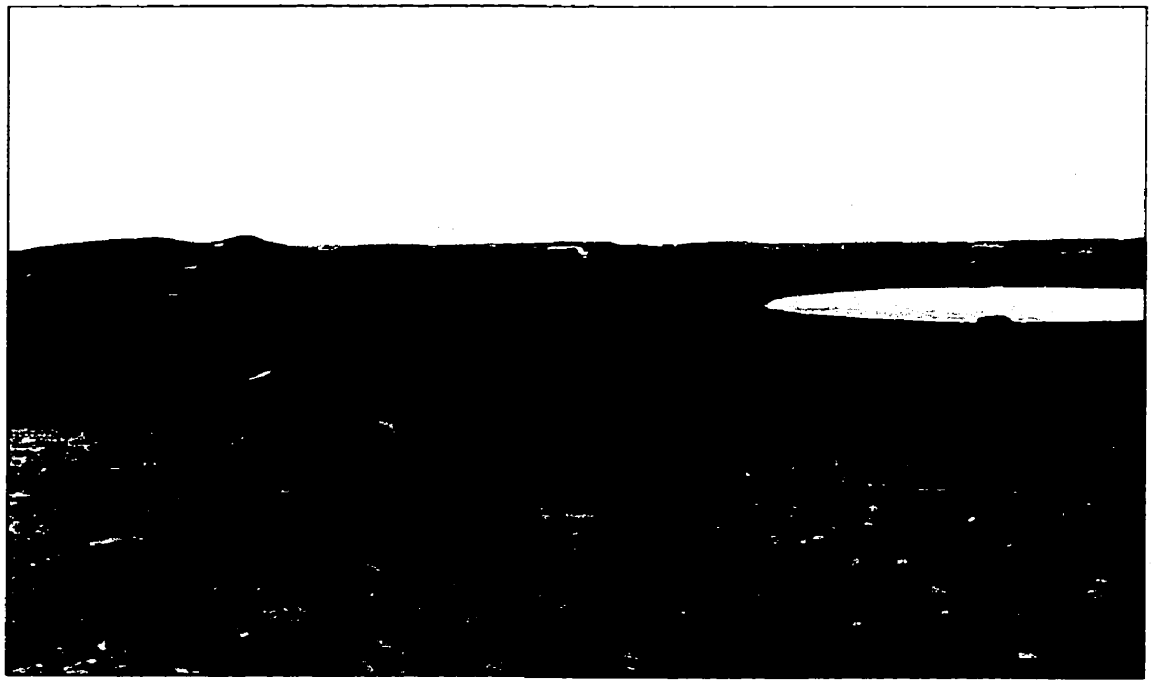

b

Figure 4.5 Photographs of the Melville Island Field Area. Photo *a* shows the prominant ridge formed by the Degerbols Formation limestone unit (at right), the Assistance Formation mudstone unit (centre), and the Sabine Bay Formation sandstone unit (at left); in the foreground are ~2 to 20 cm limestone clasts of the Degerbols Formation. Photo *b* shows the red Canyon Fiord Formation sandstones intruded by a prominent gabbro dike; in the foreground are ~2 to 20 cm limestones and sandstones of the Great Bear Cape and Canyon Fiord formations, respectively.

ground cover; locations of tundra are generally restricted to moderately to imperfectly drained soils on mid- to lower slopes where there has been a persistent snow cover in winter (Edlund, 1994)]. Common lichens noted in the Melville Island Field Area include the following: *Thamnolia subuliformis*, *Lecidea lapicida*, *Lecidea ramulosa*, and *Vulpicida tilesii* (lichen identification performed by Pak Yau Wong, Canadian Museum of Nature). A black material coats the surfaces of particularly moist areas in the Melville Island region. Several samples of this material collected from the field area have been identified as filamentous alga and fungal tissue by P.Y. Wong (Canadian Museum of Nature) and Dr. Michele Piercey-Normore (Department of Botany, University of Manitoba). The dark material is referred to in this document simply as "black algae" (see also Appendix A).

4.2.7.2 Melville Island Field Sites

In addition to the general reconnaissance of the Melville Island Field Area, 83 field sites were examined and sampled during the 1998 field season (Figures 4.6 to 4.8). These sites were chosen *in situ*, based on an understanding of the following four requirements: 1) all significant varieties of surface materials in the Field Area must be examined and sampled, 2) the locations of all field sites must be easily identifiable on aerial photographs, 3) each field site should be relatively homogeneous regarding the nature and distribution of surface materials, and 4) the surface area of each field site should be as large as possible (to allow each site to be represented in digital imagery by as many pixels as possible, and to reduce or eliminate the effects of small errors in the positioning of sites on satellite imagery).

At each of the 83 field sites, general lithological and vegetative information was

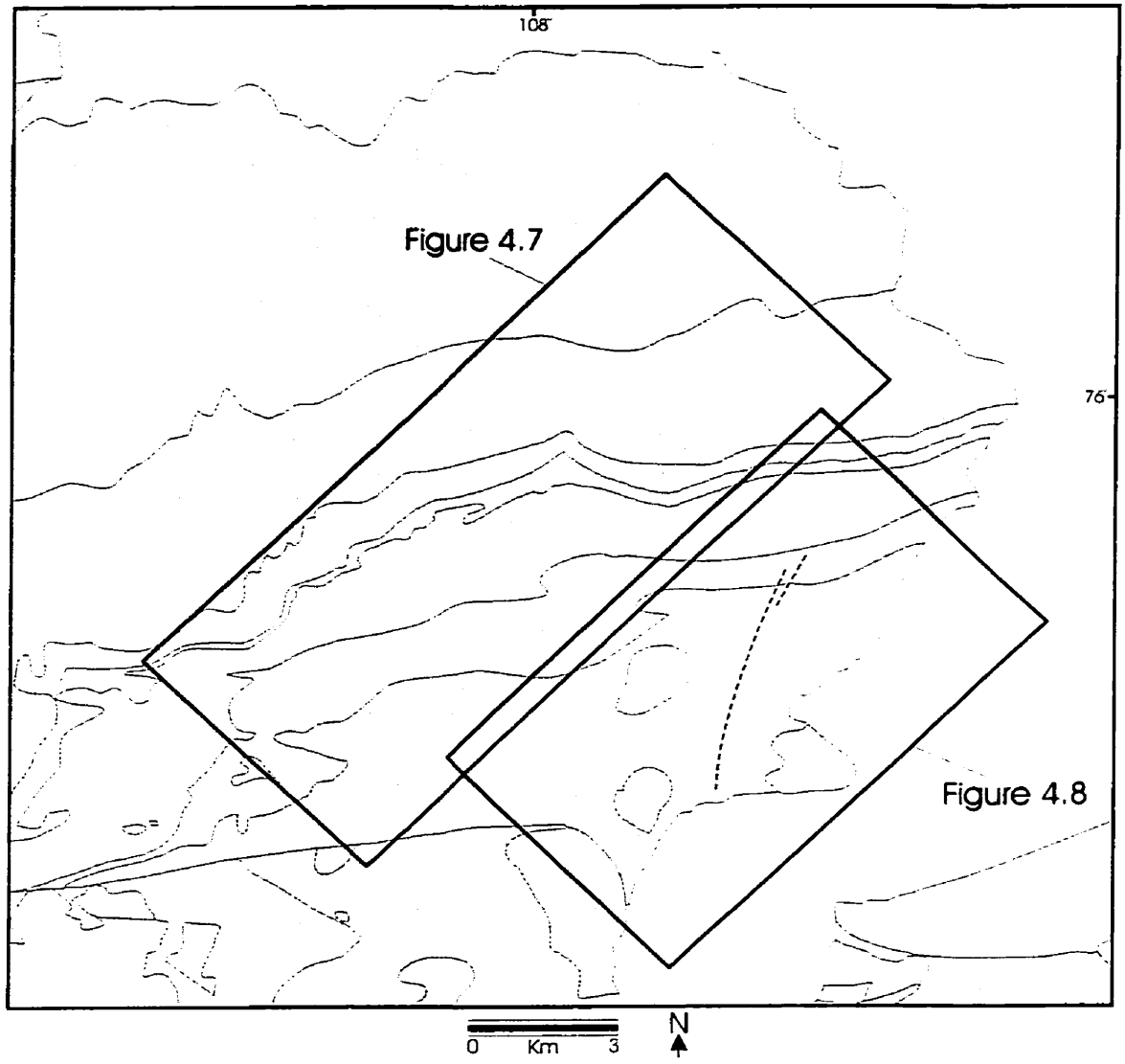

Figure 4.6 Areal extents of Figures 4.7 and 4.8 (outlines of geological units are identical to those given in Figure 4.4).

Figure 4.7 Site locations in the northwestern part of the Melville Island Field Area (aerial photos A16763-54 and A16763-93).

Figure 4.8 Site locations in the southeastern part of the Melville Island Field Area (aerial photos A16763-55 and A16763-92).

recorded (e.g., the lithologies present, the typical size range of rocks, the presence or absence of fines, the reaction of materials to HCl, the presence and nature of vegetation). In addition, representative samples of the following materials were collected at each site for later laboratory examination: 1) rocks, 2) fines, and 3) vegetation. Each site was further documented through the use of both photography and videography; at most sites, at least two photographs were taken (one oblique "landscape" photograph, and one vertical "closeup" photograph), and approximately one to ten minutes of video documentation were recorded. A summary of the information collected for each site is given in Appendix A. Most of the 83 sites were used as a basis for the generation of the database used in the evaluation of TM imagery and classification algorithms presented in Chapters 5 to 7 (see Section 5.2.1.1).

4.2.8 Melville Island Satellite Images

Two Landsat-5 TM images and two Radarsat C-band SAR images were available for use in the main Melville Island components of this research. The two TM images were acquired on July 20, 1992 (north; media id: 407298), and August 8, 1994 (south; media id: 409069), and provide coverage of essentially all of eastern Melville Island (Figure 4.9). Swath widths are 185 km, and image data have an 8-bit radiometric resolution. Both images were georeferenced to the Universal Transverse Mercator projection (Zone 13) using first-order mapping polynomials and nearest-neighbour resampling. Pixel spacing is 30 m for both images.

The two Radarsat images were acquired on July 10, 1998 (north; scene id: M0167801) and July 17, 1998 (south; scene id: M0168320), and provide coverage of all but

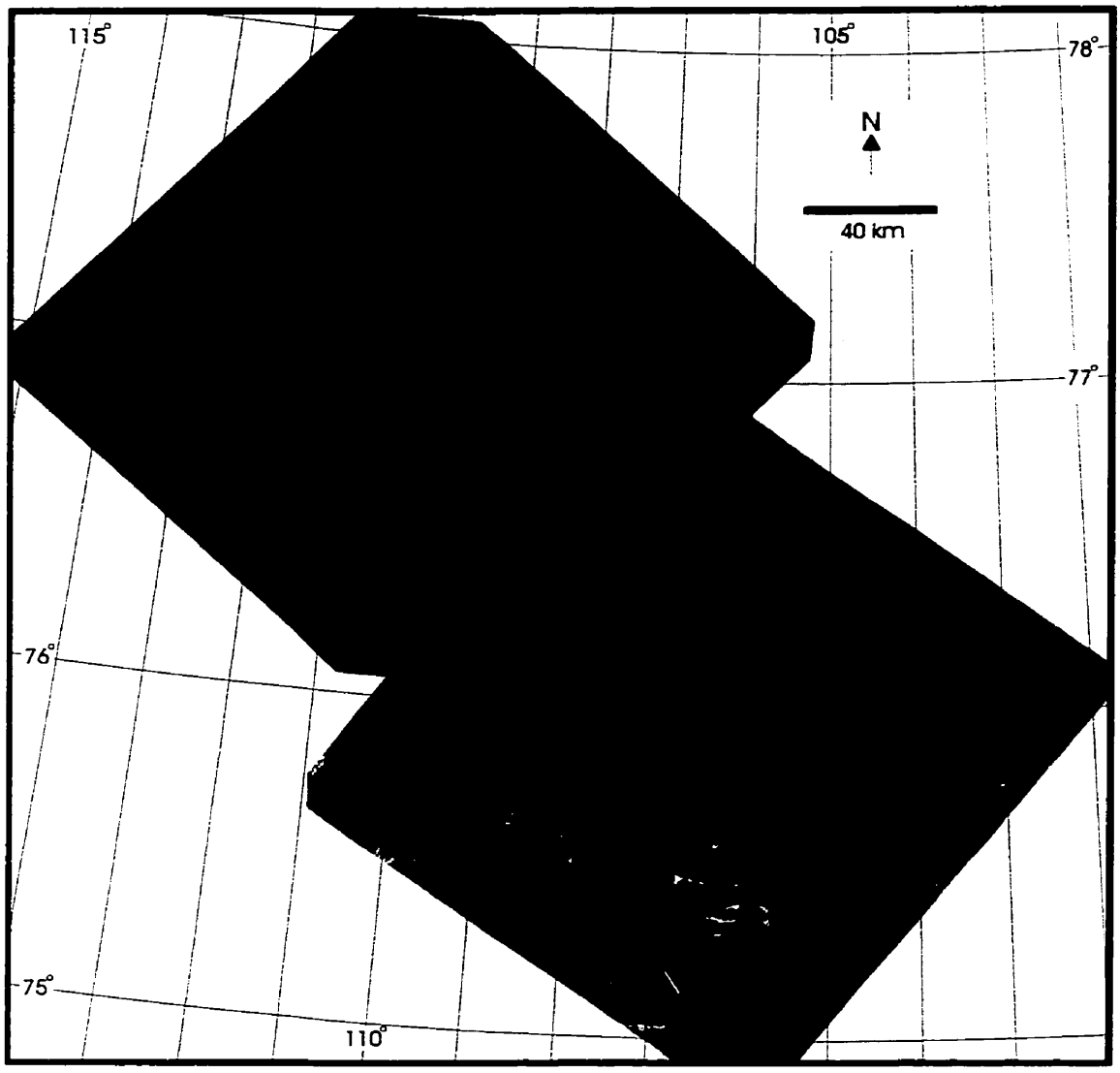

Figure 4.9 Landsat TM images for eastern Melville Island (compare with Figure 4.3). Colour composite uses channels 543:RGB.

the southernmost extent of eastern Melville Island (Figure 4.10). Both images were acquired using the *S7* beam mode [incidence angles = 44.9° to 49.4° (Luscombe *et al.*, 1993)] from an ascending orbit. Images are 100 x 100 km in dimension, and have a 16-bit dynamic range. The images were georeferenced to the Universal Transverse Mercator projection (Zone 13) using first-order mapping polynomials and nearest-neighbour resampling. Resolution of the images is 19.1 x 27 m (range x azimuth), and pixel spacing is 12.5 m. Both images were acquired during the 1998 Melville Island field season. Analyses that used and evaluated the TM and Radarsat data are documented in Chapters 5 to 8.

Both panchromatic and multispectral IKONOS images of a portion of the Melville Island Field Area were also used in this research. These images are discussed in Chapter 8.

4.3 The Cape Smith Belt Study Area

4.3.1 Geological Overview

The Archean protocraton of North America is an aggregate of former microcontinents, also referred to as the *Archean provinces*, which include: 1) the Superior Province; 2) the Wyoming Province; 3) the Slave Province; 4) the Nain Province; 5) the Hearne Province; and 6) the Rae Province (the last two of these provinces were parts of the former Churchill Province) (Figure 4.11) (Hoffman, 1989; Lucas *et al.*, 1998). The Archean provinces, which themselves are believed to be Late Archean crustal aggregates of the Archean equivalents of island arcs, are welded by Early Proterozoic collisional orogens (Figure 4.11) (Hoffman, 1989). The Archean protocraton is bordered along its west, south,

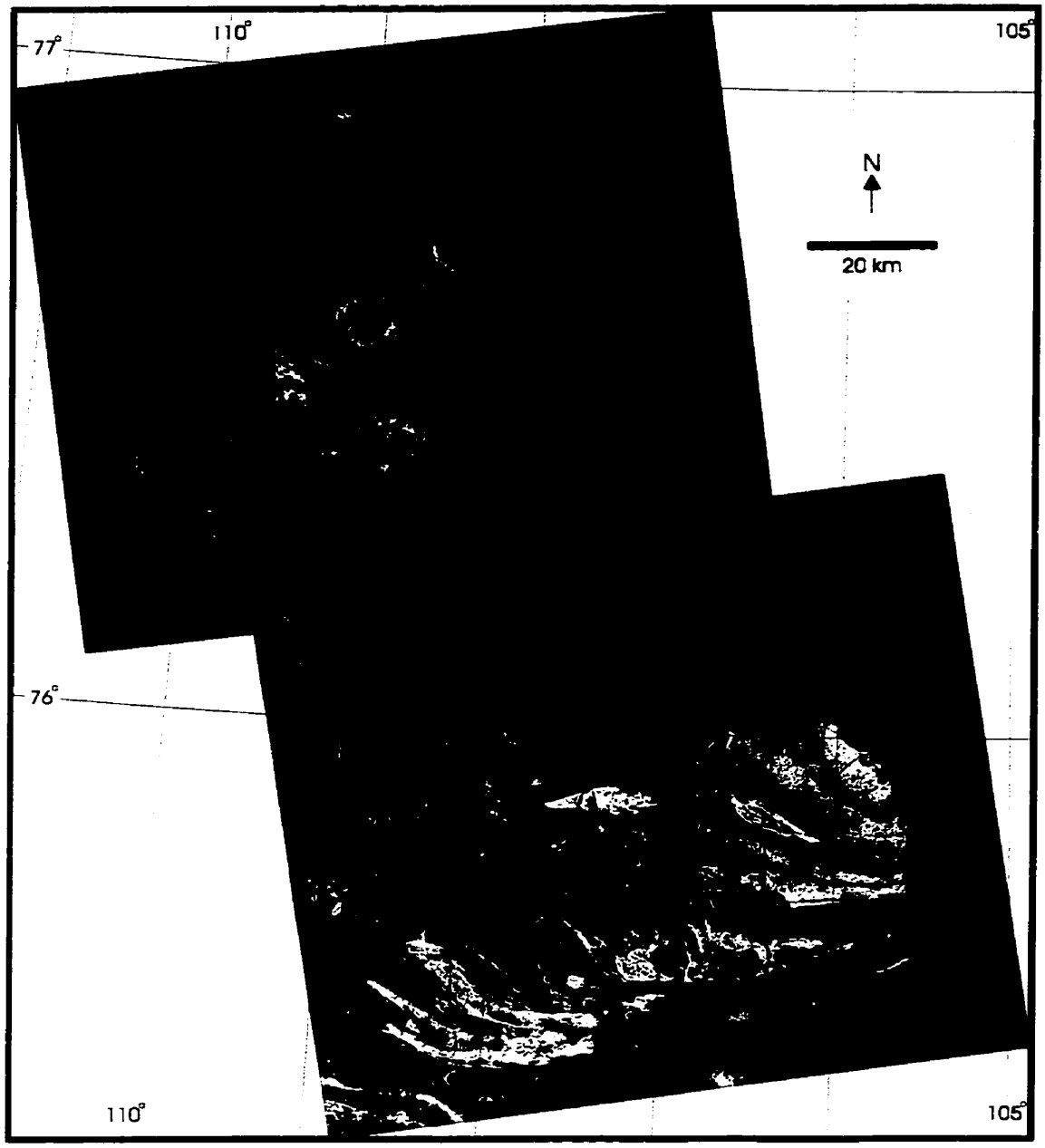

Figure 4.10 Radarsat images for eastern Melville Island (compare with Figure 4.3). The beam mode used for each image was *S7*.

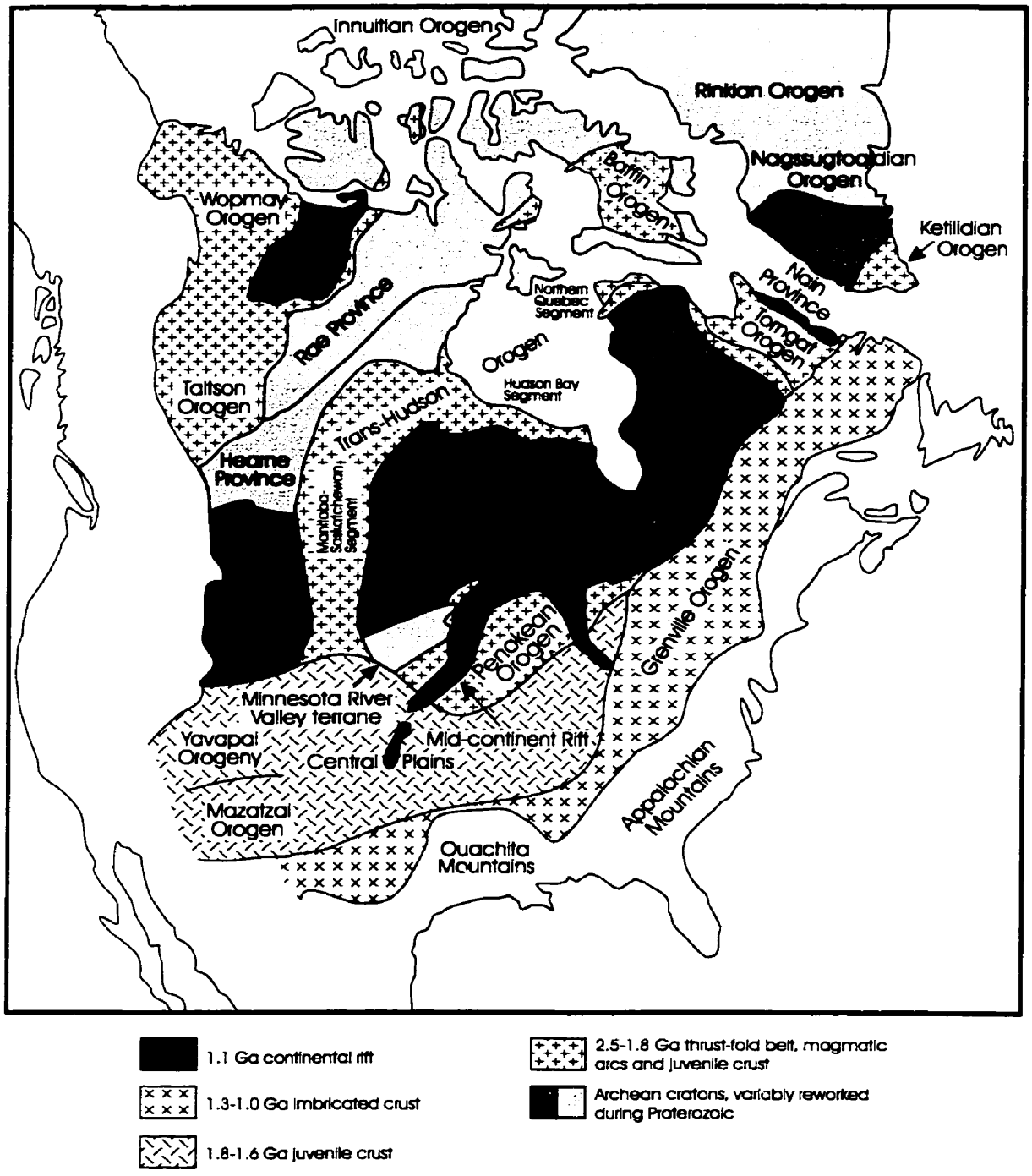

Figure 4.11 Archean Provinces of the Canadian Shield. The three main subdivisions of the Trans-Hudson Orogen (a Paleoproterozoic collision zone between the Superior Province and the Archean provinces to the north and to the west) are shown (after Card and Poulsen, 1998).

and southeast margins by crust that was accreted in the Early Proterozoic and contains little or no Archean material (Hoffman, 1989). The Grenville orogen accreted to the North American craton between 1.2 and 1.0 Ga through northwest-directed thrusting (Hoffman, 1989; Davidson, 1995).

The Superior Province is composed of subparallel east-northeast-trending belts that contrast with regard to lithology, age, and/or metamorphic grade (Card, 1990; Card and Poulsen, 1998). The belted structure of the Superior Province is truncated on its eastern and western margins by the Trans-Hudson, Grenville, and New Québec orogens, indicating that this province must be a rifted fragment of a larger Archean crustal assembly (Hoffman, 1989).

4.3.2 The Québec-Baffin Segment of the Trans-Hudson Orogen

The Trans-Hudson orogen is the Paleoproterozoic collision zone between the Superior Province and the Archean provinces to the north and to the west (Hoffman, 1988; Hoffman, 1989; Lewry and Stauffer, 1990). Within Canada, the orogen may be divided into three segments: 1) the northern Québec [Québec-Baffin] segment, 2) the Hudson Bay segment, and 3) the Manitoba-Saskatchewan segment (Hoffman, 1989; St-Onge *et al.*, 1999) (Figure 4.11).

The Québec-Baffin segment of the Trans-Hudson orogen has been interpreted in northern Québec as an arc-continent collisional belt (the Ungava Orogen) (St-Onge and Lucas, 1990a). This belt consists of tectonostratigraphic elements accumulated on or accreted to the northern margin of the Superior Province during divergent- and convergent-margin tectonic activity that occurred over a period of >0.2 Ga (St-Onge and Lucas, 1990a,

1992, 1993). The external zone of the Québec-Baffin segment of the Trans-Hudson Orogen is peripheral to the Superior Province in northern Québec, while the internal zone is exposed on southern Baffin Island (St-Onge *et al.*, 1999).

4.3.3 The Geology of the Cape Smith Belt and Surrounding Region

Cape Smith Belt of northern Québec is a 20 000 km^2 Early Proterozoic greenstone belt that forms a portion of the Québec-Baffin segment of the Trans-Hudson Orogen (Figure 4.12) (Hoffman, 1985; St-Onge *et al.*, 1986; St-Onge and Lucas, 1989, 1990a, 1993; St-Onge *et al.*, 1999). Geographically, the surface expression of the belt lies between that of the Minto block (Superior Province) to the south, and the Kovic Domain (Superior Province) and Narsajuak arc to the north (Figure 4.12) (Card, 1998; St-Onge *et al.*, 1999). The Cape Smith Belt is a zone of east-west trending mafic-ultramafic thrust sheets that was produced by southward-directed thrusting of allochthonous crust onto the Superior Province (Hoffman, 1985). The belt is preserved in a doubly-plunging synclinorium as a stack of klippen (Hoffman, 1985, St-Onge *et al.*, 1989, St-Onge and Lucas, 1990a). The belt provides evidence for ancient plate tectonics through 1) the presence of an ophiolite, and 2) indications of continental subduction (St-Onge *et al.*, 1988; Scott *et al.*, 1989; St-Onge and Lucas, 1990a).

The Cape Smith Belt is contiguous along its northwestern, northeastern, eastern, and southern exposed margins with Archean tonalites of the Superior Province (Figure 4.12) (Taylor, 1982; Doig, 1987; St-Onge *et al.*, 1988; St-Onge and Lucas, 1992). The belt is separated from the underlying basement of the Superior Province, and its autochthonous

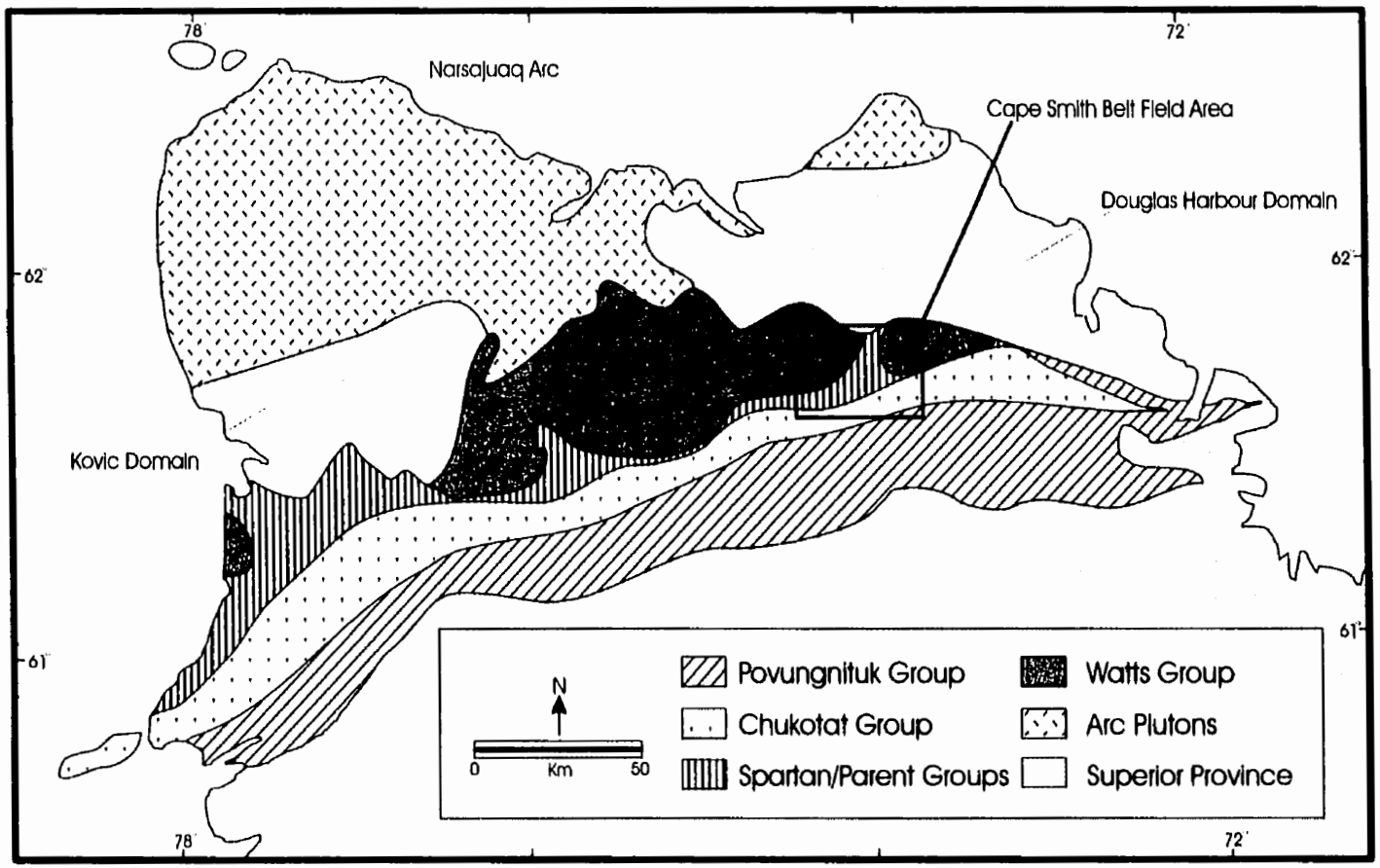

Figure 4.12 Simplified geological map of the Cape Smith Belt, which consists of the Povungnituk, Chukotat, Spartan/Parent, and Watts groups (after Giovenazzo *et al.*, 1989, St-Onge and Lucas, 1992; St-Onge *et al.*, 1999). The outline of the Cape Smith Belt Field Area is given.

Early Proterozoic cover, by a continuous décollement (Hoffman, 1985; St-Onge *et al.*, 1986). This décollement is hypothesized to be rooted in the vicinity of Baffin Island (St. Onge *et al.*, 1999).

The high-grade (granulite) rocks located north of the Cape Smith Belt in the vicinity of Sugluk Inlet are known as the Narsajuaq arc (Figure 4.12), and are interpreted to be allochthonous with respect to the Superior Province (Hoffman, 1985; St-Onge and Lucas, 1990b, 1992, 1997). The autochthonous Superior Province rocks of the Kovic and Douglas Harbour domains, located northwest and northeast of the belt respectively (Figure 4.12), were exposed by the post-thrust formation of an east-trending regional antiform [termed the Kovik Antiform by Hoffman (1985)], and by the interference between this antiform and later north-trending antiforms to produce a saddle (St-Onge and Lucas, 1992). The subsequent erosion of the thrusted allochthon through the basal décollement at the east-trending antiform exposed the basement rocks of the Kovic and Douglas Harbour domains (Lucas and St-Onge 1991; St-Onge and Lucas, 1992). The rocks of the Cape Smith Belt are associated with strong positive gravity anomalies, reflecting the higher density of the constituent mafic and ultramafic rocks (in contrast to the felsic plutonic rocks that characterize the areas to the south and north) (e.g., Thomas *et al.*, 1991).

Most of the Cape Smith Belt is composed of north-dipping imbricate thrust sheets (Hoffman ,1985), the configuration of which constrain the distribution of tectonostratigraphic units within the belt (St-Onge *et al.*, 1989). Although the Cape Smith Belt can be structurally divided into southern, midbelt, and northern thrust sheets, a more useful lithological and tectonostratigraphic subdivision of the belt produces five distinct Early Proterozoic suites,

generally distributed from south to north (St-Onge *et al.*,1989; St-Onge and Lucas, 1993) (Figure 4.12):

1) fluvio-deltaic sediments of the Povungnituk Group (preserved south of the belt, on unstretched continental crust of the Superior Province),

2) rift-fill sediments of the Povungnituk Group,

3) transitional crust basalts (pillowed and massive basalt flows) of the Chukotat Group,

4) deep-water sediments (pelites interbedded with semipelite and minor sandstone) of the Spartan Group, and

5) ophiolitic units (basalts, sheeted dykes, and mafic-ultramafic plutonics) of the 2.00 Ga Purtuniq ophiolite (Watts Group).

The northern half of the belt is sparsely intruded by granitoid plutons (Hoffman, 1985). All rocks of the Cape Smith Belt have been metamorphosed to between greenschist and amphibolite facies (St-Onge and Lucas, 1990a). Tectonostratigraphic units of the Cape Smith Belt and surrounding region are summarized in Table 4.2.

A general summary of the groups and suites of the region of the Cape Smith Belt, based mainly on the summary of St-Onge and Lucas (1993) and references therein (except where noted), follows. This summary is divided into the following sections: 1) Superior Province, 2) Povungnituk Group, 3) Chukotat Group, 4) Spartan Group, 5) Parent Group, 6) Watts Group, and 7) Narsajuak Arc.

1) Superior Province: The Superior Province in this region consists of three main units: the Kovik Domain, the Douglas Harbour Domain, and the Minto Block (Figure 4.12)

(Card, 1998). These units consist of Archean (typically 2600 to 3000 Ma) rocks that occur as the stratigraphic or structural basement to the Cape Smith Belt and the Narsajuaq arc, and that, at the scale of the orogen, may be considered (par)-autochthonous with regard to the overlying thrust belt (Card, 1998; St-Onge *et al.*, 1999). The lithologies of the region's three main units are generally similar, consisting primarily of plutonic rocks ranging from quartz diorite to syenogranite, with screens and inclusions of mafic-ultramafic and metasedimentary rocks (Card, 1998). Tonalite is the dominant rock type in the region (Card 1998). Both granulite-facies (older) and amphibolite-facies (younger) mineral assemblages are present (Card, 1998).

2) Povungnituk Group: In the Early Proterozoic, the rocks of the Povungnituk and Chukotat groups were accumulated on or adjacent to the rifted Superior Province craton. The rocks of these groups are progressively more allochthonous from south to north, with respect to the underlying basement of the Superior Province. The Povungnituk Group may be divided into the lower Povungnituk Group (autochthonous and allochthonous, mainly sedimentary rocks) and the upper Povungnituk Group (allochthonous, mainly volcanic rocks). Both the sedimentary and volcanic rocks of the Povungnituk Group are intruded by massive gabbroic sills which are hypothesized to be part of a feeder system to the volcanic rocks of the upper Povungnituk Group.

2a) Lower Povungnituk Group: The lower Povungnituk Group includes, in part, areally-restricted autochthonous, clastic sedimentary rocks that occur in thin sequences along the southern margin of the belt, and as small outliers in the vicinity of Burgoyne Bay. These autochthonous rocks rest unconformably on Archean tonalite or monzogranite, and are

Table 4.2 Tectonostratigraphic units in the eastern Cape Smith Belt and surrounding region (St-Onge and Lucas, 1993).

Group / Suite	Dominant Lithology
n/a	Diabase dykes (Late Proterozoic).
Narsajuaq Arc	Tonalite, granite, quartz diorite, semi-pelite.
Spartan Group	Semipelite, pelite, quartzite, gabbro.
Watts Group	Basalt, gabbro sills, sheeted gabbroic dykes.
	Pyroxenite.
	Layered gabbro.
	Layered peridotite.
Chukotat Group	Dominantly plagioclase phyric basalt, gabbro.
	Dominantly pyroxene phyric basalt, gabbro.
	Dominantly olivine phyric basalt, gabbro, peridotite, layered gabbro-peridotite sills.
Povungnituk Group (Upper)	Basalt, volcaniclastic sedimentary rock, rhyolite, minor semipelite and quartzite, gabbro, peridotite, layered gabbro-peridotite sills.
Povungnituk Group (Lower)	Micaceous quartzite.
	Basalt, volcaniclastic sedimentary rock, rhyolite, minor quartzite, dolomite and calc-silicate, gabbro, peridotite, layered
	Semipelite, pelite, micaceous quartzite, quartzite, conglomerate, ironstone, dolomite, calc-silicate, minor basalt and volcaniclastic rocks, gabbro, peridotite, layered peridotite-gabbro sills.
	Ironstone, minor quartzite and semipelite.
	Quartzite, ironstone, conglomerate, semipelite.
Superior Province	Tonalite, granite, amphibolite.

capped by the basal décollement of the thrust belt. Most of the lower Povungnituk Group, however, consists of allochthonous sedimentary and volcanic rocks. From south to north, ironstone and semipelite are found to grade into mafic volcaniclastic rocks interlayered with basalt flows. The tectonostratigraphic changes of the allochthonous units are interpreted to have resulted from an increase in water depth and the accumulation of units which represent more distal facies from south-to-north along a north-facing rift margin. A gabbroic sill emplaced in the lower Povungnituk Group has been dated at 2038 Ma (U-Pb), providing a minimum age for the commencement of continental-margin subsidence and accumulation of sedimentary rocks along the northern margin of the Superior Province.

2b) Upper Povungnituk Group: The upper Povungnituk group includes tholeiitic basalt flows that conformably overlie or are interfingered with the upper clastic sedimentary rocks. Thin pillowed mafic flows, thicker tabular flows, and volcaniclastic sedimentary units occur in this group. Flows are separated by dolomite and black semipelite throughout the sequence. A rhyolite sample dated from near the top of the volcanic sequence is dated at 1959 Ma (U-Pb). The upper Povungnituk Group is believed to be associated with rifting of the Superior Province.

3) Chukotat Group: The Chukotat group is almost entirely igneous, consisting of lava flows with individual thicknesses between 2 and 100 m. Submarine accumulation is indicated by the presence of structures such as pillowed flows and pillow tubes. Rock compositions range from komatiitic basalts to normal MORBs (mid-ocean-ridge basalts). Mapped lithological units of the Chukotat Group include the following: olivine-phyric (komatiitic) basalt, pyroxene-phyric basalt, plagioclase-phyric basalt (normal MORB), and

layered mafic-ultramafic (gabbro-peridotite) sills. Based in part on the presence of these sills, the fault-bounded Chukotat Group is believed to be related to the northern rifted margin of the Superior Province. Sills and ultramafic intrusions in the Upper Povungnituk Group form part of the feeder system to the lower Chukotat Group; economic Ni-Cu-PGE sulfide deposits are associated with elements of this feeder system, with the best developed deposits occurring near the contact between the Povungnituk and Chukotat groups (Giovenazzo *et al.*, 1989). The Ni-Cu-PGE mineralization is most notable in the Raglan horizon, within which deposits are hosted mainly by ultramafic sills that are typically thinner than 150 m and can be traced for several kilometres (Giovenazzo *et al.*, 1989).

The Chukotat Group is interpreted to record the shift from the production of continental rift-type volcanic rocks to the formation of transitional (and possibly oceanic) crust. With a sill intruding the lower Chukotat Group dated at 1918 Ma (U-Pb), the hypothesized U-Pb chronology of rifting is as follows: 1) rifting initiated by 2038 Ma, 2) accumulation of >5 km of continental tholeiitic basalts by 1959 Ma, and 3) transition toward the formation of an ocean basin by ca. 1918 Ma.

4) Spartan Group: The Spartan Group is a fault-bounded assemblage of clastic sedimentary rocks, with no known tectonostratigraphic or magmatic link with the rocks of the Superior Province, the Povungnituk Group, or the Chukotat Group. Lithologies include mainly laminated dark pelites and semipelite. Fine-grained mafic sills intrude the sedimentary rocks of the Spartan Group south of Lac Watts. The Spartan Group may represent a clastic apron marginal to the hypothesized Parent Group magmatic arc, or it may alternatively represent distal deposits associated with the rift margin of the northern Superior Province.

5) Parent Group: The Parent Group, located in the western portion of the Cape Smith Belt, is in the analogous structural position to that of the Spartan Group (i.e., it is in fault contact with the underlying Chukotat Group and the overlying Watts Group). The rocks of the Parent Group are dominantly volcanic, and have been interpreted as having been deposited in a subduction-related magmatic arc.

6) Watts Group: The Watts Group is a fault-bounded assemblage of layered mafic and ultramafic rocks, massive and pillowed basalt flows, mafic sills and sheeted dykes, and rare plagiogranite intrusions. Like the Spartan Group, there is no known tectonostratigraphic or magmatic link between the Watts Group and the rocks of the Superior Province, the Povungnituk Group, or the Chukotat Group. Mapped lithological units of the Watts Group include the following: layered peridotite, layered gabbro, pyroxenite, and a sheeted dyke complex. The layered gabbro unit forms the most volumetric unit of the Watts Group, and is defined by two end-member mineral assemblages: 1) hornblende (after primary pyroxene), and 2) plagioclase-zoisite (after primary plagioclase) (the two end-members represent black meta-pyroxenite and meta-anorthosite layers, respectively). Two gabbro layers are dated at 1998 and 1997.5 Ma (U-Pb). The rocks of the Watts Group have been interpreted to represent the crustal remnants of a tectonically dismembered ophiolite suite (e.g., Scott *et al.* 1989). The relation, if any, of the ophiolite to the basin into which much of the Puvungnituk and Chukotat groups accumulated, is unclear. The rocks of the Watts and Parent groups are intruded by large tonalite plutons which are dated from 1898 Ma to 1839 Ma. These rocks are interpreted to be correlative with the plutonic rocks of the Early Proterozoic Narsajuaq arc.

7) Narsajuaq Arc: The Narsajuak arc is a distinct terrane that has been dated from about 1860 to 1830 Ma, and that collided with the Superior Province sometime after 1830 Ma (St-Onge and Lucas, 1992). The Narsajuak arc is comprised of a layered calc-alkaline plutonic sequence as well as deepwater sedimentary rocks, all cut by voluminous plutons (St-Onge and Lucas, 1992, 1997). Common calc-alkaline lithologies in the layered sequence include tonalite and quartz diorite, while the deepwater sedimentary lithologies include mainly graphitic, sulphidic semi-pelites. The layered plutonic and sedimentary rocks were intruded by tonalite, granite, and quartz diorite plutonic bodies, which have been dated at about 1844-1826 Ma. Granulite metamorphism, coeval with the plutonism, affected all lithologies, and was overprinted by amphibolite-grade assemblages associated with the collision of the Narsajuak arc with the margin of the Superior Province (St-Onge and Lucas, 1992).

4.3.4 The Surface State of Geological Materials in the Cape Smith Belt Region

The entire region is mantled by a thin, discontinuous cover of glacial drift, with boulder fields commonly resting on glacially-polished bedrock surfaces (St-Onge and Scott, 1986). Most boulders in the region appear to be glacially-transported erratics, although a felsenmeer appears to be slowly developing near ridge summits (St-Onge and Scott 1986). Despite the presence of glacial deposits, bedrock is exposed over much of the region (St-Onge and Scott, 1986; Daigneault, 1996a, 1996b, 1997).

4.3.5 Glacial Deposits in the Cape Smith Belt Region

During the peak of the late Wisconsinan glaciation, the region was overlain by the

Labrador Sector of the Laurentide Ice Sheet (Fulton, 1989). Deglaciation began about 8000 years ago (Dyke and Prest, 1987), with the ice front retreating from the northeast toward the southwest (Daigneault, 1993). Deglaciation was followed by marine submergence, and raised deltas produced during this submergence are now found at elevations of up to ~135 m. Numerous ice-marginal and proglacial meltwater channels are found in the Purtuniq area; these landforms generally indicate a retreat of ice toward the south (Daigneault, 1993). Scattered throughout the region are eskers and other meltwater landforms that have lengths of up to 40 km (Daigneault, 1993, 1996a, 1996b, 1997). Although a thin and discontinuous cover of glacial drift is present throughout the region, bedrock exposure is generally good (St-Onge and Scott, 1986; St-Onge and Lucas, 1993; Daigneault, 1996a, 1996b, 1997).

4.3.6 The Vegetation of the Cape Smith Belt Region

The Cape Smith Belt Study Area is mainly characterized by barrens communities, including mosses, grasses, and similar low-growing plants (St-Onge and Lucas, 1993). Apart from small alders and willows which grow in sheltered locations at low elevations, dwarf tundra vegetation dominates the region. Most bedrock outcrops are partially covered by lichens, except in areas associated with late-melting snowbanks (St-Onge and Lucas, 1993). Information on the specific varieties of vegetation present in the Cape Smith Belt Field Area is given in Section 4.3.8.1.

4.3.7 The Climate of the Cape Smith Belt Region

The Cape Smith Belt region is within the Low Arctic Ecoclimatic Region (Ecoregions

Working Group, 1989), and the northern portion of the region lies within the Hudson Strait sub-region of the Eastern climate region of the Canadian Arctic Islands (Maxwell, 1980). The Cape Smith Belt region has an annual mean air temperature of about -7°C. Mean January temperatures are about -23°C, while mean July temperatures are about 8.5°C (Maxwell, 1980). Winter, defined as the period of sub-zero mean daily temperatures, typically extends from about October 20 to May 30 (Maxwell, 1980). Terrain generally becomes snow free by June, although some high-elevation locations are not snow free until as late as early August (St-Onge and Lucas, 1993). The region is within the zone of continuous permafrost (ACGR, 1988).

4.3.8 Cape Smith Belt Field Area

The author and one field assistant (Ian Fieldhouse) were transported by helicopter from a location near the Raglan Mine (operated by Falconbridge Ltd.) to a location southeast of Lac Watts on August 11, 1999 (Figures 4.12 and 4.13). The base camp used for the duration of the field period was established at this drop-off location. Over a period of 13 days, ground-truth reconnaissance of portions of a ~30 x 20 km region located southeast of Lac Watts was conducted (Figure 4.13); this region is referred to in this document as the Cape Smith Belt *Field Area*, to differentiate it from the *study area*, which encompasses much of the central portion of the Cape Smith Belt. Departure from the field area occurred on August 23, 1999. The Cape Smith Belt Field Area was used as the basis for the evaluation of classification algorithms and TM imagery presented in Chapters 5, 6, and 7, as well as an evaluation of TM and Radarsat imagery in Chapter 8.

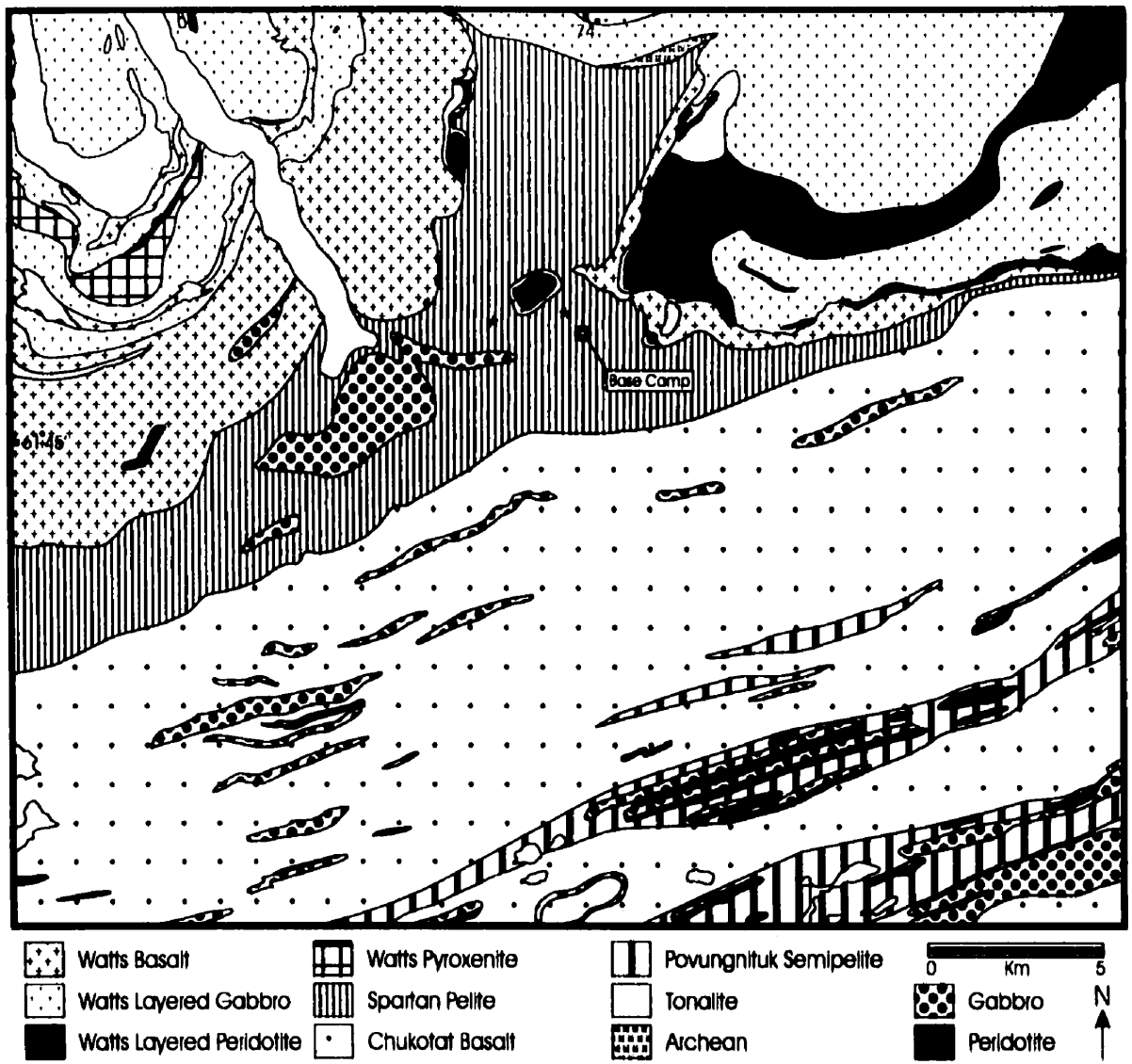

Figure 4.13 Geology of the Cape Smith Belt Field Area (after St-Onge and Lucas, 1989). Bedrock units are described in Table 4.3. Areas where mafic and ultramafic lithologies are variably present as surficial deposits on Spartan Group materials are indicated by (*).

4.3.8.1 Geology and Vegetation of the Cape Smith Belt Field Area

Geological materials exposed at the surface are mainly: 1) basalt, gabbro, and peridotite of the Watts Group, 2) pelite of the Spartan Group, and 3) basalt of the Chukotat Group (St-Onge and Lucas 1989; Scott and Bickle, 1991; Scott *et al.*, 1989; St-Onge and Lucas, 1993) (Figure 4.13). Brief descriptions of geological units are given in Table 4.3 below; further information is given above in Section 4.3.3.

Table 4.3 Bedrock units of the Cape Smith Belt Field Area (St-Onge and Lucas, 1989; 1993). Further details are given in Section 4.3.3.

GROUP / LITHOLOGY	DESCRIPTION AND INTERPRETATION
Watts Group basalt	basalt, gabbro sills, sheeted gabbroic dykes; Purtuniq ophiolite.
Watts Group gabbro	layered gabbro; Purtuniq ophiolite.
Watts Group peridotite	layered peridotite; Purtuniq ophiolite.
Watts Group pyroxenite	pyroxenite; Purtuniq ophiolite.
Spartan Group pelite	graphitic pelite, semipelite, sandstone, gabbro; marine clastic apron or distal deposits.
Chukotat Group basalt	plagioclase-phyric basalt, pyroxene-phyric basalt, olivine-phyric basalt, gabbro; transitional crust accumulated in a submarine environment.
Tonalite	tonalite; 1898-1839 Ma plutons.
Povungnituk semipelite	includes semipelite, pelite, micaceous sandstone, sandstone, conglomerate, ironstone, dolomite, calc-silicate, minor basalt, gabbro, and peridotite; rift-related deposits.
Archean units	tonalite gneiss, granodiorite gneiss, granite gneiss, minor amphibolite
Peridotite and gabbro intrusions	peridotite and gabbro.

In general, peridotite, tonalite, gabbro, and basalt are associated with positive topographic features, while pelite and semi-pelite units are associated with lower elevations. Elevations in the field area range from about 100 to 600 m above sea level. Although a thin,

discontinuous cover of glacial drift is present in the field area, much of the surface of the field area consists of exposed bedrock (St-Onge and Scott, 1986; St-Onge and Lucas, 1993; Daigneault, 1996b, 1997) (Figure 4.14).

In the field area, vegetative cover is generally very sparse on tonalite, peridotite, and Chukotat Group basalt units, and on these units is limited mainly to lichens and scattered *Cassiope tetragona* (heather) and moss. Vegetative cover is variable on Watts Group basalt and gabbro units, with cover mainly made up of heather, moss, grasses, and lichens. Vegetation cover is nearly complete on the pelite units of the Spartan Group, and consists mainly of moss and grasses, although a diverse variety of other vegetation is present as well. Lichens noted in the field area include the following: *Orphniospora moriopsis*, *Allantoparmelia alpicola*, *Rhizocarpon geographicum*, *Lecidella sp.*, *Aspicilia sp.*, *Stereocaulon arenarium*, and *Pertusaria sp.* (lichen identification performed by Pak Yau Wong, Canadian Museum of Nature). The most common variety of moss in the field area is *Rhacomitrium lanuginosum* (moss identification performed by Dr. Michele Piercey-Normore, Department of Botany, University of Manitoba).

4.3.8.2 Cape Smith Belt Field Sites

In addition to the general reconnaissance of the Cape Smith Belt Field Area, 53 field sites were examined and sampled (Figures 4.15 to 4.18). These sites were chosen *in situ*, based on the same criteria given for the Melville Island Field Area in Section 4.2.7.2. At each of the 53 field sites, general lithological and vegetative information was recorded. Samples

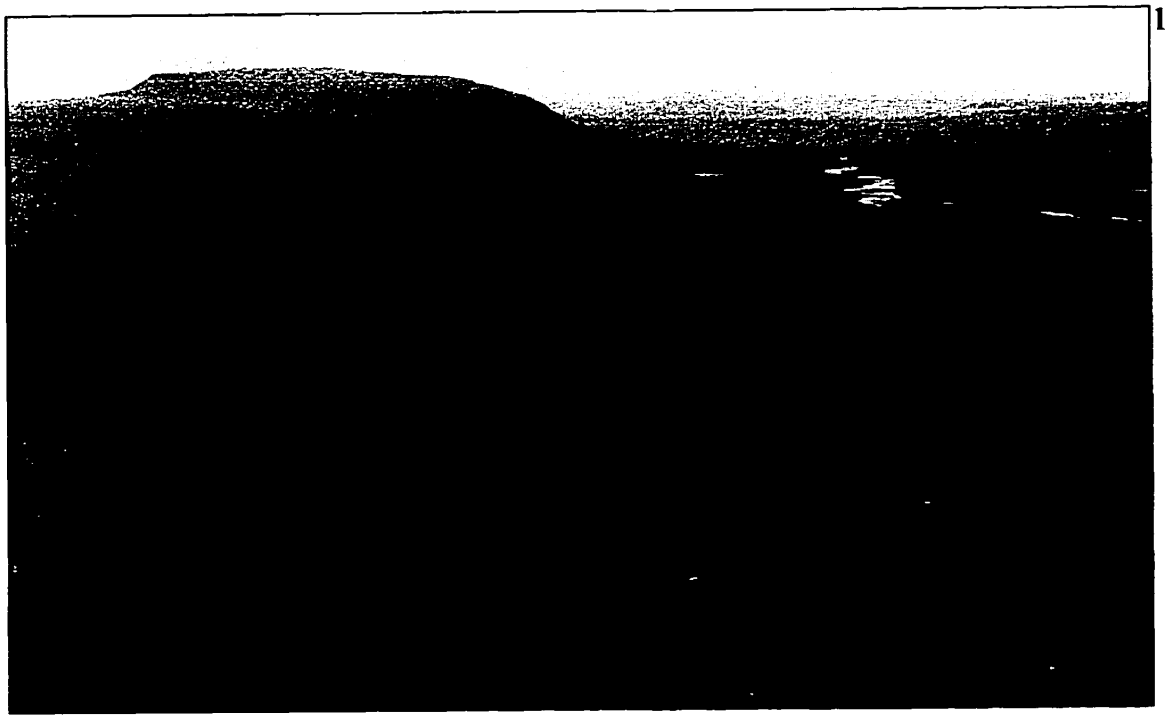

a

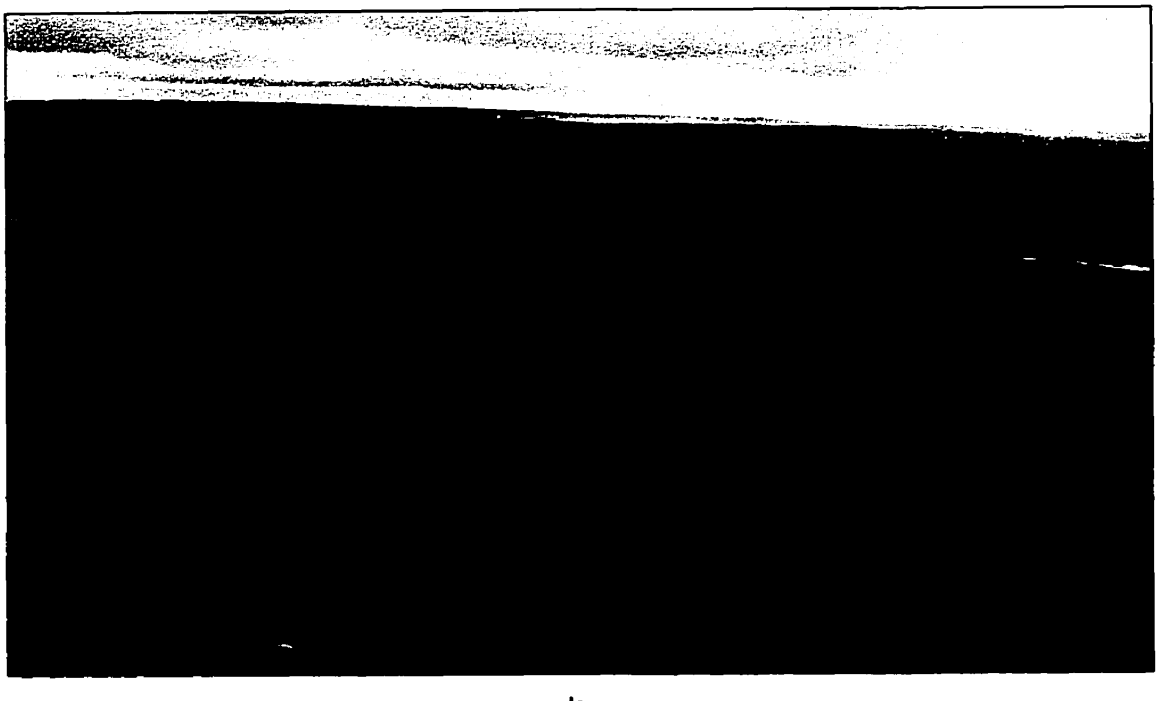

b

Figure 4.14 Photographs of the Cape Smith Belt Field Area. Photo *a* shows a prominant Watts Group peridotite mound (background at left, about 1 km across), localized outcrops of Spartan Group pelite surrounded by grassland (centre), and continuous bedrock exposure of Chukotat Group basalts (foreground). Photo *b*, taken at low altitude from a helicopter, shows a slightly elevated peridotite unit (about 2 km long) surrounded by pelites of the Povungnituk Group and basalts of the Chukotat Group.

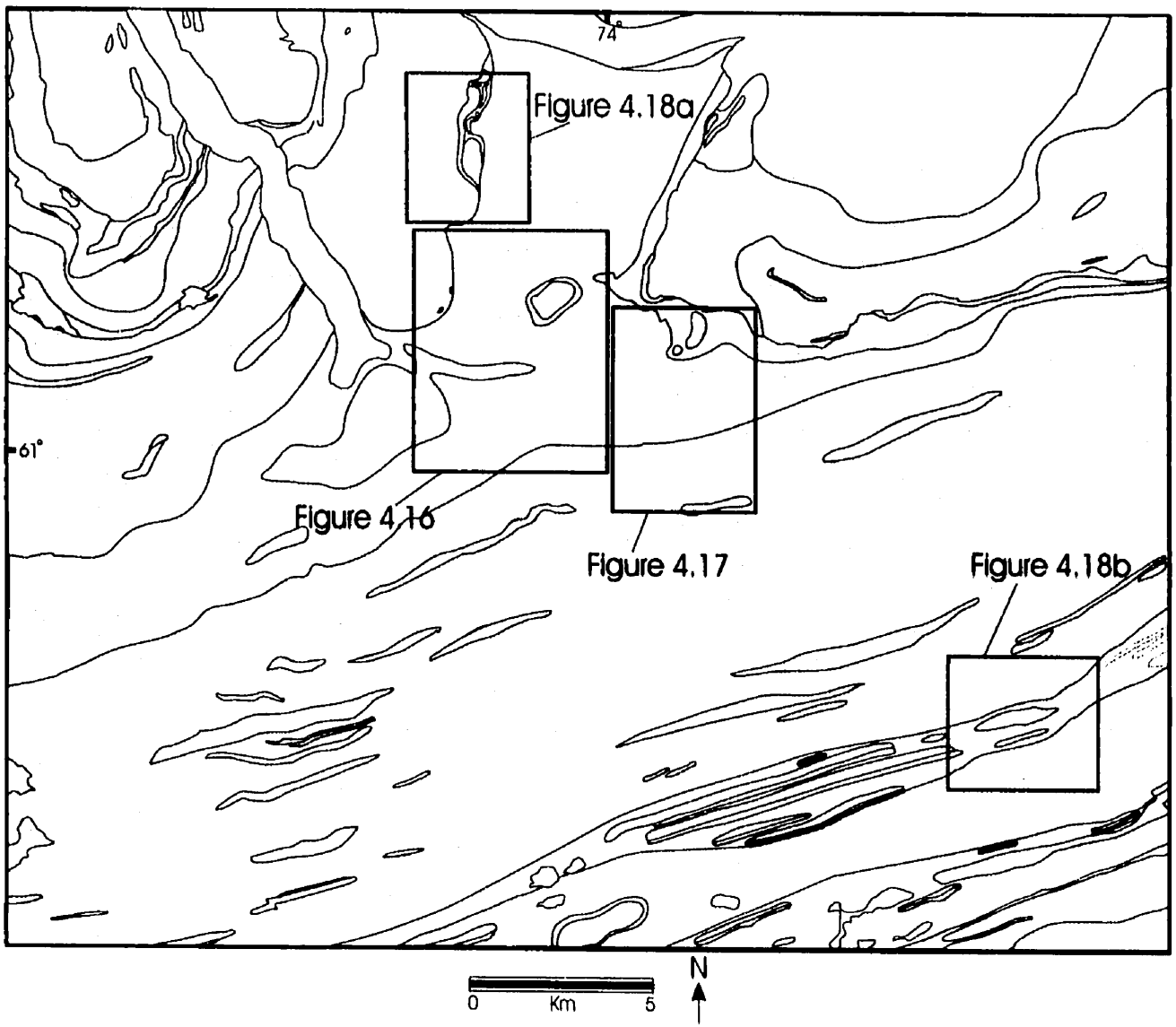

Figure 4.15 Areal extents of Figures 4.16 to 4.18 (outlines of geological units are identical to those given in Figure 4.13).

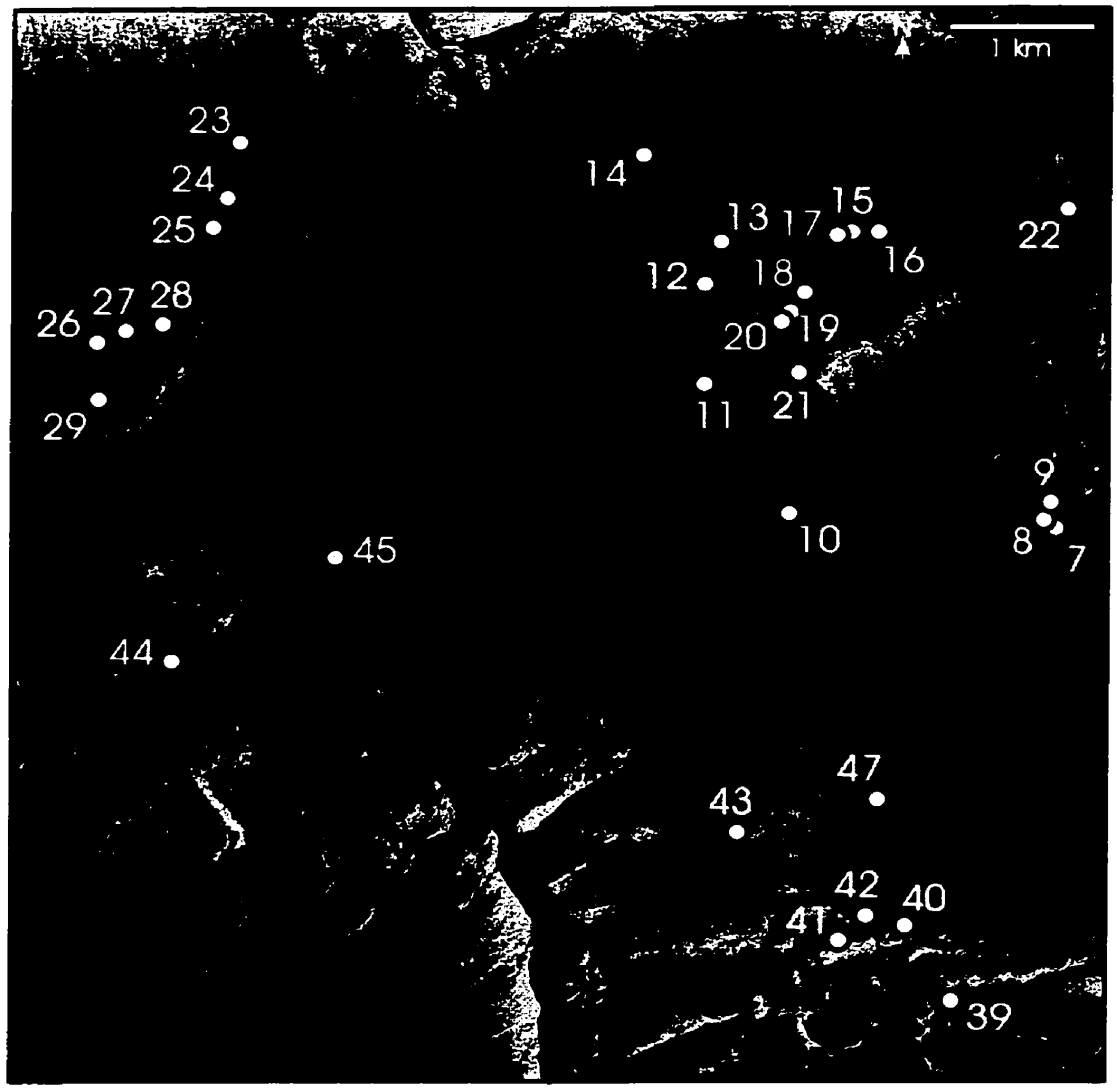

Figure 4.16 Site locations in the central part of the Cape Smith Belt Field Area (aerial photo A16251-60).

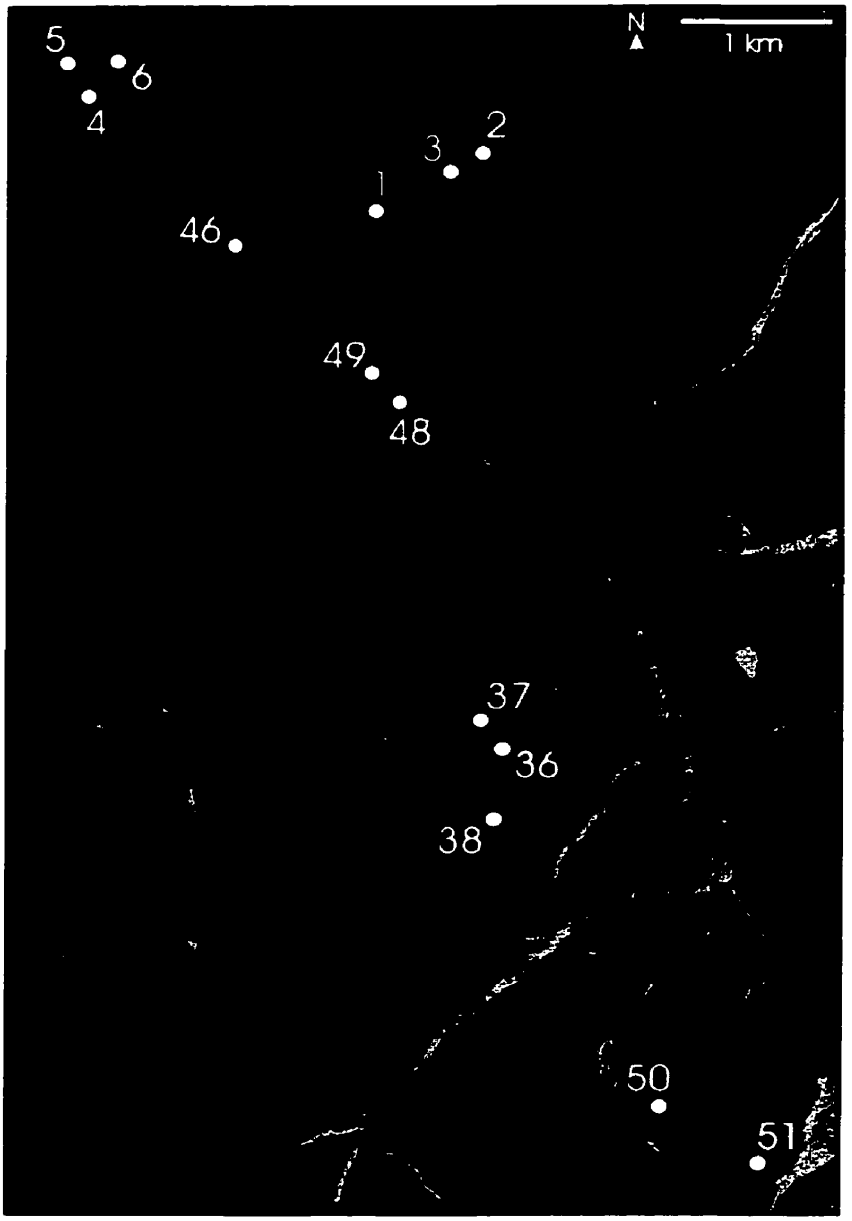

Figure 4.17 Site locations in the eastern part of the Cape Smith Belt Field Area (aerial photo A16251-62).

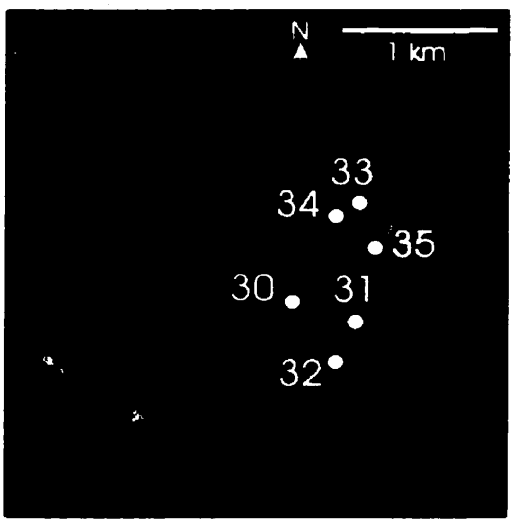

a

b

Figure 4.18 Site locations in the northern and southeastern parts of the Cape Smith Belt Field Area (aerial photos A16215-72 and A16251-30).

of the following materials were collected at each site for later laboratory examination: 1) rock samples, 2) fines, and 3) vegetation. Each site was further documented through the use of both photography and videography. A summary of the information collected for each site is given in Appendix B. Most of the 53 sites were used as a basis for the generation of the database used in the evaluation of TM imagery and classification algorithms presented in Chapters 5 to 7 (see Section 5.2.1.2).

4.3.9 Cape Smith Belt Satellite Images

Two Landsat-5 TM images and two Radarsat C-band SAR images for were available for use in the Cape Smith Belt components of this research. The two TM images were acquired on August 16, 1997 (west; media id: 972282), and September 3, 1997 (east; media id: 972462), and provide coverage of much of the central portion of the Cape Smith Belt, as well as regions north to Hudson Strait and south nearly to the southern margin of the Cape Smith Belt (Figure 4.19). Swath widths are 185 km, and image data have an 8-bit radiometric resolution. Both images were georeferenced to the Universal Transverse Mercator projection (Zone 18) using first-order mapping polynomials and nearest-neighbour resampling. Pixel spacing is 30 m for both images.

The two Radarsat images were acquired on July 23, 1998 (west; scene id: M0168069) and July 30, 1998 (east; scene id: M0168684), and provide coverage of the central portion of Cape Smith Belt as well as regions north to Hudson Strait (Figure 4.20); both Radarsat images were acquired using the *S7* beam mode [incidence angles = 44.9° to 49.4° (Luscombe *et al.*, 1993)] from an ascending orbit. Images are 100 x 100 km in dimension, and have a 16-

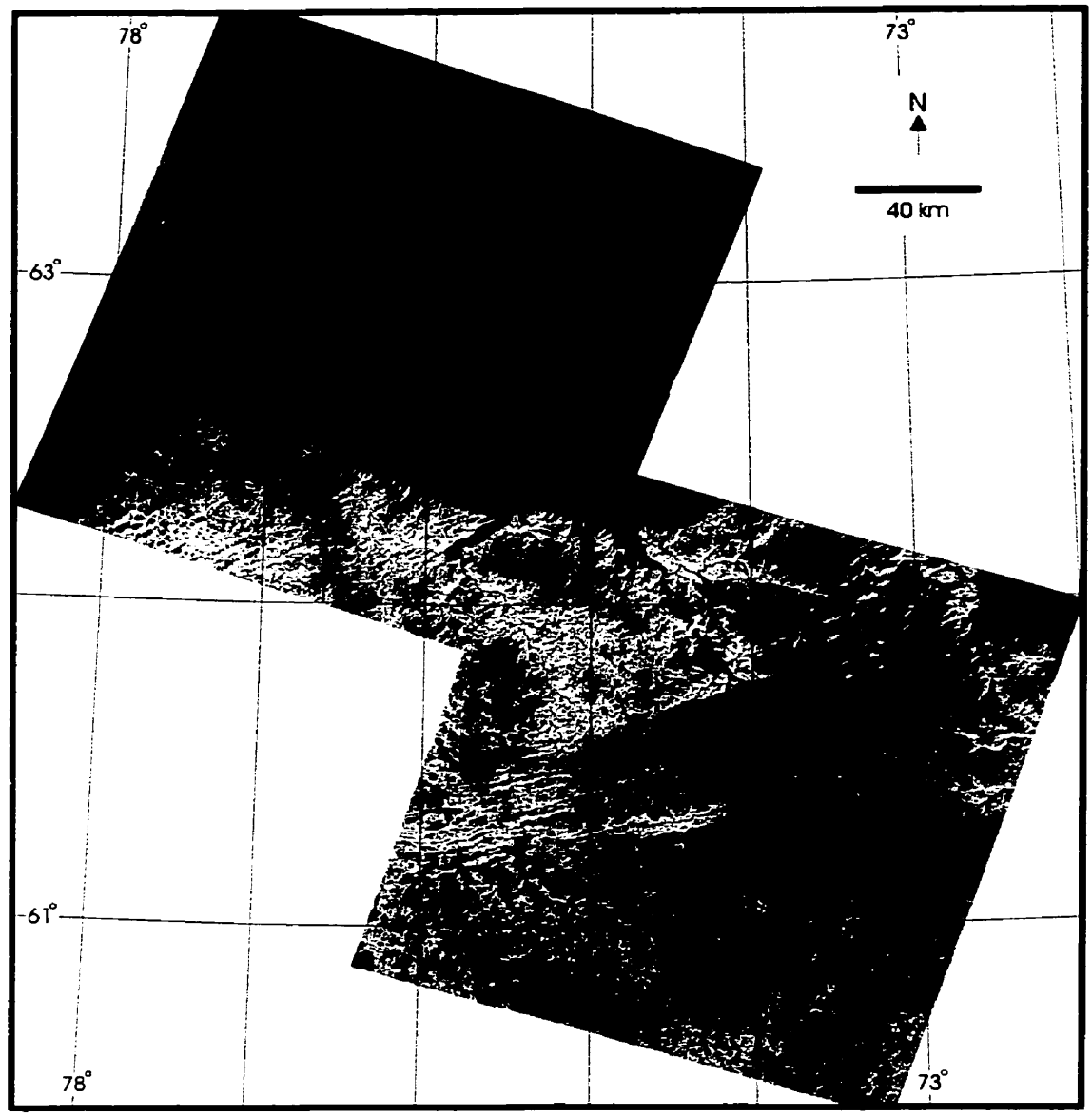

Figure 4.19 TM images for central Cape Smith Belt and surrounding areas (compare with Figure 4.12). Colour composite uses channels 543:RGB.

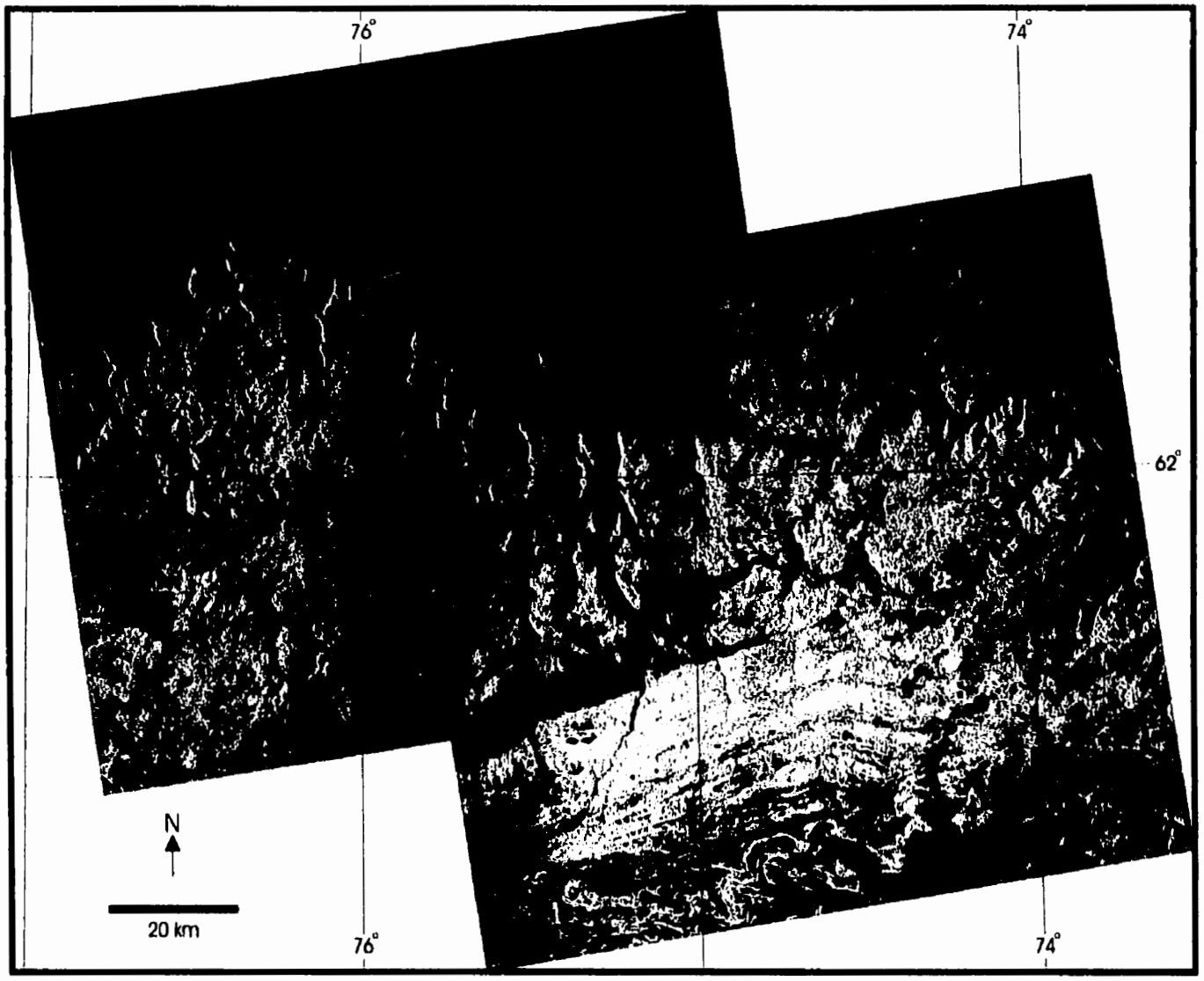

Figure 4.20 Radarsat images for central Cape Smith Belt and areas to the north (compare with Figure 4.12). The beam mode used for each image was *S7*.

bit dynamic range. The images were georeferenced to the Universal Transverse Mercator projection (Zone 18) using first-order mapping polynomials and nearest-neighbour resampling. Resolution of the images is 19.1 x 27 m (range x azimuth), and pixel spacing is 12.5 m. Analyses that used and evaluated the TM and Radarsat data are documented in Chapters 5 to 8.

4.4 Chapter Summary

Two study areas were used in this research: 1) eastern Melville Island, Nunavut, and 2) central Cape Smith Belt, northern Québec. The geology of eastern Melville Island consists mainly of sedimentary lithologies, including sandstones, shales, mudstones, carbonates, and evaporites. Exposed materials are mostly infill of a Devonian foredeep (south) and the Sverdrup Basin (north). The Melville Island Field Area, used in the evaluation of satellite imagery and classification algorithms (Chapters 5 to 8), is about 20 x 20 km in dimension and is located in the vicinity of the West Arm of Weatherall Bay. Exposed lithologies in the field area, mainly in the form of weathered and frost-shattered felsenmeer, include clastics, carbonates, and a gabbro intrusion. Vegetation cover is sparse, and consists mainly of *Saxifraga oppositifolia* barrens. A total of 83 field sites were examined and sampled in the field area during a 24-day period in July, 1998. Melville Island satellite images available for this research include two Landsat TM images, two Radarsat *S7* images, and one set of IKONOS panchromatic and multispectral images.

The Cape Smith Belt is an Early Proterozoic greenstone belt that forms a portion of the Québec-Baffin segment of the Trans-Hudson Orogen. The geology of the central Cape

Smith Belt consists of a wide variety of metamorphosed sedimentary and igneous rocks, including tonalite, peridotite, gabbro, basalt, pyroxenite, and pelite. The Cape Smith Belt Field Area, used in the evaluation of satellite imagery and classification algorithms (Chapters 5 to 8), is about 30 x 20 km in dimension and is located in the vicinity of southern Lac Watts. Exposed lithologies include metamorphosed pelite, basalt, gabbro, peridotite, and tonalite. The extent of vegetation cover is variable in the field area; vegetation mainly consists of barrens communities, with the most common constituents including *Cassiope tetragona* (heather), mosses (predominantly *Rhacomitrium lanuginosum*), grasses, and lichens. A total of 53 field sites were examined and sampled in the field area during a 13-day period in August, 1999. Cape Smith Belt satellite images available for this research include two Landsat TM images, and two Radarsat *S7* images.

5 EVALUATION OF THREE CLASSIFICATION ALGORITHMS FOR LITHOLOGICAL DISCRIMINATION

5.1 Introduction

This chapter documents the generation of the training and test databases for the Melville Island and Cape Smith Belt study areas, and the use of these databases in the evaluation of three supervised-classification algorithms: 1) maximum likelihood; 2) evidential reasoning; and 3) a backpropagation feedforward neural network (these three algorithms are described in Sections 3.2, 3.3, and 3.4, respectively). As noted in Chapter 3, the maximum likelihood classifier is the most commonly used classification algorithm (Richards, 1993), but has limitations related to its use of Gaussian normal models to parameterize training data. The evidential reasoning classifier, in comparison, is capable of modelling training data using more complex models. The neural network algorithm is unique in that it does not explicitly define training-data models, and thus is not constrained in the same manner as the other two algorithms. The ability of a classification algorithm to deal with surface-cover classes whose spectral characteristics are complex (e.g., due to spatial variations in vegetation cover or rock weathering characteristics) can be an important factor in the successful use of classification algorithms for lithological discrimination, since an inability in this regard has the potential to result in poor classification results, or may at least necessitate the subdivision of recognized lithological classes into spectral sub-classes prior to image classification (Section 3.2).

Landsat TM images were used in the evaluation of classification algorithms because TM images, which have been widely used by the remote sensing community for over 15 years

as a basis for land-cover classifications, have superior spectral characteristics compared to almost all other types of imagery generated from Earth orbit (Section 2.4.1). The general findings given in this chapter should be valid for classifications involving other image types.

The work presented in this chapter focussed on several key questions: 1) how do the three algorithms compare to each other with regard to overall classification results?; 2) how do the three algorithms compare with regard to their utility in the discrimination of particular lithological classes?; and 3) how do the algorithms compare in terms of ease of use and practicality? This research builds on previous work (e.g., Peddle, 1995; Leverington and Duguay, 1996a; Benediktsson *et al.*, 1997a; Tian *et al.*, 1999) by evaluating the algorithms using six different training and test databases for each of two study areas, by examining the utility of consensus-based neural-network classifications versus individual neural-network classifications, by investigating potential weaknesses of the evidential reasoning algorithm, and by evaluating the classification algorithms from a geological perspective.

5.2 Methodology

Evaluation of the classification algorithms involved three main steps: 1) construction of training and test databases for the Melville Island and Cape Smith Belt field areas; 2) execution of all classifications using the training and test databases; and 3) evaluation of classification results. Classification results were evaluated in the following ways: 1) by comparing overall percentages of test pixels that were correctly classified; 2) by comparing overall Kappa values [see Section 2.5.4]; 3) by comparing the nature of typical errors of omission and commission for individual lithological classes; and 4) by comparing qualitative

evaluations of classified images. Additional descriptions and analyses of evidential reasoning and consensus neural network results were also performed.

5.2.1 Construction of Training and Test Databases

The geological maps of Harrison (1995) and St-Onge and Lucas (1989) are very useful sources of information regarding the surficial distribution of lithologies at the Melville Island and Cape Smith Belt field areas, respectively. However, these maps do not provide sufficient information to be used as the sole foundation for the selection of training- and test-pixel locations. For example, these maps do not provide high-resolution information on the nature of vegetation cover, the distribution of specific lithologies, or the presence of distinct spectral sub-classes. As a result, the selection of training- and test-pixel locations used in the evaluation of the classification algorithms was based primarily on information gained through *in situ* reconnaissance and sampling of the Melville Island and Cape Smith Belt field areas (see Sections 4.2.7.2 and 4.3.8.2, respectively).

5.2.1.1 Melville Island Training and Test Database

The 83 Melville Island field sites (Section 4.2.7.2) were used as a guide to select a total of 851 pixel locations for use as training- and test-pixel locations for 14 different surface-cover classes (Table 5.1). Individual field sites were represented by as few as 1 pixel and as many as 25 pixels. The following sites were not directly used in the construction of the field databases, mainly because of limitations related to site size or heterogeneity: Sites 6, 12, 24, 26, 28, 36, 38, 43, 50, 51, 63, 64, 56, and 68 (Section 4.2.7.2).

Supplemental pixel locations (i.e., pixel locations corresponding to field locations which were observed *in situ* but were not sampled or documented in the more detailed manner used at the main field sites) were used to help define the following surface-cover classes: 1) Canyon Fiord Formation [pink]; 2) Canyon Fiord Formation [yellow], 3) gabbro, 4) Assistance Formation mudstone, 5) green vegetation, 6) snow cover, and 7) water (Table 5.1). Even with the use of supplemental field sites, several classes are represented by a relatively small number of pixels [e.g., the Canyon Fiord Formation (yellow) class; Table 5.1]. Most of these classes are areally restricted in the field area. Given the potential for significant lithological or surface-cover changes in relatively short distances, it was deemed preferable to restrict all training and test data to pixel locations associated with sites visited and described *in situ* (the addition of pixel locations whose lithological and surface-cover characteristics were not known from first-hand knowledge might have compromised research results by increasing the possibility of error in the assignment of surface-cover classes to individual pixels). Although the combination of lithological classes for different classification series (see below) allowed individual classes to be represented by greater numbers of pixels, the number of pixels used in these experiments was not as high as is ideally preferred [e.g., Richards (1993, p.274) recommends that, assuming stratified random sampling is performed over an entire area of interest, test-pixel sample size for each class should be about 30 to 60 pixels if a result is to be considered fully representative of the performance of the classifier; see also Swain (1978) and Mather (1987)].

In order to test the performance of the classification algorithms using classes with increasingly complex and diverse spectral characteristics, three additional series of surface-

Table 5.1 Classes used as the basis for TM classifications of the Melville Island Field Area. Field sites given in italics are supplementary sites. Site descriptions are given in Appendix A. Table is continued on the following page.

Class	Field Sites	Number of Pixels	Summary of Lithological and Vegetative Characteristics
1. Canyon Fiord Fm (Red-Weathering)	9, 10, 13b, 14, 22, 32, 33, 39, 82.	Total: 86 Training: 56 Test: 30	Red-weathering fine- to coarse-grained calcareous sandstone and conglomerate, and associated fines; common vegetation: *Saxifraga oppositifolia*, *Salix arctica*, lichens, localized black algae.
2. Canyon Fiord Fm (Yellow)	7, 11, 13a, *13-1*, 81.	Total: 20 Training: 13 Test: 7	Yellow-coloured calcareous fines often mixed with heterolithic rounded clasts weathered from pebble conglomerate; no vegetation cover.
3. Canyon Fiord Fm (Pink)	31, *31-1*, *31-2*, *31-3*, *31-4*.	Total: 20 Training: 13 Test: 7	Pink-coloured fines; typically no significant vegetation cover (scattered *Saxifraga oppositifolia*).
4. Tingmisut Inlier Dolomite (Beverly Inlet Fm)	1, 2, 3, 4, 5.	Total: 74 Training: 48 Test: 26	Gray and yellowish-orange dolostone, sometimes covered with gray-orange fines that may be wind-blown Canyon Fiord sediments; common vegetation: lichens.
5. Gabbro	8, *8-1*, 15, *15-1*, 27, *27-1*, *27-2*.	Total: 40 Training: 26 Test: 14	Dark gray gabbro sometimes found with gray-orange fines that may be wind-blown Canyon Fiord sediments; common vegetation: lichens.
6. Great Bear Cape Fm Limestone	16, 17, 18a, 18b, 19, 20, 21, 23, 30, 75, 76, 77, 78, 79, 80.	Total: 135 Training: 89 Test: 46	Pale yellowish brown impure limestone and minor calcareous sandstone; common vegetation: *Saxifraga oppositifolia*, lichens, localized black algae.

Table 5.1 (continued).

7. Sabine Bay Fm Sandstone	29, 34, 35, 41, 42, 49, 52, 53, 55, 57, 58, 59, 60.	Total: 90 Training: 59 Test: 31	Uncemented, non-calcareous, gray sandstone and conglomerate, and associated fines and heterolithic clasts; common vegetation: *Saxifraga oppositifolia*, lichens.
8. Assistance Fm Mudstone	37, 40, *40-1*, *40-2*, 48, *48-1*, 54.	Total: 35 Training: 23 Test: 12	Red- and brown-weathering mudstone and associated fines; typically no significant vegetation cover (scattered lichens).
9. Degerbōls Fm Limestone	25, 44, 45, 46, 47.	Total: 48 Training: 31 Test: 17	Gray and yellowish-gray limestone which in places mainly consists of loose bioclasts; common vegetation: *Saxifraga oppositifolia*, lichens
10. Trold Fiord Fm Sandstone	61, 62, 65, 66, 67, 73a, 74.	Total: 78 Training: 51 Test: 27	Yellowish-gray sandstone, and minor limestone; common vegetation: *Saxifraga oppositifolia*, lichens.
11. Bjorn Fm Sandstone	69, 70, 71, 72.	Total: 32 Training: 21 Test: 11	Brown sandstone and conglomerate, and associated fines and heterolithic clasts; Fe-concretions present (?); typically no significant vegetation (scattered *Saxifraga oppositifolia* and lichens).
12. Green Vegetation	*G-1*, *G-2*, *G-3*, *G-4*, *G-5*, *G-6*, *G-7*, *G-8*.	Total: 41 Training: 27 Test: 14	Dense moss and lichen cover typically characterized by a diverse range of vegetation varieties.
13. Snow Cover	*S-1*, *S-2*, *S-3*, *S-4*, *S-5*.	Total: 35 Training: 23 Test: 12	White snow and ice; perennial snow cover is typically distributed along the steep sides of cuestas.
14. Water	*W-1*, *W-2*, *W-3*, *W-4*, *W-5*, *W-6*, *W-7*, *W-8*.	Total: 117 Training: 77 Test: 40	Ice-free fresh and salt water.

cover classes were generated from the 14 classes through the progressive combination of these classes (Figure 5.1). Thus, in total, four Melville Island classification series were evaluated, with each series defined by a different number of surface-cover classes: the *B* series is defined by the 14 classes given in Table 5.1, while the *C*, *D*, and *E* series are defined by 10, 9, and 6 classes, respectively (Figure 5.1). Because the total number of training and test pixels did not change from series to series, the number of pixels used to define individual classes generally increased from the *B* series to the *E* series (Table 5.2).

5.2.1.2 Cape Smith Belt Training and Test Database

The 53 Cape Smith Belt field sites (Section 4.3.8.2) were used as a guide to select a total of 686 pixel locations for use as training- and test-pixel locations for 7 different surface-cover classes (Table 5.3). Individual field sites were represented by as few as 1 pixel and as many as 30 pixels. The following sites were not directly used in the construction of the field databases, mainly because of limitations related to site size or heterogeneity: Sites 7, 10, 12, 27, 35, 40, 41, 43, 45, 47, 48 (Section 4.3.8.2). Supplemental pixel locations were used to help define the water class.

5.2.2 Classification Methodology

Classifications were performed for each of the four Melville Island series of surface-cover classes (Section 5.2.1.1), and for the one Cape Smith Belt series of surface cover classes (Section 5.2.1.2). Because the results of image classifications are dependent to some extent on exactly which pixels are used for training and which are used for testing, six

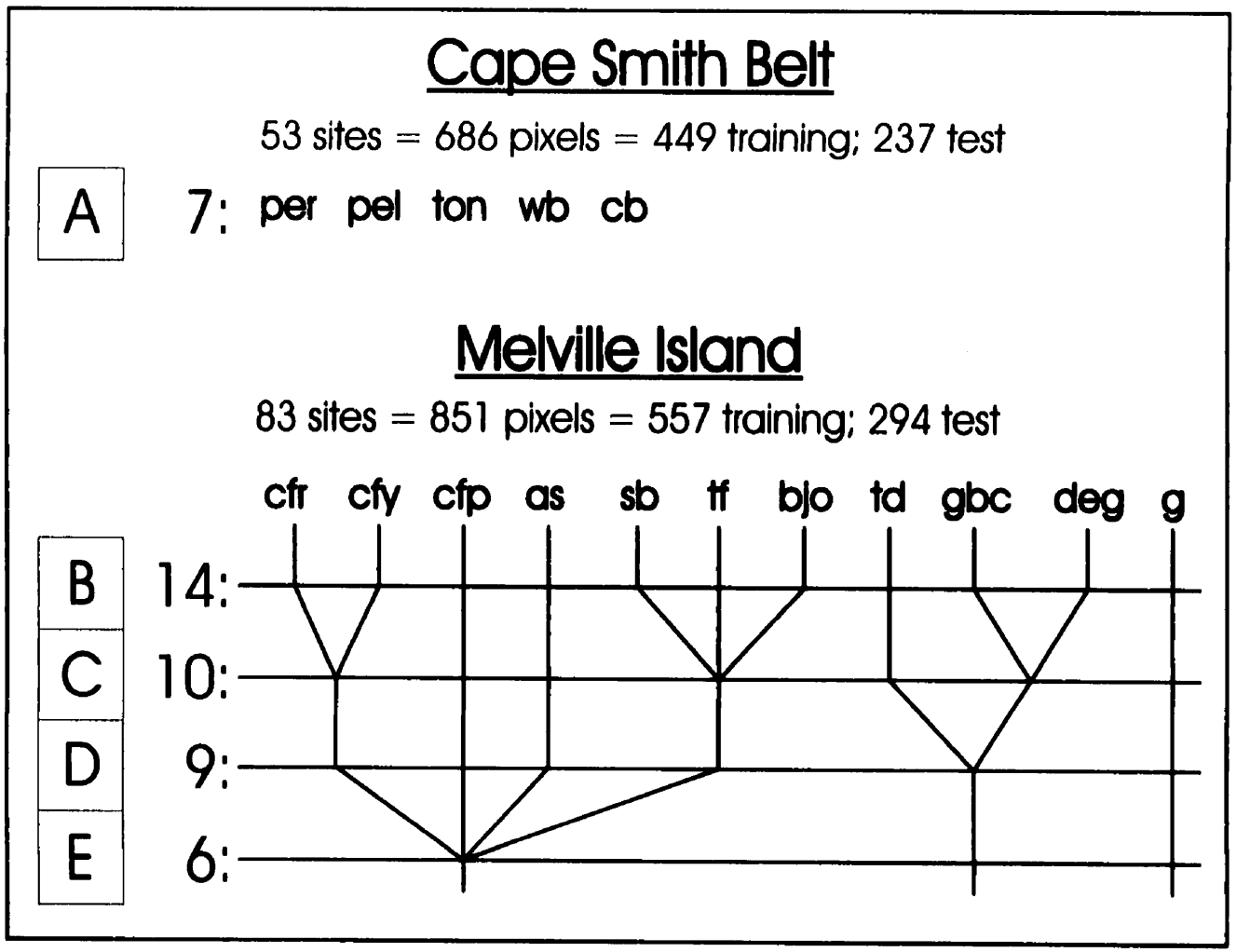

Figure 5.1 Classes used in the *A* to *E* Series of classifications (involving 7, 14, 10, 9, and 6 classes, respectively). Combination of *B* Series classes to form the *C* to *E* Series classes is shown. Class labels: *cfr*, *cfy*, *cfp*: Canyon Fiord red-, yellow-, and pink-coloured clastics; *as*: Assistance mudstone; *sb*: Sabine Bay sandstone; *tf*: Trold Fiord sandstone; *bjo*: Bjorn sandstone; *td*: Tingmisut dolostone; *gbc*: Great Bear Cape limestone; *deg*: Degerbols limestone; *g*: gabbro.

Table 5.2 Classes used in the four series (*B*, *C*, *D*, and *E*) of TM classifications of the Melville Island Field Area. The three values given below each label refer to total number of training and test pixels, number of training pixels, and number of test pixels, respectively. Numbers preceding class labels refer to the class numbering system used in this research. Classes are combined from left to right, in the same manner as that depicted in Figure 5.1.

B Series	C Series	D Series	E Series
1. Canyon Fiord (Red-Weathering) 86; 56; 30	1. Canyon Fiord (Red/Yellow) 106; 69; 37	1. Canyon Fiord (Red/Yellow) 106; 69; 37	1. Clastics 361; 236; 125
2. Canyon Fiord (Yellow) 20; 13; 7			
3. Canyon Fiord (Pink) 20; 13; 7	2. Canyon Fiord (Pink) 20; 13; 7	2. Canyon Fiord (Pink) 20; 13; 7	
8. Assistance Mudstone 35; 23; 12	7. Assistance Mudstone 35; 23; 12	6. Assistance Mudstone 35; 23; 12	
7. Sabine Bay Sandstone 90; 59; 31	6. Sabine Bay and Trold Fiord and Bjorn Sandstone 200; 131; 69	5. Sabine Bay and Trold Fiord and Bjorn Sandstone 200; 131; 69	
10. Trold Fiord Sandstone 78; 51; 27			
11. Bjorn Sandstone 32; 21; 11			
4. Tingmisut Inlier Dolomite 74; 48; 26	3. Tingmisut Inlier Dolomite 74; 48; 26	4. Carbonates 257; 168; 89	2. Carbonates 257; 168; 89
6. Great Bear Cape Limestone 135; 89; 46	5. Great Bear Cape and Degerböls Limestone 183; 120; 63		
9. Degerböls Limestone 48; 31; 17			
5. Gabbro 40; 26; 14	4. Gabbro 40; 26; 14	3. Gabbro 40; 26; 14	3. Gabbro 40; 26; 14
12. Green Vegetation 41; 27; 14	8. Green Vegetation 41; 27; 14	7. Green Vegetation 41; 27; 14	4. Green Vegetation 41; 27; 14
13. Snow Cover 35; 23; 12	9. Snow Cover 35; 23; 12	8. Snow Cover 35; 23; 12	5. Snow Cover 35; 23; 12
14. Water 117; 77; 40	10. Water 117; 77; 40	9. Water 117; 77; 40	6. Water 117; 77; 40

Table 5.3 Classes used in TM classifications of the Cape Smith Belt Field Area. Field sites listed in italics are supplementary sites. Site details given in Appendix B.

Class	Field Sites	Number of Pixels	Summary of Lithological and Vegetative Characteristics
1. Peridotite	1,15,16,17,18,19, 20,21,25,33,34, 52,53.	Total: 162 Training: 106 Test: 56	Red-, brown-, and tan-weathering peridotite bedrock and boulders; common vegetation: lichens.
2. Pelite	9,13,14,49.	Total: 70 Training: 46 Test: 24	Dark gray pelite bedrock; common vegetation: grass, moss (dominantly *Rhacomitrium lanuginosum*), heather (*Cassiope tetragona*), lichens.
3. Chukotat Group Basalt	36,37,38,39,50, 51.	Total: 158 Training: 104 Test: 54	Green- and tan-weathering basalt bedrock and boulders; common vegetation: lichen.
4. Watts Group Basalt	22,23,24,26,28, 29,30,31,32.	Total: 112 Training: 73 Test: 39	Dark greenish-gray basalt and gabbro boulders and bedrock; common vegetation: moss (dominantly *Rhacomitrium lanuginosum*), heather (*Cassiope tetragona*), grass, *Salix spp.*, lichens.
5. Tonalite	2,3.	Total: 36 Training: 23 Test: 13	Gray tonalite boulders and bedrock; common vegetation: lichens.
6. Green Vegetation	4,5,6,8,11,42,44, 46.	Total: 84 Training: 55 Test: 29	Dense vegetation cover, typically including moss (dominantly *Rhacomitrium lanuginosum*), heather (*Cassiope tetragona*), grass, *Salix spp.*, lichens, and numerous other vegetation varieties.
7. Water	*W-1, W-2, W-3, W-4.*	Total: 64 Training: 42 Test: 22	Ice-free fresh water.

different training and test databases were generated for the evaluation of each series, in order to more clearly discern trends in the classification results (this method helped reduce the impact of the use of a small number of test pixels for certain classes). The number of training and test databases used in this research was limited by two main factors: 1) time constraints; and 2) recognition that classification trends are generally consistent between each of the six sets of classification results (see below), suggesting that there would be little value in generating further results using additional training and test databases.

Each of the six databases for the Melville Island *B* series was generated by dividing the 851 pixel locations (Section 5.2.1.1) into 557 training pixels and 294 test pixels (the ratio of training pixels to test pixels using this scheme is roughly 2:1). Allocation of training and test pixels was performed by random sampling within the database of 851 pixel locations, stratified by class, using the program *R99_51* (programmed by the author and discussed further in Appendix C). The training and test databases used in the *C*, *D*, and *E* Series were generated by combining the respective *B* series databases, as shown above in Figure 5.1 and Table 5.2.

Each of the six databases for the Cape Smith Belt series was generated by dividing the 686 pixel locations (Section 5.2.1.2) into 449 training pixels and 237 test pixels (again, the ratio of training pixels to test pixels using this scheme is roughly 2:1). As with the Melville Island database, pixel locations were divided into test and training pixels based on random sampling within the main pixel database, stratified by class.

Thus, a total of 24 different sets of image classifications was generated in this research for the Melville Island Field Area (six different training and test datasets applied to each of

the four different groups of surface-cover classes discussed above), and a further 6 sets of image classifications were generated for the Cape Smith Belt Field Area (six different training and test datasets applied to the one group of surface-cover classes discussed above) (Figure 5.2). TM channels 3, 4, 5, and 7 were used in all classifications (see Section 2.4.1).

For each set of classifications, the following were generated: 1) one maximum likelihood classification, 2) one evidential reasoning classification, 3) ten individual neural network classifications, each based on a different initial (randomly-generated) set of weights, and 4) one consensus neural network classification that used as input the results of the ten individual neural network classifications.

5.2.2.1 Algorithm Parameters

A bin size of 51 was used in the interpolation and extrapolation of training data for the evidential reasoning algorithm. All input sources received equal weighting in the evidential reasoning executions.

The neural network algorithm applied here is described in Section 3.4.6. Standard values for the learning rate (0.1) and momentum (0.9) were used (Sections 3.4.5.7 and 3.4.6). All input sources were weighted equally. Target values for "correct" and "incorrect" nodes were 0.9 and 0.1, respectively (Section 3.4.6). Artificial noise (jitter) was not applied during training (Sections 3.4.5.8 and 3.4.6). Two intermediate (hidden) layers were used for all executions, and were defined with as many nodes as the maximum of the number of nodes in the input and output layers; such a topology is consistent with common "rules of thumb" (Section 3.4.5.5) as well as the results of the topological tests discussed in Chapter 6.

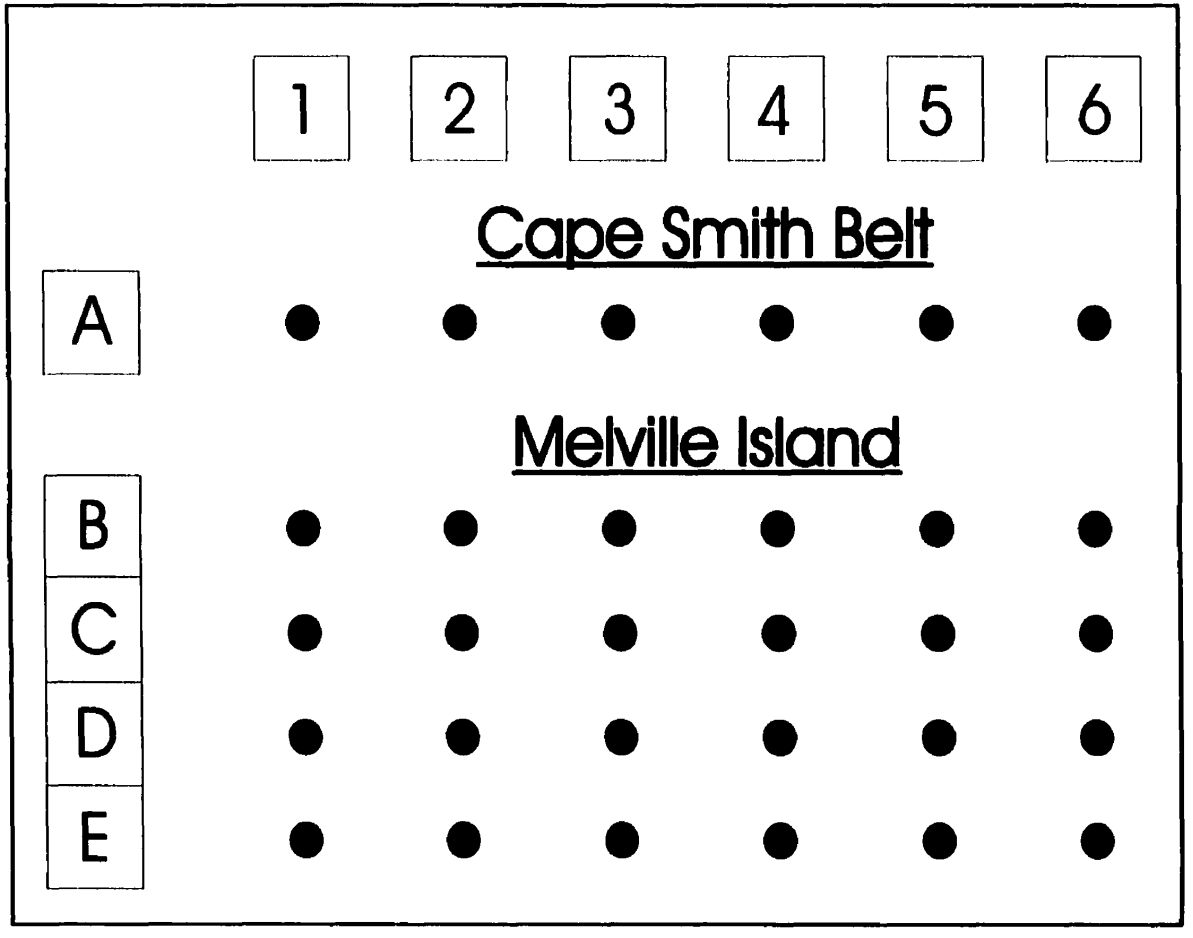

Figure 5.2 Sets of classifications performed for the Melville Island (*B* to *E* Series) and Cape Smith Belt (*A* Series) Field Areas. Six different training/testing datasets were used for each series. Each dot represents one evidential reasoning execution, one maximum likelihood execution, ten neural network executions, and one consensus execution (which used the ten neural network results as input).

The training of a neural network is normally halted when either: 1) an acceptable level of error has been reached; or 2) a specific number of iterations have passed (Section 3.4.5). The use of either of these options for terminating training is valid, and there is no specific rule on when to use one or the other method (e.g., Bishop, 1995a; Reed and Marks, 1999). For the neural network classifications presented in this chapter, neural network training was halted when an "acceptable" level of error was reached. The target tss error values (i.e., the acceptable levels of error) used for the *B*, *C*, *D*, *E*, and *A* series of tests were 80, 70, 65, 65, and 35, respectively (corresponding to average errors per node of 0.10 to 0.14, from the *B* to the *E* Series, and an average error per node per iteration of 0.11 for the *A* Series). These values were selected based on visual analyses of learning curves produced by running several training executions for about 10 000 iterations; target values were chosen to correspond to the approximate location in the learning curve where learning has essentially levelled out (note: initially, this simple method was used only for the *B* and *A* Series; an attempt was made to calculate target values for the *C* to *E* Series by assuming that tss error per node per iteration of the *B* Series would remain approximately constant; this did not prove to be a valid assumption, since it produced target values that were generally too low for the network to converge on a solution; thus, selection of target values for all Series was based on the empirical visual method given above, instead). The number of iterations taken to reach the target tss error values typically ranged between about 2000 and 8000.

An equally valid manner for determining the conditions for the halt of training would have been to specify a maximum number of iterations. This option was used for the investigations discussed in Chapter 6, for reasons noted in Sections 6.2.1.2 and 6.3.1.2.

5.3 Results

Evaluations of classifier performance are given below in Section 5.3.1 (Melville Island Field Area) and Section 5.3.2 (Cape Smith Belt Field Area). Note that visual comparisons between geological maps and classified images in these sections should be made primarily with regard to the portions of the field areas that are properly represented in the training and test databases (Figures 4.6 and 4.15). The materials of peripheral areas, if not properly represented in the training and test databases, of course should not be considered in the evaluation of the classified images (e.g., the pyroxenite class is not present in the areas visited in the Cape Smith Belt Field Area; because the classifiers were therefore not trained for this particular class, peripheral areas where this class is exposed could not possibly have been labelled correctly).

5.3.1 Melville Island Field Area

Melville Island classification results are given below, expressed as percentages of test pixels correctly labelled (Table 5.4) and as Kappa coefficients (Table 5.5). As can be seen from Tables 5.4 and 5.5, the consensus neural network is consistently associated with higher general percentage and Kappa values, compared to the maximum likelihood and evidential reasoning classifier. The evidential reasoning classifier is consistently associated with the lowest general percentage and Kappa values. The performance of the evidential reasoning, maximum likelihood, and neural network classifiers is discussed in Sections 5.3.1.1, 5.3.1.2, and 5.3.1.3, respectively. The ranking system used in these sections in the description of overall errors of omission and commission is given in Table 5.6.

Table 5.4 Summary of Melville Island classification results. Values are expressed as proportions of test pixels classified correctly, and may be converted to percentages by multiplying by 100%. Classification algorithms are labelled as follows: NN-B (best neural network result of 10 neural network jobs), NN-M (majority-vote consensus neural network result), ML (maximum likelihood result), ER (evidential reasoning result).

Series	Algor.	Set 1	Set 2	Set 3	Set 4	Set 5	Set 6	Avg.
B	NN-B	0.7755	0.7755	0.8027	0.7857	0.7721	0.7789	0.7817
	NN-M	0.7857	0.7891	0.7891	0.7789	0.7687	0.7789	0.7817
	ML	0.7653	0.7347	0.7313	0.7211	0.7415	0.7585	0.7421
	ER	0.5442	0.5272	0.5340	0.5408	0.5272	0.5442	0.5363
C	NN-B	0.8197	0.8197	0.8265	0.8537	0.8163	0.8163	0.8254
	NN-M	0.8129	0.8163	0.8197	0.8401	0.7959	0.8197	0.8174
	ML	0.8095	0.7619	0.7755	0.7653	0.7517	0.7585	0.7704
	ER	0.4694	0.4660	0.4728	0.4694	0.4592	0.4456	0.4637
D	NN-B	0.8571	0.8469	0.8367	0.8503	0.8299	0.8265	0.8412
	NN-M	0.8571	0.8537	0.8435	0.8639	0.8197	0.8299	0.8446
	ML	0.8231	0.7653	0.7755	0.7891	0.7687	0.7517	0.7789
	ER	0.4592	0.4524	0.4490	0.4456	0.4626	0.4320	0.4501
E	NN-B	0.8503	0.8639	0.8469	0.8707	0.8605	0.8435	0.8560
	NN-M	0.8469	0.8537	0.8571	0.8741	0.8707	0.8299	0.8554
	ML	0.7891	0.7823	0.7857	0.7789	0.7755	0.7721	0.7806
	ER	0.6020	0.6190	0.6531	0.6190	0.6327	0.6190	0.6241

Table 5.5 Summary of Melville Island classification results, expressed as Kappa coefficients. The Kappa ("KHAT") statistic measures the percentage of test pixels correctly labelled, beyond that which is to be expected based on chance alone (see Section 2.5.4 for details). Values in this table are expressed as proportions, and may be converted to percentages by multiplying by 100%. Classification algorithms are labelled as follows: NN-B (best neural network result of 10 neural network jobs), NN-M (majority-vote consensus neural network result), ML (maximum likelihood result), ER (evidential reasoning result).

Series	Algor.	Set 1	Set 2	Set 3	Set 4	Set 5	Set 6	Avg.
B	NN-B	0.7506	0.7522	0.7810	0.7620	0.7475	0.7550	0.7581
	NN-M	0.7624	0.7668	0.7661	0.7552	0.7440	0.7559	0.7584
	ML	0.7411	0.7087	0.7037	0.6933	0.7157	0.7344	0.7162
	ER	0.5031	0.4833	0.4908	0.4995	0.4835	0.5038	0.4940
C	NN-B	0.7877	0.7876	0.7964	0.8262	0.7830	0.7854	0.7944
	NN-M	0.7806	0.7842	0.7881	0.8110	0.7619	0.7890	0.7858
	ML	0.7770	0.7229	0.7365	0.7261	0.7101	0.7197	0.7321
	ER	0.4111	0.4075	0.4139	0.5306	0.4017	0.3893	0.4257
D	NN-B	0.8215	0.8113	0.7984	0.8146	0.7895	0.7874	0.8038
	NN-M	0.8230	0.8197	0.8051	0.8321	0.7773	0.7913	0.8081
	ML	0.7804	0.7134	0.7238	0.7415	0.7155	0.6964	0.7285
	ER	0.3983	0.3938	0.3918	0.3832	0.4042	0.3732	0.3908
E	NN-B	0.7921	0.8061	0.7854	0.8165	0.8024	0.7784	0.7968
	NN-M	0.7851	0.7940	0.7996	0.8214	0.8173	0.7592	0.7961
	ML	0.7076	0.6985	0.7006	0.6899	0.6894	0.6828	0.6948
	ER	0.4686	0.4903	0.5370	0.4833	0.5056	0.4902	0.4958

Table 5.6 Ranking system used to categorize classes in terms of the ability of the algorithm and TM imagery to discriminate them (i.e., ranks are based on success in class identification and separation from other classes). Errors are averaged for both errors of omission and commission, over all 6 sets of results.

Discrimination Ranking	Average of Errors of Commission and Omission
"Excellent"	<5%
"Very Good"	5-10%
"Good"	10-15%
"Fair"	15-20%
"Poor"	20-30%
"Very Poor"	>30%

5.3.1.1 Evidential Reasoning

The average proportions of test pixels correctly labelled by the evidential reasoning algorithm for the *B*, *C*, *D*, and *E* series are 54%, 46%, 45%, and 62%, respectively (Table 5.4). Average Kappa values for these four series are 49%, 43%, 39%, and 50%, respectively (Table 5.5). The evidential reasoning values given in Tables 5.4 and 5.5 are 20 to 30% less than the corresponding values of the other two classifiers, and are indicative of a failure of the algorithm to produce a useful database of surface lithologies or surface cover.

Errors of omission and commission for all 24 evidential reasoning executions for the Melville Island Field Area are given in Table 5.7, while generalizations of the evidential reasoning results, by class, are given in Tables 5.8 to 5.11; these generalizations are based on the confusion matrices that describe all evidential reasoning results for the Melville Island Field Area. As can be seen from these tables, errors are very high for all but the water and ice classes. Some classes are not even represented in the classification results of the test sites [e.g., the Sabine Bay sandstone class was not used as a classification label for any test sites used in the *B* Series; similarly, the Canyon Fiord (yellow) as well as the Sabine Bay and Bjorn and Trold Fiord sandstone class are not included in results in some of the *B* and *C* Series classifications].

The images produced by the evidential reasoning algorithm have very little value as geological or land-cover databases (Figures 5.3 to 5.6; compare with the corresponding map of bedrock geology, Figure 4.4) (note: as with all classified images presented in this chapter, the Weatherall Bay and Sherard Bay waters have been masked, so that only land classes are shown). A discussion of the failure of the evidential reasoning algorithm is given separately

Table 5.7 Summary of the magnitude of errors of omission and commission for all evidential reasoning classifications of the Melville Island Field Area. Values are expressed as proportions, and may be converted to percentages by multiplying by 100%.

B: ER	1		2		3		4		5		6		
CLASS	EO	EC	EO	EC	EO	EC	EO	EC	EO	EC	EO	EC	AVG
1	0.07	0.51	0.10	0.56	0.07	0.62	0.10	0.53	0.17	0.64	0.07	0.53	0.33
2	1.00		1.00		0.86	0.80	1.00	1.00	0.86	0.00	0.86	0.00	0.74
3	0.14	0.81	0.00	0.71	0.00	0.73	0.00	0.71	0.14	0.78	0.00	0.78	0.40
4	0.96	0.00	0.92	0.00	0.96	0.87	0.88	0.00	0.96	0.00	0.96	0.00	0.53
5	0.64	0.64	0.64	0.71	0.57	0.45	0.71	0.71	0.29	0.50	0.64	0.71	0.60
6	0.70	0.52	0.67	0.57	0.63	0.48	0.65	0.27	0.70	0.52	0.67	0.40	0.57
7	1.00		1.00		1.00		1.00		1.00		1.00		1.00
8	0.33	0.20	0.25	0.31	0.17	0.33	0.33	0.38	0.33	0.38	0.33	0.33	0.31
9	0.06	0.64	0.12	0.69	0.12	0.67	0.12	0.68	0.06	0.64	0.06	0.64	0.37
10	0.63	0.57	0.81	0.55	0.93	0.50	0.56	0.65	0.78	0.65	0.70	0.65	0.68
11	0.45	0.25	0.55	0.36	0.55	0.00	0.82	0.33	0.82	0.00	0.55	0.17	0.40
12	0.00	0.39	0.00	0.39	0.00	0.36	0.00	0.36	0.00	0.18	0.00	0.36	0.17
13	0.00	0.00	0.06	0.00	0.06	0.00	0.06	0.00	0.00	0.00	0.00	0.00	0.02
14	0.00	0.00	0.00	0.00	0.00	0.00	0.00	0.00	0.00	0.00	0.00	0.00	0.00

C: ER	1		2		3		4		5		6		
CLASS	EO	EC	EO	EC	EO	EC	EO	EC	EO	EC	EO	EC	AVG
1	0.16	0.63	0.19	0.63	0.14	0.63	0.16	0.67	0.22	0.69	0.19	0.65	0.41
2	0.14	0.90	0.00	0.89	0.00	0.88	0.00	0.87	0.14	0.90	0.00	0.90	0.47
3	0.96	0.00	0.92	0.00	0.96	0.87	0.88	0.00	0.96	0.00	0.96	0.00	0.53
4	0.64	0.64	0.64	0.71	0.64	0.50	0.71	0.71	0.29	0.50	0.64	0.71	0.61
5	0.70	0.53	0.73	0.59	0.71	0.55	0.73	0.50	0.78	0.53	0.78	0.54	0.64
6	1.00		1.00		1.00		1.00		1.00		1.00		1.00
7	0.17	0.41	0.17	0.38	0.17	0.57	0.08	0.45	0.25	0.50	0.25	0.50	0.32
8	0.00	0.39	0.00	0.39	0.00	0.39	0.00	0.36	0.00	0.18	0.00	0.36	0.17
9	0.00	0.00	0.00	0.00	0.00	0.00	0.08	0.00	0.00	0.00	0.00	0.00	0.01
10	0.00	0.00	0.00	0.00	0.00	0.00	0.00	0.00	0.00	0.00	0.00	0.00	0.00

D: ER	1		2		3		4		5		6		
CLASS	EO	EC	EO	EC	EO	EC	EO	EC	EO	EC	EO	EC	AVG
1	0.14	0.67	0.14	0.68	0.11	0.67	0.16	0.70	0.19	0.71	0.16	0.68	0.42
2	0.00	0.89	0.00	0.90	0.00	0.90	0.00	0.88	0.00	0.89	0.00	0.90	0.45
3	0.64	0.64	0.64	0.71	0.64	0.50	0.71	0.71	0.29	0.50	0.64	0.71	0.61
4	0.83	0.40	0.85	0.32	0.88	0.31	0.85	0.41	0.84	0.26	0.90	0.47	0.61
5	1.00		1.00		1.00		1.00		1.00		1.00		1.00
6	0.17	0.41	0.17	0.38	0.17	0.57	0.08	0.45	0.25	0.50	0.25	0.50	0.32
7	0.00	0.39	0.00	0.39	0.00	0.39	0.00	0.36	0.00	0.18	0.00	0.36	0.17
8	0.00	0.00	0.00	0.00	0.00	0.00	0.08	0.08	0.00	0.00	0.00	0.08	0.02
9	0.00	0.00	0.00	0.00	0.00	0.00	0.00	0.00	0.00	0.00	0.00	0.00	0.00

E: ER	1		2		3		4		5		6		
CLASS	EO	EC	EO	EC	EO	EC	EO	EC	EO	EC	EO	EC	AVG
1	0.55	0.33	0.54	0.31	0.50	0.28	0.50	0.38	0.50	0.34	0.51	0.32	0.42
2	0.45	0.49	0.40	0.47	0.35	0.37	0.47	0.45	0.47	0.47	0.45	0.46	0.44
3	0.57	0.77	0.57	0.78	0.64	0.84	0.57	0.78	0.21	0.62	0.57	0.78	0.64
4	0.00	0.39	0.00	0.39	0.00	0.39	0.00	0.36	0.00	0.18	0.00	0.36	0.17
5	0.00	0.50	0.00	0.43	0.00	0.43	0.00	0.37	0.00	0.52	0.00	0.52	0.23
6	0.00	0.00	0.00	0.00	0.00	0.00	0.00	0.00	0.00	0.00	0.00	0.00	0.00

Table 5.8 Summary of ability of evidential reasoning and TM imagery combination to discriminate the surface-cover classes in the Melville Island Field Area (*B* Series).

Class	Discrimination	Typically Confused Classes
1. Canyon Fiord (Red-Weathering)	Very Poor	Great Bear Cape Limestone, Sabine Bay Sandstone, Trold Fiord Sandstone, Assistance Mudstone, Canyon Fiord (Yellow), Gabbro
2. Canyon Fiord (Yellow)	Very Poor	Canyon Fiord (Red-Weathering), Degerböls Limestone
3. Canyon Fiord (Pink)	Very Poor	Tingmisut Inlier Dolomite, Sabine Bay Sandstone, Bjorn Sandstone
4. Tingmisut Inlier Dolomite	Very Poor	Canyon Fiord (Pink Weathering), Degerböls Limestone, Gabbro, Great Bear Cape Limestone
5. Gabbro	Very Poor	Trold Fiord Sandstone, Tingmisut Inlier Dolomite, Green Vegetation, Canyon Fiord (Red-Weathering), Assistance Mudstone
6. Great Bear Cape Limestone	Very Poor	Canyon Fiord (Red-Weathering), Trold Fiord Sandstone, Degerböls Limestone, Sabine Bay Sandstone, Tingmisut Inlier Dolomite
7. Sabine Bay Sandstone	Very Poor	Canyon Fiord (Red-Weathering), Canyon Fiord (Pink), Great Bear Cape Limestone, Degerböls Limestone
8. Assistance Mudstone	Very Poor	Canyon Fiord (Red-Weathering), Gabbro, Trold Fiord Sandstone
9. Degerböls Limestone	Very Poor	Canyon Fiord (Yellow), Tingmisut Inlier Dolomite, Great Bear Cape Limestone, Sabine Bay Sandstone, Bjorn Sandstone
10. Trold Fiord Sandstone	Very Poor	Canyon Fiord (Red-Weathering), Gabbro, Great Bear Cape Limestone, Assistance Mudstone
11. Bjorn Sandstone	Very Poor	Degerböls Limestone, Canyon Fiord (Pink), Great Bear Cape Limestone
12. Green Vegetation	Fair	Gabbro
13. Snow Cover	Excellent	None
14. Water	Excellent	None

Table 5.9 Summary of ability of evidential reasoning and TM imagery combo to discriminate the surface-cover classes in the Melville Island Field Area (*C* Series).

Class	Discrimination	Typically Confused Classes
1. Canyon Fiord (Red/Yellow)	Very Poor	Great Bear Cape and Degerböls Limestone, Sabine Bay and Bjorn and Trold Fiord Sandstone, Gabbro, Tingmisut Inlier Dolomite, Canyon Fiord (Pink), Assistance Formation
2. Canyon Fiord (Pink)	Very Poor	Canyon Fiord (Red/Yellow), Tingmisut Inlier Dolomite, Great Bear Cape and Degerböls Limestone, Sabine Bay and Bjorn and Trold Fiord Sandstone
3. Tingmisut Inlier Dolomite	Very Poor	Canyon Fiord (Red/Yellow), Canyon Fiord (Pink), Great Bear Cape and Degerböls Limestone, Gabbro
4. Gabbro	Very Poor	Canyon Fiord (Red/Yellow), Green Vegetation, Tingmisut Inlier Dolomite, Sabine Bay and Bjorn and Trold Fiord Sandstone
5. Great Bear Cape and Degerböls Limestone	Very Poor	Canyon Fiord (Red-Weathering), Canyon Fiord (Pink Weathering), Tingmisut Inlier Dolomite, Sabine Bay and Bjorn and Trold Fiord Sandstone
6. Sabine Bay and Bjorn and Trold Fiord Sandstone.	Very Poor	Canyon Fiord (Red/Yellow), Canyon Fiord (Pink), Gabbro, Great Bear Cape and Degerböls Limestone, Assistance Mudstone
7. Assistance Mudstone	Very Poor	Sabine Bay and Bjorn and Trold Fiord Sandstone, Canyon Fiord Sandstone (Red-Weathering)
8. Green Vegetation	Fair	Gabbro
9. Snow Cover	Excellent	None
10. Water	Excellent	None

Table 5.10 Summary of ability of evidential reasoning and TM imagery combo to discriminate the surface-cover classes in the Melville Island Field Area (*D* Series).

Class	Discrimination	Typically Confused Classes
1. Canyon Fiord (Red/Yellow)	Very Poor	Carbonates, Sabine Bay and Bjorn and Trold Fiord Sandstone, Canyon Fiord (Pink), Gabbro
2. Canyon Fiord (Pink)	Very Poor	Carbonates, Sabine Bay and Bjorn and Trold Fiord Sandstone, Canyon Fiord (Red-Weathering)
3. Gabbro	Very Poor	Green Vegetation, Carbonates, Sabine Bay and Bjorn and Trold Fiord Sandstone, Assistance Mudstone, Canyon Fiord (Red-Weathering)
4.Carbonates	Very Poor	Canyon Fiord (Red-Weathering), Canyon Fiord (Yellow), Gabbro, Sabine Bay and Bjorn and Trold Fiord Sandstone
5. Sabine Bay and Bjorn and Trold Fiord Sandstone.	Very Poor	Canyon Fiord (Red-Weathering), Canyon Fiord (Pink), Gabbro, Carbonates, Assistance Mudstone
6. Assistance Mudstone	Very Poor	Gabbro, Sabine Bay and Bjorn and Trold Fiord Sandstone
7. Green Vegetation	Fair	Gabbro
8. Snow Cover	Excellent	None
9. Water	Excellent	None

Table 5.11 Summary of ability of evidential reasoning and TM imagery combo to discriminate the surface-cover classes in the Melville Island Field Area (*E* Series).

Class	Discrimination	Typically Confused Classes
1. Clastics	Very Poor	Carbonates, Gabbro, Snow Cover
2. Carbonates	Very Poor	Clastics, Gabbro, Snow Cover
3. Gabbro	Very Poor	Clastics, Carbonates, Green Vegetation
4. Green Vegetation	Fair	Gabbro
5. Snow Cover	Poor	Clastics, Carbonates
6. Water	Excellent	None

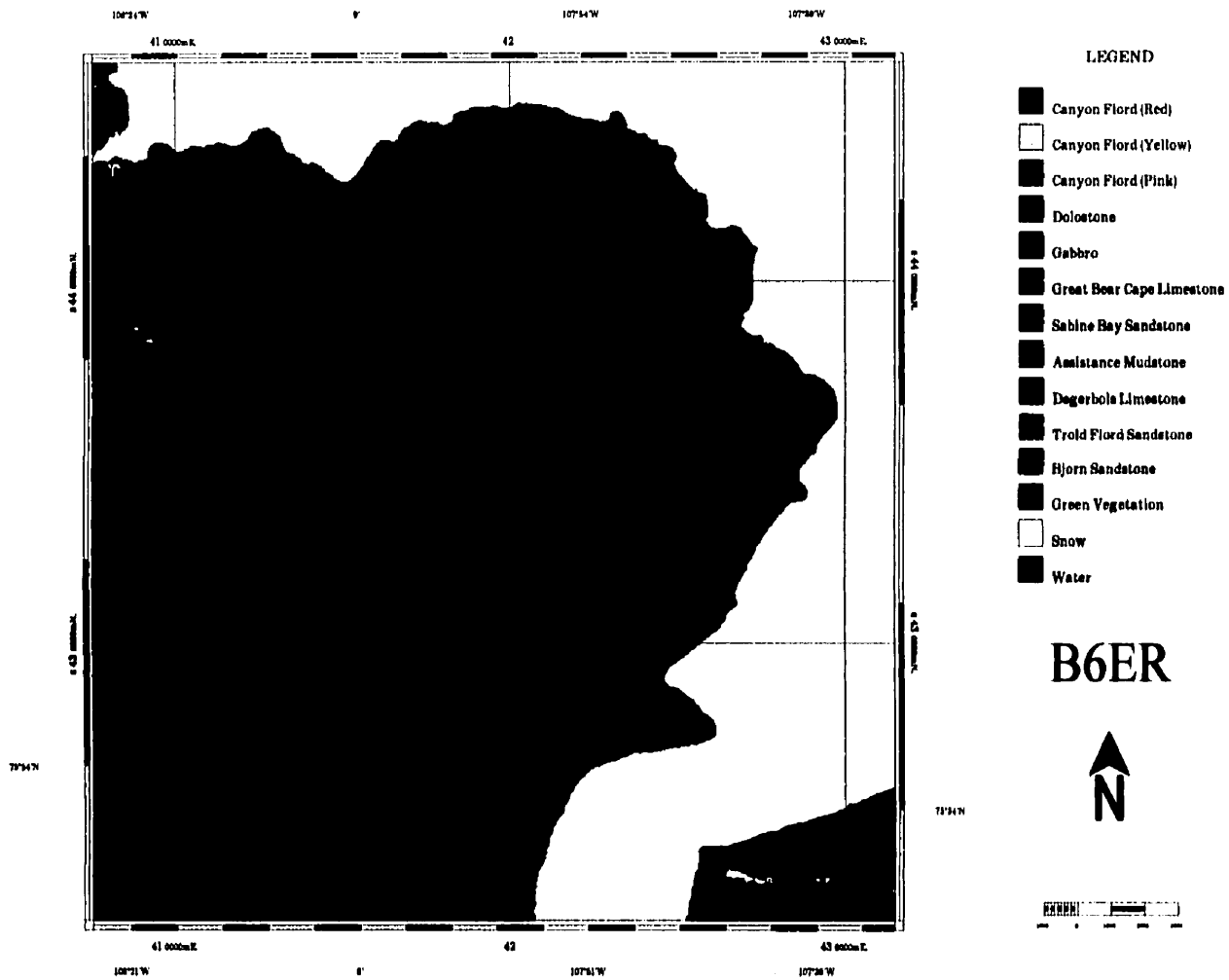

Figure 5.3 Classified image of the Melville Island Field Area, produced by the evidential reasoning algorithm (*B* Series, Execution #6). Compare with the map of bedrock geology (Figure 4.4) for areas represented in the training and test database (Figure 4.6).

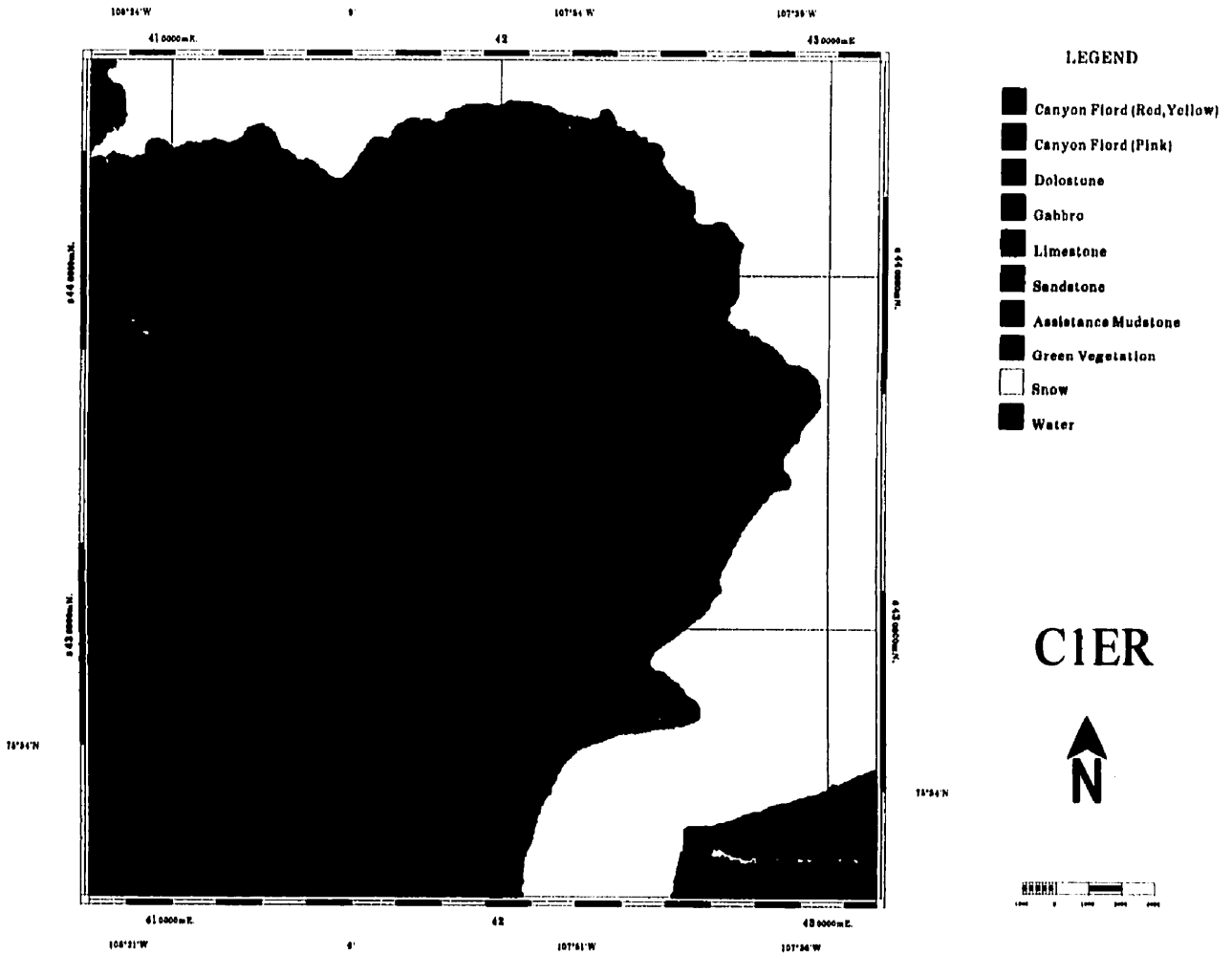

Figure 5.4 Classified image of the Melville Island Field Area, produced by the evidential reasoning algorithm (*C* Series, Execution #1). Compare with the map of bedrock geology (Figure 4.4) for areas represented in the training and test database (Figure 4.6).

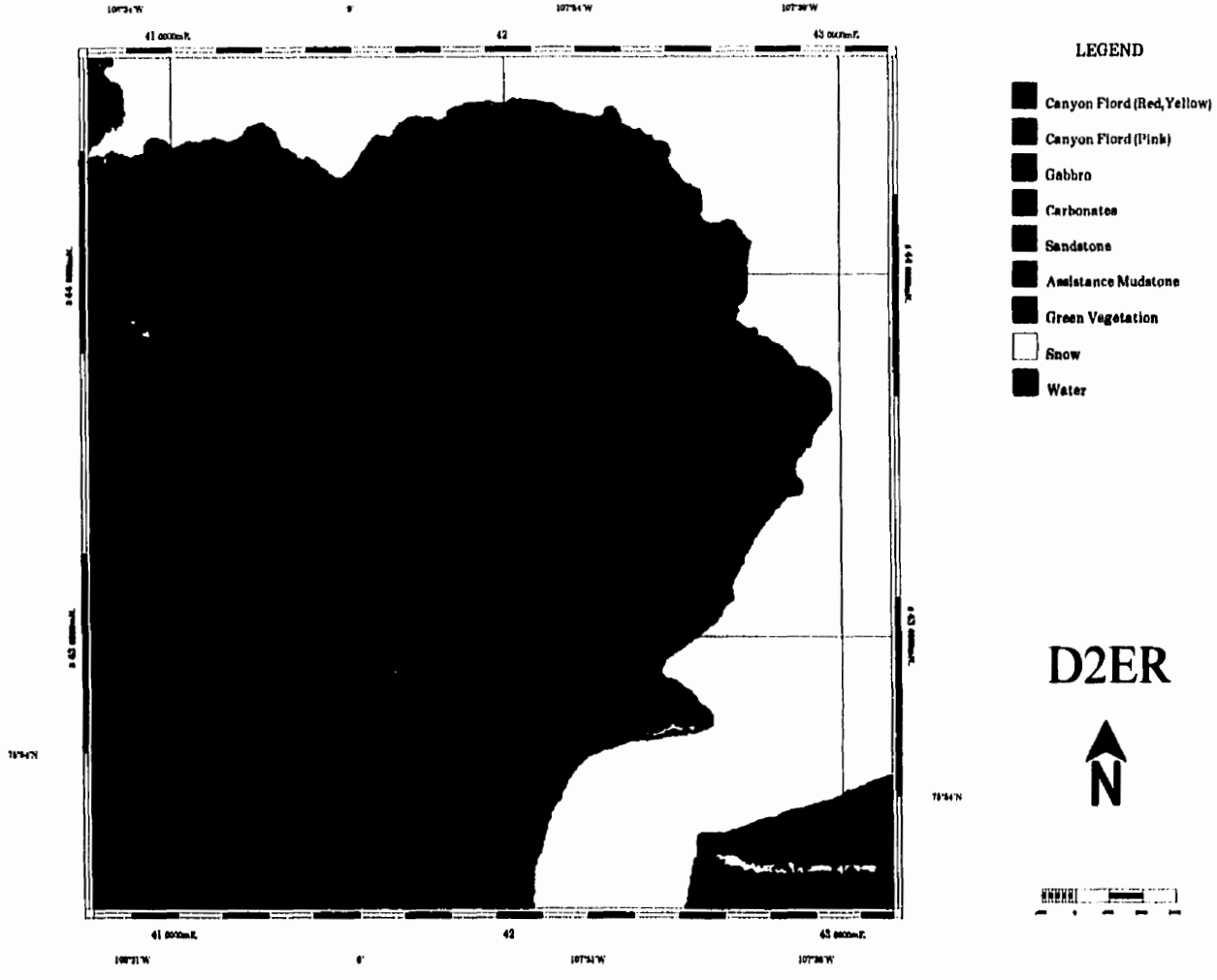

Figure 5.5 Classified image of the Melville Island Field Area, produced by the evidential reasoning algorithm (*D* Series, Execution #2). Compare with the map of bedrock geology (Figure 4.4) for areas represented in the training and test database (Figure 4.6).

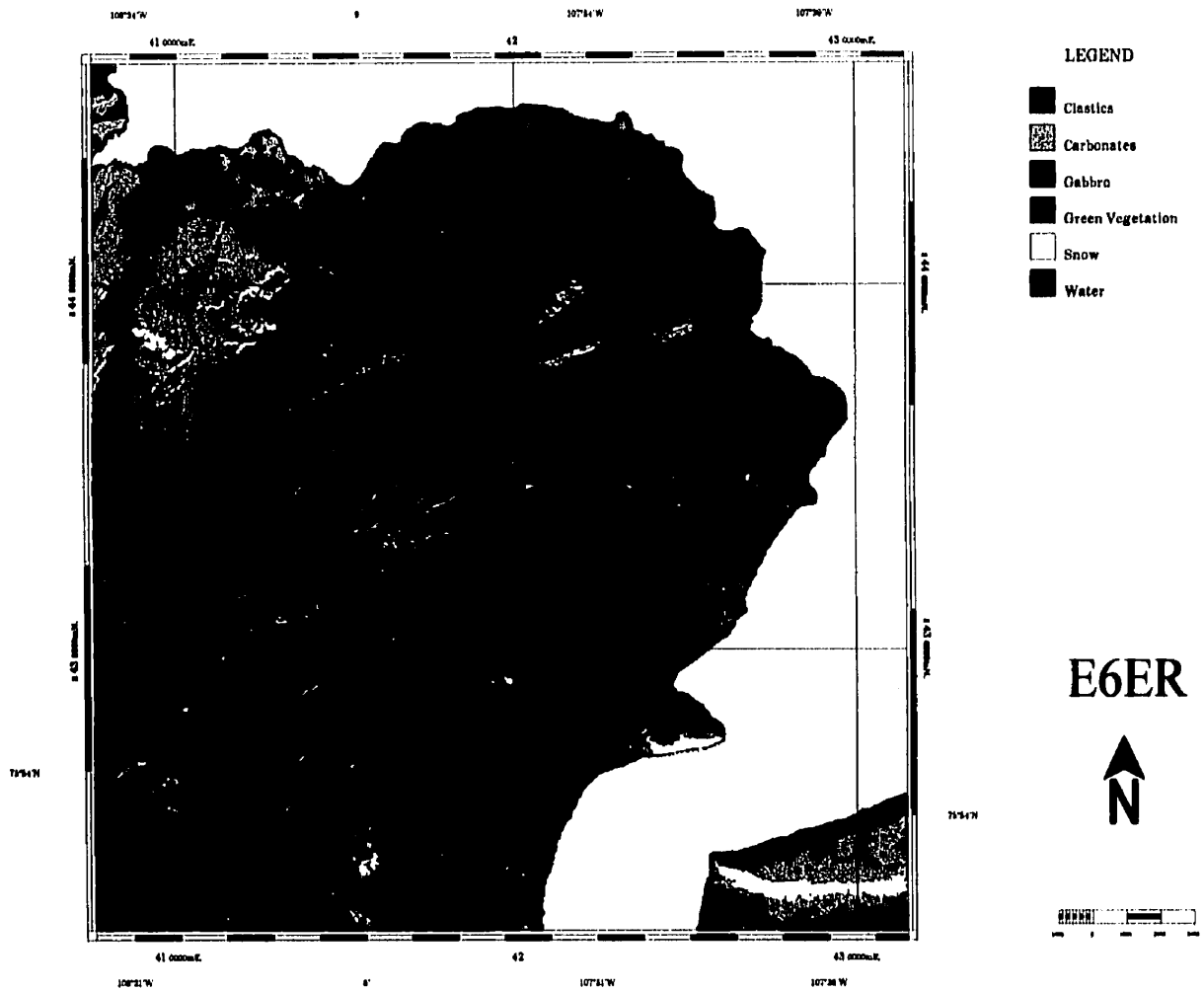

Figure 5.6 Classified image of the Melville Island Field Area, produced by the evidential reasoning algorithm (*E* Series, Execution #6). Compare with the map of bedrock geology (Figure 4.4) for areas represented in the training and test database (Figure 4.6).

in Section 5.4.

5.3.1.2 Maximum Likelihood

Classification results obtained using the maximum likelihood classifier are much stronger than those of the evidential reasoning classifier. The average general percentages of test pixels correctly labelled for the *B*, *C*, *D*, and *E* series are 74%, 77%, 78%, and 78%, respectively (Table 5.4). Average Kappa values for these series are 72%, 73%, 73%, and 69%, indicating that when expected results due to chance are taken into account, classification results produced by the maximum likelihood algorithm do not improve from Series *B* to *E* (Table 5.5).

Although the maximum likelihood values given in Tables 5.4 and 5.5 are 20 to 30% higher than those of the evidential reasoning algorithm, they are consistently 3 to 10% less than the corresponding values of the consensus neural network algorithm. A more detailed comparison between the results of the maximum likelihood and consensus neural network algorithms is given in Section 5.3.1.3.

The total errors of omission and commission for all maximum likelihood classifications of the Melville Island Field Area are given in Table 5.12. A summary of these errors with specific reference to the classes most confused is given in Tables 5.13 to 5.16; these tables are based on confusion matrices generated for each maximum likelihood execution. From these data, it can be seen that the best discriminated geological classes in the *B* Series of tests were Canyon Fiord (red-weathering), Canyon Fiord (pink), gabbro, Assistance mudstone, and Bjorn sandstone (Table 5.13). Classes relatively well discriminated in the *C* and *D* Series

Table 5.12 Summary of the magnitude of errors of omission and commission for all maximum likelihood classifications of the Melville Island Field Area. Values are expressed as proportions, and may be converted to percentages by multiplying by 100%.

B: ML	1		2		3		4		5		6		
CLASS	EO	EC	EO	EC	EO	EC	EO	EC	EO	EC	EO	EC	AVG
1	0.10	0.10	0.13	0.13	0.07	0.07	0.10	0.10	0.17	0.17	0.10	0.10	0.11
2	0.43	0.50	0.43	0.60	0.29	0.50	0.29	0.38	0.71	0.67	0.57	0.57	0.49
3	0.00	0.00	0.00	0.00	0.00	0.00	0.00	0.00	0.00	0.00	0.00	0.00	0.00
4	0.38	0.38	0.58	0.31	0.62	0.41	0.65	0.40	0.50	0.43	0.54	0.48	0.47
5	0.29	0.17	0.07	0.24	0.14	0.08	0.29	0.23	0.07	0.28	0.14	0.14	0.18
6	0.30	0.30	0.41	0.34	0.30	0.32	0.35	0.21	0.35	0.25	0.28	0.20	0.30
7	0.61	0.40	0.61	0.40	0.74	0.65	0.74	0.619	0.61	0.4	0.58	0.35	0.56
8	0.17	0.00	0.00	0.25	0.00	0.14	0.08	0.31	0.08	0.21	0.08	0.31	0.14
9	0.29	0.52	0.24	0.55	0.53	0.60	0.35	0.59	0.24	0.50	0.47	0.67	0.46
10	0.30	0.44	0.41	0.45	0.33	0.50	0.30	0.56	0.41	0.50	0.26	0.33	0.40
11	0.09	0.09	0.00	0.27	0.09	0.09	0.09	0.09	0.09	0.09	0.09	0.17	0.10
12	0.00	0.00	0.14	0.00	0.07	0.00	0.07	0.00	0.00	0.00	0.00	0.00	0.02
13	0.00	0.00	0.00	0.00	0.00	0.08	0.00	0.00	0.00	0.08	0.00	0.08	0.02
14	0.00	0.00	0.00	0.00	0.00	0.00	0.00	0.00	0.00	0.00	0.00	0.00	0.00

C: ML	1		2		3		4		5		6		
CLASS	EO	EC	EO	EC	EO	EC	EO	EC	EO	EC	EO	EC	AVG
1	0.14	0.16	0.16	0.14	0.11	0.15	0.14	0.20	0.27	0.27	0.16	0.16	0.17
2	0.00	0.00	0.00	0.00	0.00	0.00	0.00	0.00	0.00	0.00	0.00	0.00	0.00
3	0.12	0.39	0.35	0.47	0.38	0.41	0.35	0.47	0.38	0.45	0.19	0.49	0.37
4	0.29	0.17	0.00	0.22	0.14	0.08	0.29	0.23	0.07	0.32	0.14	0.14	0.17
5	0.11	0.32	0.22	0.36	0.21	0.36	0.25	0.30	0.19	0.39	0.25	0.34	0.27
6	0.52	0.18	0.57	0.23	0.51	0.31	0.48	0.28	0.57	0.21	0.59	0.26	0.39
7	0.08	0.00	0.00	0.43	0.08	0.31	0.08	0.45	0.08	0.27	0.08	0.45	0.19
8	0.00	0.00	0.14	0.00	0.07	0.00	0.07	0.00	0.00	0.00	0.00	0.00	0.02
9	0.00	0.00	0.00	0.00	0.00	0.00	0.00	0.00	0.00	0.00	0.00	0.00	0.00
10	0.00	0.00	0.00	0.00	0.00	0.00	0.00	0.00	0.00	0.00	0.00	0.00	0.00

D: ML	1		2		3		4		5		6		
CLASS	EO	EC	EO	EC	EO	EC	EO	EC	EO	EC	EO	EC	AVG
1	0.14	0.18	0.14	0.24	0.14	0.22	0.11	0.21	0.24	0.28	0.16	0.24	0.19
2	0.00	0.00	0.00	0.00	0.00	0.00	0.00	0.00	0.00	0.00	0.00	0.13	0.01
3	0.29	0.23	0.00	0.30	0.14	0.08	0.29	0.23	0.07	0.28	0.14	0.25	0.19
4	0.12	0.28	0.26	0.30	0.25	0.31	0.24	0.26	0.21	0.33	0.27	0.34	0.26
5	0.45	0.24	0.57	0.36	0.51	0.36	0.45	0.31	0.55	0.30	0.58	0.34	0.42
6	0.08	0.00	0.00	0.40	0.08	0.39	0.08	0.45	0.08	0.31	0.08	0.48	0.20
7	0.00	0.00	0.14	0.00	0.07	0.00	0.07	0.00	0.00	0.00	0.00	0.00	0.02
8	0.00	0.00	0.00	0.00	0.00	0.00	0.00	0.00	0.00	0.00	0.00	0.00	0.00
9	0.00	0.00	0.00	0.00	0.00	0.00	0.00	0.00	0.00	0.00	0.00	0.00	0.00

E: ML	1		2		3		4		5		6		
CLASS	EO	EC	EO	EC	EO	EC	EO	EC	EO	EC	EO	EC	AVG
1	0.39	0.13	0.35	0.16	0.38	0.14	0.34	0.19	0.40	0.17	0.38	0.19	0.27
2	0.10	0.35	0.20	0.35	0.12	0.38	0.18	0.35	0.17	0.37	0.20	0.38	0.26
3	0.29	0.41	0.00	0.42	0.21	0.15	0.36	0.40	0.07	0.35	0.14	0.33	0.26
4	0.00	0.00	0.14	0.00	0.07	0.00	0.07	0.00	0.00	0.00	0.00	0.00	0.02
5	0.00	0.00	0.00	0.00	0.00	0.00	0.00	0.00	0.00	0.00	0.00	0.00	0.00
6	0.00	0.00	0.00	0.00	0.00	0.00	0.00	0.00	0.00	0.00	0.00	0.00	0.00

Table 5.13 Summary of ability of maximum likelihood and TM imagery combination to discriminate the surface-cover classes in the Melville Island Field Area (*B* Series).

Class	Discrimination	Typically Confused Classes
1. Canyon Fiord (Red-Weathering)	Good	Gabbro
2. Canyon Fiord (Yellow)	Very Poor	Tingmisut Inlier Dolomite
3. Canyon Fiord (Pink)	Excellent	None
4. Tingmisut Inlier Dolomite	Very Poor	Canyon Fiord (Yellow), Degerböls Limestone, Sabine Bay Sandstone, Trold Fiord Sandstone
5. Gabbro	Fair	Canyon Fiord (Red-Weathering)
6. Great Bear Cape Limestone	Very Poor	Trold Fiord Sandstone, Sabine Bay Sandstone, Degerböls Limestone
7. Sabine Bay Sandstone	Very Poor	Trold Fiord Sandstone, Tingmisut Inlier Dolomite, Degerböls Limestone, Great Bear Cape Limestone
8. Assistance Mudstone	Good	Trold Fiord Sandstone
9. Degerböls Limestone	Very Poor	Tingmisut Inlier Dolomite, Great Bear Cape Limestone, Sabine Bay Sandstone
10. Trold Fiord Sandstone	Very Poor	Tingmisut Inlier, Great Bear Cape Limestone, Sabine Bay Sandstone,
11. Bjorn Sandstone	Good	Great Bear Cape Limestone, Sabine Bay Sandstone
12. Green Vegetation	Excellent	None
13. Snow Cover	Excellent	None
14. Water	Excellent	None

Table 5.14 Summary of ability of maximum likelihood and TM imagery combo to discriminate the surface-cover classes in the Melville Island Field Area (*C* Series).

Class	Discrimination	Typically Confused Classes
1. Canyon Fiord (Red/Yellow)	Fair	Tingmisut Inlier Dolomite, Sabine Bay and Bjorn and Trold Fiord Sandstone, Gabbro, Great Bear Cape Limestone
2. Canyon Fiord (Pink)	Excellent	None
3. Tingmisut Inlier Dolomite	Very Poor	Great Bear Cape and Degerböls Limestone, Sabine Bay and Bjorn and Trold Fiord Sandstone, Canyon Fiord (Red/Yellow)
4. Gabbro	Fair	Canyon Fiord (Red/Yellow)
5. Great Bear Cape and Degerböls Limestone	Poor	Canyon Fiord (Red/Yellow), Tingmisut Inlier Dolomite, Sabine Bay and Bjorn and Trold Fiord Sandstone
6. Sabine Bay and Bjorn and Trold Fiord Sandstone.	Very Poor	Canyon Fiord (Red/Yellow), Tingmisut Inlier Dolomite, Great Bear Cape and Degerböls Limestone, Assistance Mudstone
7. Assistance Mudstone	Fair	Sabine Bay and Bjorn and Trold Fiord Sandstone
8. Green Vegetation	Excellent	None
9. Snow Cover	Excellent	None
10. Water	Excellent	None

Table 5.15 Summary of ability of maximum likelihood and TM imagery combo to discriminate the surface-cover classes in the Melville Island Field Area (*D* Series).

Class	Discrimination	Typically Confused Classes
1. Canyon Fiord (Red/Yellow)	Fair	Carbonates, Sabine Bay and Bjorn and Trold Fiord Sandstone, Gabbro
2. Canyon Fiord (Pink)	Excellent	None
3. Gabbro	Fair	Canyon Fiord (Red/Yellow), Carbonates
4.Carbonates	Poor	Canyon Fiord (Red/Yellow), Sabine Bay and Bjorn and Trold Fiord Sandstone, Gabbro
5. Sabine Bay and Bjorn and Trold Fiord Sandstone	Very Poor	Carbonates, Canyon Fiord (Red/Yellow), Assistance Mudstone
6. Assistance Mudstone	Poor	Sabine Bay and Bjorn and Trold Fiord Sandstone
7. Green Vegetation	Excellent	None
8. Snow Cover	Excellent	None
9. Water	Excellent	None

Table 5.16 Summary of ability of maximum likelihood and TM imagery combo to discriminate the surface-cover classes in the Melville Island Field Area (*E* Series).

Class	Discrimination	Typically Confused Classes
1. Clastics	Poor	Carbonates, Gabbro
2. Carbonates	Poor	Clastics, Gabbro
3. Gabbro	Poor	Clastics, Carbonates
4. Green Vegetation	Excellent	None
5. Snow Cover	Excellent	None
6. Water	Excellent	None

were Canyon Fiord (red/yellow), Canyon Fiord (pink), gabbro, and Assistance mudstone (Tables 5.14 and 5.15). None of the geological classes were well discriminated in the *E* Series using the maximum likelihood algorithm (Table 5.16). Particularly poorly discriminated lithologies in the *B* Series included Canyon Fiord (yellow), Tingmisut Inlier dolomite, Great Bear Cape limestone, Sabine Bay sandstone, Degerböls limestone, and Trold Fiord sandstone (Table 5.13). When these classes were combined with other classes in the *C*, *D*, and *E* Series, the associated results generally remained poor (Tables 5.14, 5.15, and 5.16).

As can be seen in Figures 5.7 to 5.10 (selected *B* to *E* Series results), the images produced by the maximum likelihood algorithm have value as geological and land-cover databases, at least with regard to the better discriminated classes noted above (compare these results with the corresponding map of bedrock geology, given in Figure 4.4). More detailed evaluation of the classified images is given in Section 5.3.1.4.

5.3.1.3 Neural Network

Classification results obtained using the consensus neural network classifier are the strongest of the three classifiers examined here. The average general percentages of test pixels correctly labelled for the *B*, *C*, *D*, and *E* series are 78%, 82%, 84%, and 86%, respectively (Table 5.4). Average Kappa values for the same series are 76%, 79%, 81%, and 80% (Table 5.5). For each of the 24 comparisons between consensus neural network jobs and their corresponding maximum likelihood jobs, the neural network produced similar or superior results (strictly speaking, all consensus neural network percentages are slightly to

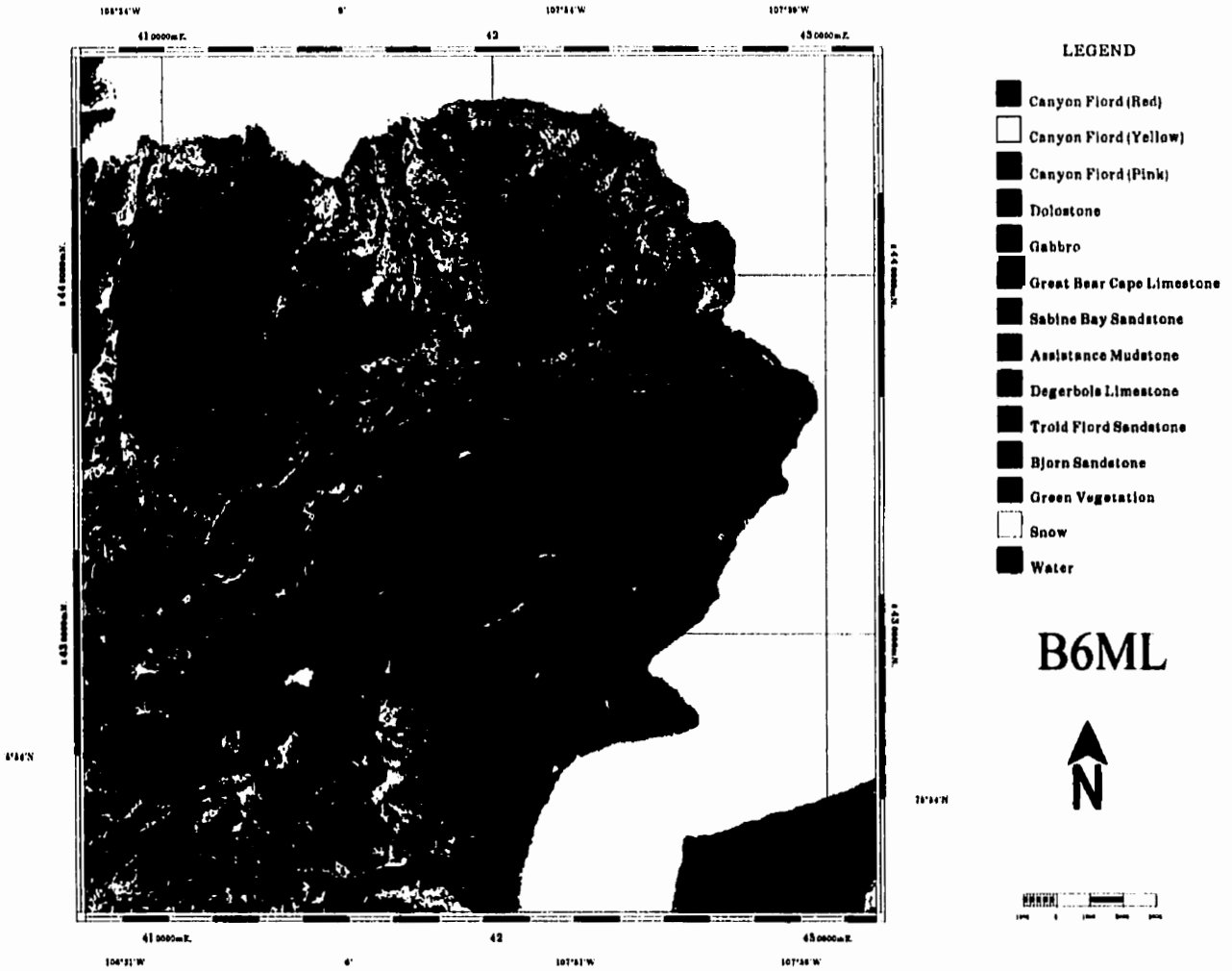

Figure 5.7 Classified image of the Melville Island Field Area, produced by the maximum likelihood algorithm (*B* Series, Execution #6). Compare with the map of bedrock geology (Figure 4.4) for areas represented in the training and test database (Figure 4.6).

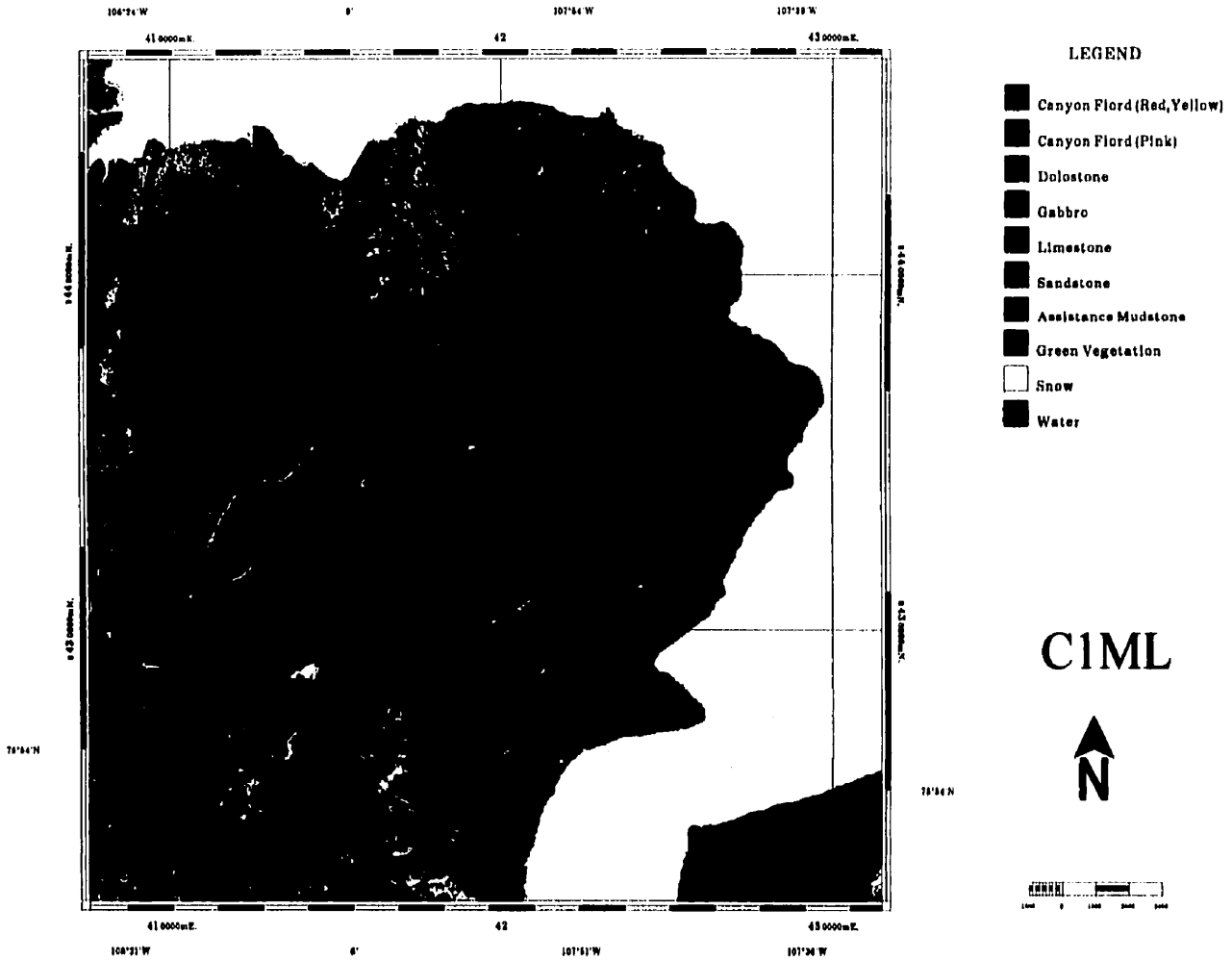

Figure 5.8 Classified image of the Melville Island Field Area, produced by the maximum likelihood algorithm (*C* Series, Execution #1). Compare with the map of geology (Figure 4.4) for areas represented in the training and test database (Figure 4.6).

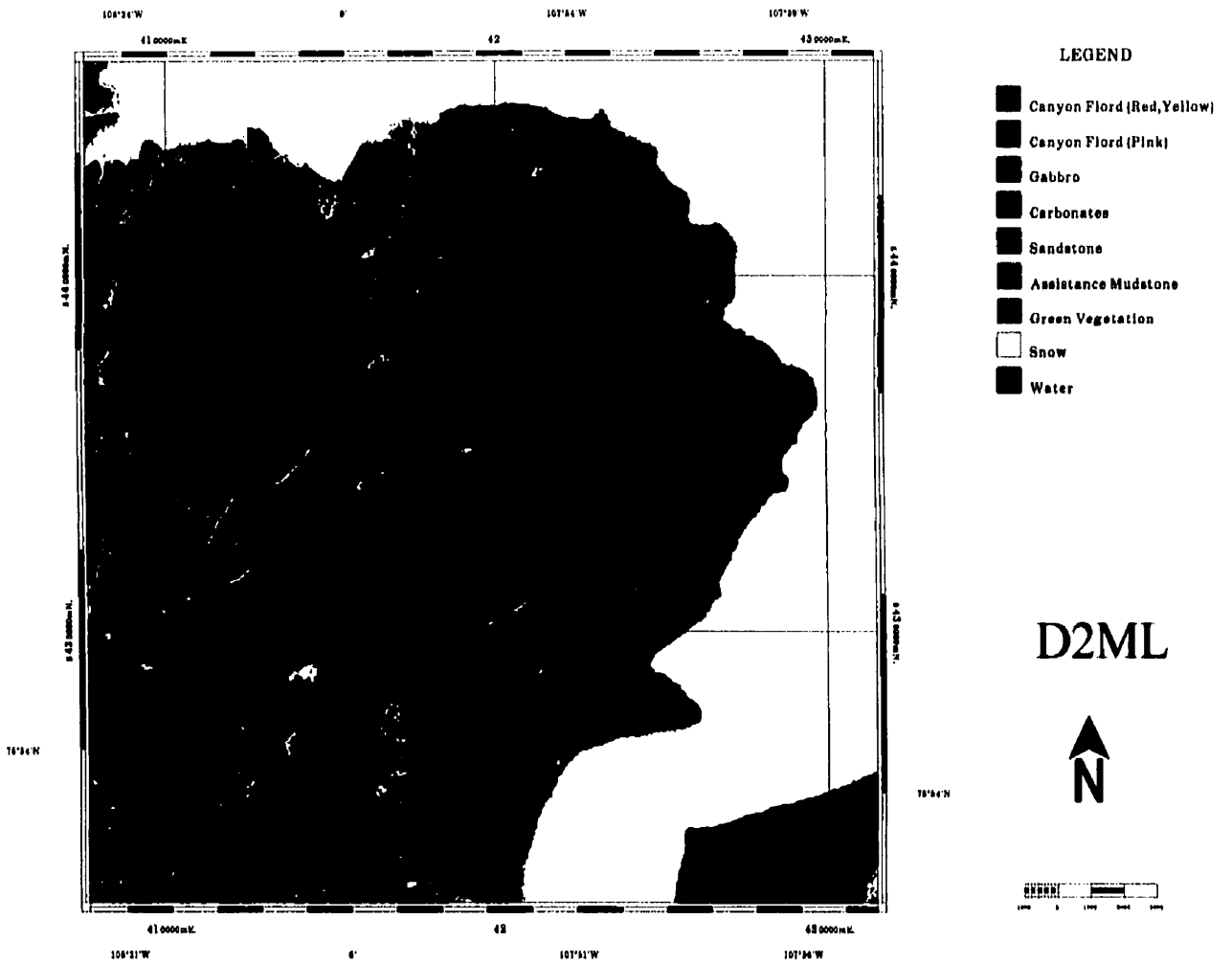

Figure 5.9 Classified image of the Melville Island Field Area, produced by the maximum likelihood algorithm (*D* Series, Execution #2). Compare with the map of geology (Figure 4.4) for areas represented in the training and test database (Figure 4.6).

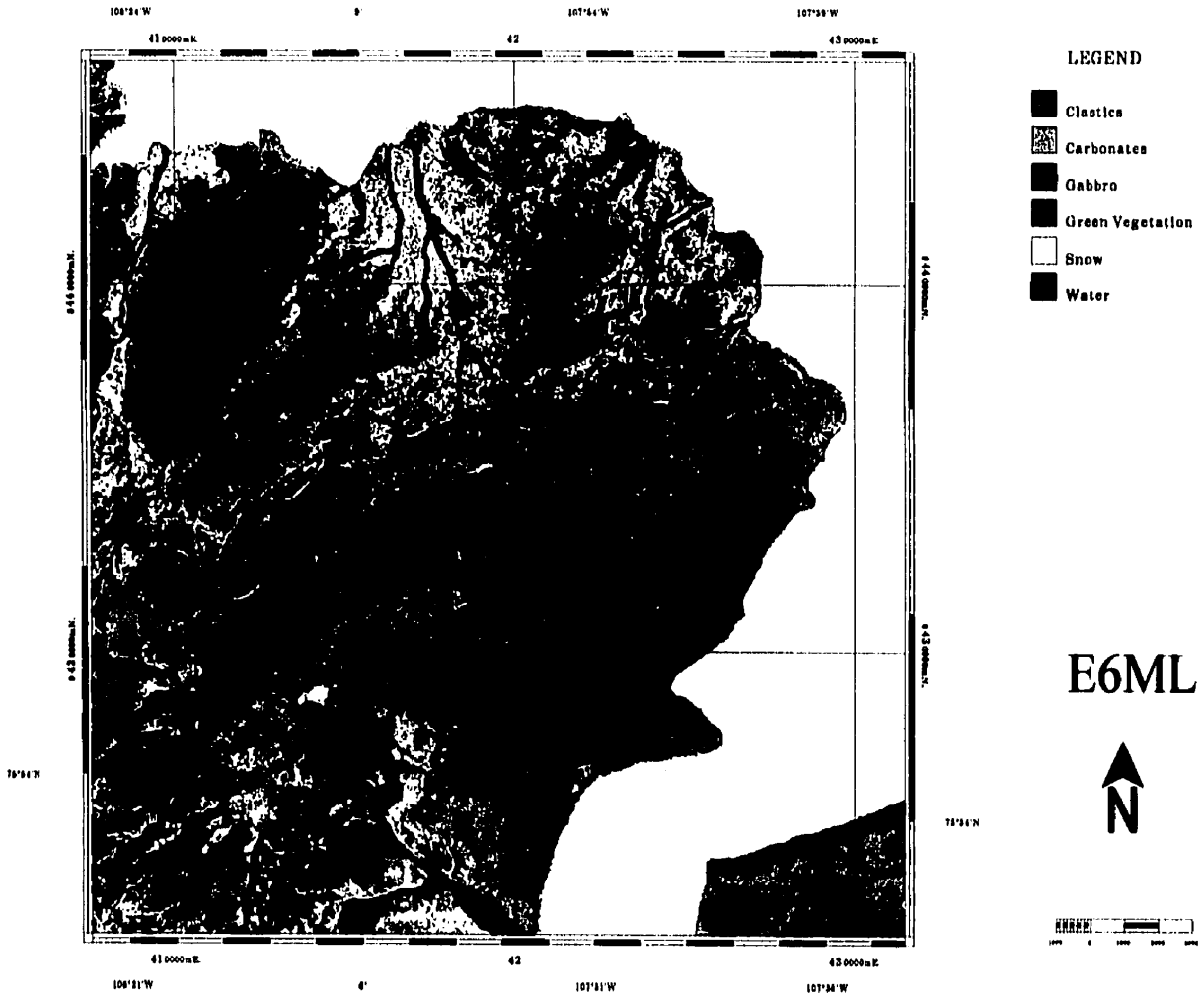

Figure 5.10 Classified image of the Melville Island Field Area, produced by the maximum likelihood algorithm (*E* Series, Execution #6). Compare with the map of geology (Figure 4.4) for areas represented in the training and test database (Figure 4.6).

significantly higher than those of the maximum likelihood algorithm). The difference between each consensus neural network result and its corresponding maximum likelihood result increases from an average of 4% for the *B* series to an average of 7% for the *E* series (Table 5.17). The differences are even greater for the average Kappa results, for which differences of up to 10% occurred (Table 5.18). The trend of increasing differences between the performance of the neural network and the maximum likelihood classifiers in the *B* to *E* Series is believed to be the result of the increasingly variable and complex nature of the frequency histograms describing the training data of the lithological classes, from series *B* to *E* (for example, in the *B* Series, several geological classes are spectrally distinct; as these and other classes are combined in the *C*, *D*, and *E* Series, the spectral nature of the resulting classes necessarily becomes much more complicated - see Figure 5.11). This trend in results is interesting in that it shows that the consensus neural network classifier can consistently produce results that are better than those of the maximum likelihood classifier, and that the difference between the results increases with the complexity of training-data frequency distributions.

Although the results of individual neural network executions vary considerably (Figure 5.12), the consensus neural network results given in Table 5.4 are typically within about 1% of the result of the best individual neural network job for a given training and test data set (standard deviations of the differences between these values for the *B*, *C*, *D*, and *E* series are 0.9%, 0.8%, 0.7%, and 0.9%, respectively). The strong similarity between the best individual results and the corresponding consensus results is of interest, since one of the most serious practical limitations of the application of neural networks for classification purposes is the

Table 5.17 Differences between the proportions of test pixels correctly classified for the consensus neural network and the corresponding maximum likelihood executions: Melville Island Field Area.

Series	Set 1	Set 2	Set 3	Set 4	Set 5	Set 6	Avg.
B	0.0204	0.0544	0.0578	0.0578	0.0272	0.0204	0.0397
C	0.0034	0.0544	0.0442	0.0748	0.0442	0.0612	0.0470
D	0.0340	0.0884	0.0680	0.0748	0.0510	0.0782	0.0657
E	0.0578	0.0714	0.0714	0.0952	0.0952	0.0578	0.0748

Table 5.18 Differences between Kappa values for the consensus neural network and the corresponding maximum likelihood executions: Melville Island Field Area.

Series	Set 1	Set 2	Set 3	Set 4	Set 5	Set 6	Avg.
B	0.0213	0.0581	0.0624	0.0619	0.0283	0.0215	0.0423
C	0.0036	0.0613	0.0516	0.0849	0.0518	0.0693	0.0538
D	0.0426	0.1063	0.0813	0.0906	0.0618	0.0949	0.0796
E	0.0775	0.0955	0.0990	0.1315	0.1279	0.0764	0.1013

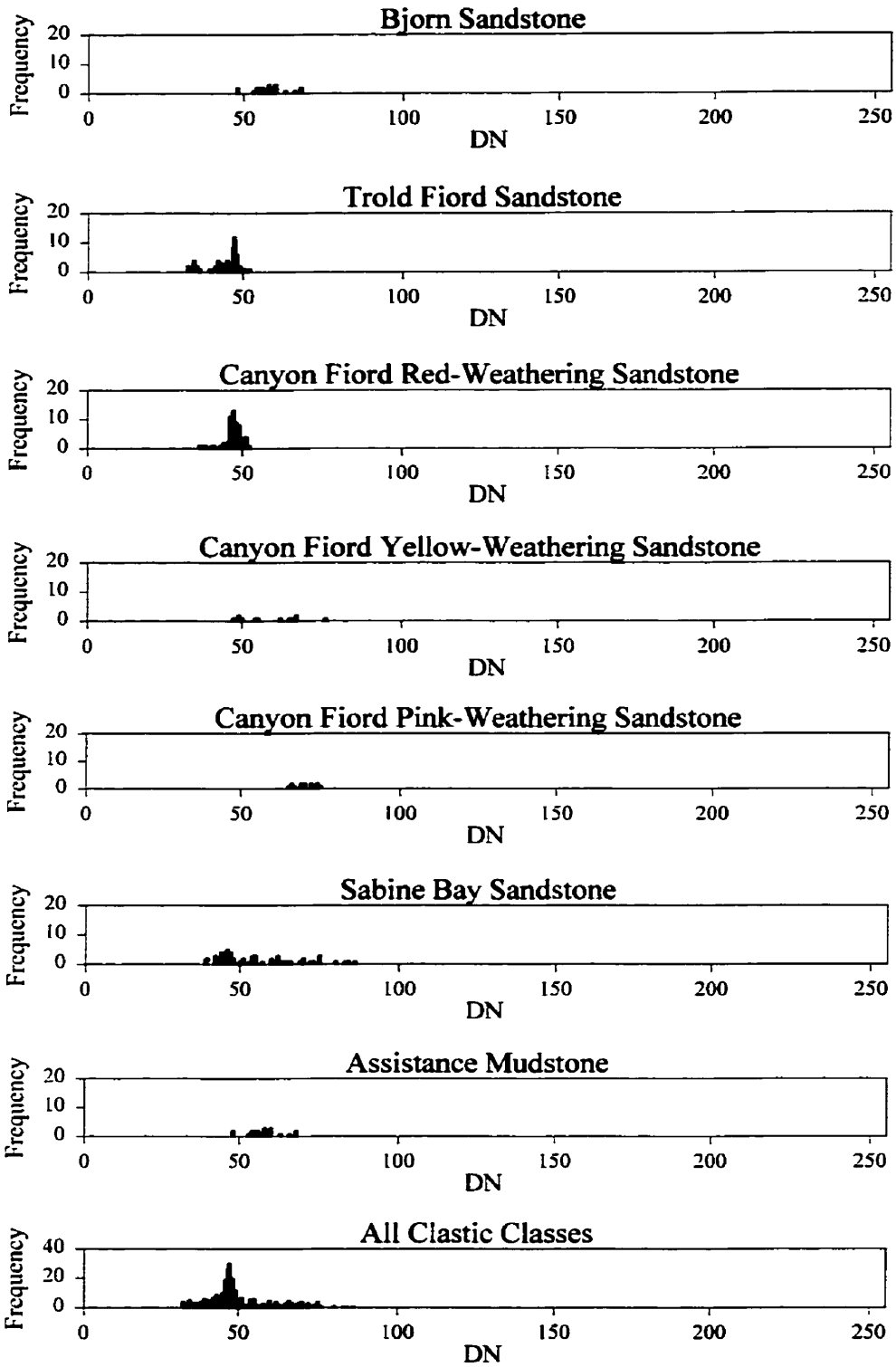

Figure 5.11 The complexity of class histograms increases from the *B* Series to the *E* Series, as is shown here for the *E* Series class "clastics". This class is made up of the following *B* Series classes: Bjorn sandstone, Trold Fiord sandstone, Canyon Fiord red-, yellow-, and pink-coloured clastics, Sabine Bay sandstone, and Assistance mudstone.

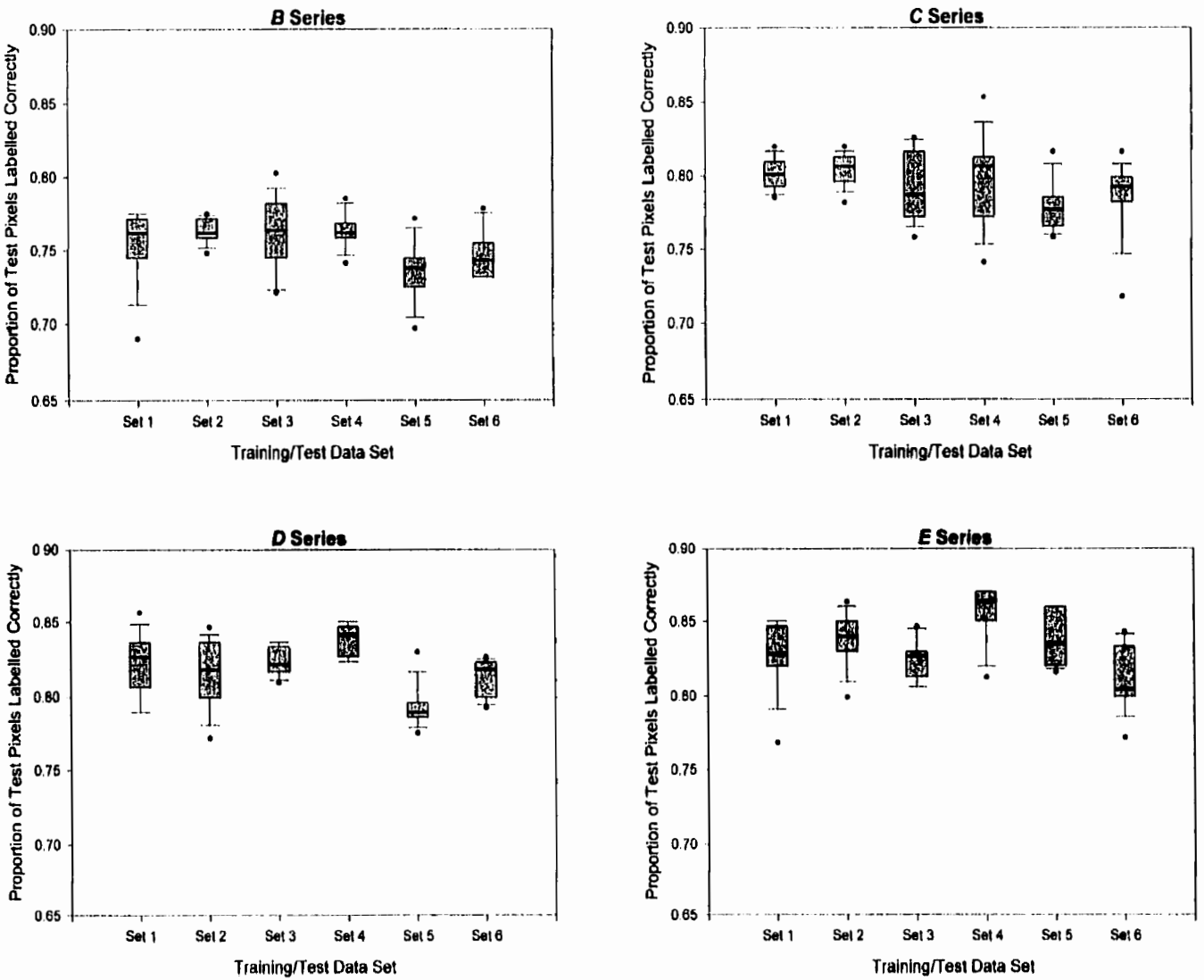

Figure 5.12 Boxplots showing the considerable variation in individual overall classification results produced by the neural network classifier (*B* to *E* Series results for the Melville Island Field Area). Boxes give the 25th, 50th (median), and 75th percentiles, and the whiskers and circles give the 5th, 10th, 90th, and 95th percentiles.

considerable amount of variation in results that typically occurs from execution to execution (as a result of the random initialization of network weights that takes place prior to network training). This limitation normally necessitates the generation and evaluation of multiple neural network results, in order for the user to be able to pick the best result from all results available. By utilizing a neural network algorithm that automatically runs 10 separate executions and generates a consensus database from the results of these executions, the user can generate the best possible results without having to evaluate the results of each neural network execution. A related benefit is that, because the evaluation of results is not necessary, the user does not have to set aside test data for classification evaluation (i.e., all field data may be used to train the network, if the sole reason for testing would have been to choose the results of the best individual neural network execution).

The total errors of omission and commission for all neural network classifications of the Melville Island Field Area are given in Table 5.19. A summary of these errors with specific reference to the classes most confused is given in Tables 5.20 to 5.23. From these data, it can be seen that geological classes that were relatively well discriminated in the *B* Series of tests were Canyon Fiord (red-weathering), Canyon Fiord (pink), gabbro, Assistance mudstone, and Bjorn sandstone (Table 5.20); these are the same classes that were relatively well discriminated by the maximum likelihood classifier (Section 5.3.1.2 above), although the neural network results are generally slightly better. Classes relatively well discriminated by the neural network algorithm in the *C* and *D* Series were Canyon Fiord (red/yellow), Canyon Fiord (pink), gabbro, and Assistance mudstone (Tables 5.21 and 5.22). None of the

Table 5.19 Summary of the magnitude of errors of omission and commission for all consensus neural network classifications of the Melville Island Field Area. Values are expressed as proportions, and may be converted to percentages by multiplying by 100%.

B: NN	1		2		3		4		5		6		
CLASS	EO	EC	EO	EC	EO	EC	EO	EC	EO	EC	EO	EC	AVG
1	0.10	0.10	0.10	0.13	0.10	0.04	0.10	0.18	0.20	0.17	0.07	0.10	0.12
2	0.57	0.00	0.29	0.29	0.43	0.33	0.43	0.50	0.57	0.63	0.43	0.56	0.42
3	0.00	0.00	0.00	0.00	0.00	0.00	0.00	0.00	0.00	0.00	0.00	0.36	0.03
4	0.12	0.43	0.23	0.36	0.23	0.36	0.46	0.33	0.23	0.36	0.42	0.40	0.33
5	0.14	0.29	0.14	0.29	0.14	0.00	0.29	0.33	0.00	0.13	0.21	0.08	0.17
6	0.17	0.30	0.20	0.33	0.13	0.33	0.15	0.32	0.20	0.36	0.17	0.28	0.24
7	0.42	0.36	0.52	0.32	0.55	0.50	0.48	0.33	0.58	0.35	0.61	0.43	0.46
8	0.33	0.00	0.00	0.14	0.00	0.14	0.08	0.21	0.25	0.10	0.00	0.25	0.13
9	0.71	0.36	0.59	0.42	0.53	0.20	0.53	0.27	0.41	0.33	0.65	0.45	0.48
10	0.48	0.30	0.44	0.21	0.56	0.40	0.33	0.33	0.52	0.36	0.26	0.26	0.37
11	0.09	0.09	0.00	0.15	0.09	0.00	0.09	0.17	0.09	0.17	0.09	0.17	0.10
12	0.00	0.07	0.14	0.08	0.00	0.00	0.07	0.00	0.00	0.00	0.00	0.00	0.03
13	0.00	0.00	0.00	0.00	0.00	0.08	0.00	0.00	0.00	0.00	0.00	0.00	0.01
14	0.00	0.00	0.00	0.00	0.00	0.00	0.00	0.00	0.00	0.00	0.00	0.00	0.00

C: NN	1		2		3		4		5		6		
CLASS	EO	EC	EO	EC	EO	EC	EO	EC	EO	EC	EO	EC	AVG
1	0.18	0.09	0.14	0.14	0.14	0.18	0.14	0.14	0.19	0.25	0.11	0.13	0.15
2	0.00	0.00	0.00	0.13	0.00	0.00	0.00	0.00	0.00	0.13	0.00	0.30	0.05
3	0.23	0.44	0.35	0.29	0.35	0.39	0.50	0.28	0.19	0.46	0.42	0.42	0.36
4	0.14	0.29	0.07	0.24	0.07	0.00	0.29	0.29	0.00	0.22	0.00	0.07	0.14
5	0.19	0.27	0.24	0.29	0.14	0.33	0.13	0.25	0.27	0.23	0.22	0.26	0.23
6	0.36	0.20	0.33	0.25	0.41	0.16	0.22	0.18	0.41	0.24	0.35	0.21	0.26
7	0.33	0.00	0.00	0.08	0.08	0.08	0.08	0.21	0.25	0.00	0.00	0.25	0.11
8	0.00	0.07	0.07	0.07	0.00	0.00	0.07	0.00	0.00	0.00	0.00	0.00	0.02
9	0.00	0.00	0.00	0.00	0.00	0.00	0.00	0.00	0.00	0.00	0.00	0.00	0.00
10	0.00	0.00	0.00	0.00	0.00	0.00	0.00	0.00	0.00	0.00	0.00	0.00	0.00

D: NN	1		2		3		4		5		6		
CLASS	EO	EC	EO	EC	EO	EC	EO	EC	EO	EC	EO	EC	AVG
1	0.16	0.06	0.16	0.06	0.14	0.11	0.16	0.14	0.24	0.24	0.11	0.21	0.15
2	0.00	0.00	0.00	0.13	0.00	0.00	0.00	0.13	0.00	0.00	0.00	0.00	0.02
3	0.00	0.30	0.00	0.33	0.14	0.00	0.21	0.21	0.00	0.26	0.07	0.24	0.15
4	0.10	0.25	0.15	0.22	0.09	0.30	0.16	0.18	0.16	0.24	0.26	0.24	0.20
5	0.35	0.15	0.32	0.20	0.43	0.15	0.20	0.21	0.38	0.25	0.30	0.24	0.27
6	0.25	0.00	0.00	0.00	0.08	0.00	0.08	0.00	0.33	0.11	0.08	0.08	0.09
7	0.00	0.00	0.14	0.00	0.00	0.07	0.00	0.00	0.00	0.00	0.00	0.00	0.02
8	0.00	0.00	0.00	0.00	0.00	0.00	0.00	0.00	0.00	0.00	0.00	0.00	0.00
9	0.00	0.00	0.00	0.00	0.00	0.00	0.00	0.00	0.00	0.00	0.00	0.00	0.00

E: NN	1		2		3		4		5		6		
CLASS	EO	EC	EO	EC	EO	EC	EO	EC	EO	EC	EO	EC	AVG
1	0.22	0.13	0.18	0.14	0.25	0.09	0.16	0.13	0.16	0.14	0.21	0.18	0.17
2	0.17	0.25	0.21	0.23	0.11	0.26	0.16	0.19	0.20	0.19	0.25	0.26	0.21
3	0.14	0.29	0.00	0.30	0.07	0.13	0.21	0.21	0.00	0.18	0.14	0.25	0.16
4	0.00	0.07	0.07	0.00	0.00	0.00	0.00	0.00	0.00	0.07	0.00	0.00	0.02
5	0.00	0.00	0.00	0.00	0.00	0.00	0.00	0.00	0.00	0.00	0.00	0.00	0.00
6	0.00	0.00	0.00	0.00	0.00	0.00	0.00	0.00	0.00	0.00	0.00	0.00	0.00

Table 5.20 Summary of ability of the consensus neural network and TM imagery combination to discriminate the surface-cover classes in the Melville Island Field Area (*B* Series).

Class	Discrimination	Typically Confused Classes
1. Canyon Fiord (Red-Weathering)	Good	Gabbro, Sabine Bay Sandstone
2. Canyon Fiord (Yellow)	Very Poor	Canyon Fiord (Red-Weathering), Tingmisut Inlier Dolomite, Degerböls Limestone, Great Bear Cape Limestone, Trold Fiord Sandstone
3. Canyon Fiord (Pink)	Excellent	None
4. Tingmisut Inlier Dolomite	Very Poor	Sabine Bay Sandstone, Trold Fiord Sandstone
5. Gabbro	Fair	Canyon Fiord (Red-Weathering)
6. Great Bear Cape Limestone	Poor	Sabine Bay Sandstone, Trold Fiord Sandstone, Degerböls Limestone
7. Sabine Bay Sandstone	Very Poor	Tingmisut Inlier Dolomite, Great Bear Cape Limestone, Degerböls Limestone, Trold Fiord Sandstone
8. Assistance Mudstone	Good	Trold Fiord Sandstone
9. Degerböls Limestone	Very Poor	Canyon Fiord (Yellow), Tingmisut Inlier, Great Bear Cape Limestone, Sabine Bay Sandstone
10. Trold Fiord Sandstone	Very Poor	Great Bear Cape Limestone, Sabine Bay Sandstone
11. Bjorn Sandstone	Good	None
12. Green Vegetation	Excellent	None
13. Snow Cover	Excellent	None
14. Water	Excellent	None

Table 5.21 Summary of ability of neural-network and TM imagery combo to discriminate the surface-cover classes in the Melville Island Field Area (*C* Series).

Class	Discrimination	Typically Confused Classes
1. Canyon Fiord (Red/Yellow)	Fair	Great Bear Cape and Degerböls Limestone, Gabbro, Sabine Bay and Bjorn and Trold Fiord Sandstone
2. Canyon Fiord (Pink)	Very Good	None
3. Tingmisut Inlier Dolomite	Very Poor	Great Bear Cape and Degerböls Limestone, Sabine Bay and Bjorn and Trold Fiord Sandstone
4. Gabbro	Good	None
5. Great Bear Cape and Degerböls Limestone	Poor	Tingmisut Inlier Dolomite, Sabine Bay and Bjorn and Trold Fiord Sandstone
6. Sabine Bay and Bjorn and Trold Fiord Sandstone.	Poor	Great Bear Cape and Degerböls Limestone, Tingmisut Inlier Dolomite, Canyon Fiord (Red/Yellow)
7. Assistance Mudstone	Good	None
8. Green Vegetation	Excellent	None
9. Snow Cover	Excellent	None
10. Water	Excellent	None

Table 5.22 Summary of ability of neural-network and TM imagery combo to discriminate the surface-cover classes in the Melville Island Field Area (*D* Series).

Class	Discrimination	Typically Confused Classes
1. Canyon Fiord (Red/Yellow)	Fair	Carbonates, Gabbro
2. Canyon Fiord (Pink)	Excellent	None
3. Gabbro	Fair	Canyon Fiord (Red/Yellow), Carbonates
4.Carbonates	Poor	Canyon Fiord (Red/Yellow), Sabine Bay and Bjorne and Trold Fiord Sandstone, Gabbro
5. Sabine Bay and Bjorn and Trold Fiord Sandstone.	Poor	Carbonates, Canyon Fiord (Red/Yellow)
6. Assistance Mudstone	Very Good	Sabine Bay and Bjorn and Trold Fiord Sandstone
7. Green Vegetation	Excellent	None
8. Snow Cover	Excellent	None
9. Water	Excellent	None

Table 5.23 Summary of ability of neural-network and TM imagery combo to discriminate the surface-cover classes in the Melville Island Field Area (*E* Series).

Class	Discrimination	Typically Confused Classes
1. Clastics	Fair	Carbonates, Gabbro
2. Carbonates	Poor	Clastics, Gabbro
3. Gabbro	Fair	Carbonates, Clastics
4. Green Vegetation	Excellent	None
5. Snow Cover	Excellent	None
6. Water	Excellent	None

geological classes was particularly well discriminated in the *E* Series (Table 5.23), although the results of this series are better than those produced by the maximum likelihood classifier. Geological classes that were very poorly discriminated by the neural network algorithm in the *B* Series included Canyon Fiord (yellow), Tingmisut Inlier dolomite, Sabine Bay sandstone, Degerböls limestone, and Trold Fiord sandstone; again, these are the same classes that were poorly discriminated by the maximum likelihood classifier (Section 5.3.1.2 above). As with the maximum likelihood classifier, these poorly differentiated classes kept results poor in the *C*, *D*, and *E* Series as they were combined with other, better differentiated classes (Tables 5.21, 5.22, and 5.23).

The images produced by the consensus neural network algorithm have value as geological and land-cover databases; as with the images produced by the maximum likelihood classifier, the classes best shown on the images are those noted above as having been well discriminated (Figures 5.13 to 5.16; compare with the corresponding map of bedrock geology, Figure 4.4). The level of overall information provided in these images regarding geological classes is good (see Section 5.3.1.4 for further discussion).

5.3.1.4 Evaluation of the Melville-Island Field Area Classified Databases

In all maximum likelihood and neural network classifications of the Melville Island Field Area, the surface-cover classes of water and green vegetation were very well discriminated. However, shadows associated with the steep north-facing slope of the Blue Fiord Formation limestone unit (in the southeast corner of the field area) were consistently confused with water; such shadow effects are typical of optical images of polar regions, where

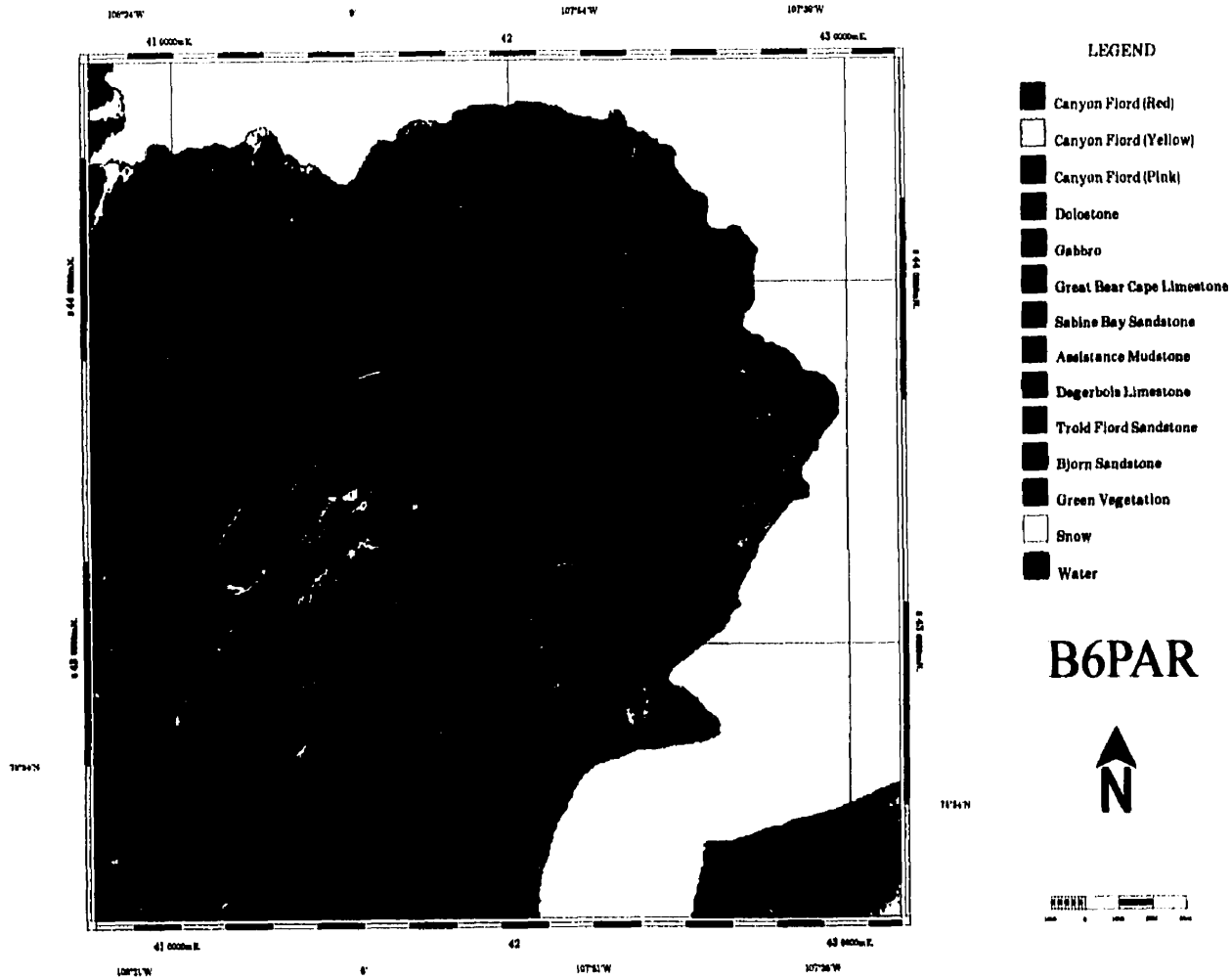

Figure 5.13 Classified image of the Melville Island Field Area, produced by the consensus neural network algorithm (*B* Series, Execution #6). Compare with the map of geology (Figure 4.4) for areas represented in the training and test database (Figure 4.6).

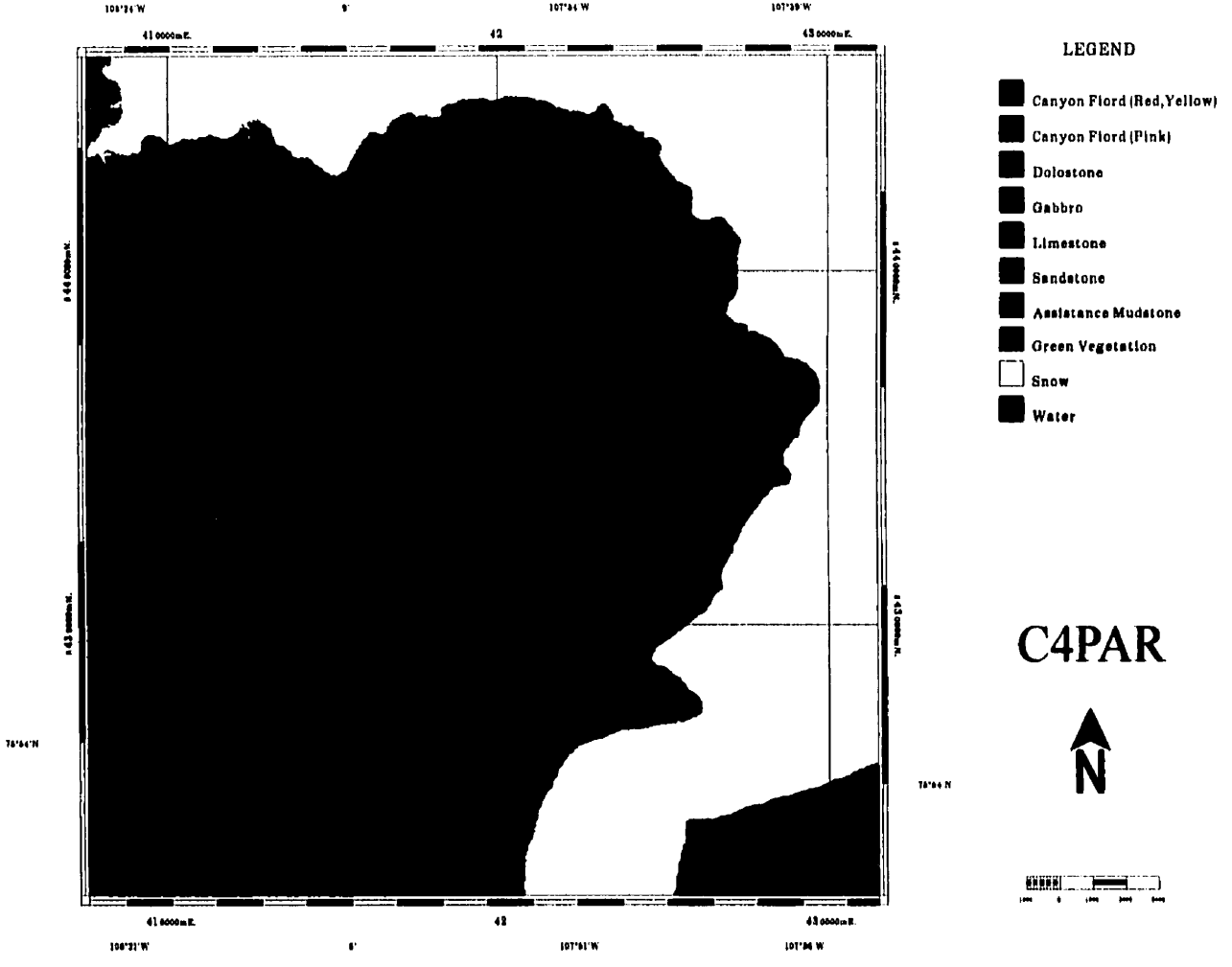

Figure 5.14 Classified image of the Melville Island Field Area, produced by the consensus neural network algorithm (*C* Series, Execution #4). Compare with the map of geology (Figure 4.4) for areas represented in the training and test database (Figure 4.6).

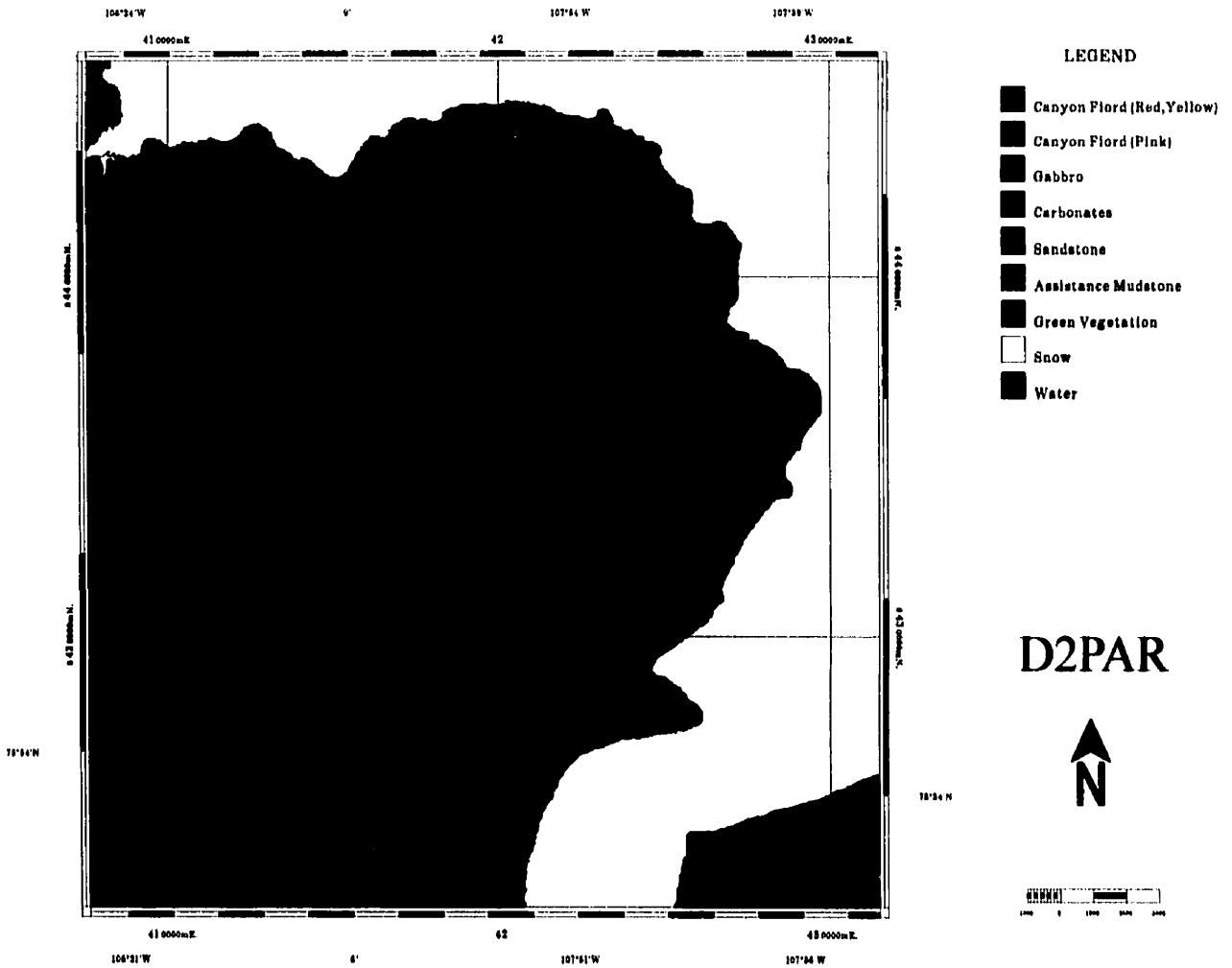

Figure 5.15 Classified image of the Melville Island Field Area, produced by the consensus neural network algorithm (*D* Series, Execution #2). Compare with the map of bedrock geology (Figure 4.4) for areas represented in the training and test database (Figure 4.6).

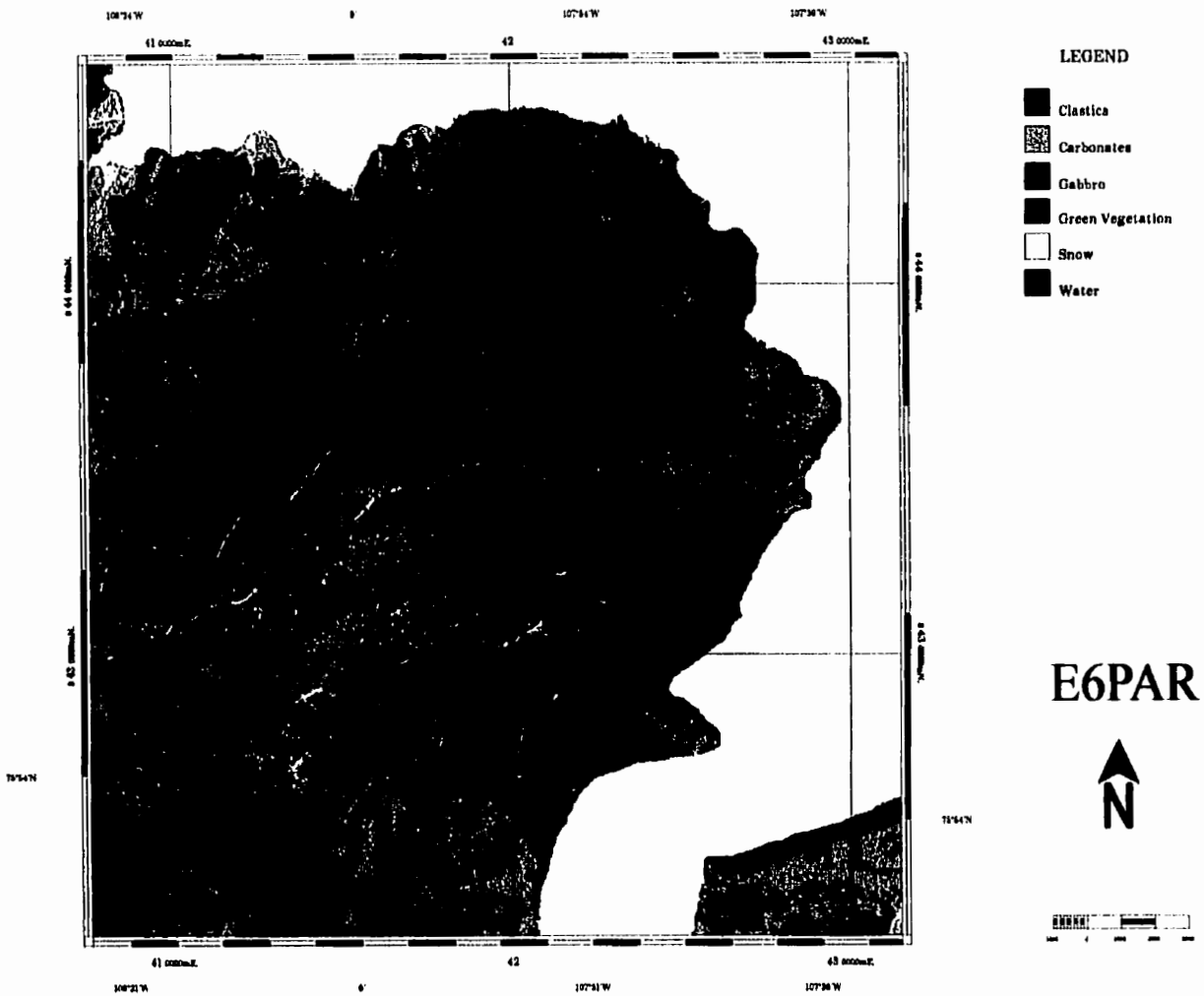

Figure 5.16 Classified image of the Melville Island Field Area, produced by the consensus neural network algorithm (*E* Series, Execution #6). Compare with the map of bedrock geology (Figure 4.4) for areas represented in the training and test database (Figure 4.6).

low sun elevations are common (e.g., Birnie *et al.*, 1989; Harding *et al.*, 1989; Lyberis *et al.*, 1990). This is to be expected since these classes have spectral signatures that are distinct from those of the other classes. The snow class, which is also spectrally distinct, was very well discriminated by the neural network classifier, but was more poorly discriminated by the maximum likelihood algorithm. Numerous maximum likelihood results overestimate the surface area of snow cover, and the prevalence of these errors increases from the results of the *B* Series to those of the *E* Series.

The best differentiated geological classes in the *B* Series produced by the maximum likelihood and neural network algorithms were: Canyon Fiord (red-weathering), Canyon Fiord (pink), gabbro, Assistance mudstone, and Bjorn sandstone. Those best differentiated in the *C* and *D* Series were: Canyon Fiord (red/yellow), Canyon Fiord (pink), gabbro, and Assistance mudstone. None of the geological classes were particularly well discriminated in the *E* Series. For all four Melville Island series, the neural network generally produced better results than those of the other algorithms.

In the *B* to *E* Series of classifications, many classes were confused with classes whose lithological characteristics are disparate. For example, the following five classes were commonly confused with each other in the *B* Series of classifications: Great Bear Cape limestone, Trold Fiord sandstone, Sabine Bay sandstone, Degerböls limestone, Tingmisut dolomite. Also commonly confused with each other were the gabbro and Canyon Fiord (red-weathering) classes; interestingly, this error was more frequently encountered in the results of the neural network, compared with those of the maximum likelihood algorithm. The confusion between the gabbro and Canyon Fiord (red-weathering) classes can be explained

in part by 1) the spatial characteristics of the gabbro class (i.e., the narrow extent of the dike results in a proportionately greater chance for mixed pixels in the gabbro class), 2) close association of black algae with both the Canyon Fiord materials and the eastern slopes of the gabbro dike, and 3) the geographical proximity of the two classes (wind-blown red-weathering Canyon Fiord fines discontinuously cover localized portions of the gabbro dike). Confusion between other classes (such as the carbonate and clastic classes) is likely related to other factors, including: 1) similarities in the types of vegetation cover that characterize these classes; 2) greater similarities in lithology than the class labels imply [e.g., as noted above, the Great Bear Cape limestones are generally impure; also, the Trold Fiord sandstones locally grade into limestone]; and 3) limitations of the TM imagery in the spectral separation of these lithologies.

Despite the limitations of the land-cover databases produced by the classification algorithms, they nevertheless have value for geological investigation. The databases provide specific and generally accurate information on the spatial distribution of numerous lithologies; this information complements the information provided by the geological map (Figure 4.4), which necessarily is a more general resource of information. For example, the geological map for the field area depicts the Canyon Fiord formation as a well-defined polygon with a sharp and relatively simple outline. The true nature of the formation's surficial exposure is given by the classified database (e.g., Figure 5.8), which indicates that the exposed portion of the formation is not as extensive as the geological map indicates. Further, the classified database indicates that Canyon Fiord materials extend northward into an eastern area labelled on the geological map as Great Bear Cape limestones (field evidence confirms that the classified

database is correct in this regard - see documentation for Sites 26 and 28 in Appendix A). Of course, the classified database also provides information on the spatial distribution of a distinctive Canyon Fiord sub-class, the pink clastic unit.

Another example of the value of the classified databases for geological investigation involves the Assistance Formation. Although the geological map (Figure 4.4) properly portrays the mudstones of the Assistance Formation as extending roughly southwest-northeast in a continuous fashion across the field area, the classified database (e.g., Figure 5.14) provides specific information on the spatial distribution of exposed Assistance Formation materials. The database shows that these materials are only discontinuously exposed from beneath limestone materials weathering from the overlying Degerböls Formation.

Finally, the classified databases can provide useful information even for geological classes that are not particularly well discriminated. For example, despite the limitations of the *C4* consensus neural network image (Figure 5.14) (a significant problem is the erroneous depiction of the presence of gabbro materials where Canyon Fiord materials are found with black algae), the distributions of relatively poorly-discriminated classes (e.g., Great Bear Cape limestones) are nevertheless generally accurate.

5.3.2 Cape Smith Belt Field Area

Cape Smith Belt classification results, expressed as percentages of test pixels correctly labelled, are summarized in Table 5.24. Kappa values are given in Table 5.25.

Table 5.24 Summary of Cape Smith Belt classification results (values give the proportion of all test pixels correctly classified). Classification algorithms are labelled as follows: NN-B (best neural network result of 10 neural network jobs), NN-M (majority-vote consensus neural network result), ML (maximum likelihood result), ER (evidential reasoning result).

Series	Algor.	Set 1	Set 2	Set 3	Set 4	Set 5	Set 6	Avg.
A	NN-B	0.9156	0.8776	0.8987	0.8903	0.8861	0.8945	0.8938
	NN-M	0.9030	0.8776	0.8987	0.8945	0.8734	0.8692	0.8861
	ML	0.8734	0.7890	0.8523	0.8692	0.8608	0.8397	0.8474
	ER	0.6371	0.6076	0.6034	0.6456	0.7046	0.6456	0.6407

Table 5.25 Summary of Melville Island classification results, expressed as Kappa ("KHAT") values (see Section 2.5.4 for details). Classification algorithms are labelled as follows: NN-B (best neural network result of 10 neural network jobs), NN-M (majority-vote consensus neural network result), ML (maximum likelihood result), ER (evidential reasoning result).

Series	Algor.	Set 1	Set 2	Set 3	Set 4	Set 5	Set 6	Avg.
A	NN-B	0.8981	0.8517	0.8775	0.8678	0.8627	0.8727	0.8718
	NN-M	0.8823	0.8516	0.8778	0.8725	0.8474	0.8422	0.8623
	ML	0.8484	0.7485	0.8244	0.8435	0.8334	0.8084	0.8178
	ER	0.5655	0.5284	0.5266	0.5755	0.6445	0.5752	0.5693

5.3.2.1 Evidential Reasoning

It can be seen from Tables 5.24 and 5.25 above that, like the classification results for the Melville Island Field Area, the Cape Smith Belt classification results obtained using the evidential reasoning classifier are poor. The average proportions of test pixels correctly labelled for the *A* Series is 64%. This value is approximately 20% less than the average values of the remaining two classifiers, and is again indicative of a failure of the algorithm to produce a very useful database of surface lithologies.

Errors of omission and commission for all 6 evidential reasoning jobs for the Cape Smith Belt Field Area are documented in Table 5.26, while generalizations of the evidential reasoning results, by class, are given in Table 5.27. Errors are very high for all but the water and green vegetation classes. Some classes are not even represented in the classification results of the test sites (e.g., the tonalite class was not used as a classification label for test sites in 5 of the 6 evidential reasoning classifications performed).

Despite the relatively high error associated with the evidential reasoning results, the images produced by the evidential reasoning algorithm have some value as geological and land-cover databases (Figure 5.17; compare with the corresponding map of bedrock geology, Figure 4.12). For example, the image given in Figure 5.17 provides relatively good general information on the water, vegetation, and peridotite classes. A further discussion of the evidential reasoning classified images is given in Section 5.3.2.4. A discussion of the generally poor results associated with the evidential reasoning algorithm is given in Section 5.4.

Table 5.26 Summary of the magnitude of errors of omission and commission for all classifications of the Cape Smith Belt Field Area (including evidential reasoning, maximum likelihood, and neural network results). Values are expressed as proportions, and may be converted to percentages by multiplying by 100%.

A: ER	1		2		3		4		5		6		
CLASS	EO	EC	EO	EC	EO	EC	EO	EC	EO	EC	EO	EC	AVG
1	0.48	0.19	0.55	0.26	0.57	0.27	0.55	0.19	0.38	0.10	0.55	0.17	0.36
2	0.21	0.65	0.33	0.71	0.21	0.68	0.25	0.67	0.17	0.50	0.25	0.64	0.44
3	0.33	0.37	0.22	0.40	0.37	0.36	0.20	0.31	0.33	0.37	0.28	0.38	0.33
4	0.44	0.49	0.56	0.47	0.44	0.53	0.41	0.48	0.28	0.45	0.44	0.51	0.46
5	1.00		1.00		1.00		1.00		1.00		1.00		1.00
6	0.21	0.00	0.24	0.08	0.24	0.00	0.24	0.04	0.10	0.07	0.07	0.00	0.11
7	0.00	0.00	0.00	0.00	0.00	0.00	0.00	0.00	0.00	0.00	0.00	0.00	0.00

A: ML	1		2		3		4		5		6		
CLASS	EO	EC	EO	EC	EO	EC	EO	EC	EO	EC	EO	EC	AVG
1	0.21	0.12	0.30	0.19	0.36	0.10	0.25	0.07	0.21	0.06	0.32	0.14	0.19
2	0.04	0.08	0.17	0.09	0.13	0.19	0.04	0.12	0.00	0.17	0.00	0.11	0.09
3	0.15	0.13	0.35	0.19	0.09	0.11	0.17	0.13	0.22	0.16	0.17	0.15	0.17
4	0.21	0.14	0.21	0.34	0.18	0.06	0.15	0.21	0.21	0.24	0.21	0.23	0.20
5	0.08	0.45	0.15	0.56	0.00	0.54	0.08	0.33	0.08	0.33	0.23	0.52	0.28
6	0.00	0.00	0.00	0.03	0.00	0.09	0.00	0.09	0.00	0.03	0.00	0.03	0.02
7	0.00	0.00	0.00	0.00	0.00	0.00	0.00	0.00	0.00	0.00	0.00	0.00	0.00

A: NN-M	1		2		3		4		5		6		
CLASS	EO	EC	EO	EC	EO	EC	EO	EC	EO	EC	EO	EC	AVG
1	0.05	0.20	0.07	0.17	0.14	0.14	0.11	0.12	0.13	0.13	0.20	0.06	0.13
2	0.13	0.09	0.21	0.00	0.21	0.24	0.13	0.13	0.04	0.08	0.00	0.14	0.12
3	0.09	0.09	0.17	0.17	0.06	0.09	0.13	0.11	0.24	0.13	0.09	0.23	0.13
4	0.21	0.03	0.23	0.19	0.15	0.03	0.15	0.18	0.13	0.26	0.28	0.18	0.17
5	0.23	0.17	0.15	0.08	0.15	0.27	0.23	0.00	0.31	0.18	0.31	0.25	0.19
6	0.03	0.00	0.00	0.03	0.00	0.00	0.00	0.06	0.00	0.03	0.00	0.00	0.01
7	0.00	0.00	0.00	0.00	0.00	0.00	0.00	0.00	0.00	0.00	0.00	0.00	0.00

Table 5.27 Summary of ability of evidential reasoning and TM imagery combo to discriminate the surface-cover classes in the Cape Smith Belt Field Area (*A* Series).

Class	Discrimination	Typically Confused Classes
1. Peridotite	Very Poor	Pelite, Chukotat Basalt, Tonalite, Watts Basalt, Tonalite, Green Vegetation
2. Pelite	Very Poor	Peridotite, Chukotat Basalt, Watts Basalt, Tonalite, Green Vegetation
3. Chukotat Basalt	Very Poor	Peridotite, Pelite, Watts Basalt
4. Watts Basalt	Very Poor	Chukotat Basalt, Peridotite, Pelite, Tonalite
5. Tonalite	Very Poor	Peridotite, Pelite, Watts Basalt
6 .Green Vegetation	Good	Pelite, Peridotite
7. Water	Excellent	None

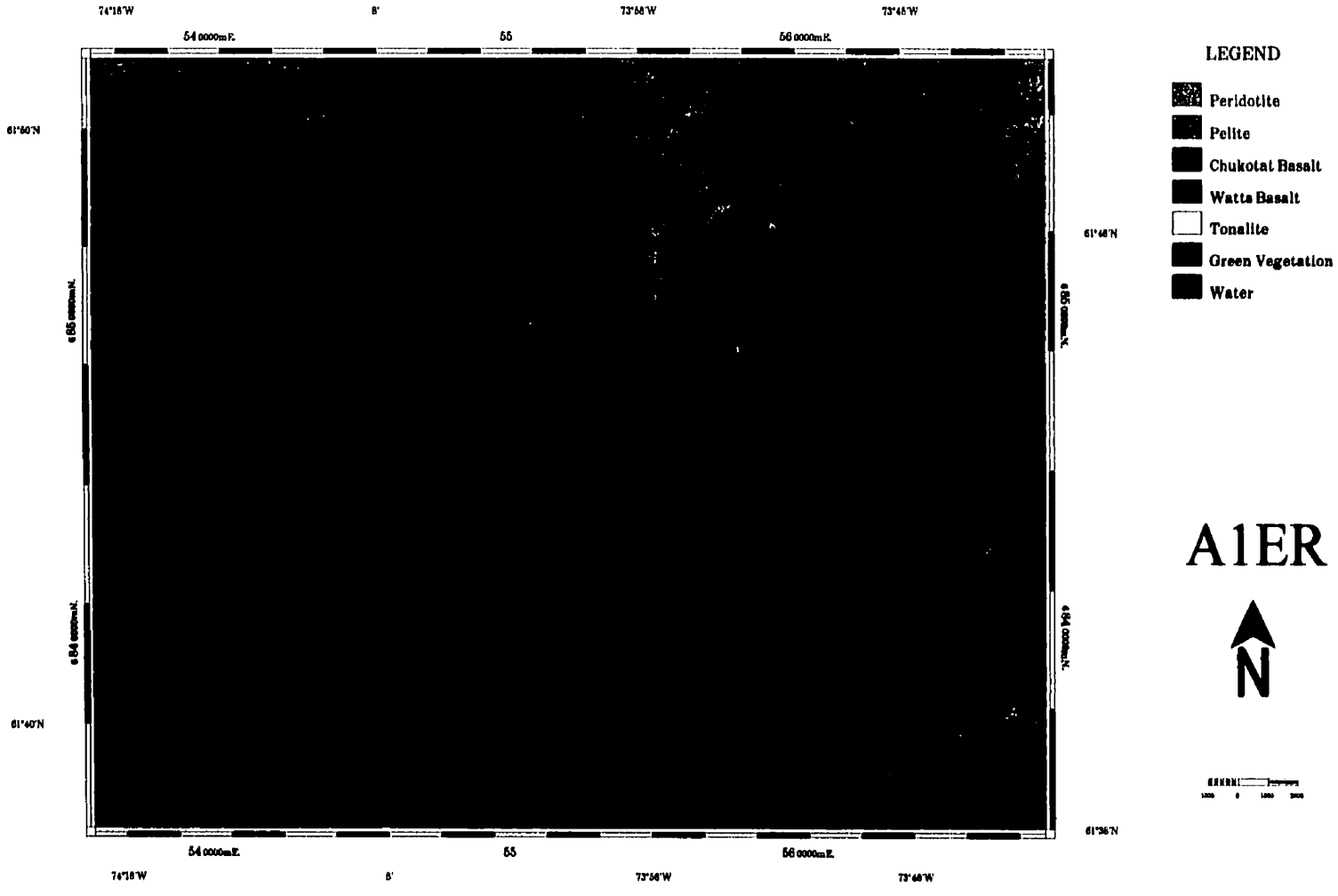

Figure 5.17 Classified image of the Cape Smith Belt Field Area, produced by the evidential reasoning algorithm (*A* Series, Execution #1). Compare with the map of bedrock geology (Figure 4.13) for areas represented in the training and test database (Figure 4.15).

5.3.2.2 Maximum Likelihood

Classification results obtained using the maximum likelihood classifier are much stronger than those of the evidential reasoning classifier. The average proportion of test pixels correctly labelled for the *A* Series is 85% (Table 5.24), and the average Kappa coefficient for the same series is 82% (Table 5.25). These average values are about 20 to 25% greater than the evidential reasoning results, and about 3 to 5% less than the neural network results. A more detailed comparison between the results of the maximum likelihood and consensus neural network algorithms is given in Section 5.3.2.3, below.

The total errors of omission and commission for all maximum likelihood classifications of the Cape Smith Belt Field Area are given in Table 5.26. A summary of these errors with specific reference to the classes most confused is given in Table 5.28; these tables are based on confusion matrices generated for each maximum likelihood execution. From these data, it can be seen that geological classes that were relatively well discriminated were pelite and to a lesser extent peridotite and Chukotat basalt. Poorly discriminated lithological classes included tonalite and Watts basalt (Table 5.28).

As can be seen in Figure 5.18, the images produced by the maximum likelihood algorithm have value as geological and land-cover databases (compare with the corresponding map of bedrock geology, Figure 4.12). Further discussion on this topic is given in Section 5.3.2.4.

5.3.2.3 Neural Network

Classification results obtained for the Cape Smith Belt Field Area using the consensus

Table 5.28 Summary of ability of maximum likelihood and TM imagery combo to discriminate the surface-cover classes in the Cape Smith Belt Field Area (*A* Series).

Class	Discrimination	Typically Confused Classes
1. Peridotite	Fair	Tonalite, Pelite, Chukotat Basalt
2. Pelite	Very Good	Peridotite
3. Chukotat Basalt	Fair	Watts Basalt, Peridotite
4. Watts Basalt	Poor	Chukotat Basalt
5. Tonalite	Poor	Peridotite
6. Green Vegetation	Excellent	None
7. Water	Excellent	None

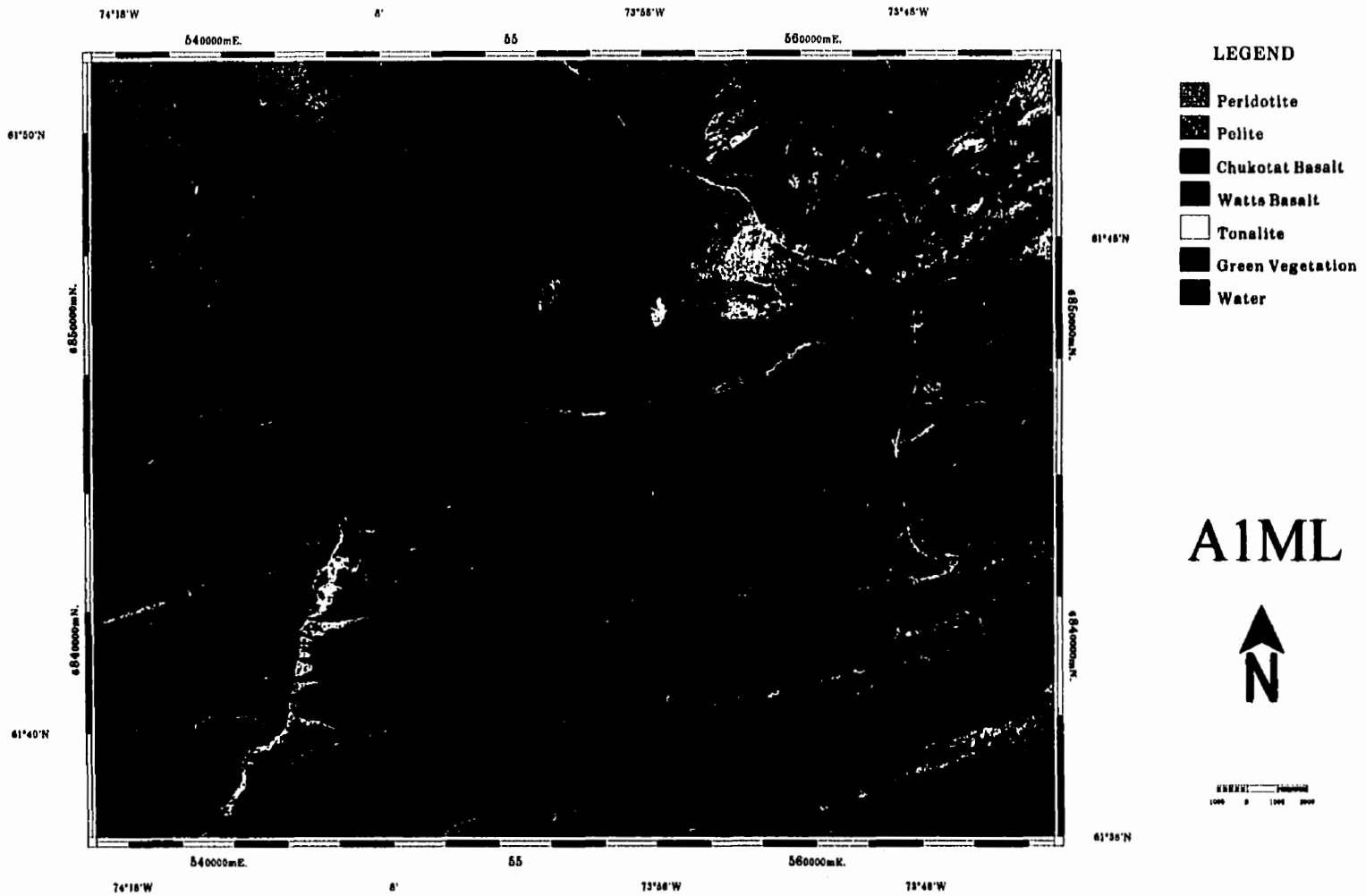

Figure 5.18 Classified image of the Cape Smith Belt Field Area, produced by the maximum likelihood algorithm (*A* Series, Execution #1). Compare with the map of bedrock geology (Figure 4.13) for areas represented in the training and test database (Figure 4.15).

neural network classifier are the strongest of the three classifiers examined here. The average proportion of test pixels correctly labelled for the A series is 89% (Table 5.24), while the average Kappa coefficient for this series is 86% (Table 5.25); these values are about 3 to 6% greater than the corresponding values for the maximum likelihood classifier. For each of the 6 comparisons between consensus neural network jobs and their corresponding maximum likelihood jobs, the neural network produced similar or superior results (strictly, all consensus neural network percentages are higher than those of the other two classification algorithms). These results support the Melville Island results (Section 5.3.1) which indicate that the consensus neural network classifier can consistently produce results that are better than those of the maximum likelihood classifier.

Although individual neural network results vary considerably (Figure 5.19), the general overall percentage results for the consensus neural network algorithm are typically within about 1.5% of the result of the best individual neural network job for a given training/test data set (standard deviation of the differences between these values is 1%). These results support the hypothesis that a consensus neural network execution can produce a result that is comparable to that of the best neural network execution of a series of neural network executions (see also Section 5.3.1.3).

The total errors of omission and commission for all consensus neural network classifications of the Cape Smith Belt Field Area are given in Table 5.26. A summary of these errors with specific reference to the classes most confused is given in Table 5.29; these tables are based on confusion matrices generated for each consensus neural network execution. From these data, it can be seen that all five geological classes were relatively well

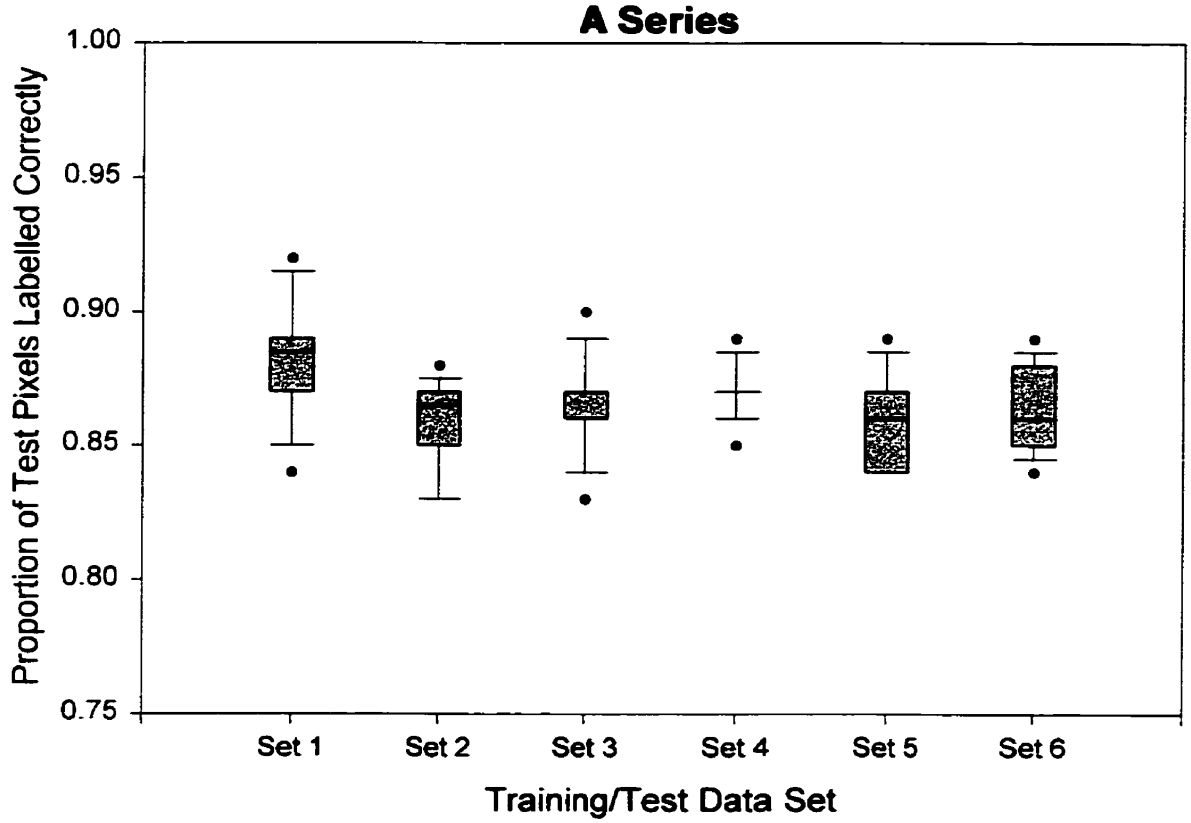

Figure 5.19 Boxplots showing the considerable variation in individual overall classification results produced by the neural network classifier (*A* Series results for the Cape Smith Belt Field Area). Boxes give the 25th, 50th, and 75th percentiles, and the whiskers and circles give the 5th, 10th, 90th, and 95th percentiles.

Table 5.29 Summary of ability of neural network and TM imagery combo to discriminate the surface-cover classes in the Cape Smith Belt Field Area (*A* Series).

Class	Discrimination	Typically Confused Classes
1. Peridotite	Good	Pelite, Tonalite, Chukotat Basalt
2. Pelite	Good	Peridotite, Watts Basalt
3. Chukotat Basalt	Good	Watts Basalt, Peridotite
4. Watts Basalt	Fair	Chukotat Basalt, Pelite
5. Tonalite	Fair	Peridotite
6. Green Vegetation	Excellent	None
7. Water	Excellent	None

discriminated, with the peridotite, pelite, and Chukotat basalt classes being the best discriminated.

As can be seen in Figure 5.20, the images produced by the consensus neural network algorithm have value as geological and land-cover databases (compare with the corresponding map of bedrock geology: Figure 4.12). Further discussion is given in Section 5.3.2.4.

5.3.2.4 Evaluation of the Cape Smith Belt Field Area Classified Databases

The surface-cover classes of water and green vegetation were very well discriminated in all maximum likelihood and neural network classifications of the Cape Smith Belt Field Area (and in most of the evidential reasoning classifications as well). This is to be expected since these classes have spectral signatures that are distinct from those of the other classes. Nevertheless, as with the Melville Island Field Area, areas associated with shadows (e.g., the steep north-facing slopes of valleys and hills) were commonly confused with the water class.

The best differentiated geological classes in the *A* Series produced by the evidential reasoning algorithm was the peridotite class. Although basalt exposures of the Watts Group were generally well discriminated by the evidential reasoning algorithm in the north half of the field area, there was considerable confusion between the basalts of the Watts Group and the Chukotat Group in the southern half. The best differentiated geological classes in the *A* Series produced by the maximum likelihood algorithm were pelite, peridotite, and Chukotat basalt. All five geological classes were relatively well discriminated by the neural network algorithm. In general, the neural network algorithm produced better results than those of the other two algorithms.

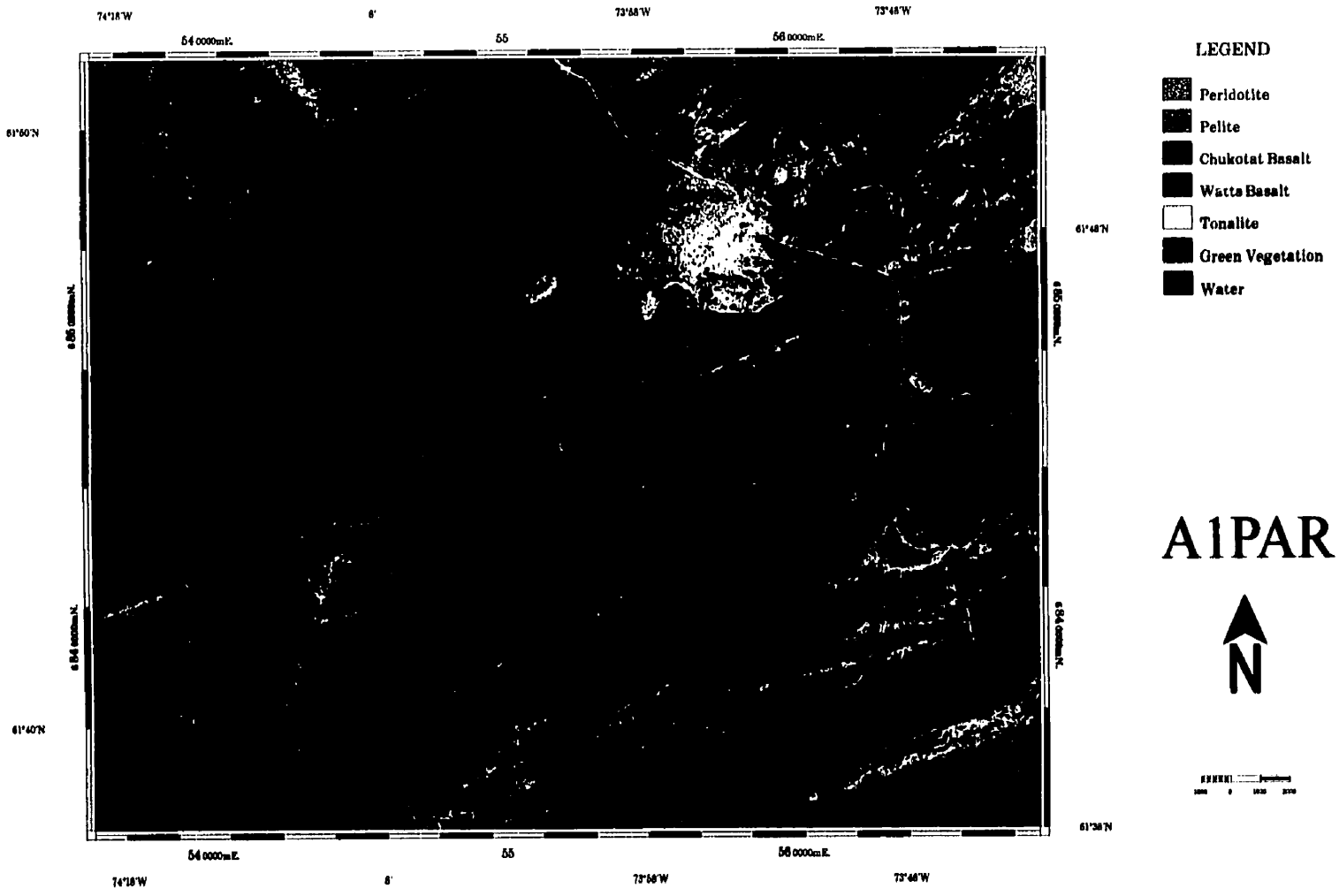

Figure 5.20 Classified image of the Cape Smith Belt Field Area, produced by the consensus neural network algorithm (*A* Series, Execution #1). Compare with the map of bedrock geology (Figure 4.13) for areas represented in the training and test database (Figure 4.15).

Many of the lithological classes in the Cape Smith Belt Field Area were confused with similar classes (e.g., peridotite with Chukotat basalt, and Chukotat basalt with Watts basalt; this latter problem is especially evident in the results of the evidential reasoning classifier). As with the Melville Island Field Area, however, some lithological classes in the Cape Smith Belt Field Area were confused with classes with very different lithological characteristics. For example, tonalite, pelite, and peridotite were commonly confused with each other. Reasons behind the confusion between disparate lithologies is likely related to similarities in lichen cover and vegetation. Also, mafic and ultramafic rocks (typically <30 cm across) are scattered throughout much of the region (probably as a result of past glaciation); the widespread presence of these materials is likely to contribute to confusion between different lithologies by making the spectral signatures of classes less distinct. As with the Melville Island results, shortcomings in the spectral properties of TM data must have contributed to confusion between classes.

The land-cover databases produced by the classification algorithms have value for geological investigation, despite the limitations noted above. The databases produced by the maximum likelihood and neural network classifiers provide specific and generally accurate information on the spatial distribution of lithologies in the field area; this information complements the information provided by the geological map (Figure 4.12) by providing more specific information on the surface distribution of lithological classes. The databases produced by the consensus neural network, for example, successfully depict the distribution of peridotite in the field area (the maximum likelihood algorithm also produced a useful peridotite database, although the area of peridotite exposure is believed to have been over

estimated). In these images, there is a relatively clear distinction between Chukotat Group basalts and other lithologies, including Watts Group basalts. Tonalite is relatively well discriminated in the neural network classifications, but its area of exposure is over estimated by the maximum likelihood algorithm.

5.4 Failure of the Evidential Reasoning Algorithm

Compared to the maximum likelihood and neural network algorithms, the evidential reasoning algorithm did not produce especially useful surface-cover databases (Tables 5.4 and 5.24; Figures 5.3 to 5.6, and Figure 5.17). For the Melville Island Field Area, the algorithm failed to discriminate between different geological classes and routinely failed to properly separate geological classes from other spectrally-distinct classes such as the green vegetation and snow and ice classes. The poor results of this study are not consistent with numerous other studies (Peddle, 1993, 1995; Peddle *et al.*, 1994, Leverington and Duguay, 1996a; Duguay and Peddle, 1996), which have found the evidential reasoning algorithm to be a viable alternative to the maximum likelihood algorithm for classification of satellite images. Because of the unexpected discrepancy between evidential reasoning results and the results of the other two classifiers examined here, an investigation into the causes of the poor performance of the evidential reasoning algorithm was conducted, with special emphasis on finding programming errors or errors in the handling of training and test data (as with the neural network software, the evidential reasoning software used in this research was written by the author).

The investigation confirmed the following: 1) the raw training data submitted to the

evidential reasoning algorithm is the same as that submitted to the other two algorithms, 2) the evidence propagation software (Section 3.3.3) properly interpolated and extrapolated this raw training data according to the methodology of Peddle [1991, 1995], and 3) the main evidential reasoning program properly utilized the interpolated and extrapolated training data as a basis for the classification of test pixels, using the principles of orthogonal summation as described by Richards (1993). No errors of any kind were found at any stage of the classification process, from the initial generation of evidence to the final assignment of class labels (the valid generation of evidence from training data is demonstrated for the *E1* series of tests in Figures 5.21, 5.22, and 5.23). Furthermore, the same algorithm (using different measures of evidence) was successfully applied in classification tests reported in Chapter 7. Thus, the poor performance of the evidential reasoning algorithm as documented in this chapter does not appear to be in any way attributable to file-handling or software errors.

The reason for the large discrepency between the evidential reasoning results of this study and those of previous studies (Peddle, 1993, 1995; Peddle *et al.*, 1994; Leverington and Duguay, 1996a; Duguay and Peddle, 1996) is unknown, but is presumably related to differences in the datasets and images involved in the classifications [e.g., the study by Leverington and Duguay (1996a) involved only two classes, and involved the classification of satellite image as well as landcover and geomorphological databases].

5.5 Operational Considerations

Each of the three classification algorithms used in this research is unique with respect to the exact manner in which it is used to classify satellite images. The most notable

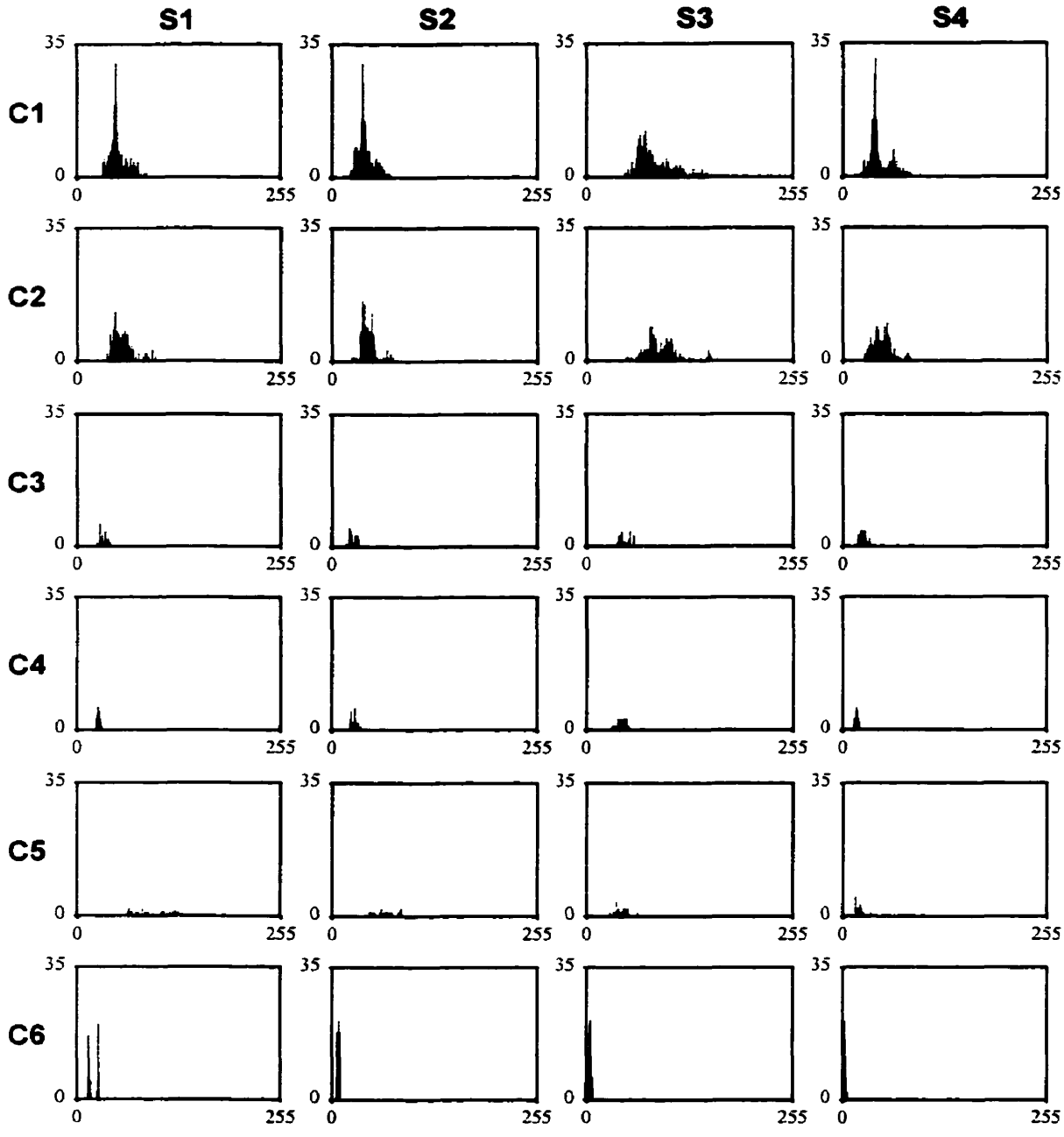

Figure 5.21 Frequency histograms of original (raw) training data for the *E1* Series of tests. Pixel totals are plotted on the y-axis against DN's on the x-axis. Histograms are arranged by source (*S*) and class (*C*).

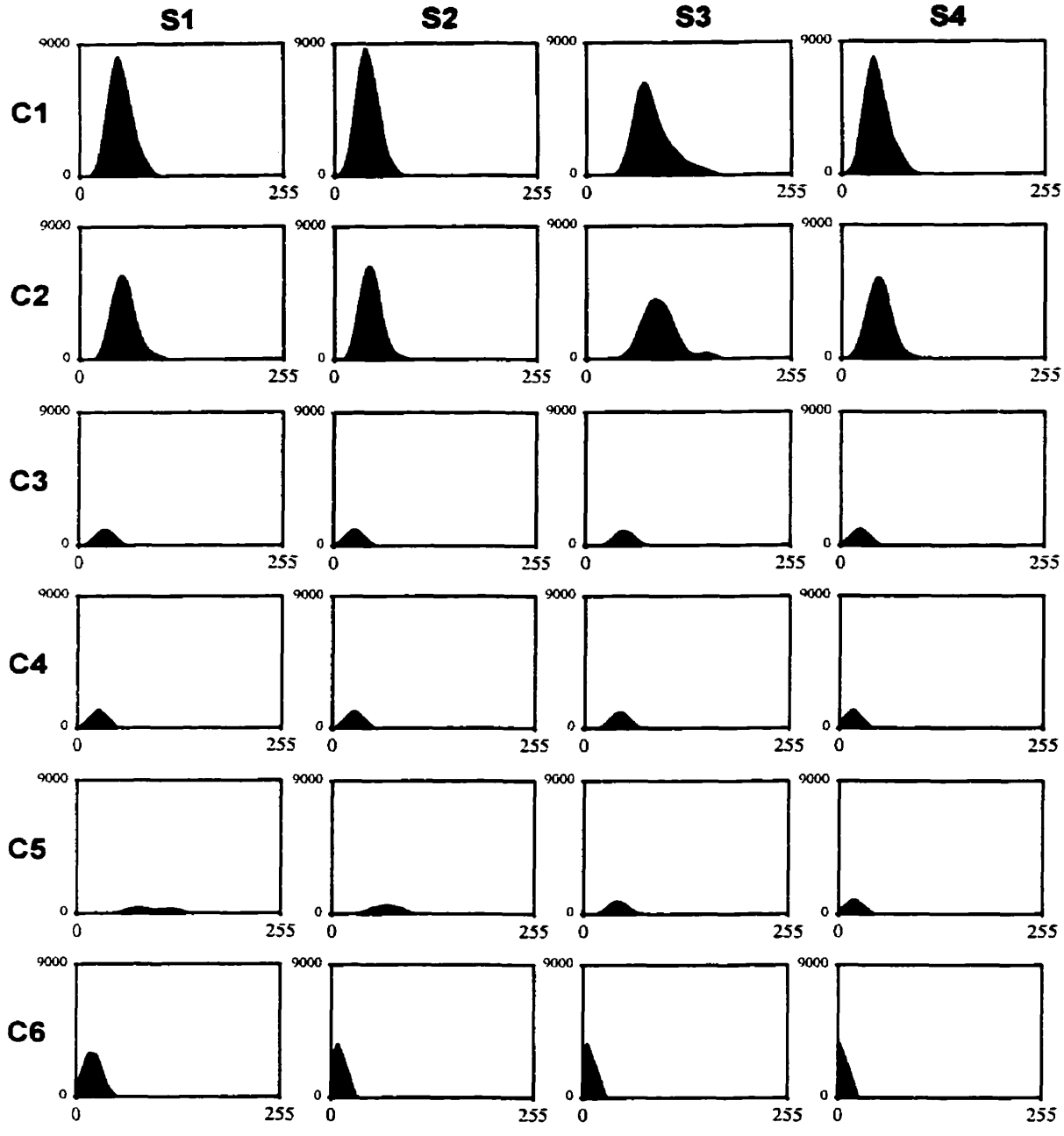

Figure 5.22 Frequency histograms of interpolated and extrapolated training data for the *E1* Series of tests. These data were derived from the data summarized in Figure 5.21 using the methods of Peddle (1991, 1995). Pixel totals are plotted on the y-axis against DN's on the x-axis. Histograms are arranged by source (*S*) and class (*C*).

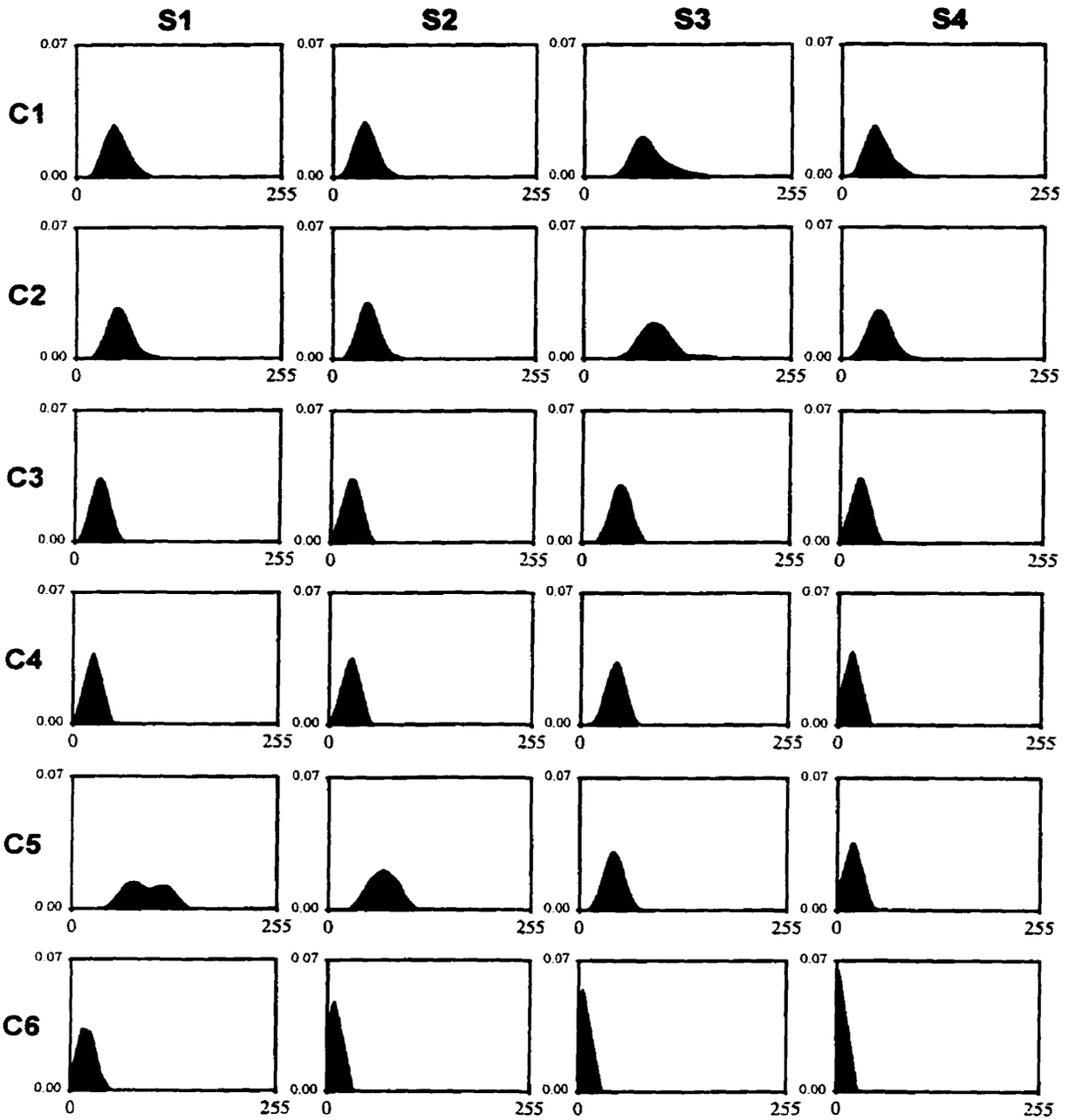

Figure 5.23 Frequency histograms of interpolated and extrapolated training data for the *E1* Series of tests. These data are the same as those summarized in Figure 5.22, but are given in terms of evidential support (i.e., the y-axis values of Figure 5.22 are divided by the total number of pixels in the respective histograms). Evidence values are plotted on the y-axis against DN's on the x-axis. Histograms are arranged by source (*S*) and class (*C*).

difference in the practical operation of the algorithms is the relatively long training period required of the neural network software. The three algorithms were otherwise generally comparable with regard to the time taken to classify images after training.

5.5.1 Maximum Likelihood Algorithm

The commercial "PCI Easi/Pace" maximum likelihood software was used in this research. Because the broad assumptions involved in its parameterization of training data are common to all cases in which the algorithm is applied (Section 3.2), the algorithm does not require the user to make crucial decisions regarding algorithm setup (although the user may choose to define certain classification parameters such as minimum probability thresholds). As a result, the algorithm is easy to use, and classified images can be generated relatively quickly. Once training data were parameterized, classification of the imagery used in this research took less than one minute on a "Sun SPARCstation 20" workstation.

5.5.2 Evidential Reasoning Algorithm

With the evidential reasoning software used in this research, interpolation and extrapolation of raw training data is a labourious operation that is completely separate from the actual classification of satellite images (the labourious nature of this step is a function of the custom software used in this research, rather than a necessary element of extrapolation itself). A bin size of 51 was defined for all evidential reasoning extrapolations; the user did not need to make crucial decisions regarding algorithm setup prior to classification. Once training data were processed, classification of the imagery used in this research generally took

less than one minute on a Pentium II personal computer.

5.5.3 Neural Network Algorithm

The target tss error to be used for each of the five main series (*A* to *E*) of this research was experimentally determined using several test classifications. Apart from this step, the algorithm did not require the user to make any decisions regarding key algorithm properties such as network topology [network characteristics were set by standard rules of thumb (Section 5.2.2.1) that are demonstrated in Chapter 6 to be generally valid for the training and test datasets used here]. Training for a single classification typically took about 15 to 80 minutes (for 2000- to 8000-iteration executions) on "Sun ULTRA5" and "Sun ULTRA10" workstations. The classification of satellite imagery using a trained network took less than 5 minutes on a Pentium II personal computer. Because the consensus neural network routine requires the results of 10 different training and classification processes, the consensus classifier used in this research took considerably longer than the other classifiers to produce a final image (it is estimated that the generation of 10 different classified images and the final consensus image would take about 4 hours if it were to take place using a single "Sun ULTRA5" workstation). Thus, although the neural network results were consistently superior to those of the other two classifiers, the use of the algorithm requires considerably more of the user's attention and time to execute. It would not be difficult to automate all of the steps involved in consensus neural network classification, eliminating the need of the user to monitor all stages of the classification.

5.6 Chapter Summary

Based on fieldwork conducted in the summers of 1998 and 1999, ground-truth databases were constructed for two study areas: one located on Melville Island, Nunavut, and the other in the north-central portion of the Cape Smith Belt of Québec. An evaluation of three supervised classifiers (evidential reasoning, maximum likelihood, and neural network) for lithological discrimination was performed for these northern study areas using the ground-truth databases, which consist of five sets of surface-cover classes, and six training and test databases. Results indicate that the neural network algorithm (which implements a standard feedforward network that uses backpropagation in training and which combines the results of 10 separate classifications by consensus) consistently produced results that are superior to those of the standard maximum-likelihood classifier and the experimental evidential-reasoning classifier (strictly speaking, the neural network algorithm produced the best results in all 30 tests reported in this chapter). For the Melville Island Field Area, average overall percentages of test pixels correctly labelled ranged from 78% (*B* Series) to 86% (*E* Series), and were typically 4 to 7% higher than the percentages of the next best classifier (maximum likelihood). For the Cape Smith Belt Field Area, the average overall percentage of test pixels correctly labelled was 89%, and percentages were typically 3 to 6% greater than those of the next best classifier (maximum likelihood). The overall lithological information content of images produced by the neural network algorithm is considered good, although all images are characterized by variable amounts of confusion between sometimes diverse lithologies. The best discriminated lithological classes were found to be those with distinctive weathering characteristics.

Although individual neural network accuracies were found to vary considerably, the consensus neural network results were found to consistently be within about one percent of overall percentages associated with the highest individual neural network results. This suggests that the consensus neural network algorithm can be used to generate useful neural network results without the need to evaluate the results of multiple individual neural network results. The use of a simple majority-vote consensus routine to reduce or eliminate the effect of variability between individual neural network is supported by these results, although such a routine necessarily extends the length of classification time considerably.

The maximum likelihood algorithm produced results that are visually similar to those of the neural network, although the percentages of all test pixels correctly classified were typically about 3 to 10% less than those of the neural network. The evidential reasoning algorithm produced relatively poor results (overall percentages are typically 20 to 30% less than those of the maximum likelihood and neural network classifiers), in contrast to the results of prior studies. The results presented in this chapter suggest that the evidential reasoning classifier itself, and / or the method for evidence calculation used here (which calculates evidence as a function of the proportions of class training data that contain the image values being classified) are unsuitable for use in the classification of databases such as those used in this research (see Chapter 7 for evaluation of the evidential reasoning classifier as a consensus algorithm for combination of neural network results).

6 EMPIRICAL NEURAL NETWORK INVESTIGATIONS REGARDING NETWORK TOPOLOGY AND THE USE OF NOISE DURING TRAINING

6.1 Introduction

In the research presented in this chapter, the feedforward backpropagation neural network algorithm is empirically evaluated with regard to: 1) over-generalization [Section 3.4.5.8] and the influence of jitter [artificial noise applied during training] on classification results; and 2) the influence of changes in the number of intermediate layers, and the number of nodes used to define these layers, on classification results [Section 3.4.5.5].

6.2 Noise

The purpose of the research presented in this section was: 1) to determine if over-generalization occurs during the training of a feedforward backpropagation network using the satellite image and surface-cover databases assembled for this project [Chapter 5]; and 2) to determine if additive noise applied during training helps to increase the percentage of test pixels successfully classified [Section 3.4.5.8]; the author is not aware of any prior neural network research that has tested the use of jitter in the classification of satellite imagery. Given the small training dataset available in this study, the potential for over-generalization was considered to be relatively high (a larger training dataset, meanwhile, could conceivably be less problematic in this regard, since there would presumably be fewer peculiarities in such a dataset for the network weights to adapt to).

6.2.1 Methodology

6.2.1.1 Training and Test Databases

Jitter tests were performed using the six *D* Series training and testing databases of the Melville Island Field Area, and the six *A* Series training and testing databases of the Cape Smith Belt Field Area (Sections 5.2.1 and 5.2.2). The Melville Island *D* Series databases involve 557 training pixels and 294 test pixels representing 9 surface-cover classes (Table 5.2). The Cape Smith Belt *A* Series databases involve 449 training pixels and 237 test pixels representing 7 surface-cover classes (Table 5.3).

6.2.1.2 Classification Methodology

For non-jitter tests, ten neural network classifications were performed for each of the six training and test databases, for each of the two field areas (*D* and *A* Series). The results of each set of 10 neural network results were used to generate majority-vote consensus results. Thus, 60 neural network classifications were generated for each field area, from which 6 consensus results were produced. The number of iterations used in to generate the neural network classifications was 20,000; this figure was chosen since it is sufficiently large to ensure the onset of over-generalization, if over-generalization should occur at all (recall that the number of iterations needed for neural network classifications discussed in Chapter 5 was typically only about 2000 to 8000). The results produced by the 20,000-iteration non-jitter executions were compared with those of the relevant 2000-8000 iteration non-jitter jobs of Chapter 5 to determine if over-generalization is a difficulty for these datasets.

The same methodology described above was used for tests with jitter, except the

neural network training module had a jitter routine implemented that randomly added noise (±4) to all training data during the training stage [strictly speaking the jitter used in the tests was actually ±4/255 because training data (originally falling in the 8-bit range of 0 to 255) is normalized to 1.0 prior to submission to the classifier] (note: analyses of values generated using the *C* random number generator implemented in this research demonstrate that the frequency distribution of random values approximates a Gaussian distribution, and has a standard deviation of about 1.58). The choice of ±4 as the noise interval was based on an expectation, derived through examination of class histograms, that a choice of, e.g., ±1 would be too low to influence classification results, and a choice of, e.g., ±10 would be so large as to create significant overlap between certain "numerically-adjacent" classes; thus, statistical methods for the calculation of useful noise levels (e.g., Bishop, 1995a, pp. 346-349) were foregone here in favour of a more *ad hoc* and intuitive method. Although the use of jitter necessarily slowed learning and raised tss errors (Figure 6.1), the learning curve of all classifications was essentially horizontal well before the 20,000 iterations were completed, indicating that the network was trained to (or beyond) its potential. TM channels 3, 4, 5, and 7 were used as input images.

6.2.2 Results

A comparison of overall classification results for the *D* and *A* Series are given in Tables 6.1 and 6.2, respectively. From these tables, it can be seen that overall classification results are similar between classifications executed with about 2000 to 8000 iterations, and those executed with 20,000 iterations. This indicates that over-generalization is not a

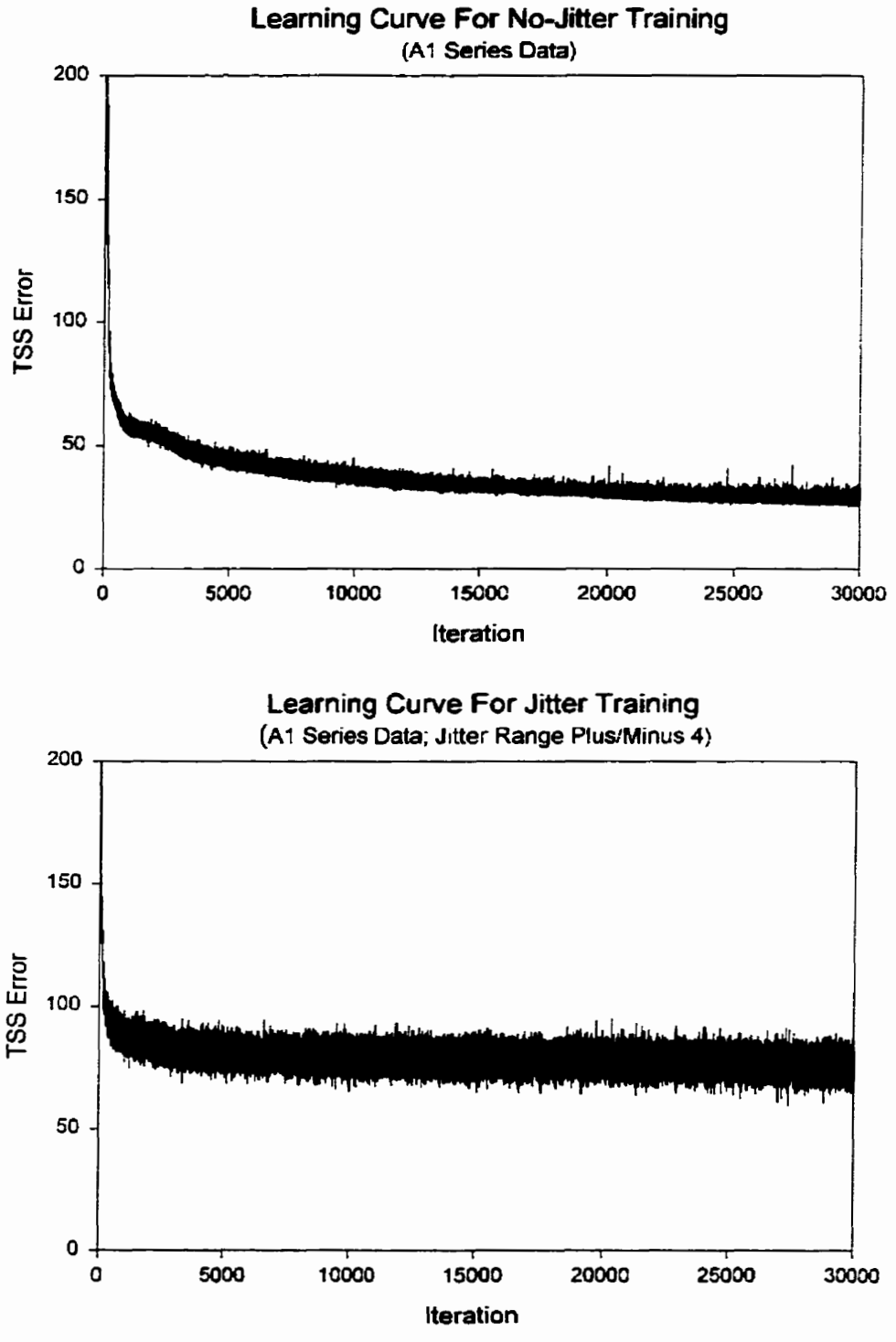

Figure 6.1 Learning curves for non-jitter and jitter training (plus / minus 4).

Table 6.1 Comparison of the *D* Series overall results (percentage of test pixels correctly classified for Melville Island Field Area) for 1) no jitter (2000-8000 iterations), 2) no jitter (20,000 iterations), and 3) ±4 jitter (20,000 iterations) classifications. Classifications labelled as follows NN-B: best individual neural network result of 10 neural network jobs, NN-M: majority-vote consensus neural network results.

		D1	D2	D3	D4	D5	D6
No Jitter	NN-B	0.8571	0.8469	0.8367	0.8503	0.8299	0.8265
2-8000 it.	NN-M	0.8571	0.8537	0.8435	0.8639	0.8197	0.8299
No Jitter	NN-B	0.8435	0.8537	0.8435	0.8639	0.8163	0.8333
20,000 it.	NN-M	0.8503	0.8537	0.8435	0.8605	0.8197	0.8333
Jitter ±4	NN-B	0.8197	0.8401	0.8639	0.8776	0.8299	0.8401
20,000 it.	NN-M	0.8027	0.8401	0.8469	0.8707	0.8197	0.8299

Table 6.2 Comparison of the *A* Series overall results (percentage of test pixels correctly classified for Cape Smith Belt Field Area) for 1) no jitter (2000-8000 iterations), 2) no jitter (20,000 iterations), and 3) ±4 jitter (20,000 iterations) classifications. Classifications labelled as follows NN-B: best individual neural network result of 10 neural network jobs, NN-M: majority-vote consensus neural network results.

		A1	A2	A3	A4	A5	A6
No Jitter	NN-B	0.9156	0.8776	0.8987	0.8903	0.8861	0.8945
2-8000 it.	NN-M	0.9030	0.8776	0.8987	0.8945	0.8734	0.8692
No Jitter	NN-B	0.9198	0.8861	0.8987	0.8861	0.8987	0.8903
20,000 it.	NN-M	0.9072	0.8945	0.9030	0.8819	0.9072	0.9030
Jitter ±4	NN-B	0.9030	0.8734	0.8692	0.9030	0.8945	0.8650
20,000 it.	NN-M	0.8945	0.8650	0.8650	0.8987	0.8903	0.8523

significant problem for the Melville Island *D* Series training and test databases and the Cape Smith Belt *A* Series training and test databases.

Although some results obtained using ±4 jitter are slightly higher than the corresponding results obtained without jitter, the results given in Tables 6.1 and 6.2 provide no consistent evidence that is indicative of a benefit associated with jitter. In fact, some jitter results (e.g., those of the *D1*, *A3*, and *A6* experiments) are about 3 to 4% below those of the corresponding non-jitter classifications, indicating that the use of ±4 jitter can produce results that are significantly below those produced without jitter.

Errors of omission and commission are summarized for the *D* and *A* Series in Tables 6.3 and 6.4. These tables indicate that 1) the 20,000-iteration non-jitter results are essentially the same as the 2000-8000 iteration results, and 2) the ±4-jitter 20,000-iteration results are essentially the same or worse than the 20,000-iteration non-jitter results. Thus, as with the data in Tables 6.1 and 6.2, these data support the hypotheses that 1) over-generalization is not a problem with the databases tested, and 2) ±4 jitter is not helpful in improving classification success.

6.3 Network Topology

There is no mathematical method for determining the optimum network topology for solving a particular problem using a feedforward backpropagation neural network (Section 3.4.5.5). Nevertheless, theoretical and empirical studies have helped to define general guidelines for the definition of network topologies. For example, it has been understood since the late 1960's that many problems cannot be solved at all without at least

Table 6.3 Summary of the magnitude of errors of omission and commission for *D* Series non-jitter and jitter classifications of the Melville Island Field Area. Classifications are listed as follows: NJ1: no-jitter, approximately 2000-8000 iterations; NJ2: no jitter, 20000 iterations; J: ±4 jitter, 20000 iterations. The class numbering scheme is the same as that used in Chapter 5 for the Melville Island Field Area (see Table 5.2). Values are expressed as proportions, and may be converted to percentages by multiplying by 100%.

D: NJ1	1		2		3		4		5		6		
CLASS	EO	EC	EO	EC	EO	EC	EO	EC	EO	EC	EO	EC	AVG
1	0.16	0.06	0.16	0.06	0.14	0.11	0.16	0.14	0.24	0.24	0.11	0.21	0.15
2	0.00	0.00	0.00	0.13	0.00	0.00	0.00	0.13	0.00	0.00	0.00	0.00	0.02
3	0.00	0.30	0.00	0.33	0.14	0.00	0.21	0.21	0.00	0.26	0.07	0.24	0.15
4	0.10	0.25	0.15	0.22	0.09	0.30	0.18	0.18	0.16	0.24	0.26	0.24	0.20
5	0.35	0.15	0.32	0.20	0.43	0.15	0.20	0.21	0.38	0.25	0.30	0.24	0.27
6	0.25	0.00	0.00	0.00	0.08	0.00	0.08	0.00	0.33	0.11	0.08	0.08	0.09
7	0.00	0.00	0.14	0.00	0.00	0.07	0.00	0.00	0.00	0.00	0.00	0.00	0.02
8	0.00	0.00	0.00	0.00	0.00	0.00	0.00	0.00	0.00	0.00	0.00	0.00	0.00
9	0.00	0.00	0.00	0.00	0.00	0.00	0.00	0.00	0.00	0.00	0.00	0.00	0.00

D: NJ2	1		2		3		4		5		6		
CLASS	EO	EC	EO	EC	EO	EC	EO	EC	EO	EC	EO	EC	AVG
1	0.16	0.11	0.14	0.14	0.14	0.09	0.16	0.11	0.22	0.26	0.14	0.20	0.15
2	0.00	0.00	0.00	0.13	0.00	0.00	0.00	0.13	0.00	0.00	0.00	0.00	0.02
3	0.07	0.28	0.00	0.26	0.07	0.07	0.21	0.21	0.07	0.24	0.00	0.07	0.13
4	0.12	0.25	0.17	0.20	0.10	0.29	0.17	0.19	0.18	0.26	0.26	0.24	0.20
5	0.36	0.15	0.32	0.22	0.43	0.17	0.23	0.20	0.36	0.21	0.30	0.23	0.27
6	0.08	0.00	0.00	0.08	0.08	0.08	0.08	0.21	0.25	0.18	0.00	0.29	0.11
7	0.00	0.07	0.07	0.00	0.00	0.00	0.00	0.00	0.00	0.00	0.00	0.00	0.01
8	0.00	0.00	0.00	0.00	0.00	0.00	0.00	0.00	0.00	0.00	0.00	0.00	0.00
9	0.00	0.00	0.00	0.00	0.00	0.00	0.00	0.00	0.00	0.00	0.00	0.00	0.00

D: J	1		2		3		4		5		6		
CLASS	EO	EC	EO	EC	EO	EC	EO	EC	EO	EC	EO	EC	AVG
1	0.27	0.04	0.14	0.09	0.14	0.03	0.16	0.00	0.24	0.20	0.14	0.18	0.13
2	0.00	0.00	0.00	0.00	0.00	0.00	0.00	0.00	0.00	0.00	0.00	0.22	0.02
3	0.07	0.28	0.00	0.39	0.00	0.18	0.07	0.19	0.00	0.22	0.07	0.32	0.15
4	0.12	0.33	0.15	0.25	0.07	0.29	0.06	0.24	0.06	0.30	0.17	0.27	0.19
5	0.46	0.26	0.38	0.19	0.46	0.14	0.35	0.17	0.51	0.15	0.39	0.16	0.30
6	0.33	0.00	0.08	0.00	0.08	0.08	0.17	0.00	0.33	0.00	0.17	0.00	0.10
7	0.00	0.07	0.14	0.00	0.07	0.00	0.00	0.00	0.00	0.00	0.00	0.00	0.02
8	0.00	0.00	0.00	0.00	0.00	0.00	0.00	0.00	0.00	0.00	0.00	0.00	0.00
9	0.00	0.00	0.00	0.00	0.00	0.00	0.00	0.00	0.00	0.00	0.00	0.00	0.00

Table 6.4 Summary of the magnitude of errors of omission and commission for *A* Series non-jitter and jitter classifications of the Cape Smith Belt Field Area. Classifications are listed as follows: NJ1: no-jitter, approximately 2000-8000 iterations; NJ2: no jitter, 20000 iterations; J: ±4 jitter, 20000 iterations. The class numbering scheme is the same as that used in Chapter 6 for the Cape Smith Belt Field Area (see Table 5.3). Values are expressed as proportions, and may be converted to percentages by multiplying by 100%.

A:NJ1	1		2		3		4		5		6		
CLASS	EO	EC	EO	EC	EO	EC	EO	EC	EO	EC	EO	EC	AVG
1	0.05	0.20	0.07	0.17	0.14	0.14	0.11	0.12	0.13	0.13	0.20	0.06	0.13
2	0.13	0.09	0.21	0.00	0.21	0.24	0.13	0.13	0.04	0.08	0.00	0.14	0.12
3	0.09	0.09	0.17	0.17	0.06	0.09	0.13	0.11	0.24	0.13	0.09	0.23	0.13
4	0.21	0.03	0.23	0.19	0.15	0.03	0.15	0.18	0.13	0.26	0.28	0.18	0.17
5	0.23	0.17	0.15	0.08	0.15	0.27	0.23	0.00	0.31	0.18	0.31	0.25	0.19
6	0.03	0.00	0.00	0.03	0.00	0.00	0.00	0.06	0.00	0.03	0.00	0.00	0.01
7	0.00	0.00	0.00	0.00	0.00	0.00	0.00	0.00	0.00	0.00	0.00	0.00	0.00

A: NJ2	1		2		3		4		5		6		
CLASS	EO	EC	EO	EC	EO	EC	EO	EC	EO	EC	EO	EC	AVG
1	0.05	0.20	0.04	0.17	0.16	0.13	0.14	0.13	0.07	0.12	0.11	0.11	0.12
2	0.17	0.09	0.17	0.05	0.17	0.23	0.13	0.16	0.04	0.08	0.04	0.12	0.12
3	0.11	0.08	0.13	0.15	0.02	0.12	0.13	0.13	0.15	0.13	0.09	0.13	0.11
4	0.15	0.03	0.23	0.12	0.18	0.00	0.15	0.15	0.13	0.13	0.15	0.13	0.13
5	0.23	0.17	0.23	0.00	0.15	0.21	0.23	0.17	0.31	0.00	0.38	0.11	0.18
6	0.00	0.00	0.00	0.03	0.00	0.00	0.03	0.07	0.00	0.03	0.00	0.03	0.02
7	0.00	0.00	0.00	0.00	0.00	0.00	0.00	0.00	0.00	0.00	0.00	0.00	0.00

A: J	1		2		3		4		5		6		
CLASS	EO	EC	EO	EC	EO	EC	EO	EC	EO	EC	EO	EC	AVG
1	0.05	0.17	0.07	0.15	0.13	0.16	0.14	0.09	0.14	0.11	0.16	0.10	0.12
2	0.08	0.08	0.13	0.00	0.17	0.23	0.08	0.19	0.00	0.14	0.00	0.23	0.11
3	0.11	0.14	0.15	0.23	0.13	0.18	0.13	0.10	0.13	0.15	0.17	0.21	0.15
4	0.26	0.06	0.33	0.21	0.26	0.12	0.13	0.19	0.13	0.17	0.31	0.27	0.20
5	0.31	0.18	0.31	0.10	0.31	0.25	0.15	0.00	0.46	0.00	0.38	0.11	0.21
6	0.00	0.00	0.00	0.03	0.00	0.00	0.00	0.03	0.00	0.03	0.00	0.00	0.01
7	0.00	0.00	0.00	0.00	0.00	0.00	0.00	0.00	0.00	0.00	0.00	0.00	0.00

one hidden layer (Section 3.4.5), and thus the use of a single hidden layer greatly improves the potential of that network for solving problems. The addition of further hidden layers increases the potential of the network to solve problems, although this comes at a price with regard to other factors such as training time (Section 3.4.5). It has been shown that most problems can be solved using a 2-layer network, and that virtually any solvable problem can be solved with a three-or four-layer network (e.g., Huang and Huang, 1991; Tamura and Tateishi, 1997), although in practice it is rarely clear exactly how many nodes must be used for each hidden layer in order to solve a particular problem.

The following general "rules of thumb" have been devised regarding the definition of network topologies for classification purposes: 1) use 1 or 2 hidden layers; and 2) define each hidden layer with a number of nodes between the number of nodes used to define the input and output layers (Section 3.4.5.5; Richards, 1993). The purpose of the research presented in this section was to determine the number of nodes and layers that produced the best overall classification results, by progressively varying network topology in a simple manner. Of interest was whether or not established rules of thumb would be supported or contradicted by empirical tests using the databases assembled for this study.

6.3.1 Methodology

6.3.1.1 Training and Test Databases

The tests were performed using the first training and testing database of the Melville Island *D* Series, and the first training and testing database of the Cape Smith Belt *A* Series (see Sections 5.2.1 and 5.2.2). The Melville Island *D* Series involves 557 training pixels and

294 test pixels representing 9 surface-cover classes. The Cape Smith Belt *A* Series involves 449 training pixels and 237 test pixels representing 7 surface-cover classes.

6.3.1.2 Classification Methodology

Two sets of tests were performed for each field area. The first set of tests involved the use of a single intermediate layer, while the second set of tests involved the use of two intermediate layers. The number of nodes used to define the intermediate layers in each of these two sets of tests ranged from 1 to the maximum number of nodes in the output layer (9 for the *D1* database, and 7 for the *A1* database). Thus, a series of classifications was generated for each set of tests, with each set of 10 neural network classifications and one consensus classification corresponding to a different network topology (Figure 6.2). TM channels 3, 4, 5, and 7 were used as input images.

For each classification, training occurred for 20,000 iterations, in order to be sure that weights had converged on essentially as good a solution as was possible, given the network topology. There is no evidence for a tendency toward over-generalization when using these datasets, as shown above in Section 6.2.

6.3.2 Results

Plots of overall consensus results (given as the proportion of test pixels classified correctly), and the corresponding average tss error after 20,000 iterations, are given for one-hidden-layer cases in Figures 6.3 and 6.5 (*D1* and *A1* results, respectively), and for two-hidden-layer cases in Figures 6.4 and 6.6 (*D1* and *A1* results, respectively). The plots show

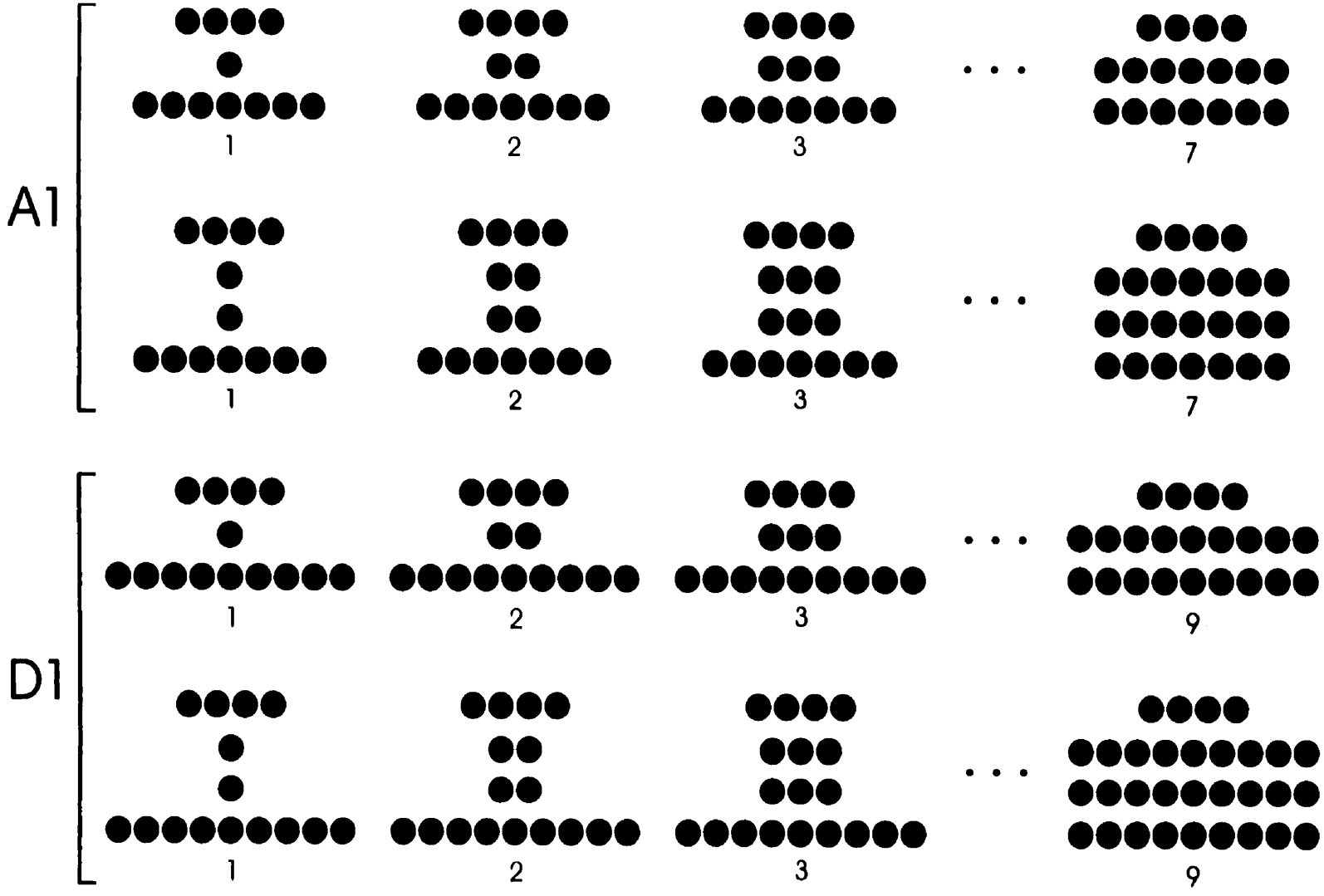

Figure 6.2 Changes in network topology performed for one- and two-hidden layer tests, for the Melville Island Field Area (*D1* Series) and the Cape Smith Belt Field Area (*A1* Series).

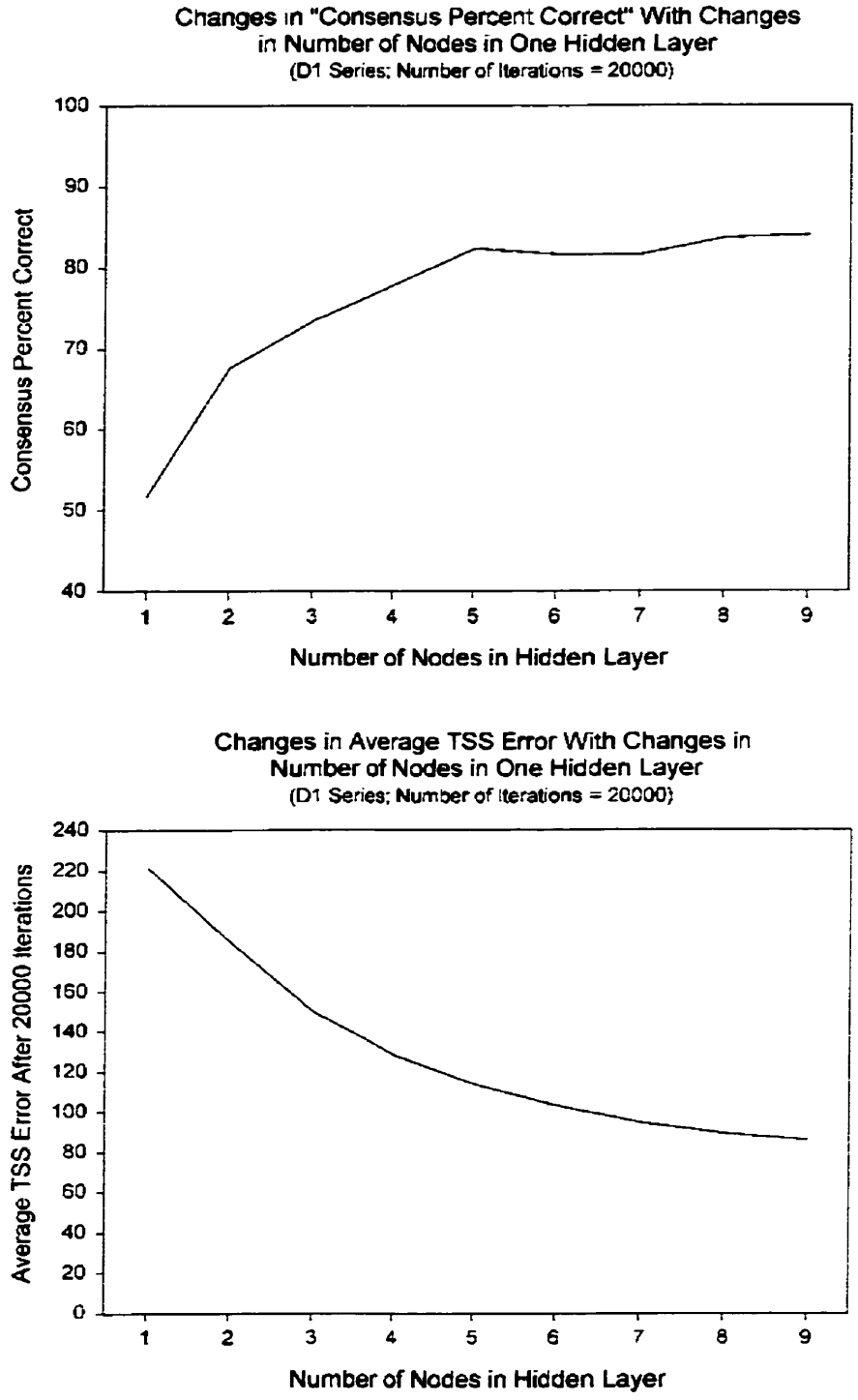

Figure 6.3 Plot of changes in consensus results, and corresponding results in average tss error after 20000 iterations, with changing number of nodes in a network with one hidden layer (*D1* Series).

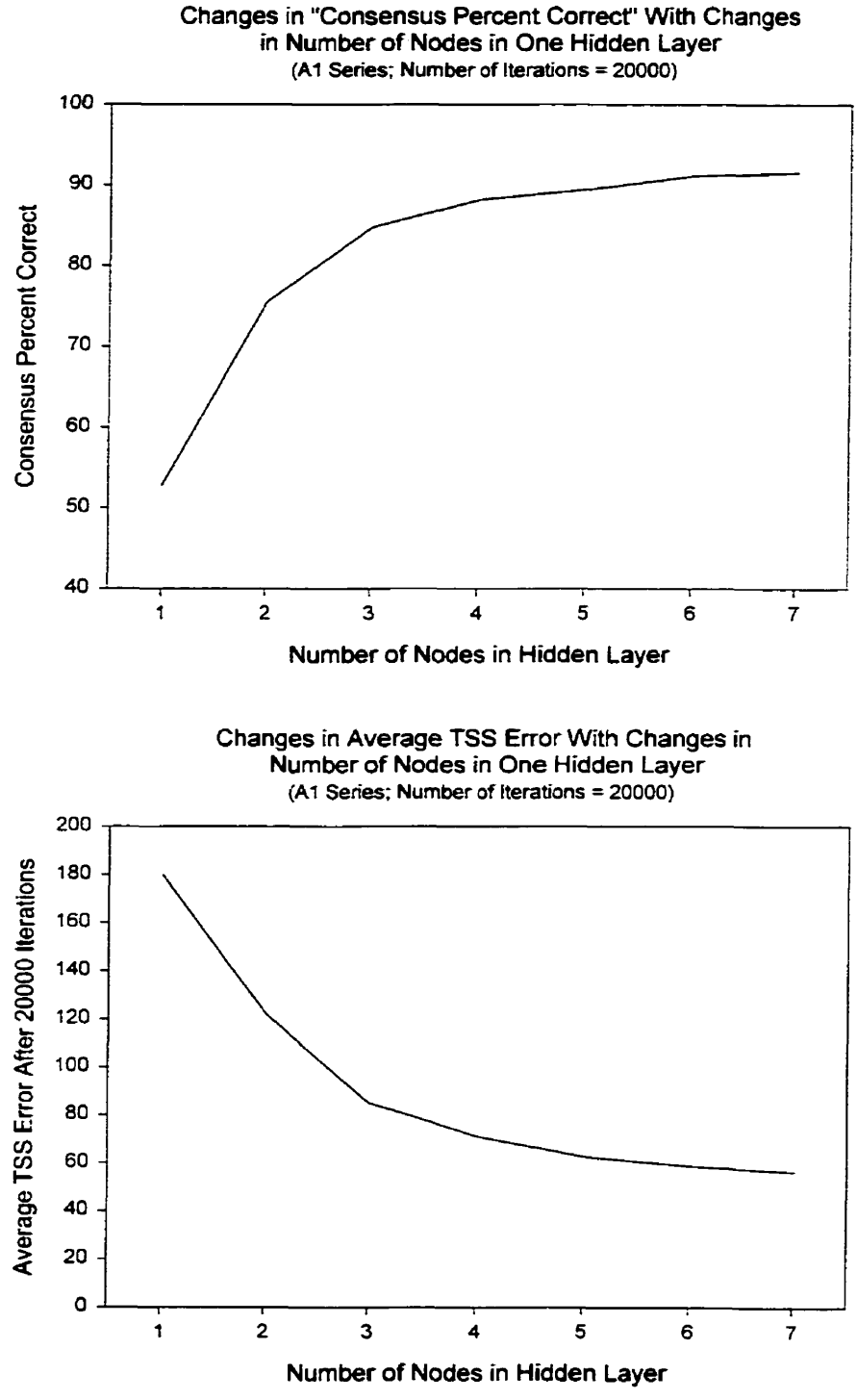

Figure 6.4 Plot of changes in consensus results, and corresponding results in average tss error after 20000 iterations, with changing number of nodes in a network with one hidden layer (*A1* Series).

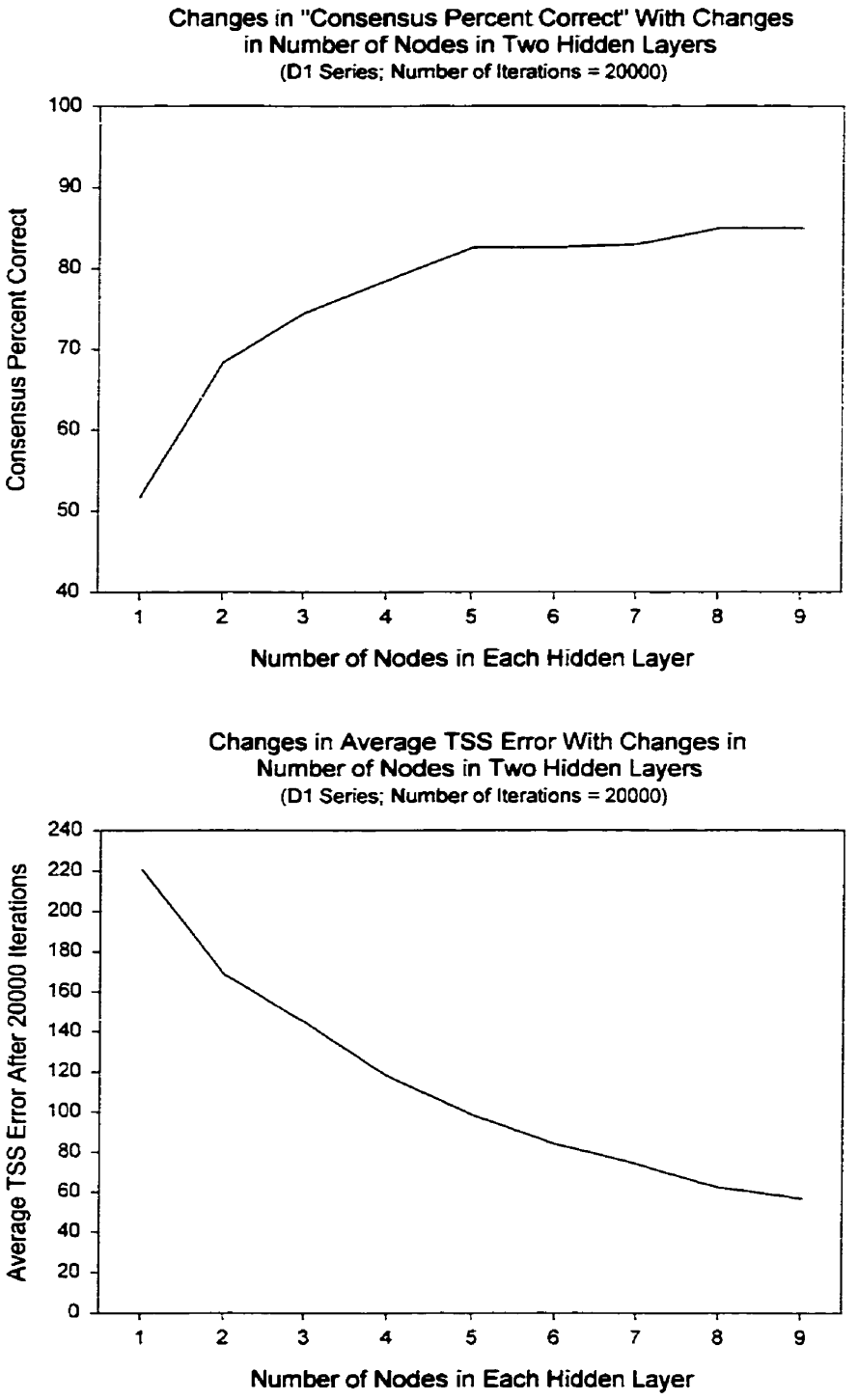

Figure 6.5 Plot of changes in consensus results, and corresponding results in average tss error after 20000 iterations, with changing number of nodes in a network with two hidden layers (*D1* Series).

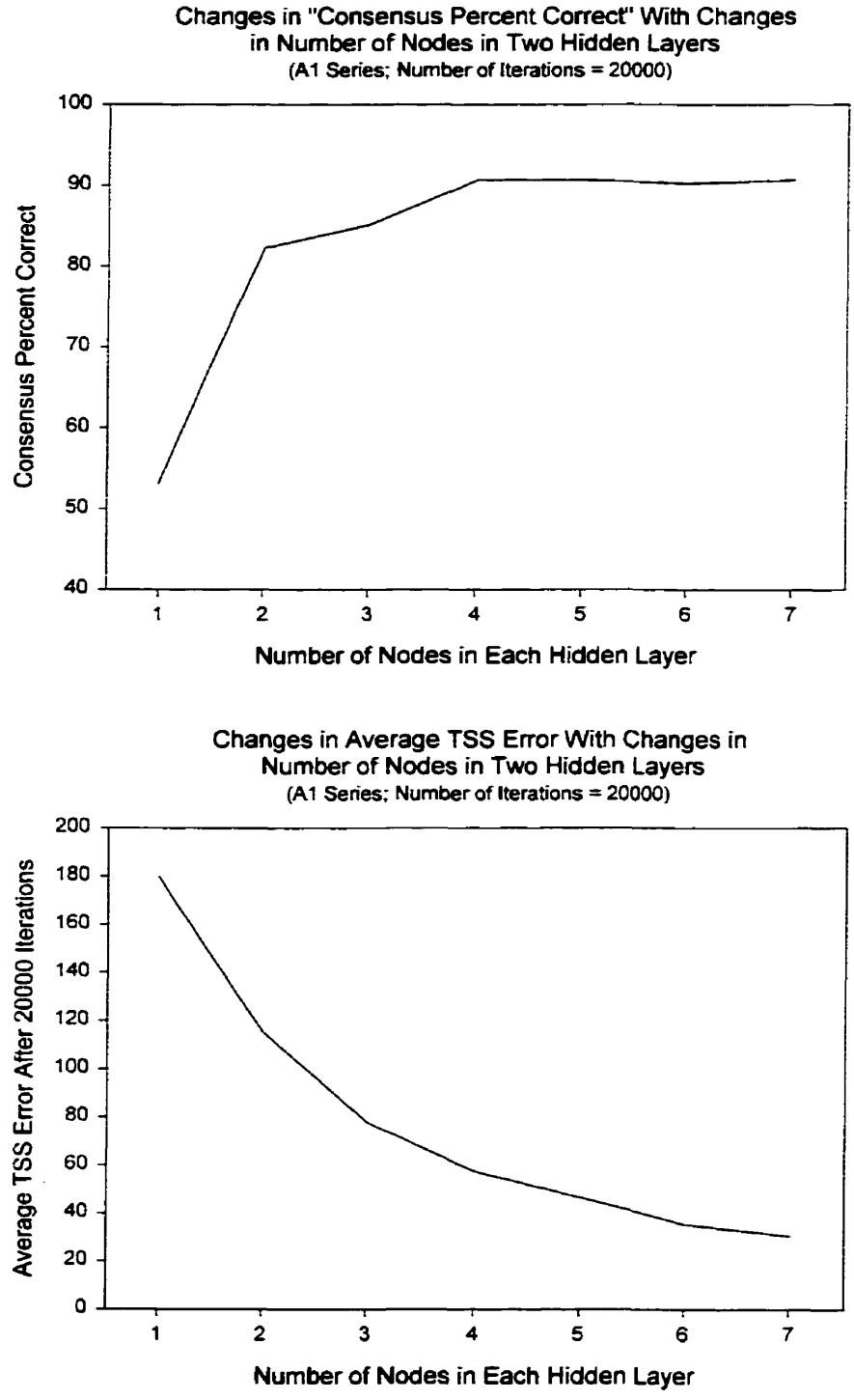

Figure 6.6 Plot of changes in consensus results, and corresponding results in average tss error after 20000 iterations, with changing number of nodes in a network with two hidden layers (*A1* Series).

that overall classification results improve as the number of nodes in the hidden layer(s) increase, and that the best overall results are generally associated with the largest 2-hidden-layer networks. For each of the four sets of results, classification results approach their maximums in a generally asymptotic manner. The results presented in Figures 6.3 to 6.6 are consistent with recognized "rules of thumb" (Section 3.4.4.5; Richards, 1993)

The average tss error after 20,000 iterations can continue to drop in instances in which changes in consensus percent correct have flattened out (e.g Figure 6.4). This is to be expected, since tss error is a measure of how close output values are to desired output values (Sections 3.4.4 and 3.4.6), rather than a measure of the percentage of test pixels correctly classified (i.e., output values can continue to approach the idealized target values without changing the corresponding classification results).

When the number of training samples used in a classification problem is small relative to the dimensionality of the problem at hand, classification results may be unsatisfactory. The negative effect that relatively small training datasets and large problem dimensionalities can have on classification results is known as the Hughes phenomenon (Section 3.4.5.5). The classification results presented in Figures 6.3 to 6.6 suggest that a sufficient amount of training data was available (relative to the dimensionality of the problems investigated), since, in general, classification results continue to improve with increases in the number of weights used in the networks. However, it is conceivable that a larger and more fully representative training dataset could have produced overall classification results that are superior to those given in Figures 6.3 to 6.6 (for the same reasons, a smaller and less representative training dataset could have produced worse results, possibly even involving a decreasing trend in

overall classification accuracies with increasing network size (e.g., Shahshahani and Landgrebe, 1994).

6.4 Chapter Summary

Tests indicate that over-generalization is not present in the training of a feedforward backpropagation neural network using databases such as those of the Melville Island and Cape Smith Belt Field Areas. Also, given the slow training time and generally poor results associated with jitter training, there is no evidence favouring the use of jitter for the classification of databases such as those used here.

Empirical investigations regarding the influence of network topology on overall results suggest that two hidden layers should be used in the classification of databases such as those used here; each of these layers should be defined by the greatest of the number of nodes in the input and output layers. These results are consistent with recognized "rules of thumb" (e.g., Richards, 1993).

7 EMPIRICAL NEURAL NETWORK INVESTIGATIONS REGARDING EVIDENTIAL-REASONING CONSENSUS AND THE GENERATION OF CONFIDENCE IMAGES

7.1 Introduction

The output layer of a neural network can consist of any number of nodes. When neural networks are applied toward regression problems, there may be as few as one output node, and the output activations (or scaled versions of these numbers) are themselves usually the values of interest to the investigator. In contrast, when neural networks are applied toward classification problems, the output layer most often consists of the same number of nodes as there are classes. Under this arrangement, each class is assigned a single output node, and the predicted class for a given input vector corresponds to the class whose output node has the greatest activation [during training, target output activations for correct and incorrect class labels are typically high (e.g., 1) and low (e.g., 0), respectively; as noted in Section 3.4.6, the neural network used in this research used respective target activations of 0.9 and 0.1 as targets for correct and incorrect class labels]. The above arrangement thus means that typical neural network classification decisions are based on a simple majority vote of output activations. Beyond this, the magnitudes (both absolute and relative) of output activations are usually not considered in the classification decision.

The activations of output nodes have the potential to provide information beyond that used in majority-vote classifications. Workers have found that output activations, generated by a neural network that learns by minimizing tss error (Section 3.4.4), can approximate

posterior probabilities (Ruck *et al.*, 1990; Wan, 1990). This suggests that output activations may be used to a greater extent than they are in majority-vote classifications (e.g., they may be used in consensus operations), since they provide a general framework for ranking classes in terms of the relative likelihood that they are associated with a particular input vector (e.g., Rogova, 1994; Benediktsson *et al.*, 1997a).

This chapter presents empirical classification results involving the utilization of output activations for purposes beyond those of majority-vote classifications. Specifically, the following are tested: 1) the consensus of neural network classifications by orthogonal summation, through the treatment of output activations as measures of evidence, and 2) the use of the highest two output activations of neural network output vectors to generate "confidence images" (i.e., images whose values reflect the confidence associated with the class-labelling decisions of a corresponding classified image).

7.2 Evidential Reasoning Consensus

The evidential reasoning classification algorithm is described in Section 3.3. As noted in Section 3.3.1, the method for the combination of evidence using orthogonal summation is well established, but methods for generating initial measures of evidence are not (Moon, 1990, 1993). Peddle (1991, 1995) has suggested that evidence can be calculated as a function of the proportions of class training data that contain the values being classified (Section 3.3.1). This method of evidence calculation was used in the empirical evaluation of the evidential reasoning algorithm in Chapter 5.

In the research presented below, the evidential reasoning algorithm was investigated

as a means for improvement of overall neural network results through the consensus of multiple sets of neural network output activations (Rugova, 1994). Output activations were treated as measures of evidence, and were combined using orthogonal summation as described in Section 3.3 (Figure 7.1). The main goals of the evidential reasoning consensus tests were: 1) to determine how the evidential reasoning consensus method compares to the majority-vote consensus method tested in Chapter 5; 2) to determine if the evidential reasoning method can produce results that are superior to all individual neural network results used as input; and 3) to determine if the use of neural network activations as measures of evidence improves the utility of the evidential reasoning algorithm over that described in Chapter 5. This author is not aware of any prior research, apart from that of Rugova (1994) (which focused on the use of neural networks for character recognition), which has examined the utility of the combination of neural network activations using evidential reasoning as the consensus algorithm.

Recall that it was found in Chapter 5 that the majority-vote consensus classifications produced overall results that were typically within ±1% of those of the best individual neural network results. This was found to be of practical value, since it suggested that the majority-vote consensus method can be used to generate consistently strong neural network classifications without necessitating the evaluation of numerous individual neural network classifications (Section 5.3.1.3). It was also found in Chapter 5 that the evidential reasoning algorithm, employed using a method which calculates evidence as a function of the proportions of class training data that contain the image values being classified, produced poor classification results compared to those of the other classifiers tested (Section 5.4).

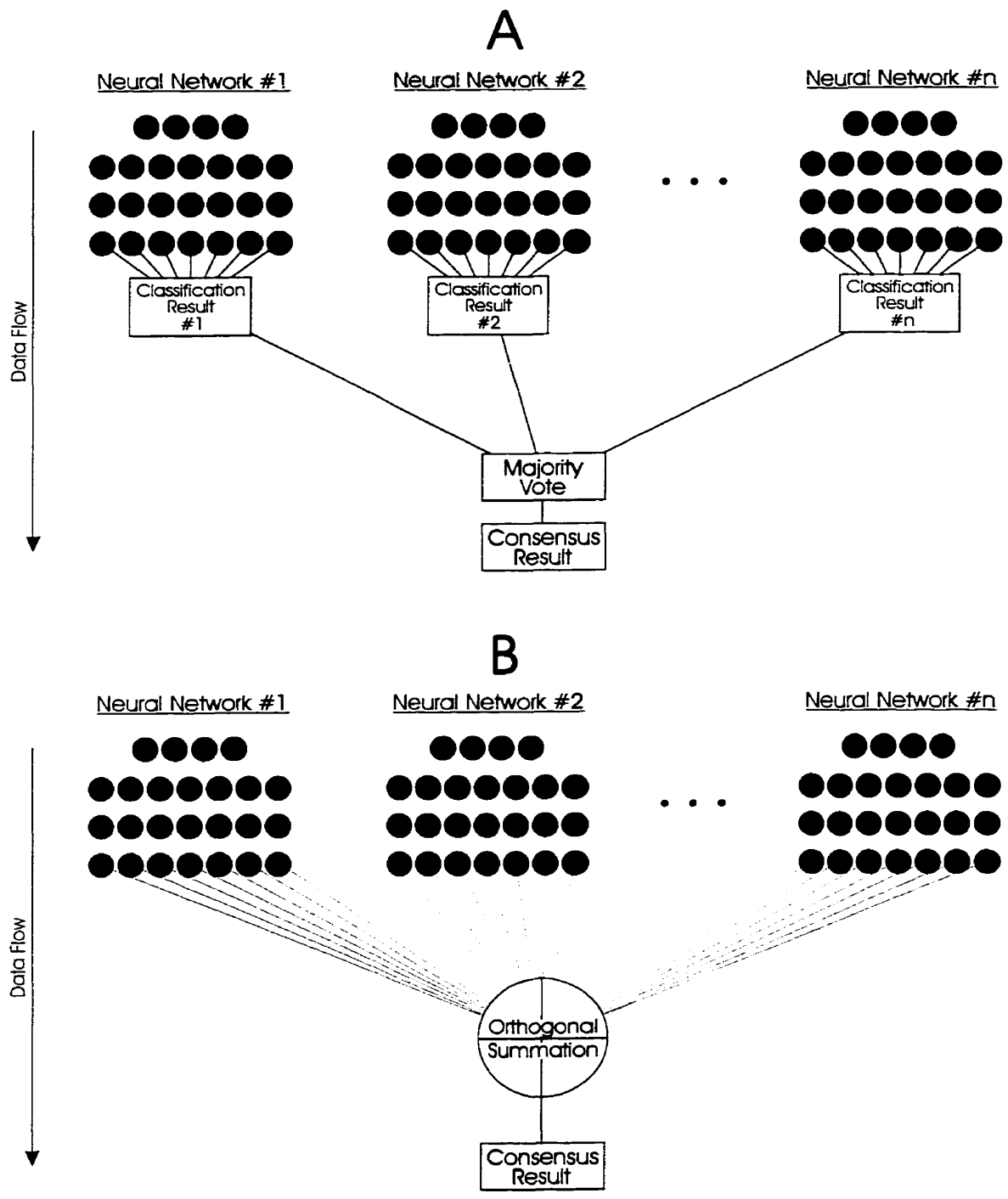

Figure 7.1 Illustration of the two consensus algorithms used in this research: A) majority vote; and B) evidential reasoning. The majority vote algorithm simply chooses the class label most frequently selected by individual neural networks. The evidential reasoning algorithm uses orthogonal summation of output activations to assign class labels.

7.2.1 Methodology

The evidential reasoning consensus tests were performed for the Melville Island Field Area using the training and test pixels of the *B, C, D* and *E* Series (Section 5.2.1.1), and for the Cape Smith Belt Field Area using the training and test pixels of the *A* Series (Section 5.2.1.2) (i.e., all training and test databases introduced in Chapter 5 were used). For each of the six training and test datasets of the five main Series, the output activations of ten individual neural network executions were treated as measures of evidence, and were combined through orthogonal summation [note: a modified version of the neural network classification software (*FEED9E.C*: Appendix C) was used to generate the databases of output activations for all test pixels; a modified version of the main evidential reasoning software (*ER129FXVA14.C*: Appendix C) was used in order to accommodate the different input requirements involved in these tests]. Because most (or all) sums of output activations exceeded 1.0, a normalization step was typically required prior to evidence combination [the frame of discernment was also necessarily set to zero in the process; this is in contrast to the executions of Chapter 5, where evidence measures were so low (with frames of discernment often as high as ~0.95) as to never require this normalization step]. As with all evidential-reasoning classifications discussed in this document, final class labels corresponded to those classes whose measures of combined evidence were greatest. Classification results were compared with those generated in Chapter 5. TM channels 3, 4, 5, and 7 were used.

7.2.2 Results

Overall evidential reasoning consensus results for the Melville Island Field Area are

given in Tables 7.1 (overall proportions) and 7.2 (overall Kappa values). Results for the Cape Smith Belt Field Area are given in Tables 7.3 (overall proportions) and 7.4 (overall Kappa values). For the *A* to *D* Series, the evidential reasoning results are approximately the same as those produced by the majority vote algorithm. For the *E* Series, evidential reasoning results are consistently ~3% lower than those produced by the majority-vote algorithm (a notable exception to this finding is the evidential reasoning result for *E6*, which is about 10% higher than the corresponding majority-vote result).

Thus, in general, the results given in Tables 7.1 to 7.4 show that the evidential reasoning consensus algorithm generally performed only slightly worse than the majority-vote consensus algorithm. The evidential reasoning consensus results compare favourably to the maximum likelihood and evidential reasoning results reported in Chapter 5 (Tables 5.4, 5.5, 5.24, and 5.25). Nevertheless, the results suggest that the evidential-reasoning consensus algorithm is not a superior alternative to the simple majority-vote consensus algorithm evaluated in Chapter 5 (at least, for training and test data such as those used in this research).

As noted in Section 3.4.5.9, the generation of consensus results that are consistently superior to those produced by the best individual neural network classification can only be performed if individual results are error-independent. The failure of both of the consensus algorithms tested in this research (Chapters 5 and 7) to produce results that are consistently superior to those of the best individual neural network results suggests that the individual results are not sufficiently error-independent. The only differences between the individual neural network executions were those related to weight initializations, whereas some workers

Table 7.1 Summary of evidential-reasoning consensus results for all Series of the Melville Island Field Area. Values give the proportion of all test pixels classified correctly, and may be converted to percentages by multiplying by 100%. Compare with Table 5.4.

Series	Set 1	Set 2	Set 3	Set 4	Set 5	Set 6	Avg.
B	0.7925	0.7857	0.7925	0.7687	0.7517	0.7755	0.7778
C	0.7993	0.8129	0.8061	0.7959	0.8129	0.8163	0.8072
D	0.8503	0.8265	0.8401	0.8571	0.8129	0.8163	0.8339
E	0.8163	0.8197	0.8265	0.8061	0.8299	0.9252	0.8373

Table 7.2 Summary of evidential-reasoning consensus results for all Series of the Melville Island Field Area, expressed as Kappa coefficients. Values give the proportion of all test pixels correctly classified, beyond that which is to be expected based on chance alone (see Section 2.5.4 for details). Compare with Table 5.5.

Series	Set 1	Set 2	Set 3	Set 4	Set 5	Set 6	Avg.
B	0.7696	0.7632	0.7701	0.7442	0.7262	0.7521	0.7542
C	0.7627	0.7800	0.7718	0.7592	0.7805	0.7849	0.7732
D	0.8145	0.7861	0.8011	0.8238	0.7688	0.7742	0.7948
E	0.7451	0.7494	0.7574	0.7294	0.7636	0.8957	0.7734

Table 7.3 Summary of evidential reasoning consensus results for the *A* Series of the Cape Smith Belt Field Area. Values give the proportion of all test pixels classified correctly, and may be converted to percentages by multiplying by 100%. Compare with Table 5.24.

Series	Set 1	Set 2	Set 3	Set 4	Set 5	Set 6	Avg.
A	0.9156	0.8565	0.8987	0.8819	0.8903	0.8861	0.8882

Table 7.4 Summary of evidential reasoning consensus results for the *A* Series of the Cape Smith Belt Field Area, expressed as Kappa coefficients. Values give the proportion of all test pixels correctly classified, beyond that which is to be expected based on chance alone (see Section 2.5.4 for details). Compare with Table 5.25.

Series	Set 1	Set 2	Set 3	Set 4	Set 5	Set 6	Avg.
A	0.8978	0.8263	0.8778	0.8567	0.8674	0.8620	0.8647

have made use of much more diverse input data sets. For example, Rogova's (1994) tests of the evidential reasoning consensus algorithm for "character recognition" were based on the combination of results produced by neural networks with different topologies, learning algorithms, and training data.

7.2.2.1 Implications for the Evidential Reasoning Algorithm

The evidential reasoning consensus results presented here validate the contention that orthogonal summation of evidence is a useful means for the classification of satellite imagery. The only differences between the generally strong evidential reasoning consensus executions presented here and the poor evidential reasoning classifications presented in Chapter 5 are related to the initial measurement of evidence; the former tests used neural network output activations as measures of evidence, while the latter tests calculated evidence as a function of the proportions of class training data that contain the image values being classified (note: the evidential reasoning programs used for both groups of classifications are identical, except for file-reading and initial data processing routines). Thus, the results presented in this section and in Chapter 5 suggest that the latter method for calculating initial evidence values is not useful for the calculation of evidence, at least for classifications involving geological classes such as those involved in this research. It is clear that the evidential reasoning algorithm itself is applicable for image classification, as long as useful measures of evidence are available.

7.3 Confidence Images

Some classification algorithms use specific measures to estimate the "confidence"

with which individual class labellings are performed. For example, in the use of the evidential reasoning classifier, information on the nature and probable success of a classification can be obtained through examination of the evidential mass allocated to particular class propositions (the *support*), the evidential mass allocated to contradictory class propositions (the *plausibility*), and the evidential mass allocated to the set of all classes (θ, or the *uncertainty*) (Section 3.3.1). The magnitudes of each of these three variables can be used to produce images whose values reflect on the confidence with which labelling decisions were made (e.g., Moon, 1990; Richards, 1993). Such images could be of value when evaluating or interpreting classified images. Shahshahani and Landgrebe (1994) similarly generated probability maps for the EM (expectation maximization) algorithm by gray coding the Mahalanobis distance of each pixel for the class to which it was classified.

In this section, two simple measures of classification confidence are proposed to accompany the generation of individual neural network image classifications. The first measure of confidence is the magnitude of the highest output activation in an output vector. The second measure of confidence is the difference between the highest output activation and the next-highest output activation. Clearly, the two error measures are not independent, since relatively large measures of the highest output activation will tend to be associated with relatively large measures of the difference between the two highest activations. These measures were derived intuitively, based on the concept that the confidence associated with pixel classifications should in part be related to the magnitude of and separation between the greatest output activations. This intuitive concept is shown below to have a valid empirical basis. This author is not the first to have proposed these measures of classification confidence

(e.g., see Wan, 1990, p.303).

7.3.1 Methodology

Investigations into the validity of the use of the two proposed measures of confidence were performed using the *C6* training and test databases of the Melville Island Field Area (Section 5.2.2). A modified version of the main neural network classification module (*FEED9E.C*: Appendix C) was used to calculate the two measures of confidence for all test pixels in the *C6* Series. These measures were plotted against the success of the corresponding classifications (i.e., whether or not the selected class label matched the known class label), in order to determine if there is a useful and consistent relation between these parameters. Sample confidence images were generated for the first of the 10 individual neural network classifications involved in the *C6* training and test databases (i.e., the *C6N1* execution), using each of the proposed measures of confidence.

7.3.2 Results

Plots of the highest output activations versus classification success are given in Figure 7.2. The differences between highest and next-highest output activations are plotted against classification success in Figure 7.3. Activation values in both figures are normalized with respect to all corresponding output activations. It is clear in both sets of plots that there is a useful and consistent relation between the proposed confidence measures and classification success. That is, higher measures of confidence are associated with higher "likelihoods" of classification success. Differences between highest and next-highest output activations are

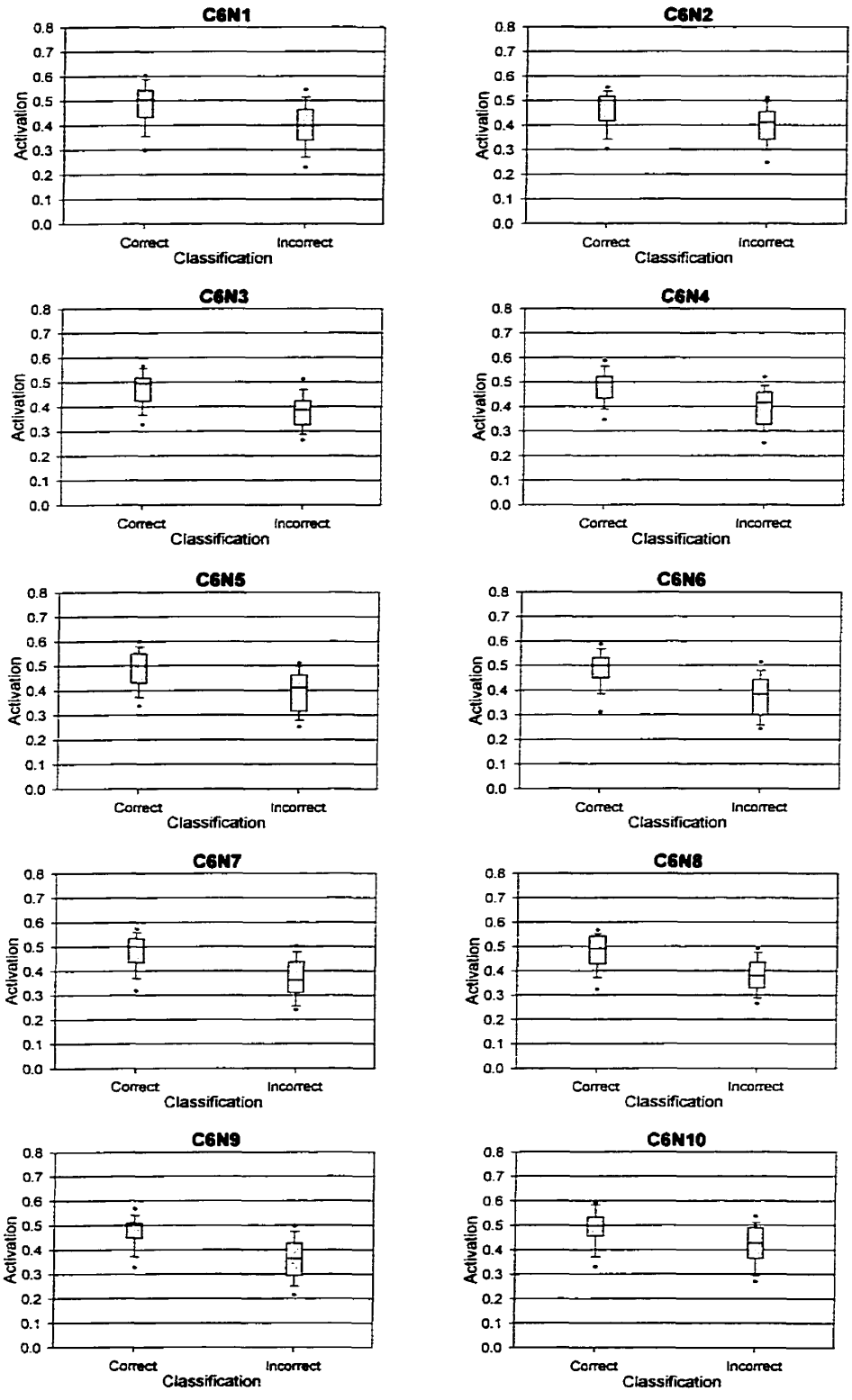

Figure 7.2 Box-plots showing the association between neural network classification success and highest output activations. Box-plots are given for each of the 10 individual neural network executions of the *C6* Series. Activations are normalized with respect to all output activations.

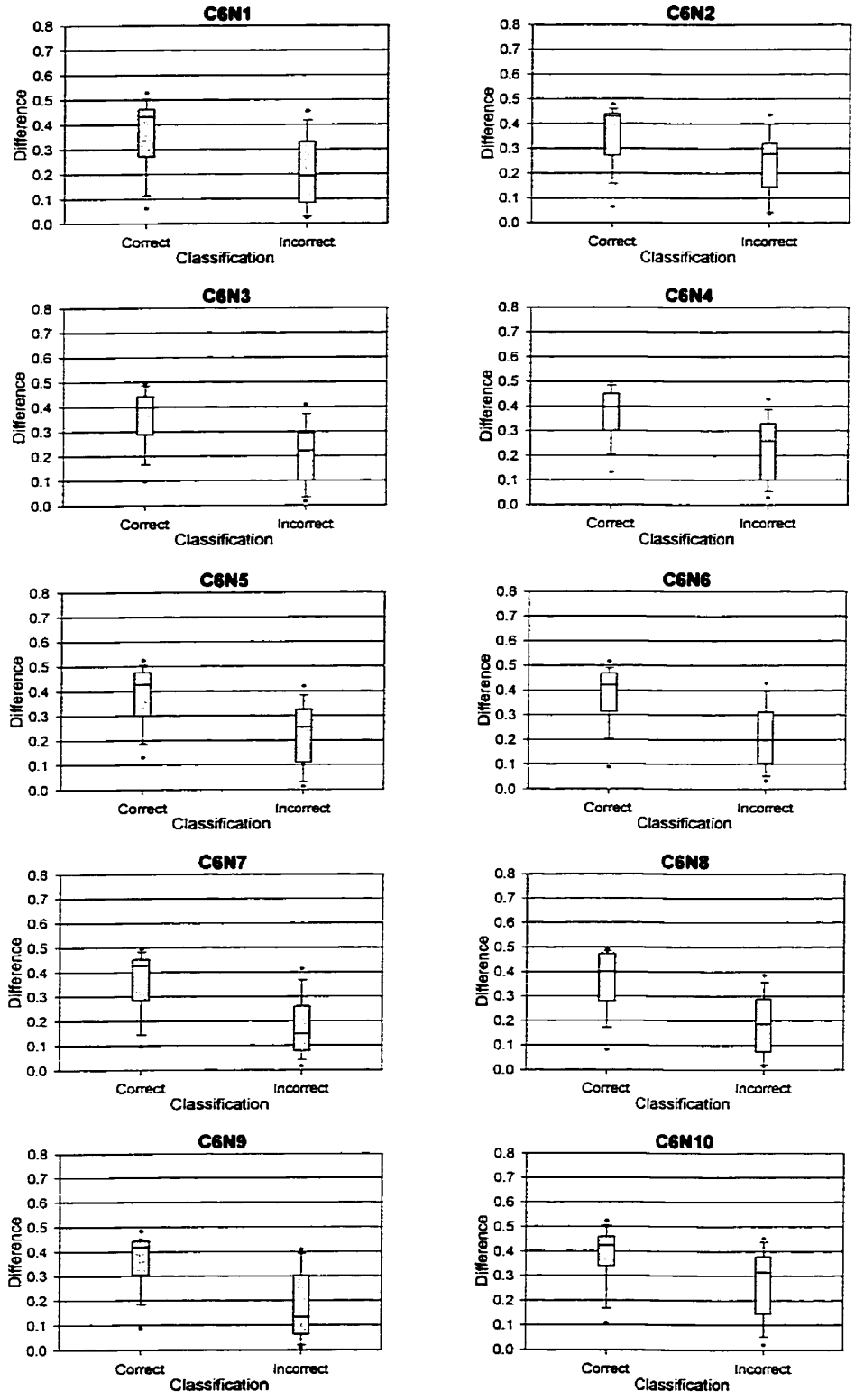

Figure 7.3 Box-plots showing the association between neural network classification success and differences between highest and next-highest output activations. Box-plots are given for each of the 10 individual neural network executions of the *C6* Series. Differences are normalized with respect to all output activations.

in particular a useful measure of confidence, given the generally good separation between the distributions of test pixels (the 25th percentile of correct classifications generally coincides with the 75th percentile of incorrect classifications for all 10 neural network classifications) (Figure 7.3).

Sample confidence images, generated for the first of the 10 individual neural network classifications involved in the *C6* training and test databases (i.e., the *C6N1* execution), are given in Figures 7.4 and 7.5. These images, which are highly correlated, show the spatial distribution of confidence over the Melville Island Field Area as determined from neural network output activations. Figure 7.5 is considered to be the most useful of the two images, given the slightly better separations shown in Figure 7.3 versus Figure 7.2. The highest confidence in Figure 7.5 is generally assigned to the green vegetation class, as well as to good exposures of the Bjorn Formation. Somewhat lower (but still high) confidence is assigned to well-discriminated geological units, including the Assistance Formation, the pink unit of the Canyon Fiord Formation, and portions of the main red-weathering unit of the Canyon Fiord Formation. The lowest confidence values are associated with exposed geological materials to the north (none of which are represented in the training dataset) as well as portions of the Trold Fiord, Great Bear Cape, and other formations.

The value of a confidence image is debatable, given that a measure of the confidence associated with classified images can be obtained simply through the generation of error matrices using test pixels (and, in the process, calculating producer's and user's percentages for each class - see, e.g., Lillesand and Kiefer, 1994). Thus, perhaps the principal value of a confidence image such as that given in Figure 7.5 is that it can provide a relative measure

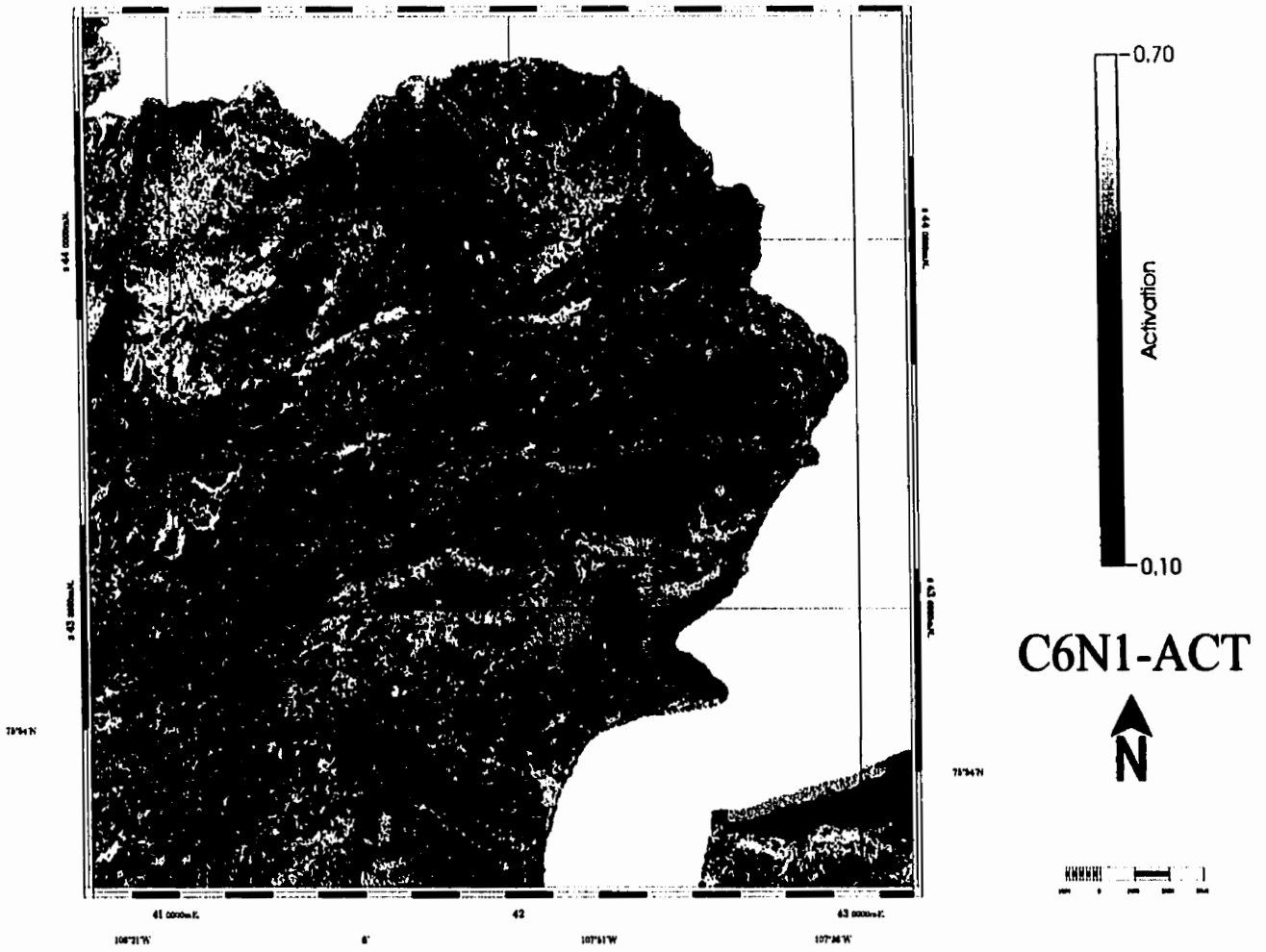

Figure 7.4 An image that gives the greatest output activations for the *C6N1* neural network execution (activations are normalized with respectt o all outputa ctivations). This type of image may be useful as a "confidence" image for individual neural network classifications,s ince higher activations are generally associated with a greater likelihood of classification success (Figure 7.2).

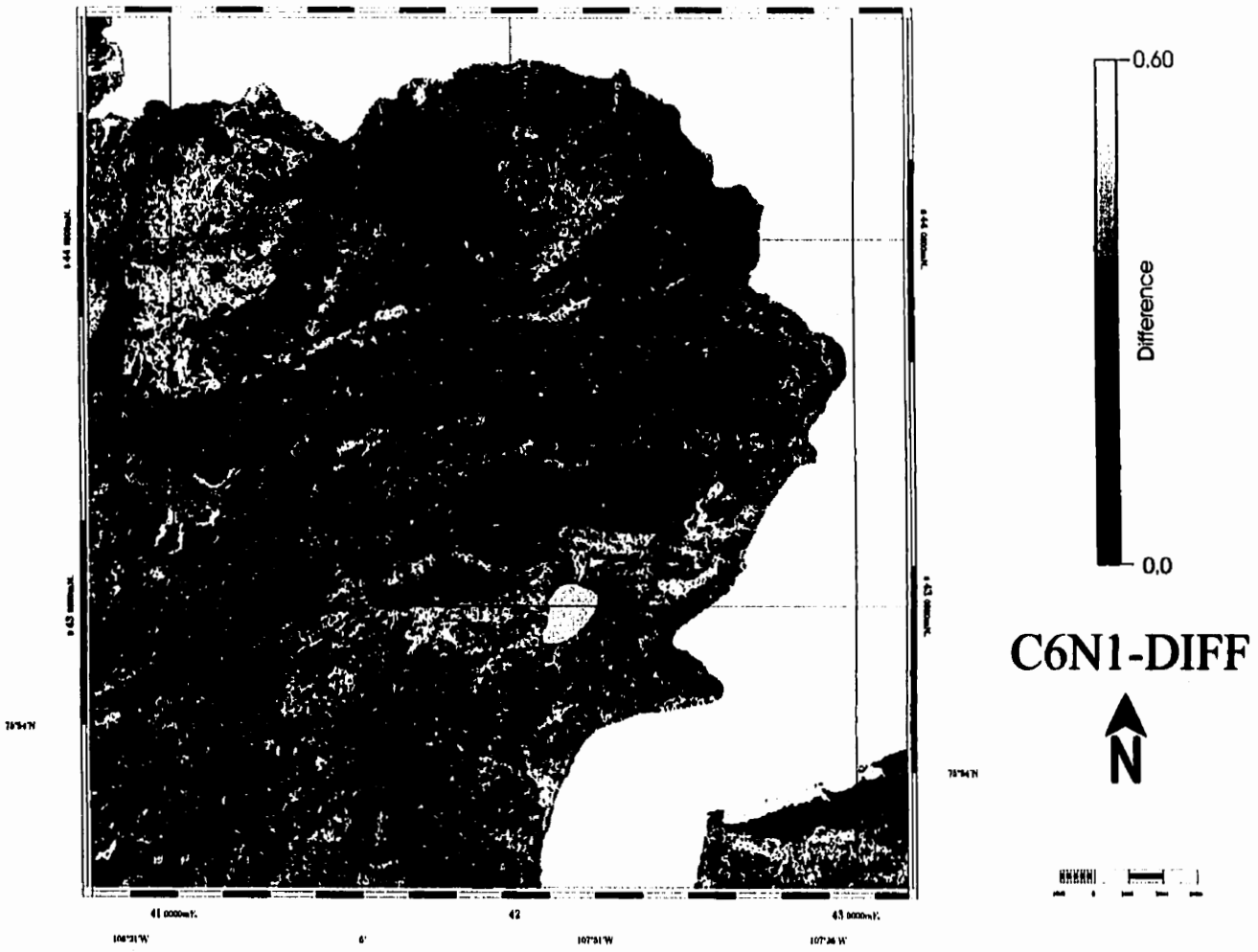

Figure 7.5 An image that gives the difference between highest and next-highest output activations for the *C6N1* neural network execution (differences are normalized with respect to all output activations). This type of image may be useful as a "confidence" image for individual neural network classifications,s ince greater differences are more often associated with correct classifications,a nd smallerd ifferences are more often associated with incorrect classifications (Figure 7.3).

of classification confidence without the need to evaluate test pixels [although the evaluation of test pixels could not only provide key class-specific information on classification success (and thus classification confidence), but could also conceivably calibrate confidence images with respect to the likelihood of classification success].

It is important to note that the value of the confidence images is limited by the quality and representativeness of the training database. For example, the shadowed portion of the large exposure of the Blue Fiord Formation (in the southeast portion of the region) is associated with relatively high confidence, but, because it was not represented in the training database, was consistently misclassified as water in all tests presented in Chapter 5. [Note further that because such a distinct mismatch between high confidence and error can occur, it is arguable that the term "confidence" as used in this chapter should be replaced by a term such as "distinctiveness". Thus, the term "confidence measure" might be replaced by "distinctiveness index", to avoid the casual use of a statistically meaningful term ("confidence"), and to make clear to any analyst using the data that image values are simply measures of the absolute or relative magnitude of output activations (and thus are indirect measures of the spectral "distinctiveness" of a given class assignment)].

7.4 Chapter Summary

Typical neural network classification decisions are based on simple majority votes of output activations. The magnitudes (both absolute and relative) of output activations are usually not considered in such classification decisions. Although this is a valid use of output activations that can produce worthwhile results (Chapter 5), the activations of output nodes

provide useful information beyond that used in majority-vote classifications, and this information may be useful in the combination of neural network results, and in the generation of confidence images.

Tests involving the consensus of neural network classifications by orthogonal summation, performed by treating output activations as measures of evidence, produced results that were found to be slightly worse than those produced by the majority-vote consensus algorithm (Chapter 5). This, along with the neural network results of Chapter 5, suggests that the individual neural network results used here are not sufficiently error-independent for the generation of consensus results that are superior to component results. This is likely related to the fact that the only differences between the individual neural network executions used here were related to weight initializations. Although the evidential reasoning consensus results presented in this chapter are not superior to those generated by majority-vote consensus, they clearly show that the evidential reasoning algorithm tested in Chapter 5 is a valid algorithm for classification of satellite imagery, as long as it is given good initial measures of evidence.

Useful measures of classification confidence can be generated from output activations. Plots of highest activations versus classification success, and differences in the two highest activations versus classification success, suggest that there is a good empirical basis for the use of these particular measures of confidence in the classification of satellite images. Relative assignments of confidence in two confidence images for the Melville Island Field Area were found to be generally consistent with the class-specific successes of neural network classifications presented in Chapter 5. This method could conceivably be adapted for use with

consensus algorithms by, e.g., averaging individual confidence images.

8 A VISUAL EVALUATION OF RADARSAT, LANDSAT TM, AND IKONOS IMAGERY FOR DISCRIMINATING LITHOLOGY

8.1 Introduction

Although automated or semi-automated techniques (such as image classification and spectral mixture modelling) can be useful for the generation of geological information from satellite images, a considerable amount of geological information can also be produced through direct visual analysis of satellite images. As noted in Section 2.5.4, geological information produced through the methods of visual analysis can be superior to that produced using other techniques, since these methods allow for the use of visual cues such as size, shape, pattern, and context to refine the quality of geological information derived from images; such cues are usually not taken into account in per-pixel classification, for example (Rivard, 1996; Costa *et al.*, 1998).

The potential utility of radar imagery in the discrimination and mapping of lithology and other geological parameters is significant, particularly when radar imagery is analysed visually (Costa *et al.*, 1998; Adam *et al.*, 1998; Shimabukuro *et al.*, 1998) (Sections 2.3.2.4 and 2.4.2), and much work continues to be focussed on evaluating the applicability of radar imagery toward geological study (e.g., Metternicht and Zinck, 1998; Paradella *et al.*, 1998; Simms and Bell, 1998; Arkin *et al.*, 1999; Rivard *et al.*, 1999; Robinson *et al.*, 1999; Sharma *et al.*, 1999; Smith *et al.*, 1999; Haack *et al.*, 2000; Lepage *et al.*, 2000) (Section 2.3.2.4). Imagery produced by the recently-launched IKONOS sensor also has considerable potential as a visual source of geological information. Although IKONOS imagery has a relatively

poor spectral resolution (Section 2.4.3), its unprecedented 1 m pixel spacing promises to advance terrestrial remote sensing by providing digital high-resolution views of surface materials from earth orbit.

In this chapter, in an effort to build on previous research regarding the application of radar imagery for lithological discrimination, Radarsat images are evaluated and compared with Landsat TM images with regard to their value in discriminating lithological units in selected regions of the Melville Island and Cape Smith Belt study areas (Landsat TM imagery has been widely used by the remote sensing community for more than 15 years, and thus is a useful standard against which newer types of imagery may be evaluated). In addition, as one of the first evaluations of IKONOS imagery, panchromatic and multispectral IKONOS images are evaluated in this chapter for a 4 by 10 km region of the Melville Island Field Area. General information on the Radarsat, Landsat TM, and IKONOS sensors is given in Section 2.4. The Landsat TM and Radarsat images used in this research are described in Sections 4.2.8 and 4.3.9, respectively. The two study areas are described in Chapter 4.

8.2 Methodology

Two regions of interest were selected for the Melville Island study area: 1) the Tingmisut Lake region; and 2) the Weatherall Bay region (Figure 8.1a). One region of interest was chosen for the Cape Smith Belt study area: the Lac Watts region (Figure 8.1b). All three regions were selected based on: 1) satellite-image coverage; 2) availability of ground-truth information; and 3) the presence and diversity of geological features of interest.

For each of the regions, Landsat TM and Radarsat images were evaluated with regard

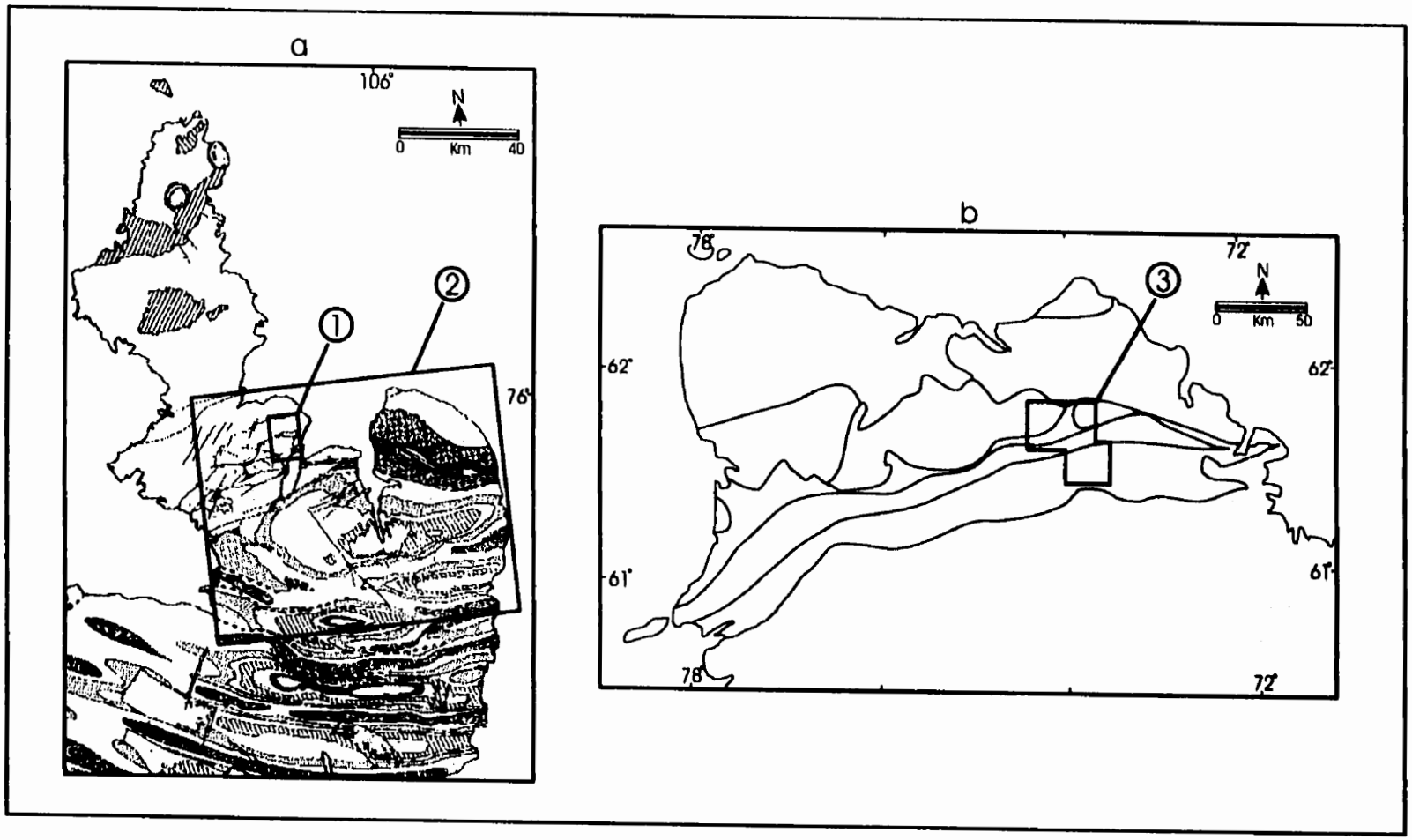

Figure 8.1 Outlines of the three regions used in the visual evaluation of satellite images; outlines are overlain on simplified geological maps of eastern Melville Island ("a"; from Figure 4.3) and the Cape Smith Belt ("b"; from Figure 4.12): 1) Tingmisut Lake Region; 2) Weatherall Bay Region; and 3) Lac Watts Region.

to their visual information content regarding the nature and extent of exposed lithological units. IKONOS imagery was also evaluated for the Tingmisut Lake region on Melville Island. In this exercise, emphasis was placed on areas visited and sampled in the course of this research (see Sections 4.2.7 and 4.3.8, respectively). Evaluations associated with other areas are necessarily more limited, and were based on consultation with aerial photographs and relevant sources of geological information.

8.3 Results

The results of the evaluation of Radarsat, TM, and IKONOS images are presented below for the Tingmisut Lake, Weatherall Bay, and Lac Watts regions.

8.3.1 Tingmisut Lake Region (Melville Island)

The Tingmisut Lake region (Figure 8.2) is 10 by 14 km in dimension and is located in the central portion of the Melville Island Field Area (Section 4.2.7). Geological materials exposed at the surface are mainly late-Paleozoic north-dipping clastic and carbonate sequences of the Sverdrup basin, although Ordovician dolostones (the Tingmisut Inlier) and a Cretaceous gabbro dike are also present (Figure 8.2; Table 4.1). Geological materials and vegetation cover in the region are documented in Section 4.2.7.1; an overview of this information, with reference to aerial photographs of the region, is given below.

A mosaic of four panchromatic aerial photographs of the Tingmisut Lake region is given in Figure 8.3. The aerial photographs were acquired in 1959 from an altitude of about 9850 m (30000 ft), with solar illumination from the northwest. In the mosaic, three

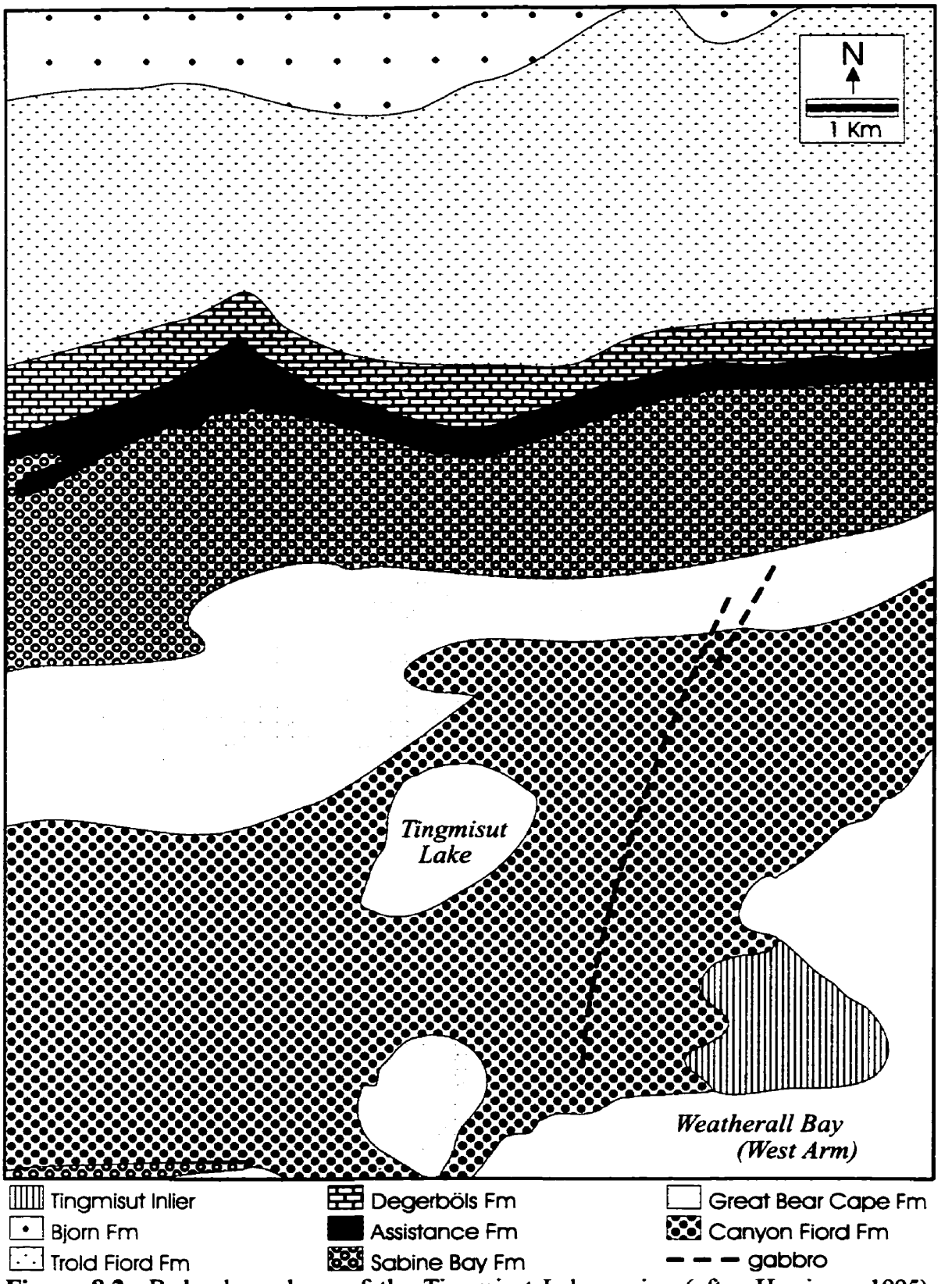

Figure 8.2 Bedrock geology of the Tingmisut Lake region (after Harrison, 1995). Geological units are described in Table 4.1.

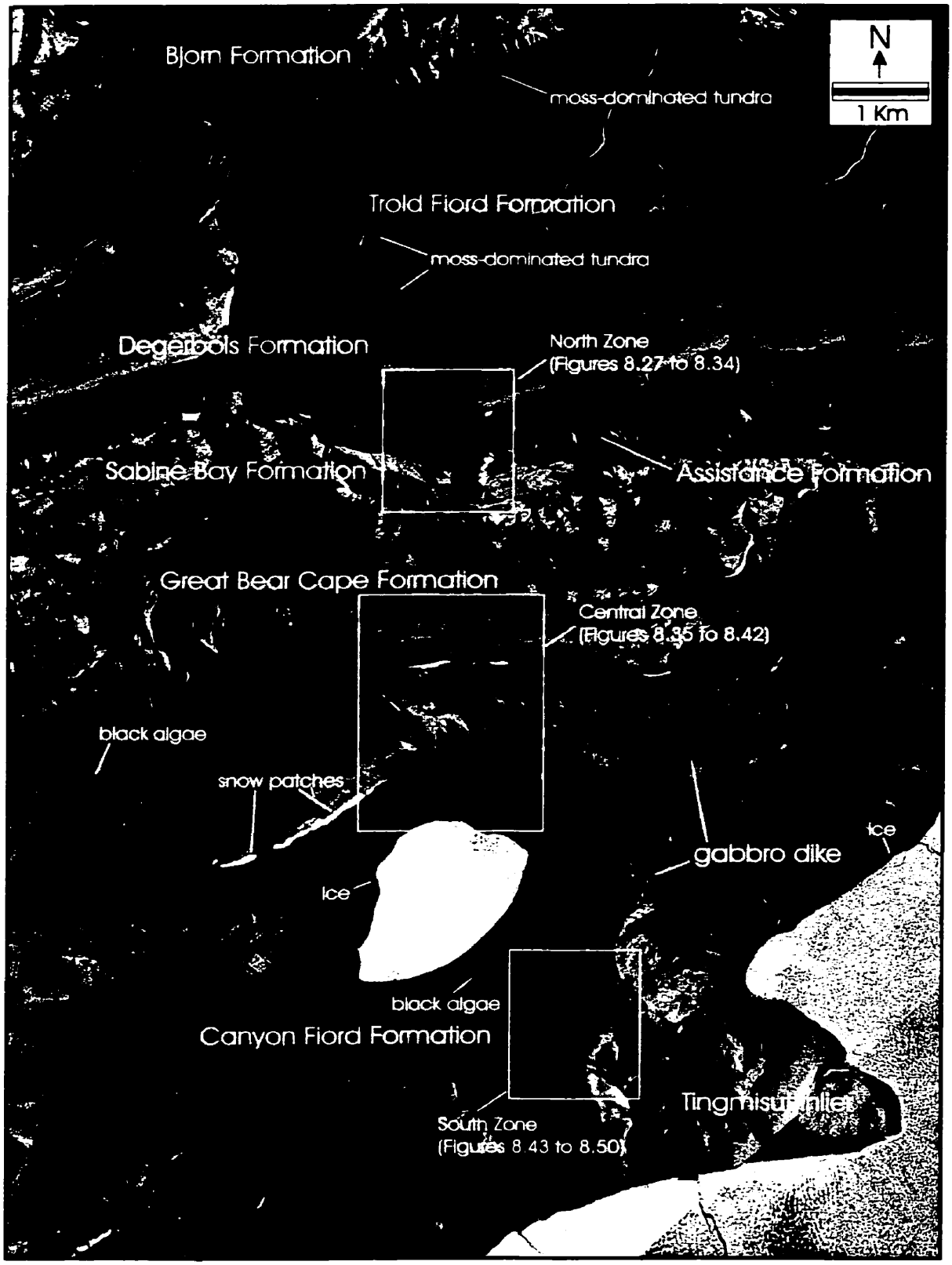

Figure 8.3 Mosaic of aerial photographs of the Tingmisut Lake region (photographs A16763-53, -54, -55, and -93). Illumination is from the northeast.

prominent east-west striking ridge-forming units are visible: 1) the Great Bear Cape Formation limestone unit; 2) the Degerböls Formation limestone unit; and 3) the Bjorn Formation sandstone unit. These units form the main ridges of the cuesta landforms that dominate the local landscape. Two additional ridge- and hill-forming units include the gabbro dyke and the Tingmisut Inlier dolostone unit (Figure 8.3). Between the ridge-forming units are less-resistant units, including the Trold Fiord Formation sandstone, the Assistance Formation mudstone, the Sabine Bay Formation sandstone, and the Canyon Fiord Formation sandstone. Because the aerial photographs were acquired relatively early in the summer season, the surfaces of both Tingmisut Lake and Weatherall Bay are covered with ice in the mosaic of aerial photographs (Figure 8.3).

Vegetation cover in the Tingmisut Lake region is generally low. The surfaces of most geological units are sparsely vegetated by variably-spaced patches (typically 10 to 30 cm across) of *Saxifraga oppositifolia* (purple saxifrage). Areas of significant vegetation cover (consisting mainly of dense accumulations of either black algae or diverse moss-dominated tundra communities) are more common in the northern half of the region, and are generally associated with dark tones in the mosaic of aerial photographs (Figure 8.3).

8.3.1.1 Landsat TM Image

Landsat TM colour composites for the Tingmisut Lake region are given in Figure 8.4 (channels 321:RGB; true colour), Figure 8.5 (channels 543:RGB), and Figure 8.6 (channels 754:RGB). Because the Landsat image was acquired late in the summer season (August 8, 1994), there is no ice cover on Tingmisut Lake in the images, and the portion of Weatherall

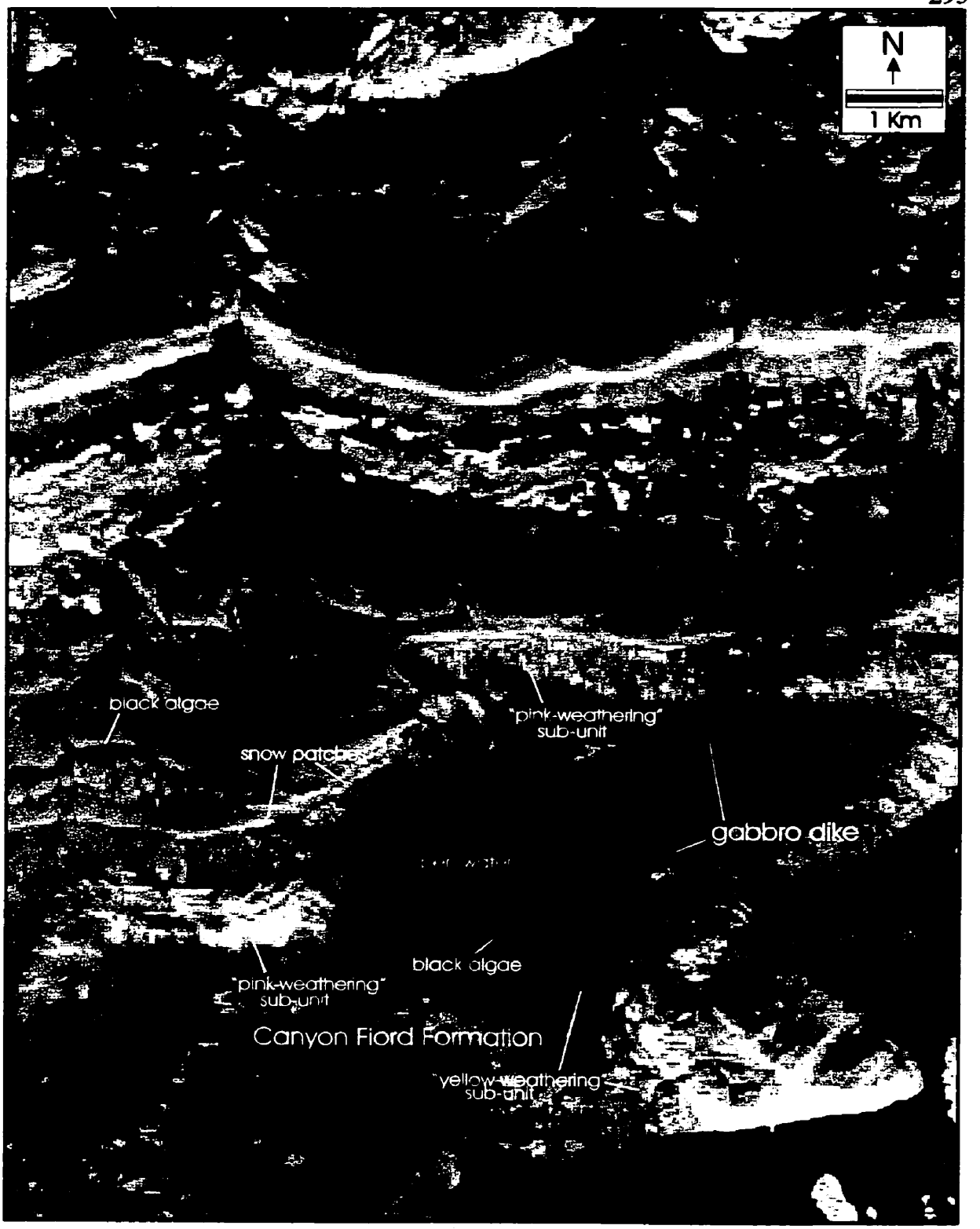

Figure 8.4 TM colour composite (channels 321:RGB; true colour) for the Tingmisut Lake region. Illumination is from the south.

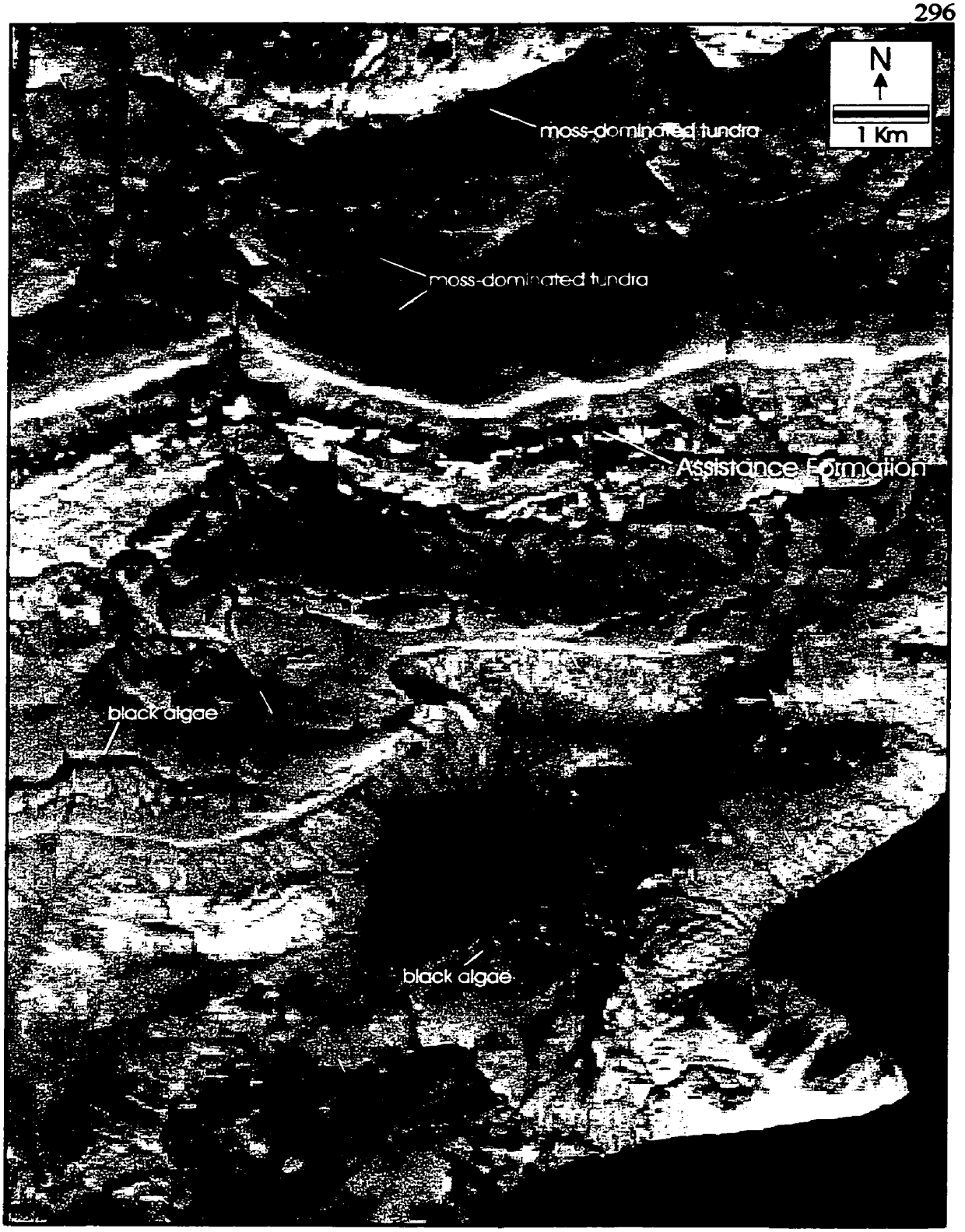

Figure 8.5 TM colour composite (channels 543:RGB) for the Tingmisut Lake region. Illumination is from the south.

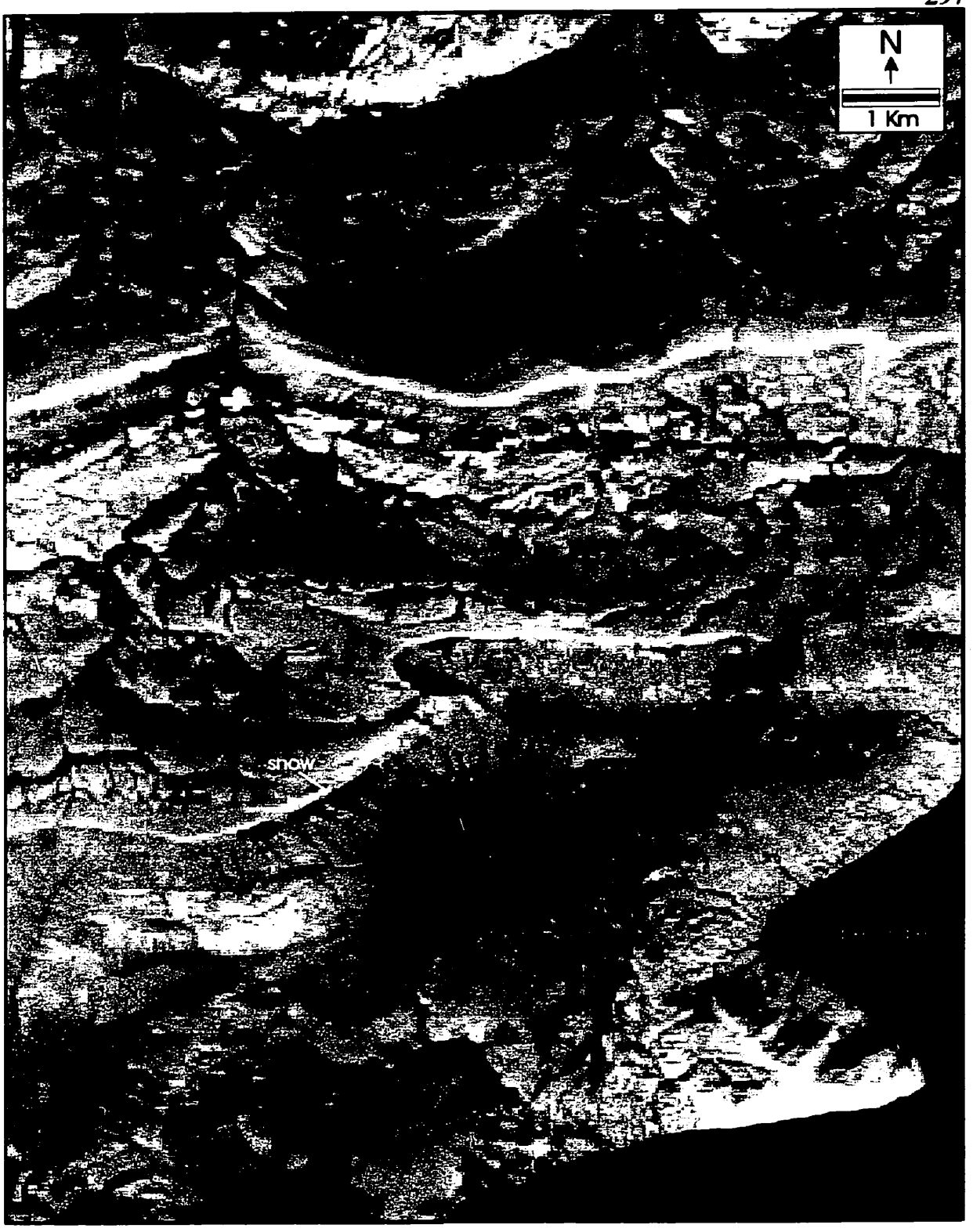

Figure 8.6 TM colour composite (channels 754:RGB) for the Tingmisut Lake region. Illumination is from the south.

Bay within the Tingmisut Lake region is mainly ice free. Solar illumination is from the south, and pixel spacing is 30 m. Contrast was enhanced in the TM images using linear histogram stretches.

Using the TM imagery, open water can be easily discriminated from other materials by its characteristically low reflectance in the visible (Figure 8.4) and negligible reflectance in the mid-infrared (Figure 8.6). Snow patches and sea ice are easily discriminated from other materials by their high reflectance in the visible (Figure 8.4) and very low reflectance in the mid-infrared (Figure 8.6). Areas of dense moss and broadleaf vegetation cover are well discriminated in the TM images, based on their characteristically high reflectance in the near-infrared and low reflectance in the red portion of the visible spectrum (vegetated areas are shown in shades of green in Figure 8.5).

Canyon Fiord Formation clastic materials, which are characterized by relatively high reflectance in the red portion of the spectrum and relatively low reflectance in the blue and green portions (presumably a result of the presence of iron oxides on exposed surfaces; see Drury, 1993, p.8), are easily discriminated from other materials in the region (Canyon Fiord Formation materials are shown in shades of brown in Figure 8.4). The TM image can be used to further discriminate the pink sub-unit of the Canyon Fiord Formation (shown in very light shades of brown in Figure 8.4). The yellow sub-unit (yellow-coloured fines which are often associated with heterolithic pebble-sized clasts; Table 5.1) of the Canyon Fiord Formation is not easily recognized visually, probably because exposures of this sub-unit are generally smaller than the TM pixel size (typically resulting in mixed pixels with other Canyon Fiord Formation materials) (Figure 8.4). The low reflectance of the gabbro dike in the visible

portion of the spectrum (Figure 8.4) causes it to contrast well with the surrounding Canyon Fiord Formation materials. The mudstones of the Assistance Formation are well discriminated using the red-to-mid-infrared channels (shown in shades of red and pink in Figure 8.5).

The generally greater reflectance, in all three TM colour composites, of the materials of the Sabine Bay, Degerböls, and Bjorn formations aids in their visual discrimination from darker units (e.g., Great Bear Cape and Trold Fiord formations). These units cannot be discriminated from each other based strictly on their spectral properties, using the TM images.

8.3.1.2 Radarsat Image

The Radarsat image of the Tingmisut Lake region is given in Figure 8.7. This image was acquired from the west-southwest, preferentially illuminating slopes oriented toward this direction. Because the Radarsat image was acquired in the middle of the brief summer season (July 17, 1998), the surfaces of Tingmisut Lake and Weatherall Bay are mostly covered by ice in the image. Speckle was reduced in the image by filtering original data using a 7 x 7 Lee filter. The image has a pixel spacing of 12.5 m. Contrast was enhanced in the Radarsat image using a linear histogram stretch.

Open water, which is associated with very low values in the Radarsat image, is easily discriminated from geological and ice classes in the region (Figure 8.7) (recall that water bodies act as specular reflectors under calm conditions - Section 2.3.2.2). Sea and lake ice are associated with low to moderate image values in the Radarsat image. Although lake ice is sometimes associated with lower image values compared to sea ice (Ulaby *et al.*, 1982,

Figure 8.7 Radarsat image of the Tingmisut Lake region. Radar illumination is from the southwest.

p.910), these two ice types are not visually distinguishable from each other in the Radarsat image; this may be due to the fact that most or all of the ice in the West Arm of Weatherall Bay is, like the ice of Tingmisut Lake, first-year ice. Sea and lake ice in the Tingmisut Lake region may generally be distinguished from land materials based on the regularity of the tonal variations of these ice classes, although because the image values and texture associated with sea and lake ice are in places similar to those associated with land materials, there is some potential for confusion between land and ice classes if additional information on shoreline positions and ice presence is not available (note, for example, that ice cover on Tingmisut Lake is associated with image values and a texture similar to those of the surrounding Canyon Fiord Formation materials).

Snow cover is associated with very low radar backscatter in the Radarsat image, making it easy to discriminate from surrounding geological materials, although without additional contextual information there is considerable potential for confusion between snow patches and open water. The snow patches in the region were in the process of melting when the Radarsat image was acquired, suggesting that the surfaces of the snow patches may have been sufficiently smooth and wet to act as specular reflectors (dry snow can typically be penetrated easily by microwave radiation, but wet snow can reflect significant amounts of incident microwave radiation, causing high or low backscatter depending on the roughness of the snow surface), or at least to significantly attenuate incident microwave radiation (see, e.g., Ulaby *et al.*, 1982; Engeset and Weydahl, 1998; Baghdadi *et al.*, 2000). A panoramic view of the immediate Tingmisut Lake area is given in Figure 8.8, showing the extent of ice, snow, and water in the area five days before acquisition of the Radarsat image (compare with

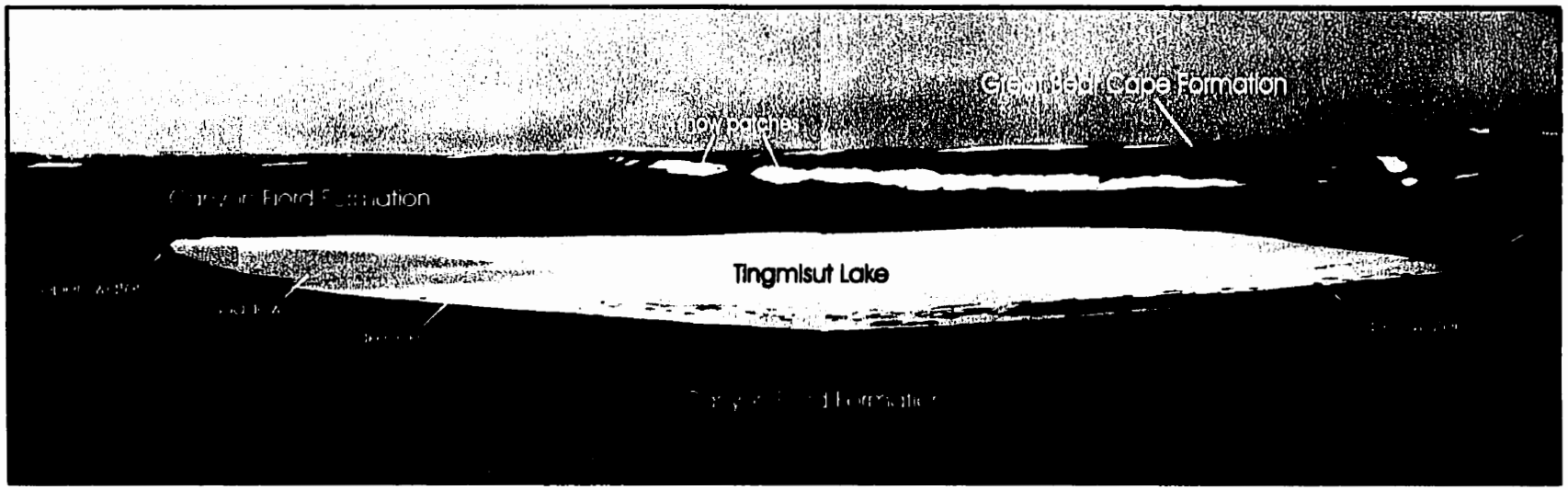

Figure 8.8 View of the immediate Tingmisut Lake area, showing the extent of ice, snow, and water five days before acquisition of the Radarsat image. View is toward the west from the mid-portion of the gabbro dike. Compare with Figure 8.7. Tingmisut Lake is about 2 km across, from left to right.

Figure 8.7).

As discussed in Section 2.3.2.4, radar can normally be used for discriminating and mapping lithological units only when there is a good correlation between lithology and the physical factors to which radar is sensitive: topography, surface roughness, and moisture. Although no geological unit in Figure 8.7 is uniquely associated with particular image values, some units stand out sufficiently well to be visually recognized. For example, the gabbro dike, which is oriented in places at relatively high angles to the look direction of the radar sensor, is well illuminated on much of its western flank and thus can be visually discriminated from the surrounding materials whose backscatter is generally lower. Although topography appears to be the main factor influencing gabbro image values, image values may also have been influenced by the sizes and shapes of gabbro materials. For example, gabbro boulders (typically up to about 50 cm across) and bedrock outcrops (which can extend for tens of metres horizontally and up to about 8 m vertically) may have acted as corner reflectors to incoming microwave radiation (Figure 8.9). Smaller, blocky gabbro materials (many of which have dimensions on the order of the radar wavelength of 5.6 cm) may in places produce radar-rough surfaces (Figure 8.9). The Canyon Fiord Formation materials that surround much of the gabbro dike are typically sand to pebble sized, producing surfaces that will appear smooth to the Radarsat sensor (see below). Coarser Canyon Fiord Formation rocks associated with small drainage gulleys and bedrock exposures may locally produce radar-rough surfaces; the larger Canyon Fiord Formation rocks are generally flat, likely reducing their contribution to surface roughness (see below).

The Tingmisut Inlier dolomite unit, like the gabbro unit, is associated with high radar

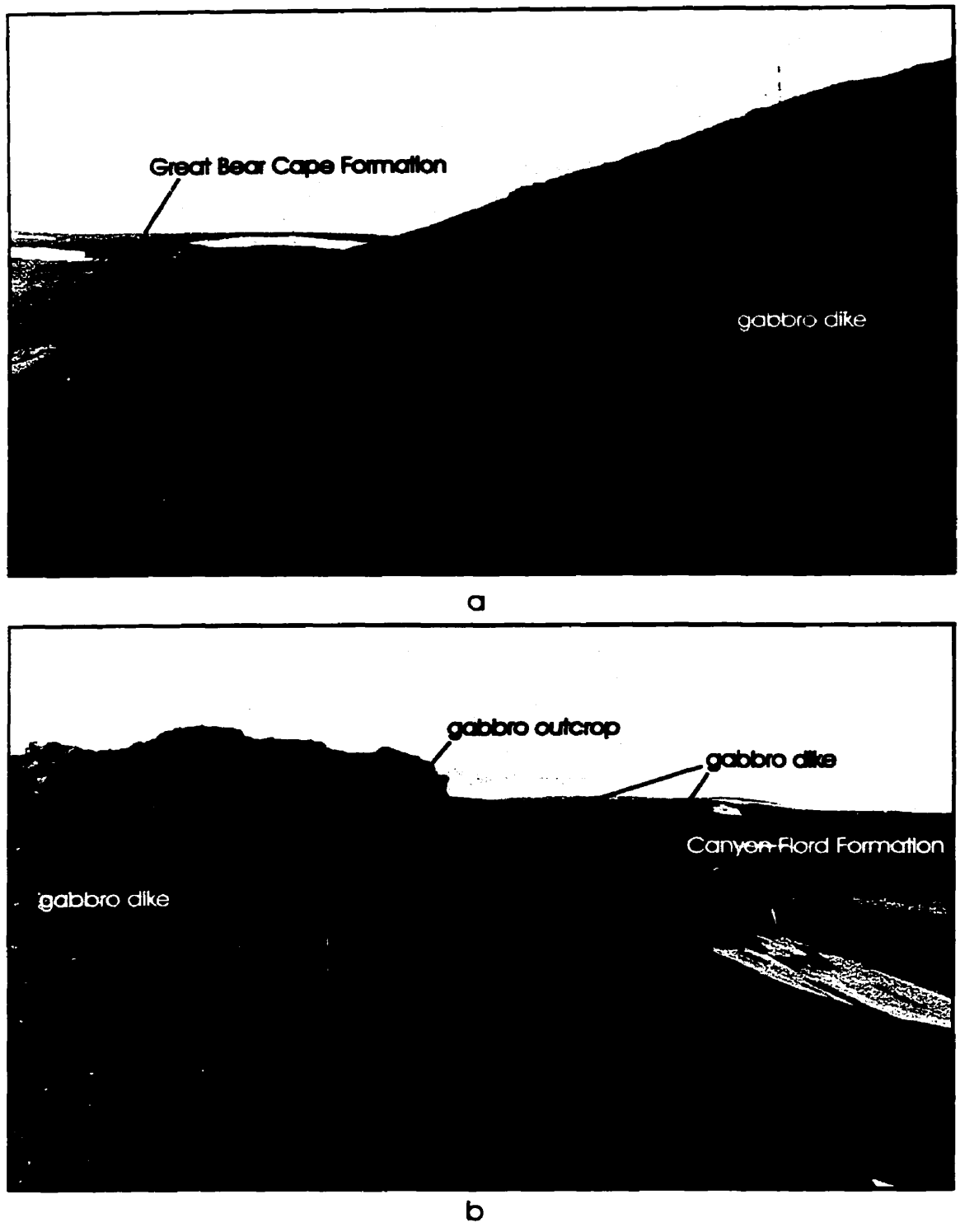

Figure 8.9 Photographs of the west ("a") and east ("b") flanks of the central portion of the gabbro dike (Site 15). Location is shown in Figure 8.7. Views are toward the north. The scale bar in both photographs is 1 m long and divided into 10 cm increments. The western flank of the gabbro ridge is well illuminated in the Radarsat image.

backscatter, making it easy to discriminate in the radar image. The high backscatter of the dolostone unit is due in large part to the favourable orientation of slopes toward the radar sensor (note that the brightest dolostone pixels are associated with south- to west-facing slopes). Radar backscatter may have been increased further because of the orientation of slopes at about 30 to 40 degrees relative to horizontal [resulting in more direct backscatter when imaging at high incidence angles such as those of the *S7* Radarsat mode (44.9° to 49.4°)] (Figure 8.10). Also, slope materials are mainly blocky dolostone rocks with dimensions close the wavelength of the radar sensor (5.6 cm), and with very little infill between clasts by fines (such materials would be expected to produce radar-rough surfaces; Figure 8.11). The faces of the large and irregularly-shaped dolostone bedrock exposures may act as corner reflectors (Figure 8.10). It is not clear why the flat and north-east facing slopes of the Tingmisut Inlier are characterized by relatively high levels of radar backscatter; this may in part be due to factors related to surface roughness (Figure 8.12) or moisture conditions.

Many geological units in the Tingmisut Lake region are not consistently related to particular levels of radar backscatter, hindering the discrimination of individual units from surrounding materials. For example, the Canyon Fiord Formation materials are associated with very low radar backscatter immediately north of Tingmisut Lake, probably due to: 1) the shallow slopes in the area; and 2) the abundance of sand- and pebble-sized fines in these locations, which produce a radar-smooth surface (Figure 8.13). Canyon Fiord Formation materials are associated with relatively high backscatter west of the gabbro dike, where the orientation of local slopes is toward the radar sensor, and where earth materials are variably

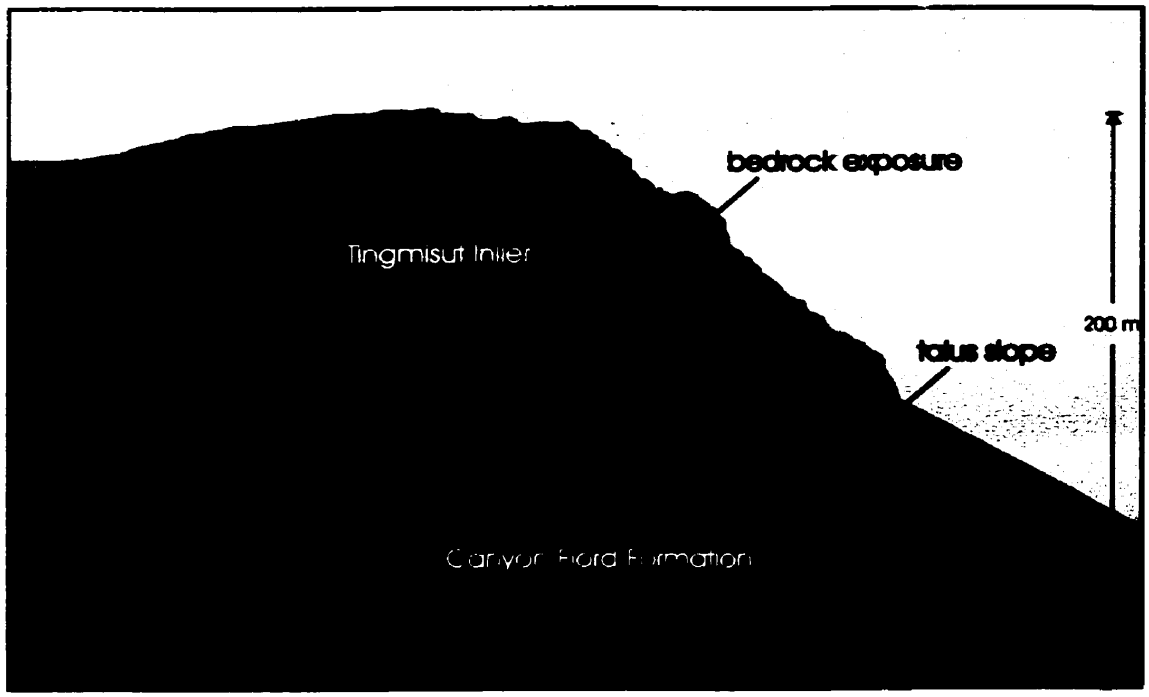

Figure 8.10 Photograph of the south slope of the Tingmisut Inlier dolostone unit. Foreground materials belong to the Canyon Fiord Formation. View is toward the northeast.

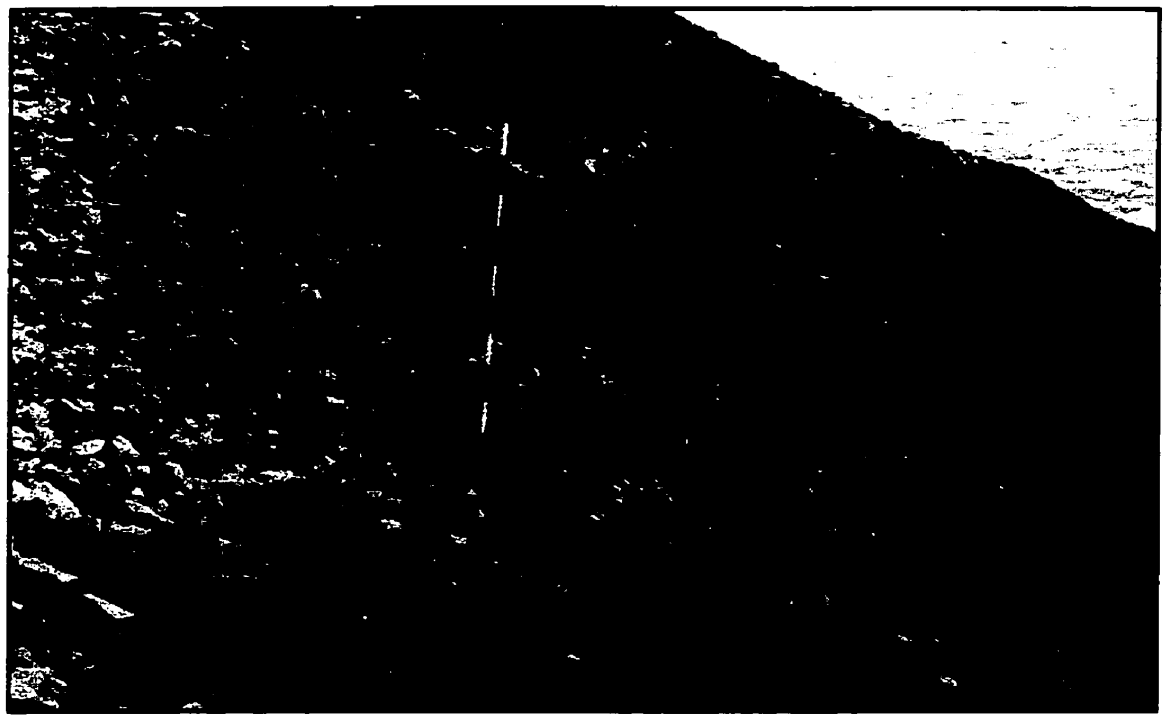

a

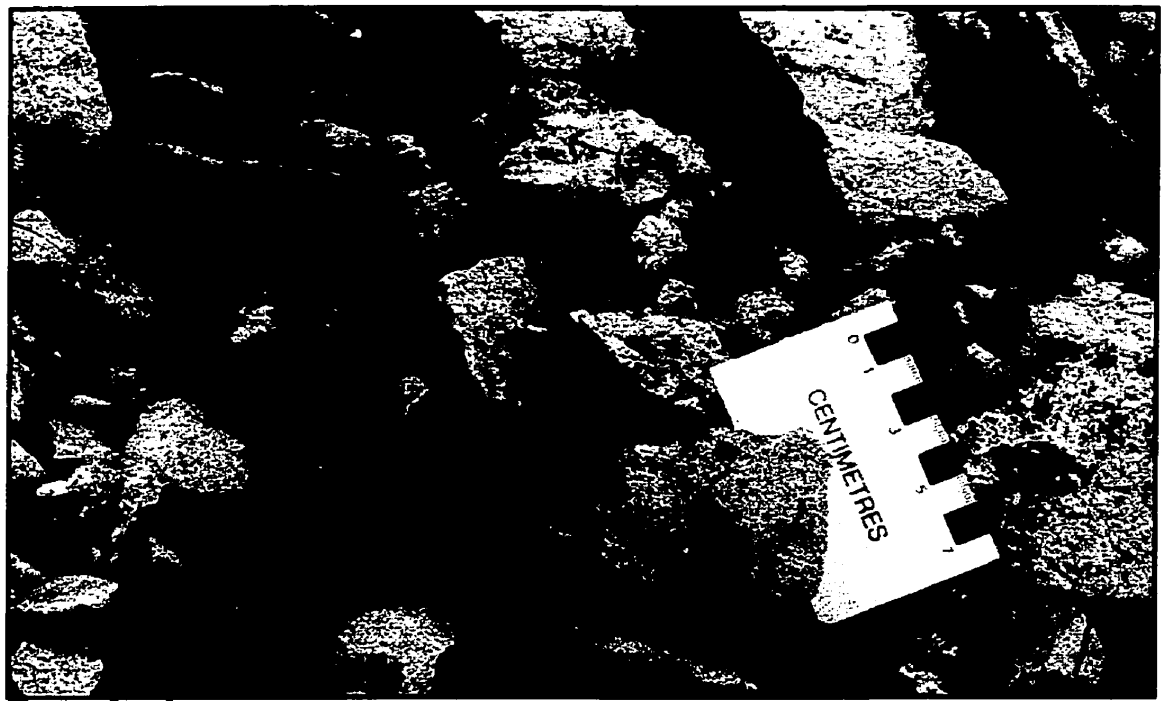

b

Figure 8.11 Photographs of talus materials of the south slope of the Tingmisut Inlier dolostone unit (Site 1). Location is shown in Figure 8.7. Scale in "a" is divided into 10 cm increments. Scale in "b" is divided into 1 cm increments.

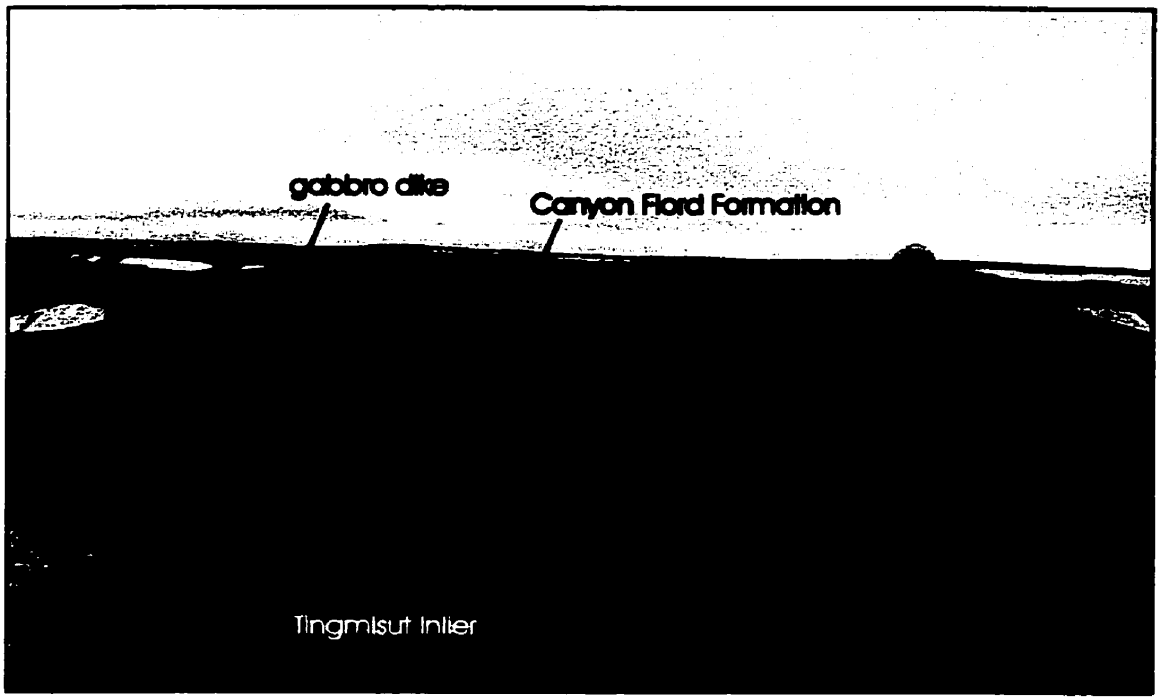

a

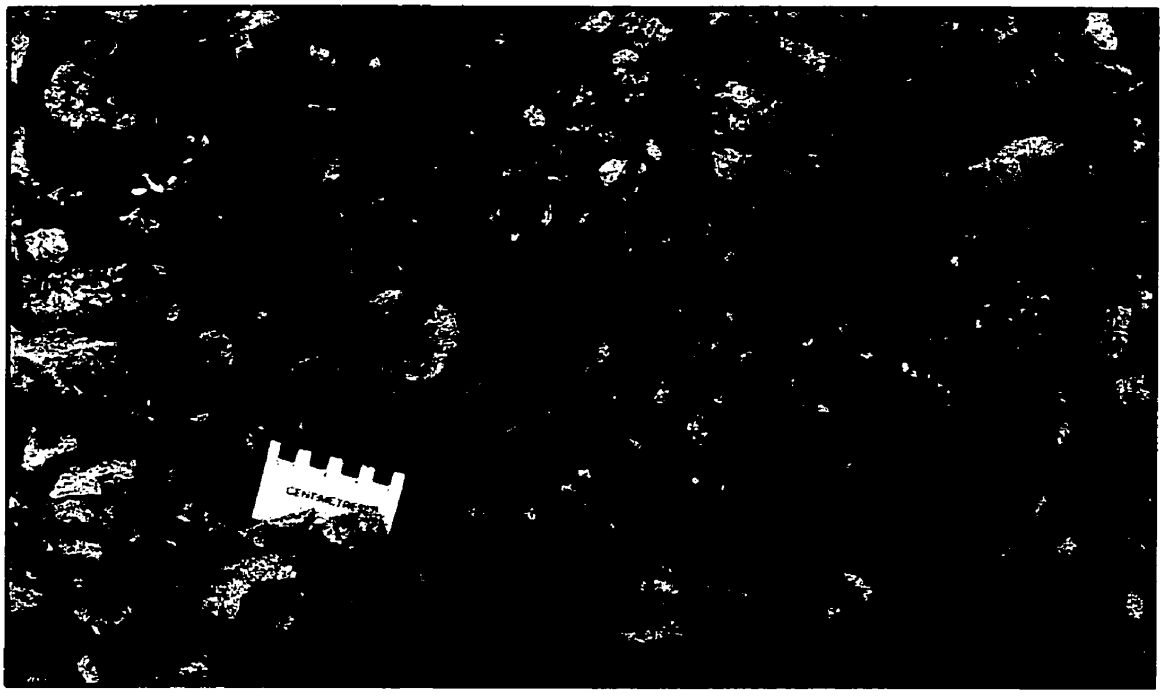

b

Figure 8.12 Photographs of dolostone materials at a location on the summit of the Tingmisut Inlier (Site 5). Location is shown in Figure 8.7. View in "a" is toward the west. Scale in "a" is 1 m long and divided into 10 cm increments. Scale in "b" is divided into 1 cm increments.

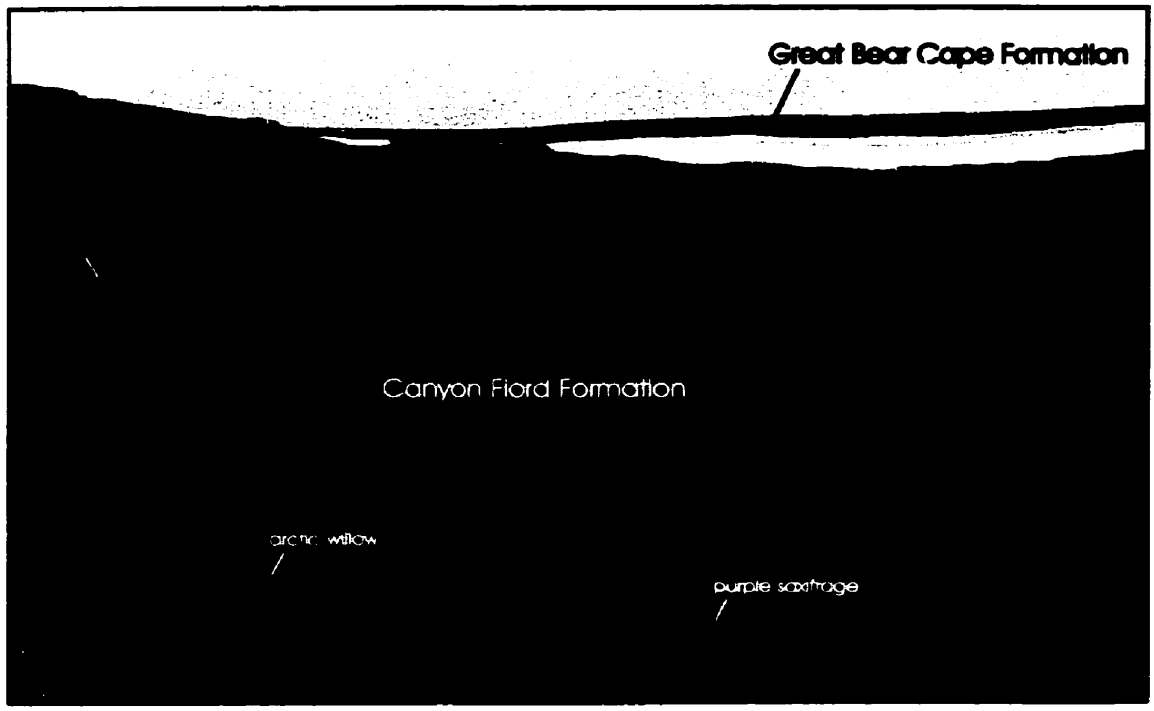

a

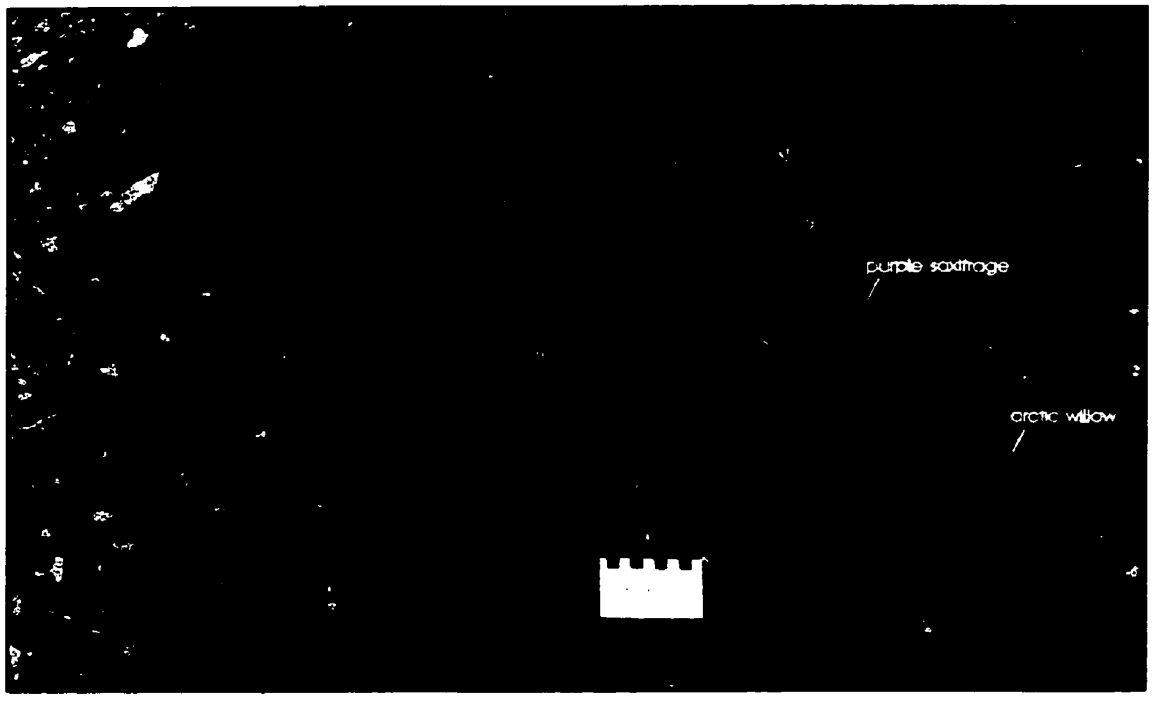

b

Figure 8.13 Photographs of small Canyon Fiord Formation materials (red-weathering calcareous sandstones and related fines) at a location north of Tingmisut Lake (Site 22). Location is shown in Figure 8.7. View in "a" is toward the north. Scale in "a" is 1 m long and divided into 10 cm increments. Scale in "b" is divided into 1 cm increments. Clast sizes shown here are typical of the smaller surficial materials of the Canyon Fiord Formation.

sized (from loose pebble-sized clasts near the summit of the ridge, to sizes between about 2 and 15 cm at lower elevations and in gulleys; Figure 8.14); localized bedrock exposures, typically several metres across and up to about one metre high, are also scattered across the slope.

Like the Canyon Fiord Formation materials, the Great Bear Cape Formation limestones are not consistently associated with particular ranges of image values. Vegetation-poor locales are typically associated with low backscatter, regardless of clast sizes (which range between about 1 and 20 cm: see Figures 8.15 and 8.16), while locations associated with southwest-oriented topography or significant amounts of moss and other vegetation cover (Figure 8.17) are associated with greater backscatter. The direct relation noted here between vegetated areas and radar backscatter is uncertain, given its seeming incompatibility with the clearly poor relation between these variables elsewhere in the region (e.g., at the Trold Fiord Formation) as well as in the Weatherall Bay region (Section 8.3.2.2).

Although the surficial materials of the Sabine Bay Formation have variable sizes (Figure 8.18), most materials of this unit are pebble-sized or smaller (Figure 8.19). A correlation between radar backscatter and clast size is not visually apparent in the Radarsat image, and most materials of the Sabine Bay Formation are associated with low backscatter. Southwest-facing slopes of large Sabine Bay Formation bedrock outcrops, which are likely good corner reflectors, are associated with high backscatter. The surficial materials of the Assistance Formation are generally small (most rocks are less than about 4 cm across; Figure 8.20), and are associated with low backscatter, even on slopes oriented at relatively high angle to the look direction. The surficial materials of the Degerböls Formation are typically

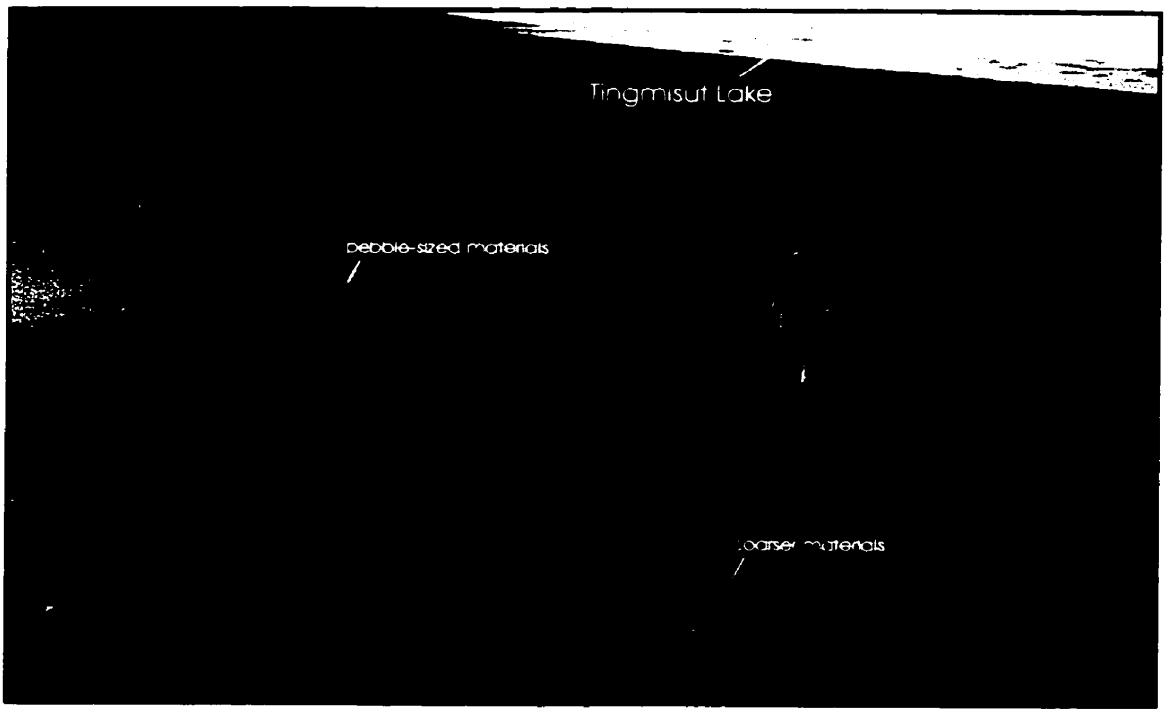

a

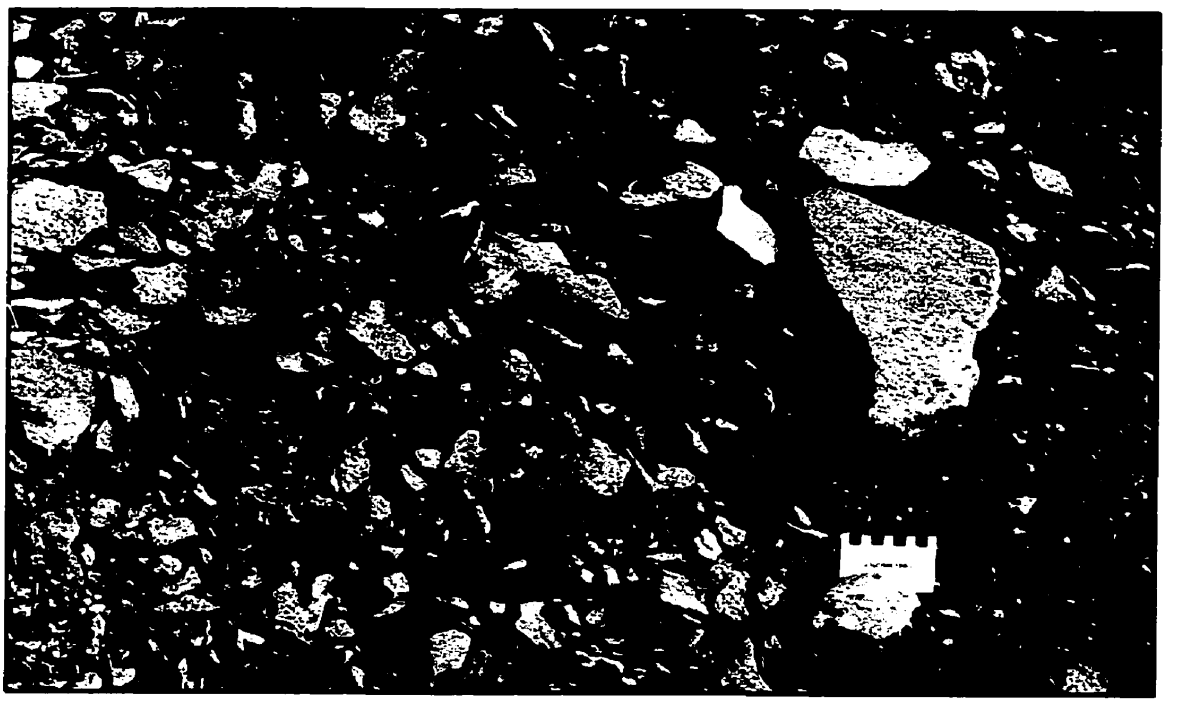

b

Figure 8.14 Photographs of large Canyon Fiord Formation materials (red-weathering calcareous sandstones and related fines) at a location west of the gabbro dike (Site 13B). Location is shown in Figure 8.7. View in "a" is toward the southwest. Scale in "a" is 1 m long and divided into 10 cm increments. Scale in "b" is divided into 1 cm increments. Clast sizes shown in the foreground of "a", and in "b", are typical of the larger surficial materials of the Canyon Fiord Formation.

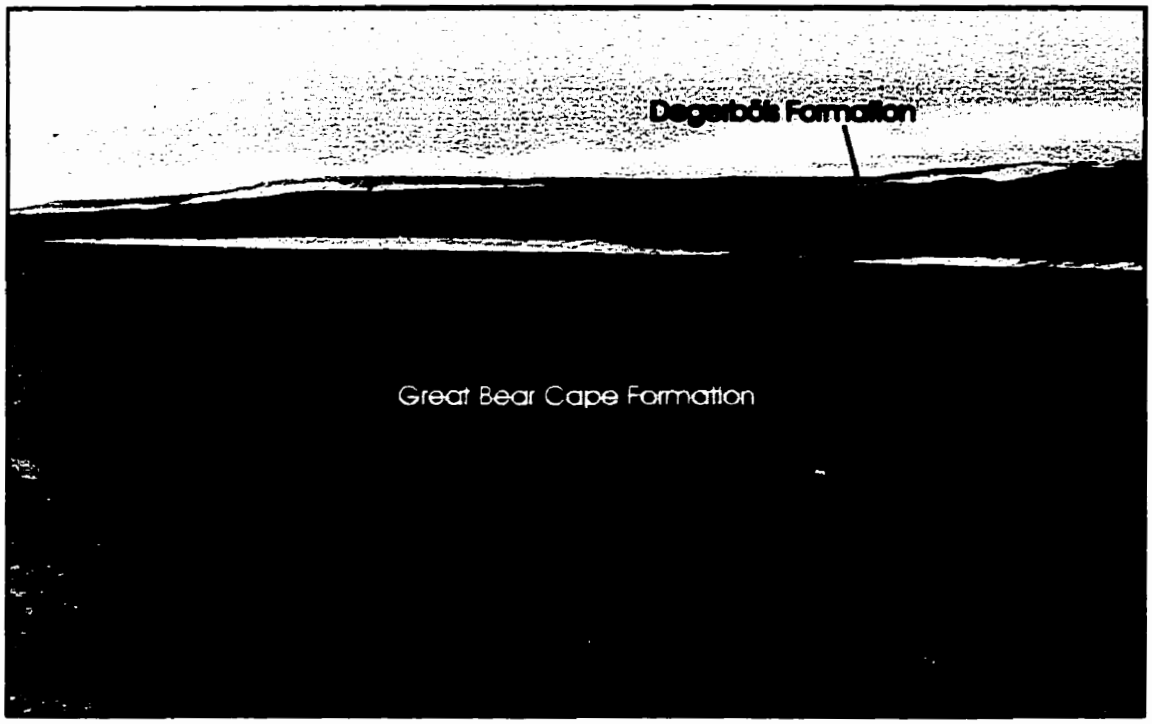

a

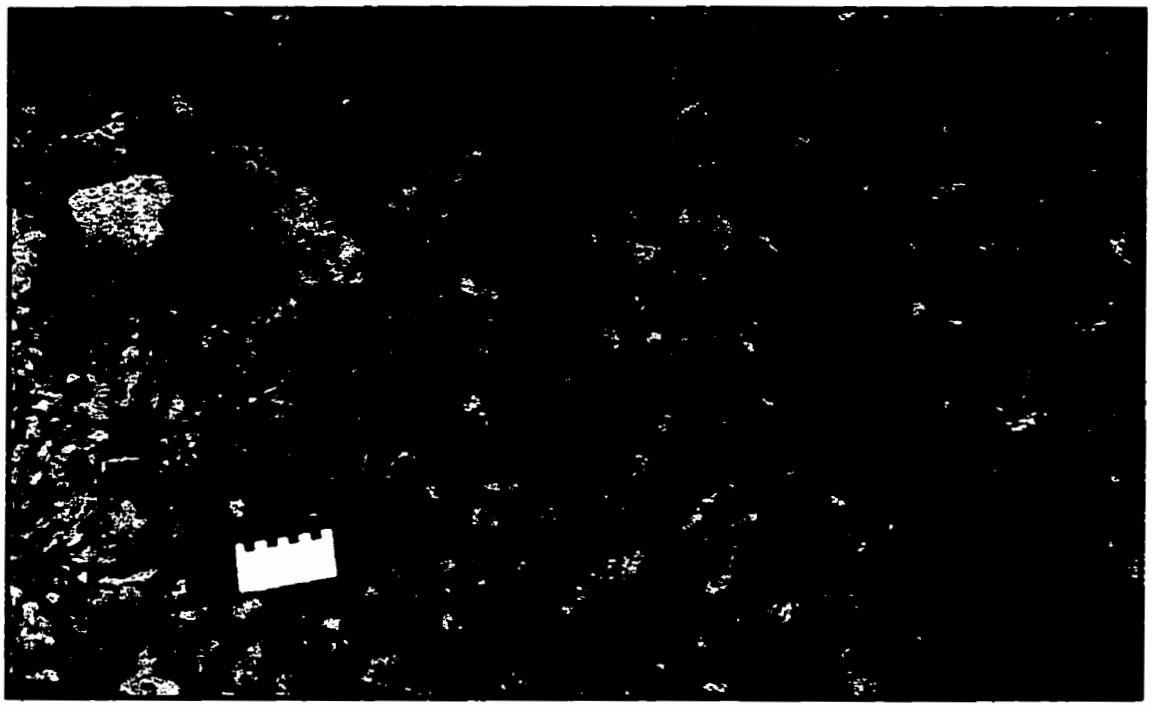

b

Figure 8.15 Photographs of large Great Bear Cape Formation materials (limestone) at a location in the western portion of the Tingmisut Lake region (Site 20). Location is shown in Figure 8.7. View in "a" is toward the northwest. Scale in "a" is divided into 10 cm increments. Scale in "b" is divided into 1 cm increments. Clast sizes shown here are typical of the larger surficial materials of the Great Bear Cape Formation.

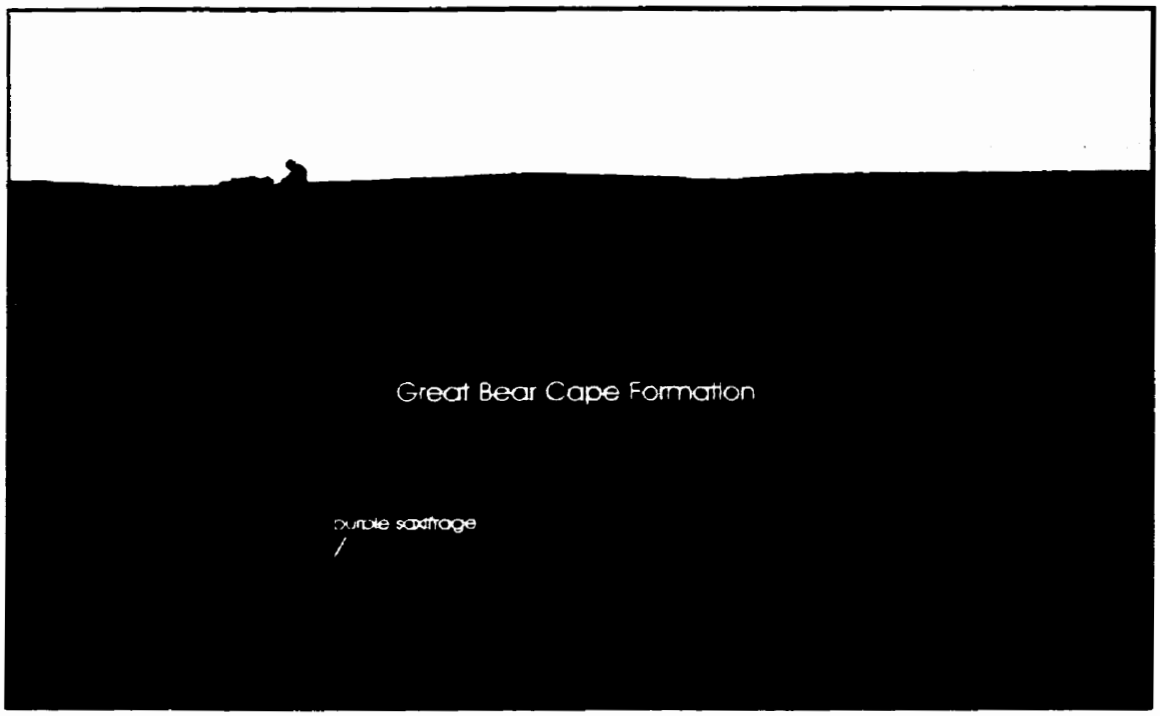

a

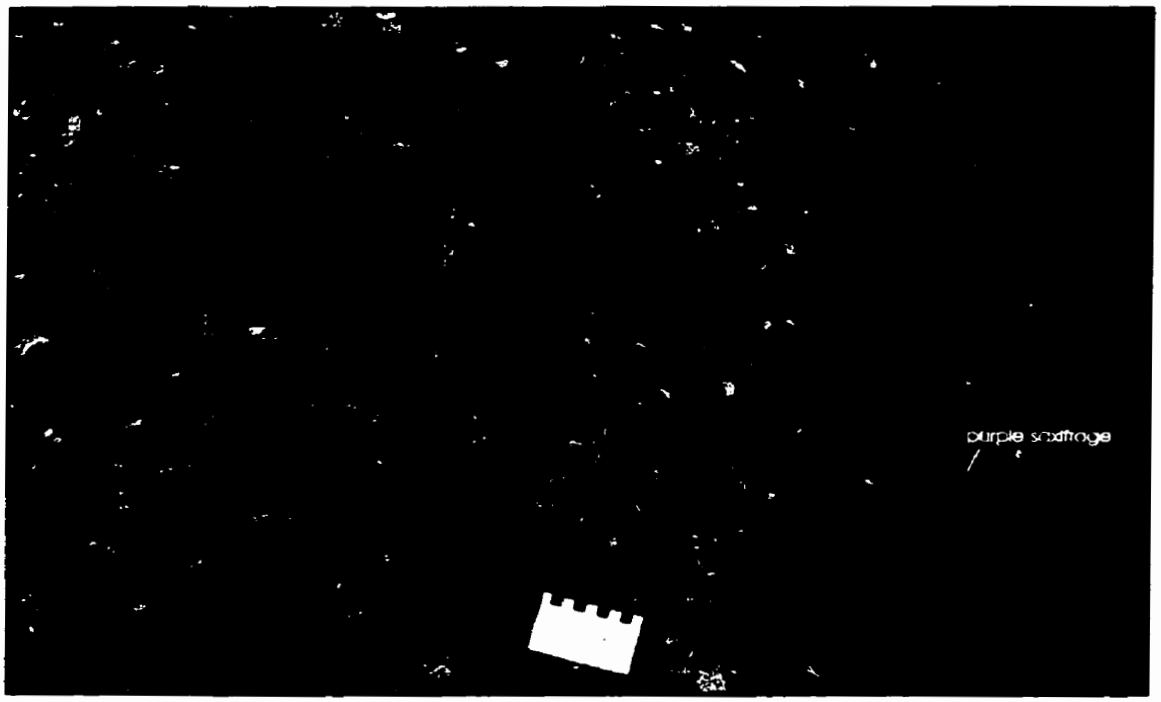

b

Figure 8.16 Photographs of small Great Bear Cape Formation materials (limestone) at a location in the western portion of the Tingmisut Lake region (Site 21). Location is shown in Figure 8.7. Note person in "a" for scale. Scale in "b" is divided into 1 cm increments. Clast sizes shown here are typical of the smaller materials of the Great Bear Cape Formation.

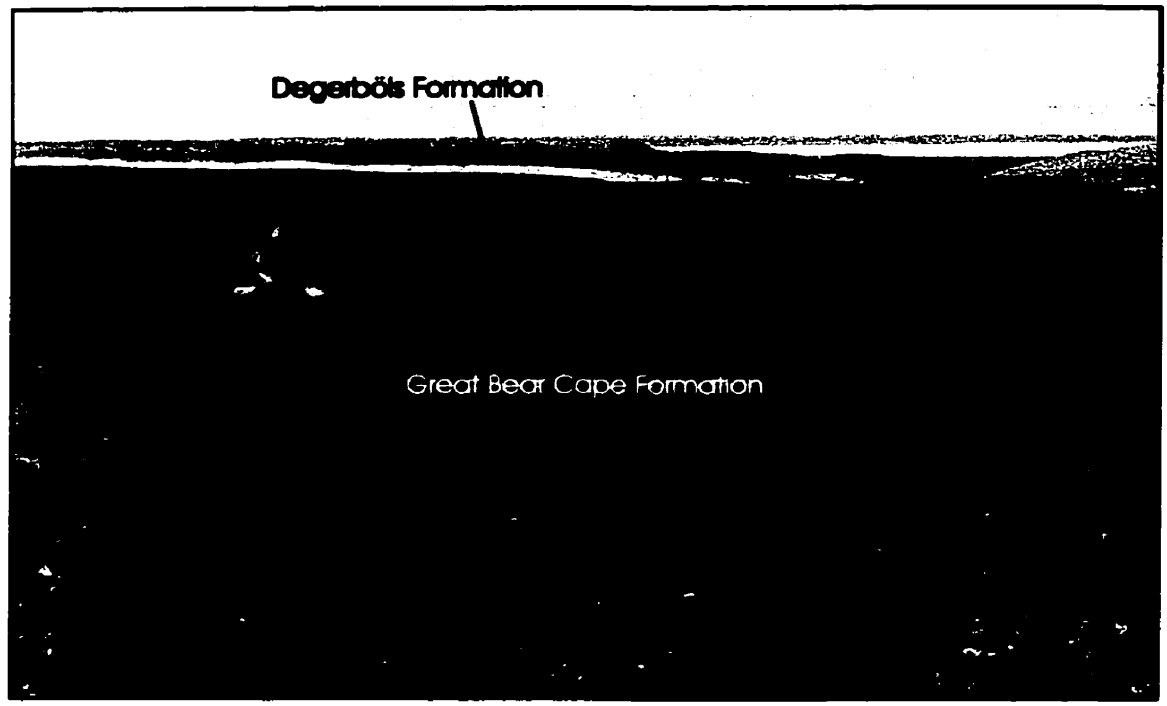

a

b

Figure 8.17 Photographs of vegetated Great Bear Cape Formation materials (limestone) at a location in the central portion of the Tingmisut Lake region (Site 24). Location is shown in Figure 8.7. Note that vegetation cover (mostly purple saxifrage, mosses, and lichens) is extensive. View in "a" is toward the north. Note person in "a" for scale. Scale in "b" is divided into 1 cm increments.

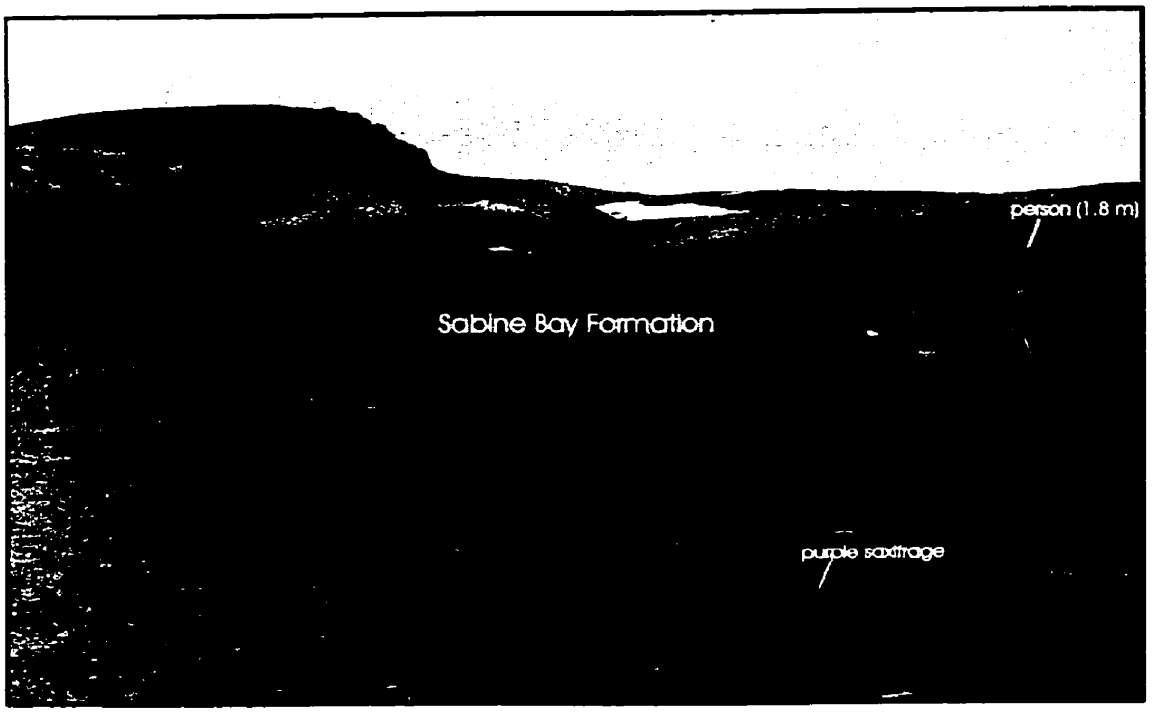

a

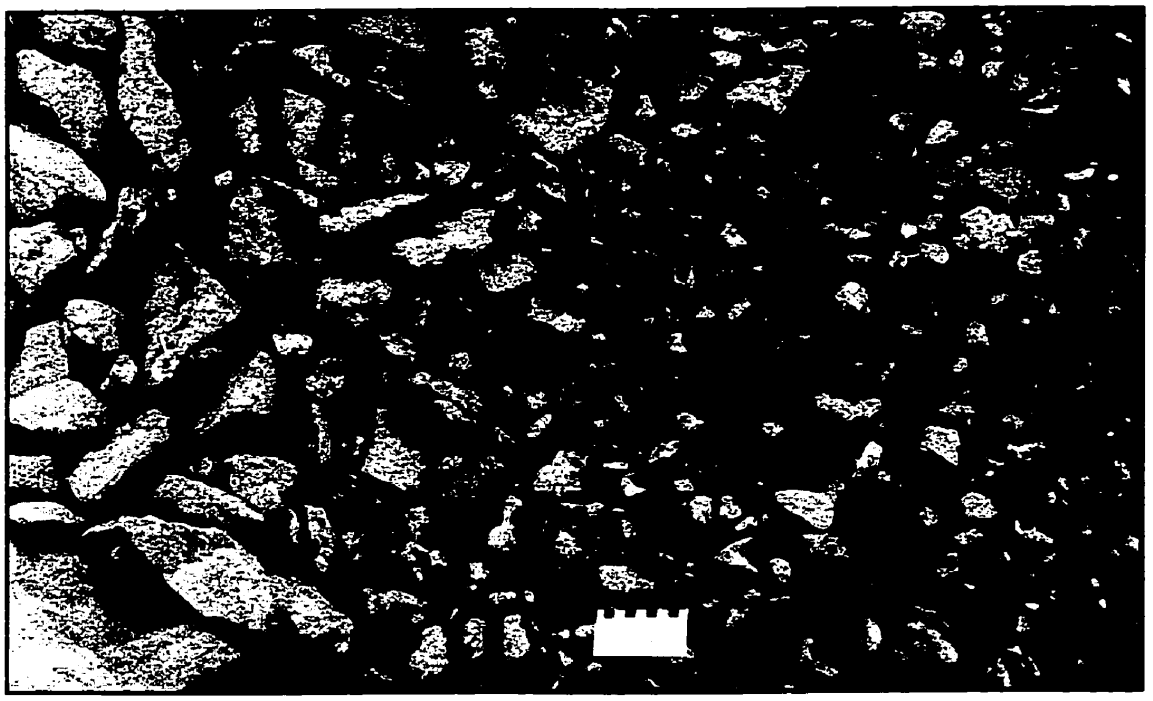

b

Figure 8.18 Photographs of large Sabine Bay Formation materials (sandstone) (Site 35). Location is shown in Figure 8.7. View in "a" is toward the east. Note person in "a" for scale. Scale in "b" is divided into 1 cm increments. Clast sizes shown here are typical of the larger surficial materials of the Sabine Bay Formation.

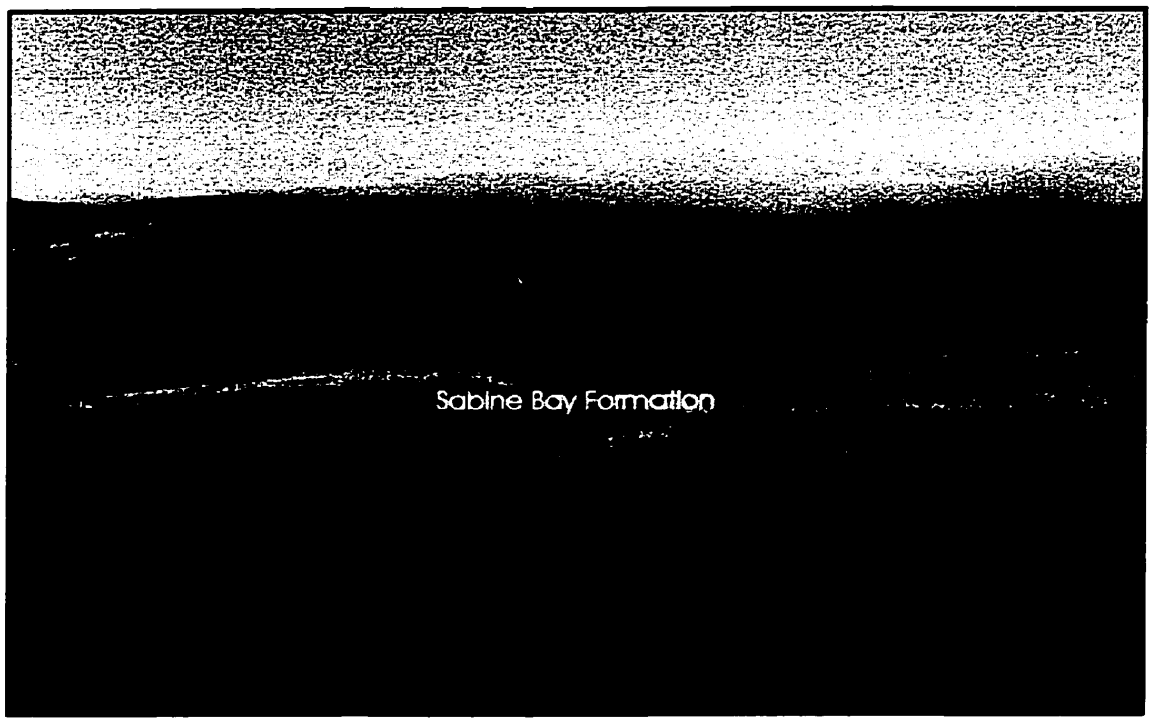

a

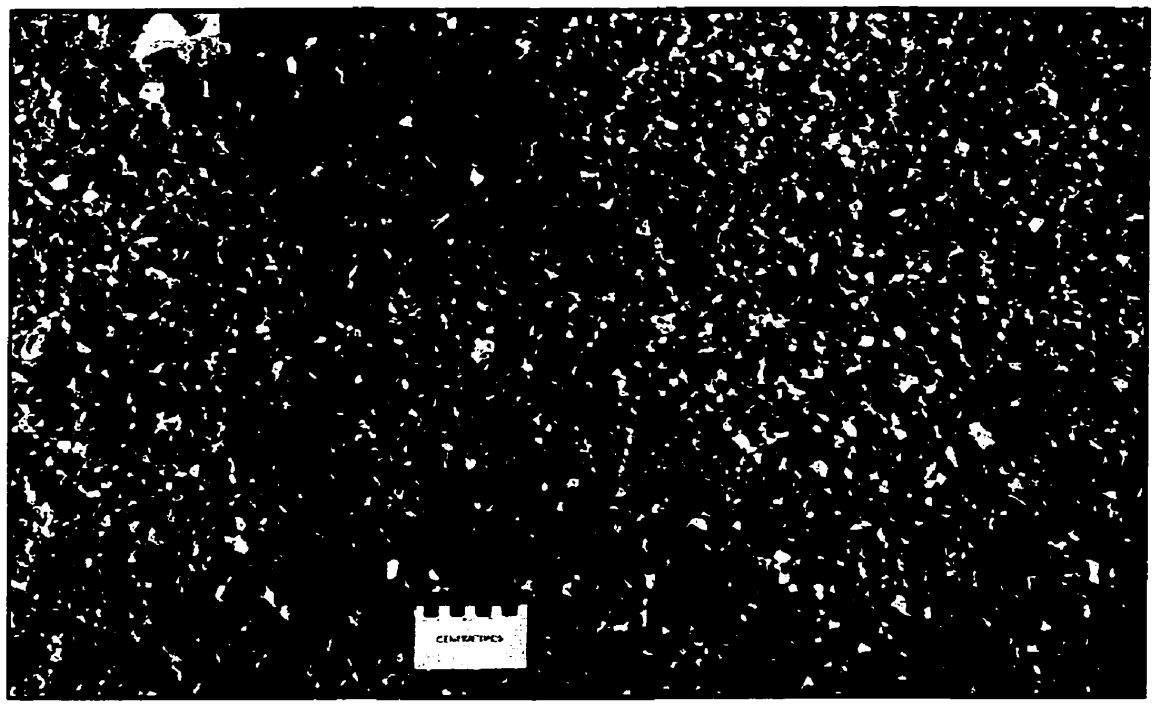

b

Figure 8.19 Photographs of small Sabine Bay Formation materials (mainly fines weathered from quartz sandstone and pebble conglomerate) (Site 53). Location is given in Figure 8.7. View in "a" is toward the east. Scale in "a" is divided into 10 cm increments. Scale in "b" is divided into 1 cm increments. Clast sizes shown here are typical of the smaller surficial materials of the Sabine Bay Formation.

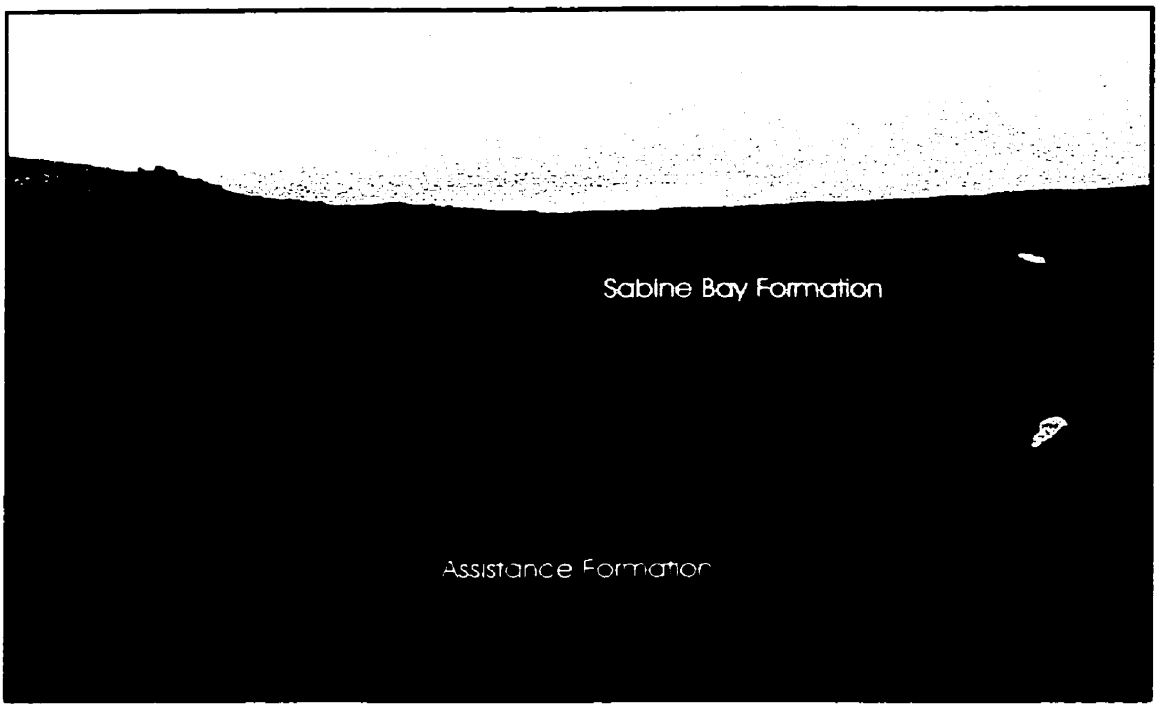

a

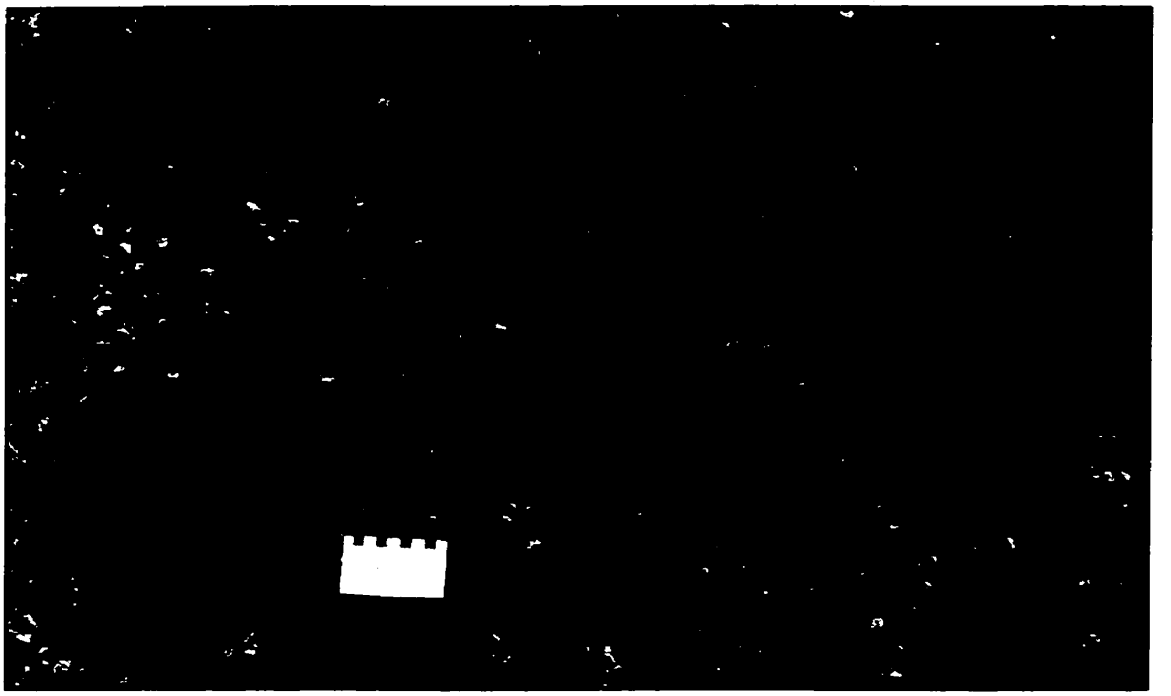

b

Figure 8.20 Photographs of Assistance Formation materials (red-weathering mudstone) (Site 40). Location is given in Figure 8.7. View in "a" is toward the southeast. Scale in "a" is divided into 10 cm increments. Scale in "b" is divided into 1 cm increments. The clast sizes shown here are typical of Assistance Formation materials in the region.

less than 3 cm across (Figure 8.21), although more coarse materials (rocks up to about 50 cm across) are common in places (e.g., Site 25). Most surficial materials of the Degerböls Formation are associated with low backscatter, regardless of clast size; this may be related in part to the gentle slope of Degerböls surfaces away from the radar sensor. The surficial materials of the Trold Fiord Formation are variable with regard to clast size, although most exposures are associated with relatively coarse materials (1 to 15 cm; Figure 8.22); the materials of this unit have variable backscatter which appears to be correlated with topography rather than roughness or amount of vegetation cover. The surficial materials of the Bjorn Formation are typically pebble-sized or smaller (Figure 8.23), and are mainly associated with low radar backscatter in the Radarsat image.

In general, most geological units in the Tingmisut Lake region are associated with moderate to low values in the Radarsat image. This may in part be due to the generally small clasts typical of many units (e.g., materials of the Sabine Bay, Assistance, and Bjorn formations), although as noted above, many units characterized by variably-sized clasts (e.g., materials of the Canyon Fiord, Great Bear Cape, Degerböls, and Trold Fiord formations) are associated with similarly moderate to low values. Overall, topography appears to be the main factor responsible for determining the backscatter properties of ground materials in the Tingmisut Lake region. Except for perhaps the dolostone (Tingmisut Inlier) and gabbro units, non-topographical factors do not produce sufficiently consistent differences in backscatter to be of any practical value (that is, topographical factors appear to dominate the effects of other factors, making it difficult to visually extract lithological information in this region). Rocks of the dolostone and gabbro units are more massive and therefore more blocky ("equant")

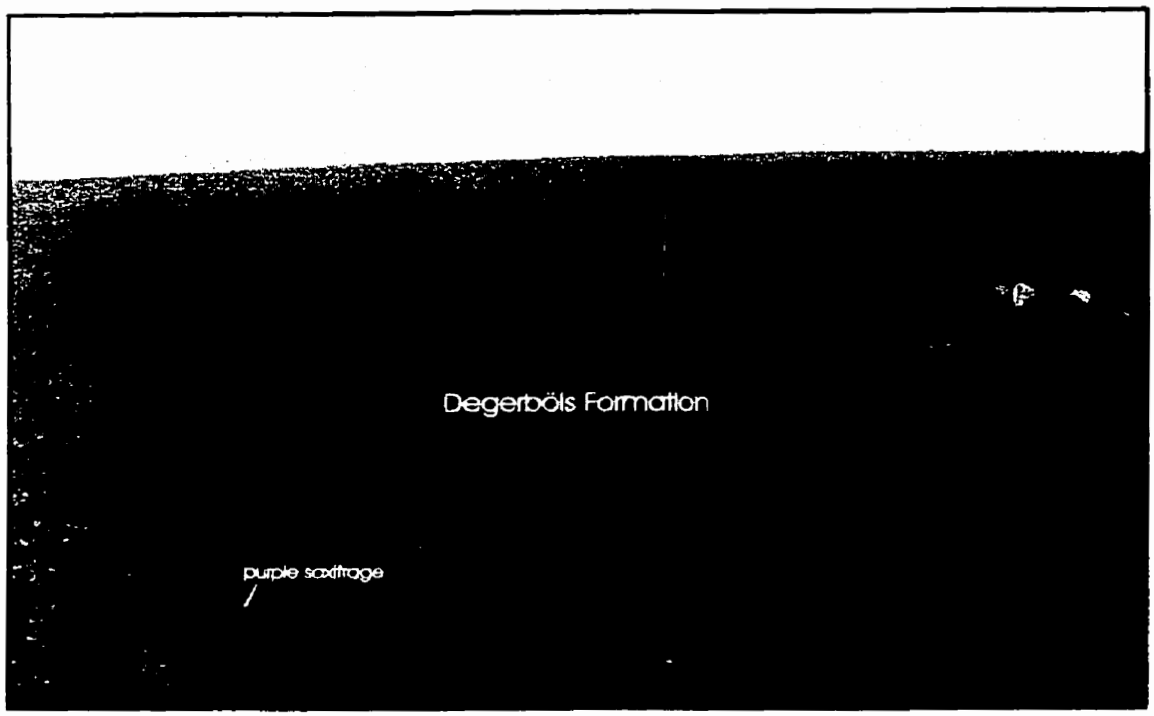

a

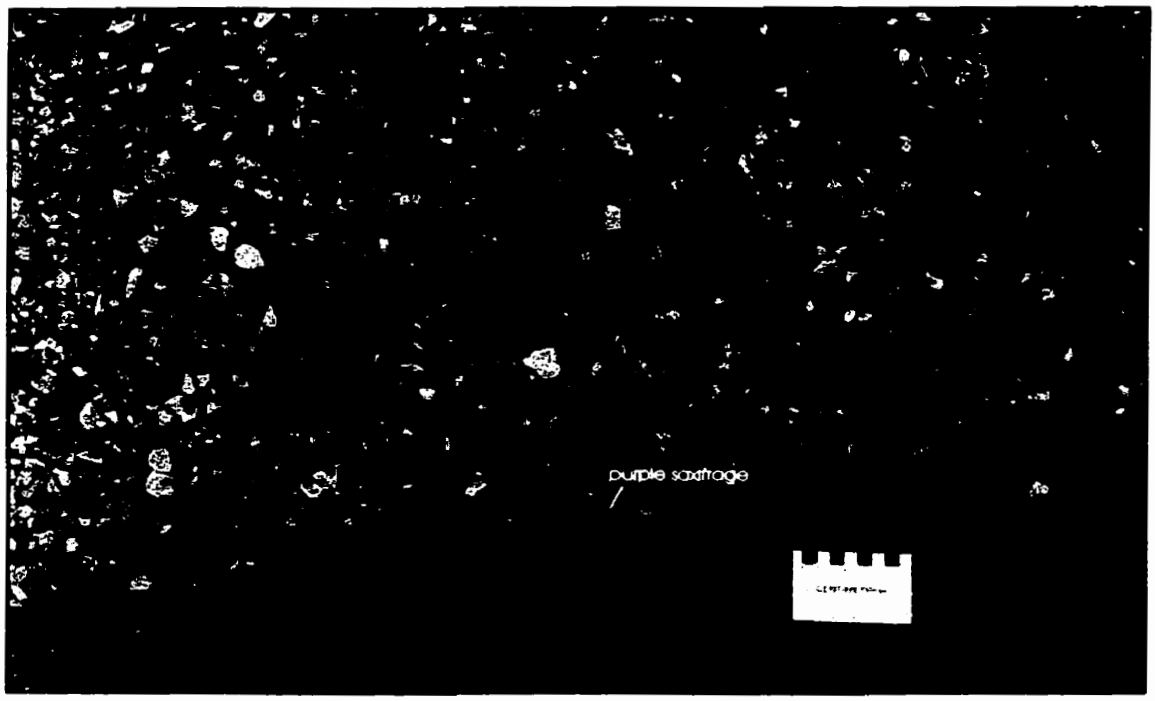

b

Figure 8.21 Photographs of Degerböls Formation materials (mainly bioclasts weathered from limestone) (Site 45). Location is given in Figure 8.7. Scale in "a" is divided into 10 cm increments. Scale in "b" is divided into 1 cm increments.

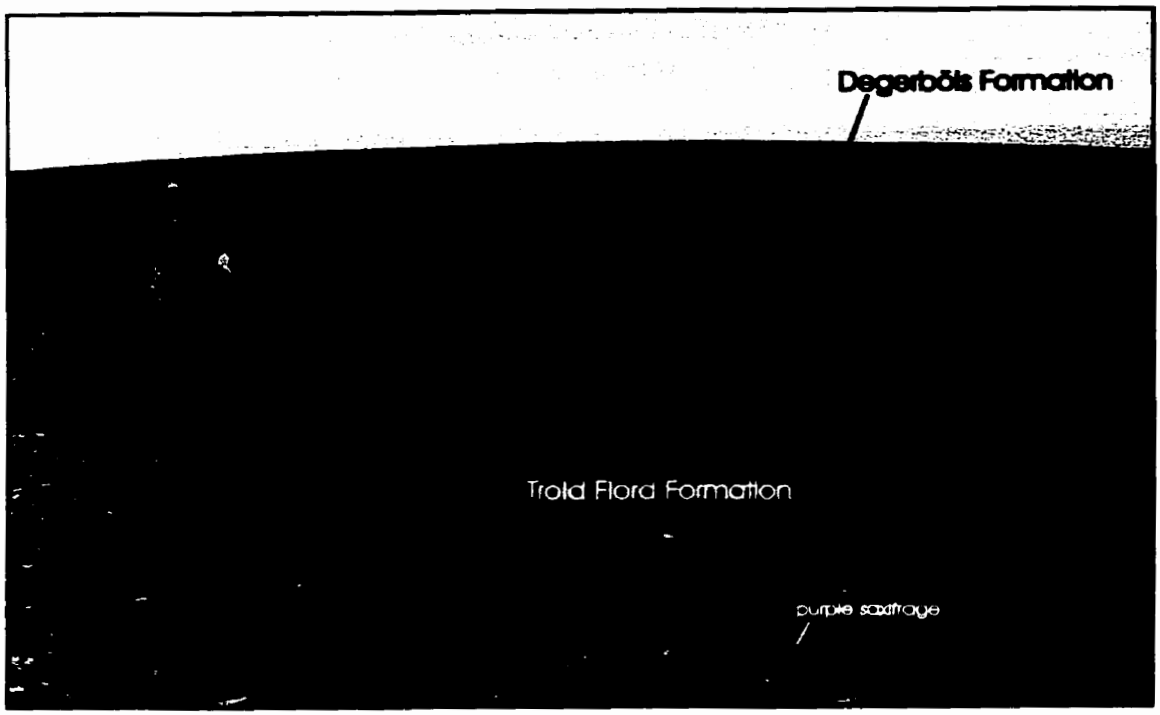

a

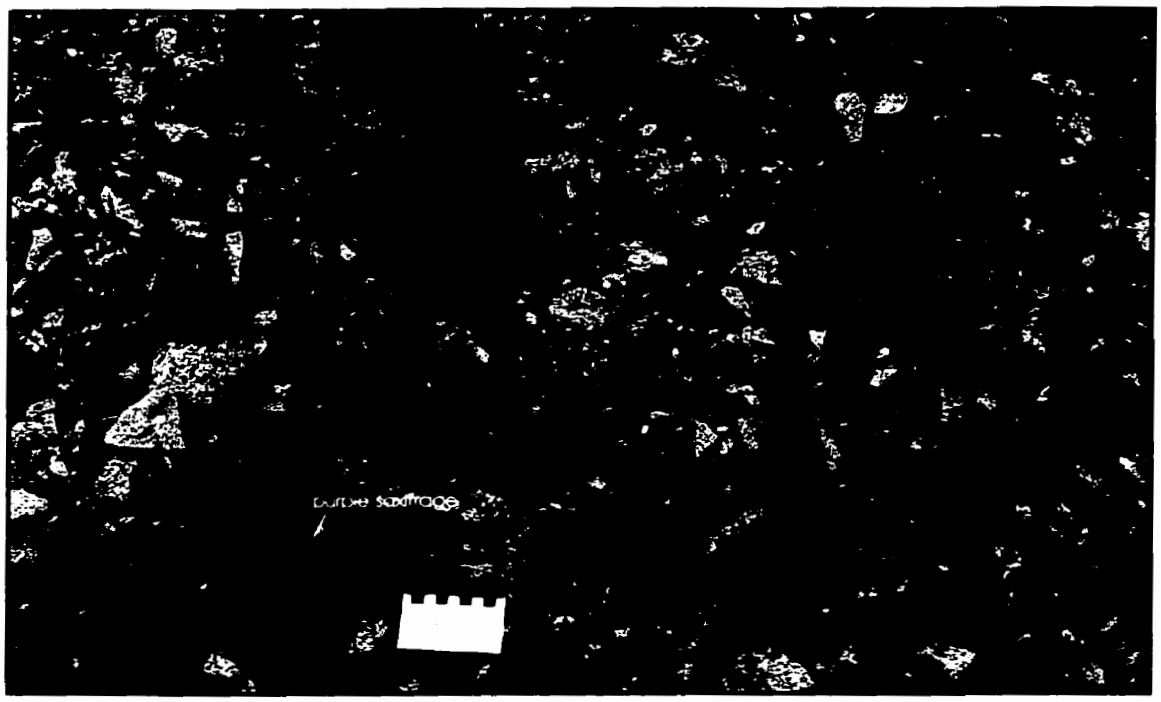

b

Figure 8.22 Photographs of Trold Fiord Formation materials (sandstone and limestone) (Site 66). Location is given in Figure 8.7. View in "a" is toward the southeast. Scale in "a" is divided into 10 cm increments. Scale in "b" is divided into 1 cm increments.

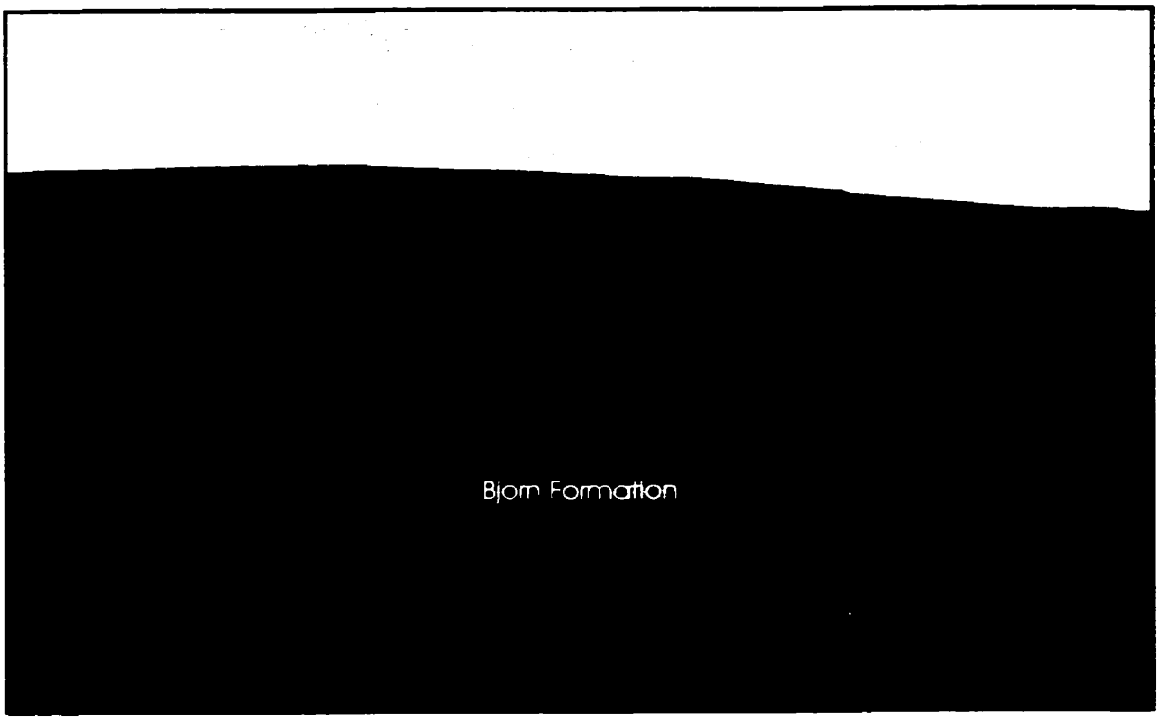

a

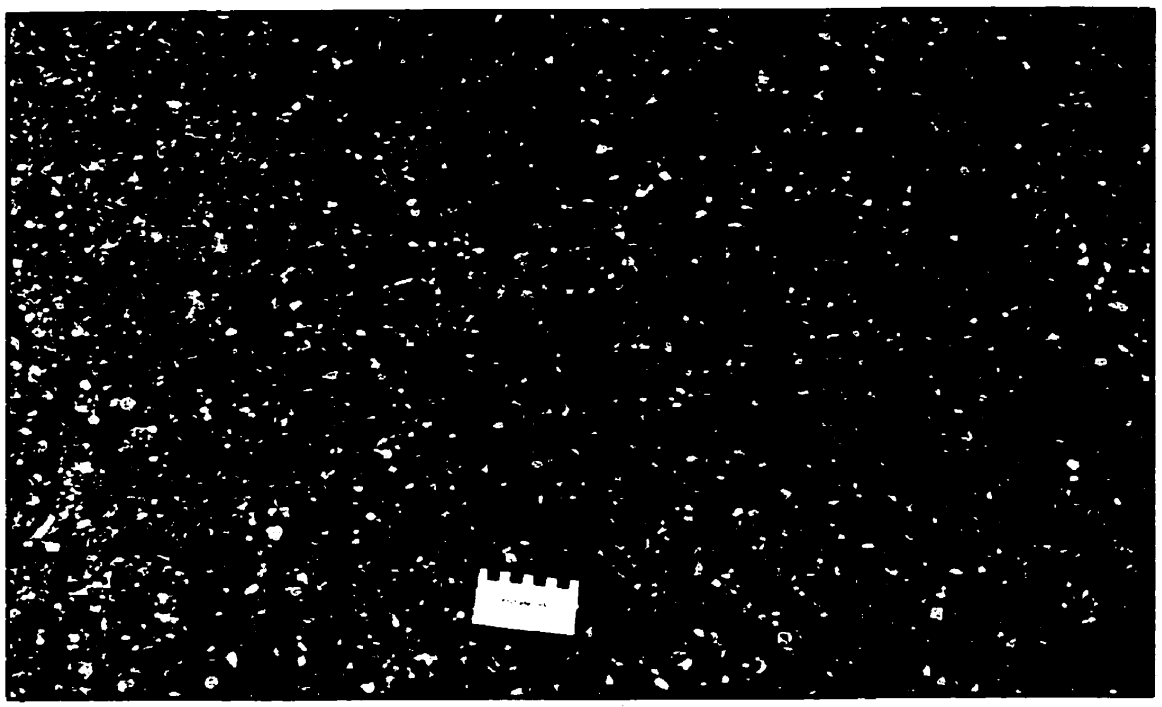

b

Figure 8.23 Photographs of Bjorn Formation materials (mainly sand- and pebble-sized clasts weathered from sandstone and conglomerate) (Site 70). Location is given in Figure 8.7. View in "a" is toward the northeast. Scale in "a" is divided into 10 cm increments. Scale in "b" is divided into 1 cm increments. The clast sizes shown here are typical of Bjorn Formation materials in the region.

than the flat-lying (planar / tabular) rocks typical of the surfaces of other units in the region. These differences in weathering style may account for the apparent differences in radar-roughness between the dolostone / gabbro units and the other geological units in the region.

8.3.1.3 IKONOS Images

The panchromatic IKONOS image of the Tingmisut Lake region is given in Figure 8.24, and corresponding colour composites of multispectral IKONOS imagery are given in Figure 8.25 (channels 321:RGB; true colour) and Figure 8.26 (channels 432:RGB; colour infrared) (image id: 2000072401485810000010000359). The IKONOS images, which have a smaller areal coverage of the Tingmisut Lake region than the TM and Radarsat images, were acquired on July 24, 2000, with solar illumination from the west. The panchromatic image has a pixel spacing of 1 m, and the multispectral images have a pixel spacing of 4 m. Contrast was enhanced in the IKONOS images using linear histogram stretches.

The visual information content of the panchromatic IKONOS image (Figure 8.24) is remarkably similar to that of the aerial photograph mosaic (Figure 8.3). Although the spectral range associated with the panchromatic IKONOS image is far too broad to allow geological units to be uniquely identified spectrally, the image provides sufficient high-resolution visual information regarding terrain tone and texture to allow for the recognition of most terrain features in the region. Like the aerial photograph mosaic, the panchromatic IKONOS image provides sufficient geomorphological and surface-cover information to allow for the visual discrimination of most geological units. While the TM images (Figures 8.4 to 8.6) are useful sources of spectral information, they provide much less morphological and contextual

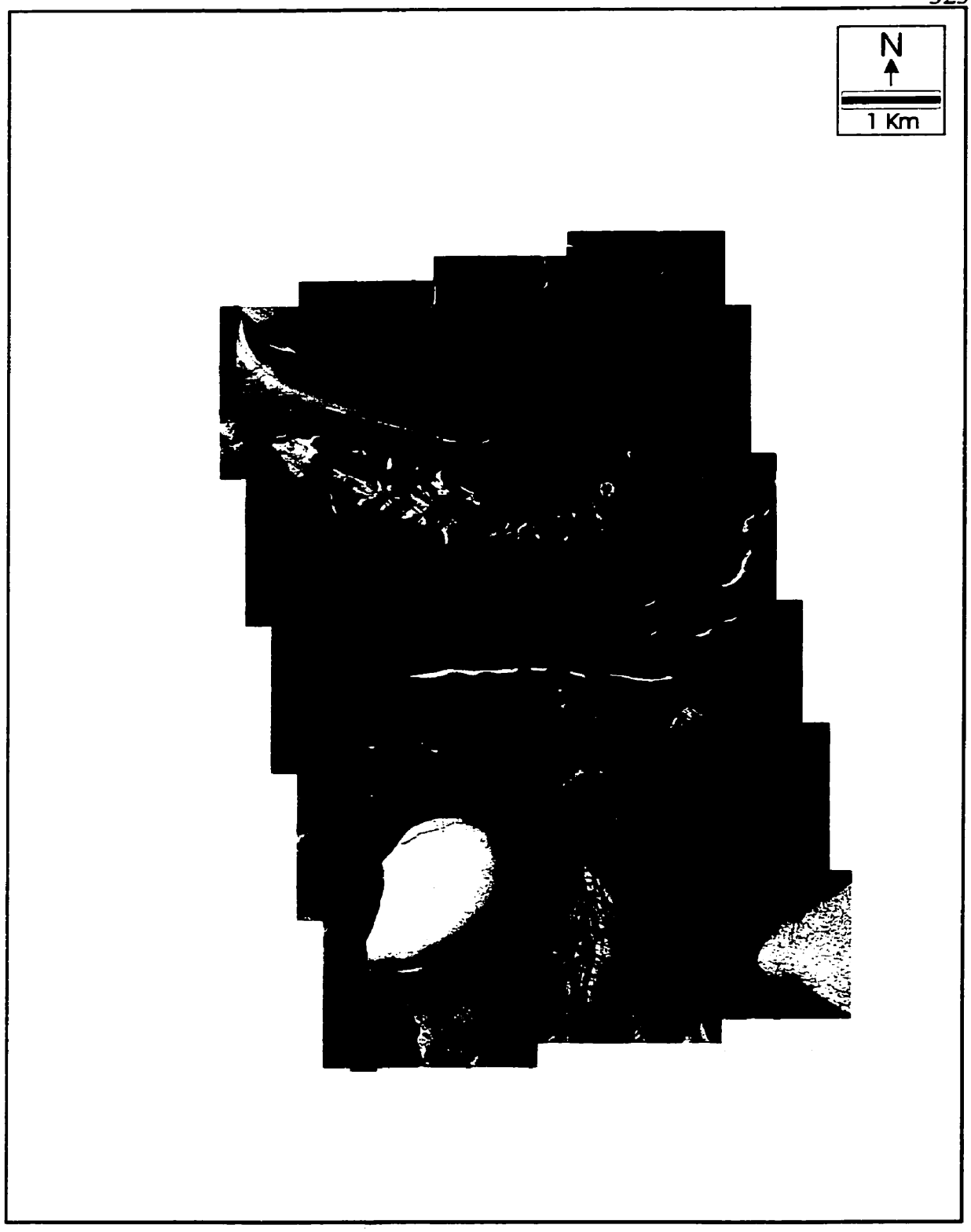

Figure 8.24 Panchromatic IKONOS image of the Tingmisut Lake region. Illumination is from the west.

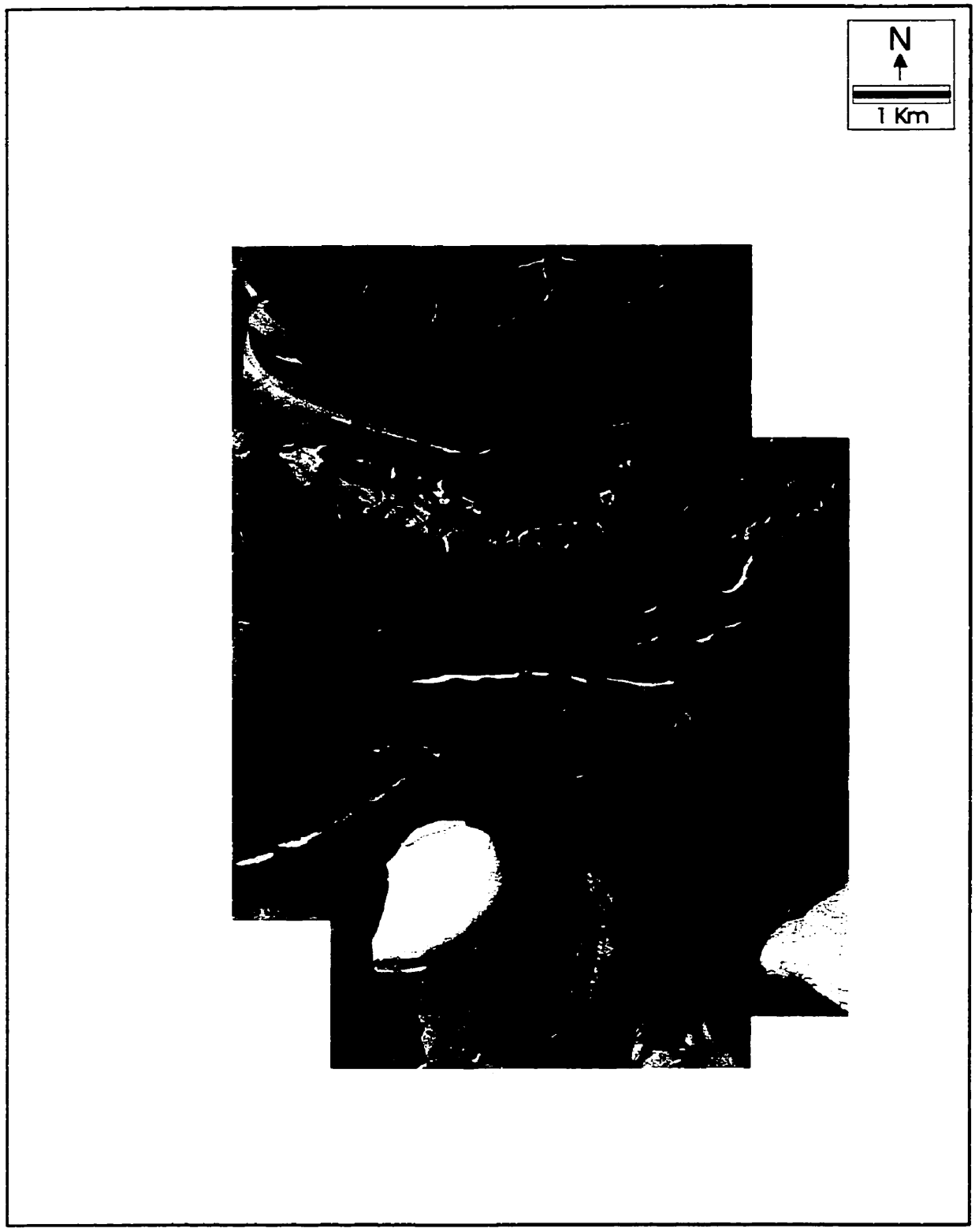

Figure 8.25 IKONOS colour composite (multispectral channels 321:RGB; true colour) for the Tingmisut Lake region. Illumination is from the west.

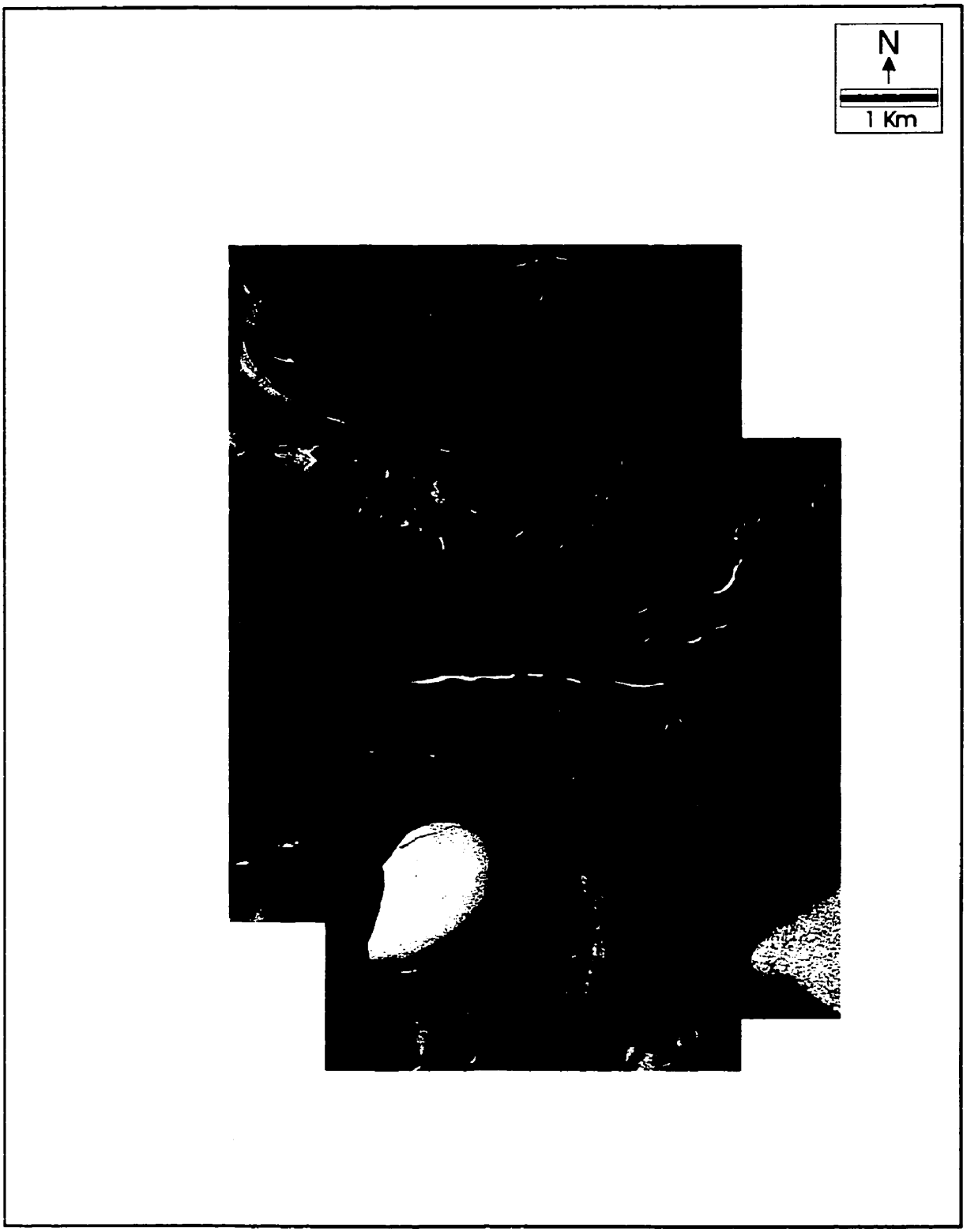

Figure 8.26 IKONOS colour composite (multispectral channels 432:RGB; colour infrared) for the Tingmisut Lake region. Illumination is from the west.

information than the panchromatic IKONOS image, at the scale of the Lake Tingmisut region.

The multispectral IKONOS images (Figures 8.25 and 8.26) also provide detailed information on surface materials in the Tingmisut Lake region. Although the spectral resolution of the multispectral IKONOS imagery is limited to that of the first four TM channels (Section 2.4.3), the imagery can nevertheless be used to uniquely discriminate the materials of certain geological units. For example, the Canyon Fiord Formation, as well as its pink- and yellow-coloured subunits, may be discriminated in the images. Well-exposed materials of the Sabine Bay Formation may be identified by their relatively high reflectance in all four multispectral IKONOS channels. High-resolution information on the distribution of remnant patches of snow is visible in both IKONOS colour composites (Figures 8.25 and 8.26), and areas where significant vegetation cover is present are identified in reddish hues on the colour-infrared IKONOS image (Figure 8.26). Like the panchromatic IKONOS image, the multispectral IKONOS images may be used to visually identify most geological units on the basis of their morphological and tonal characteristics.

8.3.1.4 Evaluation of Satellite Imagery at Three Zones Within the Tingmisut Lake Region

Aerial photographs and TM, Radarsat, and IKONOS imagery are compared below for three smaller zones of the Tingmisut Lake region (the "north zone", "central zone", and "south zone") whose locations are given in Figure 8.3. Aerial photography for the **north zone** is given in Figure 8.27, and a north-facing ground photograph of the zone is given in Figure 8.28. This zone mainly consists of the Degerböls Formation limestone, the Assistance Formation mudstone, and the Sabine Bay Formation sandstone (Figure 8.27). Although

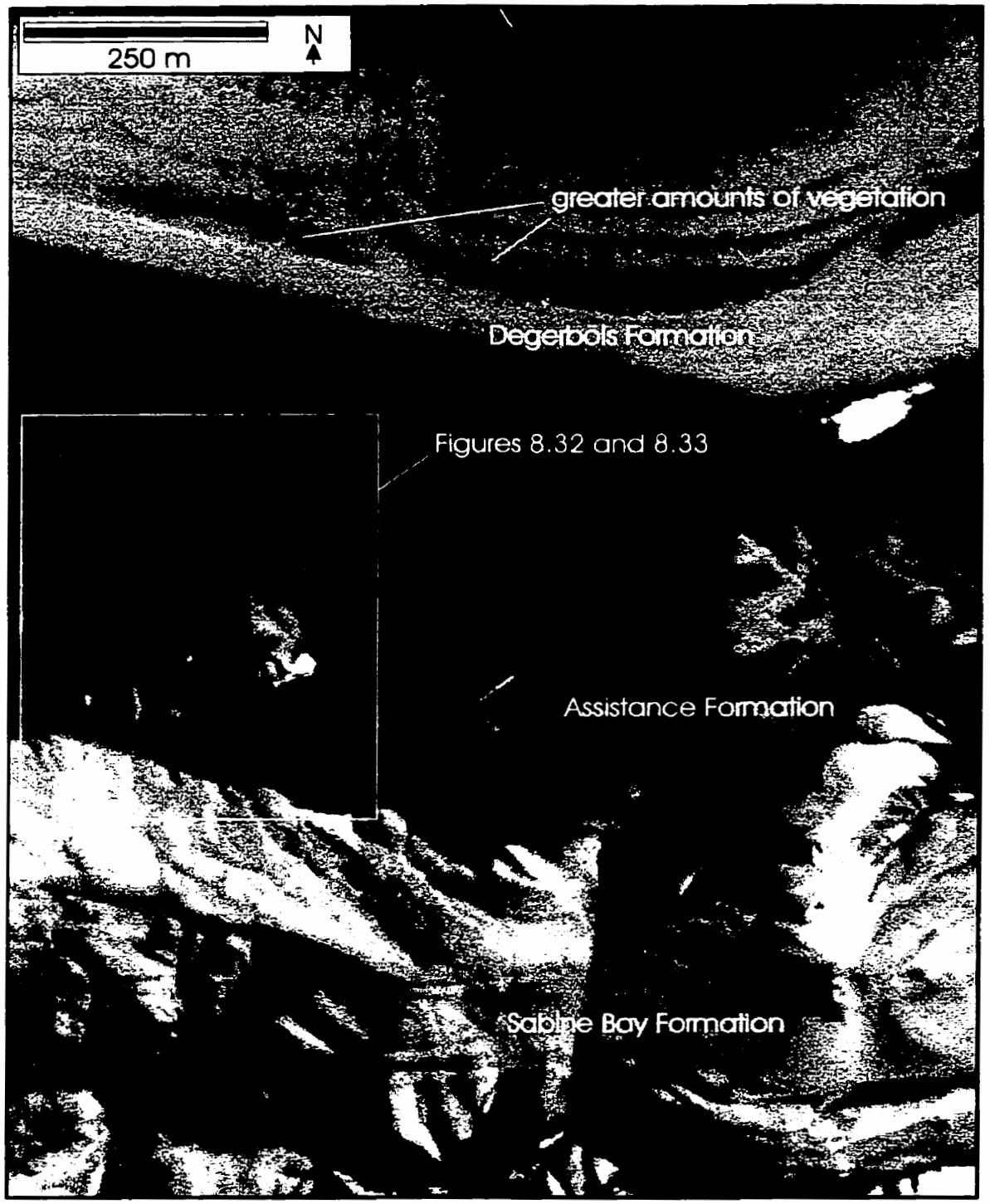

Figure 8.27 Aerial photograph of the north zone of the Tingmisut Lake region (photograph A16763-54).

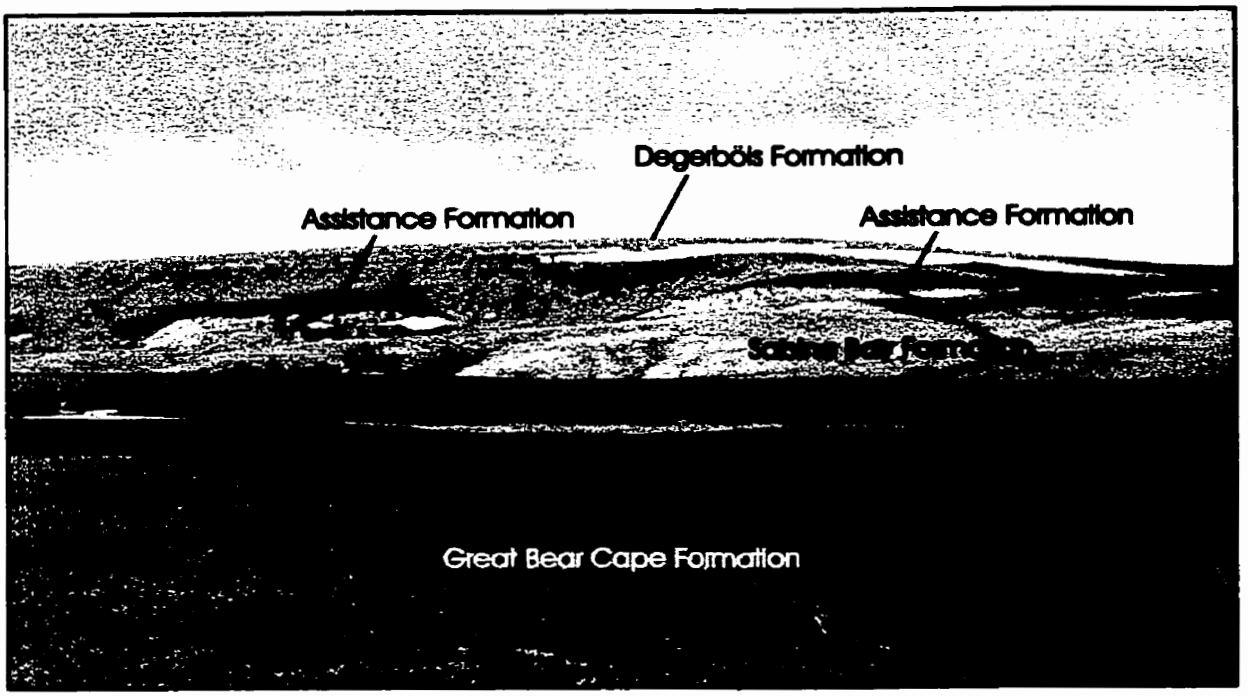

Figure 8.28 Ground photograph of the north zone of the Tingmisut Lake region. View is across strike toward the north.

useful for visualizing landforms down to features only metres in dimension, the panchromatic aerial photograph does not allow for the clear distinction between these lithological units on the basis of spectral information (although, in general, the Sabine Bay sandstone is associated with lighter tones, the Degerböls Formation with darker tones, and the Assistance Formation with the darkest tones). Areas of greater vegetation cover are associated with darker tones in the aerial photograph (Figure 8.27). The visual information provided by the TM 543:RGB and Radarsat images (Figures 8.29 and 8.30, respectively) for the north zone is limited, although the TM image does provide sufficient spectral information to discriminate the Assistance Formation mudstones from the other materials, and areas of particularly dense vegetation cover are shown in green hues. Radarsat image values are mainly a function of topographic factors (see above), although moisture or roughness factors may also be significant at certain locales (e.g., note that the gully in the southeast portion of the zone is associated with higher image values than surrounding materials: Figure 8.30). The panchromatic IKONOS image (Figure 8.31) provides an amount of spatial and tonal information that is very similar to that provided by the aerial photograph (compare details in Figures 8.32 and 8.33). The colour infrared IKONOS image (Figure 8.34; channels 432:RGB) does not have sufficient spectral resolution to provide clear information on the discrimination of lithologies in the zone, although well-exposed Sabine Bay materials are generally associated with light tones. Areas where vegetation cover is relatively high are clearly identified in the colour infrared IKONOS image by their red colour.

Aerial photography for the **central zone** is given in Figure 8.35, and an east-facing ground photograph of a portion of the zone is given in Figure 8.36. The central zone consists

Figure 8.29 TM colour composite (channels 543:RGB) for the north zone of the Tingmisut Lake region.

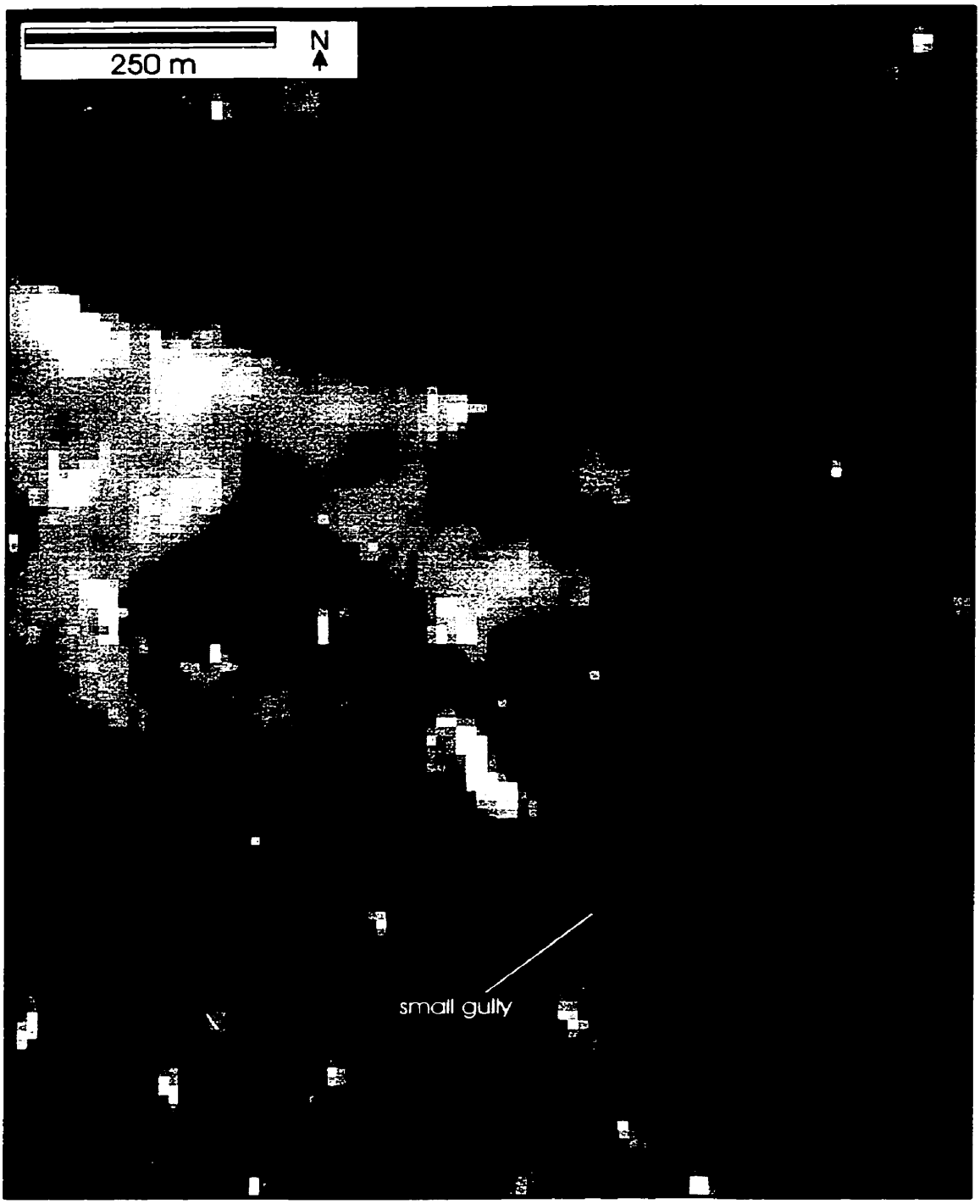

Figure 8.30 Radarsat image of the north zone of the Tingmisut Lake region.

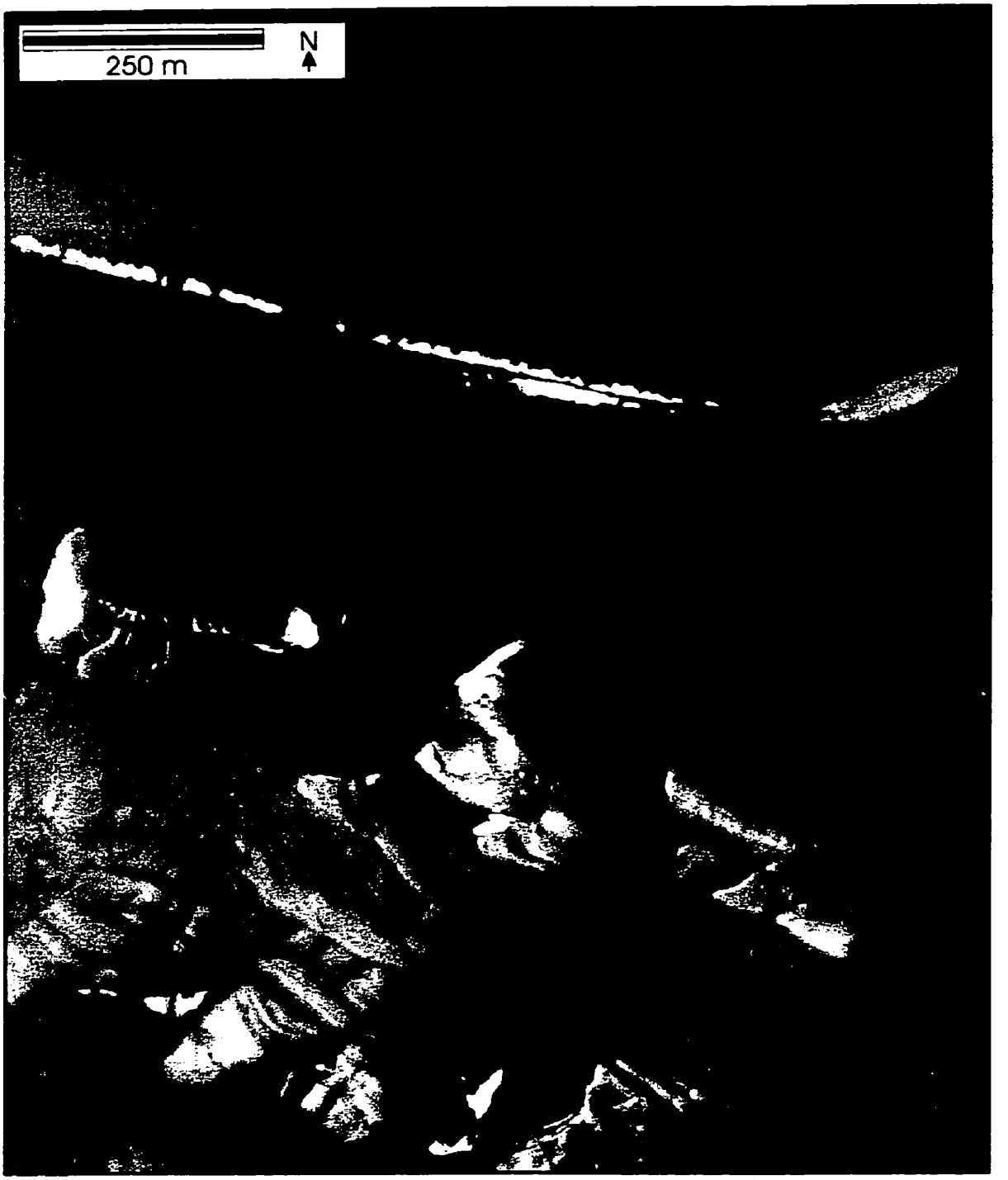

Figure 8.31 Panchromatic IKONOS image of the north zone of the Tingmisut Lake region.

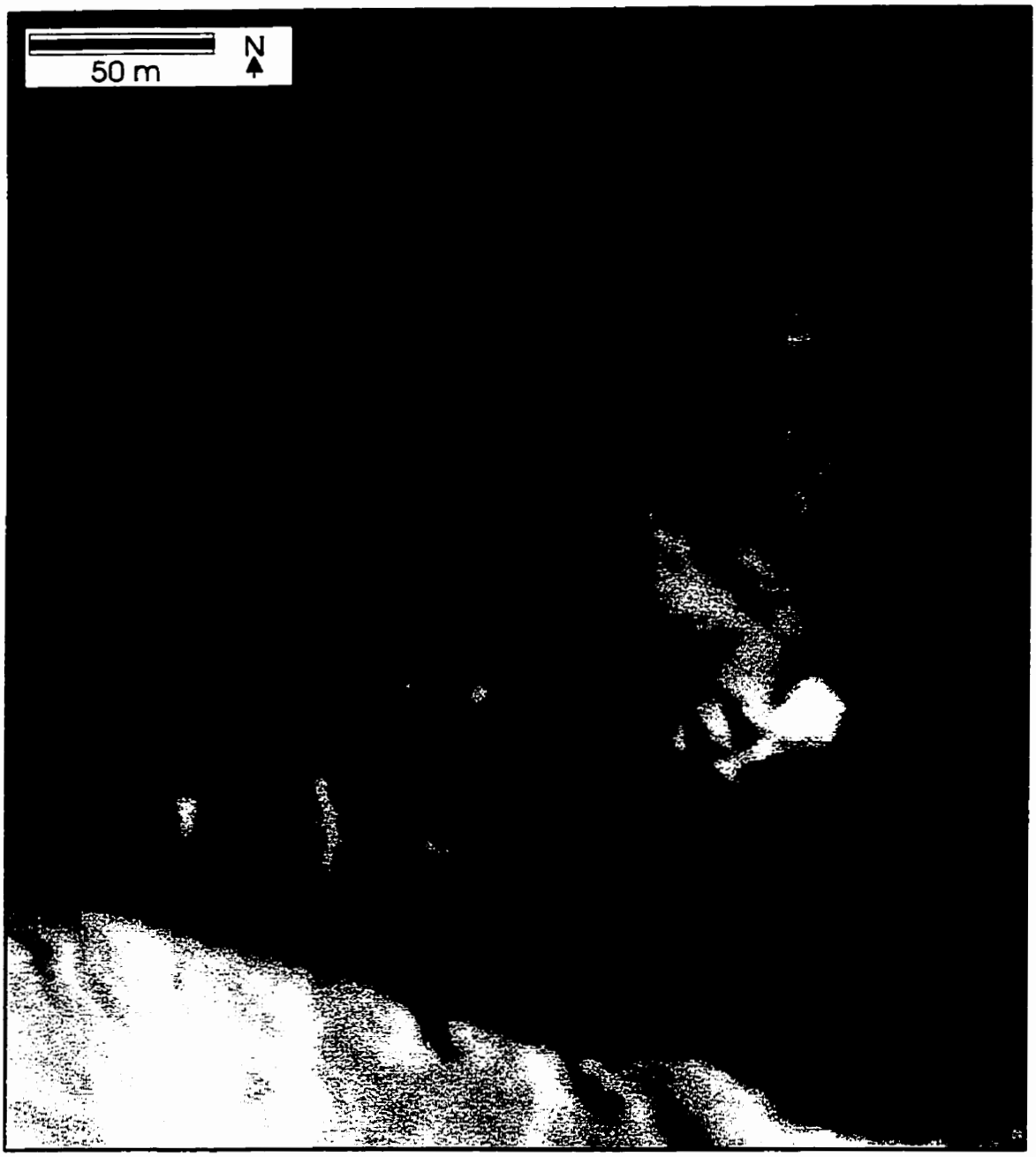

Figure 8.32 Aerial photograph of the north zone of the Tingmisut Lake region: detail (see Figure 8.27 for location).

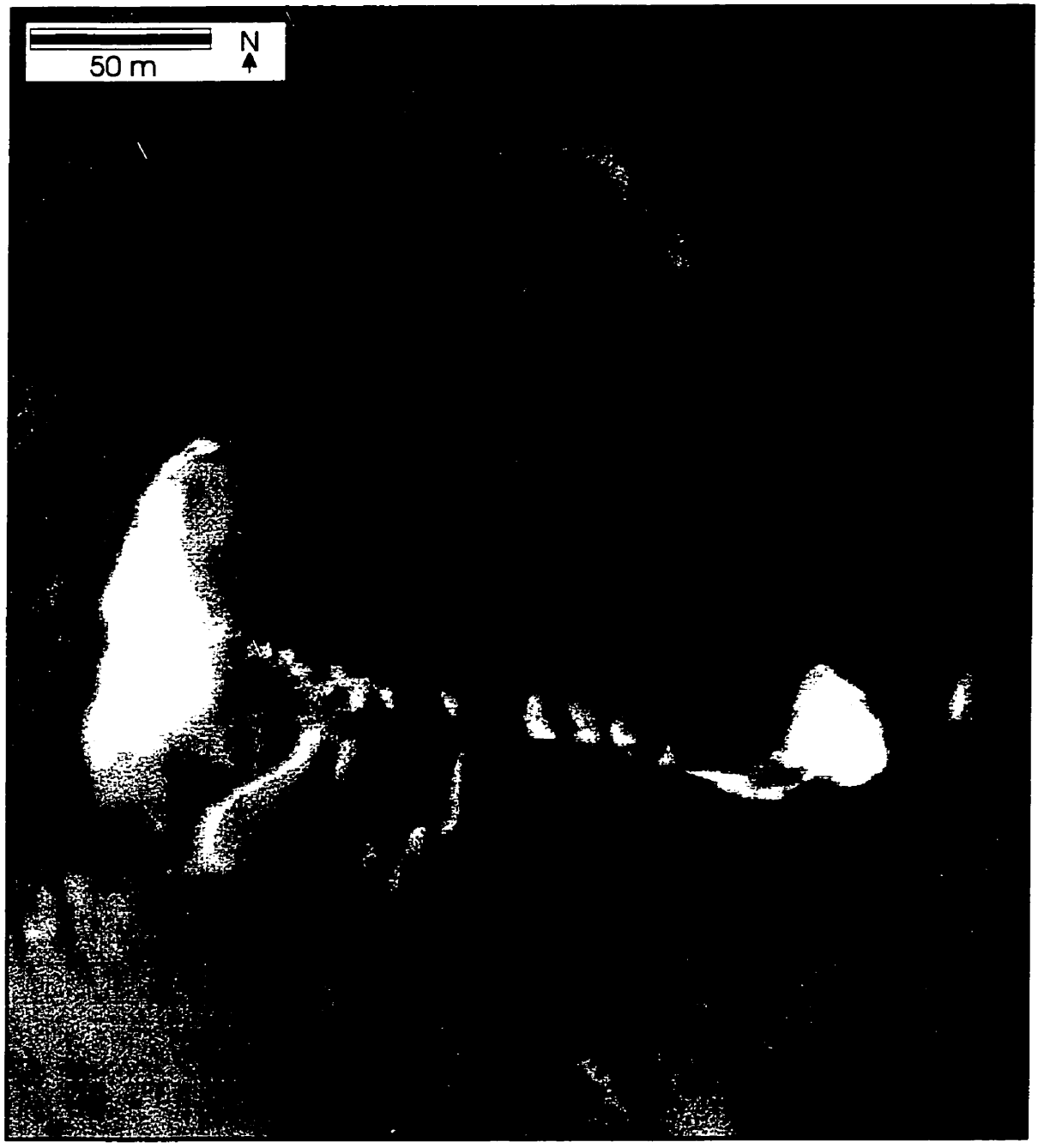

Figure 8.33 Panchromatic IKONOS image of the north zone of the Tingmisut Lake region: detail (see Figure 8.27 for location).

Figure 8.34 IKONOS colour composite (multispectral channels 432:RGB; colour infrared) for the north zone of the Tingmisut Lake region.

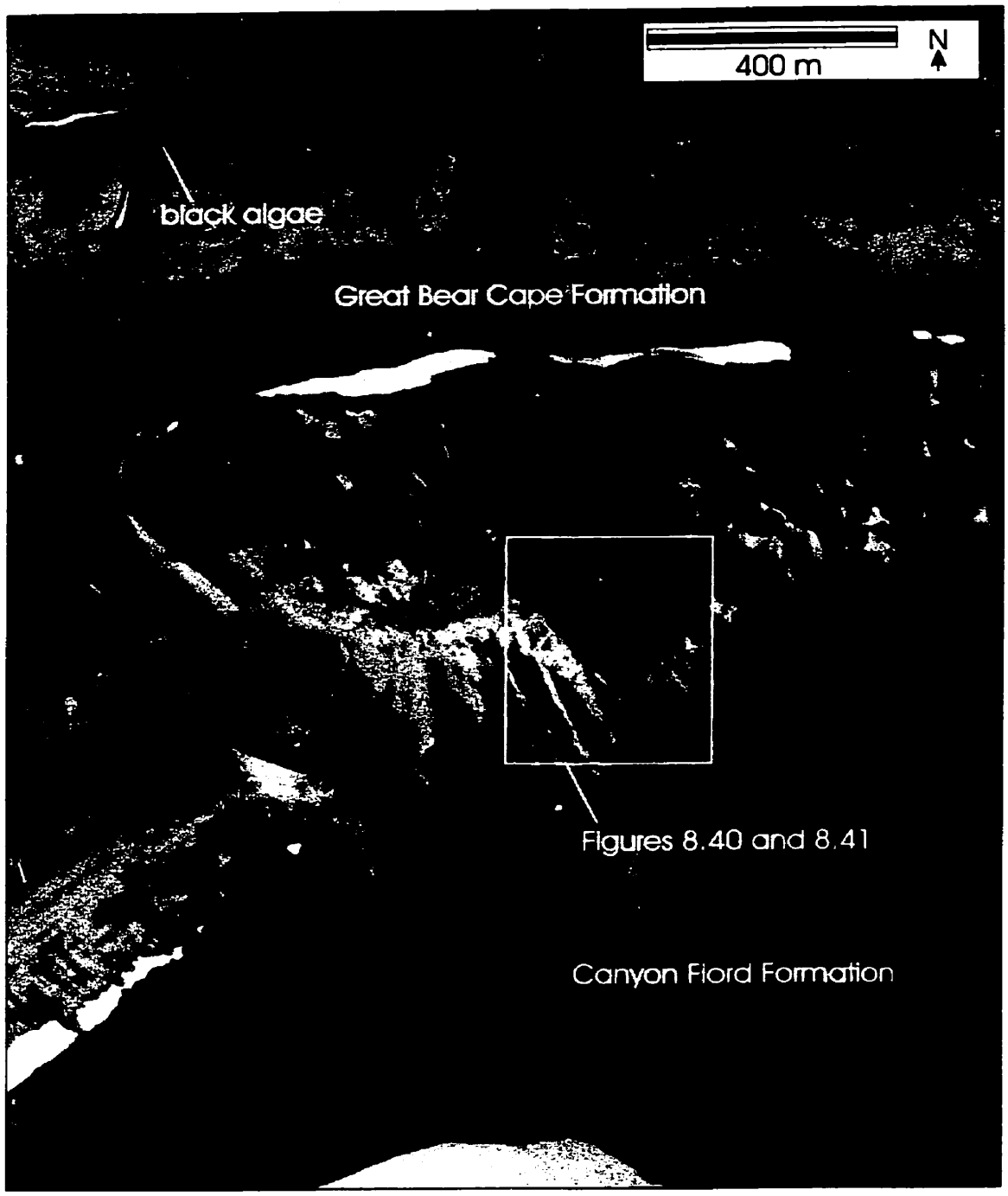

Figure 8.35 Aerial photograph of the central zone of the Tingmisut Lake region (photograph A16763-54).

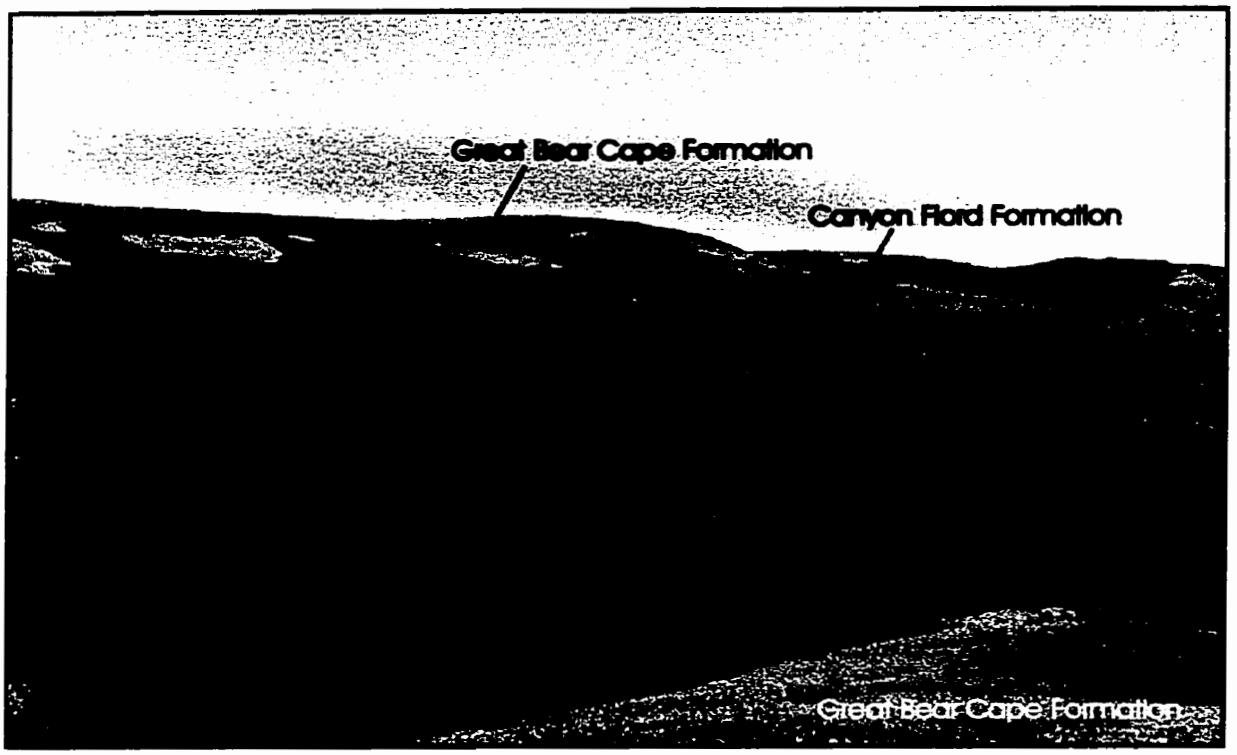

Figure 8.36 Ground photograph of the central zone of the Tingmisut Lake region. View is along strike toward the east.

of the Great Bear Cape Formation limestone and the Canyon Fiord Formation clastics. As with the north zone, the panchromatic aerial photography does not allow for the clear distinction between these lithological units on a purely spectral and tonal basis, although sufficient geomorphological and contextual information is provided for discrimination of these units. The visual information provided by the TM 543:RGB and Radarsat images (Figures 8.37 and 8.38, respectively) for the central zone is limited, although the TM image provides sufficient spectral information to easily discriminate between the materials of the two formations. Again, topographic factors appear to be the dominant control of image values in the Radarsat image [note that the fine-grained Canyon Fiord Formation materials north of Tingmisut Lake have roughly the same backscatter characteristics as the Great Bear Cape Formation limestones, which are generally more coarse (see above)] (Figure 8.38). The panchromatic IKONOS image (Figure 8.39) provides an amount of spatial and tonal information that is very similar to that provided by the aerial photograph (compare aerial and panchromatic IKONOS details in Figures 8.40 and 8.41, and the corresponding east-facing ground photograph in Figure 8.36). The true colour IKONOS image (Figure 8.42; channels 321:RGB) provides sufficient information for the high-resolution discrimination of the carbonates and clastics in the zone.

Aerial photography for the **south zone** is given in Figure 8.43, and a northeast-facing ground photograph of the zone is given in Figure 8.44. This zone mainly consists of the clastics of the Canyon Fiord Formation, as well as the gabbro dike. Once again the aerial photograph is useful for visualizing landforms at high spatial resolution, but does not allow for the clear distinction between lithological units on the basis of spectral information. Areas

Figure 8.37 TM colour composite (channels 543:RGB) for the central zone of the Tingmisut Lake region.

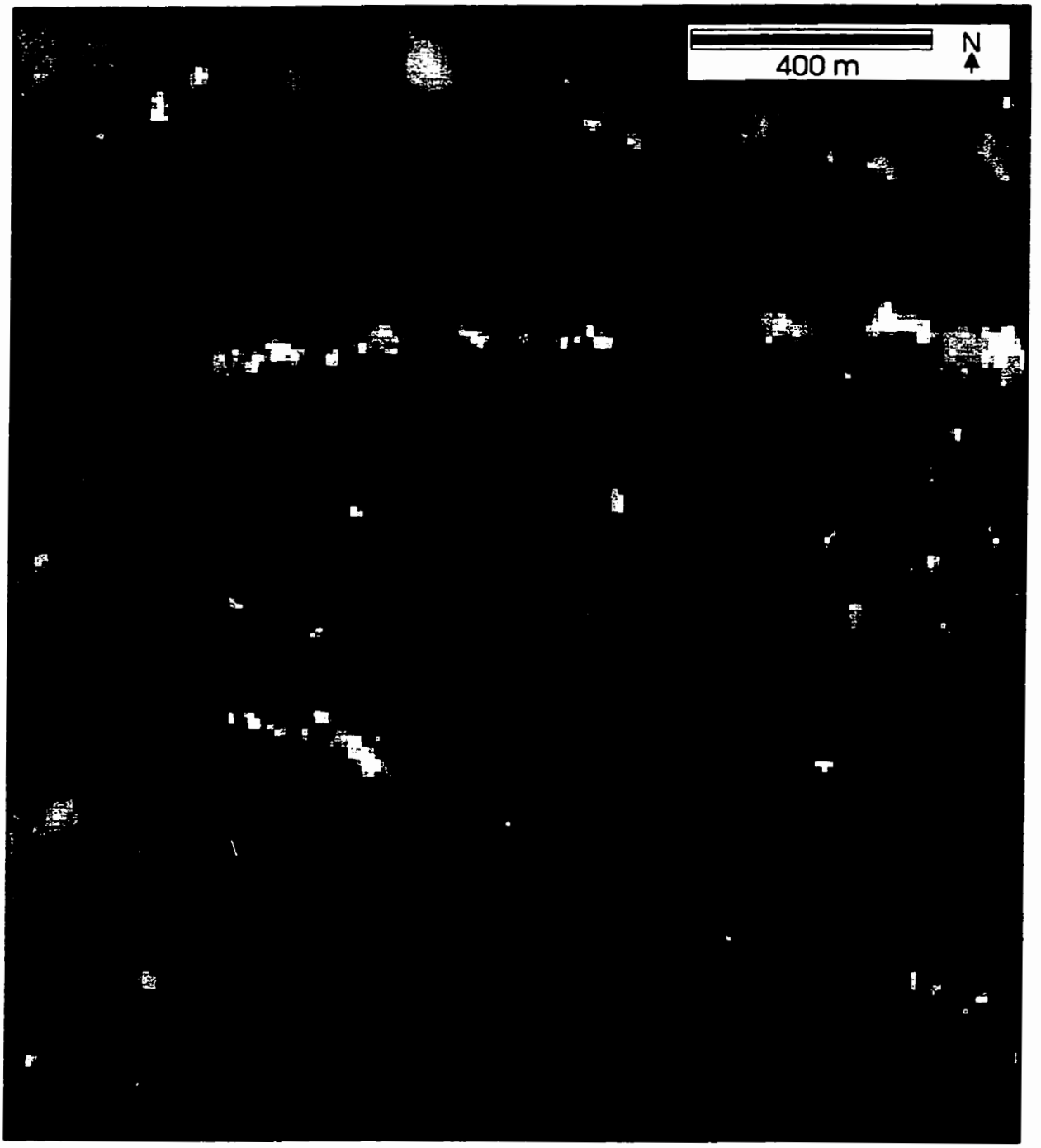

Figure 8.38 Radarsat image of the central zone of the Tingmisut Lake region.

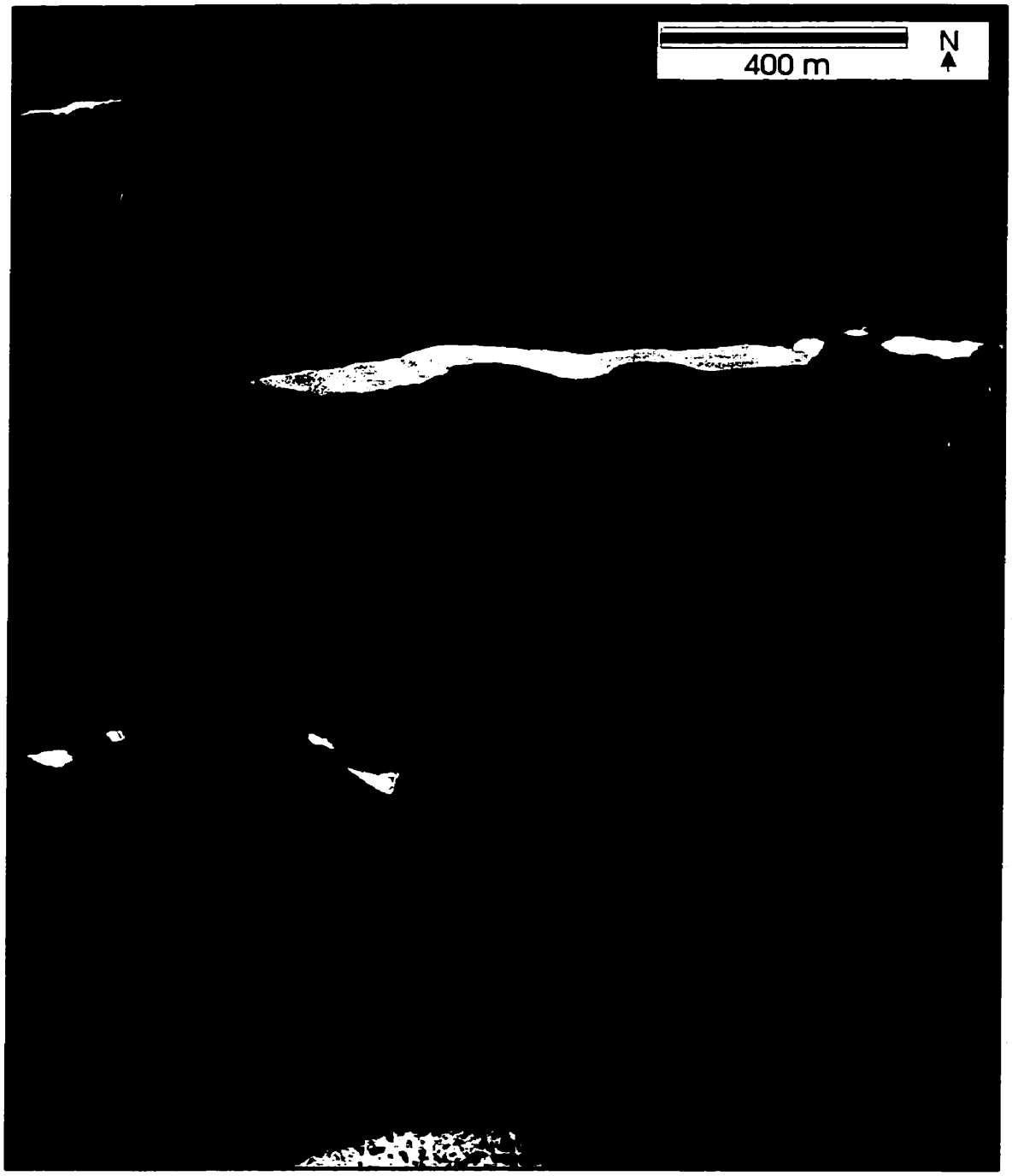

Figure 8.39 Panchromatic IKONOS image of the central zone of the Tingmisut Lake region.

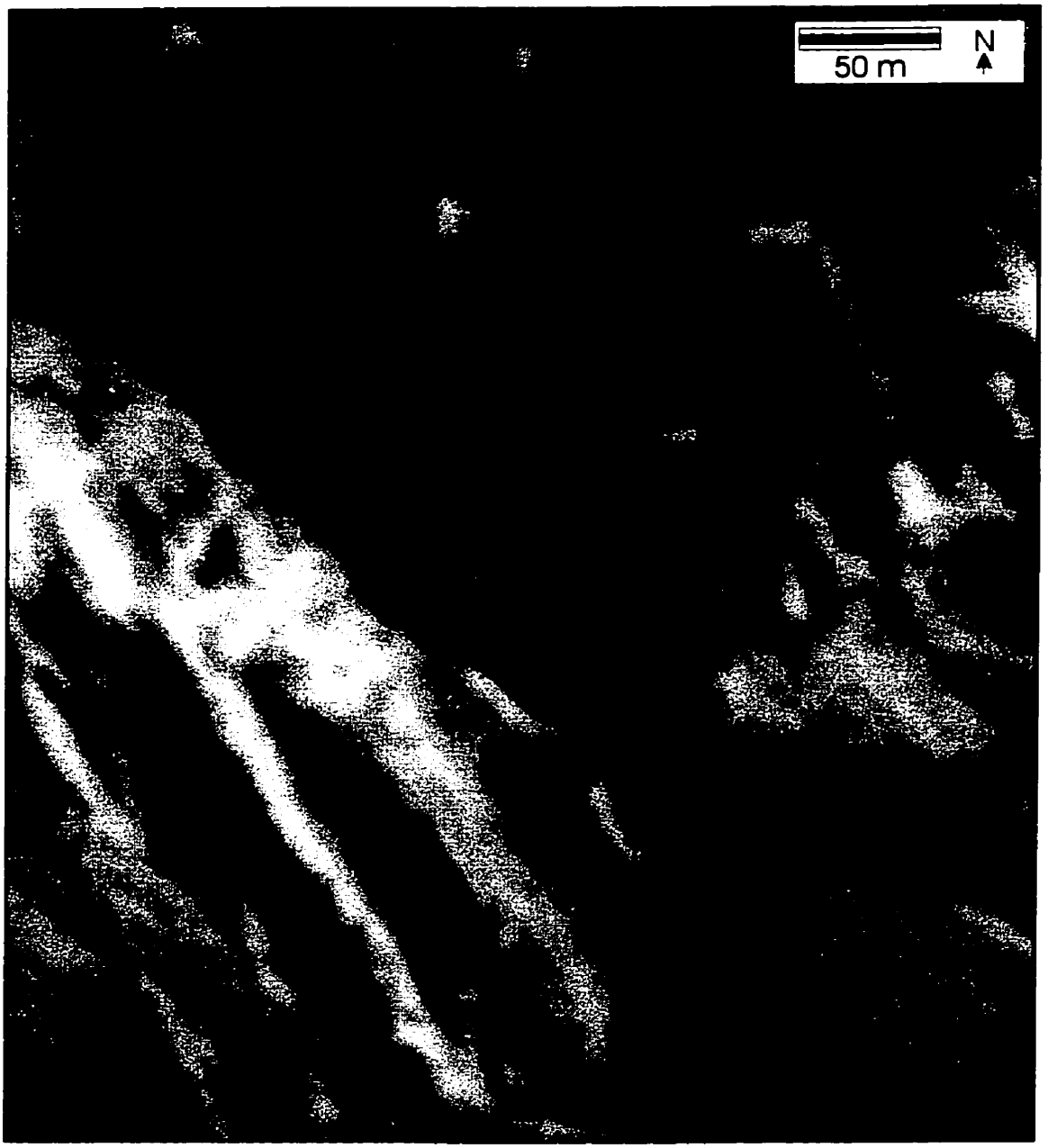

Figure 8.40 Aerial photograph of the central zone of the Tingmisut Lake region: detail (see Figure 8.35 for location).

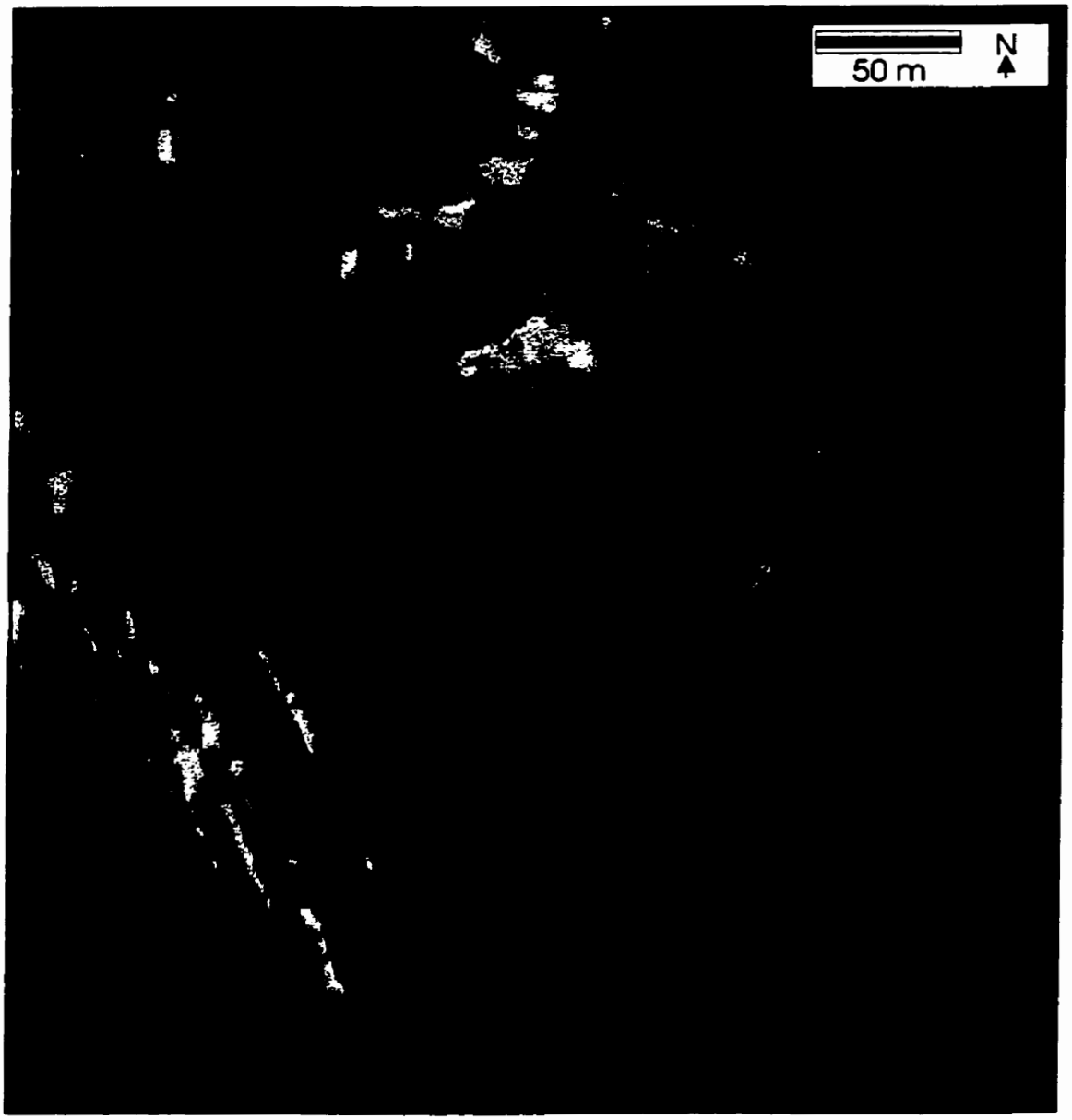

Figure 8.41 Panchromatic IKONOS image of the central zone of the Tingmisut Lake region: detail (see Figure 8.35 for location).

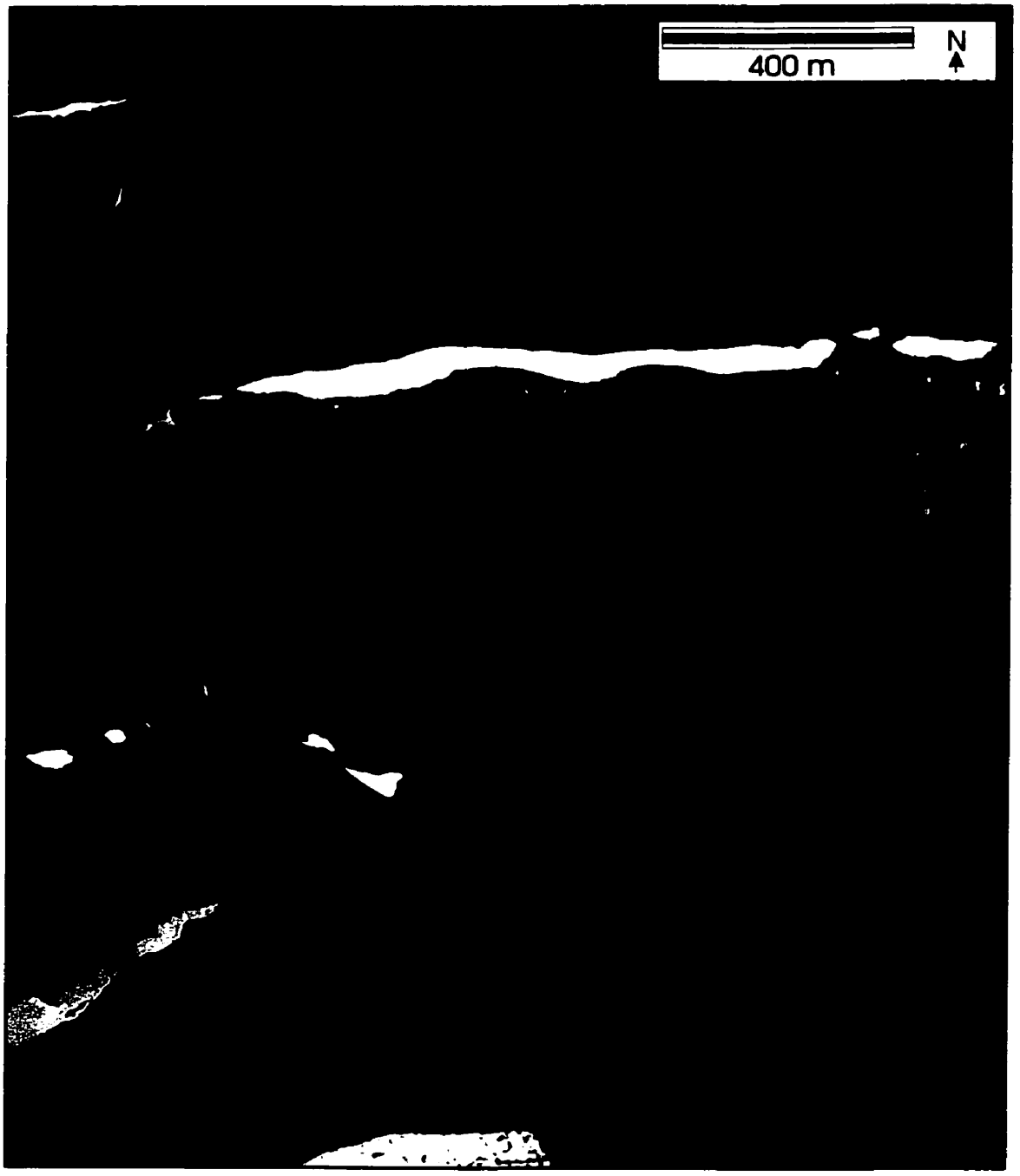

Figure 8.42 IKONOS colour composite (multispectral channels 321:RGB; true colour) for the central zone of the Tingmisut Lake region.

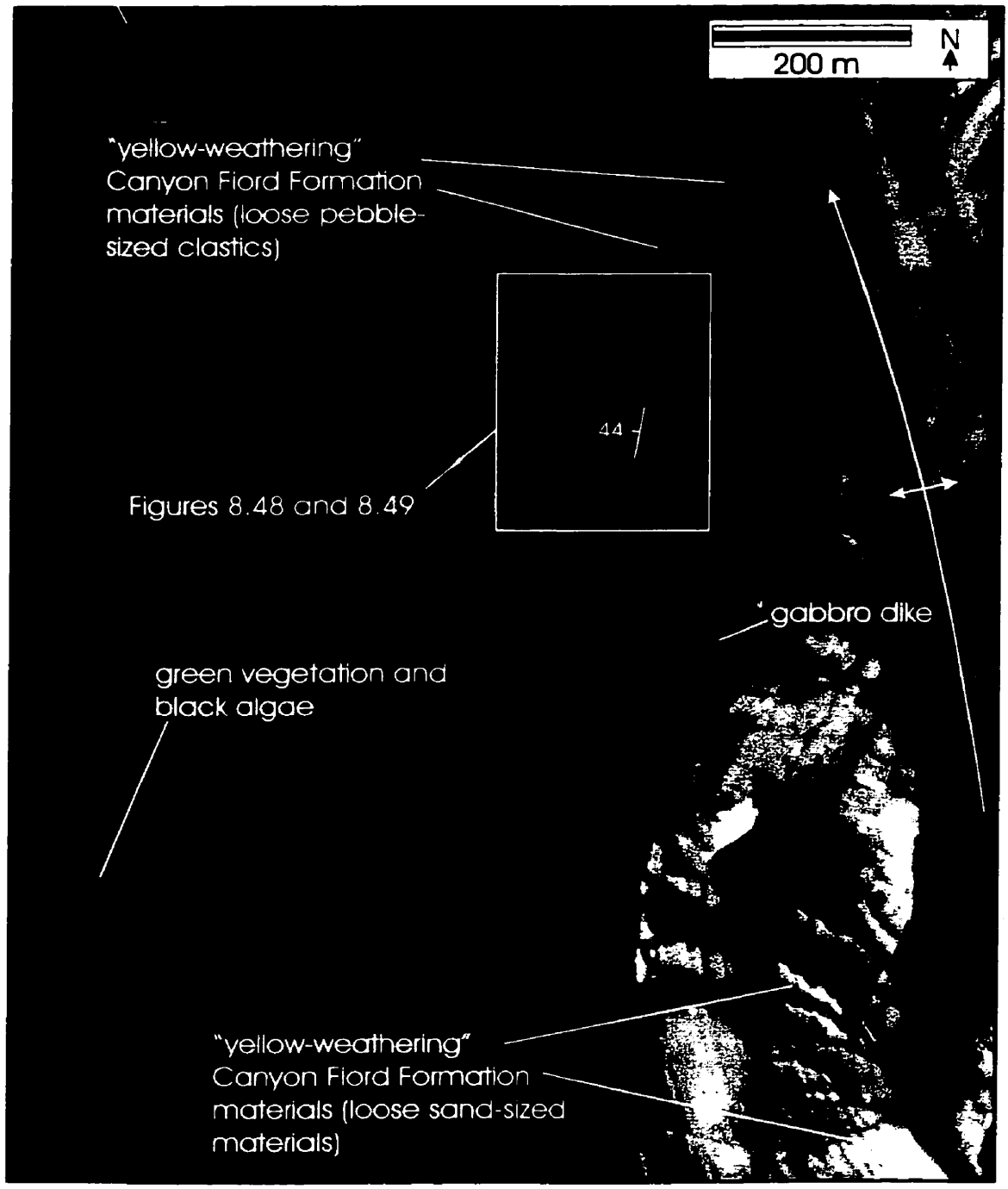

Figure 8.43 Aerial photograph of the south zone of the Tingmisut Lake region (photograph A16763-54). Structural annotation after Harrison (1995, p.114).

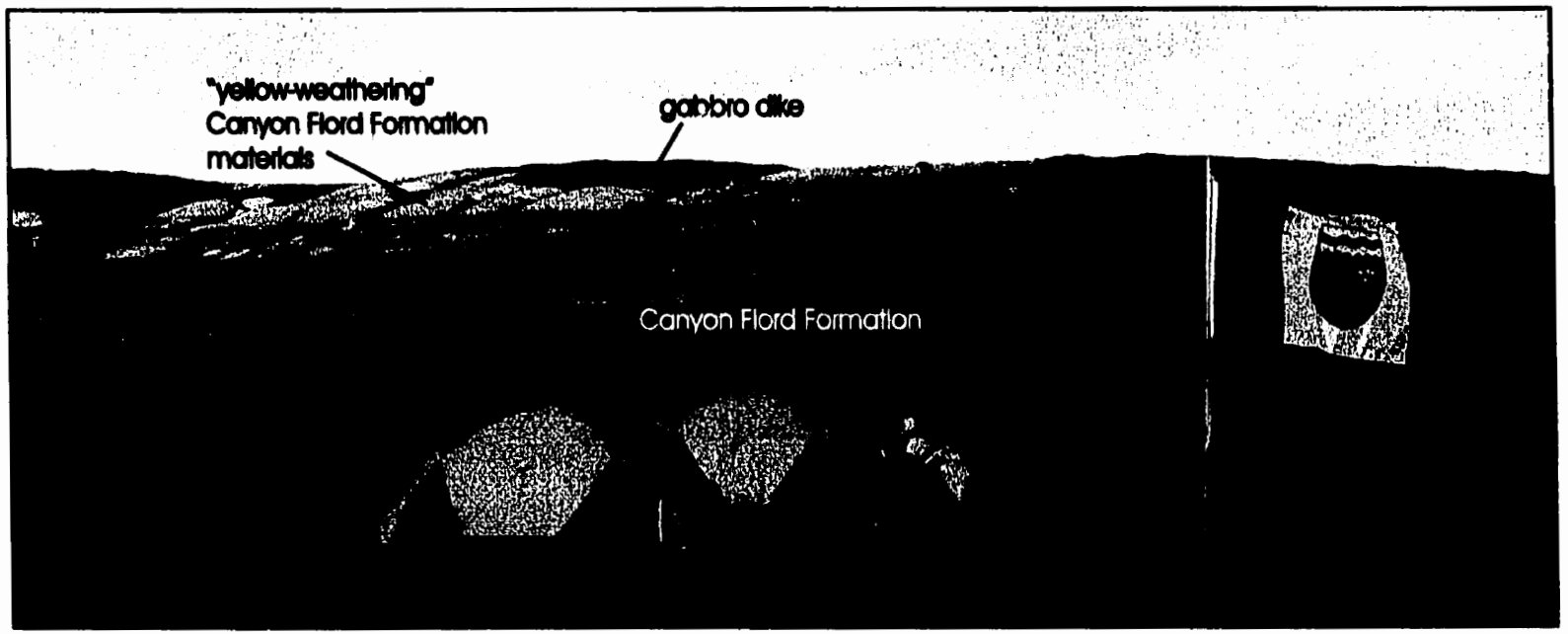

Figure 8.44 Ground photograph of the southern zone of the Tingmisut Lake region. View is across the gabbro dike, toward the northeast. The gabbro dike is about 2 km from the tents in the foreground, which are located outside of the zone.

of greater vegetation cover are associated with darker tones, although changes in lighting conditions across the zone make such tonal changes inconsistent and difficult to interpret (Figure 8.43). The visual information provided by the TM 543:RGB and Radarsat images (Figures 8.45 and 8.46, respectively) for the south zone is mainly limited to topographic features related to the gabbro dike. The panchromatic IKONOS image (Figure 8.47) provides an amount of spatial and tonal information that is very similar to that provided by the aerial photograph (compare details in Figures 8.48 and 8.49). The colour infrared IKONOS image (Figure 8.50; channels 432:RGB) has sufficient spectral resolution to clearly discriminate between the red-weathering and yellow units of the Canyon Fiord Formation. The image also provides high-resolution information on the precise position of the gabbro dike (dark brown) and black-algae cover (red) on Canyon Fiord Formation materials; this is notable, since it could conceivably allow for distinct separation between the algae and gabbro classes in the region (as noted in Section 5.3.1.4, the relatively poor spatial resolution of the TM imagery may have caused the training data for the gabbro class to be mixed with a small number of pixels dominated by black algae cover, contributing to the confusion between, for example, the Canyon Fiord Formation and gabbro classes).

8.3.2 Weatherall Bay Region (Melville Island)

The Weatherall Bay region is about 70 by 100 km in dimension and is located in the central portion of eastern Melville Island (Figures 8.1 and 8.51). Geological materials exposed at the surface mainly consist of units of the Devonian clastic wedge, which represents the depositional record of the Ellesmerian Orogeny (Section 4.2.1.3). Carboniferous and

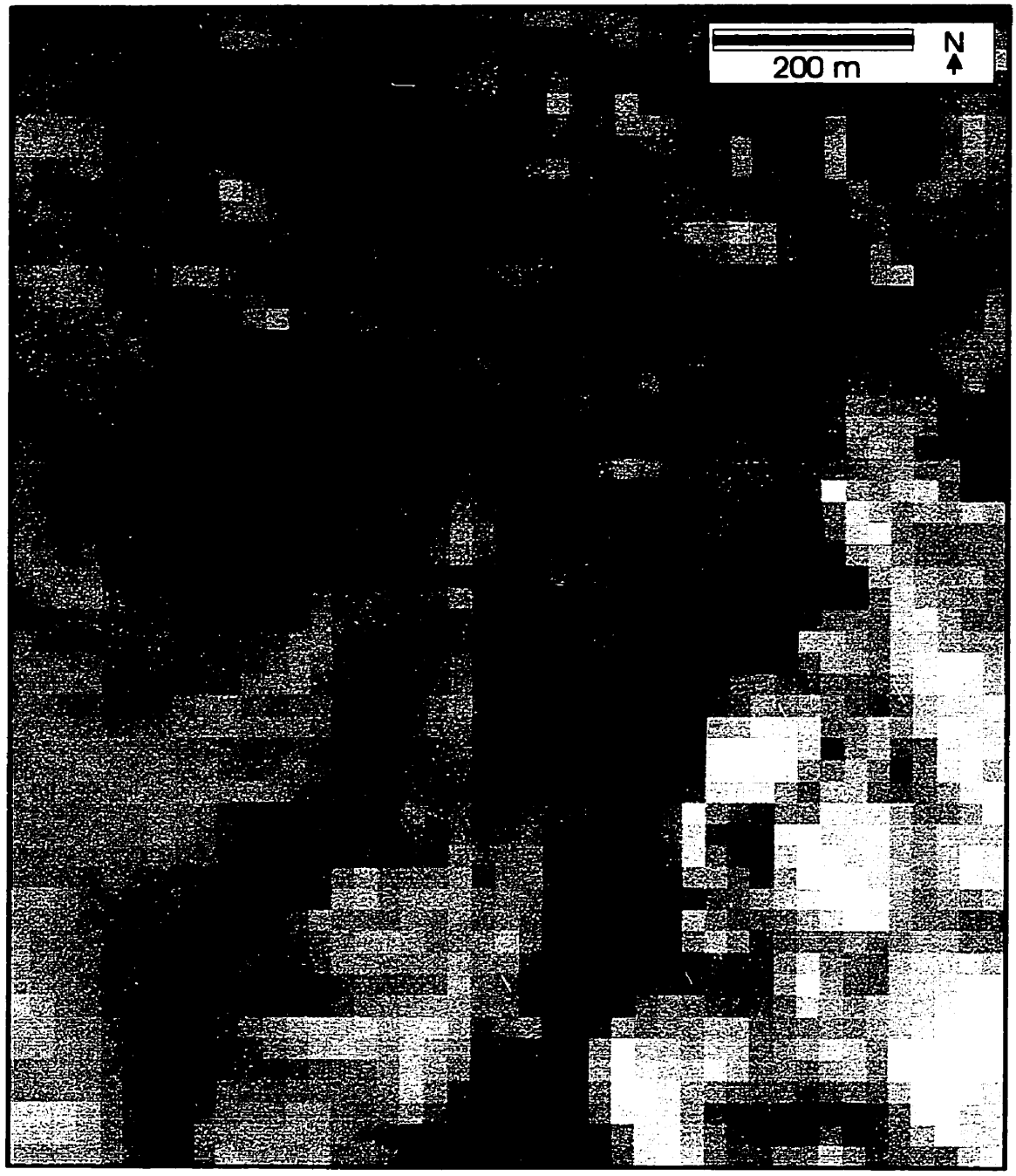

Figure 8.45 TM colour composite (channels 543:RGB) for the south zone of the Tingmisut Lake region.

Figure 8.46 Radarsat image of the south zone of the Tingmisut Lake region.

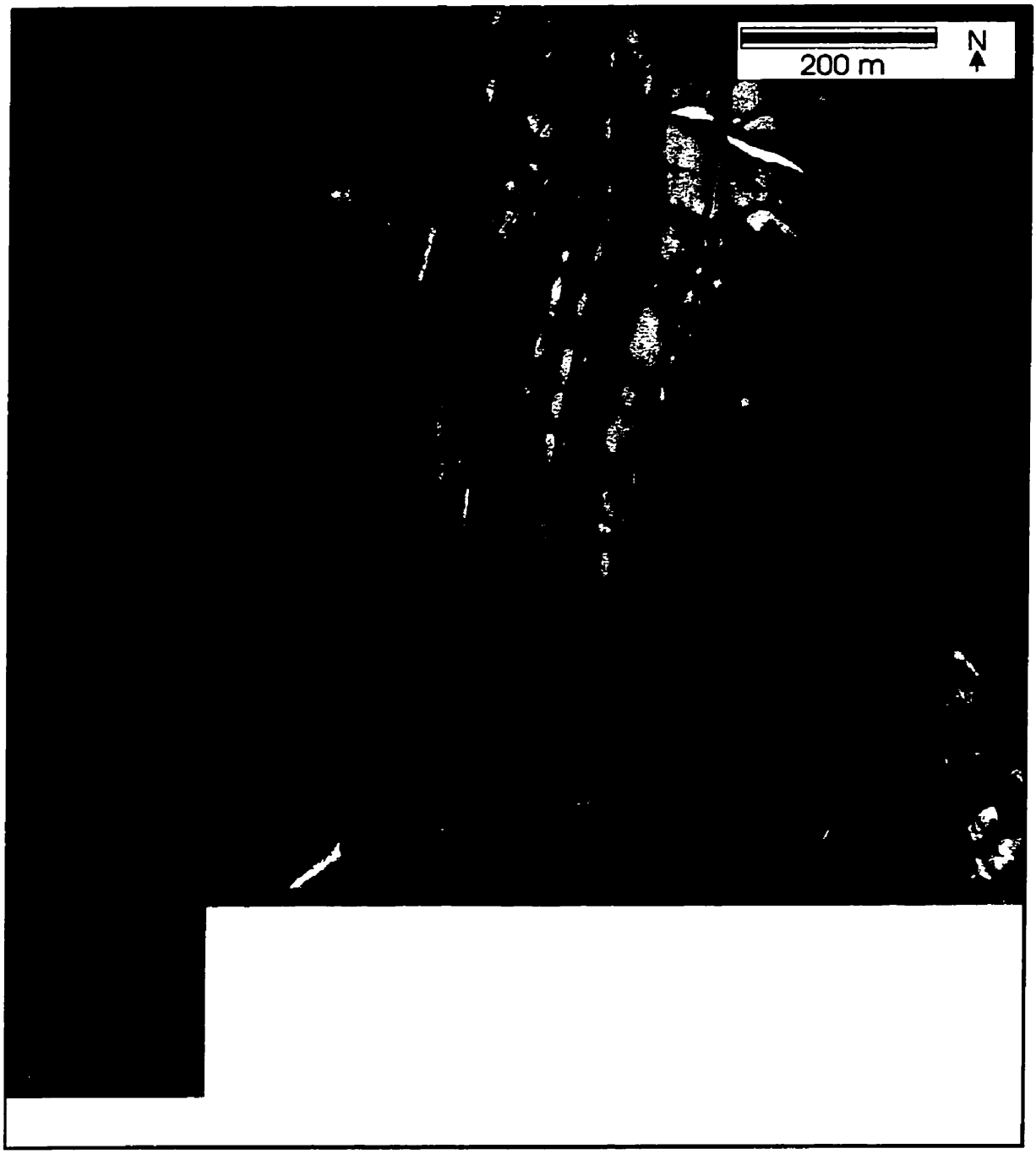

Figure 8.47 Panchromatic IKONOS image of the south zone of the Tingmisut Lake region.

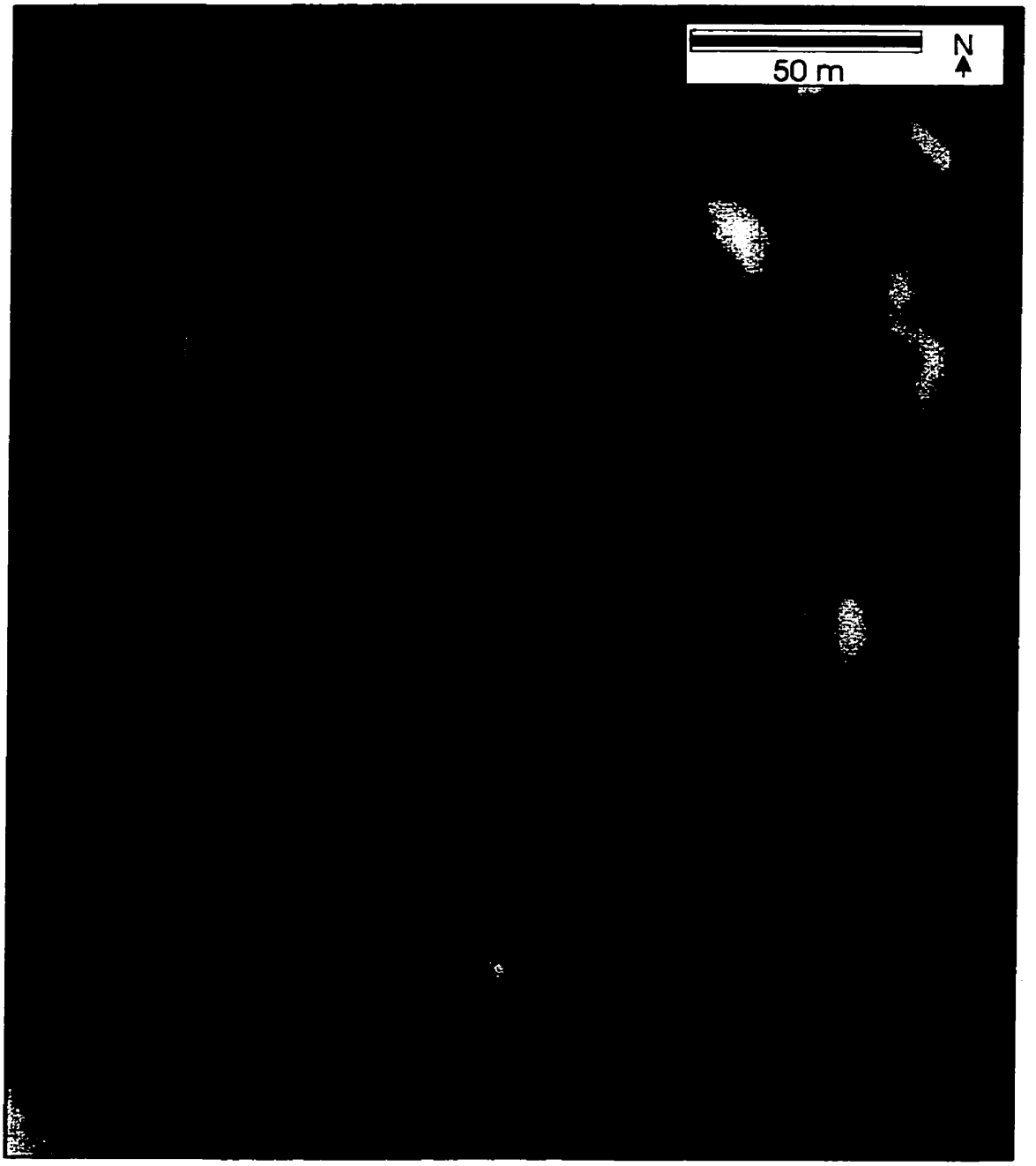

Figure 8.48 Aerial photograph of the south zone of the Tingmisut Lake region: detail (see Figure 8.43 for location).

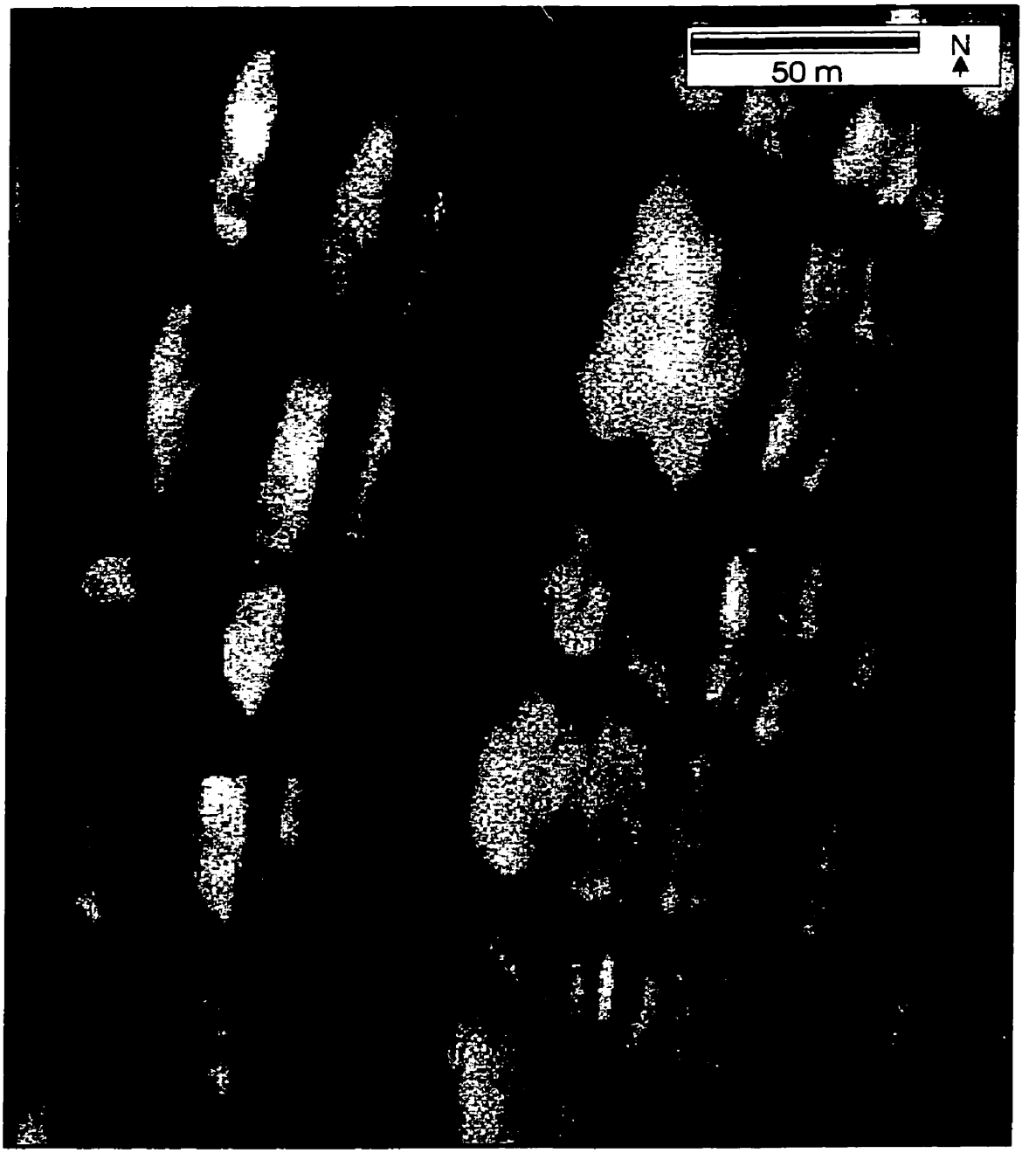

Figure 8.49 Panchromatic IKONOS image of the south zone of the Tingmisut Lake region: detail (see Figure 8.43 for location).

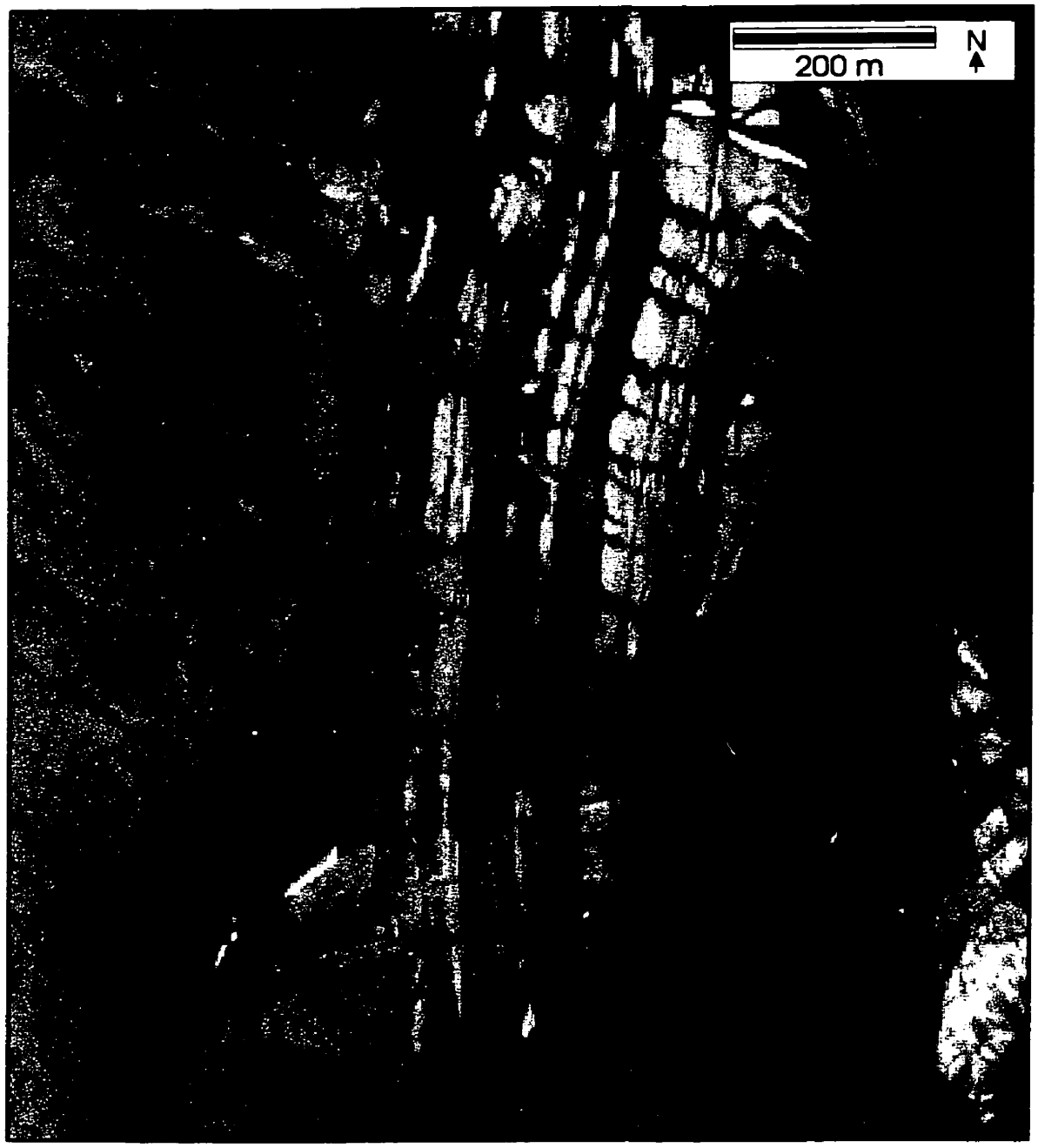

Figure 8.50 IKONOS colour composite (multispectral channels 432:RGB; colour infrared) for the south zone of the Tingmisut Lake region.

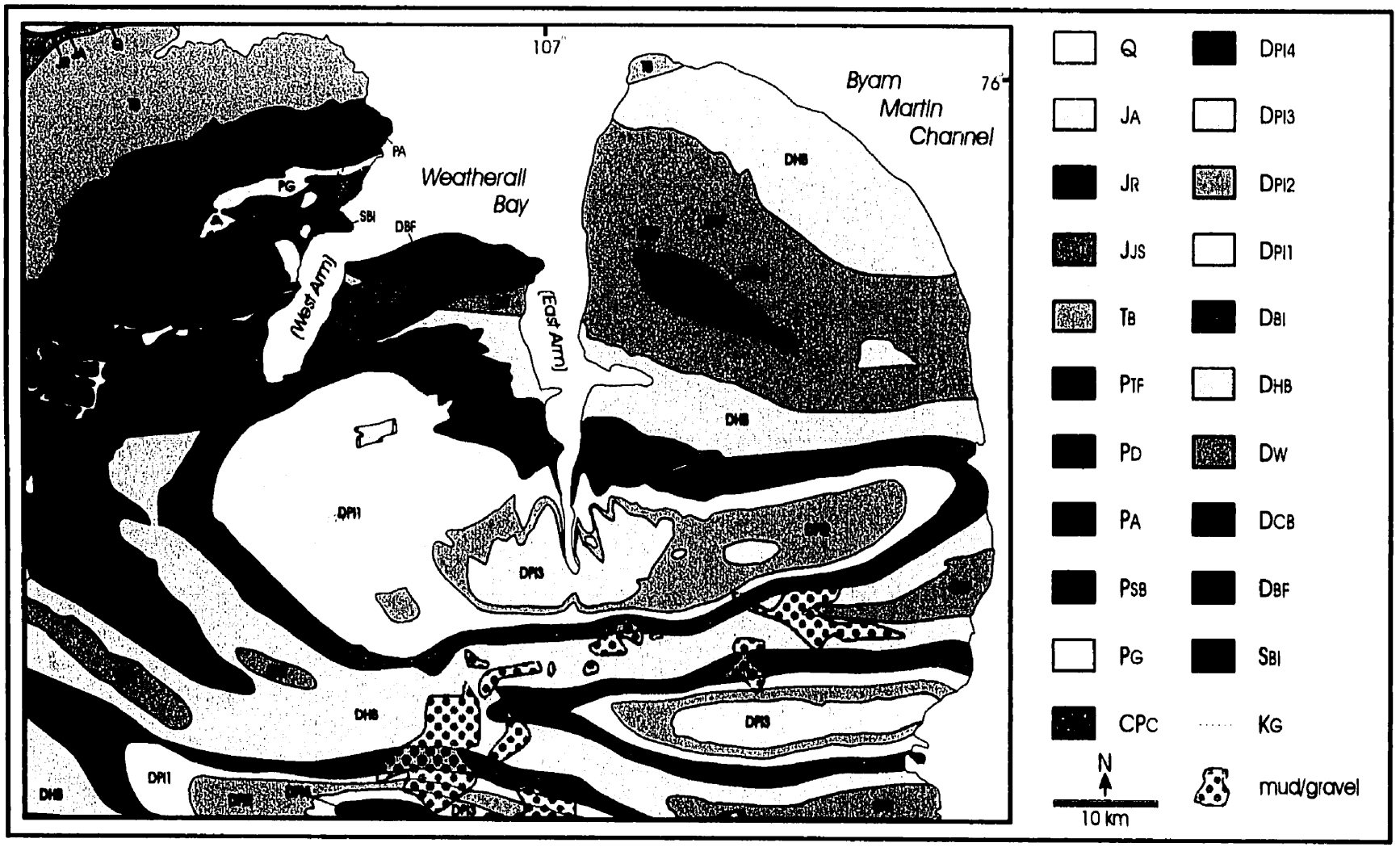

Figure 8.51 Geology of the Weatherall Bay region (after Harrison, 1995). Geological units are described in Table 8.1.

Permian units of the Sverdrup Basin are exposed in the northwest portion of the region [this portion of the region includes the Tingmisut Lake region (Section 8.3.1)] (Figure 8.51; Table 8.1; Section 4.2.1.3).

On Melville Island, the Devonian clastic wedge consists of a 3.3 to 4.6 km thick siliciclastic- and mudrock-dominated foreland succession that blankets parts of the shelf and deepwater basins of the Franklinean Mobile Belt (Section 4.2.1.3) (Harrison, 1995). The clastic wedge was subjected to southerly-directed deformation during the Ellesmerian Orogeny, producing the salt-based fold belt that is exposed over much of the southern portion of Melville Island (Sections 4.2.1.3 and 4.2.2.1) (Harrison, 1995). There are three unconformity-bounded sequences in the clastic wedge, listed here from oldest to youngest: 1) the Hecla Bay Sequence (on Melville Island comprising the Blackley, Cape De Bray, Weatherall, and Hecla Bay formations); 2) the Beverley Inlet Sequence (on Melville Island comprising only the Beverley Inlet Formation); and 3) the Parry Islands Sequence (on Melville Island comprising five locally mappable units of the Parry Islands Formation) (Embry, 1991; Harrison, 1995). The geological units of the Devonian clastic wedge lie in open folds exposed at the surface. Regional-scale folds have wavelengths of 12 to 17 km, axial planes that dip 80 to 90° north or south, and axial plunge variation that is 0 to 6 ° (Harrison, 1995).

The Sverdrup Basin units in the Weatherall Bay region include the following formations, listed from oldest to youngest: Canyon Fiord, Great Bear Cape, Sabine Bay, Assistance, Degerböls, Trold Fiord, Bjorn, Jameson Bay and Sandy Point, Ringnes, and Awingak. Brief descriptions of the geological units in the Weatherall Bay region are given

in Table 8.1. Most of the Weatherall Bay region was not visited for this study, and thus the evaluation of TM and Radarsat imagery given below is much more limited in scope than the evaluations for the other two regions.

8.3.2.1 Landsat TM Image

Landsat TM colour composites for the Weatherall Bay region are given in Figure 8.52 (channels 321:RGB; true colour), Figure 8.53 (channels 543:RGB), and Figure 8.54 (channels 754:RGB). Because the Landsat image was acquired late in the summer season (August 8, 1994), ice cover in the east and west arms of Weatherall Bay is substantially reduced (although ice cover north of Weatherall Bay and in Byam Martin Channel is extensive). Solar illumination is from the south, and pixel spacing is 30 m. Contrast was enhanced in the TM images by using linear histogram stretches.

As with the Tingmisut Lake region, open water is easily discriminated from other materials in the TM imagery by its low reflectance in the visible (Figure 8.52) and negligible reflectance in the mid-infrared (Figure 8.54). Snow patches (e.g., in valleys of the northeastern portion of the region) and sea ice are easily discriminated from other materials by their high reflectance in the visible (Figure 8.52) and very low reflectance in the mid-infrared (Figure 8.54). Areas of dense moss and broadleaf vegetation cover are well discriminated by their high reflectance in the near-infrared and low reflectance in the red portion of the visible spectrum (these areas are shown in shades of green in Figure 8.53). Geological units that are characterized by relatively extensive vegetation cover include the Trold Fiord, Weatherall Bay, Beverly Inlet, and Parry Island formations (compare Figures

Table 8.1 Exposed bedrock units of the Weatherall Bay region (continued on following page) (Harrison, 1995). A corresponding map of bedrock geology is given in Figure 8.51.

Unit Name	Symbol	Lithology and Interpretation
Quaternary Deposits	Q	Fluvial, deltaic, glacial, and marine beach sediments (mapped only where underlying geology cannot be inferred).
Awingak Fm.	JA	Sandstone, quartzose; siltstone; minor conglomerate; nearshore marine.
Ringnes Fm.	JR	Shale, dark grey to black weathering; siltstone; minor find-grained sandstone; common dolomitic concretions; offshore marine.
Jameson Bay / Sandy Point Fms.	JJS	Shale, light grey and greenish grey weathering; sandstone, quartzose, glauconitic and fossiliferous; basal oolitic ironstone and pebble conglomerate; marine.
Bjorn Fm.	TB	Sandstone, variably carbonaceous and pebbly, weathers orange, grey-green, buff and red; minor shale; fluvial and deltaic.
Trold Fiord Fm.	PTF	Sandstone, peloidal and glauconitic, green and red weathering, variably calcareous; pebbly bioclastic limestone; spiculitic chert; marine.
Degerböls Fm.	PD	Limestone, bioclastic, common brachiopods, crinoids, and bryozoans; unrestricted shallow marine.
Assistance Fm.	PA	Sandstone, grey to grey-green, variably glauconitic, quartzose, and carbonaceous; siltstone; fossiliferous ironstone; transgressive marine.
Sabine Bay Fm.	PSB	Sandstone, quartzose, cherty, and variably pebbly and carbonaceous; chert-pebble conglomerate; siltstone; minor coal; fluvial and marginal marine.
Great Bear Cape Fm.	PG	Limestone, fossiliferous, variably pebbly and arenaceous; calcareous sandstone; unrestricted shallow water marine.
Canyon Fiord Fm.	CPC	Red-bed sandstone, variably pebbly and calcareous; chert-pebble conglomerate; oligomictic conglomerate and breccia; minor limestone; fluvial and shallow water marine.

Table 8.1 (continued).

Parry Islands Fm. unit 4	DPI4	Shale: dark grey, common sideritic nodules; prodeltaic or lacustrine.
Parry Islands Fm. unit 3	DPI3	Sandstone: quartzose, deltaic.
Parry Islands Fm. unit 2	DPI2	Cape Fortune Member: Grey-green weathering; sandstone, calcareous and fossiliferous; shale; shallow water marine.
Parry Islands Fm. unit 1	DPI1	Burnett Point Member::sandstone, orange to white weathering; green siltstone; minor shale and bituminous coal; deltaic.
Bevery Inlet Fm.	DBI	Sandstone, pale green and white weathering; siltstone, red and green weathering; grey-green shale; minor coal; fluvial and marginal marine.
Hecla Bay Fm.	DHB	Sandstone, micaceous and quartzose, weathers off-white, yellowish grey, and light green; siltstone; minor shale and coal; deltaic and marginal marine.
Weatherall Fm.	DW	Siltstone, grey-green and quartzose; sandstone, variably calcareous and fossiliferous; dark grey-green shale; delta front and margin marine.
Cape De Bray Fm.	DCB	Shale, silty calcareous, and micaceous; minor sandstone, argillaceous, silty, and thin bedded; siltstone, variably fossiliferous; mudrock gravity flows.
Blue Fiord Fm.	DBF	Limestone, light brown, dark brown, and light grey, variably micritic, stromatolitic, cryptalgal, fossiliferous, and petroliferous; dolostone; subtidal and intertidal.
Barlow Inlet Fm.	SBI	Tingmisut Inlier: dolostone.
Gabbro Intrusion	KG	Near-vertical gabbro intrusion; ~123 Ma (Balkwill and Fox, 1982).

Figure 8.52 TM colour composite (channels 321:RGB; true colour) for the Weatherall Bay region.

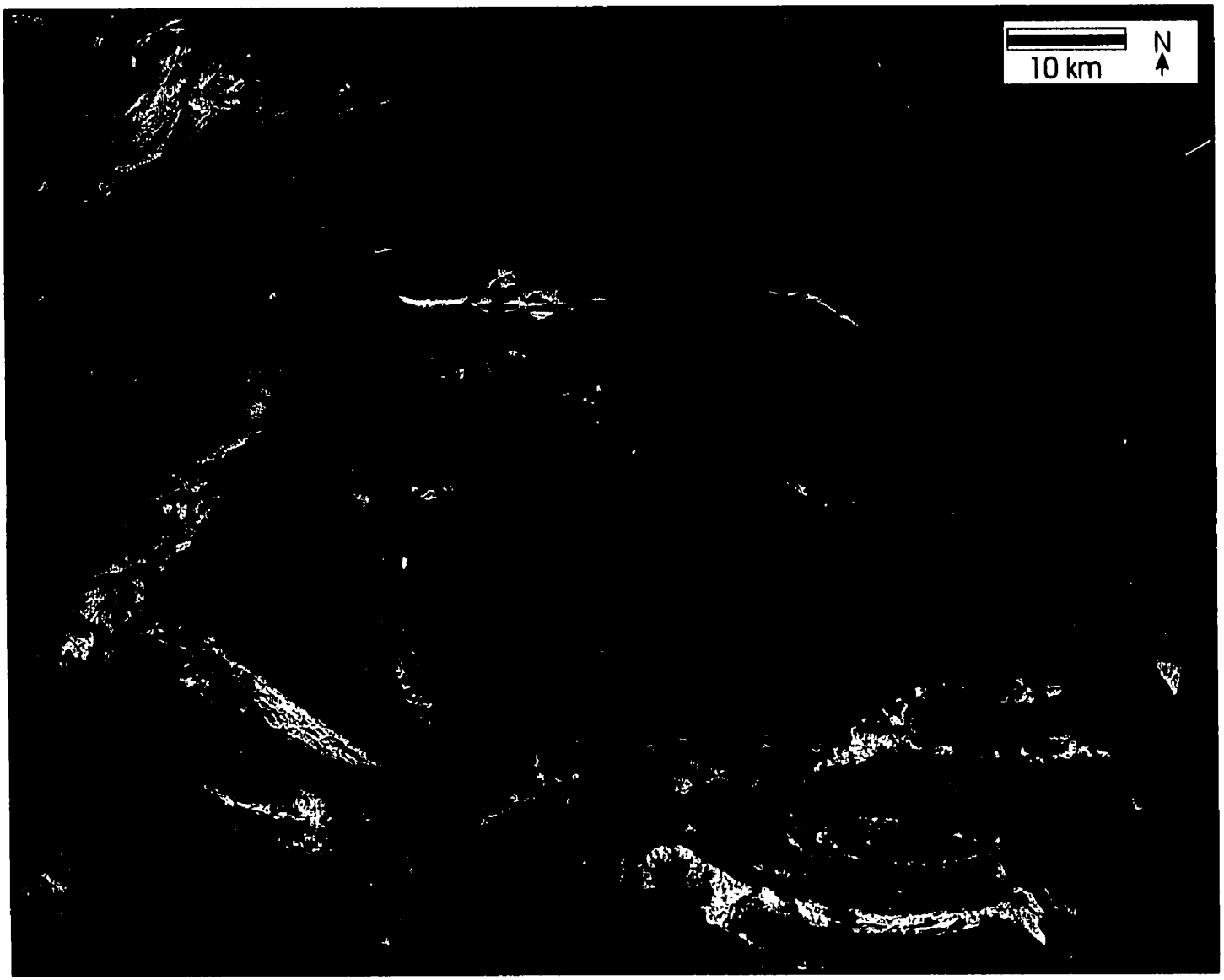

Figure 8.53 TM colour composite (channels 543:RGB) for the Weatherall Bay region.

Figure 8.54 TM colour composite (channels 754:RGB) for the Weatherall Bay region.

8.51 and 8.53). There is a good visual correlation between materials shown in shades of green in Figure 8.53 and materials shown in shades of dark brown colours in Figure 8.52. Low-level clouds are visible in all three TM colour composites (e.g., Figure 8.52). Thin high-level clouds extend in north-south directions over much of the region; contrast is not sufficiently high in Figures 8.52 to 8.54 for these clouds to be clearly visible.

The three TM colour composites provide substantial visual information regarding the distribution of lithological units exposed in the Weatherall Bay region. Geological units with relatively distinct spectral properties include the Canyon Fiord (shades of orange in Figures 8.52 and 8.54; see also Section 8.3.1), Trold Fiord (shades of light orange in 8.52, light pink in 8.53, and light green in 8.54), Blue Fiord (shades of light gray in 8.52, light pink in 8.53, and light green in 8.54), and Hecla Bay formations (shades of light gray in 8.52, light pinkish gray in 8.53, and light greenish gray in 8.54). The spectral properties of some units are not consistent across the region, presumably because of differences in lithological or cover characteristics (e.g., materials of the Hecla Bay formation do not have consistent spectral properties - compare the generally lighter southern exposures to the generally darker northern exposures). Because much of the Weatherall Bay region was not visited for this study, the specific reasons for these changes in the spectral properties of individual units are uncertain.

Numerous other geological units in the region can be visually distinguished despite their non-unique spectral properties (e.g., individual units of the Parry Islands Formation). This appears to be due to the following two factors: 1) these units tend to have significantly different spectral properties compared to adjacent units (probably related in part to differing amounts of vegetation cover); and 2) the spectral properties of these units, while not unique,

are nevertheless sufficiently consistent from location to location to allow for their visual recognition.. Large mud and gravel deposits, which obscure parts of the Hecla Bay, Beverly Inlet, Parry Islands, and Weatherall Bay formations, are visible in the TM colour composites (most notably in Figure 8.54; compare to Figure 8.51).

8.3.2.2 Radarsat Image

The Radarsat image of the Weatherall Bay region is given in Figure 8.55. The image was derived from the same original data as the image for the Tingmisut Lake region, and thus has the same basic properties (i.e., the image was acquired on July 17, 1998, from the west-southwest, preferentially illuminating slopes oriented toward this direction; speckle was reduced by filtering original data using a 7 x 7 Lee filter; the image has a pixel spacing of 12.5 m). Contrast was enhanced in the Radarsat image using a linear histogram stretch. Weatherall Bay and Byam Martin Channel are almost entirely covered by ice in the image.

Open water, which is associated with very low values in the Radarsat image, is easily discriminated from geological and ice classes (Figure 8.55). Sea and lake ice are associated with low to moderate image values in the Radarsat image. Sea and lake ice are easily distingished from land materials based on their low image values and the consistency of their texture, although as noted in Section 8.3.1, there is potential for confusion between ice and geological classes in the Tingmisut Lake region (i.e., in the northwest corner of the Weatherall Bay region). Snow cover is associated with very low radar backscatter in the Radarsat image, making it easy to discriminate from surrounding geological materials when not located within valleys. In valleys, there is some potential for confusion between snow

Figure 8.55 Radarsat image of the Weatherall Bay region. The locations of land areas with especially low image values are shown.

cover and radar shadow. As noted in Section 8.3.1, there is potential for confusion between areas of snow cover and open water.

The Radarsat image shows three large land areas that are associated with very low backscattering. The radar-dark areas consist of the area south of the West Arm of Weatherall Bay, and two large areas in the southwestern corner of the region (Figure 8.55). All three areas are floodplains, and thus it is possible that the areas are dark in the image due to shallow seasonal flooding (the areas are not shown to be flooded in the TM images). However, because the channels within the floodplains are associated with greater backscatter, this suggests that a simple layer of water cannot have covered the floodplain at the time of imaging (the channels would not have been exposed, and thus would have been associated with low values). Also, these areas are associated with similarly low values in a different Radarsat image (acquired in September, 1997) not used in this research, suggesting that the low values associated with the three floodplains are characteristic of the exposed floodplain materials themselves. It is possible that the materials are sufficiently fine to act as specular reflectors under the environmental conditions that prevail in the region; there is no field data available to substantiate this hypothesis. The underlying bedrock of all three flooded areas belongs to the Beverly Inlet Formation, a unit consisting mainly of sandstone, siltstone, and shale (Table 8.1).

The extents of several geological units may be easily recognized on the Radarsat image. Some of the most visually distinct units include the Blue Fiord, Barlow Inlet, Hecla Bay, and Weatherall Bay formations, as well as the second member of the Parry Islands Formation (Figure 8.55; compare with Figure 8.51). These units are recognizable because

of their generally higher image values relative to surrounding materials. Because fieldwork was conducted only in the northwest portion of the Weatherall Bay region, it is unknown if the materials of most of these formations are radar-bright as a result of surface-roughness, moisture conditions, or other factors. As noted in Section 8.3.1.2, dolostone materials of the Barlow Inlet formation (Tingmisut Inlier) are blocky (equant) and have dimensions on the order of the wavelength of the Radarsat sensor (5.6 cm), suggesting that they are radar-bright not only because of considerations related to topography and bedrock exposure, but also because they produce a surface that is rough. The two main exposures of Blue Fiord Formation materials were not visited for this research, but ground and aerial views of the western exposure of this formation suggest that similar conditions apply [i.e., exposures are associated with positive topographic features with extensive irregular bedrock exposures near their summits, and extensive talus deposits of blocky materials flanking their lower slopes (Figures 8.56 and 8.57)].

Inconsistency with regard to the association of image values to geological units is evident in the Radarsat image. For example, materials of the Hecla Bay Formation are associated with high image values in the southwestern portion of the region, but are associated with low to moderate values in much of the southeastern portion of the region, despite the fact that the materials are well exposed in both areas (see TM colour composites: Figures 8.52 to 8.54). The cause of this may be related to differences in surface roughness; given the good exposure of these materials (as is evident in the TM images) it cannot be related to factors such as vegetation cover or obscuration by surficial deposits. Topographic

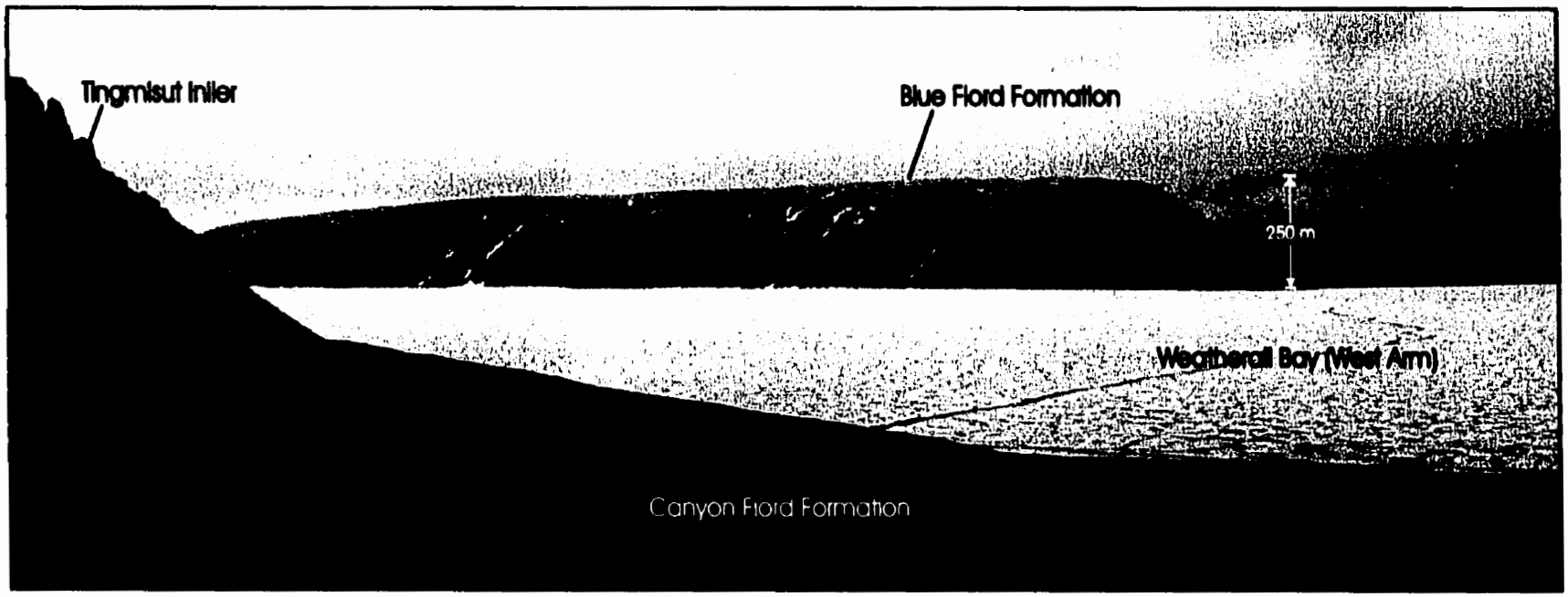

Figure 8.56 Ground view of the western exposure of the Blue Fiord Formation (limestone). Also shown are the Tingmisut Inlier (dolostone) and Canyon Fiord Formation materials (red-weathering sandstone). View is toward the east-southeast, from the west shore of the West Arm of Weatherall Bay. The width of Weatherall Bay is about 4 km in this area.

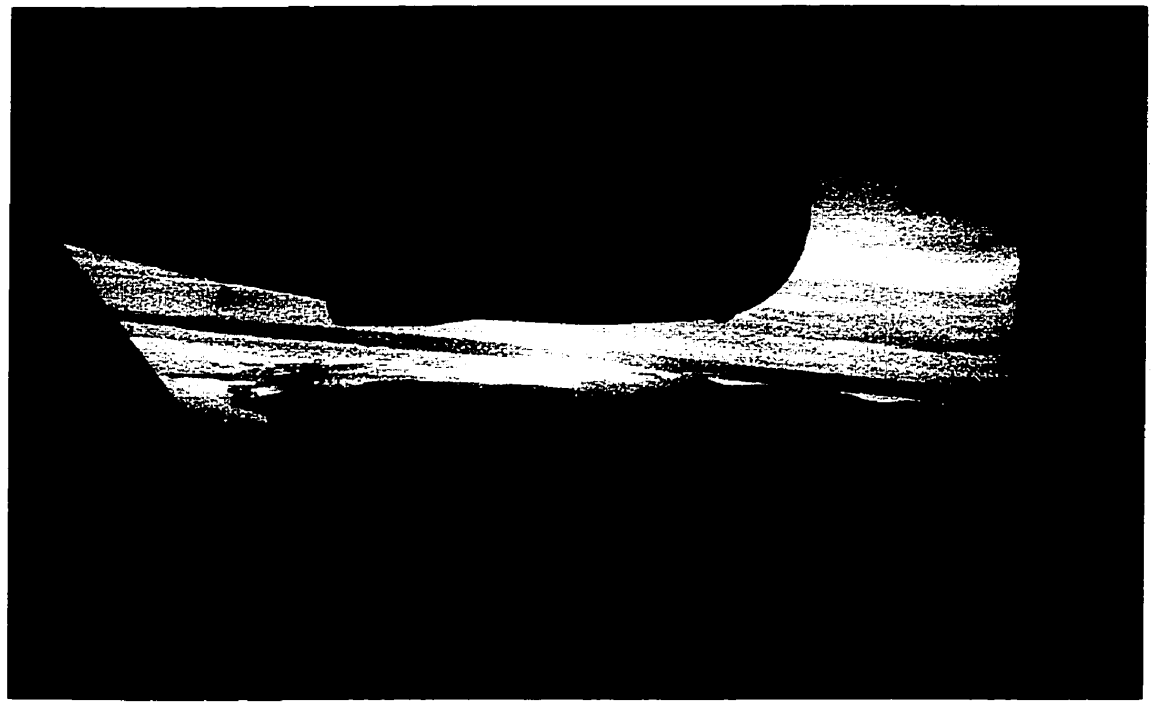

a

b

Figure 8.57 Photographs of the western exposure of the Blue Fiord Formation. The view in "a" is toward the east, and shows the westernmost portion of the exposure. The view in "b" is toward the northeast, and shows the central portion of the exposure.

factors contribute to variability in otherwise consistent ranges of image values in the Radarsat image. For example, the materials of the Canyon Fiord Formation are generally radar dark, but are brighter where slopes are more steep and are oriented toward the sensor.

The Radarsat image cannot be used to discriminate between vegetated and non-vegetated areas in the Weatherall Bay region (compare green-shaded areas in the TM colour composite in Figure 8.53 with corresponding locations in the Radarsat image - Figure 8.55). A clear example of this involves the Trold Fiord Formation, where the Radarsat image does not distinguish between well-exposed materials in the eastern portion of the formation and densely vegetated areas in the western portion.

Overall, both topography and surface roughness appear to be the most significant factors in determining the overall values in the Radarsat image of the Weatherall Bay region (although the evidence for the contribution of surface roughness to image values is very much incomplete because of the limited field data available for the region as a whole). Because of its characteristically side-lit appearance, the Radarsat image provides considerable visual information regarding the general nature of topography throughout the region. Despite inconsistencies regarding the relation between image values and individual geological units, the image may be used to clearly delineate the extent of exposures of numerous lithological units. Further field investigations in the region would aid in the recognition of the key factors involved in some of the above relations.

8.3.3 Lac Watts Region (Cape Smith Belt)

The Lac Watts region is located in the central portion of the Cape Smith Belt of

northern Québec (Figure 8.1). The Lac Watts region has an irregularly shaped boundary, and has maximum dimensions of 40 by 40 km (Figure 8.58). From south to north, exposed geological materials in the region belong to the Povungnituk, Chukotat, Spartan, and Watts groups. The geology of the central portion of the Cape Smith Belt is described in Section 4.3.3, and is briefly summarized below.

The Cape Smith Belt is 20 000 km^2 Early Proterozoic greenstone belt that forms a portion of the Québec-Baffin segment of the Trans-Hudson Orogen (Hoffman, 1985; St-Onge and Lucas, 1989, 1990a, 1993; St-Onge *et al.*, 1999). The belt consists of east-west trending mafic-ultramafic thrust sheets that were produced by southward-directed thrusting of allochthonous crust onto the Superior Province (Hoffman, 1985). The rocks of the southerly Povungnituk and Chukotat groups were accumulated in the Early Proterozoic on or adjacent to a north-facing rift margin of the Superior Province (St-Onge and Lucas, 1993). There is a south-north gradation of Povungnituk Group materials from ironstone and semipelite to mafic volcaniclastic rocks interlayered with basalt flows. The rocks of the Chukotat Group, which is fault-bounded and is interpreted to record the shift from the production of continental rift-type volcanic rocks to the formation of transition crust, are almost entirely of basaltic composition, and were accumulated in a submarine environment. Both the Povungnituk and Chukotat groups are intruded by mafic and ultramafic (gabbro and peridotite) sills. The Spartan Group is a fault-bounded assemblage of clastic sedimentary rocks (including mainly laminated dark pelites and semipelite), and has no known link with the rocks of the Superior Province, the Povungnituk Group, or the Chukotat Group (St-Onge and Lucas, 1993). The Watts Group is a fault-bounded assemblage of layered mafic and

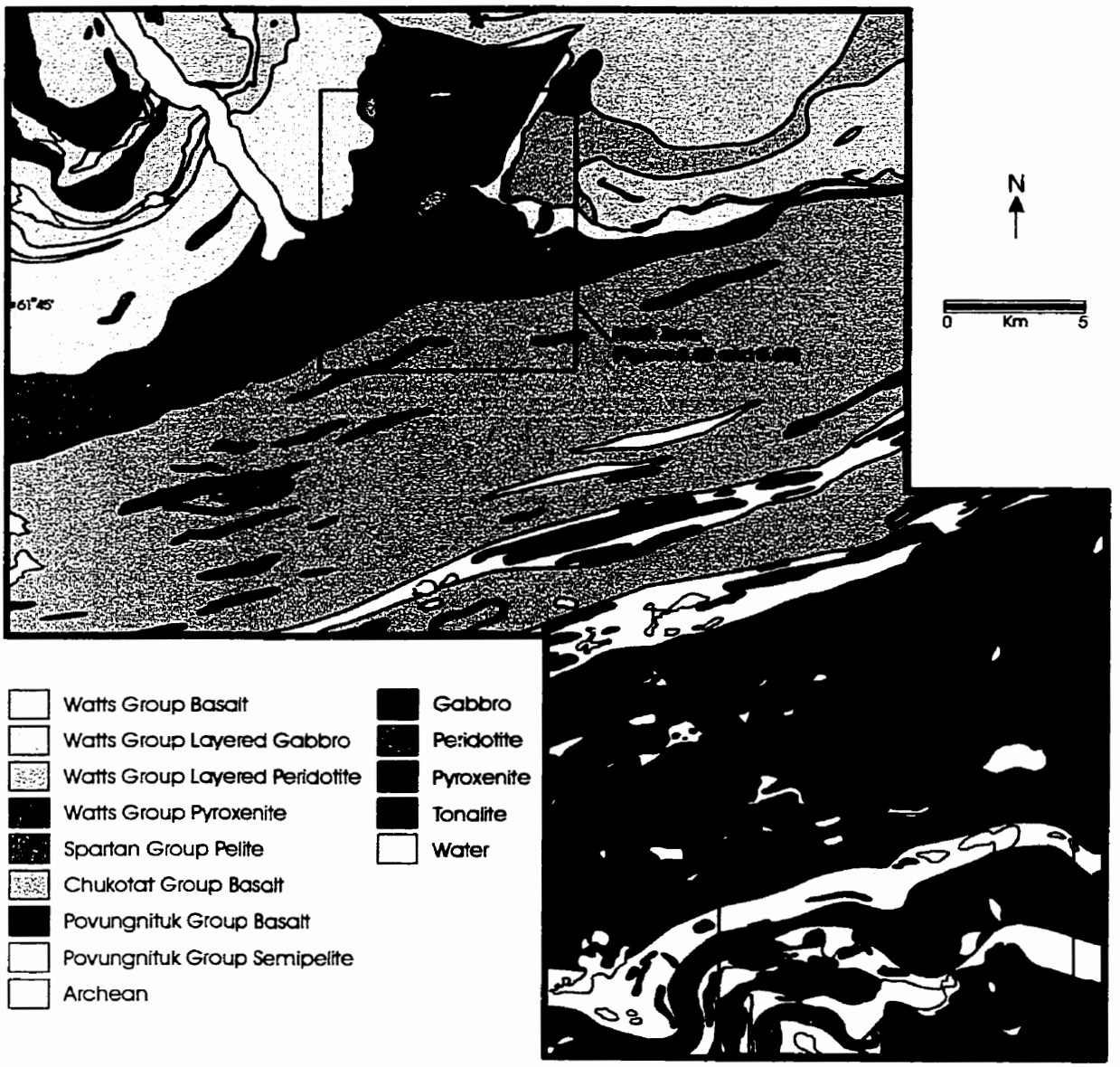

Figure 8.58 Bedrock geology of the Lac Watts region (after St-Onge and Lucas, 1989). Geological units are described in Table 4.3.

ultramafic rocks, massive and pillowed basalt flows, mafic sills and sheeted dykes, and rare plagiogranite intrusions (St-Onge and Lucas, 1993). Like the Spartan Group, there is no known link between the Watts Group and the other units of the region. The rocks of the Watts Group have been interpreted to represent the crustal remnants of a tectonically dismembered ophiolite suite (e.g., Scott *et al.*, 1989). A summary of the geological units of the Lac Watts region is given in Table 4.3 and Figure 8.58.

Exposure of bedrock is generally excellent in the region, although a discontinuous cover of glacial drift is present. Meltwater landforms associated with glaciation (e.g., eskers) are found in the region. Vegetation in the Lac Watts region is mainly characterized by barrens communities, including moss (dominantly *Rhacomitrium lanuginosum*), grass, and similar low-growing plants (Section 4.3.8.1; St-Onge and Lucas, 1993). Most rock exposures are partially covered by lichens (Section 4.3.8.1).

8.3.3.1 Landsat TM Image

Landsat TM colour composites for the Lac Watts region are given in Figure 8.59 (channels 321:RGB; true colour), Figure 8.60 (channels 543:RGB), and Figure 8.61 (channels 754:RGB). TM colour composites for the north and south zones of the region (Figure 8.58) are given in Figures 8.62 and 8.63, respectively (channels 543:RGB). Because the TM image was acquired late in the summer season (September 3, 1997), there is essentially no snow or ice cover in the region. Solar illumination is from the south-southeast, and pixel spacing is 30 m. Contrast was enhanced in the TM images using linear histogram stretches.

Using the TM imagery, open water can be easily discriminated from other materials

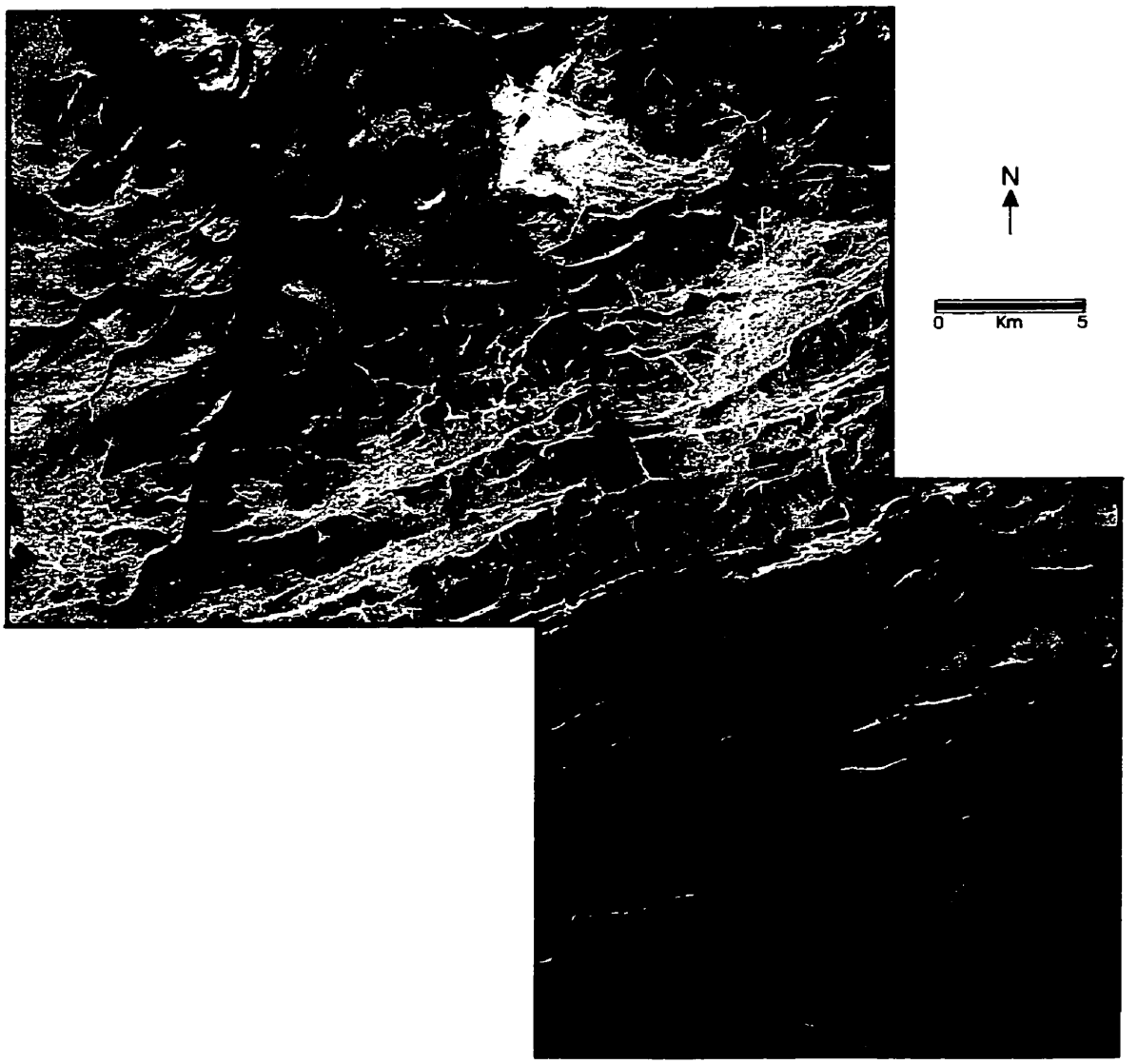

Figure 8.59 TM colour composite (channels 321:RGB; true colour) for the Lac Watts region.

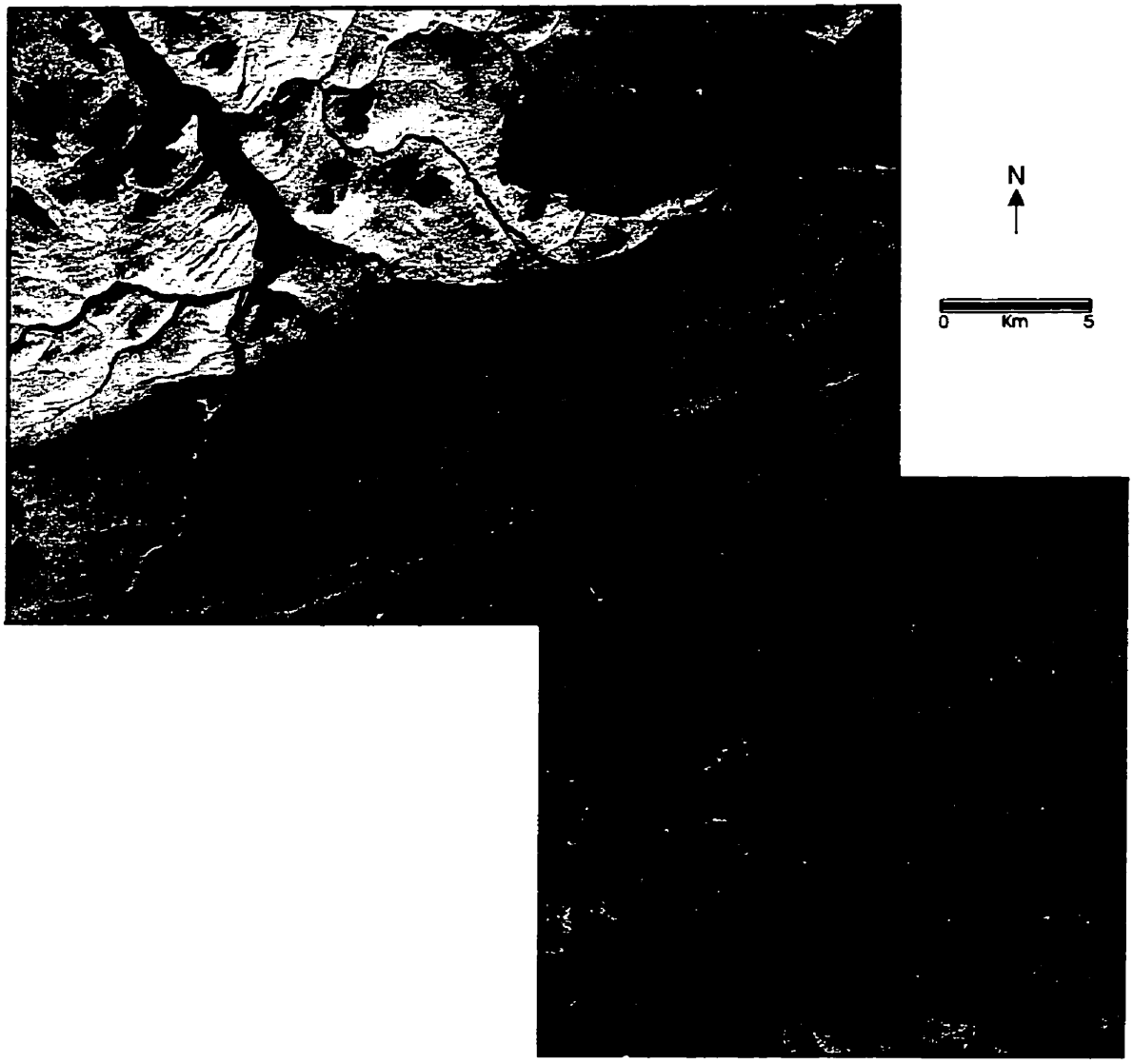

Figure 8.60 TM colour composite (channels 543:RGB) for the Lac Watts region.

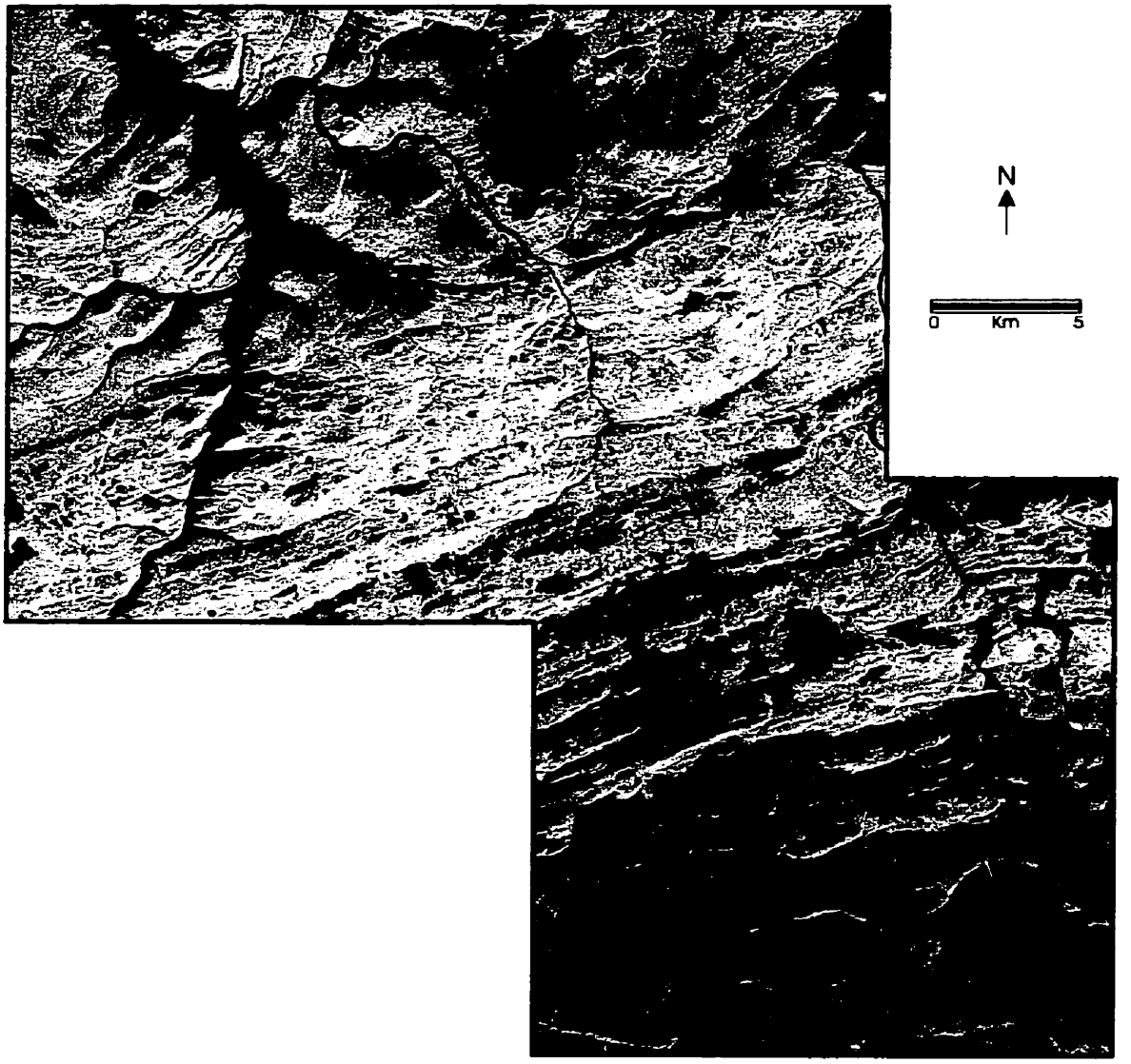

Figure 8.61 TM colour composite (channels 754:RGB) for the Lac Watts region.

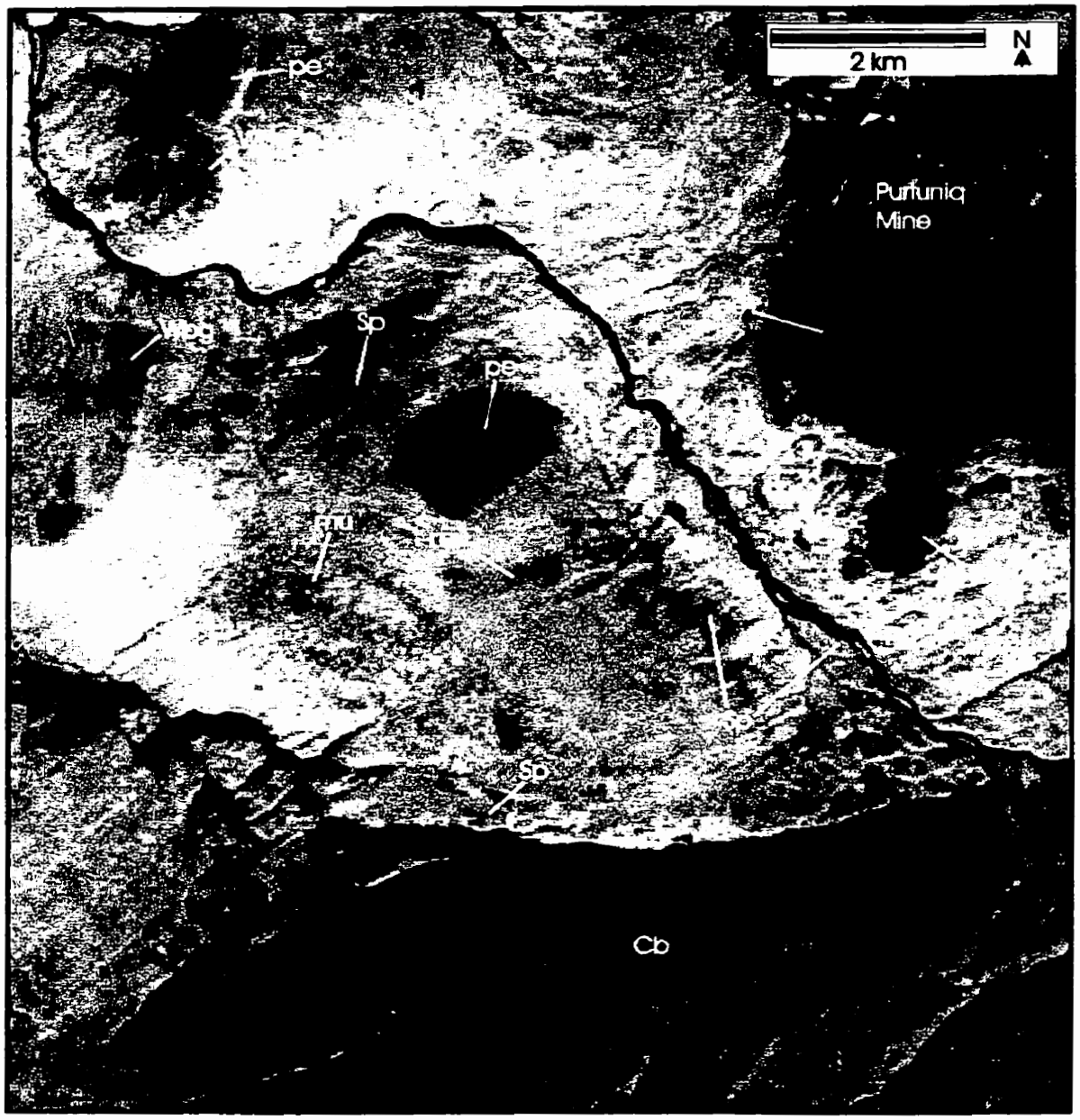

Figure 8.62 TM colour composite (channels 543:RGB) for the north zone of the Lac Watts region. Lithological symbols: *pe* - peridotite; *to* - tonalite; *Wbg* - Watts Group basalt/gabbro; *Sp* - Spartan Group pelite; *Cb* - Chukotat Group basalt; *mu* - mafic and ultramafic lithologies (mainly basalt/peridotite materials, resting on generally unexposed Spartan Group bedrock) (bedrock geology is given in Figure 8.58). Lithological information based on St-Onge and Lucas (1989), and samples collected during the 1999 field season.

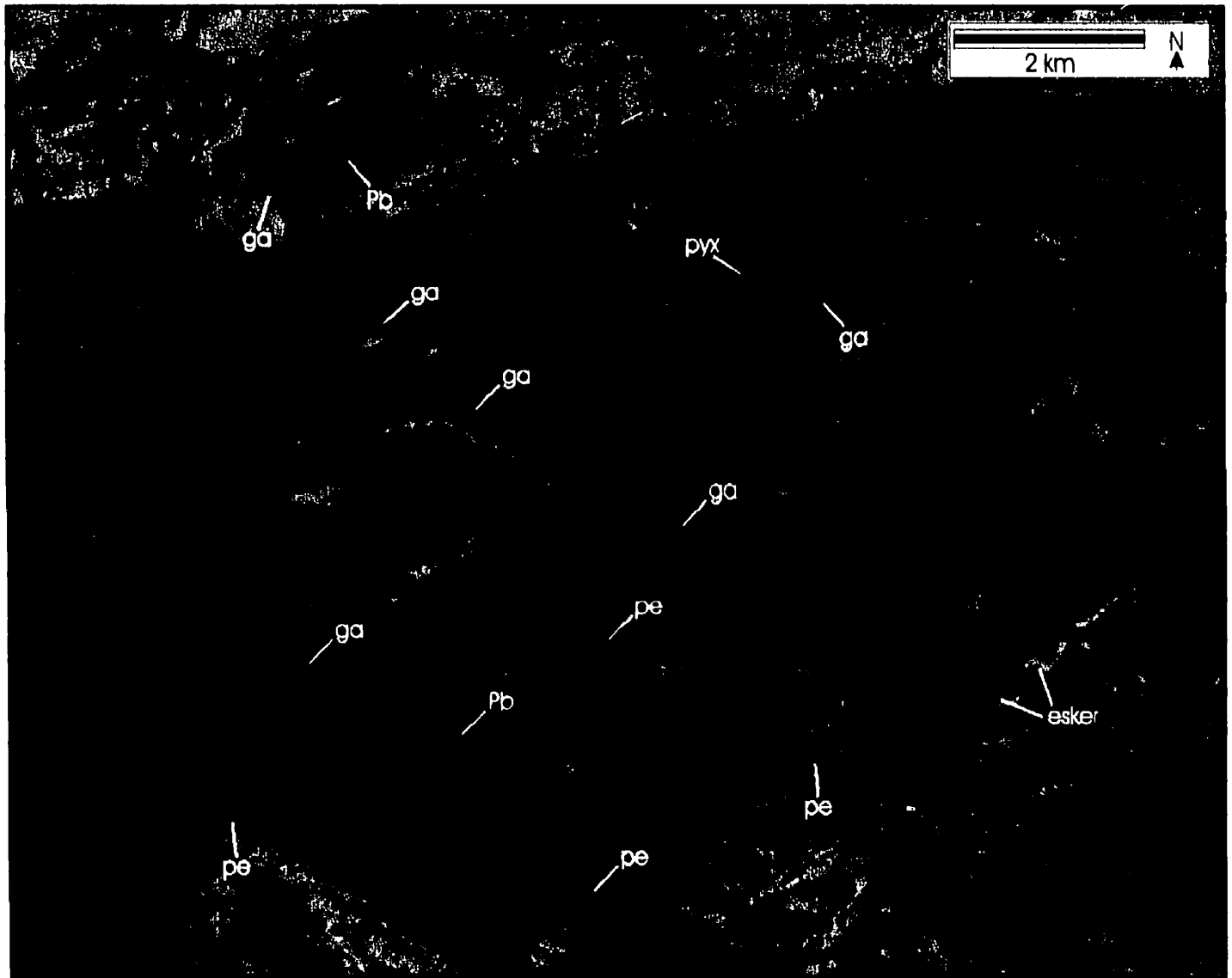

Figure 8.63 TM colour composite (channels 543:RGB) for the south zone of the Lac Watts region. Lithological symbols: *pe* - peridotite; *pyx* - pyroxenite; *Pb* - Povungnituk Group basalt; *ga* - gabbro intrusion (bedrock geology is given in Figure 8.58). Lithological information after St-Onge and Lucas (1989).

by its characteristically low reflectance in the visible (Figure 8.59) and negligible reflectance in the mid-infrared (Figure 8.61). Several lakes are associated with shades of green in the true colour image, probably due to their shallowness, or due to a greater amount of material in suspension compared to other water bodies in the region. Areas of dense moss and broadleaf vegetation cover are well discriminated in the TM images, based on their high reflectance in the near-infrared and low reflectance in the red portion of the visible spectrum (moist and densely-vegetated areas are shown in shades of green in Figure 8.60, whereas drier and rockier areas of grass and moss cover are shown in shades of yellow). Vegetation cover is relatively extensive over much of the Povungnituk Group semipelite unit, the Povungnituk Group basalt unit, the Spartan Group pelite unit, and the Watts Group basalt unit (compare Figures 8.58 and 8.60).

The TM colour composites can be used to identify the location and extent of most peridotite units in the Lac Watts region. This information is most clear in the red-to-near-infrared colour composite (Figures 8.60, 8.62, and 8.63; compare to Figure 8.58), in which peridotite units are shown in shades of purple. Although Figures 8.60 and 8.61 are useful for distinguishing exposures of other geological units from peridotite and vegetation classes, there is insufficient spectral information in the TM images to uniquely discriminate these geological units from each other visually (as shown in Section 5.3.2, however, there is sufficient numerical information in the TM images for classification algorithms to partially separate these classes for the northern portion of the Lac Watts region).

In the south zone, a good correlation between topography and lithology can be used to help distinguish certain units. Povungnituk Group semipelite and basalt units are generally

associated with topographic lows in the zone, and are thus characterized by significant amounts of vegetation cover. Gabbro and peridotite units, by comparison, are associated with well-exposed positive topographic features characterized by relatively low vegetation cover. As a result, the TM image can be used to distinguish most Povungnituk Group materials from gabbro and peridotite units; peridotite units can be further distinguished from gabbro units on the basis of their spectral properties (see above). In Figure 8.63, vegetated areas, well-correlated with Povungnituk Group materials, are shown in shades of green; gabbro intrusions are generally shown in shades of pink, and peridotite intrusions are generally shown in shades of purple. Localized pyroxenite units, as well as rare exposures of basalt and semipelite units of the Povungnituk Group, are also shown in shades of pink, and are not visually distinguishable from the gabbro units. Materials that comprise an esker (Figure 8.63) are not distinguishable from the non-peridotite lithological units.

8.3.3.2 Radarsat Image

The Radarsat image of the Lac Watts region is given in Figure 8.64. Details of the Radarsat image for the north and south zones of the region (Figure 8.58) are given in Figures 8.65 and 8.66, respectively. The Radarsat image was acquired from the west-southwest, preferentially illuminating slopes oriented toward this direction. There is no snow or ice in the image, which was acquired in the middle of the summer season on July 30, 1998. Speckle was reduced in the image by filtering original data using a 7 x 7 Lee filter. The image has a pixel spacing of 12.5 m. Contrast was enhanced in the Radarsat image using a square-root histogram stretch.

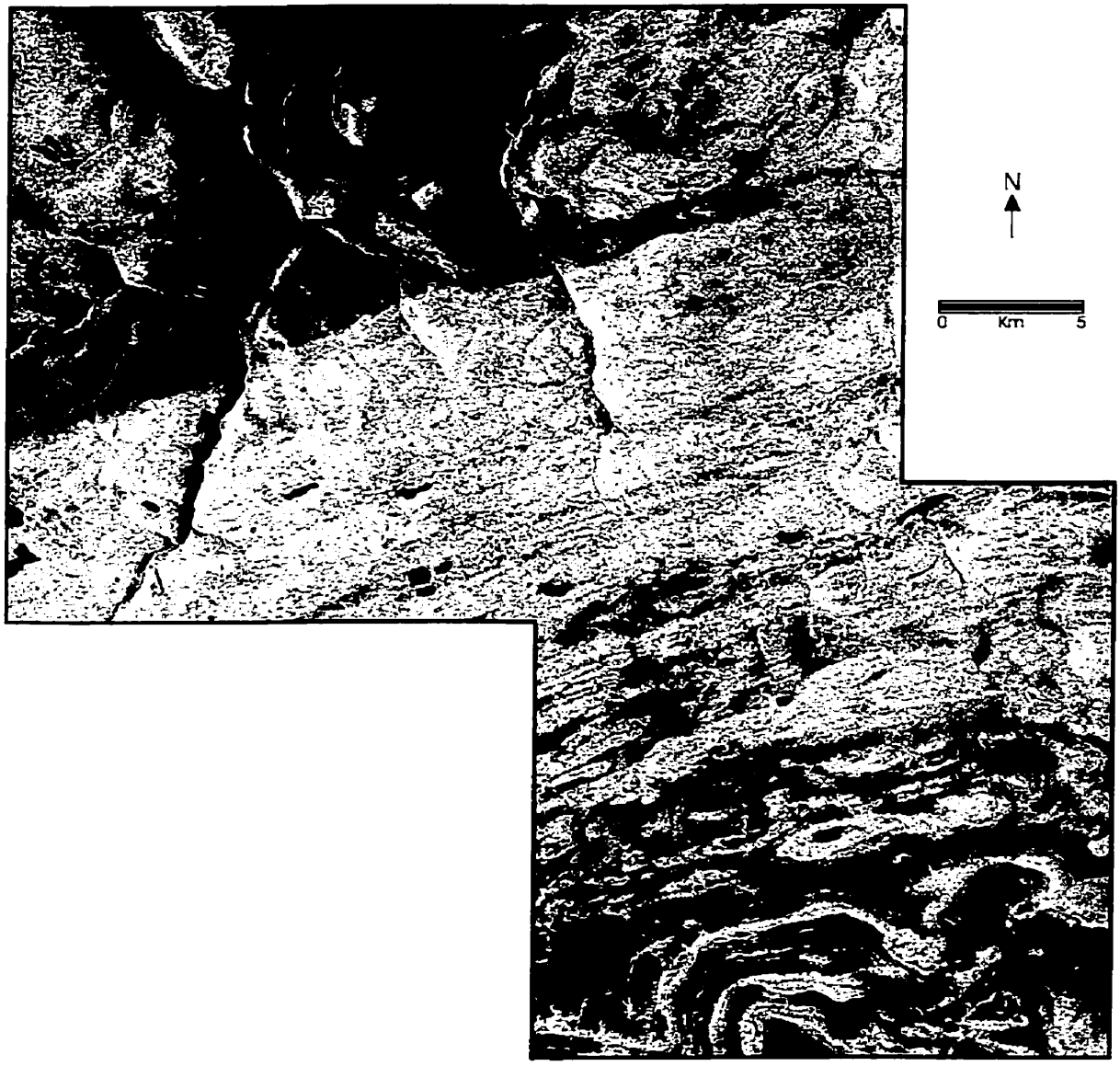

Figure 8.64 Radarsat image of the Lac Watts region.

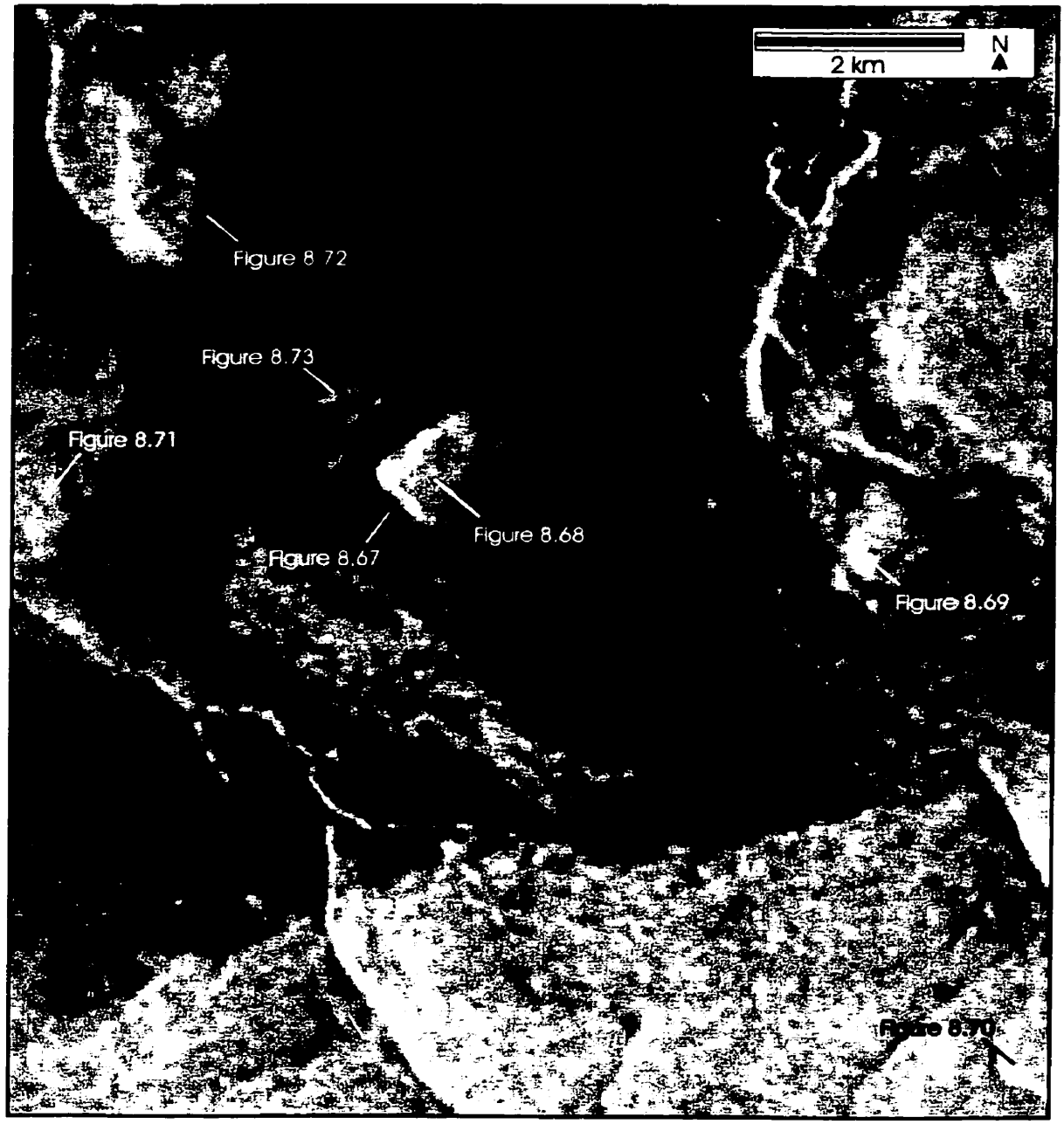

Figure 8.65 Radarsat image of the north zone of the Lac Watts region.

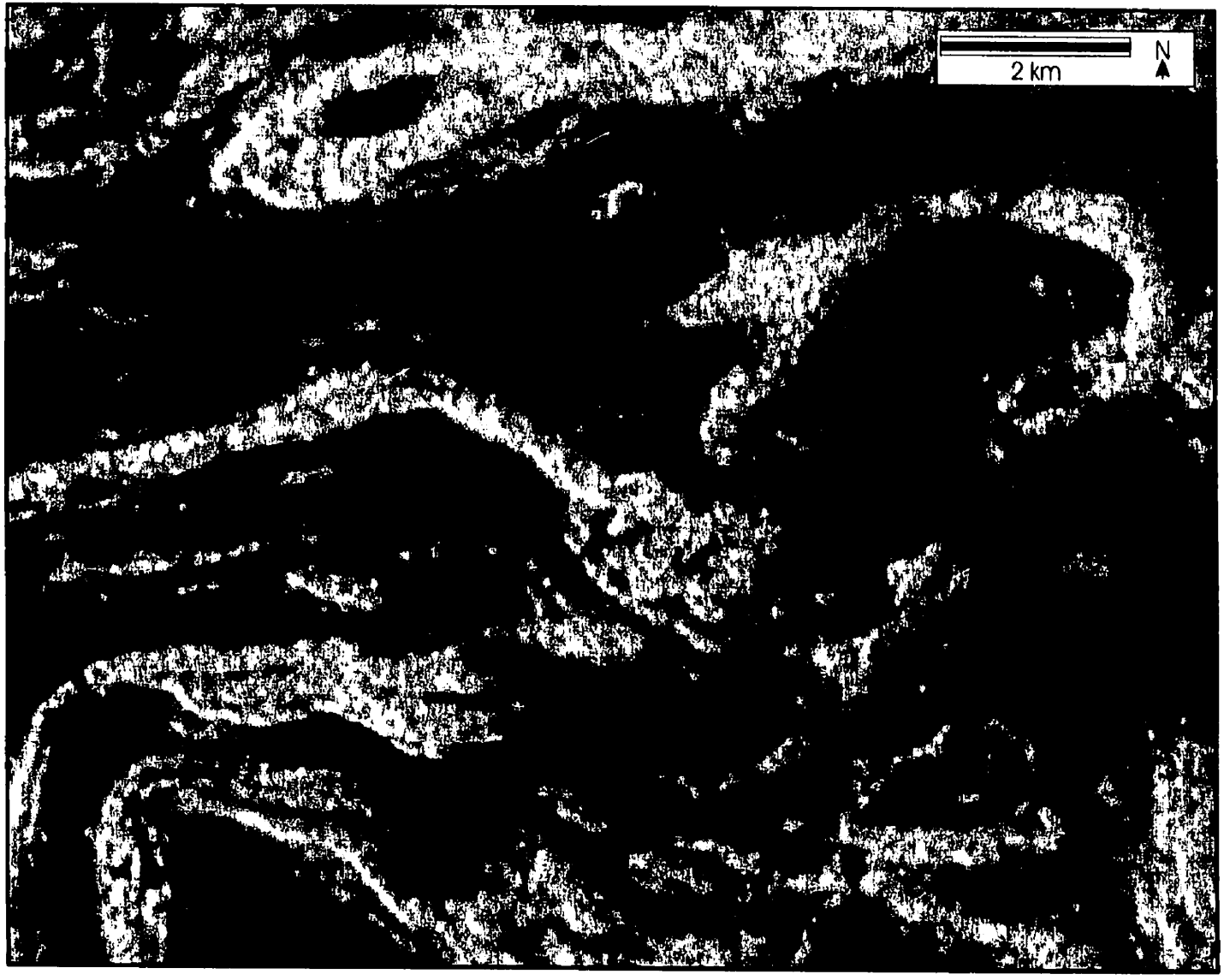

Figure 8.66 Radarsat image of the south zone of the Lac Watts region.

Open water, which is associated with very low values in the Radarsat image, is easily discriminated from geological classes in the region (Figure 8.62). In general, the Radarsat image can be used to distinguish between vegetated and non-vegetated (well-exposed rock) areas in the Lac Watts region. By comparing Figure 8.60 (which is a TM colour composite showing vegetated areas in shades of green and yellow - see above) with Figure 8.64 (the Radarsat image), it can be seen that vegetated areas are generally associated with darker tones in the Radarsat image. Well-exposed geological units are generally associated with lighter tones in the Radarsat image, presumably because of the prevalence of rough surfaces and corner reflectors in such environments (see below). In a small number of places, the relation between exposure and Radarsat image values is not consistent; for example, northeast of Lac Watts, areas shown to be well exposed in the TM images are associated with low Radarsat image values. These particular areas were not visited for this research, so the reasons for these discrepancies cannot be explored here. It is hypothesized that surface materials in these areas are radar-smooth.

The good relation between well-exposed areas and moderate to high Radarsat image values for the Lac Watts region as a whole is valid within the north zone (compare Figures 8.62 and 8.65). It is clear from the Radarsat image of the north zone (Figure 8.65) that the highest image values are associated with slopes generally oriented toward the antenna (see Figure 8.67, which shows of one of the many steep southwest-facing slopes in the zone that are associated with high image values). Moderate values in the Radarsat image are generally associated with well-exposed blockfields or bedrock. There is no visual correlation between Radarsat image values and lithology; this may in part be a result of the lack of clear

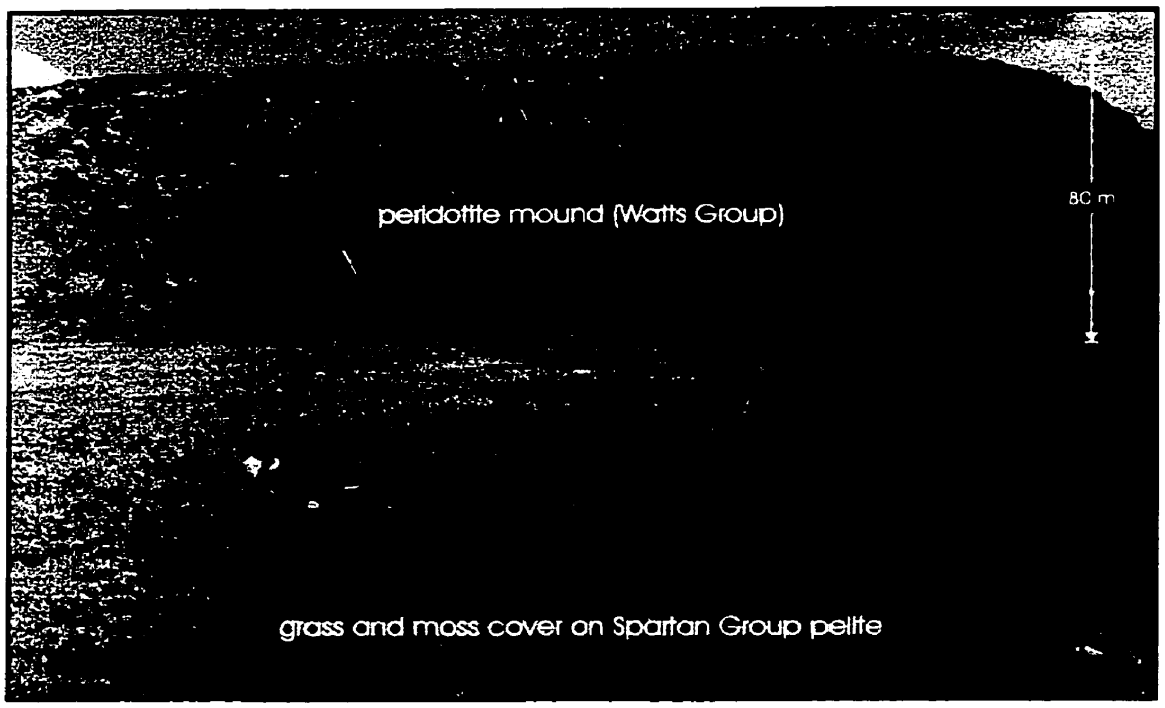

a

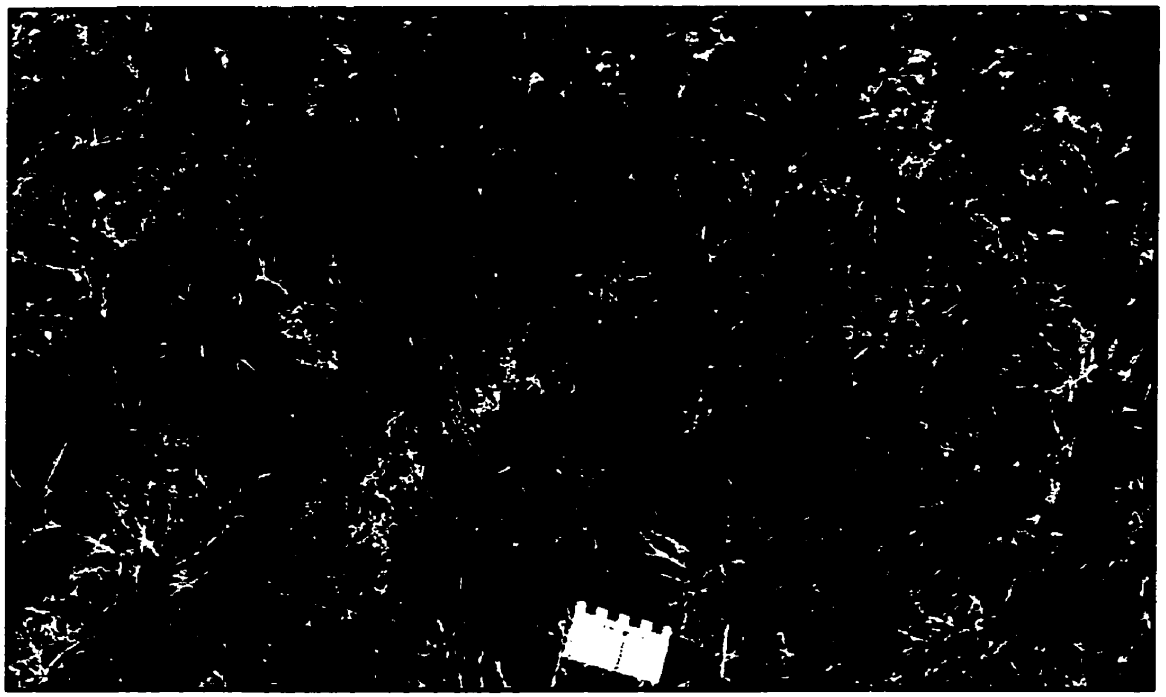

b

Figure 8.67 Photographs of an area of complete grass and moss cover, on Spartan Group pelite (Site 11). Location is shown in Figure 8.65. View in "a" is toward the northeast. Scale in "b" is divided into 1 cm increments. The slope of the peridotite mound in "a" is associated with high values in the Radarsat image; the meadow in "a" is associated with relatively low values (Figure 8.65).

and unique correlations in the region between lithology and the geometry of rocks. Although rock sizes and geometry can vary significantly within individual lithological classes in the north zone, the materials of the peridotite, tonalite, and Chukotat Group basalt units are generally blocky (equant) with common dimensions of about 15 cm to 1 m (see Figures 8.68 to 8.70, and Figure 4.14a; these figures are not fully representative of all such materials in the north zone, but depict common size ranges for geological materials in this zone). Although some exposures of Watts Group basalts also consist of large, blocky materials (Figure 8.71), some bedrock exposures of this unit consist of relatively flat materials (e.g., Site 8.72). The nature of surficial Spartan Group materials is quite variable, but typically is characterized by both blocky rockfields and generally flat bedrock exposures (e.g., Figure 8.73). In the north zone, there is no means for visually differentiating between lithologies based on Radarsat image values, since all rock types are associated with comparable image values.

Although the Radarsat image may not be used in the north zone for the discrimination of individual lithologies, the good correlation between topography and lithology in the south zone, which was found to be useful for distinguishing gabbro and peridotite units from materials of the Puvungnituk Group using the TM image (Section 8.3.3.1), can similarly be used to help distinguish the same lithologies using the Radarsat image (Figures 8.64 and 8.66) [this is consistent with the results of Mustard (1994), who found that CIRIS HH-polarized C- and X-band airborne radar images of the zone, and an area to the south and southwest, to be similarly useful sources of lithological information]. Povungnituk Group semipelite and basalt units, which are topographically low and are characterized by significant amounts of vegetation cover, are associated with low Radarsat image values. Gabbro and peridotite

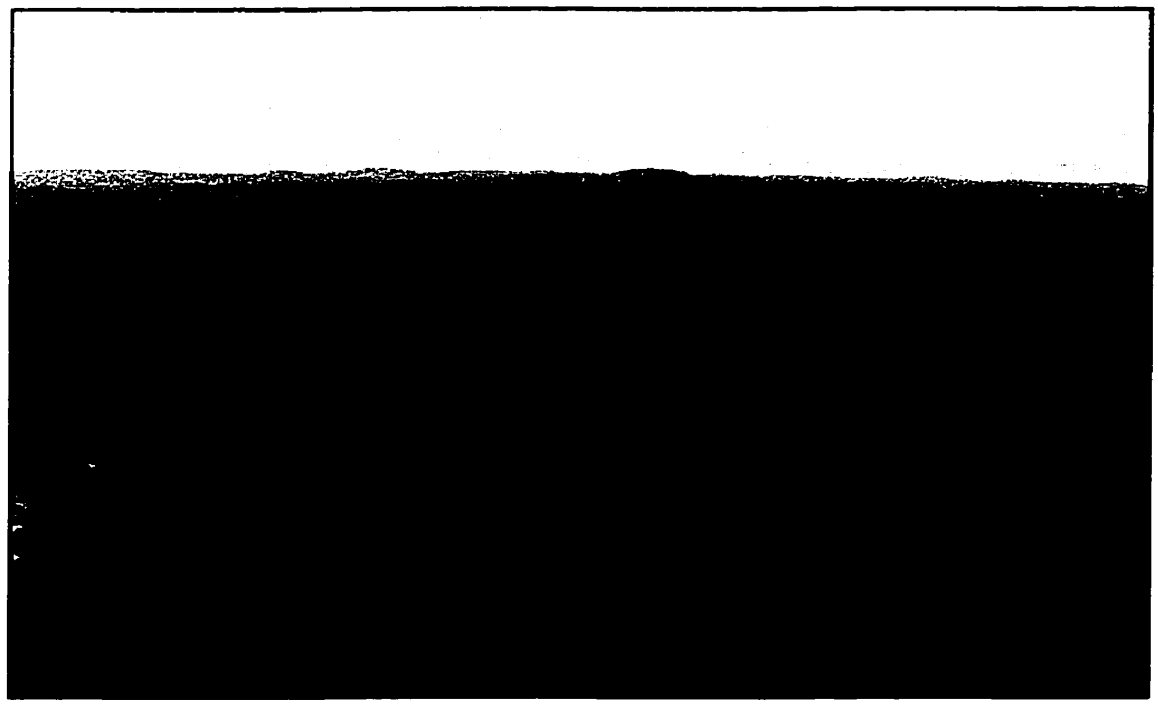

a

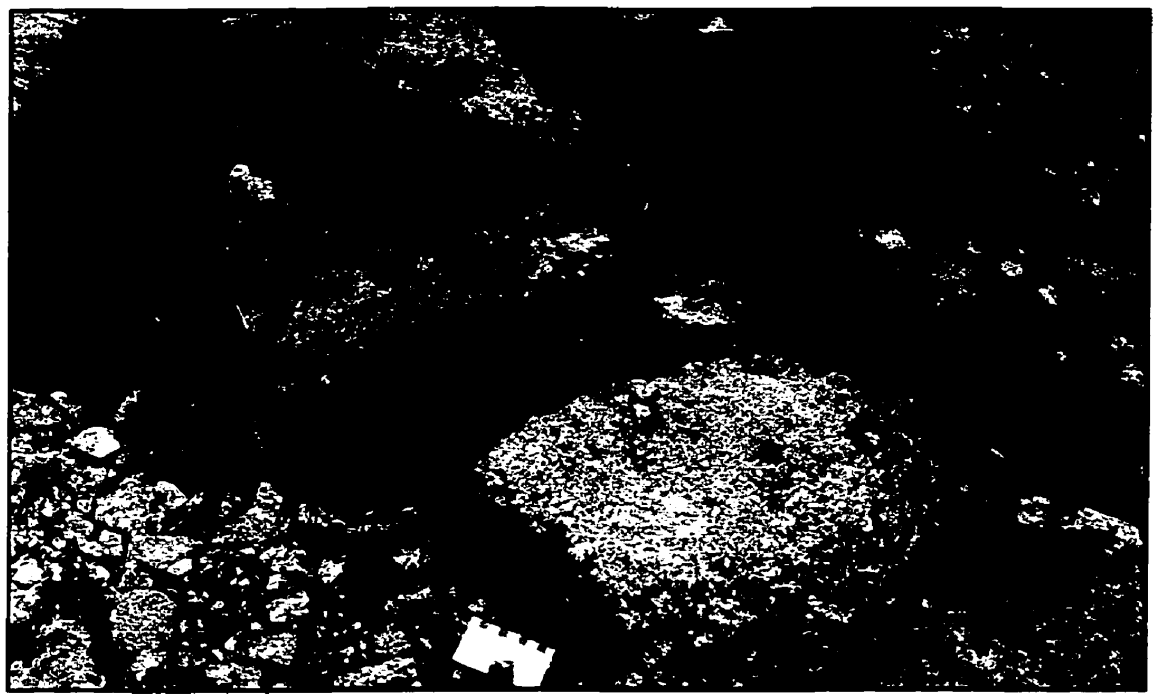

b

Figure 8.68 Photographs of peridotite materials of the Watts Group (Site 18). Location is shown in Figure 8.65). Scale in "a" is divided into 10 cm increments. Scale in "b" is divided into 1 cm increments.

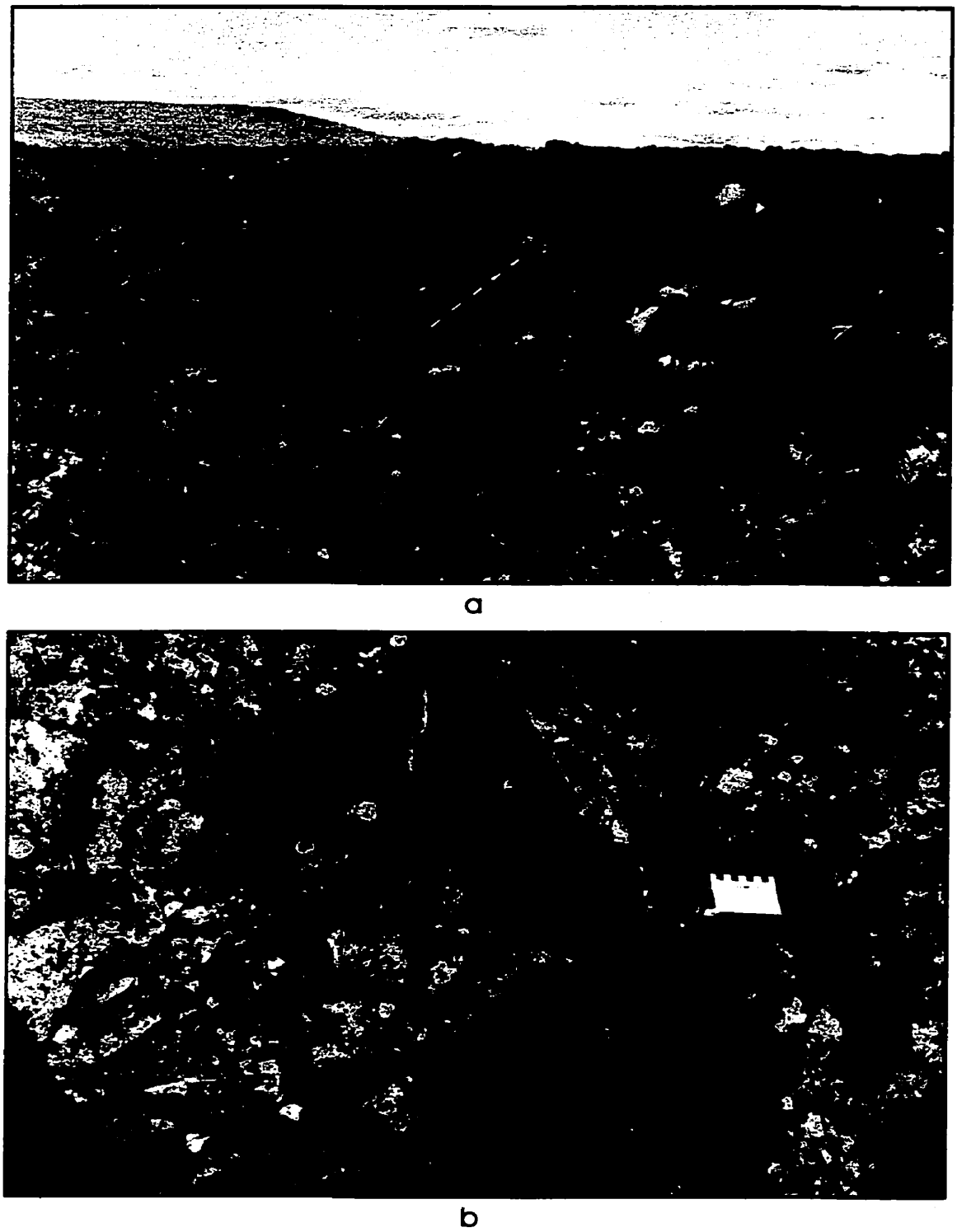

Figure 8.69 Photographs of materials of a tonalite intrusion (Site 3). Location is shown in Figure 8.65. View in "a" is toward the northwest. Scale in "a" is divided into 10 cm increments. Scale in "b" is divided into 1 cm increments.

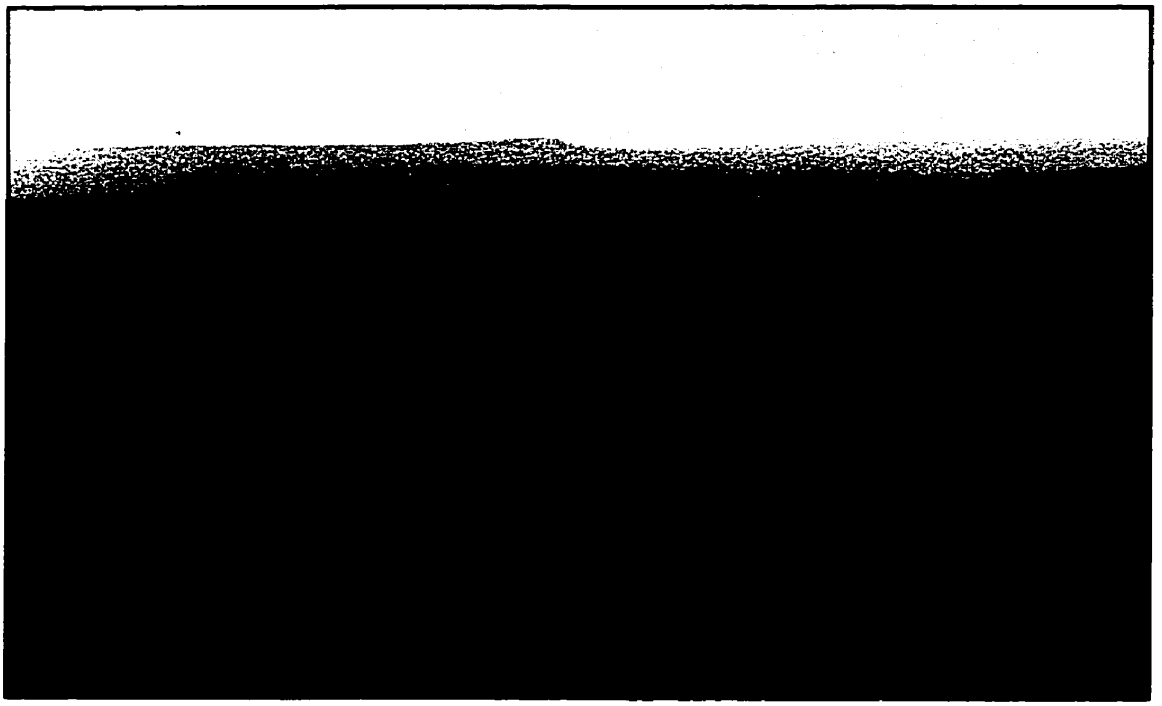

a

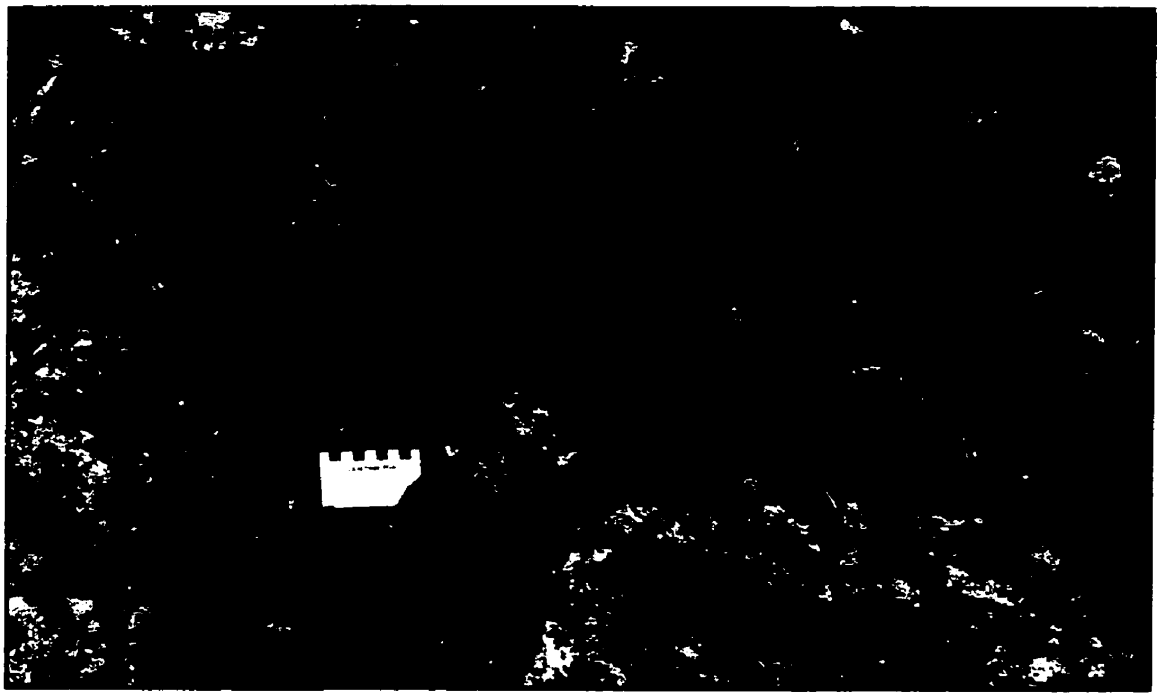

b

Figure 8.70 Photographs of basalt of the Chukotat Group (Site 50). Location is shown in Figure 8.65. Scale in "a" is divided into 10 cm increments. Scale in "b" is divided into 1 cm increments.

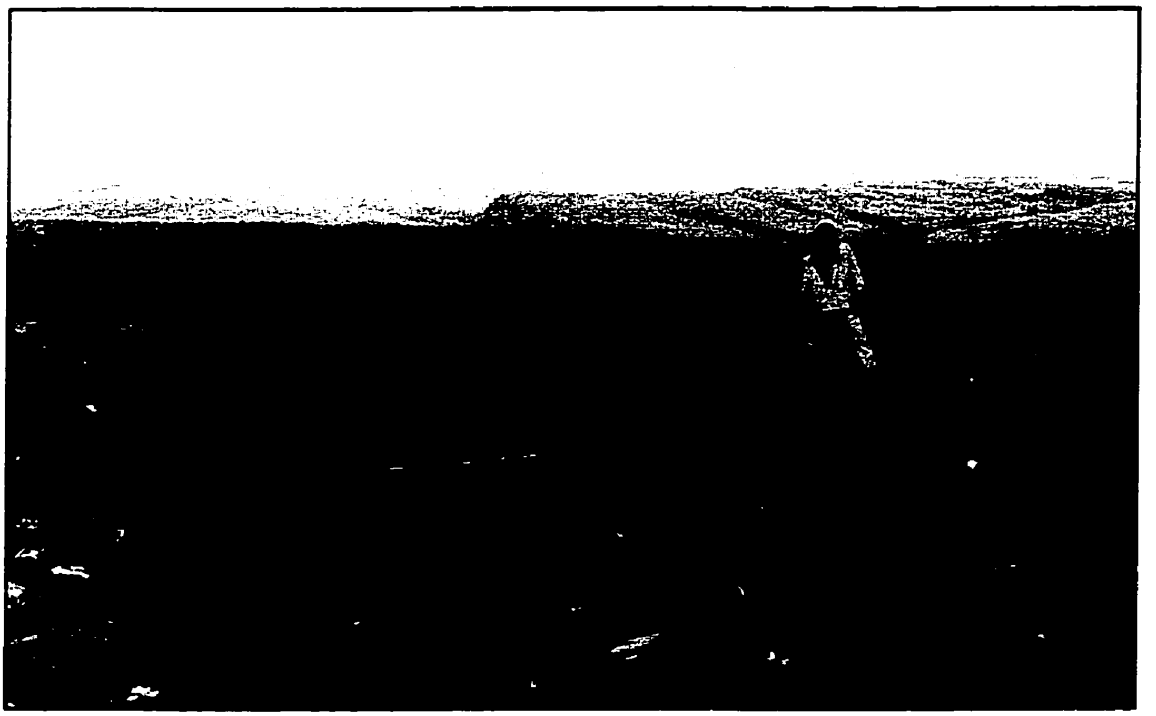

a

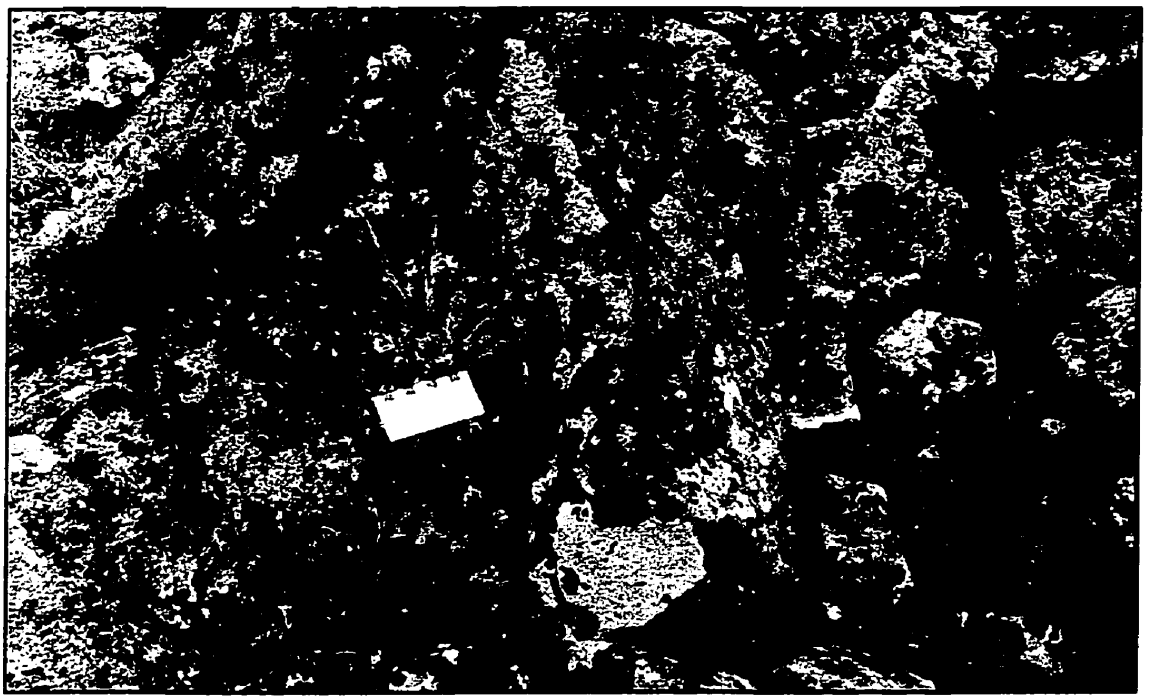

b

Figure 8.71 Photographs of gabbro / basalt of the Watts Group (Site 26).Location is shown in Figure 8.65. View in "a" is toward the west. Scale in "a" is divided into 10 cm increments. Scale in "b" is divided into 1 cm increments.

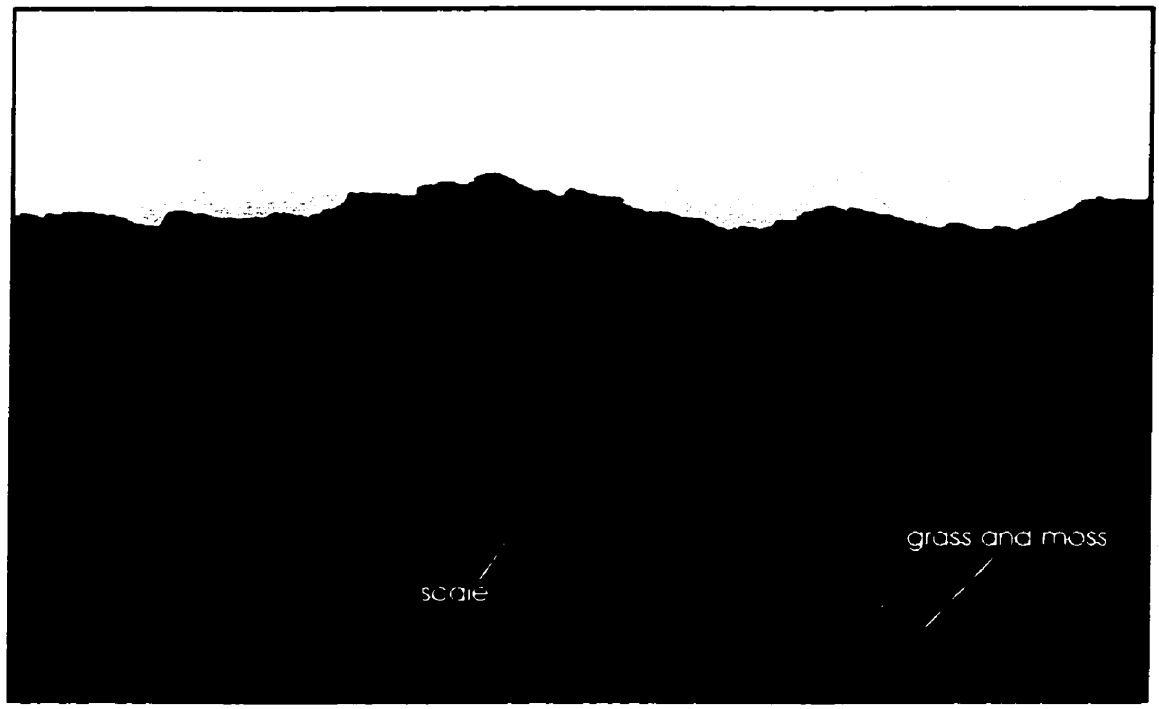

a

b

Figure 8.72 Photographs of basalts of the Watts Group (Site 31). Location is shown in Figure 8.65. View in "a" is toward the south. Scale in "a" is divided into 10 cm increments. Scale in "b" is divided into 1 cm increments.

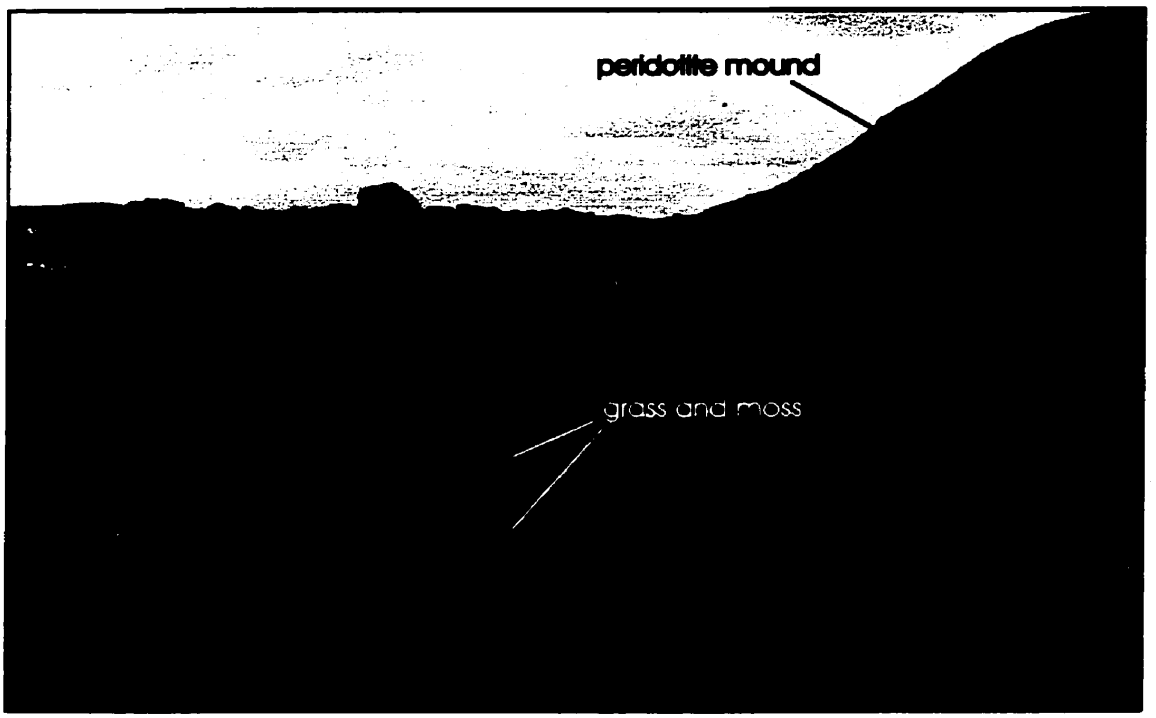

a

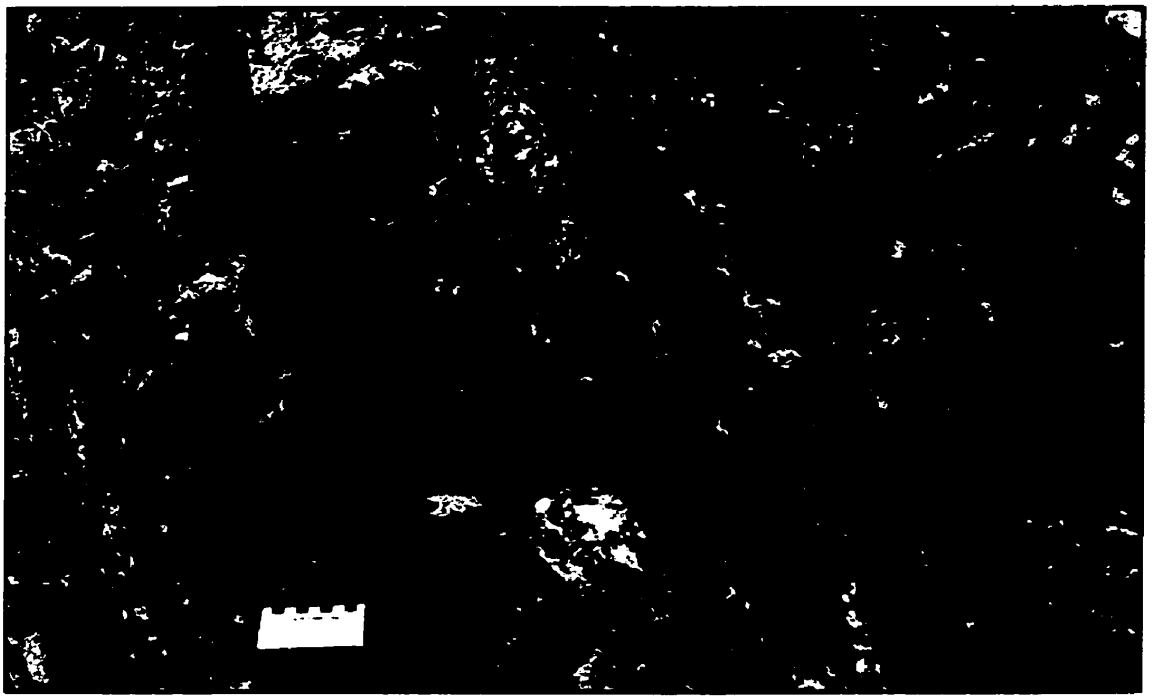

b

Figure 8.73 Photographs of scattered mafic / ultramafic rocks resting on a bedrock exposure of the Spartan Group (pelite) (Site 14). Location is given in Figure 8.65. View in "a" is toward the southeast. Scale in "a" is divided into 10 cm increments. Scale in "b" is divided into 1 cm increments.

units, which are associated with well-exposed features and are characterized by relatively low amounts of vegetation cover, are associated with higher Radarsat image values. As a result, the Radarsat image can be used to distinguish most Povungnituk Group materials from gabbro and peridotite units (Figure 8.66). The Radarsat image cannot be used to distinguish between peridotite, gabbro, pyroxenite, and other well-exposed units in the zone (compare Figures 8.66 and 8.63; see also Section 8.3.3.1).

8.4 Chapter Summary and Discussion

The Landsat TM images were found to be useful visual sources of information regarding general land cover for all three regions examined in this study. In addition to providing accurate information on the distribution of water, snow, ice, and vegetation in the three regions, the TM images were found to provide useful visual information on the distribution of numerous lithological units (although only a minority of such units could be clearly and uniquely identified based only on the spectral information contained in the colour composites examined here). The separability of geological classes in the two Melville Island regions was limited in varying degrees by lithological, and thus spectral, similarities between many of the clastic and carbonate units. The separability of geological classes in the Lac Watts region is believed to have been, in part, adversely affected by the extensive lichen cover in this region. Such problems are typical of optical imaging in arctic environments (e.g., Birnie *et al.*, 1989; Arvidson *et al.*, 1993; Cloutis, 1995b). The most unambiguous lithological information provided by the TM images was for units whose materials are characterized by distinctive iron-oxide weathering surfaces; these units include the Assistance

Formation mudstone and the Canyon Fiord Formation sandstone on Melville Island, and the peridotite units in the Cape Smith Belt. These findings are consistent with previous work, which has noted the value of distinctive weathering attributes in mapping lithology using optical satellite imagery (e.g., Harding *et al.*, 1989; Pontual, 1989; Spatz and Taranik, 1989; El Rakaiby, 1995; Glikson and Creasey, 1995; Macias, 1995).

The Radarsat images were found to be useful visual sources of information regarding the distribution of water, snow, ice, and land classes, although this information is somewhat more ambiguous than that provided by the TM imagery. For example, there was found to be potential for confusion between water and wet snow classes (since both are associated with very low image values in the Radarsat images), and more rarely between ice and land classes (since both classes were sometimes found to be associated with low to moderate image values). Of course, prior geographic knowledge of an imaged region (e.g., knowledge of the distribution of all water bodies) would greatly reduce the potential for confusion in this regard.

The Radarsat image for the Cape Smith Belt was found to be useful for distinguishing vegetated from non-vegetated areas in much of the Lac Watts region, probably because of the good correlation between non-vegetated areas and the presence of variably-sized blocky materials (which should act in many cases as corner reflectors and radar-rough surfaces). The Radarsat image for Melville Island was generally found to not be useful for mapping vegetation cover at the Tingmisut Lake and Weatherall Bay regions, probably because unvegetated areas in these regions are not consistently associated with radar-rough surfaces.

The Radarsat images were found to be useful visual sources of information regarding

the location and extent of a variety of geological units on Melville Island, including materials of the gabbro class, and the Beverly Inlet, Blue Fiord, and Hecla Bay formations. The materials of the gabbro and Beverly Inlet (Tingmisut Inlier) units are blocky, with sizes on the order of the wavelength of the Radarsat sensor, and the spaces between rocks are commonly not filled by fines or smaller clasts. These characteristics should produce radar-rough surfaces; this would be consistent with the findings of Budkewitsch *et al.* (1996), which suggest a similar relation between carbonates and radar-rough surfaces on nearby Bathurst Island.

Although distinctions between different lithologies could not be made for the northern part of the Lac Watts region using the Radarsat image, correlations between lithology and both topography and surface roughness in the southern part of the region allowed the Radarsat image to be used as a source of information regarding particular groups of lithological classes. These results are consistent with the findings of Mustard (1994), who found that radar and TM imagery can be used in the region for mapping general lithological classes.

The visual evaluation of Radarsat imagery given in this chapter is consistent with previous studies carried out in arctic and/or semi-arid environments where rock exposure is good (Sections 2.3.2.4 and 2.4.2). The practical importance of topography and surface roughness in determining the magnitude of radar backscatter, as seen here with regard to the Melville Island and Cape Smith Belt regions, is well documented in the literature (e.g., Fielding *et al.*, 1986; Lynne and Taylor, 1986; Graham and Grant, 1991; Dall *et al.*, 1995; Shimabukuro *et al.*, 1998). As McGregor *et al.* (1999) note, both obvious and subtle

geomorphic features are expressed through variation in radar backscatter due to changes in slope and aspect across the features; although this information can be very useful in detecting features and units of interest (e.g., the gabbro dike in the Tingmisut Lake region, or the esker in the Lac Watts region), it unfortunately can also play an important part in suppressing ground-cover information (e.g., lithological classes) (Rudant *et al.*, 1994; Arkin *et al.*, 1999) [this problematic situation is not restricted to geological studies; for example, Malcolm *et al.* (1998) found that changes in topography can greatly compromise the discrimination of forest classes].

The IKONOS images were found to be excellent sources of high-resolution visual information regarding the distribution of general surface classes (water, snow, ice, and land). Furthermore, despite their relatively poor spectral resolution, the IKONOS images were found to be useful not only for mapping the extent of vegetation cover, but also the distribution of certain lithological units (including, e.g., the pink-, yellow-, and red-coloured units of the Canyon Fiord Formation). Although IKONOS imagery is necessarily limited with regard to its potential for spectrally discriminating lithology, both the panchromatic and multispectral IKONOS images provide a level of visual detail that is similar to that provided by aerial photographs, and thus allow for the visual discrimination of lithological units on the basis of morphological and textural information. Because of the digital and multispectral nature of these images, their potential value is considerable for applications such as surface mapping. This should not be surprising, given that the value of airborne and planetary optical images with similar spatial resolutions is well documented (e.g., Staenz *et al.*, 1999; Carr and Malin, 2000), and given the applicability of optical imaging systems with similarly restricted

spectral characteristics (e.g., SPOT) toward the mapping of general surface classes (e.g., Gastellu-Etchegorry *et al.*, 1990; Mekarnia and Chorowicz, 1992). Unfortunately, although the visual information content of IKONOS imagery is high, the current cost of IKONOS imagery per unit area is as much as ten times greater than that of Radarsat or Landsat imagery.

9 SUMMARY AND CONCLUSIONS

9.1 Introduction

This research undertook to 1) investigate the utility of specialized algorithms and processing techniques for the classification of satellite imagery with regard to lithological and other surface classes at two northern study areas; and 2) investigate and compare the value of Landsat TM, Radarsat, and IKONOS satellite imagery in the visual discrimination of lithological and other surface classes at the same two study areas. The results of this research are summarized below in Sections 9.2 to 9.6. Research implications are given in Section 9.7, and recommendations for future research are given in Section 9.8.

9.2 Ground-Truth Databases

Based on fieldwork conducted in the summers of 1998 and 1999, ground-truth databases were constructed for two field areas in northern Canada: one located on eastern Melville Island, Nunavut, and the other in the north-central portion of the Cape Smith Belt of Québec. The Melville Island Field Area, located in the vicinity of Tingmisut Lake, is characterized by the widespread exposure of Paleozoic clastic and carbonate sequences of the Sverdrup Basin. The Melville Island database, constructed using a Landsat TM image with a pixel spacing of 30 m, consists of 851 pixels whose selection and characterization was based mainly on information collected *in situ* at 83 field sites. These 851 pixels were subdivided into surface classes in four different ways (involving 14, 10, 9, and 6 classes, and labelled the *B*, *C*, *D*, and *E* Series, respectively), and were further divided into test and training pixels in six different ways (producing a total of 24 separate collections of classification inputs for this

field area).

The Cape Smith Belt Field Area, located in the vicinity of Lac Watts, is characterized by the widespread exposure of mafic and ultramafic thrust sheets of the Cape Smith Belt, an Early Proterozoic greenstone belt. The Cape Smith Belt database, constructed using a Landsat TM image with a pixel spacing of 30 m, consists of 686 pixels whose selection and characterization was based mainly on information collected *in situ* at 53 field sites. These 686 pixels were subdivided into 7 surface classes (labelled the *A* Series), and were further divided into test and training pixels in six different ways (producing a total of 6 separate collections of classification inputs for this field area).

The two databases described above were used in this research for the empirical evaluation of supervised classification techniques for lithological discrimination using Landsat TM images (channels 3, 4, 5, and 7). The field data used to construct the databases was also used in the visual evaluation of three different types of satellite imagery (Landsat TM, Radarsat *S7*, and IKONOS panchromatic and multispectral images). It is anticipated that the databases will also be used in future as the basis for the evaluation of new image-processing algorithms and satellite sensors.

9.3 Empirical Evaluations of Classifiers

An empirical evaluation of three supervised classifiers (evidential reasoning, maximum likelihood, and neural network, as well as several variants of these algorithms) for lithological discrimination was performed using the ground-truth databases and Landsat TM images noted above. All classification software used in this research, except the commercially-available

maximum likelihood program, was written by the author and based mainly on established principles.

Classification results indicate that the neural network algorithm (which implements a standard feedforward network that uses backpropagation in training and which combines the results of 10 separate classifications by majority-vote consensus) consistently produced overall results that are superior to those of the maximum-likelihood and evidential-reasoning classifiers. For the Melville Island Field Area, average overall percentages of test pixels correctly labelled ranged from 78% (*B* Series; 14 classes) to 86% (*E* Series; 6 classes), and were typically 4 to 7% higher than the percentages of the next best classifier (maximum likelihood). For the Cape Smith Belt Field Area, the average overall percentage of test pixels correctly labelled was 89% (*A* Series; 7 classes), and percentages were typically 3 to 6% greater than those of the next best classifier (maximum likelihood). The overall lithological information content of classified images produced by the neural network algorithm is considered useful, although all images are characterized by variable amounts of confusion between sometimes diverse lithologies (complicated in part by factors such shadowing, lichen cover, and the spectral limitations of TM imagery). The best discriminated lithological classes were those with distinctive weathering characteristics.

Individual neural network results (i.e., the results of individual neural network executions prior to consensus) were found to vary considerably as a consequence of differences in weight initializations (with variation of up to ~15% in overall percentages of test pixels correctly classified), but the majority-vote consensus neural network results were found to consistently be within about one percent of overall percentages associated with the

best individual neural network results. Although the majority-vote consensus methodology did not eliminate the need for the generation of multiple neural network results (indeed, it clearly can only be applied if numerous neural network results are available), it simplified the generation of the final classification image by eliminating the need for the user to select the best results based on evaluations of individual neural network results.

In the empirical evaluation of supervised classifiers discussed above, the maximum likelihood algorithm produced results that are visually similar to those of the neural network, although the percentages of all test pixels correctly classified were typically about 3 to 10% less than those of the neural network. The evidential reasoning algorithm produced relatively poor results (overall percentages were typically 20 to 30% less than those of the maximum likelihood and neural network classifiers), in contrast to the more favourable evidential reasoning results of several prior studies (e.g., Peddle, 1993, 1995; Peddle *et al.*, 1994; Leverington and Duguay, 1996a; Duguay and Peddle, 1996). Additional results generated in this study by the evidential reasoning algorithm, using it as a consensus algorithm for neural network results (treating the output activations of 10 sets of neural network results as measures of evidence, under the assumption that neural network output activations approximate posterior probabilities), were found to approach those of the majority-vote consensus algorithm. These additional evidential reasoning results confirm that the evidential reasoning algorithm itself is a viable means for classifying satellite imagery, but that it clearly can only classify effectively if initial measures of evidence are valid. This research suggests that the measure of evidence as a function of the proportions of extrapolated class training data that contain the image values being classified (Peddle, 1991, 1995) is not appropriate

when classifying databases such as those used in this research.

The fact that neither the majority-vote nor the evidential-reasoning consensus methods produced overall results that were superior to the best individual neural network results demonstrates that the individual neural network results used here are not sufficiently error-independent for the generation of consensus results that are superior to all component results. Thus, although differences in network weight initializations are sufficient to produce quite variable results in individual neural network classifications of satellite imagery, they are not sufficient by themselves for the generation of error-independent results.

9.4 Over-Generalization and Artificial Noise in Neural Network Classifications

The results of neural network classifications involving 20,000 iterations were empirically shown to be no worse than those produced by classifications involving much fewer iterations (~2000 to 8000). This suggests that over-generalization, the progressive incorporation during training of features of the training dataset that are not characteristic of the data as a whole, does not characterize the training of a feedforward backpropagation neural network using databases such as those used here. The results of neural network classifications in which small amounts of random noise was added to input vectors during training were empirically shown to produce less satisfactory classification results compared to classifications without noise. The use of noise was also shown to increase tss (total-sum-of-squares) error and to extend training times considerably, impairing the classifier's ability to converge upon a solution with an acceptable level of tss error. Thus, the use of random noise during training does not appear to be a useful means of supplementing sparse training

datasets, and its potential use to prevent over-generalization appears to be precluded by an absence of over-generalization in the classifications performed here.

9.5 Network Topology in Neural Network Classifications

Empirical investigations regarding the influence of network topology on overall results, in which topologies were progressively varied from smaller to larger networks, show that the use of two hidden (intermediate) layers of a given size produces superior results compared with the use of one hidden layer of the same size. Furthermore, classifications in which the number of nodes used in each hidden layer were equal to the greatest of the number of nodes in the input and output layers produced superior results to those using fewer nodes to define hidden layers. In plots of 1) average tss error after 20,000 iterations, and 2) overall percentage of test pixels correctly classified, against number of nodes used to define hidden layers, average tss error was shown to typically continue to drop with increases in number of nodes in each hidden layer, while percentage of test pixels correctly classified typically levelled off as the number of nodes used in each hidden layer approached the maximum tested. These results suggest that two hidden layers rather than one should be used in the classification of databases such as those used here. Further, each of these layers should be defined by the greatest of the number of nodes in the input and output layers. These results are consistent with recognized "rules of thumb" currently used in the application of neural networks toward classification problems (e.g., Richards, 1993).

9.6 Confidence Images Generated From Output-Layer Activations

Plots of maximum output activations versus classification successes, and plots of the differences between the two highest output activations versus classification successes, show that higher values of these two measures are generally associated with a greater likelihood of classification success. Thus, there is a good empirical basis for the use of these particular measures of confidence in the generation of "confidence images" to accompany satellite-image classifications. Relative assignments of confidence in two confidence images for the Melville Island Field Area were found to be generally consistent with the classification success associated with corresponding pixel locations: distinctive lithological units were associated with higher measures of classification confidence, while certain peripheral units not represented in the training database were associated with very low measures of confidence.

9.7 Visual Evaluation of TM, Radarsat, and IKONOS Imagery

Three regions (the Tingmisut Lake and Weatherall Bay regions on Melville Island, and the Lac Watts region in the north-central Cape Smith Belt) were used to visually evaluate Landsat TM, Radarsat, and IKONOS imagery as sources of lithological information. The Landsat TM images were found to be useful visual sources of information regarding general land cover for all three regions, providing unambiguous information regarding the extent of water, snow, ice, and vegetation. Additionally, the TM images were found to provide useful visual information on the distribution of numerous lithological units, especially those with distinctive weathering characteristics. The separability of geological classes in the two Melville Island regions was limited somewhat by lithological similarities between many of the

clastic and carbonate units, and spectral limitations associated with the TM sensor itself. The separability of geological classes in the Lac Watts region is believed to have been adversely affected by the extensive lichen cover in this region, as well as the mixing of multiple lithological classes in certain areas.

The Radarsat images were found to be useful sources of visual information regarding the distribution of water, snow, ice, and land classes, although this information is somewhat more ambiguous than that provided by the TM imagery (for example, there is potential for confusion between water and wet snow in the Radarsat images examined here). The Radarsat image for the Cape Smith Belt was found to be useful for distinguishing vegetated from unvegetated areas in much of the Lac Watts region, probably because of the good correlation between non-vegetated areas and the presence of variably-sized blocky materials. The Radarsat image for Melville Island was generally found to not be useful for mapping vegetation cover at the Tingmisut Lake and Weatherall Bay regions, probably because unvegetated areas in these regions are not consistently associated with surfaces of a particular roughness.

The Radarsat images were found to be useful visual sources of information regarding the location and extent of a variety of geological units on Melville Island, including materials of the gabbro class, and the Beverly Inlet, Blue Fiord, and Hecla Bay formations. Although distinctions between different lithologies could not be made for the northern part of the Lac Watts region of the Cape Smith Belt using the Radarsat image, correlations between lithology and both topography and surface roughness in the southern part of the region allowed the Radarsat image to be used as a source of information regarding particular groups of

lithological classes. The visual evaluation of Radarsat imagery given here is consistent with previous studies carried out in arctic and/or semi-arid environments where rock exposure is good. Unfortunately, as has been found in previous studies (e.g., McGregor *et al.*, 1999; Rudant *et al.*, 1994; Arkin *et al.*, 1999), the very properties that cause radar imagery to be useful in detecting geomorphic features of interest also play an important role in suppressing ground-cover information

The IKONOS images, available in this study only for the Tingmisut Lake region of Melville Island, were found to be excellent sources of high-resolution visual information regarding the distribution of general surface classes (water, snow, ice, land, and vegetated land). Furthermore, despite their relatively poor spectral resolution, the IKONOS images were found to be useful for spectrally ascertaining the extent of certain lithological units. Although IKONOS imagery is necessarily limited with regard to its potential for spectrally discriminating lithology, both the panchromatic and multispectral IKONOS images provide a level of visual detail that is similar to that provided by aerial photographs, and thus allow for the visual discrimination of lithological units on the basis of morphological and textural information. Because of the digital and multispectral nature of these images, their potential value is considerable for surface-mapping projects.

9.8 Research Implications

This research has a number of implications for the practice of remote sensing:

- The majority-vote consensus algorithm, in combination with results produced by multiple

feedforward backpropagation neural networks, is capable of consistently producing classification results that are roughly equal to those produced in the best individual neural network execution, and that are superior to those generated by the maximum likelihood and evidential reasoning classifiers. This neural network consensus algorithm produces consistently superior classification results without the variability in final results characteristic of typical sets of neural network classifications of satellite imagery. Thus, this algorithm should be considered an appropriate and favoured means for supervised classification of satellite imagery.

Like all consensus routines, the majority-vote neural network algorithm necessarily extends the length of classification time well beyond that of other classifiers such as maximum likelihood and evidential reasoning, precluding its use when timely classifications are necessary (consensus classification times of several hours should be expected for moderately-sized images) . The consensus routine could be easily automated in neural network software such that, if desired, the user need only be concerned with final consensus results rather than the many individual results generated in support of consensus results.

- The evidential reasoning algorithm is a valid means for classifying satellite images, as long as initial measures of evidence are appropriate. The calculation of initial measures of evidence as a function of the proportions of extrapolated class training data that contain the image values being classified, will not necessarily produce satisfactory evidential reasoning classification results. The use of neural network output activations as initial measures of evidence can result in evidential reasoning results that approach those associated with the

majority-vote consensus method.

- Reliance on variation in weight initializations to produce error-independent results for input to consensus algorithms is not necessarily appropriate.

- The training of feedforward backpropagation neural networks for the classification of satellite images does not appear to be characterized by over-generalization. The use of small amounts of artificial noise during training does not favourably affect neural network classification results.

- There is an empirical basis for the use of confidence measures to supplement neural network classifications of satellite imagery. There is a generally good correlation between correct classifications and a) the magnitude of the highest output activation in an output layer, and b) the difference between the highest two activations in an output layer. Confidence images are a valid means of evaluating a classified image, in a relative sense, without needing to evaluate the classified image using test pixels. Confidence images should not to be considered replacements for the use of test pixels in the evaluation of classification results.

- Landsat TM and Radarsat images are useful, and in most cases complementary, tools for the visual discrimination of a variety of geological classes. This result is consistent with the findings reported in much of the remote sensing literature over the past decade. In general, Landsat TM images are useful for discriminating a variety of lithologies, especially those with

distinctive weathering characteristics, and Radarsat images are especially useful for visually highlighting lithological units with good correlations with surface roughness and geomorphology. Nevertheless, the value of TM imagery in lithological discrimination is limited to varying extents by its relatively poor spectral resolution, while Radarsat imagery can be limited by its often inconsistent relation between image values and lithological classes.

- Both panchromatic and multispectral IKONOS images have a visual information level that is similar to that of aerial photography taken from moderate altitudes. IKONOS images can be useful for the spectral discrimination of distinct lithological units, and for the visual identification of geomorphological features whose maximum dimensions are as small as several metres. Because of their multispectral, digital, and high-resolution characteristics, images such as those generated by the IKONOS sensor are expected to become widely utilized by remote sensing practitioners.

9.9 Recommendations for Future Research

This research suggests that differences in network weight initializations are not sufficient for the generation of error-independent results for input to consensus routines. Thus, methods which are designed to produce error-independent results through the employment of a variety of network architectures and learning algorithms (e.g., Rugova, 1994) or through mathematical transforms of network inputs (e.g., Benediktsson, 1997a) should be investigated with regard to their utility in producing consensus results that are superior to all individual component results.

This research demonstrates that Peddle's (1991, 1995) algorithm for calculating initial evidence values for input to the evidential reasoning algorithm may not be as widely applicable for the classification of satellite imagery as previous studies suggest. Additional theoretical and empirical investigations are warranted, for the purpose of refining the algorithm and to further ascertain the limits of its applicability.

Preliminary experiments involving the addition of artificial noise to input vectors during the training of neural networks were found in this research to not produce improvements in classification results. The utility of the addition of noise in the classification of satellite images was also questioned, given an absence of over-generalization. Nevertheless, specialized algorithms that statistically determine appropriate levels of noise to be used in particular classifications have been developed (e.g., Bishop, 1995a, 1995b) and should be tested with regard to their utility in improving neural network classifications from sparse training datasets.

This research tested neural networks whose topologies are defined in advance of network training using rules of thumb; these topologies did not change during training and classification. While such algorithms have been shown in this and previous research to be effective classifiers, more adaptable algorithms may ultimately be found to produce superior classification results. The use of constructive (e.g., Hirose *et al.*, 1991; Bartlett, 1994; Kwok and Yeung, 1997b; Parekh *et al.*, 2000) and pruning (e.g., Sietsma and Dow, 1991; Reed, 1993; Castellano *et al.*, 1997) algorithms, which augment network topology during training in order to improve classification results, should be examined with regard to their utility in image classification. The use of evolutionary and genetic algorithms (e.g., Odri *et al.*, 1993;

Angeline *et al.*, 1994; Maniezzo, 1994; Smalz and Conrad, 1994; Yao and Liu, 1997; Fogel, 2000), which are based on simplified principles of biological evolution and which can be used to optimize network topology, weights, and overall network behaviour, may also prove to be useful in image classification.

The current trend toward increased spectral resolution of satellite imagery [e.g., ASTER, a 14-channel instrument operational since 2000 (Fujisada, 1998; Abrams, 2000); MODIS, a 36-channel instrument operational since 2000 (Barnes *et al.*, 1998; Justice *et al.*, 1998); and ORBVIEW-4, a yet-to-be-launched platform with a 200-channel instrument (Orbital Imaging Corporation, 2000)] is expected to increase the importance of computer algorithms for extracting lithological and other surface-cover information from satellite images. In particular, algorithms such as those that perform supervised and unsupervised classification, as well as spectral mixture modelling, are expected to become essential for this purpose. The utility of the maximum likelihood, evidential reasoning, and neural network algorithms in the classification of large image databases should be investigated.

This research found that Landsat TM, Radarsat *S7*, and IKONOS imagery provide useful visual information regarding the presence and extent of general surface-cover types, as well as information regarding certain lithological units with distinctive weathering characteristics, surface roughness, and form. Additional field-based evaluations of the Radarsat and IKONOS image types, carried out in diverse regions and under a wide range of environmental conditions, will advance the assessment of these image types for geoscientific research.

REFERENCES

Abarca-Hernández, F., and Chica-Olmo, M., 1999. "Evaluation of geostatistical measures of radiometric spatial variability for lithologic discrimination in Landsat TM images", *Photogrammetric Engineering and Remote Sensing*, **65**: 705-711.

Abdelhamid, G., and Rabba, I., 1994. "An investigation of mineralized zones revealed during geological mapping, Jabal Hamra Faddan - Wadi Araba, Jordan, using Landsat TM data", *International Journal of Remote Sensing*, **15**: 1495-1506.

Abdelsalam, M.G., Robinson, C., El-Baz, F., and Stern, R.J., 2000. "Applications of orbital imaging radar for geologic studies in arid regions: the Saharan testimony", *Photogrammetric Engineering and Remote Sensing*, **66**: 717-726.

Abrams, M.J., 2000. "The advanced spaceborne thermal emission and reflection radiometer (ASTER): data products for the high spatial resolution imager on NASA's Terra platform", *International Journal of Remote Sensing*, **21**: 847-859.

Abrams, M.J., Rothery, D.A., and Pontual, A., 1988. "Mapping in the Oman ophiolite using enhanced Landsat Thematic Mapper images", *Tectonophysics*, **151**: 387-401.

Abuzar, M., and Al-Ghunaim, I., 1993. "Classification of temporal Thematic Mapper data for the delineation of an oil spill in the Arabian Gulf", *Canadian Journal of Remote Sensing*, **19**: 179-185.

ACGR (Associate Committee on Geotechnical Research), 1988. *Glossary of Permafrost and Related Ground-Ice Terms*. Permafrost Subcommittee, National Research Council of Canada, Technical Memorandum 142.

Adam, S., Wiebe, J., Collins, M., and Pietroniro, A., 1998. "Radarsat flood mapping in the Peace-Athabasca Delta, Canada", *Canadian Journal of Remote Sensing*, **24**: 69-79.

Adams, J.B., Smith, M.O., and Gillespie, A.R., 1993. "Imaging spectroscopy: interpretation based on spectral mixture analysis", *in* Remote Geochemical Analysis: Elemental and Mineralogical Composition, Pieters, C.M, and Englert, P.A. (eds.), Cambridge University Press, pp.145-166.

Ager, C.M., and Milton, N.M., 1987. "Spectral reflectance of lichens and their effects on the reflectance of rock substrates", *Geophysics*, **52**: 898-906.

Amirikian, B., and Nishimura, H., 1994. "What size network is good for generalization of a specific task of interest?", *Neural Networks*, 7: 321-329.

An, P., Chung, C.F., 1994. "Neural network approach for geological mapping: technical background and case study", *Canadian Journal of Remote Sensing*, **20**: 293-301.

Angeline, P.J., Saunders, G.M., and Pollack, J.B., 1994. "An evolutionary algorithm that constructs recurrent neural networks", *IEEE Transactions on Neural Networks*, **5**: 54-65.

Anzai, Y., 1992. *Pattern Recognition and Machine Learning*. Academic Press, Boston.

Arkin, Y., Ichoku, C., and Karnieli, A., 1999. "Fault traces in the arid Arava Valley floor, Israel, revealed by Radarsat surface roughness classification", *Canadian Journal of Remote Sensing*, **25**: 302-310.

Arvidson, R., Duncan, I., Green, G., Rivard, B., and Sultan, M., 1994. "Geological mapping using Landsat Thematic Mapper data over oak-hickory forest, arctic and hyperarid terrains", *in* Remote Geochemical Analysis: Elemental and Mineralogical Composition, C.M. Pieters and P.A. Englert (eds.), Cambridge University Press, pp.247-282.

ASD (Analytical Spectral Devices, Inc.), 2001. "Field Spectrometry: Techniques and Instrumentation", <URL:http://www.asdi.com/asd/apps/remote_sensing.html>.

Avery, T.E., and Berlin, G.L., 1992. *Fundamentals of Remote Sensing and Airphoto Interpretation*, Prentice Hall, New Jersey.

Baghdadi, N., Gauthier, Y., Bernier, M., and Fortin, J-P., 2000. "Potential and limitations of RADARSAT SAR Data for wet snow monitoring", *IEEE Transactions on Geoscience and Remote Sensing*, **38**: 316-320.

Balkwill, H.R., and Fox, F.G., 1982. "Incipient rift zone, western Sverdrup Basin", *in* Arctic Geology and Geophysics, A.F. Embry and H.R. Balkwill (eds.), Canadian Society of Petroleum Geologists, Memoir 8, p.171-187.

Barbosa, M.P., Singhroy, V., and Saint-Jean, R., 1999. "Mapping coastal erosion in southern Paraíba, Brazil, from Radarsat-1", *Canadian Journal of Remote Sensing*, **25**: 323-328.

Barnes, W.L., Pagano, T.S., and Salomonson, V.V., 1998. "Preflight characteristics of the Moderate Resolution Imaging Spectroradiometer (MODIS) on EOS-AM1", *IEEE Transactions on Geoscience and Remote Sensing*, **36**: 1088-1100.

Bartlett, E.B., 1994. "Dynamic node architecture learning: an information theoretic approach", *Neural Networks*, **7**: 129-140.

Battiti, R., and Colla, A.M., 1994. "Democracy in neural nets: voting schemes for classification", *Neural Networks*, 7: 691-707.

Beaubien, J., 1994. "Landsat TM satellite images of forests: from enhancement to classification", *Canadian Journal of Remote Sensing*, **20**: 17-26.

Bélanger, J.R., 1991. "Remote sensing of geochemical anomalies related to ultrabasic rocks and gold and uranium mineralization", *Canadian Journal of Remote Sensing*, **17**: 112-121.

Bell, R., Singhroy, V.H., Evans, C.S., and Harrington, S.E., 1991. "Investigating subtle lithologic information in forested regions of northwestern Ontario using field and remote sensing approaches", *Canadian Journal of Remote Sensing*, **17**: 85-96.

Benediktsson, J.A., Swain, P.H., and Ersoy, O.K., 1990. "Neural network approaches versus statistical methods in classification of multisource remote sensing data", *IEEE Transactions on Geoscience and Remote Sensing*, **28**: 540-552.

Benediktsson, J.A., and Swain, P.H., 1992. "Consensus theoretic classification methods", *IEEE Transactions on Systems, Man, and Cybernetics*, **22**: 688-704.

Benediktsson, J.A., Sveinsson, J.R., Ersoy, O.K., and Swain, P.H., 1997a. "Parallel consensual neural networks", *IEEE Transactions on Neural Networks*, **8**: 54-64.

Benediktsson, J.A., Sveinsson, J.R., Ingimundarson, J.I., Sigurdsson, H.S., and Ersoy, O.K., 1997b. "Multistage classifiers optimized by neural networks and genetic algorithms", *Nonlinear Analysis, Theory, Methods, and Applications*, **30**: 1323-1334.

Benediktsson, J.A., Sveinsson, J.R., and Swain, P.H., 1997c. "Hybrid consensus theoretic classification", *IEEE Transactions on Geoscience and Remote Sensing*, **35**: 833-843.

Benediktsson, J.A., and Kanellopoulos, I., 1999. "Classification of multisource and hyperspectral data based on decision fusion", *IEEE Transactions on Geoscience and Remote Sensing*, **37**: 1367-1377.

Birnie, R.W., Parr, J.T., Naslund, H.R., Nichols, J.D., and Turner, P.A., 1989. "Applications of Landsat Thematic Mapper and ground-based spectrometer data to a study of the Skaergaard and other mafic intrusions of East Greenland", *Remote Sensing of Environment*, **28**: 297-304.

Bischof, H., Schneider, W., and Pinz, A.J., 1992. "Multispectral classification of Landsat images using neural networks", *IEEE Transactions on Geoscience and Remote Sensing*, **30**: 482-490.

Bishop, C.M., 1995a. *Neural Networks for Pattern Recognition*. Oxford University Press, New York.

Bishop, C.M., 1995b. "Training with noise is equivalent to Tikhonov regularization", *Neural Computation*, 7: 108-116.

Bishop, Y.M.M., Feinberg, S.E., and Hooland, P.W., 1975. *Discrete Multivariate Analysis Theory and Practice*. MIT Press, Cambridge, Mass.

Blanchard, A.J., and Rouse, J.W. Jr., 1980. "Depolarization of electromagnetic waves scattered from an inhomogeneous half space bounded by a rough surface", *Radio Science*, **15**: 773-779.

Boggs, S., Jr., 1987. *Principles of Sedimentology and Stratigraphy*. Merrill Publishing Company, Toronto.

Bronge, L.B., and Bronge, C., 1999. "Ice and snow-type classification in the Vestfold Hills, East Antarctica, using Landsat TM data and ground radiometer measurements", *International Journal of Remote Sensing*, **20**: 225-240.

Brown, M., Lewis, H.G., and Gunn, S.R., 2000. "Linear spectral mixture models and support vector machines for remote sensing", *IEEE Transactions on Geoscience and Remote Sensing*, **38**: 2346-2360.

Bruzzone, L., Prieto, D.F., and Serpico, S.B., 1999. "A neural-statistical approach to multitemporal and multisource remote-sensing image classification", *IEEE Transactions on Geoscience and Remote Sensing*, **37**: 1350-1359.

Bryson, R.A., Wendland, W.M., Ives, J.D., and Andrews, J.T., 1969. "Radiocarbon isochrones on the disintegration of the Laurentide Ice Sheet", *Arctic and Alpine Research*, **1**: 1-14.

Budkewitsch, P., D'Iorio, M.A., and Harisson, J.C. 1996. "Signatures radar en bande C des lithologies en environement arctique: résultats préliminaires de l'Île de Bathurst, Territoires du Nord-Ouest", *in* Recherches en cours 1996-B, Commission géologique du Canada, pp.67-72.

Burns, R.G., 1993. "Origin of electronic spectra of minerals in the visible to near-infrared region", *in* Remote Geochemical Analysis: Elemental and Mineralogical Composition, C.M. Pieters and P.A. Englert (eds.), Cambridge University Press, pp.3-29.

Cahalan, R.F., and Snider, J.B., 1989. "Marine stratocumulus structure", *Remote Sensing of Environment*, **28**: 95-107.

Card, K.D. 1990. "A review of the Superior Province of the Canadian Shield, a product of Archean accretion", *Precambrian Research*, **48**: 99-156.

Card, K.D., and Poulsen, K.H., 1998. "Geology and mineral deposits of the Superior Province of the Canadian Shield", *in* Chapter 2, Geology of the Precambrian Superior and Grenville Provinces and Precambrian Fossils in North America, S.Lucas and M.R. St-Onge (co-ord), Geological Survey of Canada, Geology of Canada, no.7, pp.13-194.

Carr, M.H., and Malin, M.C., 2000. "Meter-scale characteristics of Martian channels and valleys", *Icarus*, **146**: 366-386.

Castellano, G., Fanelli, A., and Pelillo, M., 1997. "An iterative pruning algorithm for feedforward neural networks", *IEEE Transactions on Neural Networks*, **8**: 519-531.

Cavalieri, D.J., and Gloersen, P., 1984. "Determination of sea ice parameters with the Nimbus 7 SMMR", *Journal of Geophysical Research*, **89**: 5355-5369.

Chavez, P.S., Jr., and Bowell, J.A., 1988. "Comparison of the spectral information content of Landsat Thematic Mapper and SPOT for three different sites in the Phoenix, Arizona, region", *Photogrammetric Engineering and Remote Sensing*, **54**: 1699-1708.

Chen, K.S., Tzeng, Y.C., Chen, C.F., and Kao, W.L., 1995. "Land-cover classification of multispectral imagery using a dynamic learning neural network", *Photogrammetric Engineering and Remote Sensing*, **61**: 403-408.

Clark, R.N., 1999. "Spectroscopy of Rocks and Minerals, and Principles of Spectroscopy", <URL:http://speclab.cr.usgs.gov>.

Cloutis, E.A., 1992. "Weathered and unweathered surface spectra of rocks from cold deserts: identification of weathering processes and remote sensing implications", *Geologiska Föreningens i Stockholm Förhandlingar*, **114**: 181-191.

Cloutis, E.A., 1995a. "Geological mapping of the Canadian Shield by optical remote sensing: spectral resolution requirements", *in* Proceedings of the 17th Canadian Symposium on Remote Sensing, Saskatoon, pp. 748-753.

Cloutis, E.A., 1995b. "Environmental monitoring and geological exploration of the Canadian Shield by optical remote sensing of lichens", *in* Proceedings of the 17th Canadian Symposium on Remote Sensing, pp. 82-87.

Cloutis, E.A., 1997. "Manganese-rich olivines: identification from spectral reflectance properties", *Journal of Geophysical Research*, **102**: 25575-25580.

Cohen, J., 1960. "A coefficient of agreement of nominal scales", *Education Psychological Measurements*, **20**:37-46.

Costa, M.P. de F., de Moraes Novo, E.M.L., Ahern, F., Mitsuo II, F., Mantovani, J.E., Ballester, M.V., and Pietsch, R.W., 1998. "The Amazon floodplain through radar eyes: Lago Grande de Monte Alegre case study", *Canadian Journal of Remote Sensing*, **24**: 339-349.

Daigneault, R.-A., 1993. "Quaternary geology", *in* Geology of the eastern Cape Smith Belt: Parts of the Kangiqsujuaq, Cratère du Nouveau-Québec, and lacs Nuvilik map areas, Québec, St-Onge, M.R., and Lucas, S.B., Geological Survey of Canada, Memoir 438, pp.96-99.

Daigneault, R.-A., 1996a. *Géologie des Formations en Surface, Région du Cap Wolstenholme et de Kovik Bay, Québec - Territoires du Nord*, Geological Survey of Canada, Map 1861A, 1:250 000.

Daigneault, R.-A., 1996b. *Géologie des Formations en Surface, Région de Salluit et des Lacs Nuvilik, Québec - Territoires du Nord*, Geological Survey of Canada, Map 1862A, 1:250 000.

Daigneault, R.-A., 1997. *Géologie des Formations en Surface, Région du Cap de Nouvelle-France, du Cratère du Nouveau-Québec et de Kangiqsujuaq, Québec - Territoires du Nord*, Geological Survey of Canada, Map 1863A, 1:250 000.

Daily, M., Elachi, C., Farr, T., and Schaber, G., 1978. "Discrimination of geologic units in Death Valley using dual frequency and plarization imaging radar data", *Geophysical Research Letters*, **5**: 889-892.

Dall, J., Madsen, S.N., Brooks, C.K., and Nielson, T., 1995. "Geologic mapping in Greenland with Polarimetric SAR", *in* Proceedings: 1995 International Geoscience and Remote Sensing Symposium, IEEE, 2206-2208.

Davidson, A., 1995. "A review of the Grenville orogen in its North American type area", *AGSO Journal of Australian Geology and Geophysics*, **16**: 3-24.

Davies, G.R., and Nassichuk, W.W. 1991. "Carboniferous and Permian history of the Sverdrup Basin, Arctic Islands", *in* Chapter 12, Geology of the Innuitian Orogen and Arctic Platform of Canada and Greenland, H.P. Trettin (ed.), Geological Survey of Canada, no.3, pp.345-367.

Del Frate, F., Petrocchi, A., Lichtenegger, J., and Calabresi, G., 2000. "Neural networks for oil spill detection using ERS-SAR data", *IEEE Transactions on Geoscience and Remote Sensing*, **38**: 2282-2287.

Dempster, A.P., 1967. "Upper and lower probabilities induced by a multivalued mapping", *Annals of Mathematical Statistics*, **38**: 325-339.

Dobson, M.C., and Ulaby, F.T., 1986. "Preliminary evaluation of the SIR-B response to soil moisture, surface roughness, and crop canopy cover", *IEEE Transactions on Geoscience and Remote Sensing*, **GE-24**: 517-526.

Doig, R., 1987. "Rb-Sr geochronology and metamorphic history of Proterozoic to early Archean rocks north of the Cape Smith Fold Belt, Quebec", *Canadian Journal of Earth Sciences*, **24**: 813-825.

Dozier, J., 1984. "Snow reflectance from Landsat-4 Thematic Mapper", *IEEE Transactions on Geoscience and Remote Sensing*, **GE-22**: 323-328.

Dozier, J., 1989. "Spectral signature of alpine snow cover from Landsat 5 TM", *Remote Sensing of Environment*, **28**: 9-22.

Drury, S.A., 1986. "Remote sensing of geological structure in temperate agricultural terrains", *Geological Magazine*, **123**: 113-121.

Drury, S.A., 1993. *Image Interpretation in Geology*, Chapman and Hall, New York.

Duguay, C.R., 1993. "Modelling the radiation budget of alpine snowfields with remotely sensed data: model formulation and validation", *Annals of Glaciology*, **17**: 288-294.

Duguay, C.R., and Peddle, D.R., 1996. "Comparison of evidential reasoning and neural network approaches in a multi-source classification of alpine tundra vegetation", *Canadian Journal of Remote Sensing*, **22**: 433-440.

Dyke, A.S., 1984. *Quaternary Geology of Boothia Peninsula and Northern District of Keewatin, Central Canadian Arctic*. Geological Survey of Canada, Memoir 407.

Dyke, A.S., 1987. "A reinterpretation of glacial and marine limits around the northwestern Laurentide Ice Sheet", *Canadian Journal of Earth Sciences*, **24**: 591-601.

Dyke, A.S., 1999. "Last glacial maximum and deglaciation of Devon Island, arctic Canada: support for an Innuitian Ice Sheet", *Quaternary Science Reviews*, **18**: 393-420.

Dyke, A.S., Dredge, L.A., Vincent, J., 1982. "Configuration and dynamics of the Laurentide Ice Sheet during the late Wisconsin maximum", *Geographie physique et Quaternaire*, **36**: 5-14.

Dyke, A.S., and Prest, V.K., 1987. *Paleogeography of Northern North America, 18 000 - 5000 Years Ago*. Geological Survey of Canada, Map 1703A (scale: 1:12 500 000).

Ecoregions Working Group, 1989. *Ecoclimatic Regions of Canada*, Ecological Land Classification Series, No.23, Environment Canada and Canadian Wildlife Service.

Edlund, S.A., 1986. "Vegetation-geology-climate relationships of western Melville Island, District of Franklin", *in* Current Research, Part A, Geological Survey of Canada, Paper 86-1A, pp.719-726.

Edlund, S.A., 1994. "The distribution of plant communities on Melville Island, Arctic Canada", *in* The Geology of Melville Island, Arctic Canada, R.L. Christie and N.J. McMillan (eds.), Geological Survey of Canada, Bulletin 450, pp. 247-255.

Edlund, S.A., and Alt, B.T., 1989. "Regional congruence of vegetation and summer climate patterns in the Queen Elizabeth Islands, Northwest Territories, Canada", *Arctic*, **42**: 3-23.

Ehlers, M. 1997. "Rectification and registration", *in* Integration of Geographic Information Systems and Remote Sensing, L. Star, J.E. Estes, and K.C. McGwire (eds.), Cambridge University Press, New York.

El Rakaiby, M.L., 1995. "The use of enhanced Landsat-TM image in the characterization of uraniferous granitic rocks in the Central Eastern Desert of Egypt", *International Journal of Remote Sensing*, **16**: 1063-1074.

El Rakaiby, M.L., and Shalaby, M.H., 1992. "Geology of Gebel Qattar batholith, central Eastern Desert, Egypt", *International Journal of Remote Sensing*, **13**: 2337-2347.

Embry, A.F., 1991. "Middle-Upper Devonian clastic wedge of the Arctic Islands", *in* Chapter 10, Geology of the Innuitian Orogen and Arctic Platform of Canada and Greenland, H.P. Trettin (ed.), Geological Survey of Canada, Geology of Canada, no.3, pp. 263-279.

Engeset, R.V., and Weydahl, D.J., 1998. "Analysis of glaciers and geomorphology on Svalbard using multitemporal ERS-1 SAR images", *IEEE Transactions on Geoscience and Remote Sensing*, **36**: 1879-1887.

England, J., 1998. "Support for the Innuitian Ice Sheet in the Canadian High Arctic during the Last Glacial Maximum", *Journal of Quaternary Science*, **13**: 275-280.

England, J., 1999. "Coalescent Greenland and Innuitian ice during the last glacial maximum: revising the Quaternary of the Canadian High Arctic", *Quaternary Science Reviews*, **18**: 421-456.

EOSAT, 1988. *Landsat Thematic Mapper Imagery*. Earth Observation Satellite Company, Lanham, Maryland.

Ernst, W.G., and Paylor II, E.D., 1996. "Study of the Reed Dolomite aided by remotely sensed imagery, Central White-Inyo Range, Easternmost California", *AAPG Bulletin*, **80**: 1008-1026.

Evans, D.L., 1988. "Multisensor classification of sedimentary rocks", *Remote Sensing of Environment*, **25**: 129-144.

Evans, D.L., Farr, T.G., Ford, J.P., Thompson, T.W., and Werner, C.L., 1986. "Multipolarization radar images for geologic mapping and vegetation discrimination", *IEEE Transactions on Geoscience and Remote Sensing*, **GE-24**: 246-257.

Evans, L.G., Reedy, R.C., and Trombka, J.I. 1993. "Introduction to planetary remote sensing gamma ray spectroscopy", *in* Remote Geochemical Analysis: Elemental and Mineralogical Composition, C.M. Pieters and P.A. Englert (eds.), Cambridge University Press, pp.167-198.

Ferrazzoli, P., Guerriero, L., and Schiavon, G., 1999. "Experimental and model investigation on radar classification capability", *IEEE Transactions on Geoscience and Remote Sensing*, **37**: 960-968.

Fielding, E.J., Knox, Jr., W.J., and Bloom, A.L., 1986. "SIR-B radar imagery of volcanic deposits in the Andes", *IEEE Transactions on Geoscience and Remote Sensing*, **GE-24**: 582-589.

Fogel, D.B., 2000. "What is evolutionary computation?", *IEEE Spectrum*, February 2000: 26-32.

Foody, G.M., McCulloch, M.B., and Yates, W.B., 1995. "Classification of remotely sensed data by an artificial neural network: issues related to training data characteristics", *Photogrammetric Engineering and Remote Sensing*, **61**: 391-401.

Fortier, Y.O., McNair, A.H., and Thorsteinsson, R., 1954. "Geology and petroleum possibilities in Canadian Arctic Islands", *Bulletin of the American Association of Petroleum Geologists*, **38**: 2075-2109.

Francis, P.W., and De Silva, S.L., 1989. "Application of the Landsat Thematic Mapper to the identification of potentially active volcanoes in the Central Andes", *Remote Sensing of Environment*, **28**: 245-255.

Franklin, S.E., 1991. "Satellite remote sensing of mountain geomorphic surfaces", *Canadian Journal of Remote Sensing*, **17**: 218-229.

Franklin, S.E., and Wilson, B.A., 1991. "Vegetation mapping and change detection using SPOT MLA and Landsat imagery in Kluane National Park", *Canadian Journal of Remote Sensing*, **17**: 2-17.

Frisch, T., and Trettin, H.P., 1991. "Precambrian successions in the northernmost part of the Canadian Shield", *in* Chapter 6, Geology of the Innuitian Orogen and Arctic Platform of Canada and Greenland, H.P. Trettin (ed.), Geological Survey of Canada, Geology of Canada, no.3, pp.103-108.

Fujisada, H., Sakuma, F., Ono, A., and Kudoh, M., 1998. "Design and preflight performance of ASTER instrument protoflight model", *IEEE Transactions on Geoscience and Remote Sensing*, **36**, 1152-1160.

Fulton, R.J., 1989. "Forward to the Quaternary Geology of Canada and Greenland", *in* Geology of Canada and Greenland, R.J. Fulton (ed.), Geological Survey of Canada, Geology of Canada, no.1, pp. 1-11.

Fung, A.K., and Ulaby, F.T., 1978. "A scatter model for leafy vegetation", *IEEE Transactions on Geoscience Electronics*, **GE-16**: 281-286.

Gaffey, S.J., McFadden, L.A., Nash, D., and Pieters, C.M., 1993. "Ultraviolet, visible, and near-infrared reflectance spectroscopy: laboratory spectra of geologic materials", *in* Remote Geochemical Analysis: Elemental and Mineralogical Composition, C.M. Pieters and P.A. Englert (eds.), Cambridge University Press, pp.43-77.

Gallant, S.I., 1993. *Neural Network Learning and Expert Systems*. MIT Press, Cambridge.

Galvao, L.S., and Vitorello, Í., 1995. "Quantitative approach in the spectral reflectance-lithostratigraphy of the Wind River and southern Bighorn basins, Wyoming", *International Journal of Remote Sensing*, **16**: 1617-1631.

Gastellu-Etchegorry, J.P., Van der Meer Mohr, H., Handaya, A., and Surjanto, W.J., 1990. "An evaluation of SPOT capability for mapping the geology and soils of Central Java", *International Journal of Remote Sensing*, **11**: 685-702.

Gebhardt, M., Horrell, J.M., and Inggs, M.R., 1995. "Comparison of speckle reduction techniques applied to airborne SAR imagery", *in* Proceedings: 1995 International Geoscience and Remote Sensing Symposium, IEEE, 172-174.

Gibbons, D.E., Wukelic, G.E., Leighton, J.P., and Doyle, M.J., 1989. "Application of Landsat Thematic Mapper data for coastal thermal plume analysis at Diablo Canyon", *Photogrammetric Engineering and Remote Sensing*, **55**: 903-909.

Gillespie, A.R., 1980. "Digital techniques of image enhancement", *in* Remote Sensing in Geology, B.S. Siegal and A.R. Gillespie (eds.), John Wiley and Sons, Toronto.

Gillespie, A.R., 1992. "Spectral mixture analysis of multispectral thermal infrared images", *Remote Sensing of Environment*, **42**: 137-145.

Gillespie, A.R., Smith, M.O., Adams, J.B., Willis, S.C., Fischer, A.F., III, and Sabol, D.E., 1990. "Interpretation of residual images: spectral mixture analysis of AVIRIS images, Owen Valley, California", *In:* Proceedings of the Airborne Science Workshop, JPL Publication No. 90-54, pp.243-270.

Giovenazzo, D., Picard, C., and Guha, J., 1989. "Tectonic setting of Ni-Cu-PGE deposits in the central part of the Cape Smith Belt", *Geoscience Canada*, **16**: 134-136.

Giugni, L.-P., Gray, J.T., and Cavayas, F., 1998. "Utilization de la télédétection pour la cartographie des dépôts glaciers sur l'île Akpatok, Baie d'Ungava, T.N.O.", *Canadian Journal of Remote Sensing*, **24**: 402-414.

Glackin, D.L., 1998. "International space-based remote sensing overview: 1980-2007", *Canadian Journal of Remote Sensing*, **24**: 307-314.

Glikson, A.Y., and Creasey, J.W. 1995., "Application of Landsat-5 TM imagery to mapping of the Giles Complex and associated granulites, Tomkinson Ranges, western Musgrave Block, central Australia", *AGSO Journal of Australian Geology and Geophysics*, **16**: 173-193.

Goodbody, Q.H., and Christie, R.L. 1994. "Summary of stratigraphy of Melville Island, Arctic Canada", *in* The Geology of Melville Island, Arctic Canada, R.L. Christie and N.J. McMillan (eds.), Geological Survey of Canada, Bulletin 450, pp. 13-22.

Gopal, S., and Woodcock, C., 1996. "Remote sensing of forest change using artificial neural networks", *IEEE Transactions on Geoscience and Remote Sensing*, **34**: 398-404.

Graham, D.F., and Grant, D.R., 1991. "A test of airborne, side-looking synthetic-aperture radar in central Newfoundland for geological reconnaissance", *Canadian Journal of Earth Sciences*, **28**: 257-265.

Graham, D.F, and Grant, D.R., 1994. "Airborne SAR for surficial geological mapping", *Canadian Journal of Remote Sensing*, **20**: 319-323.

Gupta, R.P., 1991. *Remote Sensing Geology*. Springer-Verlag, New York.

Gutta, S., Huang, J.R.J., Jonathon, P., and Wechsler, H., 2000. "Mixture of experts for classification of gender, ethnic origin, and pose of human faces", *IEEE Transactions on Neural Networks*, **11**: 948-960.

Haack, B.N., Herold, N.D., and Bechdol, M.A., 2000. "Radar and optical data integration for land-use / land-cover mapping", *Photogrammetric Engineering and Remote Sensing*, **66**: 709-716.

Hall, D.K., Ormsby, J.P., Bindschadler, R.A., and Siddalingaiah, H., 1987. "Characterization of snow and ice zones on glaciers using Landsat Thematic Mapper data, *Annals of Glaciology*, **9**: 104-108.

Hansen, L.K., and Salamon, P., 1990. "Neural network ensembles", *IEEE Transactions on Pattern Analysis and Machine Intelligence*, **12**: 993-1001.

Hapke, B., 1993. *Theory of Reflectance and Emittance Spectroscopy*. Cambridge University Press, New York.

Harding, A.E., and Forrest, M.D., 1989. "Analysis of multiple geological datasets from the English Lake district", *IEEE Transactions on Geoscience and Remote Sensing*, **27**: 732-739.

Harding, D.J., Wirth, K.R., and Bird, J.M., 1989. "Spectral mapping of Alaskan ophiolites using Landsat Thematic Mapper data", *Remote Sensing of Environment*, **28**: 219-232.

Harris, J.R., Bowie, C., Rencz, A.N., and Graham, D., 1994. "Computer-enhancement techniques for the integration of remotely sensed, geophysical, and thematic data for the geosciences", *Canadian Journal of Remote Sensing*, **20**: 210-221.

Harrison, J.C., Goodbody, Q.H., and Christie, R.L., 1985. "Stratigraphic and structural studies on Melville Island, District of Franklin", *in* Current Research, Part A, Geological Survey of Canada, Paper 85-1A, pp.629-637.

Harrison, J.C., 1994a. "A summary of the structural geology of Melville Island, Canadian Arctic Archipelago", *in* The Geology of Melville Island, Arctic Canada, R.L. Christie and N.J. McMillan (eds.), Geological Survey of Canada, Bulletin 450, pp.257-283.

Harrison, J.C., 1994b. *Melville Island and Adjacent Smaller Islands, Canadian Arctic Achipelago, District of Franklin, Northwest Territories*. Geological Survey of Canada, Map 1844A, scale 1:250 000.

Harrison, J.C. 1995. *Melville Island's Salt-Based Fold Belt, Arctic Canada*. Geological Survey of Canada, Bulletin 472.

Harrison, J.C., Fox, F.G., and Okulitch, A.V. 1991. "Late Devonian - Early Carboniferous deformation of the Parry Islands and Canrobert Hills Fold Belts, Bathurst and Melville Islands", *in* Chapter 12, Geology of the Innuitian Orogen and Arctic Platform of Canada and Greenland, H.P. Trettin (ed.), Geological Survey of Canada, no.3, pp.321-333.

Heermann, P.D., and Khazenie, N., 1992. "Classification of multispectral remote sensing data using a backpropagation neural network", *IEEE Transactions on Geoscience and Remote Sensing*, **30**: 81-88.

Higgins, A.K., Ineson, J.R., Peel, J.S., Surlyk, F., and Sønderholm, M., 1991. "Cambrian to Silurian basin development and sedimentation, North Greenland", *in* Chapter 7 of Geology of the Innuitian Orogen and Arctic Platform of Canada and Greenland, H.P. Trettin (ed.), Geological Survey of Canada, no.3, pp.111-162.

Hirose, Y., Yamashita, K., and Hijiya, S., 1991. "Back-propagation algorithm which varies the number of hidden nodes", *Neural Networks*, **4**: 61-66.

Hodgson, D.A., Vincent, J.S., and Fyles, J.G., 1984. *Quaternary Geology of Central Melville Island, Northwest Territories*. Geological Survey of Canada, Paper 83-16.

Hodgson, D.A., and Vincent, J.S., 1984. "A 10 000 yr B.P. extensive ice shelf over Viscount Melville Sound, Arctic Canada", *Quaternary Research*, **22**: 18-30.

Hodgson, D.A., 1989. "Quaternary stratigraphy and chronology (Queen Elizabeth Islands)", *in* Chapter 6, Quaternary Geology of Canada and Greenland, R.J. Fulton (ed.), Geological Survey of Canada, Geology of Canada, no.1, pp.452-464.

Hoffman, P.F., 1985. "Is the Cape Smith Belt (northern Québec) a klippe?", *Canadian Journal of Earth Sciences*, **22**: 1361-1369.

Hoffman, P.F., 1988. "United plates of America, the birth of a craton: Early Proterozoic assembly and growth of Laurentia", *Annual Review of Earth and Planetary Sciences*, **16**: 543-603.

Hoffman, P.F., 1989. "Precambrian geology and tectonic history of North America", *in* Chapter 16, The Geology of North America - An Overview, A.W. Bally and A.R. Palmer (eds.), Geological Society of America, Volume A, pp.447-512.

Holmström, L., and Koistinen, P., 1992. "Using additive noise in back-propagation training", *IEEE Transactions on Neural Networks*, **3**: 24-38.

Holmström, L., Koistinen, P., Laaksonen, J., and Oja, E., 1997. "Neural and statistical classifiers - Taxonomy and two case studies", *IEEE Transactions on Neural Networks*, **8**: 5-17.

Horler, D.N.H., and Ahern, F.J., 1986. "Forestry information content of Thematic Mapper data", *International Journal of Remote Sensing*, **7**: 405-428.

Huang, S.C., and Huang, Y.F., 1991. "Bounds on the number of hidden neurons in multilayer perceptrons", *IEEE Transactions on Neural Networks*, **2**: 47-55.

Hughes, G.F., 1968. "On the mean accuracy of statistical pattern recognizers", *IEEE Transactions on Information Theory*, **IT-14**: 55-63.

Hunt, G.R., 1980. "Electromagnetic radiation: the communication link in remote sensing", *in* Remote Sensing in Geology, B.S. Siegal and A.R. Gillespie (eds.), John Wiley and Sons, Toronto.

Jensen, J.R., Kjerfve, B., Ramsey, E.W., III, Magill, K.E., Medeiros, C., and Sneed, J.E., 1989. "Remote sensing and numerical modelling of suspended sediment in Laguna de Terminos, Campeche, Mexico", *Remote Sensing of Environment*, **28**: 33-44.

Ji, C., and Ma, S., 1997. "Combinations of weak classifiers", *IEEE Transactions on Neural Networks*, **8**: 32-42.

Jiminez, L.O., Morales-Morell, A., and Creus, A., 1999. "Classification of hyperdimensional data based on feature and decision fusion approaches using projection pursuit, majority voting, and neural networks", *IEEE Transactions on Geoscience and Remote Sensing*, **37**: 1360-1366.

Johnson, C.A., and Harrison, C.G.A., 1989. "Tectonics and volcanism in central Mexico: a Landsat Thematic Mapper perspective", *Remote Sensing of Environment*, **28**: 273-286.

Joshi, A., Ramakrishman, N., Houtis, E.N., and Rice, J.R., 1997. "On neurobiological, neuro-fuzzy, machine learning, and statistical pattern recognition techniques", *IEEE Transactions on Neural Networks*, **8**: 18-31.

Justice, C.O., Vermote, E., Townshend, J.R.G., Defries, R., Roy, D.P., Hall, D.K., Salomonson, V.V., Privette, J.L., Riggs, G., Strahler, A., Lucht, W., Myneni, R.B., Knyazikhin, Y., Running, S.W., Nemani, R.R., Wan, Z., Huete, A.R., van Leeuwen, W., Wolfe, R.E., Giglio, L., Muller, J-P., Lewis, P., and Barnsley, M.J., 1998. "The moderate resolution imaging spectroradiometer (MODIS): land remote sensing for global change research", *IEEE Transactions on Geoscience and Remote Sensing*, **36**: 1228-1249.

Kahle, A.B., and Alley, R.E., 1992. "Separation of temperature and emittance in remotely sensed radiance measurements", *Remote Sensing of Environment*, **42**: 107-111.

Kahle, A.B., Palluconi, F.D., and Christensen, P.R., 1993. "Thermal emission spectroscopy: application to the Earth and Mars", *in* Remote Geochemical Analysis: Elemental and Mineralogical Composition, C.M. Pieters and P.A. Englert (eds.), Cambridge University Press, pp.99-120.

Kalkhan, M.A., Reich, R.M., and Czaplewski, R.L., 1997. "Variance estimates and confidence intervals for the Kappa measure of classification accuracy", *Canadian Journal of Remote Sensing*, **23**: 210-216.

Karystinos, G.N., and Pados, D.A., 2000. "On overfitting, generalization, and randomly expanded training sets", *IEEE Transactions on Neural Networks*, **11**: 1050-1057.

Kaufman, Y.J., Herring, D.D., Ranson, K.J., and Collatz, G.J., 1998. "Earth Observing System AM1 mission to Earth", *IEEE Transactions on Geoscience and Remote Sensing*, **36**:1045-1055.

Kendall, D.N., 1966. "Infrared radiation: description and simple theory of absorption by molecules", *in* Applied Infrared Spectroscopy, D.N. Kendall (ed.), Reinhold Publishing Corporation, Chapman and Hall, London.

Kenny, F.M., Barnett, P.J., and Singhroy, V.H., 1994. "Application of airborne multispectral and radar images for Quaternary geological mapping", *Canadian Journal of Remote Sensing*, **20**: 286-292.

Kettles, I.M., Rencz, A.N., and Bauke, S.D., 2000. "Integrating Landsat, geologic, and airborne gamma ray data as an aid to surficial geology mapping and mineral exploration in the Manitouwadge area, Ontario", *Photogrammetric Engineering and Remote Sensing*, **66**: 437-445.

Key, J.R., 1994. "Classification of arctic cloud and sea ice features in multispectral satellite data", *in* Neural Nets: Applications in Geography, B.C. Hewitson and R.G. Crane (eds.), pp.145-181.

Khorram, S., Brockhaus, J.A., and Cheshire, H.M., 1987. "Comparison of Landsat MSS and Landsat TM data for urban land-use classification", *IEEE Transactions on Geoscience and Remote Sensing*, **25**: 238-243.

Khotanzad, A., Elragal, H., Lu, T-L., 2000. "Combination of artificial neural-network forecasters for prediction of natural gas consumption", *IEEE Transactions on Neural Networks*, **11**: 464-473.

Klein, C., and Hurlbut, Jr., C.S., 1985. *Manual of Mineralogy*. John Wiley and Sons, Toronto.

Koutsias, N., and Karteris, M., 2000. "Burned area mapping using logistic regression modelling of a single post-fire Landsat-5 Thematic Mapper image", *International Journal of Remote Sensing*, **21**: 673-687.

Kruse, F.A., 1992. "Geologic remote sensing: new technology, new information", *in* Proceedings: 1992 International Geoscience and Remote Sensing Symposium, IEEE, 625-627.

Kůrková, V., 1992. "Kolmogorov's theorem and multilayer neural networks", *Neural Networks*, **5**: 501-506.

Kusky, T.M., Lowman, P.D. Jr., Masuoka, P., Blodget, H.W., 1993. "Analysis of Seasat L-band radar imagery of the West Bay - Indian Lake Fault System, Northwest Territories", *Journal of Geology*, **101**: 623-632.

Kux, H.J.H., dos Santos, J.R., Ahern, F.J., Pietsch, R.W., and Lacruz, M.S.P., 1998. "Evaluation of Radarsat for land use and land cover dynamics in the southwestern Brazilian Amazon State of Acre", *Canadian Journal of Remote Sensing*, **24**: 350-359.

Kwok, T., and Yeung, D., 1997a "Objective functions for training new hidden units in constructive neural networks", *IEEE Transactions on Neural Networks*, **8**: 1131-1148.

Kwok, T., and Yeung, D., 1997b. "Constructive algorithms for structure learning in feedforward neural networks for regression problems", *IEEE Transactions on Neural Networks*, **8**: 630-645.

Landgrebe, D.A., 1978. "Useful information from multispectral image data: another look", *in* Remote Sensing - the Quantitative Approach (P.H. Swain and S. Davis, Eds), Mcgraw Hill, New York, 336-374.

Leberl, F.W., 1990. *Radargrammetric Image Processing*, Artech House, Norwood, Mass.

Lee, J., Weger, R.C., Sengupta, S.K., and Welch, R.M., 1990. "A neural network approach to cloud classification", *IEEE Transactions on Geoscience and Remote Sensing*, **28**: 846-855.

Lee, T., Richards, J.A., and Swain, P.H., 1987. "Probabilistic and evidential approaches for multi-source data analysis", *IEEE Transactions on Geoscience and Remote Sensing*, **25**: 283-293.

Lepage, R., Rouhana, R.G., St-Onge, B., Noumeir, R., and Desjardins, R., 2000. "Cellular neural network for automated detection of geological lineaments on Radarsat images", *IEEE Transactions on Geoscience and Remote Sensing*, **38**: 1224-1233.

Leverington, D.W., 1995. *Prediction of 'Depth to Late-Summer Frozen Ground' Using Satellite Imagery and Digital Topographic Data, Mayo, Yukon Territory*. unpublished MSc thesis, Ottawa-Carleton Geoscience Centre, University of Ottawa.

Leverington, D.W., and Duguay, C.R., 1996a. "Evaluation of three supervised classifiers in mapping 'depth to late-summer frozen ground', central Yukon Territory", *Canadian Journal of Remote Sensing*, **22**: 163-174.

Leverington, D.W., and Duguay, C.R., 1996b. "Evaluation of neural network performance in land cover classification", in Proceedings: 26th International Symposium on Remote Sensing of Environment / 18th Annual Symposium of the Canadian Remote Sensing Society, pp.83-86.

Leverington, D.W., and Duguay, C.R. 1997. "A neural network method to determine the presence or absence of permafrost near Mayo, Yukon Territory, Canada", *Permafrost and Periglacial Processes*, **8**: 205-215.

Lewry, J.F., and Stauffer, M.R., (eds.), 1990. *The Early Proterozoic Trans-Hudson Orogen of North America*. Geological Association of Canada, Special Paper 37.

Lillesand, T.M., and Kiefer, R.W., 1994. *Remote Sensing and Image Interpretation*. John Wiley and Sons, Toronto.

Lo, I.Y., Trombka, J.I., Adler, I., and Bielefeld, M., 1993. "X-ray remote sensing techniques for geochemical analysis of planetary surfaces", *in* Remote Geochemical Analysis: Elemental and Mineralogical Composition, C.M. Pieters and P.A. Englert (eds.), Cambridge University Press, pp.199-212.

Lowe, D., 1980. "Acquisition of remotely sensed data", *in* Remote Sensing in Geology. B.S. Siegal and A.R. Gillespie (eds.), John Wiley and Sons, Toronto.

Lowman, P.D. Jr., 1991. "Original shape of the Sudbury Structure, Canada: a study with airborne imaging radar", *Canadian Journal of Remote Sensing*, **17**: 152-161.

Lowman, P.D. Jr., 1994. "Radar geology of the Canadian Shield: a 10-year review", *Canadian Journal of Remote Sensing*, **20**: 198-209.

Lowman, P.D., Jr., Whiting, P.J., Short, N.M., Lohmann, A.M., and Lee, G., 1992. "Fracture patterns on the Canadian Shield: a lineament study with Landsat and orbital radar imagery", *Basement Tectonics*, 7: 139-159.

Lucas, S.B., and St-Onge, M.R., 1991. "Evolution of Archean and early Proterozoic magmatic arcs in northeastern Ungava Peninsula, Quebec", *in* Current Research, Part C, Geological Survey of Canada, Paper 91-1C, pp.109-119.

Lucas, S.B., St-Onge, M.R., and Percival, J.A., 1998. "Introduction", *in* Chapter 1, Geology of the Precambrian Superior and Grenville Provinces and Precambrian Fossils in North America, S.B. Lucas and M.R. St-Onge (co-ord.), Geological Survey of Canada, Geology of Canada, no.7, pp.1-12.

Luger, G.F., and Stubblefield, W.A. 1993. *Artificial Intelligence: Structures and Strategies for Complex Problem Solving*. 2nd Edition, Benjamin/Cumming Publishing, Redwood City, California.

Lunetta, R.S., and Balogh, M.E., 1999. "Application of multi-temporal Landsat 5 TM imagery for wetland identification", *Photogrammetric Engineering and Remote Sensing*, **65**: 1303-1310.

Luscombe, A.P., Ferguson, I., Shepherd, N., Zimcik, D.G., Naraine, P., 1993. "The Radarsat synthetic aperture radar development", *Canadian Journal of Remote Sensing*, **19**: 298-310.

Lyberis, N., Parrot, J.F., Chorowicz, J., and Rudant, J.P., 1990. "Geological features of the Spitsbergen region obtained from multispectral SPOT data and field radiometer measurements", *International Journal of Remote Sensing*, **11**: 253-265.

Lymburner, L., Beggs, P.J., and Jacobson, C.R., 2000. "Estimation of canopy-average surface-specific leaf area using Landsat TM data", *Photogrammetric Engineering and Remote Sensing*, **66**: 183-191.

Lynne, G.J., and Taylor, G.R., 1986. "Geological assessment of SIR-B imagery of the Amadeus Basin, N.T., Australia", *IEEE Transactions on Geoscience and Remote Sensing*, **GE-24**: 575-581.

Macias, L.F. 1995. "Remote sensing of mafic-ultramafic rocks: examples from Australian Precambrian terranes", *AGSO Journal of Australian Geology and Geophysics*, **16**: 163-171.

Madon, Z., Trowell, N.F., Berger, B., and Ayer, J.A., 1999. "Geological investigation and data integration of 'typical' Canadian Shield Terrain using airborne and satellite imagery including Radarsat radar - Lightning River area, Abitibi Greenstone Belt, Ontario", *Canadian Journal of Remote Sensing*, **25**: 229-244.

Malcolm, J.R., Zimmerman, B.L., Cavalcanti, R.B., Ahern, F.J., and Pietsch, R.W., 1998. "Use of Radarsat SAR data for sustainable management of natural resources: a test case in the Kayapó Indigenous Area, Pará, Brazil", *Canadian Journal of Remote Sensing*, **24**: 360-366.

Maniezzo, V., 1994. "Genetic evolution of the topology and weight distribution of neural networks", *IEEE Transactions on Neural Networks*, **5**: 39-53.

Mather, P.M., 1987. *Computer Processing of Remotely-Sensed Images*. Wiley, Chichester.

Matthews, P.S.C., 1986. *Quantum Chemistry of Atoms and Molecules*. Cambridge University Press, New York.

Maxwell, J.B., 1980. *The Climate of the Canadian Arctic Islands and Adjacent Waters*, Vol. 1, Climatological Studies 30, Atmospheric Environment Service, Toronto.

Maxwell, J.B., 1981. "Climatic regions of the Canadian Arctic Islands", *Arctic*, **34**: 225-240.

Maxwell, J.B., 1982. *The Climate of the Canadian Arctic Islands and Adjacent Waters*, Vol. 2, Climatological Studies 30, Atmospheric Environment Service, Toronto.

Mayewski, P.A., Denson, G.H., and Hughes, T.J., 1981. "Late Wisconsin ice sheets in North America", *in* The Last Great Ice Sheets, G.H. Denton and T.J. Hughes (eds.), John Wiley and Sons, New York, pp.67-178.

McCauley, J.F., Breed, C.S., Schaber, G.G., McHugh, W.P., Issawi, B., Haynes, C.V., Grolier, M.J., and Kilani, A.E., 1986. "Paleodrainages of the eastern Sahara - the radar rivers revisited (SIR-A/B implications for a mid-Tertiary Trans-African drainage system)", *IEEE Transactions on Geoscience and Remote Sensing*, **GE-24**: 624-648.

McClelland, J.L., Rumelhart, D.E., and Hinton, G.E., 1986. "The appeal of parallel distributed processing", *in* Parallel Distributed Processing: Explorations in the Microstructure of Cognition - Foundations, Vol.1, MIT Press, Cambridge, pp.3-44.

McClelland, J.L., and Rumelhart, D.E., 1988. *Explorations in Parallel Distributed Processing - a Handbook of Models, Programs, and Exercises*. MIT Press, Cambridge.

McCulloch, W.S., and Pitts, W., 1943. "A logical calculus of the ideas immanent in nervous activity", *Bulletin of Mathematical Biophysics*, **5**: 115-133.

McGregor, R.G., Brown, A., Good, D.H., and Tomsons, D., 1994. "Potential application of synthetic aperture radar to geologic site characterization of Canadian Shield terrain", *Canadian Journal of Remote Sensing*, **20**: 333-339.

McGregor, R.G., Bruton, P., Singhroy, V.H., and Brown, A., 1999. "An application of remote sensing and GIS towards geological site characterization of a Canadian Shield terrain", *Canadian Journal of Remote Sensing*, **25**: 245-257.

McKay, G.A., 1990. "Climate and the Canadian Arctic Islands", *Canada's Missing Dimension: Science and History in the Canadian Arctic Islands*, C.R.Harrington (ed.), Vol.1, Canadian Museum of Nature, pp.273-293.

McLaren, P., and Barnett, D.M., 1978. "Holocene emergence of the south and east coasts of Melville Island, Queen Elizabeth Islands, Northwest Territories, Canada", *Arctic*, **31**: 415-427.

McNairn, H., Wood, D., Gwyn, Q.H.J., Brown, R.J., and Charbonneau, F., 1998. "Mapping tillage and crop residue management practices with Radarsat", *Canadian Journal of Remote Sensing*, **24**: 28-35.

Mekarnia, A., and Chorowicz, J., 1992. "Geological analysis of SPOT imagery at the 1:25,000 scale: example of the eastern part of the Gabian petroleum structure in southeastern France", *Remote Sensing of Environment*, **39**: 179-185.

Metternicht, G.I., and Zinck, J.A., 1998. "Evaluating the information content of JERS-1 SAR and Landsat TM data for discrimination of soil erosion features", *ISPRS Journal of Photogrammetry and Remote Sensing*, **53**: 143-153.

Miao, J., Johnsen, K-P., Kern, S., Heygster, G., and Kunzi, K., 2000. "Signature of clouds over Antarctic sea ice detected by the Special Sensor Microwave/Imager", *IEEE Transactions on Geoscience and Remote Sensing*, **38**: 2333-2344.

Minsky, M., and Papert, S., 1969. *Perceptrons*. MIT Press, Cambridge.

Moon, W.M., 1990. "Integration of geophysical and geological data using evidential belief function", *IEEE Transactions on Geoscience and Remote Sensing*, **28**: 711-720.

Moon, W.M., 1993. "On mathematical representation and integration of multiple spatial geoscience data sets", *Canadian Journal of Remote Sensing*, **19**: 63-67.

Moon, W.M., Won, J.S., Singhroy, V., and Lowman, P.D. Jr., 1994. "ERS-1 and CCRS C-SAR data integration for look-direction bias correction using wavelet transform", *Canadian Journal of Remote Sensing*, **20**: 280-285.

Mukai, Y., and Hasegawa, I., 2000. "Extraction of damaged areas of windfall trees by typhoons using Landsat TM data", *International Journal of Remote Sensing*, **21**: 647-654.

Mustard, J.F. 1994. "Lithological mapping of gabbro and peridotite sills in the Cape Smith Fold and Thrust Belt with Thematic Mapper and airborne radar data", *Canadian Journal of Remote Sensing*, **20**: 222-232.

Mustard, J.F., and Pieters, C.M., 1987. "Abundance and distribution of ultramafic microbreccia in Moses Rock Dike: quantitative application of mapping spectroscopy", *Journal of Geophysical Research*, **92**: 10376-10390.

Odri, S.V., Petrovacki, D.P., and Krstonosic, G.A., 1993. "Evolutional development of a multilevel neural network", *Neural Networks*, **6**: 583-595.

Oh, S.-H., 1997. "Improving the error backpropagation algorithm with a modified error function", *IEEE Transactions on Neural Networks*, **8**: 799-803.

Orbital Imaging Corporation, 2000. "Orbview-4: High-Resolution Imaging and Hyper-spectral Data", <URL:http://www.orbimage.com/corp/orbimage_system/ov4/index.html>.

Paradella, W.R., and Vitorello, I., 1995. "Geobotanical and soil spectral investigation for rock discrimination in the 'Caatinga' environment (Brazil) based on multitemporal remote sensing data", *Canadian Journal of Remote Sensing*, **21**: 52-59.

Paradella, W.R., dos Santos, A.R., Dall'Agnol, R., Pietsch, R.W., and Sant'Anna, M.V., 1998. "A geological investigation based on airborne (SAREX) and spaceborne (Radarsat-1) SAR integrated products in the central Serra dos Carajás granite area, Brazil", *Canadian Journal of Remote Sensing*, **24**: 376-392.

Parashar, S., Langham, E., McNally, J., and Ahmed, S., 1993. "Radarsat mission requirements and concept", *Canadian Journal of Remote Sensing*, **19**: 280-288.

Parekh, R., Yang, J., and Honavar, V., 2000. "Constructive neural-network learning algorithms for pattern recognition", *IEEE Transactions on Neural Networks*, **11**: 436-451.

Patchett, P.J., Roth, M.A., Canale, B.S., de Freitas, T.A., Harrison, J.C., Embry, A.F., and Ross, G.M., 1999. "Nd isotopes, geochemistry, and constraints on sources of sediments in the Franklinian mobile belt, Arctic Canada", *Geological Society of America Bulletin*, **111**: 578-589.

Peddle, D.R., 1991. *Evidential Classification of Land Cover and Permafrost from Multisource Remote Sensing Imagery in Mountainous Terrain, Yukon*, unpublished MSc thesis, Department of Geography, University of Calgary.

Peddle, D.R., 1993. "An empirical comparison of evidential reasoning, linear discriminant analysis, and maximum likelihood algorithms for alpine land cover classification", *Canadian Journal of Remote Sensing*, **19**: 31-44.

Peddle, D.R., 1995. "Knowledge formulation for supervised evidential classification", *Photogrammetric Engineering and Remote Sensing*, **61**: 409-417.

Peddle, D.R., Foody, G.M., Zhang, A., Franklin, S.E., LeDrew, E.F., 1994. "Multi-source image classification II: an empirical comparison of evidential reasoning and neural network approaches", *Canadian Journal of Remote Sensing*, **20**: 396-407.

Pilon, P.G., and Wiart, R.J., 1990. "Operational forest inventory applications using Landsat TM data: the British Columbia experience", *Geocarto International*, **5**: 25-30.

Pinder, III, J.E., and McLeod, K.W., 1999. "Indications of relative drought stress in longleaf pine from Thematic Mapper data", *Photogrammetric Engineering and Remote Sensing*, **65**: 495-501.

Pontual, A., 1989. "Investigations of the Cerro Colorado Pluton, northern Chile, using enhanced Thematic Mapper images", *IEEE Transactions on Geoscience and Remote Sensing*, **27**: 746-753.

Puhr, C.B., and Donoghue, D.N.M., 2000. "Remote sensing of upland conifer plantations using Landsat TM data: a case study from Galloway, south-west Scotland", *International Journal of Remote Sensing*, **21**: 633-646.

Pultz, T.J., Leconte, R., Brown, R.J., and Brisco, B., 1990. "Quantitative soil moisture extraction from airborne SAR data", *Canadian Journal of Remote Sensing*, **16**: 56-62.

Qari, M.Y.H.T., 1992. "Improving geological mapping in the Arabian Shield using Landsat Thematic Mapper imagery - Jabal Duhayyah area", *International Journal of Remote Sensing*, **13**: 2765-2772.

Quarmby, N.A., Townshend, J.R.G., Millington, A.C., White, K., and Reading, A.J., 1989. "Monitoring sediment transport systems in a semiarid area using Thematic Mapper data", *Remote Sensing of Environment*, **28**: 305-315.

Ramsay, B., Manore, M., Weir, L., Wilson, K., and Bradley, D., 1998. "Use of Radarsat data in the Canadian Ice Service", *Canadian Journal of Remote Sensing*, **24**: 36-42.

Reed, R.D., 1993. "Pruning algorithms - a survey", *IEEE Transactions on Neural Networks*, **1**: 239-242.

Reed, R.D., and Marks II, R.J., 1999. *Neural Smithing*, MIT Press, Cambridge, Mass.

Rheault, M., Simard, R., Garneau, C., and Slaney, V.R., 1991. "SAR Landsat TM-geophysical data integration utility of value-added products in geological exploration", *Canadian Journal of Remote Sensing*, **17**: 185-190.

Riaza, A., Mediavilla, R., and Santisteban, J.I., 2000. "Mapping geological stages of climate-dependant iron and clay weathering alteration on lithologically uniform sedimentary units using Thematic Mapper imagery (Tertiary Duero Basin, Spain)", *International Journal of Remote Sensing*, **21**: 937-950.

Ricchetti, E., 2000. "Multispectral satellite image and ancillary data integration for geological classification", *Photogrammetric Engineering and Remote Sensing*, **66**: 429-435.

Rich, E., and Knight, K., 1991. *Artificial Intelligence*. McGraw-Hill, New York.

Richards, J.A. 1993., *Remote Sensing Digital Image Analysis*, Springer-Verlag, New York.

Rivard, B., Petroy, S.B., and Miller, J.R., 1993. "Measured effects of desert varnish on the mid-infrared spectra of weathered rocks as an aid to TIMS imagery interpretation", *IEEE Transactions on Geoscience and Remote Sensing*, **31**: 284-291.

Rivard, B., Kellett, R.L., Saint-Jean, R., and Singhroy, V., 1994. "Characterization of faulting and dyke intrusion in the Benny Deformation Zone, North Range of Sudbury, from airborne magnetics and SAR", *Canadian Journal of Remote Sensing*, **20**: 324-328.

Rivard, B., Corriveau, L., and Harris, L.B., 1999. "Structural reconnaissance of a deep crustal orogen using Radarsat and Landsat satellite imagery and airborne geophysics", *Canadian Journal of Remote Sensing*, **25**: 258-267.

Rivard, L.A., 1996. "The use of aerospace imageries in basic geological mapping - some interpretation issues", *Canadian Journal of Remote Sensing*, **22**: 329-342.

Robinson, C., El-Baz, F., and Singhroy, V.H., 1999. "Subsurface imaging by Radarsat: comparison with Landsat TM data and implications for ground water in the Selima area, Northwestern Sudan", *Canadian Journal of Remote Sensing*, **25**: 268-277.

Rogova, G., 1994. "Combining the results of several neural network classifiers", *Neural Networks*, 7: 777-781.

Rosenblatt, F., 1962. *Principles of Neurodynamics: Perceptrons and the Theory of Brain Mechanisms*, Spartan, Washington DC.

Rothery, D.A., Francis, P.W., and Wood, C.A., 1988. "Volcano monitoring using short wavelength infrared data from satellites", *Journal of Geophysical Research*, **93**: 7993-8008.

Rowan, L.C., Anton-Pachesco, C., Brickey, D.W., Kingston, M.J., Payas, A., Vergo, N., and Crowley, J.K., 1987. "Digital classification of contact metamorphic rocks in Extremadura Spain using Landsat thematic mapper data", *Geophysics*, **52**: 885-897.

Ruck, D.W., Rogers, S.K., Kabrisky, M., Oxley, M.E., and Suter, B.W., 1990. "The multilayer perceptron as an approximation to a Bayes optimal discriminant function", *IEEE Transactions on Neural Networks*, **1**: 296-298.

Rudant, J.P., Deroin, J.-P., and Polidori, L., 1994. "Multi-resolution analysis of radar images and its application to lithological and structural mapping; Larzac (southern France) test site", *International Journal of Remote Sensing*, **15**: 2451-2468.

Rumelhart, D.E., McClelland, J.L., and the PDP Research Group, 1986. *Parallel Distributed Processing: Explorations in the Microstructure of Cognition*. Vol.1 and 2, MIT Press, Cambridge, Mass.

Saint-Jean, R., Singhroy, V., and Khalifa, S.M., 1995. "Geological interpretation of integrated SAR images in the Azraq area of Jordan", *Canadian Journal of Remote Sensing*, **21**: 511-517.

Salisbury, J.W., and Hunt, G.R., 1974. "Remote sensing of rock type in the visible and near infrared", *in* Proceedings: 9th Symposium on Remote Sensing of Environment, Vol 3, pp.1953-1958.

Salisbury, J.W., and D'Aria, D.M., 1992. "Emissivity of terrestrial materials in the 8-14 μm atmospheric window", *Remote Sensing of Environment*, **42**: 83-106.

Sartori, M.A., and Antsaklis, P.J., 1991. "A simple method to derive bounds on the size and to train multilayer neural networks", *IEEE Transactions on Neural Networks*, **2**: 467-471.

Schaber, G.G., 1999. "SAR studies in the Yuma Desert, Arizona: sand penetration, geology, and the detection of military ordnance debris", *Remote Sensing of Environment*, **67**: 320-347.

Schaber, G.G., McCauley, J.F., Breed, C.S., and Olhoeft, G.R., 1986. "Shuttle imaging radar: physical controls on signal penetration and subsurface scattering in the eastern Sahara", *IEEE Transactions on Geoscience and Remote Sensing*, **GE-24**: 603-623.

Schaber, G.G., McCauley, J.F., and Breed, C.S., 1997. "The use of multifrequency and polarimetric SIR-C/X-SAR data in geological studies of Bir Safsaf, Egypt", *Remote Sensing of Environment*, **59**: 337-363.

Schaber, G.G., and Breed, C., 1999. "The importance of SAR wavelength in penetrating blow sand in northern Arizona", *Remote Sensing of Environment*, **69**: 87-104.

Schau, M., Dredge, L., Rencz, A.N., and Chung, C.F., 1993. "Effect of surficial geology on remotely sensed data of bedrock in northern Canada", *in* Proceedings: 1993 International Geoscience and Remote Sensing Symposium, IEEE, pp.2113-2115.

Schetselaar, E.M., 1994. "A comparative evaluation on the potential of C-band airborne SAR and panchromatic SPOT images for geologic mapping in the Archean Hood River Belt, Bathurst Inlet, Northwest Territories", *Canadian Journal of Remote Sensing*, **20**: 302-316.

Scott, D.J., St-Onge, M.R., Lucas, S.B., and Helmstaedt, H., 1989. "The 1998 Ma Purtuniq ophiolite: imbricated and metamorphosed oceanic crust in the Cape Smith Thrust Belt, northern Quebec", *Geoscience Canada*, **16**: 144-147.

Scott, D.J., and Bickle, M.J., 1991. "Field relationships in the early Proterozoic Purtuniq Ophiolite, Lac Watts and Purtuniq map areas, Quebec", *in* Current Research, Part C, Geological Survey of Canada, Paper 91-1C, pp.179-188.

Sgavetti, M., Ferrari, M.C., Chiari, R., Fantozzi, P.L., and Longhi, I., 1995. "Stratigraphic correlation by integrating photostratigraphy and remote sensing multispectral data: an example from Jurassic-Eocene strata, Northern Somalia", *AAPG Bulletin*, **79**: 1571-1589.

Shafer, G., 1976. *A Mathematical Theory of Evidence*. Princeton University Press, Princeton.

Shahshahani, B.M., and Landgrebe, D.A., 1994. "The effect of unlabelled samples in reducing the small sample size problem and mitigating the Hughes phenomenon", *IEEE Transactions on Geoscience and Remote Sensing*, **32**: 1087-1095.

Sharma, K.N.M., Singhroy, V.H., Madore, L., Lévesque, J., Hébert, C., and Hinse, M., 1999. "Use of radar images in the identification of major regional structures in the Grenville Province, western Quebec", *Canadian Journal of Remote Sensing*, **25**: 278-290.

Sharpe, D.R., 1992. *Quaternary Geology of Wollaston Peninsula, Victoria Island, Northwest Territories*. Geological Survey of Canada, Memoir 434.

Shimabukuro, Y.E., Amaral, S., Ahern, F.J., and Pietsch, R.W., 1998. "Land cover classification from Radarsat data of the Tapajós National Forest, Brazil", *Canadian Journal of Remote Sensing*, **24**: 393-401.

Sietsma, J., and Dow, R.J.F., 1991. "Creating artificial neural networks that generalize", *Neural Networks*, **4**: 67-79.

Simms, É.L., and Bell, T., 1998. "Terrain mapping in an arctic environment from a Radarsat image", *Canadian Journal of Earth Sciences*, **24**: 298-306.

Singhroy, V.H., 1996. "Interpretation of SAR images for coastal zone mapping in Guyana", *Canadian Journal of Remote Sensing*, **22**: 317-328.

Singhroy, V.H., Kenny, F.M., and Barnett, P.J., 1992. "Radar imagery for Quaternary geological mapping in glaciated terrains", *Canadian Journal of Remote Sensing*, **18**: 112-117.

Singhroy, V.H., Slaney, R., Lowman, P., Harris, J., and Moon, W., 1993. "Radarsat and radar geology in Canada", *Canadian Journal of Remote Sensing*, **19**: 338-351.

Singhroy, V.H., and Saint-Jean, R., 1999. "Effects of relief on the selection of Radarsat-1 incidence angle for geological applications", *Canadian Journal of Remote Sensing*, **25**: 211-217.

Skidmore, A., and Turner, B., 1989. "Assessing the accuracy of resource inventory maps", *In* Proceedings of Global Natural Resource Monitoring and Assessment: Preparing for the 21st Century, Venice, Italy, pp. 524-535.

Smalz, R., and Conrad, M., 1994. "Combining evolution with credit apportionment: a new learning algorithm for neural nets", *Neural Networks*, 7: 341-351.

Smith, S.K., Grieve, R.A.F., Harris, J.R., and Singhroy, V., 1999. "The utilization of Radarsat-1 imagery for the characterization of terrestrial impact landforms", *Canadian Journal of Remote Sensing*, **25**: 218-228.

Sohn, Y.M., Moran, E., and Gurri, F., 1999. "Deforestation in north-central Yucatan (1985-1995): mapping secondary succession of forest and agricultural land use in Sotuta using the cosine of the angle concept", *Photogrammetric Engineering and Remote Sensing*, **65**: 947-958.

Spatz, D.M., and Taranik, J.V., 1989. "Regional analysis of Tertiary volcanic calderas (western U.S.) using Landsat Thematic Mapper imagery", *Remote Sensing of Environment*, **28**: 257-272.

Staenz, K., Neville, R.A., Lévesque, J., Szeredi, T., Singhroy, V., Borstad, G.A., and Hauff, P., 1999. "Evaluation of casi and SFSI hyperspectral data for environmental and geological applications - two case studies", *Canadian Journal of Remote Sensing*, **25**: 311-322.

St-Onge, M.R., Lucas, S.B., Scott, D.J., and Bégin, N.J., 1986. "Eastern Cape Smith Belt: an early Proterozoic thrust-fold belt and basal shear zone exposed in oblique section, Wakeham Bay and Cratère du Nouveau Québec map areas, northern Quebec", *in* Current Research, Part A, Geological Survey of Canada, Paper 86-1A, pp.1-14.

St-Onge, M.R., and Scott, J.S., 1986. "Notes on the geomorphology and Quaternary geology of northeastern Ungava Peninsula, Nouveau Québec", *in* Current Research, Part A, Geological Survey of Canada, Paper 86-1A, pp.783-785.

St-Onge, M.R., Lucas, S.B., Scott, D.J., Bégin, N.J., Helmstaedt, H., and Carmichael, D.M., 1988. "Thin-skinned imbrication and subsequent thick-skinned folding of rift-fill, transitional-crust, and ophiolite suites in the 1.9 Ga Cape Smith Belt, northern Quebec", *in* Current Research, Part C, Geological Survey of Canada, Paper 88-1C, p.1-18.

St-Onge, M.R., and Lucas, S.B., 1989. *Geology, eastern portion of the Cape Smith Thrust-Fold Belt, Parts of the Wakeham Bay, Cratere du Nouveau-Québec and Nuvilik Lakes map areas, northern Québec.* Geological Survey of Canada, Maps 1721A to 1735A (1:50 000 scale).

St-Onge, M.R., Lucas, S.B., Scott, D.J., and Begin, N.J., 1989. "Evidence for the development of oceanic crust and for continental rifting in the tectonostratigraphy of the Early Proterozoic Cape Smith Belt", *Geoscience Canada*, **16**: 119-122.

St-Onge, M.R., and Lucas, S.B., 1990a. "Evolution of the Cape Smith Belt: Early Proterozoic continental underthrusting, ophiolite obduction, and thick-skinned folding", *in* Lewry, J.F.,and Stauffer, M.R., eds., The Early Proterozoic Trans-Hudson Orogen of North America: Geological Association of Canada, Special Paper 37, 313-351.

St-Onge, M.R., and Lucas, S.B., 1990b. "Early Proterozoic collisional tectonics in the internal zone of the Ungava (Trans-Hudson) orogen, Lacs Nuvilik and Sugluk map areas, Québec", *in* Current Research, Part C, Geological Survey of Canada, Paper 90-1C, pp. 119-132.

St-Onge, M.R., and Lucas, S.B., 1992. "New insight on the crustal structure and tectonic history of the Ungava Orogen, Kovik Bay and Cap Wolstenholme, Quebec", *in* Current Research, Part C, Geological Survey of Canada, Paper 92-1C, pp.31-41.

St-Onge, M.R., and Lucas, S.B., 1993. *Geology of the Eastern Cape Smith Belt: Parts of the Kangiqsujuaq, Cratère du Nouveau-Québec, and Lacs Nuvilik Map Areas, Québec.* Geological Survey of Canada, Memoir 438.

St-Onge, M.R., and Lucas, S.B., 1997. *Geological Maps, Descriptive Notes, and Legend, Parts of Northern Québec and Northwest Territories.* Geological Survey of Canada, Maps 1911A to 1916A (1:100 000 scale).

St-Onge, M.R., Lucas, S.B., Scott, D.J., and Wodicka, N., 1999. "Upper and lower plate juxtaposition, deformation and metamorphism during crustal convergence, Trans-Hudson Orogen (Quebec-Baffin segment), Canada", *Precambrian Research*, **93**: 27-49.

Swain, P.H., 1978. "Fundamentals of pattern recognition", *in* Remote Sensing: The Quantitative Approach, P.H., Swain and S.M. Davis (eds.), New York, McGraw-Hill, pp.136-187.

Tamura, S., and Tateishi, M., 1997. "Capabilities of a four-layered feedforward neural network: four layers versus three", *IEEE Transactions on Neural Networks*, **8**: 251-255.

Taylor, F.C., 1982. *Reconnaissance Geology of a Part of the Canadian Shield, Northern Quebec and Northwest Territories*. Geological Survey of Canada, Memoir 399.

Thakur, R.S., and Dikshit, O., 1997. "Contextual classification with IRS LISS-II imagery", *ISPRS Journal of Photogrammetry and Remote Sensing*, **52**: 92-100.

Thimm, G., and Fiesler, E., 1997. "High-order and multilayer perceptron initialization", *IEEE Transactions on Neural Networks*, **8**: 349-359.

Thomas, M.D., Grover, B., Halliday, D.W., St-Onge, M.R., and Lucas, S.B., 1991. "Detailed gravity traverses across the early Proterozoic Ungava orogen, northern Quebec", *in* Current Research, Part C, Geological Survey of Canada, Paper 91-1C, pp.189-193.

Tian, B., Shaikh, A., Azimi-Sadjadi, M.R., Haar, T.H.V., and Reinke, D.L., 1999. "A study of cloud classification with neural networks using spectral and textural features", *IEEE Transactions on Neural Networks*, **10**: 138-151.

Tozer, E.T., and Thorsteinsson, R., 1964. *Western Queen Elizabeth Islands, Arctic Archipelago*. Geological Survey of Canada, Memoir 332.

Trettin, H.P., 1987. "Pearya: a composite terrane with Caledonian affinities in northern Ellesmere Island", *Canadian Journal of Earth Sciences*, **24**: 224-245.

Trettin, H.P., 1989. "The Arctic Islands", *in* Chapter 16, The Geology of North America - An Overview, A.W. Bally and A.R. Palmer (eds.), Geological Society of America, Volume A, pp.349-370.

Trettin, H.P., 1991a. "Tectonic Framework" *in* Chapter 4, Geology of the Innuitian Orogen and Arctic Platform of Canada and Greenland, H.P. Trettin (ed.), Geological Survey of Canada, Geology of Canada, no.3, pp.59-66.

Trettin, H.P., 1991b. "Introduction", *in* Chapter 12, Geology of the Innuitian Orogen and Arctic Platform of Canada and Greenland, H.P. Trettin (ed.), Geological Survey of Canada, Geology of Canada, no.3, p.295.

Trettin, H.P., Mayr, U., Long, G.D.F., and Packard, J.J., 1991. "Cambrian to Early Devonian basin development, sedimentation, and volcanism, Arctic Islands", *in* Chapter 8, Geology of the Innuitian Orogen and Arctic Platform of Canada and Greenland, H.P. Trettin (ed.), Geological Survey of Canada, Geology of Canada, no.3, pp.163-238.

Ulaby, F.T., Moore, R.K., and Fung, A.K., 1981. *Microwave Remote Sensing: Active and Passive*, Vol.1, Addison-Wesley Publishing Company, Don Mills, Ontario.

Ulaby, F.T., Moore, R.K., and Fung, A.K., 1982. *Microwave Remote Sensing: Active and Passive*, Vol.2, Addison-Wesley Publishing Company, Don Mills, Ontario.

Ulaby, F.T., Brisco, B., and Dobson, C., 1983. "Improved spatial mapping of rainfall events with spaceborne SAR imagery", *IEEE Transactions on Geoscience and Remote Sensing*, **GE-21**: 118-121.

Urai, M., 2000. "Volcano monitoring with Landsat TM short-wave infrared bands: the 1990-1994 eruption of Unzen Volcano, Japan", *International Journal of Remote Sensing*, **21**: 861-872.

Van der Meer, F., Van Dijk, P.M., and Westerhof, A.B., 1995. "Digital classification of the contact metamorphic aureole along the Los Pedroches batholith, south-central Spain, using Landsat Thematic Mapper data", *International Journal of Remote Sensing*, **16**: 1043-1062.

Vemuri, V.R., 1992. *Artificial Neural Networks: Concepts and Control Applications*. IEEE Computer Society Press, Los Alamintos, California.

Vickers, R.S., and Lyon, R.J.P., 1967. "Infrared sensing from spacecraft: a geological interpretation", *in* Thermophysics of Spacecraft and Planetary Bodies - Radiation Properties of Solids and the Electromagnetic Radiation Environment in Space. O.B. Heller (ed.), Academic Press, New York, pp. 986-988.

Voudouri-Maniati, E., 1997. "A neural network approach to nonparametric and robust classification procedures", *IEEE Transactions on Neural Networks*, **8**: 288-298.

Wald, L., 1999. "Some terms of reference in data fusion", *IEEE Transactions on Geoscience and Remote Sensing*, **37**: 1190-1193.

Wan, E.A., 1990. "Neural network classification: a Bayesian interpretation", *IEEE Transactions on Neural Networks*, **1**: 303-304.

Wang, Y., and Civco, D.L., 1994. "Evidential reasoning-based classification of multi-source spatial data for improved land cover mapping", *Canadian Journal of Remote Sensing*, **20**: 381-395.

Wang, Z., Massimo, C.D., Tham, M.T., and Morris, J., 1994. "A procedure for determining the topology of multilayer feedforward neural networks", *Neural Networks*, **7**: 291-300.

Wang, J., and Liu, W., 1994. "Road detection from multi-spectral satellite imagery", *Canadian Journal of Remote Sensing*, **20**: 180-191.

Warner, T.A., Campagna, D.J., Evans, C.S., Levandowski, D.W., and Cetin, H., 1991. "Analyzing remote sensing geobotanical trends in Quetico Provincial Park, Ontario, Canada, using digital elevation data", *Photogrammetric Engineering and Remote Sensing*, **57**: 1179-1183.

Widrow, B., and Hoff, M.E., 1960. "Adaptive switching circuits", *in* IRE WESCON Convention Record, Vol.4, New York, pp.96-104.

Winston, P.H., 1991. *Artificial Intelligence*. Addison-Wesley Publishing Co., Reading, Mass.

Wolf, A.P., and King, R.H., 1999. "A paleolimnological constraint to the extent of the last glaciation on northern Devon Island, Canadian High Arctic", *Quaternary Science Reviews*, **18**: 1563-1568.

Yam, J.Y.F., and Chow, T.W.S., 1997. "Extended least squares based algorithm for training feedforward networks", *IEEE Transactions on Neural Networks*, **8**: 806-811.

Yao, X., and Liu, Y., 1997. "A new evolutionary system for evolving artificial neural networks", *IEEE Transactions on Neural Networks*, **8**: 694-713.

Yin, L.I., Trombka, J.I., Adler, I., and Bielefeld, M., 1993. "X-ray remote sensing techniques for geochemical analysis of planetary surfaces", *in* Remote Geochemical Analysis: Elemental and Mineralogical Composition, C.M. Pieters and P.A. Englert (eds.), Cambridge University Press, pp.199-212.

Zhou, C., Luo, J., Yang, C., Li, B., and Wang, S., 2000. "Flood monitoring using multi-temporal AVHRR and Radarsat imagery", *Photogrammetric Engineering and Remote Sensing*, **66**: 633-638.

Zhou, W., 1999. "Verification of the nonparametric characteristics of backpropagation neural networks for image classification", *IEEE Transactions on Geoscience and Remote Sensing*, **37**: 771-779.

Zhou, G., and Li, R., 2000. "Accuracy evaluation of ground points from IKONOS high-resolution satellite imagery", *Photogrammetric Engineering and Remote Sensing*, **66**: 1103-1112.

APPENDIX A: Descriptions of Melville Island Field Sites

Introductory notes to Appendix A

1) Site Locations are given in Figures 4.6 to 4.8.

2) Over 300 photographs and seven hours of video tape (on four two-hour tapes) provide visual documentation of the Melville Island study area.

3) Particularly detailed video documentation of the varieties of vegetation that characterize the study area is available in the documentation of Sites 8, 15, 36, 39, 46, and 76.

4) Vegetation Cover Ranks:

0	Essentially no vegetation of any kind.
0-L	Essentially no vascular vegetation, but lichen varieties are present and significant.
1	Sparsely-scattered vegetation: ~1% to ~6% cover (lower boundary defined by Site 13A, and upper boundary defined by Sites 16 and 30).
2	~6% to ~15% vegetation cover (lower boundary defined by Site 45, and upper boundary defined by Sites 18A and 43)
3	~15% to ~25% vegetation cover.
4	~25% to ~75% vegetation cover.
5	>75% vegetation cover (lichen, moss, or vascular) (includes, e.g., Site 51)

5) The sizes of rock samples are expressed in terms of their longest dimension.

6) Carbonate lithologies are described using the terminology of Folk (1962) [see summary given by Boggs (1987, p. 230)].

7) Common Names for Melville Island Plants:

Saxifraga oppositifolia: Purple Saxifrage
Papaver radicatum: Arctic Poppy
Oxyria digyna: Mountain Sorrel
Salix arctica: Arctic Willow

8) Melville Island lichens collected by the author and identified by P.Y. Wong, Collection Division, Canadian Museum of Nature (Ottawa) (all species but *Vulpicida tilesii* are very common in the study area):

Thamnolia subuliformis (Ehrh.) Culb.
Lecidea lapicida (Ach.) Ach.
Lecidea ramulosa Th. Fr.

Vulpicida tilesii (Ach.) J.-E. Mattsson & M.J. Lai

9) A black vegetative material coats the surfaces of particularly moist areas in the Melville Island region. A sample of this material, collected by the author at Site 51, was identified as alga by P.Y. Wong, Collection Division, Canadian Museum of Nature (Ottawa). Samples of dark material collected at Sites 13B and 17 were identified as "fungal tissue with fruiting perithecia" and "filamentous alga", respectively, by Dr. Michele Piercey-Normore, Department of Botany, University of Manitoba. The dark material is referred to here simply as "black algae".

10) The list of vegetation varieties in the section "Other Varieties Noted" is not meant to be a comprehensive listing of all varieties present at a site.

11) The term "small bag" refers to a plastic bag with dimensions of approximately 18 cm x 20 cm.

Site 1

Photographs:	One landscape photo; one closeup photo.
Video:	Tape #1, 42:17 - 43:02.
Formation/Unit:	Tingmisut Inlier.
Dominant Lithology:	Dolostone.
General Information:	Site consists of angular dolostone rocks (typically 3 to 20 cm) on talus slope. Unconsolidated reddish-weathering fines are present (visually-estimated surface proportion: <10%).
Munsell Colours:	Rocks typically 5Y 8/1 (*yellowish grey*) and/or 10 YR 6/6 (*dark yellowish orange*). Fines 10 YR 7/4 (*grayish orange*).
Samples:	5 rock samples (12.5 cm, 11 cm, 9 cm, 6.5 cm, 6 cm; reaction with HCl is subdued to moderate for exposed surfaces, and is subdued for fresh surfaces).
Thin Section:	Thin section *1-1*: Interlocking anhedral dolomite crystals; bi-modal crystal-size distribution (<0.1 mm and 0.5-6.0 mm). Minor calcite fossils and cement are present.
Weathering State:	Unweathered dolostone surfaces are gray. Weathered surfaces are typically yellowish-orange. The orange fines may be derived from the local dolostone, or may be wind-blown Canyon Fiord Formation materials.
Vegetation:	Cover Rank: 0. Significant Varieties: None. Other Varieties Noted: None.

Site 2

Photographs:	One landscape photo; one closeup photo.
Video:	Tape #1, 46:35 - 46:52.
Formation/Unit:	Tingmisut Inlier.
Dominant Lithology:	Dolostone.
General Information:	Site consists of dolostone rocks (typically <5 cm, but larger rocks <20 cm are present). Unconsolidated reddish-weathering fines are present (visually-estimated surface proportion: <15%). Rocks and fines are sorted by size by frost action, forming arcuate ridges and irregular ovoid features.
Munsell Colours:	Rocks typically N8-N7 (*very light gray* to *light gray*) and 5YR 5/6 (*light brown*). Fines 10 YR 7/4 (*grayish orange*).
Samples:	3 "end-member" rock samples (each 4 cm; reaction with HCl is subdued to vigorous for exposed surfaces, and is subdued to moderate on fresh surfaces); one small sample of reddish-weathering fines (reaction with HCl is vigorous).
Thin Section:	None.
Weathering State:	Unweathered dolostone surfaces are gray. Weathered surfaces are typically yellowish-orange. The orange fines may be derived from the local dolostone, or may be wind-blown Canyon Fiord Formation materials.
Vegetation:	Cover Rank: 0. Significant Varieties: None. Other Varieties Noted: None.

Site 3

Photographs:	One landscape photo only.
Video:	Tape #1, 43:52 - 47:36.
Formation/Unit:	Tingmisut Inlier.
Dominant Lithology:	Dolostone.
General Information:	Site consists of dolostone rocks (typically <5 cm). Unconsolidated reddish-weathering fines are exposed (visually-estimated surface proportion: <40%). In places, rocks and fines are sorted by size by frost action.
Munsell Colours:	Rocks typically N8-N7 (*very light gray* to *light gray*) and 5YR 5/6 (*light brown*). Fines 10 YR 7/4 (*grayish orange*).
Samples:	None.
Thin Section:	None.
Weathering State:	Unweathered dolostone surfaces are gray. Weathered surfaces are typically yellowish-orange. The orange fines may be derived from the local dolostone, or may be wind-blown Canyon Fiord Formation materials.
Vegetation:	Cover Rank: 0. Significant Varieties: None. Other Varieties Noted: None.

Site 4

Photographs:	None taken.
Video:	Tape #1, 47:52 - 49:00.
Formation/Unit:	Tingmisut Inlier.
Dominant Lithology:	Dolostone.
General Information:	Site consists of dolostone rocks (typically <5 cm). Unconsolidated reddish-weathering fines are present. Rocks and fines are sorted by size in places by frost action.
Munsell Colours:	Rocks typically N8-N7 (*very light gray* to *light gray*) and 5YR 5/6 (*light brown*). Fines 10 YR 7/4 (*grayish orange*).
Samples:	None.
Thin Section:	None.
Weathering State:	Unweathered dolostone surfaces are gray. Weathered surfaces are typically yellowish-orange. The orange fines may be derived from the local dolostone, or may be wind-blown Canyon Fiord Formation materials.
Vegetation:	Cover Rank: 0. Significant Varieties: None. Other Varieties Noted: None.

Site 5

Photographs:	One landscape photo; one closeup photo.
Video:	Tape #1, 50:28 - 51:13.
Formation/Unit:	Tingmisut Inlier.
Dominant Lithology:	Dolostone.
General Information:	Site consists of dolostone rocks (typically <10 cm). Unconsolidated reddish-weathering fines are present (visually-estimated surface proportion: <5%).
Munsell Colours:	Rocks typically N7 (*light gray*) to 10 YR 7/4 (*grayish orange*). Fines 10 YR 7/4 (*grayish orange*).
Samples:	1 rock sample (11.5 cm: reaction with HCl is subdued for both exposed and fresh surfaces); one small sample of reddish-weathering fines (reaction with HCl is vigorous).
Thin Section:	None.
Weathering State:	Unweathered dolostone surfaces are gray. Weathered surfaces are typically yellowish-orange. The orange fines may be derived from the local dolostone, or may be wind-blown Canyon Fiord Formation materials.
Vegetation:	Cover Rank: 0. Significant Varieties: None. Other Varieties Noted: None.

Site 6

Photographs:	One landscape photo; one closeup photo.
Video:	Tape #1, 53:05 - 54:17.
Formation/Unit:	Canyon Fiord Formation.
Dominant Lithology:	Red-weathering and yellow sands and related non-calcareous sandstones.
General Information:	Most materials at this site are unconsolidated and poorly-consolidated fines (typically <2 mm), although rocks with dimensions of up to ~20 cm are also found. Rounded quartz clasts are the most dominant component of the fines and rocks.
Munsell Colours:	Fines 10 YR 6/6 (*dark yellowish orange*) and yellowish orange.
Samples:	One small bag containing red-weathering clasts (no reaction with HCl); one small bag containing yellow-weathering fines (no reaction with HCl).
Thin Section:	None.
Weathering State:	These materials appear to have been derived from weathered Canyon Fiord sandstones.
Vegetation:	Cover Rank: 0. Significant Varieties: None. Other Varieties Noted: None.

Site 7

Photographs:	One landscape photo; one closeup photo.
Video:	Tape #1, 55:34 - 56:35.
Formation/Unit:	Canyon Fiord Formation.
Dominant Lithology:	Heterolithic clasts set in unconsolidated yellow, red, and gray fines.
General Information:	Site consists of rounded heterolithic clasts (typically <1.3 cm) set in unconsolidated yellow, red, and unconsolidated gray fines (typically <2 mm).
Munsell Colours:	Fines between 5Y 8/4 (*grayish yellow*) and 5Y 8/1 (*yellowish gray*).
Samples:	One small bag of yellowish/whitish fines/clasts (fine- to coarse-grained quartz grains coated with whitish-gray material; reaction with HCl is vigorous); one small bag of reddish fines/clasts (mix of unidentified elongate and rounded grains, including quartz; reaction with HCl is subdued to moderate).
Thin Section:	None.
Weathering State:	These materials appear to have been derived from weathered Canyon Fiord sandstones and conglomerates.
Vegetation:	Cover Rank: 0. Significant Varieties: None. Other Varieties Noted: None.

Site 8

Photographs:	One landscape photo; one closeup photo.
Video:	Tape #1, 59:29 - 1:00:22.
Formation/Unit:	Unnamed gabbro intrusion.
Dominant Lithology:	Gabbro.
General Information:	Site mainly consists of angular gabbro rocks (typically 0.5 to 10 cm), unconsolidated reddish fines (visually-estimated surface proportion: <10%), and scattered gabbro bedrock outcrops (individual outcrops are typically ~3 m across).
Munsell Colours:	Rocks ~N2 (*grayish black*) to ~5YR 4/4 (*moderate brown*). Fines yellow-brown.
Samples:	Three gabbro rocks: 9.5 cm, 6.5 cm, 2.5 cm. Vegetation was sampled.
Thin Section:	None.
Weathering State:	Unweathered gabbro surfaces are gray-black. Weathered surfaces are typically brown. The yellow-brown fines appear to be wind-blown Canyon Fiord Formation materials.
Vegetation:	Cover Rank: 0-L Significant Cover: *Thamnolia subuliformis, Lecidea spp.* Other Cover: *Saxifraga oppositifolia, Vulpicida tilesii.*

Site 9

Photographs:	One landscape photo; one closeup photo.
Video:	None (refer to video of nearby Sites 5, 8, 10, and 11).
Formation/Unit:	Canyon Fiord Formation.
Dominant Lithology:	Red-weathering fine-grained calcareous sandstones, and associated fines.
General Information:	Site consists of red-weathering fine-grained calcareous sandstones (rocks typically <15 cm), associated unconsolidated red-weathering fines, and small (typically <5 cm) gabbro clasts derived from the upslope gabbro dike. The dominant constituents of the sandstones and fines are rounded fine-grained quartz grains.
Munsell Colours:	Sandstones ~5YR 4/4 (*moderate brown*); fresh surfaces ~5Y 8/1 (*yellowish gray*). Gabbro N2 (*grayish black*).
Samples:	5 small rocks (all < 6 cm): four sandstones (reaction with HCl subdued to moderate for exposed surfaces, and moderate to vigorous for fresh surfaces), and one gabbro. One small bag of red fines (composed of fine-grained quartz set loosely in a red-weathering silty matrix; reaction of fines to HCl vigorous).
Thin Section:	None.
Weathering State:	Most exposed sandstone surfaces are weathered red, while fresh sandstone surfaces are yellowish-gray. Unweathered gabbro surfaces are gray-black. Weathered gabbro surfaces are typically brown.
Vegetation:	Cover Rank: 0. Significant Varieties: None. Other Varieties Noted: None.

Site 10

Photographs:	One landscape photo; one closeup photo.
Video:	Tape #1, 1:00:22 - 1:02:10.
Formation/Unit:	Canyon Fiord Formation.
Dominant Lithology:	Red-weathering fine-grained calcareous sandstones, and associated fines.
General Information:	Site consists of red-weathering fine-grained calcareous sandstones (rocks typically <15 cm), associated unconsolidated red-weathering fines, and small (typically <5 cm) gabbro clasts derived from the upslope gabbro dike. The dominant constituents of the sandstones and fines are rounded fine-grained quartz grains.
Munsell Colours:	Sandstones ~5YR 4/4 (*moderate brown*); fresh surfaces ~5Y 8/1 (*yellowish gray*). Gabbro N2 (*grayish black*).
Samples:	Six small rocks (all <7.5 cm): five sandstones (reaction with HCl is absent to subdued for exposed surfaces, and moderate to vigorous for fresh surfaces) and one gabbro. One small bag of red fines (composed of fine-grained quartz set loosely in a red-weathering silty matrix; reaction of fines to HCl subdued).
Thin Section:	None.
Weathering State:	Most exposed sandstone surfaces are weathered red, while fresh sandstone surfaces are yellowish-gray.. Unweathered gabbro surfaces are gray-black. Weathered gabbro surfaces are typically brown.
Vegetation:	Cover Rank: 0. Significant Varieties: None. Other Varieties Noted: None.

Site 11

Photographs:	One landscape photo only (photo is of poor quality due to camera malfunction).
Video:	Tape #1, 1:00:30 - 1:00:40 (taped from Site 10).
Formation/Unit:	Canyon Fiord Formation
Dominant Lithology:	Gray- and orange-weathering unconsolidated, non-calcareous, fine-grained quartz.
General Information:	Site consists entirely of gray- and orange-weathering unconsolidated, non-calcareous, fine-grained quartz.
Munsell Colours:	Fines either 5Y 8/1 (*yellowish gray*) or yellowish orange [specifically, a cross between 10YR 8/6 (*pale yellow orange*) and 10YR 6/6 (*dark yellow orange*)].
Samples:	One small bag of orange fines (fine-grained quartz coated in part with orange-weathering material; no reaction with HCl); one small bag of gray fines (fine-grained quartz; no reaction with HCl); one friable gray calcareous sandstone sample (6 cm; reaction with HCl vigorous; this is a sample of the calcareous sandstone unit from which these fines may have been derived, and was taken from a small bedrock exposure located at the creek-ward extremity of this site.).
Thin Section:	None.
Weathering State:	These materials appear to have been derived from weathered Canyon Fiord sandstones.
Vegetation:	Cover Rank: 0. Significant Varieties: None. Other Varieties Noted: None.

Site 12

Photographs:	None (due to camera malfunction).
Video:	Tape #1, 1:03:03 - 1:03:56.
Formation/Unit:	Canyon Fiord Formation.
Dominant Lithology:	Red-weathering fine- to coarse-grained calcareous sandstone.
General Information:	Site mainly consists of materials of three size groups: 1) red-weathering silty fines, 2) smaller clasts (typically 0.1 to 3 cm): gabbro and red-weathering sandstone / conglomerate, and 3) larger clasts (typically 10-50 cm across): red-weathering sandstone, and gabbro. The dominant constituent of the sandstone / conglomerate clasts is rounded fine-grained quartz. Limestone seen in the vicinity of the site may he part of the limestone marker unit that occurs midway in the Canyon Fiord sequence, and that has been previously mapped at this site (Harrison, 1995).
Munsell Colours:	Sandstone either ~5Y 8/1 (*yellowish gray*; fresh surfaces) or 5YR 5/6 (*light brown*) to deep reddish brown (weathered surfaces). Gabbro N2 (*grayish black*).
Samples:	Samples were taken of each of the three size ranges noted above: 1) one small bag containing fines (reaction with HCl subdued; mainly fine-grained rounded quartz grains); 2) one small bag containing small clasts (<4 cm; including several gabbro clasts), and 3) five larger clasts (samples broken off of larger rocks: 6.5 cm, 6 cm, 5.5 cm, 5.5 cm, 4.5 cm). All rock samples react vigorously with HCl.
Thin Section:	None.
Weathering State:	Most exposed sandstone surfaces are weathered red, while fresh sandstone surfaces are yellowish-gray. Unweathered gabbro surfaces are gray-black. Weathered gabbro surfaces are typically brown.
Vegetation:	Cover Rank: 0. Significant Varieties: None. Other Varieties Noted: None.

Sites 13A and 13B

Photographs:	One landscape photo and one closeup photo for each of A and B (four photos total).
Video:	Tape #1, 1:04:16 - 1:06:26.
Formation/Unit:	Canyon Fiord Formation
Dominant Lithology:	Unconsolidated sandy and silty fines, pebble-sized heterolithic clasts, and calcareous sandstones.
General Information:	Site consists of two components: A) Consists mainly of rounded to subangular heterolithic clasts (typically <2.5 cm) in unconsolidated red fines. No gabbro from nearby dike is present. B) Consists mainly of angular consolidated clasts with sizes up to 25 cm (typically <10 cm), in unconsolidated red fines. This material (consisting of calcareous quartz sandstone, conglomerate, gabbro, and fines) has weathered from upslope, and extends downslope along topographic lows.
Munsell Colours:	A) Pebbles very pale yellowish to moderate reddish-brown; fines reddish brown. B) Pebbles ~5YR 5/6 (*light brown*); sandstones ~5YR 3/4 (*moderate brown*; exposed surface) and ~5Y 8/1 (*yellowish gray*; fresh surface); fines reddish brown.
Samples:	One small bag containing pebbles / fines of A (reaction with HCl subdued); one small bag containing pebbles / fines of B (reaction with HCl vigorous); four small rock samples from B (9 cm to 4.5 cm; two samples are calcareous sandstones, one sample is calcareous pebble conglomerate, and one sample is gabbro) (sandstones and conglomerate: reaction with HCl absent to moderate for exposed surfaces, and moderate to vigorous for fresh surfaces). Vegetation was sampled at 13B.
Thin Section:	None.
Weathering State:	Most exposed sandstone surfaces weathered red, while fresh sandstone surfaces yellowish gray. Unweathered gabbro surfaces gray-black. Weathered gabbro surfaces are typically brown.
Vegetation:	Cover Rank: 1. Significant Cover: *Saxifraga oppositifolia* (sparsely scattered, ~7cm mounds). Other Cover: None. Notes: Small portions of 13B are covered with black algae.

Site 14

Photographs:	None.
Video:	Tape #1, 1:06:35 - 1:09:38 (note: on video, Site 15 is erroneously referred to as Site 14).
Formation/Unit:	Canyon Fiord Formation.
Dominant Lithology:	Red-weathering calcareous sandstone and conglomerate, and unconsolidated red-weathering fines.
General Information:	Site consists of red-weathering calcareous sandstones (typically <10 cm), and unconsolidated red-weathering fines. Metre-scale bedrock outcrops and rocks are present immediately downslope from site.
Munsell Colours:	Both exposed and fresh rock surfaces are ~10R 4/6 (*moderate reddish brown*) and 5Y 8/1 (*yellowish gray*). Fines weather to ~10R 4/6 (*moderate reddish brown*).
Samples:	Seven rock samples (8 cm to 5 cm; calcareous sandstone and conglomerate): (reaction with HCl moderate to vigorous for both exposed and fresh surfaces); one small bag containing red silt- and clay-sized fines. Quartz grains are the main constituent of the sandstones and conglomerates.
Thin Section:	None.
Weathering State:	Most exposed sandstone surfaces are weathered red, while fresh sandstone surfaces are yellowish gray.
Vegetation:	Cover Rank: 0. Significant Cover: None. Other Cover: None. Notes: Black algae is present.

Site 15

Photographs:	Two landscape photos (SW side; NE side) and one closeup photo on SW side.
Video:	Tape #1, 1:09::38 - 1:12:50.
Formation/Unit:	Unnamed gabbro intrusion.
Dominant Lithology:	Gabbro.
General Information:	Site consists dominantly of angular gabbro rocks (typically 2-30 cm). Both gray and red-weathering sand / pebble fines are present; the red fines appear to be wind-blown Canyon Fiord materials.
Munsell Colours:	Rocks N3 (*dark gray*) to 5YR 4/1 (*brownish gray*) to minor 5YR 5/6 (*light brown*). Fines reddish brown.
Samples:	Two gabbro samples (14 cm and 7.5 cm); one small bag containing dark fines. The surfaces of the rock samples are representative of the local rocks, being variably covered by lichens. Vegetation was sampled.
Thin Section:	Thin section *15-1*: Medium- to fine-grained phenocrysts of plagioclase and magnetite set in fine-grained groundmass of plagioclase, pyroxene, and microcrystalline hematite.
Weathering State:	Unweathered gabbro surfaces gray-black. Weathered gabbro surfaces are typically brown.
Vegetation:	Cover Rank: 0-L. Significant Varieties: *Thamnolia subuliformis, Lecidea spp.* Other Varieties Noted: *Saxifraga oppositifolia, Papaver radicatum.*

Site 16

Photographs:	One landscape photo; one closeup photo.
Video:	Tape #1, 1:19:21 - 1:20:40.
Formation/Unit:	Great Bear Cape Formation.
Dominant Lithology:	Limestone and calcareous sandstone.
General Information:	Site consists of limestones and calcareous sandstones (typically <7 cm). Sparry calcite, bioclasts (up to at least 2 cm), and subangular to subrounded quartz grains (<0.4 mm) are the three dominant components of the limestones. The presence of a significant proportion of quartz grains in the calcareous sandstone clasts (<0.4 mm) was verified by HCl dissolution tests. Reddish-brown fines are present at this site.
Munsell Colours:	Rocks ~N7 (*light gray*) to 10YR 6/6 (*dark yellowish orange*) and 10YR 5/4 (*moderate yellowish brown*). Fines reddish-brown.
Samples:	One 8 cm calcareous sandstone sample: reaction with HCl vigorous for both exposed and fresh surfaces; one small bag containing smaller clasts (including biosparites): <4 cm; reaction with HCl vigorous for both exposed and fresh surfaces.
Thin Section:	None.
Weathering State:	Most exposed limestone and calcareous sandstone surfaces weathered orange / brown; fresh surfaces yellowish-gray.
Vegetation:	Cover Rank: 1. Significant Cover: *Saxifraga oppositifolia* (scattered, ~12 cm mounds). Other Cover: *Papaver radicatum, Vulpicida tilesii, Thamnolia subuliformis, Lecidea spp.* (on fines, not rocks), black algae. Notes: Analysis of digitized closeup photo (saxifrage value: hand-digitized results; others: classification results): 6% saxifrage; 0.06% yellow lichen, 2% white lichen (mainly antler lichen; is an overestimation, since some white rock surfaces counted); dark shadows or dark lichen: 9% (mostly shadow).

Site 17

Photographs:	One landscape photo; one closeup photo.
Video:	Tape #1, 1:22::25 - 1:23:44.
Formation/Unit:	Great Bear Cape Formation.
Dominant Lithology:	Limestone and calcareous sandstone.
General Information:	Site consists of limestones and calcareous sandstones (typically <7 cm). Sparry calcite, bioclasts (up to at least 2 cm), and subangular to subrounded quartz grains (<0.25 mm) are the three dominant components of the limestones. The presence of a significant proportion of quartz grains in the calcareous sandstone clasts (typically subangular to subrounded; <0.25 mm) was verified by HCl dissolution tests.
Munsell Colours:	Rocks ~10YR 7/4 (*grayish orange*) to yellowish brown. Fresh rock surfaces N7 to N8 (*light gray* to *very light gray*).
Samples:	One 7.5 cm dismicrite sample; one small bag full of small clasts (< 4.5 cm; includes dismicrites; reaction with HCl vigorous for both exposed and fresh surfaces); vegetation was sampled.
Thin Section:	None.
Weathering State:	Most exposed limestone surfaces are weathered orange-brown, while fresh limestone surfaces are gray.
Vegetation:	Cover Rank: 1. Significant Varieties: *Saxifraga oppositifolia* (sparsely scattered, ~10 cm mounds). Other Varieties Noted: *Thamnolia subuliformis, Lecidea spp.* (on fines, not rocks), *Vulpicida tilesii*, black algae.

Sites 18A and 18B

Photographs:	One landscape photo for A/B; one closeup photo for each of A and B.
Video:	Tape #1, 1:23:44 - 1:25:24.
Formation/Unit:	Great Bear Cape Formation
Dominant Lithology:	Limestone.
General Information:	Site consists of limestones (typically <7 cm) in which sparry calcite is typically a major constituent (biosparites are most notable in the rocks sampled); rounded glauconite grains are very sparsely distributed in some clasts. Sites 18A and 18B are differentiated mainly based on their vegetation characteristics: 18B has a greater vegetation cover compared to 18A.
Munsell Colours:	Rocks N6 to N8 (*medium light gray* to *very light gray*), to 5Y 8/1 (*yellowish gray*), to 10YR 7/4 (*grayish orange*) to 10YR 6/6 (*dark yellowish orange*) to 10YR 5/4 (*moderate yellowish brown*).
Samples:	One small bag containing mainly biosparite clasts (<5 cm; reaction with HCl vigorous for both exposed and fresh surfaces), and a small amount of grey fines. Vegetation was sampled at 18A.
Thin Section:	None.
Weathering State:	Most exposed limestone surfaces are either gray, or are weathered orange-brown. Fresh limestone surfaces are gray.
Vegetation:	Cover Ranks: 2 (Site 18A) to 3 (Site 18B). Significant Varieties: *Saxifraga oppositifolia* (scattered to densely scattered, 10-20 cm mounds). Other Varieties Noted: *Thamnolia subuliformis, Lecidea spp.* (on fines, not rocks), *Vulpicida tilesii*, black algae.

Site 19

Photographs:	One landscape photo; one closeup photo.
Video:	Tape #1, 1:25:24 - 1:26:50.
Formation/Unit:	Great Bear Cape Formation.
Dominant Lithology:	Limestone.
General Information:	Site consists of limestones (typically <15 cm) in which sparry calcite is typically a major constituent (essentially all rock samples are biosparites); rounded glauconite grains are very sparsely distributed in some clasts.
Munsell Colours:	Rocks 5Y 8/1 (*yellowish gray*) to 10YR 8/2 (*very pale orange*) to 10YR 6/6 (*dark yellowish orange*) to N8 (*very light gray*).
Samples:	Numerous biosparite rocks, including 22.5 cm, 15 cm, 10 cm, and a cloth bag containing smaller biosparite clasts (<9 cm).
Thin Section:	Thin section *19-1*: Biosparite consisting predominantly of calcite bioclasts and pore-filling calcite cement. Subangular to subrounded quartz grains (typically <0.5 mm) are present.
Weathering State:	Most exposed limestone surfaces are either gray, or are weathered orange-brown. Fresh limestone surfaces are gray.
Vegetation:	Cover Rank: 3. Significant Varieties: *Saxifraga oppositifolia* (densely-scattered, ~10-50 cm mounds). Other Varieties Noted: *Thamnolia subuliformis, Lecidea spp.* (on fines, not rocks), *Vulpicida tilesii*, black algae.

Site 20

Photographs:	One landscape photo; one closeup photo.
Video:	Tape #1, 1:26:50 - 1:29:37.
Formation/Unit:	Great Bear Cape Formation.
Dominant Lithology:	Limestone.
General Information:	Site consists of limestones (typically <25 cm) in which sparry calcite is typically a major constituent [essentially all rock samples are biosparites that are notably indurated relative to certain other limestones in the region (e.g., Site 16)].
Munsell Colours:	Rocks N8 (*light gray*) to 5YR 5/6 (*light brown*) to 5YR 4/4 (*moderate brown*) to 10YR 7/4 (*grayish orange*) to 10YR 5/4 (*moderate yellowish brown*). Some rock undersides are weathered to SG 8/1 (*light greenish gray*). Fresh surfaces are ~10YR 6/2 (*pale yellowish brown*).
Samples:	Numerous biosparite rocks, including 25 cm , 13 cm, and one cloth bag containing smaller biosparite clasts (< 6 cm). Reaction with HCl moderate to vigorous for both exposed and fresh surfaces. Vegetation was sampled.
Thin Section:	None.
Weathering State:	Most exposed limestone surfaces are weathered orange-brown; the undersides of a minority of rocks are weathered to greenish gray. Fresh limestone surfaces are gray.
Vegetation:	Cover Rank: ~1. Significant Varieties: *Saxifraga oppositifolia* (sparsely scattered, ~6 cm mounds). Other Varieties Noted: *Thamnolia subuliformis, Lecidea spp.* (on fines, not rocks), *Vulpicida tilesii*, black algae.

Site 21

Photographs:	One landscape photo; one closeup photo.
Video:	Tape #1, 1:30:22 - 1:31:49.
Formation/Unit:	Great Bear Cape Formation.
Dominant Lithology:	Limestone and calcareous sandstone.
General Information:	Site consists of both biosparite and calcareous sandstone clasts (typically <3 cm). Rounded fine- to medium-grained quartz is the dominant constituent of the sandstone.
Munsell Colours:	Rocks 5Y 8/1 (*yellowish gray*) to 10YR 8/6 (*pale yellowish orange*) to 10YR 6/6 (*dark yellowish orange*) to 10YR 6/2 (*pale yellowish brown*). Some rock undersides are weathered to SG 8/1 (*light greenish gray*). Fines brown.
Samples:	One small bag containing grey-brown biosparite and calcareous sandstone clasts (all < 3.5 cm; reaction with HCl vigorous for both exposed and fresh surfaces), and brown fines. Vegetation was sampled.
Thin Section:	None.
Weathering State:	Most exposed limestone surfaces are weathered orange, and are characterized by ~1mm pedestal-like features that impart a highly variable surface relief. The undersides of a minority of rocks are weathered to greenish gray. Fresh rock surfaces are gray-brown.
Vegetation:	Cover Rank: 2. Significant Varieties: *Saxifraga oppositifolia* (scattered, ~15 cm mounds). Other Varieties Noted: *Thamnolia subuliformis, Lecidea spp.* (on fines, not rocks), *Vulpicida tilesii*, black algae.

Site 22

Photographs:	One landscape photo; one closeup photo.
Video:	Tape #1, 1:35:30 - 1:36:49.
Formation/Unit:	Canyon Fiord Formation.
Dominant Lithology:	Calcareous sandstone and limestone.
General Information:	Site consists of red-weathering calcareous sandstone and limestone clasts (typically <5 cm), in red-weathering unconsolidated fines. Rounded fine- to medium-grained quartz, and rounded lithic clasts, are significant constituents of both rock types.
Munsell Colours:	Rocks 5YR 5/6 (*light brown*) to light reddish brown to moderate gray brown. Fresh surfaces N8 (*very light gray*) to 10YR 6/2 (*pale yellowish brown*). Fines reddish brown.
Samples:	Calcareous sandstone and impure limestone clasts (<10 cm; reaction with HCl vigorous for exposed and fresh surfaces), including one small bag containing clasts smaller than 6.5 cm, and also containing red sandy and silty fines (reaction with HCl vigorous). Vegetation was sampled.
Thin Section:	None.
Weathering State:	Most exposed rock surfaces are weathered red, while fresh surfaces are gray to brown.
Vegetation:	Cover Rank: 2. Significant Varieties: *Saxifraga oppositifolia* (sparsely scattered, 10 cm mounds), *Salix arctica* (scattered, 10-30 cm mounds). Other Varieties Noted: *Thamnolia subuliformis, Lecidea spp.* (on fines, not rocks), *Vulpicida tilesii*, black algae.

Site 23

Photographs:	One landscape photo; one closeup photo.
Video:	Tape #1, 1:37:51 - 1:40:23.
Formation/Unit:	Great Bear Cape Formation
Dominant Lithology:	Limestone.
General Information:	Site consists of limestones (typically <12 cm) in which bioclasts, sparry calcite, and fine-to medium-grained quartz are important constituents (most rocks are impure biosparites). Red-weathering fines are present. Arcuate and circular zones (typically <50 cm across), containing somewhat smaller clasts and a greater proportion of fines, appear to have been produced by frost action.
Munsell Colours:	Rocks N8 (*very light gray*) to 10YR 6/6 (*dark orangish gray*) to medium orangish gray. Fresh rock surfaces 10YR 6/2 (*pale yellowish brown*) to orangish gray. Fines medium orangish gray.
Samples:	Impure biosparite samples (<11 cm; reaction with HCl vigorous for both exposed and fresh surfaces); one small bag containing clasts (<4 cm; reaction with HCl vigorous for both exposed and fresh surfaces), as well as brown fines (reaction with HCl vigorous). Vegetation was sampled.
Thin Section:	None.
Weathering State:	Most exposed limestone surfaces are weathered orange. Fresh rock surfaces are gray-brown. The undersides of a minority of rocks are weathered to greenish gray.
Vegetation:	Cover Rank: ~2. Significant Varieties: *Saxifraga oppositifolia* (scattered, ~10-20 cm mounds). Other Varieties Noted: *Papaver radicatum, Thamnolia subuliformis, Vulpicida tilesii*, unidentified mosses.

Site 24

Photographs:	One landscape photo; one closeup photo.
Video:	Tape #1, 1:41:51 - 1:45:28.
Formation/Unit:	Great Bear Cape Formation.
Dominant Lithology:	Limestone.
General Information:	Site consists of limestones (typically <6 cm) in which sparry calcite is typically a major constituent (essentially all rock samples are impure biosparites). Red/brown-weathering fines are present.
Munsell Colours:	Rocks N8 (*very light gray*) to 5Y 8/1 (*yellowish gray*) to 10YR 6/2 (*pale yellowish brown*) to 10YR 7/4 (*grayish orange*). Fines medium grayish brown.
Samples:	Three impure biosparite samples: 8.5 cm, 8 cm, 5.5 cm (reaction with HCl vigorous for both exposed and fresh surfaces); one small bag containing limestone clasts (< 4.5 cm; reaction with HCl vigorous for both exposed and fresh surfaces) and fines (reaction with HCl vigorous). Vegetation was sampled.
Thin Section:	None.
Weathering State:	Most exposed limestone surfaces are weathered orange. Fresh rock surfaces are gray-brown. The undersides of a minority of rocks are weathered to greenish gray.
Vegetation:	Cover Rank: 3. Significant Varieties: *Saxifraga oppositifolia* (arcs, and densely-scattered, ~10-50 cm mounds). Other Varieties Noted: *Thamnolia subuliformis, Lecidea spp., Vulpicida tilesii*, black algae.

Site 25

Photographs:	One landscape photo; one closeup photo.
Video:	Tape #1, 1:49:05 - 1:50:43.
Formation/Unit:	Degerbōls Formation.
Dominant Lithology:	Limestone.
General Information:	Site consists predominantly of limestone (typically <20 cm, but rocks up to ~60 cm are present rarely) in which sparry calcite is typically a major constituent. A smaller proportion of rocks are fine-grained calcareous sandstones (the presence of a significant proportion of quartz grains in these rocks was verified by HCl dissolution tests). Yellow-gray fines are present but minor.
Munsell Colours:	Rocks 5Y 8/1 (*yellowish gray*) to 5GY 8/1 (*light greenish gray*) to 10YR 5/4 (*moderate yellowish brown*) to medium brownish gray. Fresh rock surfaces are ~N7 (*light gray*) and brownish gray. Fines yellow-gray.
Samples:	Biosparites, dismicrites, and minor calcareous sandstones (all <7.5 cm; reaction with HCl vigorous for both exposed and fresh surfaces of limestone; calcareous sandstones: reaction with HCl absent to moderate for exposed surfaces, and subdued for fresh surfaces). Vegetation was sampled.
Thin Section:	None.
Weathering State:	Most exposed rock surfaces are weathered brown. Fresh rock surfaces are gray-brown. The undersides of a minority of rocks are weathered greenish gray.
Vegetation:	Cover Rank: 2. Significant Varieties: *Saxifraga oppositifolia* (arcs, and scattered, ~20 cm mounds). Other Varieties Noted: *Vulpicida tilesii*, black algae.

Site 26

Photographs:	Two landscape photos; one closeup photo.
Video:	Tape #2, 0:00:35 - 0:04:50.
Formation/Unit:	Canyon Fiord Formation [Note: mapped as Great Bear Cape Formation by Harrison (1995)].
Dominant Lithology:	Red-weathering fine-grained calcareous sandstone.
General Information:	Site consists of red-weathering fine-grained calcareous sandstone clasts (typically <15 cm, with a slight increase in size toward the nearby ridge). The presence of a significant proportion of quartz grains (typically <0.3 mm) in these rocks was verified by HCl dissolution tests. The lithological characteristics of this site, along with those of Site 28, are very similar to the characteristics of Canyon Fiord Formation materials, while they contrast with lithological characteristics seen at all Great Bear Cape Formation sites visited.
Munsell Colours:	Rocks ~5Y 7/2 (*yellowish gray*) to reddish brown: fresh rock surfaces are ~5Y 6/4 (*dusky yellow*) to 5Y 7/6 (*moderate yellow*). Fines ~5YR 4/4 (*moderate brown*).
Samples:	Seven fine-grained calcareous sandstone samples (<9 cm; reaction with HCl vigorous for both exposed and fresh surfaces); one small bag containing smaller clasts (<2.5 cm), and fines. Vegetation was sampled.
Thin Section:	None.
Weathering State:	Most exposed rock surfaces are weathered reddish brown. Fresh rock surfaces are yellowish.
Vegetation:	Cover Rank: 1. Significant Varieties: *Saxifraga oppositifolia* (sparsely scattered, 10 cm mounds). Other Varieties Noted: *Thamnolia subuliformis*.

Site 27

Photographs:	Two landscape photos; no closeup photo.
Video:	Tape #2, 0:04:50 - 0:07:34.
Formation/Unit:	Unnamed gabbro intrusion.
Dominant Lithology:	Gabbro.
General Information:	Site consists of gabbro, exposed as both bedrock and as individual rocks (typically 2 to 40 cm). Red-weathering fines are present, and are likely weathering products of the Canyon Fiord Formation.
Munsell Colours:	Rocks N3 (*dark gray*), 5YR 5/6 (*light brown*). Fines reddish brown.
Samples:	Gabbro clasts (<8 cm). Vegetation was sampled.
Thin Section:	None.
Weathering State:	Many of the upper exposed surfaces of gabbro are weathered slightly red, while the bottom surfaces of coated with the red (Fe-oxide?) material that has been noted at many other sites of varying lithologies.
Vegetation:	Cover Ranking: 0-L to 2. Significant Varieties: *Saxifraga oppositifolia, Lecidea spp.* Other Varieties Noted: *Papaver radicatum, Oxyria digyna., Thamnolia subuliformis,.* black algae, unidentified mosses. Notes: Black algae extends downslope from the gabbro ridge.

Site 28

Photographs:	One landscape photo; one closeup photo.
Video:	Tape #2, 0:07:34 - 0:09:04.
Formation/Unit:	Canyon Fiord Formation [Note: mapped as Great Bear Cape Formation by Harrison (1995)].
Dominant Lithology:	Red-weathering fine- to medium-grained calcareous sandstone.
General Information:	Site consists of red-weathering fine- to medium-grained calcareous sandstone (typically <5 cm). The presence of a significant proportion of quartz grains in these rocks was verified by HCl dissolution tests. Unconsolidated, heterolithic, rounded pebbles (typically <2 cm) are present. The lithological characteristics of this site, along with those of Site 28, are similar to the characteristics of Canyon Fiord Formation materials, while they contrast with lithological characteristics seen at all Great Bear Cape Formation sites visited.
Munsell Colours:	Rocks 10YR 8/2 (very pale orange) to 5Y 8/1 (yellowish gray), and 5YR 4/4 (moderate brown). Fines reddish brown.
Samples:	Six calcareous sandstone samples (<9 cm; reaction with HCl vigorous for both exposed and fresh surfaces); one small bag containing calcareous sandstone clasts (<3.5 cm), and red fines.
Thin Section:	None.
Weathering State:	Most exposed rock surfaces are weathered reddish brown. Fresh rock surfaces are yellowish gray.
Vegetation:	Cover Rank: 2. Significant Varieties: *Saxifraga oppositifolia* (scattered, 10 cm mounds). Other Varieties Noted: *Thamnolia subuliformis.*

Site 29

Photographs:	Two landscape photos; no closeup photo.
Video:	Tape #2, 0:09:04 - 0:10:49.
Formation/Unit:	Sabine Bay Formation.
Dominant Lithology:	Unconsolidated brown calcareous fines.
General Information:	Site consists predominantly of grey fines (fine- to medium-grained materials consisting predominantly of quartz). Also present are scattered rocks (mainly fossil fragments and biosparite; typically <3 cm), and unconsolidated pebble-sized heterolithic clasts. The absence of a significant proportion of quartz grains in the limestones was verified by HCl dissolution tests.
Munsell Colours:	Fines ~10YR 6/2 (*pale yellowish brown*). Rocks 5Y 8/1 (*yellowish gray*) to ~10YR 6/2 (*pale yellowish brown*).
Samples:	Six limestone samples (<9.5 cm; reaction with HCl vigorous for both exposed and fresh surfaces; there are rounded green grains present that may be glauconite); one small bag containing smaller clasts (<3 cm), including rounded heterolithic clasts; one small bag containing brown fines (reaction with HCl vigorous).
Thin Section:	None.
Weathering State:	Most exposed rock surfaces are weathered brown. Fresh rock surfaces are yellowish gray.
Vegetation:	Cover Rank: 3. Significant Varieties: *Saxifraga oppositifolia* (densely scattered, 15 cm mounds), *Lecidea spp.* Other Varieties Noted: None.

Site 30

Photographs:	One landscape photo; one closeup photo.
Video:	Tape #2, 0:10:49 - 0:13:15.
Formation/Unit:	Great Bear Cape Formation.
Dominant Lithology:	Limestone and calcareous sandstone.
General Information:	Site consists of both impure biosparite and fine-grained calcareous sandstone clasts (typically <6 cm). Bioclasts of at least 1 cm have been noted in the limestones. Subangular to rounded quartz grains are dominant in the sandstones; the presence of a significant proportion of quartz grains in the limestones was verified by HCl dissolution tests. Brown fines are present. Materials are sorted by size through frost action, into irregular arcuate patterns whose widths are typically <50 cm.
Munsell Colours:	Rocks N5 (*medium gray*), 10YR 6/6 (*dark yellowish orange*), 10YR 7/4 (*grayish orange*), and 10YR 6/2 (*pale yellowish brown*). Fines brown.
Samples:	Several impure biosparite and calcareous sandstone samples (<10 cm; reaction with HCl vigorous for exposed surfaces, and moderate for fresh surfaces); one small bag containing smaller clasts (<4 cm), and brown fines.
Thin Section:	None.
Weathering State:	Most exposed rock surfaces are weathered brown. Fresh rock surfaces are gray.
Vegetation:	Cover Rank: 1. Significant Varieties: *Saxifraga oppositifolia* (sparsely scattered, 15 cm mounds). Other Varieties Noted: *Papaver radicatum, Thamnolia subuliformis, Lecidea spp.* (on fines, not rocks), black algae.

Site 31

Photographs:	One landscape photos; one closeup photo.
Video:	Tape #2, 0:14:21 - 0:16:08.
Formation/Unit:	Canyon Fiord Formation.
Dominant Lithology:	Red-weathering and gray calcareous fines.
General Information:	Site consists of red-weathering and gray calcareous fines (quartz grains, typically <0.1 mm) that make up a hard crust. Red-weathering fine-grained calcareous sandstones make up a small proportion of the surface materials (typically <1 cm; up to ~10 cm).
Munsell Colours:	Fines N8 (*very light gray*) and ~5YR 7/2 (*grayish orange pink*). Rocks ~10R 5/4 (*pale reddish brown*) to 10R 3/4 (*dark reddish brown*); fresh surfaces medium reddish brown.
Samples:	One small bag containing fines (reaction with HCl vigorous) and small calcareous sandstone clasts; four rock samples (<9.5 cm) and small rock fragments (<3 cm) are loose in the cloth sample bag (reaction of rocks with HCl subdued to moderate for both exposed and fresh surfaces).
Thin Section:	None.
Weathering State:	Most exposed rock surfaces, and a significant proportion of the fines, are weathered red. Fresh rock surfaces are brown.
Vegetation:	Cover Rank: 0. Significant Varieties: None. Other Varieties Noted: grass (isolated mounds of <12 cm).

Site 32

Photographs:	One landscape photo; one closeup photo.
Video:	Tape #2, 0:16:08 - 0:21:28.
Formation/Unit:	Canyon Fiord Formation.
Dominant Lithology:	Unconsolidated heterolithic clasts, and red-weathering unconsolidated fines.
General Information:	Site consists of unconsolidated heterolithic clasts (<2.5 cm) and red-weathering fines. Small bedrock outcrops of red-weathering calcareous sandstone (grains mainly quartz: <0.5 mm) are present.
Munsell Colours:	Heterolithic clasts: variable. Fines reddish brown. Calcareous sandstone ~moderate orange brown to 10R 4/6 (*moderate reddish brown*); fresh rock surfaces N8 (*very light gray*) and reddish brown.
Samples:	One small bag of mainly pebble-sized clasts; three calcareous sandstone samples taken from bedrock exposures (<14.5 cm).
Thin Section:	None.
Weathering State:	Most exposed rock surfaces, and a significant proportion of the fines, are weathered red. Fresh rock surfaces are gray.
Vegetation:	Cover Rank: 0. Significant Varieties: None. Other Varieties Noted: *Saxifraga oppositifolia* (isolated mounds of ~10 cm).

Site 33

Photographs:	One landscape photo; one closeup photo.
Video:	Tape #2, 0:21:28 - 0:23:18.
Formation/Unit:	Canyon Fiord Formation.
Dominant Lithology:	Calcareous, red-weathering, fine- to medium-grained sandstone, and red-weathering fines.
General Information:	Site consists of calcareous, red-weathering, sandstone clasts (typically <10 cm; mainly composed of quartz grains that are typically <0.6 mm). Also present are notable proportions of red-weathering fines, and heterolithic pebbles.
Munsell Colours:	Fines reddish brown. Rocks reddish brown; fresh surfaces ~N8 (*very light gray*).
Samples:	One small bag containing calcareous sandstone clasts (<4 cm; reaction with HCl subdued to vigorous for exposed surfaces, and vigorous for fresh surfaces) and red-weathering fines (reaction with HCl vigorous); one small bag containing larger rocks (<10 cm; reaction with HCl as that of smaller clasts).
Thin Section:	None.
Weathering State:	Fines are weathered reddish brown, and most exposed rock surfaces are weathered red. Fresh rock surfaces are gray.
Vegetation:	Cover Rank: 0. Significant Varieties: None. Other Varieties Noted: *Salix arctica, Saxifraga oppositifolia, Thamnolia subuliformis.*

Site 34

Photographs:	One landscape photo; one panoramic photo; one wide-angle photo.
Video:	Tape #2, 0:25:33 - 0:28:59, and Tape #2, 0:31:40 - 0:32:15.
Formation/Unit:	Sabine Bay Formation.
Dominant Lithology:	Uncemented, non-calcareous, gray sandstone.
General Information:	Site consists of a large bedrock outcrop (uncemented, non-calcareous, gray sandstone and conglomerate) and an associated apron of debris extending downslope to a nearby stream. The dominant sandstone constituent is fine- to coarse-grained quartz. Conglomerates are composed of rounded clasts (typically < 1.5 cm; most are chert) set in quartz sands.
Munsell Colours:	Rocks N8 (*very light gray*) to 5Y 8/1 (*yellowish gray*), 10YR 7/4 (*grayish orange*) to N4 (*medium dark gray*).
Samples:	One small bag full of medium-sized sandstone / conglomerate clasts (~7 cm), and a small amount of sandy fines; numerous medium-sized sandstone / conglomerate clasts (<11 cm). None of the sampled materials react with HCl.
Thin Section:	None.
Weathering State:	Some rock surfaces are weathered brownish or dark gray, but many surfaces are unweathered (gray).
Vegetation:	Cover Rank: 0. Significant Varieties: black algae (discontinuous cover). Other Varieties Noted: unidentified grasses (isolated mounds). Notes: Black algae is found in the more moist portions of the local debris apron, extending downslope toward the local stream.

Site 35

Photographs:	One landscape photo; one closeup photo.
Video:	Tape #2, 0:25:33 - 0:28:59; and Tape #2, 0:31:40 - 0:32:15.
Formation/Unit:	Sabine Bay Formation.
Dominant Lithology:	Uncemented, non-calcareous, gray sandstone.
General Information:	Site consists predominantly of uncemented non-calcareous sandstone and conglomerate (typically <6 cm; rocks with dimensions of up to 40 cm are sparsely scattered). Brownish gray sandy fines are present.
Munsell Colours:	Rocks N8 (*very light gray*) to 5Y 8/1 (*yellowish gray*), 10YR 7/4 (*grayish orange*) to N4 (*medium dark gray*).
Samples:	One small bag of sandy fines and small clasts; one small bag of clasts (<8 cm); one plastic bag of larger clasts (<9 cm). None of the sampled materials react with HCl.
Thin Section:	None.
Weathering State:	Some rock surfaces are weathered brownish or dark gray, but many surfaces are unweathered (gray).
Vegetation:	Cover Rank: 2. Significant Varieties: *Saxifraga oppositifolia*. Other Varieties Noted: *Papaver radicatum*. Notes: Black algae seen in moist environs at other sites does not adapt well to surfaces present at Site 35, perhaps because the Sabine Bay materials are better drained. There is a clear contrast between the algal coverage of the Great Bear Cape Formation limestones versus the algae-free surfaces of the Sabine Bay Formation non-calcareous clastics (see, e.g., Tape #2, 0:41:00).

Site 36

Photographs:	One landscape photo; one closeup photo.
Video:	Tape #2, 0:41:47 - 0:44:32.
Formation/Unit:	n/a
Dominant Lithology:	Mix of Degerböls limestone, Trold Fiord clastics, and minor Assistance mudstone.
General Information:	Site consists of a mix of Degerböls limestone, Trold Fiord clastics, and minor Assistance mudstone.
Munsell Colours:	Limestone: 5Y 7/2 (*yellowish gray*) to 10YR 6/6 (*dark yellowish orange*), N7 (*light gray*) (fresh surface). "Trold Fiord" rocks: 5Y4 8/1 (*yellowish gray*) to 5Y 7/2 (*yellowish gray*), N5 (*medium gray*) (for both exposed and fresh surfaces). Mudstone: 10YR 5/4 (*moderate yellow brown*) to 10YR 6/6 (*dark yellowish orange*) to 10YR 7/4 (*grayish orange*). Fines 5Y 7/2 (*yellowish gray*).
Samples:	Several baggies containing a variety of lithologies [clasts <8 cm; reaction to HCl vigorous (limestones) to absent (Trold Fiord and mudstone rocks); one small bag containing mainly fines (reaction to HCl subdued to moderate)]. Vegetation was sampled.
Thin Section:	None.
Weathering State:	Limestones typically weathered orange from gray; Trold Fiord rocks typically unweathered (gray) or weathered yellowish gray; Assistance mudstones typically weathered orange-brown.
Vegetation:	Cover Rank 2-3. Significant Varieties: *Saxifraga oppositifolia*. Other Varieties Noted: *Oxyria digyna, Papaver radicatum, Thamnolia subuliformis*, unidentified mosses, black algae.

Site 37

Photographs:	Three landscape photos; one closeup photo.
Video:	Tape #2, 0:44:38 - 0:47:38.
Formation/Unit:	Assistance Formation.
Dominant Lithology:	Red-weathering mudstone and associated fines.
General Information:	Site consists of red-weathering fossiliferous mudstone clasts (typically <2 cm), and associated red-weathering fines. There is a gray calcareous material between the two red topographic highs that make up this site.
Munsell Colours:	Rocks 5R 4/2 (*grayish red*) to orangish olive to ~10YR 5/4 (*moderate yellowish brown*). Fines reddish brown.
Samples:	One small bag containing fines and small mudstone clasts (<3 cm); three larger clasts (<11.5 cm). None of the site materials react with HCl. Vegetation was sampled.
Thin Section:	None. Refer to thin section *AS-1*: Subangular mono and polycrystalline quartz grains (~0.1 mm) set in red-stained (Fe-oxide) fines or cement (grains ~0.01 mm).
Weathering State:	Exposed and fresh mudrock surfaces are weathered red.
Vegetation:	Cover Rank: 0. Significant Varieties: None. Other Varieties Noted: *Papaver radicatum*, *Thamnolia subuliformis*, *Lecidea spp.* (on fines, not rocks), unidentified mosses.
Topography:	

Site 38

Photographs:	None.
Video:	None (refer to video of nearby Site 37).
Formation/Unit:	n/a.
Dominant Lithology:	Trold Fiord sandstone.
General Information:	Site located just upslope from the lower mound of Site 37. Site consists of variably-sized materials with characteristics similar to those of materials of the Trold Fiord Formation: 1) elongate silicic grains, 2) unique trace fossils, and 3) similar or identical lichen cover. Some samples are lithologically identical to known Trold Fiord samples taken from sites to the north.
Munsell Colours:	Rocks 10YR 8/6 (*pale yellowish orange*), 10YR 6/2 (*pale yellowish brown*), and 5Y 7/2 (*yellowish gray*). Fines 5Y 7/2 (*yellowish gray*).
Samples:	Small bag containing smaller clasts (<5 cm) and fines; four rock samples (<11 cm). None of the site materials react with HCl. Vegetation was sampled.
Thin Section:	None.
Weathering State:	Exposed rock surfaces are weathered to yellowish gray.
Vegetation:	Cover Rank: 0. Significant Varieties: None. Other Varieties Noted: *Lecidea spp.*

Site 39

Photographs:	Numerous landscape photographs.
Video:	Tape #2, 0:49:39 - 0:52:33.
Formation/Unit:	Canyon Fiord Formation.
Dominant Lithology:	Red-weathering calcareous sandstone and conglomerate, and associated fines and heterolithic pebbles.
General Information:	Site consists of red-weathering calcareous sandstone and conglomerate (typically <2 cm, but up to 50 cm), and associated sandy fines / heterolithic pebbles. The predominant constituents of the sandstones are quartz grains (typically <1 mm).
Munsell Colours:	Rocks moderate orangish red, N8 (*very light gray*). Fines moderate orangish red.
Samples:	Small bag containing heterolithic clasts (<4.5 cm) and red sandy fines; sandstone and conglomerate clasts (<13 cm), two of which were sampled from large boulders exposed along a nearby stream. All site materials react with HCl vigorously. Vegetation was sampled.
Thin Section:	Thin section *39-1*: Subangular to subrounded quartz crystals, and rounded to subrounded polycrystalline quartz and lithic grains, with pore space filled with calcite cement. Quartz grains typically 0.2-0.6 mm; polycrystalline quartz and lithic grains typically 0.2-0.9 mm.
Weathering State:	Exposed sandstone and conglomerate surfaces are weathered red. Fresh rock surfaces gray.
Vegetation:	Cover Rank: 1. Significant Varieties: *Saxifraga oppositifolia* (scattered, 10 cm mounds), *Salix arctica*. Other Varieties Noted: *Papaver radicatum*.

Site 40

Photographs:	One landscape photo; one closeup photo.
Video:	Tape #2, 0:54:20 - 0:58:40; brief footage at 0:59:38 and at 1:09:46.
Formation/Unit:	Assistance Formation.
Dominant Lithology:	Red-weathering mudstone, and associated fines.
General Information:	Site consists of red-weathering mudstone (typically <2.5 cm; rarely larger than 5 cm), and associated red-weathering fines.
Munsell Colours:	Rocks 5R 4/2 (*grayish red*) to orangish olive to ~10YR 5/4 (*moderate yellowish brown*). Fines reddish brown.
Samples:	Small bag containing mudstone clasts (<5 cm) and fines; numerous larger mudstone clasts (<11 cm). None of the site materials react with HCl.
Thin Section:	None. Refer to thin section *AS-1*: Subangular mono and polycrystalline quartz grains (~0.1 mm) set in red-stained (Fe-oxide) fines or cement (grains ~0.01 mm).
Weathering State:	Exposed and fresh mudrock surfaces are weathered red.
Vegetation:	Cover Rank: 0. Significant Varieties: None. Other Varieties Noted: *Thamnolia subuliformis, Lecidea spp.*

Site 41

Photographs:	One landscape photo; one closeup photo.
Video:	Tape #2, 0:59:15 - 1:01:51.
Formation/Unit:	Sabine Bay Formation.
Dominant Lithology:	Heterolithic clasts, and unconsolidated sandy fines.
General Information:	Site consists of a mix of lithologies (clasts typically <1.5 cm, but occur up to 5 cm), and unconsolidated yellowish-gray sandy quartz fines (grains typically <1 mm). Lithologies include 1) rounded heterolithic pebbles, 2) Assistance Formation mudstones, and 3) others, including calcareous quartz sandstone (possibly Sabine Bay Formation sandstones), biosparite, and glauconitic sandstone (possibly Trold Fiord materials). There are sparsely-distributed bedrock outcrops (typically ~3 m across) of fine- to medium-grained sandstone.
Munsell Colours:	Fines 5Y 7/2 (*yellowish gray*). Rocks variable, including 5Y 7/2 (*yellowish gray*), N8 (*very light gray*), ~10YR 4/2 (*dark yellowish brown*), and 10R 5/4 (*pale reddish brown*).
Samples:	Small bag containing smaller heterolithic clasts (<3 cm) and brown fines (reaction of fines with HCl subdued); seven rock samples (<9 cm; reaction with HCl absent to vigorous, depending on lithology).
Thin Section:	None.
Weathering State:	Exposed rock surfaces variably weathered.
Vegetation:	Cover Rank: 0. Significant Varieties: None. Other Varieties Noted: None.

Site 42

Photographs:	One landscape photo only.
Video:	Tape #2, 1:01:51 - 1:07:58.
Formation/Unit:	Sabine Bay Formation.
Dominant Lithology:	Heterolithic clasts, quartz sandstone, and unconsolidated sandy fines.
General Information:	Site consists of heterolithic clasts, and unconsolidated fines (mainly quartz grains; typically <0.5 mm). Also present are larger clasts (typically 5 to 15 cm) of fine- to medium-grained quartz sandstone (non-calcareous and uncemented; quartz grains dominant, and chert grains present). Large localized boulders and bedrock outcrops are present (typically 1 to 4 m across).
Munsell Colours:	Fines ~5Y 7/2 (*yellowish gray*). Rocks ~N8 (*very light gray*), N4 (*medium dark gray*), 10YR 6/6 (*dark yellowish orange*) to yellowish brown.
Samples:	Small bag containing smaller clasts (<2.5 cm) and gray sands; small bag containing reddish sands and sandstone clasts (<6 cm); several sandstone clasts loose in cloth bag (<7 cm). None of the site materials react with HCl.
Thin Section:	None.
Weathering State:	Exposed sandstone surfaces are weathered yellowish brown.
Vegetation:	Cover Rank: 0. Significant Varieties: None. Other Varieties Noted: None.

Site 43

Photographs:	One landscape photo; one closeup photo.
Video:	Tape #2, 1:07:58 - 1:10:19.
Formation/Unit:	Apparently materials of the Degerbōls Formation.
Dominant Lithology:	Limestone.
General Information:	Site consists of biosparite clasts (typically <3 cm; rarely >6 cm), as well as loose bioclasts (brachiopod and bryozoan clasts are common, with sizes up to at least 4 cm). Gray fines are present as a minor component.
Munsell Colours:	Rocks and bioclasts 5Y 7/2 (*yellowish gray*) to 5Y 6//1 (*light olive gray*) to N8 (*very light gray*). Fines gray.
Samples:	Small bag containing gray limestone clasts (<4 cm) and gray fines. All materials react moderately to vigorously with HCl. Vegetation was sampled.
Thin Section:	None.
Weathering State:	Some exposed limestone surfaces are weathered yellowish or brownish gray.
Vegetation:	Cover Rank: 2. Significant Varieties: *Saxifraga oppositifolia* (scattered, 5-25 cm mounds). Other Varieties Noted: *Papaver radicatum*, *Oxyria digyna*, *Thamnolia subuliformis*, black algae.

Site 44

Photographs:	One landscape photo; one closeup photo.
Video:	Tape #2, 1:10:19 - 1:13:40.
Formation/Unit:	Degerbōls Formation.
Dominant Lithology:	Limestone and calcareous sandstone.
General Information:	Site consists of both biosparite (impure, and containing bioclasts with dimensions >5 cm) and calcareous sandstone (quartz grains dominate; grains typically <0.3 mm). Gray fines are present.
Munsell Colours:	Rocks 5Y 7/2 (yellowish gray) to ~10YR 7/4 (grayish orange), and N8 (very light gray) to N7 (light gray) (fresh surfaces). Fines gray.
Samples:	Small bag containing gray biosparite clasts (<7 cm) and gray fines; cloth bag containing numerous clasts (<7.5 cm; several samples are notably coated by crustose lichens); plastic bag containing numerous larger clasts (<20 cm). Reaction with HCl subdued to moderate for exposed biosparite surfaces, and moderate to vigorous for fresh surfaces. Reaction with HCl absent to moderate for exposed sandstone surfaces, and subdued for fresh surfaces. Vegetation was sampled.
Thin Section:	Thin section *44-1*: Impure biosparite consisting mainly of bioclasts (many <1 cm, but larger clasts are present). Subangular to subrounded monocrystalline quartz grains (typically ~0.1 mm) are present. Thin section *44-2*: Mainly subangular to subrounded mono and polycrystalline quartz grains, and minor lithic clasts (all typically <0.1 mm). Voids filled by calcite cement, which has weathered orange.
Weathering State:	A proportion of exposed limestone surfaces are weathered yellowish or brownish gray.
Vegetation:	Cover Rank: 2. Significant Varieties: *Saxifraga oppositifolia* (scattered, 10-20 cm mounds), *Lecidea lapicida*. Other Varieties Noted: *Thamnolia subuliformis*.

Site 45

Photographs:	One landscape photo; one closeup photo.
Video:	Tape #2, 1:13:40 - 1:15:36.
Formation/Unit:	Degerbōls Formation.
Dominant Lithology:	Limestone (predominantly loose bioclasts).
General Information:	Site consists predominantly of loose bioclasts (typically <3 cm; mostly brachiopods and bryozoans). Biosparite clasts are present but minor. Brownish gray fines are present.
Munsell Colours:	Biosparite/bioclasts 5Y 7/2 (*yellowish gray*), ~5YR 8/1 (*pinkish gray*), ~N6 (*medium light gray*). Fines 5Y 7/2 (*yellowish gray*).
Samples:	One small bag containing gray bioclasts and fines; three limestone samples (<9 cm). All materials at this site react moderately to vigorously with HCl. Vegetation was sampled.
Thin Section:	None.
Weathering State:	A proportion of clast surfaces are weathered yellowish or brownish gray.
Vegetation:	Cover Rank: 2. Significant Varieties: *Saxifraga oppositifolia* (scattered, 10 cm mounds). Other Varieties Noted: *Thamnolia subuliformis*.

Site 46

Photographs:	No photos, because of fog.
Video:	Tape #2, 1:15:36 - 1: 18:08.
Formation/Unit:	Degerbōls Formation.
Dominant Lithology:	Limestone (predominantly loose bioclasts).
General Information:	Site consists predominantly of loose bioclasts (typically <4 cm; mostly brachiopods and bryozoans); biosparite clasts are present but minor. Brownish gray fines are present.
Munsell Colours:	Bioclasts/biosparite 5Y 7/2 (*yellowish gray*) to 10YR 7/4 (*grayish orange*). Fines 5Y 7/2 (*yellowish gray*).
Samples:	Small bag containing bioclasts and limestone clasts (all <4 cm). All site materials react vigorously to HCl. Vegetation was sampled.
Thin Section:	None.
Weathering State:	A proportion of clast surfaces are weathered yellowish or brownish gray.
Vegetation:	Cover Rank: 2. Significant Varieties: *Saxifraga oppositifolia*. Other Varieties Noted: *Papaver radicatum*, *Thamnolia subuliformis*, black algae.

Site 47

Photographs:	One landscape photo; one closeup photo.
Video:	Tape #2, 1:18:08 - 1:19:00
Formation/Unit:	Degerböls Formation.
Dominant Lithology:	Limestone.
General Information:	Site consists of biosparite and loose bioclasts (clasts typically <5 cm). Brownish gray fines are present.
Munsell Colours:	Rocks 5Y 7/2 (*yellowish gray*), 10YR 7/4 (*grayish orange*), 10YR 6//6 (*dark yellowish orange*), N8 (*very light gray*) to N7 (*light gray*).
Samples:	One small bag containing bioclasts and rock fragments (all <2.5 cm); several biosparite samples (<8.5 cm). All materials react vigorously to HCl.
Thin Section:	None.
Weathering State:	A proportion of clast surfaces are weathered yellowish or brownish gray; fresh surfaces are gray.
Vegetation:	Cover Rank: 2. Significant Varieties: *Saxifraga oppositifolia*. Other Varieties Noted: *Papaver radicatum, Thamnolia subuliformis*, black algae.

Site 48

Photographs:	One landscape photo only.
Video:	Tape #2, 1:19:00 - 1:20:03.
Formation/Unit:	Assistance Formation.
Dominant Lithology:	Red-weathering mudstone, and associated fines.
General Information:	Site consists of red-weathering mudstone clasts (typically <4 cm, but as large as ~11 cm), and associated fines. A small proportion of clasts are yellowish gray biosparite.
Munsell Colours:	Mudstone ~10YR 6/6 (*dark yellowish orange*) to 10YR 5/4 (*moderate yellowish brown*) to reddish orange.
Samples:	One small bag containing reddish-brown mudstone (<4.5 cm; reaction to HCl absent) and reddish-brown fines. A very small proportion of sampled clasts are yellowish gray biosparite. Vegetation was sampled.
Thin Section:	None. Refer to thin section *AS-1*: Subangular mono and polycrystalline quartz grains set in red-stained (Fe-oxide) fines or cement (grains ~0.01 mm).
Weathering State:	Exposed and fresh mudrock surfaces are weathered red.
Vegetation:	Cover Rank: 0. Significant Varieties: None. Other Varieties Noted: *Papaver radicatum, Thamnolia subuliformis, Lecidea spp.*

Site 49

Photographs:	One landscape photo only.
Video:	Tape #2, 1:20:03 - 1:21:16.
Formation/Unit:	Sabine Bay Formation.
Dominant Lithology:	Gray, non-calcareous, quartz sandstone, and associated fines.
General Information:	Site consists of gray, non-calcareous sandstone (rocks typically <10 cm); predominantly composed of quartz grains, typically <0.5 mm), and associated fines (quartz, typically <0.5 mm).
Munsell Colours:	Rocks ~5Y 7/2 (*yellowish gray*) to 10YR 7/4 (*grayish orange*) to 10YR 6/6 (*dark yellowish orange*). Fresh surfaces ~N8 (*very light gray*).
Samples:	One small bag containing gray sandstone clasts (<7 cm) and gray fines; four other sandstone clasts were sampled (<8 cm). No site materials react to HCl.
Thin Section:	None.
Weathering State:	A proportion of clast surfaces are weathered yellowish or orangish gray; fresh surfaces are gray. Chemistry of the material typical of weathered surfaces has not yet been identified.
Vegetation:	Cover Rank: 0. Significant Varieties: None. Other Varieties Noted: *Saxifraga oppositifolia*, *Papaver radicatum*, *Thamnolia subuliformis*, black algae.

Site 50

Photographs:	One landscape photo; one closeup photo.
Video:	Tape #2, 1:39:23 - 1:42:26.
Formation/Unit:	Mix of materials, including Great Bear Cape Formation rocks.
Dominant Lithology:	Brown fines, limestone, and red-weathering calcareous sandstone.
General Information:	Site consists of brown, fine-grained sands, gray biosparite clasts, and red-weathering calcareous sandstone. The red-weathering sandstone may be related to Assistance Formation materials, such as those found at, e.g., Site 54. Clasts at this site are typically <5 cm, and only rarely >7 cm.
Munsell Colours:	Fines ~10YR 5/4 (*moderate yellowish brown*). Biosparite ~10YR 6/2 (*pale yellowish brown*) to ~10YR 5/4 (*moderate yellowish brown*) to ~N7 (*light gray*); fresh surfaces 5GY 8/1 (*light greenish gray*) to N8 (*very light gray*). Calcareous sandstone reddish brown to 10YR 6/2 (*pale yellowish brown*).
Samples:	One small bag containing brown fines (reaction to HCl absent to subdued), and crustose lichens. Numerous biosparite and calcareous sandstone clasts (<7.5 cm; reaction to HCl vigorous for biosparite, and absent to subdued for sandstone), some of which are covered with white/black crustose lichens. Vegetation was sampled.
Thin Section:	None.
Weathering State:	Biosparite surfaces typically weathered yellowish or orangish gray; fresh surfaces gray. Exposed and fresh sandstone surfaces typically reddish brown.
Vegetation:	Cover Rank: 3. Significant Varieties: *Saxifraga oppositifolia* (densely scattered, ~10 - 40 cm mounds). Other Varieties Noted: *Papaver radicatum*, *Oxyria digyna*, unidentified grasses, *Thamnolia subuliformis*, *Lecidea spp.* on fines, not rocks), black algae Notes: Analysis of digitized closeup photo: *Saxifraga oppositifolia*: 22%, Papaver radicatum: 0.5%, Oxyria digyna 0.5%.

Site 51

Photographs:	One landscape photo; one closeup photo.
Video:	Tape #2, 1:42:26 - 1:44:12.
Formation/Unit:	Great Bear Cape Formation.
Dominant Lithology:	Brown fines and limestone.
General Information:	Site consists of brown sandy fines (quartz grains typically <0.5 mm) covered by black algae. Biosparite clasts are present but minor.
Munsell Colours:	Fines brownish gray. Biosparite ~10YR 7/4 (*grayish orange*) to ~10YR 5/4 (*moderate yellowish brown*) to N8 (*very light gray*); fresh surfaces N8 (*very light gray*) to ~10YR 6/2 (*pale yellowish brown*).
Samples:	One small bag containing brownish gray sandy fines (quartz grains <0.5 mm). Biosparite clasts (<8 cm; reaction with HCl vigorous). Vegetation was sampled.
Thin Section:	None.
Weathering State:	Biosparite surfaces typically weathered yellowish or orangish gray; fresh surfaces gray.
Vegetation:	Cover Rank: 5. Significant Varieties: black algae. Other Varieties Noted: *Saxifraga oppositifolia*, *Papaver radicatum*, *Thamnolia subuliformis*. Notes: Site almost entirely covered by black algae.

Site 52

Photographs:	One landscape photo; one closeup photo.
Video:	Tape #2, 1:44:13 - 1:46:00.
Formation/Unit:	Sabine Bay Formation.
Dominant Lithology:	Brownish gray fines and scattered heterolithic pebble-sized clasts.
General Information:	Site dominated by brownish gray fines (quartz grains; typically <0.2 mm). Pebble-sized clasts of variable lithology are present (typically <3 cm; rarely >10 cm), including gray biosparite, gray sandstone, and red-weathering sandstone (quartz grains dominant; typically <0.5 mm; materials resemble Assistance Formation materials found at, e.g., Site 54). Rocks of the Sabine Bay Formation are not found at this site; the brown fines may be derived from this formation.
Munsell Colours:	Fines ~yellowish gray. Biosparite ~5Y 7/2 (*yellowish gray*) to ~pale yellowish brown. Red-weathering sandstone ~5YR 5/6 (*light brown*) to ~5YR 3/2 (*grayish brown*).
Samples:	One small bag containing gray fines (reaction with HCl subdued). Numerous rock samples (<7 cm; reaction with HCl vigorous for biosparite clasts, and absent to subdued for red-weathering sandstone).
Thin Section:	None.
Weathering State:	Biosparite surfaces typically weathered brown; fresh surfaces gray.
Vegetation:	Cover Rank: 2-3. Significant Varieties: *Saxifraga oppositifolia*. Other Varieties Noted: *Papaver radicatum*, *Oxyria digyna*, *Thamnolia subuliformis*.

Site 53

Photographs:	One landscape photo; one closeup photo.
Video:	Tape #2, 1:46:00 - 1:51:25.
Formation/Unit:	Sabine Bay Formation.
Dominant Lithology:	Brown sandy fines and heterolithic clasts.
General Information:	Site consists of brown sandy fines (quartz grains, typically <0.5 mm), and rounded heterolithic clasts (typically <4 cm; mainly gray chert, although red-weathering Assistance Formation mudstones are also present).
Munsell Colours:	Fines ~10YR 7/4 (*grayish orange*). Chert yellowish gray. Assistance Formation mudstones ~5YR 3/2 (*grayish brown*) to reddish brown.
Samples:	One small bag containing pebble-sized (<2 cm) chert clasts, and brown sandy fines; one small bag containing rounded to angular heterolithic clasts (<5 cm; some are Assistance Formation red-weathering mudstones), and brown sandy fines. None of the materials react with HCl.
Thin Section:	None.
Weathering State:	The chert clasts are not weathered. Assistance Formation mudstones are weathered reddish brown.
Vegetation:	Cover Rank: 0. Significant Varieties: None. Other Varieties Noted: None.

Site 54

Photographs:	One landscape photo only.
Video:	Tape #2, 1:51:25 - 1:58:32.
Formation/Unit:	Assistance Formation.
Dominant Lithology:	Red-weathering mudstone.
General Information:	Site consists predominantly of red-weathering mudstone clasts (typically <3 cm; few >5 cm); some of the mudstone samples resemble the red-weathering sandstones of, e.g., certain Sabine Bay Formation sites. Brown fines (fine quartz sands) are present. Also present are minor yellowish gray biosparite clasts.
Munsell Colours:	Mudstone reddish brown and yellowish gray. Fines 10YR 5/4 (*moderate yellowish brown*). Biosparite ~N6 (*medium light gray*) to ~yellowish gray.
Samples:	One small bag containing mudstone and biosparite clasts (<4 cm), and brown sandy quartz fines. Four mudstone / biosparite samples (<8 cm). Reaction with HCl absent for mudstone, absent to very subdued for fines, and vigorous for biosparite.
Thin Section:	None.
Weathering State:	Assistance Formation mudstones are weathered reddish brown. Biosparites weathered yellowish gray.
Vegetation:	Cover Rank: 0. Significant Varieties: None. Other Varieties Noted: *Saxifraga oppositifolia*, *Papaver radicatum*, *Oxyria digyna*, unidentified grasses, *Thamnolia subuliformis*, unidentified mosses.

Site 55

Photographs:	One landscape photo; one closeup photo.
Video:	Tape #3, 0:00:00 - 0:02:12.
Formation/Unit:	Sabine Bay Formation.
Dominant Lithology:	Yellowish gray sandy fines, and heterolithic clasts.
General Information:	Site consists mainly of yellowish gray fines (quartz grains, typically <0.5 mm), and pebble-sized heterolithic clasts that predominantly include red-weathering Assistance Formation mudstones, chert pebbles, and uncemented Sabine Bay Formation quartz sandstones (quartz grains typically <0.5 mm). Small bedrock outcrops (uncemented sandstone) are present.
Munsell Colours:	Fines ~5Y 7/2 (*yellowish gray*). Sandstone 5Y 8/1 (*yellowish gray*). Chert yellowish gray.
Samples:	One small bag containing a variety of lithologies (< 3.5 cm), and yellowish gray fines. One rock sample has the characteristics of Trold Fiord Formation materials. Small bedrock rocks were sampled (<5 cm). Except for the single Trold Fiord sample noted, the materials do not react with HCl.
Thin Section:	None.
Weathering State:	Sandstones generally weathered yellowish gray from gray. Assistance Formation mudstones weathered reddish brown.
Vegetation:	Cover Rank: 0. Significant Varieties: black algae. Other Varieties Noted: None.

Site 56

Photographs:	One landscape photo; one closeup photo.
Video:	Tape #3, 0:02:12 - 0:04:59.
Formation/Unit:	Sabine Bay Formation or Assistance Formation.
Dominant Lithology:	n/a
General Information:	No rocks are exposed at this site. Vegetation coverage is almost 100%.
Munsell Colours:	n/a
Samples:	None.
Thin Section:	n/a
Weathering State:	n/a
Vegetation:	Cover Rank: 5. Significant Varieties: *Saxifraga oppositifolia*, unidentified mosses. Other Varieties Noted: *Papaver radicatum*, unidentified grasses, *Thamnolia subuliformis*, *Lecidea spp.*

Site 57

Photographs:	One landscape photo only.
Video:	Tape #3, 0:04:59 - 0:15:38.
Formation/Unit:	Sabine Bay Formation.
Dominant Lithology:	Yellowish gray sandy fines, and heterolithic clasts.
General Information:	Site consists mainly of yellowish gray fines (quartz grains, typically <0.5 mm), and pebble-sized heterolithic clasts that predominantly include red-weathering Assistance Formation mudstones, chert pebbles, and uncemented Sabine Bay Formation quartz sandstones (quartz grains typically <0.5 mm). Large bedrock outcrops (10's of metres of exposed uncemented sandstone) are present.
Munsell Colours:	Fines yellowish gray. Uncemented sandstone yellowish gray. Chert 5Y 8/1 (*yellowish gray*). Cemented sandstone 10YR 6/6 (*dark yellowish orange*).
Samples:	One small bag containing heterolithic clasts (<4.5 cm) and brown sandy fines; three small gray bedrock samples (uncemented sandstone, <6.5 cm). A non-calcareous, orange, cemented sandstone was sampled. No site materials react with HCl.
Thin Section:	None.
Weathering State:	Sandstones generally weathered yellowish gray from gray. Assistance Formation mudstones weathered reddish brown.
Vegetation:	Cover Rank: 0. Significant Varieties: None. Other Varieties Noted: None.

Site 58

Photographs:	No photo.
Video:	Tape #3, 0:15:38 - 0:18:54.
Formation/Unit:	Sabine Bay Formation.
Dominant Lithology:	Non-calcareous sandstones, conglomerates, and brown sandy fines.
General Information:	Site consists of brown sandy fines, pebble-sized heterolithic clasts (typically <3 cm; including chert), and reddish brown cemented sandstone and conglomerate (typically <12 cm; although cemented, the sandstone is not difficult to break by hand). The sandstone is similar to other reddish sandstone clasts noted at other Sabine Bay Formation sites. A small sandstone outcrop is present. Patch-like variations in surface materials occur on scale of 5-10 m.
Munsell Colours:	Fines brown. Chert 5Y 8/1 (*yellowish gray*). Cemented sandstone 5YR 3/4 (*grayish brown*) to yellowish brown.
Samples:	One small bag containing heterolithic clasts (<2 cm) and brown sandstone clasts (<5 cm); one reddish-brown conglomerate sample: 6 cm; several brown sandstone samples (<9 cm). No site materials react with HCl.
Thin Section:	None.
Weathering State:	Sandstones generally weathered reddish brown or yellowish gray, from gray.
Vegetation:	Cover Rank: 0. Significant Varieties: None. Other Varieties Noted: None.

Site 59

Photographs:	One landscape photo only.
Video:	Tape #3, 0:18:54 - 0:21:34.
Formation/Unit:	Sabine Bay Formation.
Dominant Lithology:	Red-weathering non-calcareous sandstone, and brown fines.
General Information:	Site consists of red-weathering quartz sandstone, in brown sandy fines (quartz grains typically <0.5 mm). The sandstone clasts are locally present in one of two general size classes (<3 cm, and <15 cm); frost action has sorted site materials by size into polygon and stripe features. The weathered-out conglomerate materials seen at nearby Sabine Bay Formation sites are not present here.
Munsell Colours:	Fines ~10YR 6/6 (*dark yellow brown*). Sandstone 10YR 6/6 (*dark yellowish orange*) and ~light gray.
Samples:	One small bag containing small brown sandstone clasts (<3.5 cm), and brown sandy fines; five small sandstone samples (<6.5 cm). No site materials react with HCl.
Thin Section:	None.
Weathering State:	Sandstones generally weathered orange from gray.
Vegetation:	Cover Rank: 0. Significant Varieties: None. Other Varieties Noted: *Lecidea spp.*

Site 60

Photographs:	One landscape photo only.
Video:	Tape #3, 0:21:34 - 0:23:48.
Formation/Unit:	Sabine Bay Formation.
Dominant Lithology:	Non-calcareous fine-grained quartz sandstone, and yellowish gray sandy fines.
General Information:	Site consists of yellowish gray sandy fines (quartz grains, typically <0.3 mm), and two size classes of sandstone (<2 cm and ~5-15 cm). The site is divided into Sections A and B, with B being characterized a slightly greater cover of vegetation.
Munsell Colours:	Fines 5Y 7/2 (*yellowish gray*). Two sandstone endmembers: 5YR 3/2 (*grayish brown*) and 5Y 7/2 (*yellowish gray*).
Samples:	One small bag containing sandstone clasts (<3 cm) and yellowish gray sandy fines; five quartz sandstones (<8 cm). No site materials react with HCl.
Thin Section:	None.
Weathering State:	Sandstones generally weathered yellowish gray or grayish brown, from gray.
Vegetation:	Cover Rank: 1. Significant Varieties: None. Other Varieties Noted: *Saxifraga oppositifolia, Papaver radicatum, Oxyria digyna, Thamnolia subuliformis.*

Sites 61A and 61B

Photographs:	One landscape photo; one closeup for each of Sites 61A and 61B.
Video:	Tape #3, 0:32:07 - 0:37:35.
Formation/Unit:	Trold Fiord Formation.
Dominant Lithology:	Trold Fiord sandstone and brown fines.
General Information:	Site consists of Trold Fiord sandstone clasts (typically <15 cm and most <7 cm), and associated gray fines. 61B is characterized by a greater proportion of vegetation and fines coverage, compared to 61A.
Munsell Colours:	Fines yellowish brown. Trold Fiord sandstones weathered 5Y 7/2 (*yellowish gray*) and grayish orange; fresh surfaces N6 (*medium light gray*) to N8 (*very light gray*).
Samples:	One small bag containing small clasts (most <3 cm) and gray fines (reaction with HCl subdued; some fines materials were clearly derived from Trold Fiord sandstones); six Trold Fiord sandstone clasts (<10.5 cm; surfaces are notably covered by crustose lichen). Reaction of Trold Fiord sandstones to HCl very subdued.
Thin Section:	None.
Weathering State:	Trold Fiord sandstones generally weathered yellowish gray from gray.
Vegetation:	Cover Rank: 1. Significant Varieties: *Saxifraga oppositifolia, Lecidea spp.* Other Varieties Noted: *Papaver radicatum, Thamnolia subuliformis.*

Site 62

Photographs:	One landscape photo; one closeup photo.
Video:	Tape #3, 0:37:35 - 0:41:47.
Formation/Unit:	Trold Fiord Formation.
Dominant Lithology:	Trold Fiord sandstone and brown fines.
General Information:	Site consists of Trold Fiord sandstone clasts (typically <7 cm), and associated gray fines.
Munsell Colours:	Fines yellowish brown. Trold Fiord sandstones ~5Y 8/1 (*yellowish gray*) and orangish gray.
Samples:	One small bag containing clasts (<2.5 cm) and brown fines; six rock samples (<8 cm; surfaces are notably covered by crustose lichen). No site materials react with HCl.
Thin Section:	None.
Weathering State:	Trold Fiord sandstones generally weathered yellowish gray from gray.
Vegetation:	Cover Rank: 1. Significant Varieties: *Saxifraga oppositifolia.* Other Varieties Noted: *Papaver radicatum, Lecidea spp.*

Site 63

Photographs:	One landscape photo only.
Video:	Tape #3, 0:43:26 - 0:45:22.
Formation/Unit:	Trold Fiord Formation.
Dominant Lithology:	Trold Fiord sandstone and brown fines.
General Information:	Site consists of Trold Fiord sandstone clasts (typically <7 cm), as well as clasts that look similar to the common type of Trold Fiord sandstone, but lack the elongate grains (cylindrical voids in these materials have been noted, suggesting that the characteristic Trold Fiord elongate grains were once present). Also present are associated gray sandy fines.
Munsell Colours:	Fines ~5Y 5/2 (*light olive gray*). Rocks 5Y 7/2 (*yellowish gray*) to pale yellow to ~5Y 5/2 (*light olive gray*).
Samples:	One small bag containing brown fines; eight sandstone samples (<8 cm; some samples are clearly Trold Fiord sandstones, while others are Trold Fiord clasts that lack the elongate grains and have cylindrical voids). No site materials react with HCl. Vegetation was sampled.
Thin Section:	None.
Weathering State:	Trold Fiord sandstones and other variations generally weathered yellowish gray from gray.
Vegetation:	Cover Rank: 4. Significant Varieties: *Saxifraga oppositifolia*, unidentified mosses. Other Varieties Noted: *Papaver radicatum, Thamnolia subuliformis, Lecidea spp.*

Site 64

Photographs:	One landscape photo only.
Video:	Tape #3, 0:47:40 - 0:49:27.
Formation/Unit:	Trold Fiord Formation.
Dominant Lithology:	Trold Fiord sandstone and brown fines.
General Information:	Site consists of Trold Fiord sandstone clasts (typically <7 cm), as well as clasts that look similar to the common type of Trold Fiord sandstone, but lack the elongate grains (cylindrical voids in these materials have been noted, suggesting that the characteristic Trold Fiord elongate grains were once present). Some samples contain a significant proportion of rounded glauconite grains. Also present at the site are associated gray sandy fines (predominantly quartz).
Munsell Colours:	Fines between yellowish gray and olive gray. Rocks 5Y 7/2 (*yellowish gray*) to pale yellow to ~5Y 5/2 (*light olive gray*).
Samples:	One small bag containing clasts (<3 cm) and gray fines; seven rock samples (<9 cm; one rock contains a notable proportion of glauconite grains). No site materials react with HCl.
Thin Section:	None.
Weathering State:	Trold Fiord sandstones and other variations generally weathered yellowish gray from gray.
Vegetation:	Cover Rank: 3-4. Significant Varieties: *Saxifraga oppositifolia*, unidentified mosses. Other Varieties Noted: *Papaver radicatum, Thamnolia subuliformis, Lecidea spp.*

Site 65

Photographs:	One landscape photo only.
Video:	Tape #3, 0:46:10 - 0:47:40.
Formation/Unit:	Trold Fiord Formation.
Dominant Lithology:	Trold Fiord sandstone and brown fines.
General Information:	Site consists of Trold Fiord sandstone clasts (typically <7 cm), as well as clasts that look similar to the common type of Trold Fiord sandstone, but lack the elongate grains (cylindrical voids in these materials have been noted, suggesting that the characteristic Trold Fiord elongate grains were once present). Also present are associated gray sandy fines. This site is located between Sites 63 and 64.
Munsell Colours:	Fines between yellowish gray and olive gray. Rocks 5Y 7/2 (*yellowish gray*) to pale yellow to ~5Y 5/2 (*light olive gray*).
Samples:	One small bag containing Trold Fiord clasts (<5 cm) and gray fines; six Trold Fiord sandstone clasts (<10 cm). No site materials react with HCl. Vegetation was sampled.
Thin Section:	None.
Weathering State:	Trold Fiord sandstones and other variations generally weathered yellowish gray from gray. Chemistry of the material typical of weathered surfaces has not yet been identified.
Vegetation:	Cover Rank: 3-4. Significant Varieties: *Saxifraga oppositifolia*, *Lecidea spp.* Other Varieties Noted: None.

Site 66

Photographs:	One landscape photo; one closeup photo.
Video:	Tape #3, 0:50:29 - 0:55:33.
Formation/Unit:	Trold Fiord Formation.
Dominant Lithology:	Trold Fiord sandstone (including a calcareous variety) and brown fines.
General Information:	Site consists of Trold Fiord sandstone clasts (typically <15 cm), as well as clasts that look similar to the common type of Trold Fiord sandstone, but lack the elongate grains (cylindrical voids in these materials have been noted, suggesting that the characteristic Trold Fiord elongate grains were once present). A minority of Trold Fiord sandstones are calcareous. Also present are associated gray sandy fines (predominantly quartz)
Munsell Colours:	Fines ~5Y 5/2 (*light olive gray*). Rocks 5Y 7/2 (*yellowish gray*) to pale yellow to ~5Y 5/2 (*light olive gray*).
Samples:	One small bag containing clasts (<4 cm) and gray fines (fines react vigorously to HCl); three small rock samples (<8 cm; at least one sample is calcareous, reacting vigorously with HCl); two larger rock samples (<16 cm).
Thin Section:	Thin section *66-1*: Sandstone consisting mainly of anhedral quartz grains (most <0.1 mm), elongate recrystallized quartz grains (typically <1.5 mm; very complex undulatory extinction; shapes and textures suggest that the grains are biogenic but that original crystals have recrystallized or have been replaced), rounded lithic clasts (typically <0.1 mm), scattered opaques (typically <0.04 mm), and scattered calcite grains that appear biogenic.
Weathering State:	Trold Fiord sandstones and other variations generally weathered yellowish gray from gray.
Vegetation:	Cover Rank: ~2 Significant Varieties: *Saxifraga oppositifolia* (scattered, 10-20 cm mounds), *Lecidea spp.* Other Varieties Noted: *Thamnolia subuliformis.*

Site 67

Photographs:	One landscape photo only.
Video:	Tape #3, 0:55:33 - 1:00:36.
Formation/Unit:	Trold Fiord Formation.
Dominant Lithology:	Trold Fiord sandstone (including a calcareous variety), Trold Fiord limestone, and brown fines.
General Information:	Site consists of Trold Fiord sandstone clasts (typically <15 cm), as well as clasts that look similar to the common type of Trold Fiord sandstone, but lack the elongate grains (cylindrical voids in these materials have been noted, suggesting that the characteristic Trold Fiord elongate grains were once present). A minority of Trold Fiord sandstones are calcareous. Also present are limestone clasts, some of which are fossiliferous. Brown fines are present.
Munsell Colours:	Fines 5Y 5/2 (*light olive gray*). Rocks 5Y 7/2 (*yellowish gray*) to pale yellow to 10Y 8/2 (*pale greenish yellow*) to 5Y 6/1 (*light olive gray*) to ~N7 (*light gray*).
Samples:	One small bag containing clasts (<3 cm), and brownish-gray fines. Six rock samples (<9 cm; sandstone clasts, including one fossiliferous sample). Reaction with HCl moderate for fines, absent for most sandstones, and moderate to vigorous for calcareous and fossiliferous lithologies. Vegetation was sampled.
Thin Section:	None.
Weathering State:	Trold Fiord sandstones and other variations generally weathered yellowish gray from gray.
Vegetation:	Cover Rank: 0. Significant Varieties: None. Other Varieties Noted: *Lecidea spp.*

Site 68

Photographs:	One landscape photo only.
Video:	Tape #3, 1:00:36 - 1:03:40.
Formation/Unit:	Trold Fiord Formation.
Dominant Lithology:	Vegetation cover is at least 50%.
General Information:	Vegetation cover is at least 50%. The remainder of the site consists of frost-sorted mounds of brown fines (mounds are typically <40 cm across).
Munsell Colours:	n/a.
Samples:	Vegetation was sampled.
Thin Section:	n/a.
Weathering State:	n/a.
Vegetation:	Cover Rank: 4-5. Significant Varieties: Unidentified mosses. Other Varieties Noted: *Papaver radicatum*, unidentified grasses, *Thamnolia subuliformis*, *Lecidea spp.*

Site 69

Photographs:	One landscape photo; one closeup photo.
Video:	Tape #3, 1:06:01 - 1:10:26.
Formation/Unit:	Bjorn Formation.
Dominant Lithology:	Fine- to medium-grained sandstone, and associated sandy fines.
General Information:	Site consists of brown sandy clasts composed of a variable number of individual dark brown and sandy "spheres" (each sphere is typically 1.5 cm across, and is composed of <0.5 mm quartz grains), separated from each other by a lighter brown sandy matrix (this matrix is variably calcareous, with some quartz grains being coated by calcite). Related unconsolidated brown sandy fines are present. Bedrock outcrops consisting entirely of these materials are sparsely scattered in the area.
Munsell Colours:	Fines ~orange brown. Spheres 5YR 3/2 (*grayish brown*). Matrix ~orange brown.
Samples:	One small bag containing both individual and fused brown spherical clasts (clasts <10 cm); other clasts (<11 cm). Reaction with HCl absent for fines, and vigorous for the lighter brown sandy matrix.
Thin Section:	None.
Weathering State:	Spheres generally weathered dark brown.
Vegetation:	Cover Rank: 0. Significant Varieties: None. Other Varieties Noted: None.

Site 70

Photographs:	One landscape photo; one closeup photo.
Video:	Tape #3, 1:10:26 - 1:13:29.
Formation/Unit:	Bjorn Formation.
Dominant Lithology:	Heterolithic clasts and brown sandy fines.
General Information:	Site consists of rounded to subangular heterolithic clasts (typically <1.5 cm) in unconsolidated brown sandy fines (quartz grains dominant; typically <1 mm). Lighter-appearing surfaces are characterized by greater amounts of pebble-sized clasts, while darker-appearing surfaces are characterized by a greater cover of sand-sized particles.
Munsell Colours:	Fines ~10YR 5/4 (*moderate yellow brown*). Colours of heterolithic clasts variable.
Samples:	One small bag containing heterolithic rounded to subangular clasts (<3.5 cm) and brown sandy fines (quartz grains <1 mm).
Thin Section:	None.
Weathering State:	Heterolithic clasts variably weathered.
Vegetation:	Cover Rank: 0. Significant Varieties: None. Other Varieties Noted: *Saxifraga oppositifolia* (sparsely scattered).

Site 71

Photographs:	None.
Video:	Tape #3, 1:24:00 - 1:28:42.
Formation/Unit:	Bjorn Formation.
Dominant Lithology:	Fine- to medium-grained sandstone, associated sandy fines, and heterolithic clasts.
General Information:	Site consists of rounded heterolithic clasts (typically <1.5 cm) and brown sandy clasts composed of a variable number of individual dark brown and sandy "spheres" (each sphere is typically 1.5 cm across, and is composed of <0.5 mm quartz grains), separated from each other by a lighter brown sandy matrix (this matrix is variably calcareous, with some quartz grains being coated by calcite). Related unconsolidated brown sandy fines are present.
Munsell Colours:	Fines ~orange brown. Spheres 5YR 3/2 (*grayish brown*) and ~orange brown. Heterolithic clasts variable.
Samples:	One small bag containing brown sandy spheres, weathered-out heterolithic clasts, and brown sandy fines; one rock sample (7 cm; a combination of brown spheres, much like samples of Site 69). Reaction with HCl vigorous for most brown sandy materials.
Thin Section:	None.
Weathering State:	Sphere-related materials sometimes weathered dark brown. Heterolithic clasts variably weathered.
Vegetation:	Cover Rank: 0. Significant Varieties: None. Other Varieties Noted: *Saxifraga oppositifolia, Lecidea spp.*

Site 72

Photographs:	One closeup photo only.
Video:	Tape #3, 1:28:42 - 1:30:56.
Formation/Unit:	Bjorn Formation.
Dominant Lithology:	Fine- to medium-grained sandstone, associated sandy fines, and heterolithic clasts.
General Information:	Site consists of rounded heterolithic clasts (typically <1.5 cm) and brown sandy clasts composed of a variable number of individual dark brown and sandy "spheres" (each sphere is typically 1.5 cm across, and is composed of <0.5 mm quartz grains), separated from each other by a lighter brown sandy matrix (this matrix is variably calcareous, with some quartz grains being coated by calcite). Related unconsolidated brown sandy fines are present. The site is unique in that relatively large (typically <15 cm) sandy "Fe-concretions" are locally abundant.
Munsell Colours:	Fines ~orange brown. Spheres 5YR 3/2 (grayish brown) and ~orange brown. Heterolithic clasts variable.
Samples:	One small bag containing clasts (<4.5 cm; many are sandy "Fe-concretions") and brown sandy fines; two rock samples(<9.5 cm). One rusty sandstone clasts notably resembles the red-weathering sandstone of certain Sabine Bay Formation sites. Sandstone minerals and cement are not magnetic.
Thin Section:	None.
Weathering State:	Sphere-related materials sometimes weathered dark brown. Heterolithic clasts variably weathered.
Vegetation:	Cover Rank: 0. Significant Varieties: None. Other Varieties Noted: *Lecidea lapicida.*

Site 73

Photographs:	One landscape photo only.
Video:	Tape #3, 1:30:56 - 1:36:49.
Formation/Unit:	Trold Fiord Formation.
Dominant Lithology:	Trold Fiord sandstone, Trold Fiord biosparite, and brown fines.
General Information:	Site consists of three surface types: A) light-shaded frost-sorted circles [Trold Fiord sandstone and minor Trold Fiord calcareous sandstone/limestone (typically <3 cm), brown fines, and estimated <10% vegetation], B) darker areas outside of circles (as "A", but vegetation <15%), and C) zone along creek to the north of site (dominantly consists of moss cover; estimated vegetation <40 % - <100%). Circles of "A" evident in aerial photographs. The biosparite variety of Trold Fiord materials consists almost entirely of calcite, but contains a very minor amount of cylindrical, non-carbonate grains.
Munsell Colours:	Fines ~10YR 5/4 (*moderate yellowish brown*). TF-sandstones 5Y 8/1 (*yellowish gray*) to ~5YR 5/2 (*pale brown*). Biosparite ~pale yellowish brown.
Samples:	One small bag mainly containing Trold Fiord sandstones (<3.5 cm) and sandy brown fines (quartz grains typically <0.5 mm; subdued reaction with HCl); four Trold Fiord samples (<9 cm); several biosparite samples (<9 cm). Reaction with HCl absent for all Trold Fiord sandstones (except for whitish fines on the surfaces of some of these clasts) and vigorous for the biosparite samples.
Thin Section:	None.
Weathering State:	Trold Fiord sandstones and limestones generally weathered yellowish gray from gray.
Vegetation:	Cover Rank: 3-4. Significant Varieties: *Saxifraga oppositifolia* (densely-scattered mounds and arcs). Other Varieties Noted: *Papaver radicatum*, *Salix spp.*, unidentified mosses, *Thamnolia subuliformis*, *Lecidea spp.*

Site 74

Photographs:	One landscape photo only.
Video:	Tape #3, 1:40:57 - 1:46:10.
Formation/Unit:	Trold Fiord Formation.
Dominant Lithology:	Variably calcareous Trold Fiord sandstone and brown fines.
General Information:	Site consists of Trold Fiord sandstone clasts (typically <10 cm; variably calcareous), and associated gray fines.
Munsell Colours:	Trold Fiord sandstones 5Y 8/1 (*yellowish gray*), N8 (*very light gray*), and orangish gray. Fines brown.
Samples:	One small bag containing clasts (<3 cm) and brown sandy fines (quartz grains typically <0.5 mm; reaction with HCl subdued); six sandstone samples (<8 cm; reaction with HCl absent to moderate for exposed surfaces, and very subdued to moderate for fresh surfaces).
Thin Section:	None.
Weathering State:	Trold Fiord sandstones generally weathered yellowish gray from gray.
Vegetation:	Cover Rank: 2. Significant Varieties: *Saxifraga oppositifolia* (scattered 20 cm mounds). Other Varieties Noted: *Lecidea spp.* Notes: On nearby slopes, vegetation found in elongated strips which follow local surface gradient.

Site 75

Photographs:	One landscape photo only.
Video:	Tape #4, 0:10:08 - 0:12:35.
Formation/Unit:	Great Bear Cape Formation.
Dominant Lithology:	Limestone.
General Information:	Site consists of impure biosparite (typically <6 cm) and unconsolidated calcareous brown fines (quartz grains typically <0.4 mm).
Munsell Colours:	Limestone ~10YR 7/4 (*grayish orange*) to 5Y 7/2 (*yellowish gray*) to N8 (*very light gray*). Fines ~moderate yellowish brown.
Samples:	One small bag containing brown sandy fines (quartz grains typically <0.4 mm; reaction with HCl vigorous); six limestone samples (<6.5 cm), and smaller clasts (reaction with HCl vigorous for both exposed and fresh surfaces).
Thin Section:	None.
Weathering State:	Limestones generally weathered yellowish gray from gray.
Vegetation:	Cover Rank: 3. Significant Varieties: *Saxifraga oppositifolia* (scattered, 20 cm mounds). Other Varieties Noted: *Papaver radicatum, Oxyria digyna*, unidentified mosses, *Thamnolia subuliformis, Lecidea spp.*

Site 76

Photographs:	One landscape photo only.
Video:	Tape #4, 0:12:35 - 0:15:49.
Formation/Unit:	Great Bear Cape Formation.
Dominant Lithology:	Limestone.
General Information:	Site consists of impure biosparite (typically <4 cm) and unconsolidated calcareous brown sandy fines (quartz grains typically <0.3 mm).
Munsell Colours:	Limestone ~yellowish gray to N7 (*light gray*) to 10YR 7/4 (*grayish orange*) to 10YR 6/6 (*dark yellowish orange*). Fines ~yellowish brown.
Samples:	One small bag containing clasts and brown sandy fines (reaction with HCl vigorous; quartz grains typically <0.3 mm); seven limestone samples (<8 cm; all biosparites; reaction with HCl vigorous for both exposed and fresh surfaces).
Thin Section:	None.
Weathering State:	Limestones generally weathered yellowish gray from gray.
Vegetation:	Cover Rank: 2-3. Significant Varieties: *Saxifraga oppositifolia* (scattered 10-20 cm mounds). Other Varieties Noted: *Papaver radicatum, Oxyria digyna*, unidentified mosses, *Thamnolia subuliformis, Lecidea spp.*

Site 77

Photographs:	None.
Video:	Tape #4, 0:22:34 - 0:28:41.
Formation/Unit:	Great Bear Cape Formation.
Dominant Lithology:	Limestone and calcareous sandstone.
General Information:	Site consists of impure biosparite and calcareous sandstone (typically <3 cm), rounded heterolithic clasts (typically <1.5 cm), and unconsolidated calcareous brown sandy fines (quartz grains typically <1 mm).
Munsell Colours:	Rocks ~yellowish brown to 10YR 7/4 (*grayish orange*) to 10YR 6/6 (*dark yellowish orange*). Fines 10YR 5/4 (*moderate yellowish brown*).
Samples:	One cloth bag containing biosparite and calcareous sandstone, brown sandy fines, and rounded heterolithic clasts. Reaction with HCl vigorous for fines, biosparite and calcareous sandstone.
Thin Section:	None.
Weathering State:	Limestones and calcareous sandstones generally weathered yellowish gray or orange from gray.
Vegetation:	Cover Rank: 0 in vicinity of hilltop. Significant Varieties: *Saxifraga oppositifolia*. Other Varieties Noted: *Lecidea spp.* Notes: Vegetation very sparse at summit of hill, increasing in density at hill sides; vegetation especially dense at far margins of hill. At nearby creek (outside site), black algae covers moist locales.

Site 78

Photographs:	One landscape photo only.
Video:	Tape #4, 0:28:41 - 0:31:00.
Formation/Unit:	Great Bear Cape Formation.
Dominant Lithology:	Impure limestone, calcareous sandstone, and brown sandy fines.
General Information:	Site consists of pebbly calcareous sandstone and impure biosparite (typically <4 cm), and brown sandy fines.
Munsell Colours:	Rocks ~10YR 8/2 (*very pale orange*) to 10YR 7/4 (*grayish orange*) to 10YR 6/6 (*dark yellowish orange*) to N8 (*very light gray*). Fines yellowish brown.
Samples:	One paper bag containing calcareous sandstone clasts and brown sandy fines (reaction with HCl vigorous); five impure biosparite and pebbly calcareous sandstone samples (<10 cm; reaction with HCl vigorous for both exposed and fresh surfaces).
Thin Section:	None.
Weathering State:	Limestones and calcareous sandstones generally weathered yellowish gray or orange from gray.
Vegetation:	Cover Rank: 3. Significant Vegetation: *Saxifraga oppositifolia* (scattered 10-40 cm mounds). Other Varieties Noted: *Thamnolia subuliformis, Lecidea spp.*

Site 79

Photographs:	One landscape photo only.
Video:	Tape #4, 0:31:00 - 0:34:00.
Formation/Unit:	Great Bear Cape Formation.
Dominant Lithology:	Pebbly calcareous sandstone and brown sandy fines.
General Information:	Site consists of pebbly calcareous sandstone clasts (typically <12 cm; quartz grains typically <0.5 mm), and sandy brown fines.
Munsell Colours:	Rocks ~10YR 8/2 (*very pale orange*) to 10YR 7/4 (*grayish orange*) to 10YR 6/6 (*dark yellowish orange*) to N8 (*very light gray*). Fines yellowish brown.
Samples:	One paper bag containing small calcareous sandstone clasts and brown sandy fines (reaction with HCl vigorous); six calcareous sandstone samples (<11 cm).
Thin Section:	Thin section *79-1*: Impure biosparite consisting of calcite bioclasts, pore-filling calcite cement, subrounded to rounded monocrystalline quartz grains (typically 0.5 mm), and subrounded to rounded polycrystalline quartz grains and lithic grains.
Weathering State:	Calcareous sandstones generally weathered yellowish gray or orange from gray.
Vegetation:	Cover Rank: 2. Significant Varieties: *Saxifraga oppositifolia*. Other Varieties Noted: *Thamnolia subuliformis, Lecidea spp.*

Site 80

Photographs:	One landscape photo only.
Video:	Tape #4, 0:34:00 - 0:37:40.
Formation/Unit:	Great Bear Cape Formation.
Dominant Lithology:	Limestone.
General Information:	Site consists of biosparite clasts (typically <10 cm) and brown sandy fines. A red-weathering, calcareous, fossiliferous mudstone clast was sampled, and may be Assistance Formation material.
Munsell Colours:	Biosparite 5Y 7/2 (*yellowish gray*) to 10YR 7/4 (*grayish orange*) to 10YR 6/6 (*dark yellowish orange*), N6 (*medium light gray*). Fines brown. Mudstone reddish-brown.
Samples:	One paper bag containing clasts and brown sandy fines; numerous biosparite samples (<12.5 cm), and one red-weathering, calcareous, fossiliferous mudstone. All biosparites react vigorously with HCl. Vegetation was sampled.
Thin Section:	Thin section *80-1*: Impure biosparite consisting mainly of bioclasts (typically <0.7 mm) and calcite cement. Subangular to rounded mono and polycrystalline quartz grains. Rounded green mineral (glauconite?) present.
Weathering State:	Limestones generally weathered yellowish gray or orange from gray.
Vegetation:	Cover Rank: 3. Significant Varieties: *Saxifraga oppositifolia* (scattered 10-20 cm mounds). Other Varieties Noted: *Papaver radicatum*, unidentified mosses, *Thamnolia subuliformis, Lecidea spp., Vulpicida tilesii.*

Site 81

Photographs:	One landscape photo only.
Video:	None (batteries dead).
Formation/Unit:	Canyon Fiord Formation.
Dominant Lithology:	Heterolithic clasts and unconsolidated red-weathering sandy fines.
General Information:	Site consists of rounded heterolithic clasts (typically <2 cm) and unconsolidated red sandy fines (quartz grains typically <0.5 mm). Pebbly calcareous sandstone and calcareous pebble conglomerate clasts are present.
Munsell Colours:	Sandstones and conglomerates: ~5YR 6/4 (*light brown*) to 5YR 5/6 (*light brown*). Fines brown. Heterolithic pebbles variably coloured.
Samples:	Cloth bag containing red sandy fines (quartz dominant; grains typically <0.5 mm; reaction with HCl very subdued), and heterolithic clasts (<4 cm); one conglomerate clast (7.5 cm; reaction with HCl vigorous), which represents the source material of the pebble-sized casts.
Thin Section:	None.
Weathering State:	Sandstones and conglomerates generally weathered brown.
Vegetation:	Cover Rank: 0. Significant Varieties: None. Other Varieties Noted: None.

Site 82

Photographs:	One landscape photo only.
Video:	None (batteries dead).
Formation/Unit:	Canyon Fiord Formation.
Dominant Lithology:	Red-weathering fine-grained calcareous sandstone and conglomerate, and red-weathering sandy fines.
General Information:	Site consists of red-weathering fine-grained calcareous sandstone clasts (quartz grains typically <0.5 mm) and red-weathering unconsolidated sandy fines.
Munsell Colours:	Rocks deep reddish brown; fresh surfaces 5Y 8/1 (*yellowish gray*). Heterolithic pebbles variably coloured.
Samples:	Cloth bag containing red sandy fines, and calcareous sandstone (<7 cm).
Thin Section:	None.
Weathering State:	Sandstones and conglomerates generally weathered reddish brown.
Vegetation:	Cover Rank: 0. Significant Varieties: None. Other Varieties Noted: None.

Site 83

Photographs:	None.
Video:	None (batteries dead).
Formation/Unit:	Canyon Fiord Formation.
Dominant Lithology:	Calcareous conglomerate and associated weathering products.
General Information:	Site consists of a light-coloured mound associated with a small bedrock exposure (only metres in dimension; seen in the photograph taken of Site 82). Exposed are pebbly calcareous sandstones, and pebble conglomerates (these materials are the source of the lighter-shaded ("yellow") materials on the western slopes of the gabbro dike).
Munsell Colours:	Rocks ~5YR 6/4 (*light brown*) to 5Y 8/1 (*yellowish gray*). Heterolithic pebbles variably coloured.
Samples:	One cloth bag containing calcareous sandstone and conglomerate clasts (< 3.5 cm), and one larger conglomerate clast (<8 cm). Reaction of sandstones and conglomerates with HCl vigorous for both exposed and fresh surfaces.
Thin Section:	None.
Weathering State:	Conglomerates generally weathered yellowish gray.
Vegetation:	Cover Rank: 0. Significant Varieties: None. Other Varieties Noted: None.

APPENDIX B: Descriptions of Cape Smith Belt Field Sites

Introductory notes to Appendix B

1) Site Locations are given in Figures 4.15 to 4.18.

2) Over 250 photographs and five hours of video tape (on three two-hour tapes) provide visual documentation of the Cape Smith Belt study area.

3) Particularly detailed video documentation of the varieties of vegetation that characterize the study area is available in the documentation of Site 46.

4) Vegetation Cover Ranks:

0	Essentially no vegetation except lichens.
1	Sparsely-scattered vegetation: ~1% to ~5% cover (e.g., Sites 2 and 9).
2	~5% to 15% vegetation cover (e.g., Site 10).
3	~15% to ~55% vegetation cover (e.g., Sites 22 and 23).
4	~55% to ~80% vegetation cover.
5	>80% vegetation cover (lichen, moss, or vascular) (e.g., Sites 4, 5, 6, and 11)

5) The sizes of rock samples are generally expressed in terms of their longest dimension.

7) Common Names for Cape Smith Belt Plants:

Cassiope tetragona: White Arctic Bell-heather, or Four-angled Mountain-heather.
Betula sp.: Birches
Papaver radicatum: Arctic Poppy
Oxyria digyna: Mountain Sorrel
Salix spp.: Willows

8) Lichen cover is very prevalent on rocks in the Cape Smith Belt region. Cape Smith Belt lichens collected by the author and identified by P.Y. Wong, Collection Division, Canadian Museum of Nature (Ottawa) include the following:

Orphniospora moriopsis (A. Massal.) D. Hawksw.
Allantoparmelia alpicola (Th. Fr.) Essl.
Rhizocarpon geographicum (L.) DC.
Lecidella sp.
Aspicilia sp.
Stereocaulon arenarium (Savicz) Lamb
Pertusaria sp.

9) Specific lichen varieties are not identified below except where materials were classified by a specialist (P.Y. Wong - see above). Generalized terms (e.g., "green/black lichens") are used below to describe varieties which have not been conclusively identified.

10) The most common variety of moss in the in the field area is *Rhacomitrium lanuginosum* (identification performed by Dr. Michele Piercey-Normore, Department of Botany, University of Manitoba).

11) The list of vegetation varieties in the section "Other Varieties Noted" is not meant to be a comprehensive listing of all varieties present at a site.

12) The prefix "meta" precedes all lithological determinations for the Cape Smith Belt Field Area (thus, a "pelite" is actually a "metapelite") (see Chapter 4; St-Onge and Lucas, 1989).

Site 1

Photographs:	One landscape photo; one closeup photo.
Video:	Tape #1, 0:17:50 - 0:24:11.
Formation/Unit:	Unnamed peridotite intrusion.
Dominant Lithology:	Peridotite.
General Information:	Peridotite rocks (typically up to 50 cm) dominant. Other ultramafics or mafics may be present.
Munsell Colours:	Fresh and weathered surfaces typically pale green (10G 6/2) to grayish green (10G 4/2). Weathered surfaces also commonly ~moderate reddish brown (10R 4/6).
Samples:	6 ultramafic samples (13 cm, 11 cm, 11 cm, 9 cm, 7 cm, 6.5 cm). Vegetation sampled.
Thin Section:	Thin Section *1-1*: Sample mainly composed of augite (typically ~2 mm; have lamelli - "exolved phase"). Original orthopyroxene has been replaced by carbonate and chlorite (this is seen most easily along the left-hand edge of the thin section).
Weathering State:	Many exposed surfaces weathered reddish brown from green.
Vegetation:	Cover Rank: 1-2 (strips of vegetation ~4 m across are locally present). Significant Varieties: Black/green lichens, grass, moss (predominantly *Rhacomitrium lanuginosum*). Other Varieties Noted: None.

Site 2

Photographs:	One landscape photo; one closeup photo.
Video:	Tape #1, 0:25:37 - 0:27:54.
Formation/Unit:	Unnamed tonalite intrusion.
Dominant Lithology:	Tonalite.
General Information:	Tonalite rocks (typically up to 70 cm). Very scattered tan-weathering rocks are present (typically <20 cm).
Munsell Colours:	Fresh and weathered surfaces typically medium gray (N5) to medium dark gray (N4).
Samples:	3 tonalite samples (10, 8, 7 cm). Vegetation sampled.
Thin Section:	Thin Section *2-1*: Sample has a mortar texture (grain-size reduction / recrystallization around edges of larger crystals). Sample mainly composed of quartz (typically <1.5 mm), plagioclase feldspar (typically <1.5 mm), and epidote. Also present are sericite and radiating / fibrous chlorite (anomalous blue birefringence noted).
Weathering State:	Surface minerals not appreciably altered.
Vegetation:	Cover Rank: 1. Significant Varieties: Green/black lichens (including *Orphniospora moriopsis*). Other Varieties Noted: grass, *Cassiope tetragona*, moss (predominantly *Rhacomitrium lanuginosum*).

Site 3

Photographs:	One landscape photo; one closeup photo.
Video:	Tape #1, 0:27:54 - 0:31:01.
Formation/Unit:	Unnamed tonalite intrusion.
Dominant Lithology:	Tonalite.
General Information:	Tonalite rocks (typically up to 70 cm). Bedrock is locally exposed. Tan-weathering mafic and ultramafic rocks (typically <20 cm) are present but minor.
Munsell Colours:	Fresh and weathered tonalite surfaces typically medium gray (N5) to medium dark gray (N4).
Samples:	5 rock samples: 3 tonalite rocks (9 cm, 9 cm, 8 cm), and 2 tan-weathering rocks (11 cm, 8 cm).
Thin Section:	None. Refer to thin section *2-1*.
Weathering State:	Surface minerals of tonalite rocks not appreciably altered.
Vegetation:	Cover Rank: 0. Significant Varieties: Green/black lichens (including *Orphniospora moriopsis*). Other Varieties Noted: None.

Site 4

Photographs:	One landscape photo; one closeup photo.
Video:	Tape #1, 0:32:14 - 0:33:51.
Formation/Unit:	Spartan Group.
Dominant Lithology:	Vegetation cover is at least 80%. Most exposed rocks are pelites (schists).
General Information:	Site is a relatively poorly drained, grassy meadow, with very little exposure of rock (rocks typically <30 cm). Most exposed rocks are schists; tan-weathering mafic and ultramafic rocks are present but minor.
Munsell Colours:	Schists medium gray (N5) to medium dark gray (N4).
Samples:	2 schist samples (8 cm, 7 cm). Vegetation sampled.
Thin Section:	None.
Weathering State:	Surface minerals of schist not appreciably altered.
Vegetation:	Cover Rank: 5. Significant Varieties: green/black lichens, grass, and scattered *Salix spp.* Other Varieties Noted: None.

Site 5

Photographs:	One landscape photo; one closeup photo.
Video:	Tape #1, 0:34:07 - 0:36:02.
Formation/Unit:	Spartan Group.
Dominant Lithology:	Vegetation cover is at least 90%.
General Information:	Site is a relatively poorly drained, grassy, vegetationally diverse meadow, with essentially no exposure of rock. Small pools of standing water are present but minor.
Munsell Colours:	n/a
Samples:	Vegetation sampled.
Thin Section:	None.
Weathering State:	n/a
Vegetation:	Cover Rank: 5. Significant Varieties: grass, scattered *Salix spp.*, and moss (predominantly *Rhacomitrium lanuginosum*). Other Varieties Noted: cotton.

Site 6

Photographs:	One landscape photo; one closeup photo.
Video:	Tape #1, 0:36:02 - 0:38:40.
Formation/Unit:	Spartan Group.
Dominant Lithology:	Vegetation cover is at least 90%.
General Information:	Site is a relatively well drained meadow consisting mainly of grass and moss. Rock exposures with dimensions of up to ~5 m are present but minor. Frost-sorted circles consisting of smaller rocks (typically <7 cm) are present but minor.
Munsell Colours:	n/a
Samples:	Vegetation sampled.
Thin Section:	None.
Weathering State:	n/a
Vegetation:	Cover Rank: 5. Significant Varieties: moss (predominantly *Rhacomitrium lanuginosum*) and scattered grass. Other Varieties Noted: *Salix spp.*

Site 7

Photographs:	One landscape photo; one closeup photo.
Video:	Tape #1, 0:38:40 - 0:42:57.
Formation/Unit:	Spartan Group.
Dominant Lithology:	Pelite.
General Information:	Site dominated by schist (rocks typically up to 30 cm, frost-sorted circles consisting of smaller rocks (typically <5 cm) are present. Tan-weathering mafic and ultramafic rocks (typically <20 cm) are present in significant amounts.
Munsell Colours:	Schists medium gray (N5) to medium dark gray (N4) to brownish gray (5YR 4/1) to greenish gray (5GY 4/1). Fresh surfaces of tan-weathering rocks greenish gray (5GY 6/1); weathered surfaces ~moderate brown (5YR 4/4).
Samples:	5 schists: 9 cm, 8 cm, 7 cm, 6 cm, 5 cm; 1 tan-weathering mafic rock: 6 cm.
Thin Section:	None.
Weathering State:	Some schist surfaces weathered greenish or brownish gray from gray.
Vegetation:	Cover Rank: 3. Significant Varieties: moss (predominantly *Rhacomitrium lanuginosum*), green-black lichens, *Cassiope tetragona*. Other Varieties Noted: grass.

Site 8

Photographs:	One landscape photo only.
Video:	Tape #1, 0:42:57 - 0:43:48.
Formation/Unit:	Spartan Group.
Dominant Lithology:	Vegetation cover is at least 95%.
General Information:	Site is a poorly drained grassy meadow with essentially no rock exposure.
Munsell Colours:	n/a
Samples:	Vegetation sampled.
Thin Section:	None.
Weathering State:	n/a
Vegetation:	Cover Rank: 5. Significant Varieties: grass. Other Varieties Noted: cotton.

Site 9

Photographs:	One landscape photo; one closeup photo.
Video:	Tape #1, 0:44:30 - 0:48:33.
Formation/Unit:	Spartan Group.
Dominant Lithology:	Pelite.
General Information:	Site consists of dominant schist (rocks typically up to 110 cm), and scattered tan-weathering mafic and ultramafic rocks (typically up to 30 cm).
Munsell Colours:	Schist light gray (N7) to dark gray (N4). Tan-weathering rocks dark yellowish orange (10YR 6/6) to medium brown (5YR 4/4); fresh surfaces greenish gray (5G 6/1) to medium dark gray (N4).
Samples:	4 schist samples (11 cm, 9 cm, 9 cm, 5 cm); 2 tan-weathering samples (8 cm, 8 cm).
Thin Section:	None.
Weathering State:	Surface minerals of schist are not appreciably altered. Surface coating of schists by green/black lichen is significant. Tan rocks weathered reddish brown from green.
Vegetation:	Cover Rank: 1 (but is a thin, long site, surrounded by grasses, so peripheral pixels will be mixed). Significant Varieties: green/black lichens, scattered *Cassiope tetragona* and moss (predominantly *Rhacomitrium lanuginosum*). Other Varieties Noted: None.

Site 10

Photographs:	One landscape photo; one closeup photo.
Video:	Tape #1, 0:48:33 - 0.:48:56.
Formation/Unit:	Spartan Group.
Dominant Lithology:	Pelite.
General Information:	Site consists of dominant schist (rocks typically up to 60 cm, and >120 cm in places), and significant tan-weathering mafic and ultramafic rocks (typically up to 30 cm).
Munsell Colours:	Schist light gray (N7) to dark gray (N4). Tan-weathering rocks dark yellowish orange (10YR 6/6) to medium brown (5YR 4/4); fresh surfaces greenish gray (5G 6/1) to medium dark gray (N4).
Samples:	4 schist samples (9 cm, 9 cm, 8 cm, 6 cm); 5 tan-weathering samples (9 cm, 9 cm, 7 cm, 7 cm, 5 cm). Vegetation sampled.
Thin Section:	None.
Weathering State:	Surface minerals of schist not appreciably altered. Surface coating of schists by green/black lichen is significant. Tan rocks weathered reddish brown from green.
Vegetation:	Cover Rank: 2 . Significant Varieties: *Cassiope tetragona* and moss (predominantly *Rhacomitrium lanuginosum*). Other Varieties Noted: None.

Site 11

Photographs:	One landscape photo; one closeup photo.
Video:	Tape #1, 0:48:56 - 0:49:07.
Formation/Unit:	Spartan Group.
Dominant Lithology:	Vegetation cover at least 95%.
General Information:	Site is a well drained grassy meadow.
Munsell Colours:	n/a
Samples:	Vegetation sampled.
Thin Section:	None.
Weathering State:	n/a
Vegetation:	Cover Rank: 5. Significant Varieties: dry grass, *Salix spp.*, and moss (predominantly *Rhacomitrium lanuginosum*). Other Varieties Noted: None.

Site 12

Photographs:	One landscape photo; one closeup photo.
Video:	Tape #1, 0:49:07 - 0:49:21 (batter power low).
Formation/Unit:	Watts Group.
Dominant Lithology:	Peridotite and pelite.
General Information:	Surface covered mainly with ultramafic materials derived from adjacent peridotite mound. Spartan Group schist is also present in significant amounts.
Munsell Colours:	Fresh surfaces of peridotite: dusky yellow green (5GY 5/2) to dark greenish gray (5GY 4/1) to dark gray (N3). Weathered surfaces of peridotite: light brown (5YR 5/6) to moderate brown (5YR 4/4).
Samples:	10 rocks (<11 cm); schist and mafic/ultramafic samples.
Thin Section:	None.
Weathering State:	Many peridotite rocks weathered reddish brown from green.
Vegetation:	Cover Rank: 3 overall (1-4). Significant Varieties: moss (predominantly *Rhacomitrium lanuginosum*), grass. Other Varieties Noted: *Cassiope tetragona*.

Site 13

Photographs:	One landscape photo; one closeup photo.
Video:	Tape #1, 0:49:21 - 0:49:37 (battery power low).
Formation/Unit:	Spartan Group.
Dominant Lithology:	Pelite.
General Information:	Rocks and bedrock exposures typically up to 3 m across, separated by areas of moss and grass cover.
Munsell Colours:	Schist light gray (N7) to dark gray (N3).
Samples:	2 schist samples (14 cm, 13 cm). Vegetation sampled.
Thin Section:	None.
Weathering State:	Surface minerals of schist not altered.
Vegetation:	Cover Rank: 3 overall. Significant Varieties: green/black lichens (including *Allantoparmelia alpicola*), moss (predominantly *Rhacomitrium lanuginosum*), grass, *Cassiope tetragona*. Other Varieties Noted: None.

Site 14

Photographs:	Two landscape photos; one closeup photo.
Video:	Tape #1, 0:49:37 - 0:49:47.
Formation/Unit:	Spartan Group.
Dominant Lithology:	Pelite.
General Information:	Pelite is exposed mainly in the form of bedrock ridges ~20-40 m across; ridge lengths can exceed 100 m. Bedrock ridges are separated by variable extents of moss and grass cover. Individual rocks are typically <1 m.
Munsell Colours:	Schist light gray (N7) to dark gray (N3).
Samples:	6 pelite samples (all <8 cm). Vegetation sampled.
Thin Section:	None.
Weathering State:	Surface minerals of schist not altered.
Vegetation:	Cover rank: ~3 overall (lower at bedrock ridges, and higher between bedrock ridges). Significant Varieties: green/black lichens (including *Allantoparmelia alpicola*), moss (predominantly *Rhacomitrium lanuginosum*), grass. Other Varieties Noted: None.

Site 15

Photographs:	One landscape photo; one closeup photo.
Video:	Tape #1, 0:51:30 - 0:53:30.
Formation/Unit:	Watts Group.
Dominant Lithology:	Peridotite.
General Information:	Ultramafic rocks are typically <20 cm (note: these rocks are generally much smaller than in surrounding areas, where the dimensions of rocks can typically exceed one metre).
Munsell Colours:	Fresh peridotite surfaces: medium light gray (N6) to medium dark gray (N4) to greenish. Weathered peridotite surfaces commonly pale yellowish orange (10YR 8/6) to dark yellowish orange (10YR 6/6) to light brown (5YR 5/6).
Samples:	10 peridotite samples (all <8 cm).
Thin Section:	None.
Weathering State:	Rocks weather orange/brown from gray and greenish gray.
Vegetation:	Cover Rank: 0. Significant Varieties: green/black lichens (including *Orphniospora moriopsis*). Other Varieties Noted: None.

Site 16

Photographs:	One landscape photo; one closeup photo.
Video:	Tape #1, 0:53:30 - 0:56:09.
Formation/Unit:	Watts Group.
Dominant Lithology:	Peridotite.
General Information:	Surfaces of rocks are mostly darker (dark gray) than surrounding materials, which are more red/orange (or, at Site 15, lighter gray). Individual rocks typically <1 m; some bedrock exposures larger.
Munsell Colours:	Fresh peridotite surfaces: medium dark gray (N4). Exposed peridotite surfaces: dark greenish gray (5G 4/1) and dark gray (N3; possibly from lichen cover) and moderate brown (5YR 4/4 and 5YR 3/4).
Samples:	6 peridotite samples (all <8 cm).
Thin Section:	None.
Weathering State:	Rocks weather brown and gray from gray.
Vegetation:	Cover Rank: 0. Significant Varieties: green/black lichens (including *Orphniospora moriopsis*). Other Varieties Noted: None.

Site 17

Photographs:	One landscape photo; one closeup photo.
Video:	Tape #1, 0:56:09 - 0:58:16.
Formation/Unit:	Watts Group.
Dominant Lithology:	Peridotite.
General Information:	Red- and orange-weathering boulder terrain. Individual boulders and bedrock exposures typically <3 m.
Munsell Colours:	Fresh peridotite surfaces: greenish gray (5G 6/1) to grayish black (N2). Weathered peridotite surfaces: light brown (5YR 5/6) to moderate brown (5YR 3/4).
Samples:	4 peridotite samples (all <8 cm).
Thin Section:	None.
Weathering State:	Rocks weather brown from greenish gray and grayish black.
Vegetation:	Cover Rank: 0. Significant Varieties: green/black lichens (including *Orphniospora moriopsis*). Other Varieties Noted: None.

Site 18

Photographs:	One landscape photo; one closeup photo.
Video:	Tape #1, 0:58:16 - 1:00:13.
Formation/Unit:	Watts Group.
Dominant Lithology:	Peridotite.
General Information:	Red- and orange-weathering bouldery terrain. Boulders typically <1.2 m. Bedrock exposures are present but minor.
Munsell Colours:	Fresh peridotite surfaces: greenish gray (5G 6/1) to grayish black (N2). Weathered peridotite surfaces: light brown (5YR 5/6) to moderate brown (5YR 3/4); surfaces also commonly dark gray (N3; possibly from lichen cover).
Samples:	5 peridotite samples (all <8 cm).
Thin Section:	Thin Section *18-1*: Sample is similar to that of 1-1, but degree of alteration is greater. Augite is present (typically ~1.5 mm, with exolution textures), as well as chlorite (in the form of veins and commonly with a fibrous and radiating habit). This sample had more orthopyroxene to start with than that of 1-1; all orthopyroxene in *18-1* has altered to opaques (original crystal centre), fibrous talc (middle), and epidote (rim).
Weathering State:	Rocks weather brown and gray from greenish gray and grayish black.
Vegetation:	Cover Rank: 0. Significant Varieties: green/black lichens (including *Orphniospora moriopsis*, and probably *Aspicilia sp.*). Other varieties: None.

Site 19

Photographs:	One landscape photo; one closeup photo.
Video:	Tape #1, 1:00:13 - 1:03:26.
Formation/Unit:	Watts Group.
Dominant Lithology:	Peridotite.
General Information:	Red- and orange-weathering boulder terrain. Boulders typically <1.2 m. In places, darker grayish rocks such as those seen at Site 16 are present. Bedrock exposures are present but minor.
Munsell Colours:	Fresh peridotite surfaces: combination of dark gray (N3) and greenish gray (5GY). Most exposed surfaces: grayish orange (10YR 7/4) to light brown (5YR 5/6) to medium brown (5YR 4/4).
Samples:	7 peridotite samples (all <9 cm).
Thin Section:	None.
Weathering State:	Most surfaces are weathered reddish brown from dark gray / green.
Vegetation:	Cover Rank: 0. Significant Varieties: green/black lichens (including *Orphniospora moriopsis*). Other Varieties Noted: None.

Site 20

Photographs:	One landscape photo; one closeup photo.
Video:	Tape #1, 1:03:26 - 1:07:15.
Formation/Unit:	Watts Group.
Dominant Lithology:	Peridotite.
General Information:	Variably green ultramafic rocks (some highly serpentinized; others orange-weathering as seen at previous sites). Rocks typically <1 m; smaller rocks (on the order of tens of cm's) are more prevalent at this site than at previous sites.
Munsell Colours:	Fresh and exposed surfaces: grayish yellow green (5GY 7/2) and dark gray (N3). Some surfaces weathered dark yellowish orange (10YR 6/6) to moderate brown (5YR 4/4).
Samples:	13 ultramafic samples (all <9 cm).
Thin Section:	None.
Weathering State:	Some rocks weathered brown from dark gray and green.
Vegetation:	Cover Rank: 1. Significant Varieties: green/black lichens (including *Orphniospora moriopsis*),moss (predominantly *Rhacomitrium lanuginosum*), grass. Other Varieties Noted: None.

Site 21

Photographs:	One landscape photo; one closeup photo.
Video:	Tape #1, 1:07:15 - 1:09:03.
Formation/Unit:	Watts Group.
Dominant Lithology:	Peridotite.
General Information:	Rocks typically <30 cm; larger rocks are present. Frost-heaved and frost-sorted features present.
Munsell Colours:	Fresh peridotite surfaces: medium dark gray (N4) and pale yellowish green (10GY 7/2). Most surfaces weathered pale yellowish brown (10YR 6/2) to dark yellowish orange (10YR 6/6) to light brown (5YR 5/6) to moderate brown (5YR 4/4).
Samples:	14 ultramafic samples, most of which have similar characteristics to the peridotite samples of nearby sites (all <8 cm).
Thin Section:	None.
Weathering State:	Some rocks weathered brown from dark gray / green.
Vegetation:	Cover Rank: 0 or 1. Significant Varieties: moss (predominantly *Rhacomitrium lanuginosum*), scattered grasses. Other Varieties Noted: None.

Site 22

Photographs:	One landscape photo; one closeup photo.
Video:	Tape #1, 1:09:03-1:09:51.
Formation/Unit:	Watts Group.
Dominant Lithology:	Basalt.
General Information:	Outcrops of basalt (outcrops typically 1-10 m across). Surface collections of individual rocks are generally not present; relatively smooth bedrock dominates. There are no tan- or orange-weathering rocks.
Munsell Colours:	Basalt dark gray (N4) to medium gray (N5). Surfaces rarely weathered to light brown (5YR 5/6).
Samples:	3 basalt samples (11 cm, 8 cm, 7 cm).
Thin Section:	Thin Section *22-1*: Basalt sample mainly composed of amphibole (<0.6 mm; probably actinolite) and epidote (<0.1 mm), which are arranged in thin layers and lenses.
Weathering State:	Most surfaces not appreciably altered.
Vegetation:	Cover Rank: 3-2. Significant Varieties: grass, moss (predominantly *Rhacomitrium lanuginosum*), green/black lichens. Other Varieties Noted: None.

Site 23

Photographs:	One landscape photo; one closeup photo.
Video:	Tape #1, 1:10:38 - 1:13::03.
Formation/Unit:	Watts Group.
Dominant Lithology:	Basalt.
General Information:	Bedrock (individual outcrops typically 1-7 m across) and rocks (typically <40 cm). There are no tan- or orange-weathering rocks.
Munsell Colours:	Fresh basalt surfaces: greenish gray (5G 6/1). Exposed surfaces typically weathered dark greenish gray (5GY 4/1), and rarely brownish gray (5YR 4/1).
Samples:	4 basalt samples (9 cm, 6 cm, 5 cm, 5 cm). Vegetation sampled.
Thin Section:	Thin Section *23-1*: (very similar to 29-1). Basalt sample mainly composed of actinolite (<0.1 mm) and epidote (<0.1 mm).
Weathering State:	Surface minerals of basalt generally not appreciably altered.
Vegetation:	Cover Rank: 3. Significant Varieties: green/black lichens, grass, .moss (predominantly *Rhacomitrium lanuginosum*), *Cassiope tetragona*. Other Varieties Noted: None.

Site 24

Photographs:	One landscape photo; one closeup photo.
Video:	Tape #1, 1:13:03 - 1:15:54.
Formation/Unit:	Watts Group.
Dominant Lithology:	Basalt.
General Information:	Site consists of rocks (typically 8-40 cm across) and bedrock exposures. Bedrock exposures are not as widespread here as they are at Site 23. Frost-sorted features are present. Tan- and orange-weathering rocks (typically 10-30 cm) are present but minor.
Munsell Colours:	Fresh basalt: greenish gray (5G 6/1) and medium bluish gray (5B 6/1). Exposed basalt surfaces greenish gray (5GY 6/1) and rarely brown or reddish brown. Tan- and orange-weathering rocks: fresh: medium dark gray (N4); exposed: moderate yellowish brown (10YR 5/4) to reddish brown).
Samples:	2 basalt samples (11 cm, 9 cm) and 2 tan- and orange-weathering ultramafic rocks (9 cm, 6 cm).
Thin Section:	None. Refer to thin section *23-1*.
Weathering State:	Surface minerals of basalt generally not appreciably altered.
Vegetation:	Cover Rank: ~3. Significant Varieties: green/black lichens, moss (predominantly *Rhacomitrium lanuginosum*), *Cassiope tetragona*, grass. Other Varieties Noted: None.

Site 25

Photographs:	One landscape photo; one closeup photo.
Video:	Tape #1, 1:15:54 - 1:18:11.
Formation/Unit:	Mapped as Watts Group basalts, but rocks clearly are ultramafic.
Dominant Lithology:	Mainly ultramafic rocks (peridotite).
General Information:	Mound of tan- and orange-weathering rocks (rocks typically 10-20 cm; up to ~1 m rocks present). There are very few or no rocks with similar characteristics to those of nearby Site 24 and Site 23.
Munsell Colours:	Fresh surfaces: dark gray (N3) and dark greenish gray (5GY 4/1). Exposed surfaces: ~moderate brown (5YR 4/4).
Samples:	4 ultramafic samples: 8 cm, 7 cm, 6 cm, 6 cm.
Thin Section:	None.
Weathering State:	Rocks weathered brown from dark gray and green.
Vegetation:	Cover Rank: 2-1. Significant Varieties: grass, moss (predominantly *Rhacomitrium lanuginosum*), *Cassiope tetragona*. Other Varieties Noted: None.

Site 26

Photographs:	One landscape photo; one closeup photo.
Video:	Tape #1, 1:18:11 - 1:21:07.
Formation/Unit:	Watts Group.
Dominant Lithology:	Basalt and gabbro.
General Information:	Surface covered by large (typically 60-110 cm) rocks of basaltic composition (variable grain sizes). The rocks weather tan and orange in small patches, but otherwise are coloured much as the materials at, e.g., Sites 23 and 24.
Munsell Colours:	Fresh gabbro surfaces: dark greenish gray (5GY 4/1) minerals in grayish yellow green matrix (5GY 7/2). Exposed surfaces typically greenish gray (5GY 6/1) and occasionally light brown (5YR 5/6).
Samples:	9 samples (all <8 cm), 6 of which are coarse-grained (crystals up to ~1.5 mm).
Thin Section:	Thin Section *26-1*: Sample has gabbroic texture, and consists mainly of amphiboles (<0.8 mm) that are pseudomorphs after augite, and that are being replaced by fibrous actinolite (<0.1 mm). Also present are fine-grained epidote and albite, unidentified brown fine-grained materials, and Fe-oxides.
Weathering State:	Rocks typically weathered greenish gray from gray and green.
Vegetation:	Cover Rank: ~1. Significant Varieties: green/black lichens, dark lichens, moss (predominantly *Rhacomitrium lanuginosum*), grass, *Cassiope tetragona*. Other Varieties Noted: None.

Site 27

Photographs:	One landscape photo; one closeup photo.
Video:	Tape #1, 1:21:07 - 1:23:28.
Formation/Unit:	Watts Group.
Dominant Lithology:	Basalt.
General Information:	Frost-sorted circles (circles typically 1-1.5 m in across) of small basaltic rocks (typically <4 cm).
Munsell Colours:	n/a
Samples:	Vegetation sampled.
Thin Section:	None.
Weathering State:	n/a
Vegetation:	Cover Rank: ~4-5. Significant Varieties: grass, moss (predominantly *Rhacomitrium lanuginosum*), *Cassiope tetragona*, and others. Other Varieties Noted: cotton, lichens.

Site 28

Photographs:	One landscape photo; one closeup photo.
Video:	Tape #1, 1:23:28 - 1:25:28.
Formation/Unit:	Watts Group.
Dominant Lithology:	Basalt.
General Information:	Rocks similar to those of Site 27, but rocks are larger (typically <20 cm), and the sorted circles are also slightly larger (typically 1-2 m across). Tan-weathering rocks are present but minor.
Munsell Colours:	Fresh surfaces: greenish gray (5G 6/1). Exposed surfaces: dark greenish gray (5GY 4/1) and more rarely grayish orange.
Samples:	18 samples (all < 8 cm); dominantly basalts.
Thin Section:	None.
Weathering State:	Rocks weathered different shades of greenish gray and brown, from greenish gray.
Vegetation:	Cover Rank: ~4. Significant Varieties: green/black lichens, grass, moss (predominantly *Rhacomitrium lanuginosum*), *Cassiope tetragona*, other unidentified vascular plants. Other Varieties Noted: cotton, other lichens.

Site 29

Photographs:	One landscape photo; one closeup photo.
Video:	Tape #1, 1:25:28 - 1:29:20.
Formation/Unit:	Watts Group.
Dominant Lithology:	Basalt.
General Information:	Surface covered by rocks (typically <70 cm) of basaltic composition.. The rocks weather tan and orange in small patches, but otherwise are coloured much as the materials at, e.g., Sites 23 and 24.
Munsell Colours:	Fresh surfaces: greenish gray (5G 6/1). Exposed surfaces: greenish gray (5GY 6/1).
Samples:	8 basalt samples (all <9 cm).
Thin Section:	Thin Section *29-1*: Sample composed mainly of actinolite (<0.2 mm) which forms pseudomorphs after augite. Also present are epidote (<0.2 mm; replacing plagioclase feldspar) and calcite (in a vein).
Weathering State:	Weathered greenish gray from greenish gray.
Vegetation:	Cover Rank: 2-3. Significant Varieties: green/black lichens, moss (predominantly *Rhacomitrium lanuginosum*), *Cassiope tetragona*, grass, *Salix spp.* Other Varieties Noted: None.

Site 30

Photographs:	Two landscape photos; one closeup photo.
Video:	Tape #1, 1:30:33 - 1:35:06.
Formation/Unit:	Watts Group.
Dominant Lithology:	Basalt.
General Information:	Outcrops of basaltic bedrock (outcrops typically 1-5 m). Loose rocks are also present (typically <30 cm). Site located at small but distinctive H-shaped lake.
Munsell Colours:	Fresh surfaces: greenish gray (5G 6/1). Exposed surfaces: ~dark greenish gray (5GY 4/1).
Samples:	5 basalt samples (all <6 cm).
Thin Section:	Thin Section *30-1*: Sample composed of actinolite (<0.1 mm), epidote (<0.05 mm), albite (<0.05 mm), and calcite (<0.6 mm).
Weathering State:	Weathered greenish gray from greenish gray.
Vegetation:	Cover Rank: 2-3. Significant Varieties: green/black lichens (including *Orphniospora moriopsis*), grass, moss (predominantly *Rhacomitrium lanuginosum*), *Salix spp.* Other Varieties Noted: None.

Site 31

Photographs:	Two landscape photos; one closeup photo.
Video:	Tape #1, 1:35:06 - 1:37:27.
Formation/Unit:	Watts Group.
Dominant Lithology:	Basalt.
General Information:	Large bedrock outcrops dominate (exposures have dimensions on the order of 10's of metres). Site located at distinctive "double lake".
Munsell Colours:	Fresh surfaces: greenish gray (5G 6/1). Exposed surfaces: dark greenish gray (5GY 4/11) to light olive gray (5Y 6/1).
Samples:	5 basalt samples (< 11 cm).
Thin Section:	None.
Weathering State:	Weathered greenish gray from greenish gray. Green/black lichen significant.
Vegetation:	Cover Rank: 2.-3. Significant Varieties: green/black lichens (including *Orphniospora moriopsis*), grass, moss (predominantly *Rhacomitrium lanuginosum*), *Cassiope tetragona*, *Salix spp.* Other Varieties Noted: Other lichens.

Site 32

Photographs:	Two landscape photos; one closeup photo.
Video:	Tape #1, 1:37:27 - 1:40:30.
Formation/Unit:	Watts Group.
Dominant Lithology:	Basalt.
General Information:	Large bedrock outcrops dominate (exposures have dimensions on the order of 10's of metres). Site properties are very similar to those of Site 31.
Munsell Colours:	Fresh surfaces: greenish gray (5G 6/1). Exposed surfaces: greenish gray to light olive gray (5Y 6/1).
Samples:	7 basalt samples (12-4 cm).
Thin Section:	None.
Weathering State:	Weathered greenish gray and olive from greenish gray.
Vegetation:	Cover Rank: 2-3. Significant Varieties: green/black lichens (including *Orphniospora moriopsis*), grass, moss (predominantly *Rhacomitrium lanuginosum*), *Cassiope tetragona*, *Salix spp.* Other Varieties Noted: None.

Site 33

Photographs:	Two landscape photos; one closeup photo.
Video:	Tape #1, 1:41:47 - 1:43:33.
Formation/Unit:	Watts Group.
Dominant Lithology:	Peridotite.
General Information:	Outcrop of tan-weathering ultramafic bedrock.
Munsell Colours:	Fresh surfaces: ~medium gray (N5). Most exposed surfaces: very pale orange (10YR 8/2) to grayish orange (10YR 7/4).
Samples:	7 peridotite samples (<9 cm).
Thin Section:	Thin Section *33-1*: Sample is almost entirely serpentinized (serpentine crystals typically ~0.05 mm). Trains of opaques (possibly magnetite; trains are ~0-.05 mm wide) extend for up to 10 mm. Olivine or augite are also present (crystals typically ~0.5 mm).
Weathering State:	Rocks weathered pale orange from gray.
Vegetation:	Cover Rank: 1-0. Significant Varieties: white/green/black lichens on rock surfaces, moss (predominantly *Rhacomitrium lanuginosum*), *Salix spp.*, *Cassiope tetragona*, grass. Other Varieties Noted: None.

Site 34

Photographs:	One landscape photo; two closeup photos.
Video:	Tape #1, 1:43:33 - 1:48:56.
Formation/Unit:	Watts Group.
Dominant Lithology:	Peridotite.
General Information:	Outcrop of ultramafic rock. Most rock is weathered reddish-tan. Large serpentine masses extend for cm's to m's in bedrock. This site is representative of much of the surrounding bedrock outcrop, apart from the zone that makes up Site 33 (which is weathered a tan colour).
Munsell Colours:	Fresh surfaces: dark gray (N3) and crystals that are dark greenish gray (SGY 4/1). Exposed surfaces: light brown (5YR 5/6) to moderate brown (5YR 4/4).
Samples:	5 peridotite samples (11-5 cm).
Thin Section:	None.
Weathering State:	Rocks weathered brown from gray/green.
Vegetation:	Cover Rank: 0-1. Significant Varieties: None. Other Varieties Noted: None.

Site 35

Photographs:	One landscape photo only.
Video:	None.
Formation/Unit:	Spartan Group.
Dominant Lithology:	Pelite.
General Information:	Pelitic rocks on edge of much larger outcrop of ultramafic rocks. This site is very small, and, because of time constraints, was not examined as thoroughly as the other sites.
Munsell Colours:	Fresh surfaces: medium dark gray (N4). Exposed surfaces: lighter shades of gray.
Samples:	1 pelite (biotite schist) sample (11 cm).
Thin Section:	None.
Weathering State:	Weathered to lighter shades of gray.
Vegetation:	Cover Rank: 3-4. Significant Varieties: grass, green/black lichens, moss (predominantly *Rhacomitrium lanuginosum*). Other Varieties Noted: None.

Site 36

Photographs:	One landscape photo; one closeup photo.
Video:	Tape #2, 0:7:41 - 0:10:16.
Formation/Unit:	Chukotat Group.
Dominant Lithology:	Basalt.
General Information:	Both a) tan-weathering and b) dark greenish rocks present (both sampled). Bedrock exposure <20%. Most rocks <60 cm, but some >1 m. Metre-scale, lens-shaped features in bedrock outcrops may be flattened pillows.
Munsell Colours:	Fresh surfaces: greenish gray (5G 6/1). Exposed surfaces: moderate brown (5YR 4/4) to light brown (5YR 5/6).
Samples:	6 basalt samples (all <9 cm).
Thin Section:	None.
Weathering State:	Weathered to brown from gray.
Vegetation:	Cover Rank: 0-1. Significant Varieties: green/black lichens (including *Rhizocarpon geographicum*), grass, moss (predominantly *Rhacomitrium lanuginosum*). Other Varieties Noted: None.

Site 37

Photographs:	Three landscape photos; one closeup photo.
Video:	Tape #2, 0:11:23 - 0:13:32.
Formation/Unit:	Chukotat Group.
Dominant Lithology:	Basalt.
General Information:	Large site consisting mainly of bedrock exposures, which are continuous over 10's of metres. Loose rocks of a wide variety of sizes are also present. Metre-scale, lens-shaped features in bedrock outcrops may be flattened pillows.
Munsell Colours:	Fresh surfaces: greenish gray (5G 6/1). Exposed surfaces: moderate brown (5YR 4/4) to light brown (5YR 5/6).
Samples:	4 samples (12-9 cm).
Thin Section:	None.
Weathering State:	Weathered to brown from gray.
Vegetation:	Cover Rank: 0. Significant Varieties: green/black lichens (including *Rhizocarpon geographicum*). Other Varieties Noted: None.

Site 38

Photographs:	One landscape photo; one closeup photo.
Video:	Tape #2, 0:13:22 - 0:15:05.
Formation/Unit:	Chukotat Group.
Dominant Lithology:	Basalt.
General Information:	Wide range of rock sizes; rocks typically <1.5 m.
Munsell Colours:	Fresh surfaces: greenish gray (5GY 6/1) to medium gray (N4). Exposed surfaces: moderate brown (5YR 4/4) to light brown (5YR 5/6).
Samples:	9 samples (all <9 cm).
Thin Section:	Thin Section *38-1*: Sample is very much like thin section 51-1, but degree of alteration is greater (no plagioclase feldspar seen; all replaced by a high-birefringence mineral; crystals typically <<0.4 mm).
Weathering State:	Weathered brown from gray.
Vegetation:	Cover Rank: 0. Significant Varieties: green/black lichens (including *Rhizocarpon geographicum*). Other Varieties Noted: None.

Site 39

Photographs:	One landscape photo; one closeup photo.
Video:	Tape #2, 0:17:12 - 0:17:44.
Formation/Unit:	Chukotat Group.
Dominant Lithology:	Basalt.
General Information:	Large basalt boulders (typically <2 m; a minority of boulders are larger).
Munsell Colours:	Fresh surfaces: medium light gray (N6) to greenish gray. Exposed surfaces: grayish orange (10YR 7/4) to pale yellowish brown (10YR 6/2) to light brown (10YR 5/6).
Samples:	4 samples (10-5 cm).
Thin Section:	Thin Section *39-1*: Sample consists mainly of fibrous and radiating actinolite (crystals typically <0.2 mm); thus, the sample is perhaps best labelled as amphibolite. Also present are epidote and small amounts of albite and opaques (possibly magnetite).
Weathering State:	Weathered brown from gray.
Vegetation:	Cover Rank: 0. Significant Varieties: green/black lichens. Other Varieties Noted: None.

Site 40

Photographs:	One landscape photo; one closeup photo.
Video:	Tape #2, 0:17:44 - 0:19:01.
Formation/Unit:	Spartan Group.
Dominant Lithology:	Pelite.
General Information:	Mostly small rocks (typically <40 cm, but most ~2-15 cm). Mafic / ultramafic rocks are present (see samples).
Munsell Colours:	Fresh pelite surfaces: ~medium gray (N5). Fresh mafic/ultramafic surfaces: greenish gray. Exposed mafic or ultramafic surfaces: grayish orange (10YR 7/4) to light brown (5YR 5/6).
Samples:	9 (all <9 cm); 5 samples are pelite, and 4 are mafic / ultramafic. Vegetation sampled.
Thin Section:	None.
Weathering State:	Surface minerals of pelite not appreciably altered. Surface coating by green/black lichen is significant.
Vegetation:	Cover Rank: 3. Significant Varieties: grass, *Salix spp.*, black/green lichens on rocks. Other Varieties Noted: white lichens.

Site 41

Photographs:	One landscape photo; one closeup photo.
Video:	Tape #2, 0:19:01 - 0:21:26.
Formation/Unit:	Spartan Group.
Dominant Lithology:	Pelite.
General Information:	Mostly small rocks (typically <40 cm, but most ~2-10 cm), many of which are frost sorted into irregular groupings that have dimensions of ~1-1.5 m. One sample taken from the site is a basalt.
Munsell Colours:	Fresh and weathered pelite surfaces: medium dark gray (N4). Mafic and ultramafic rocks weathered pale yellowish brown.
Samples:	4 pelite samples (all <11 cm); one basalt sample.
Thin Section:	None.
Weathering State:	Surfaces of pelite not appreciably altered.
Vegetation:	Cover Rank: 4-3. Significant Varieties: green/black lichens, *Salix spp.*, moss (predominantly *Rhacomitrium lanuginosum*), grass. Other Varieties Noted: white lichens.

Site 42

Photographs:	One landscape photo; one closeup photo.
Video:	Tape #2, 0:21:26 - 0:23:24.
Formation/Unit:	Site rests on Spartan Group rocks.
Dominant Lithology:	n/a.
General Information:	Essentially full vegetation cover dominated by green grass. Standing water is present in the form of small (5-8 m) interconnected ponds.
Munsell Colours:	n/a.
Samples:	Vegetation sampled.
Thin Section:	None.
Weathering State:	n/a.
Vegetation:	Cover Rank: 5. Significant Varieties: grass. Other Varieties Noted: cotton.

Site 43

Photographs:	Two landscape photos; one closeup photo.
Video:	Tape #2, 0:23:24 - 0:26:00.
Formation/Unit:	Spartan Group.
Dominant Lithology:	Pelite and basalt.
General Information:	Mixed pelite (typically <20 cm) and mafic lithologies (basalts; typically <10 cm).
Munsell Colours:	Fresh and exposed pelite surfaces: medium gray (N5) to light gray (N7). Fresh mafic surfaces: greenish gray (5GY 6/1). Exposed mafic/ultramafic surfaces: dark yellowish orange (10YR 6/6) to ~light olive gray (5Y 6/1).
Samples:	6 pelite samples (<10 cm); 3 basalt samples (<10 cm).
Thin Section:	None.
Weathering State:	Surfaces of pelite not appreciably altered. Mafic / ultramafic surfaces weathered orange and gray from greenish gray.
Vegetation:	Cover Rank: 2-3. Significant Varieties: green/black lichens, *Cassiope tetragona*, moss (predominantly *Rhacomitrium lanuginosum*), grass. Other Varieties Noted: None.

Site 44

Photographs:	Two landscape photos; two closeup photos.
Video:	Tape #2, 0:27:53 - 0:31:34.
Formation/Unit:	Spartan Group.
Dominant Lithology:	n/a.
General Information:	Complete vegetation cover.
Munsell Colours:	n/a.
Samples:	Vegetation sampled.
Thin Section:	None.
Weathering State:	n/a.
Vegetation:	Cover Rank: 5. Significant Varieties: grass and shrubs dominate; shrubs heights are up to ~1 m. Other Varieties Noted: None.

Site 45

Photographs:	One landscape photo; one closeup photo.
Video:	Tape #2, 0:31:34 - 0:35:27.
Formation/Unit:	Spartan Group.
Dominant Lithology:	Pelite and basalt.
General Information:	Pelite and mafic lithologies (typically <30 cm).
Munsell Colours:	Fresh pelite surfaces: light gray (N7). Exposed pelite surfaces: darker gray. Fresh mafic surfaces: greenish gray (5GY 6/1). Exposed mafic / ultramafic surfaces: pale yellowish brown (10YR 6/2) to grayish orange (10YR 7/4).
Samples:	7 samples (all <12 cm); 5 samples are pelite (schist); 2 are basalts.
Thin Section:	None.
Weathering State:	Surfaces of pelite not appreciably altered. Mafic surfaces weathered orange and gray from greenish gray.
Vegetation:	Cover Rank: 3 -4. Significant Varieties: Green/black lichens, *Cassiope tetragona*, grasses, white lichen, moss (predominantly *Rhacomitrium lanuginosum*). Other Varieties Noted: None.

Site 46

Photographs:	Camp site.
Video:	Tape #2, 0:37:10 - 0:50:49, and 0:52:00 - 0:57:52.
Formation/Unit:	Spartan Group.
Dominant Lithology:	n/a.
General Information:	This is the main camp site. Essentially full vegetation cover, with scattered rocks and boulders present (boulders are up to several metres across).
Munsell Colours:	n/a.
Samples:	Vegetation sampled in detail.
Thin Section:	None.
Weathering State:	n/a.
Vegetation:	Cover Rank: 5. Significant Varieties: grass and moss (predominantly *Rhacomitrium lanuginosum*) dominate. Other varieties noted: *Salix spp.*, cotton, *Papaver radicatum*, green/black lichens, *Cassiope tetragona*, *Oxyria digyna*, mushrooms, other lichens.

Site 47

Photographs:	One landscape photo; one closeup photo.
Video:	Tape #2, 1:01:30 - 1:05:11.
Formation/Unit:	Spartan Group.
Dominant Lithology:	Pelite and basalt.
General Information:	Pelite and mafic / ultramafic lithologies (rocks typically <40 cm).
Munsell Colours:	Fresh and exposed pelite surfaces: medium light gray (N6) to medium dark gray (N4). Fresh peridotite surfaces: medium dark gray (N4); exposed surfaces moderate brown (5YR 4/4). Fresh basalt surfaces: greenish gray (5GY 6/1); exposed surfaces pale yellowish orange (10YR 8/6) to light brown (5YR 5/6).
Samples:	6 pelite samples (all <11 cm), 1 ultramafic (peridotite) sample (8 cm), and 9 mafic (basalt) samples (all <13 cm; variable green/black lichen cover).
Thin Section:	None.
Weathering State:	Surfaces of pelite not appreciably altered. Mafic and ultramafic surfaces weathered orange and brown from greenish gray and gray.
Vegetation:	Cover Rank: 2-1. Significant Varieties: Green/black lichens, grass, moss (predominantly *Rhacomitrium lanuginosum*), *Cassiope tetragona*. Other Varieties Noted: other lichens.

Site 48

Photographs:	One landscape photo; one closeup photo.
Video:	Tape #2, 1:09:56 - 1:16:43.
Formation/Unit:	Site is located on materials of the Spartan Group, but rocks at surface are mainly basaltic.
Dominant Lithology:	Basalt.
General Information:	Mafic and minor ultramafic rocks (typically < 40 cm, some up to ~1 m). No pelite rocks are present.
Munsell Colours:	Fresh basalt surfaces: greenish gray (5GY 6/1 to 5G 6/1); exposed surfaces: pale yellowish orange (10YR 8/6) to moderate brown (5YR 3/4).
Samples:	10 basalt samples (all <10 cm).
Thin Section:	None.
Weathering State:	Basalt weathered orange and brown from greenish gray.
Vegetation:	Cover Rank: 3-2. Significant Varieties: grass, moss (predominantly *Rhacomitrium lanuginosum*), *Salix spp.* Other Varieties Noted: None.

Site 49

Photographs:	One landscape photo; one closeup photo (disposable camera).
Video:	Tape #2, 1:16:43 - 1:26:43.
Formation/Unit:	Spartan Group.
Dominant Lithology:	Pelite.
General Information:	Elongate bedrock outcrops, typically 1-2 m across and several metres in length, separated by vegetation-covered fines. Small ponds (metres across) are present. Tan-weathering mafic and ultramafic rocks are present but minor.
Munsell Colours:	Fresh and weathered surfaces: medium dark gray (N4) to light gray (N7).
Samples:	5 pelite samples (11-7 cm). Green/black lichen cover not extensive on samples.
Thin Section:	Thin Section *49-1*: Sample is a schistose pelite that is mainly composed of quartz (typically 0.05 mm), plagioclase feldspar (typically <0.2 mm), and chlorite (laths typically <0.05 mm). Also present are muscovite (sericite), calcite, and opaques.
Weathering State:	Surfaces of pelite materials not appreciably altered.
Vegetation:	Cover Rank: 3-4. Significant Varieties: grass, moss (predominantly *Rhacomitrium lanuginosum*), *Cassiope tetragona*, green/black lichens (including *Lecidella sp.*). Other Varieties Noted: other lichens.

Site 50

Photographs:	One landscape photo; one closeup photo.
Video:	Tape #2, 1:29:31 - 1:32:24.
Formation/Unit:	Chukotat Group.
Dominant Lithology:	Basalt.
General Information:	Rocks typically <40 cm; some up to ~1.2 m.
Munsell Colours:	Fresh basalt surfaces: greenish gray (5GY 6/1); exposed surfaces: light brown (5YR 5/6) to moderate brown (5YR 3/4).
Samples:	7 basalt samples (all <10 cm).
Thin Section:	None.
Weathering State:	Basalt weathered brown from greenish gray.
Vegetation:	Cover Rank: 0. Significant Varieties: None. Other Varieties Noted: None.

Site 51

Photographs:	One landscape photo; one closeup photo.
Video:	Tape #2, 1:32:24 - 1:37:44.
Formation/Unit:	Chukotat Group.
Dominant Lithology:	Basalt.
General Information:	Rocks typically <60 cm.
Munsell Colours:	Fresh basalt surfaces: greenish gray (5GY 6/1) to dark greenish gray (5GY 4/1); exposed surfaces: ~dark yellowish brown (10YR 4/2) and light brown (5YR 5/6).
Samples:	10 samples (all <10 cm); all samples basalt except 1 (ultramafic). Green/black lichen cover sparse to extensive.
Thin Section:	Thin Section *51-1*: Sample mainly composed of plagioclase feldspar (albite: laths typically <0.2 mm) and epidote (typically <0.05 mm). Also present are actinolite (fibrous and radiating) and chlorite.
Weathering State:	Basalt weathered brown from greenish gray.
Vegetation:	Cover Rank: 0. Varieties Noted: moss (predominantly *Rhacomitrium lanuginosum*), white lichens, grass, *Cassiope tetragona*. Other Varieties Noted: None.

Site 52

Photographs:	One landscape photo; one closeup photo.
Video:	Tape #3, 0:25:41 - 0:35:32.
Formation/Unit:	Unnamed peridotite intrusion.
Dominant Lithology:	Peridotite.
General Information:	1) Peridotite (>80% cover); mostly boulders (typically 0.6 - 1.2 m); larger boulders, as well as bedrock outcrops, are also present, and 2) scattered gray rounded rocks (<20% cover; rocks typically <40 cm).
Munsell Colours:	Fresh peridotite surfaces: dark gray (N3); exposed surfaces: light brown (5YR 5/6) to moderate brown (5YR 3/4).
Samples:	11 peridotite samples (all <14 cm).
Thin Section:	Thin Section *52-1*: Sample consists mainly of serpentine pseudomorphs after olivine, and augite which has survived serpentinization (typically ~2 mm). Also present are opaques (possibly chromite) and Fe-oxides. Thin Section *52-2*: Sample is a "mafic tonalite", and is thus much more felsic than might be expected for the immediate area. Sample is mainly composed of plagioclase feldspar and quartz (crystals typically <0.8 mm). Also present are biotite, possibly sericite, and epidote (euhedral; often found in plagioclase crystals).
Weathering State:	Peridotite weathered brown from dark gray.
Vegetation:	Cover Rank: 0. Varieties Noted: moss (predominantly *Rhacomitrium lanuginosum*), *Cassiope tetragona*, grass, green/black lichens. Other Varieties Noted: other lichens.

Site 53

Photographs:	One landscape photo; one closeup photo.
Video:	Tape #3, 0:35:32 - 0:41:49.
Formation/Unit:	Unnamed peridotite intrusion.
Dominant Lithology:	Peridotite.
General Information:	1) Peridotite (>90% cover); mainly boulders (typically 30 - 120 cm, but 2-3 m not uncommon), and 2) gray, rounded rocks variably covered by green/black lichens (<10% cover; rocks typically <40 cm).
Munsell Colours:	Fresh peridotite surfaces: dark gray (N3) to grayish black (N2); exposed surfaces: pale yellowish brown (10YR 6/2) to dark yellowish brown (10YR 4/2) to moderate brown (10YR 4/4). Gray rock surfaces: greenish gray (5GY 6/1); exposed surfaces: pale yellowish brown (10YR 6/2) to dark yellowish brown (10YR 4/2) to moderate brown (10YR 4/4).
Samples:	10 peridotite samples (all <9 cm); 3 basalt samples.
Thin Section:	None.
Weathering State:	Peridotite weathered brown from dark gray.
Vegetation:	Cover Rank: 0. Varieties Noted: *Cassiope tetragona*, moss (predominantly *Rhacomitrium lanuginosum*), grass. Other Varieties Noted: Green/black lichens.

APPENDIX C: List of Original Programs

List of Programs

A number of programs were written by the author for this research, including those of the neural network and evidential reasoning classifiers. A list of the key programs written for this research is given below, and individual programs are described on subsequent pages:

A) Test and Training File Generator: *R99_51.C*

B) Neural Network Programs:	Training:	*N400X.C, N401XJ2.C, N401XJ4.C, N401XJ5.C,*
	Classification:	*FEEDX.C*
	Consensus:	*PARAL294.C, PARAL237.C*
C) Evidential Reasoning Programs:	Interpolation:	*INT256.C*
	Classification:	*ER129FX.C*
	Consensus:	*ER129FXVA14.C*

List of C-Code In this Document

C-Code for *ER129F6.C* is given in Appendix D.
C-Code for *ER129F10VA14.C* is given in Appendix E.
C-Code for *N400X.C* is given in Appendix F.
C-Code for *FEED9.C* is given in Appendix G.

Test and Training File Generation

R99_51.C

Purpose: To generate test and training files from ground-truth files.

Inputs:

"p.txt": - a parameter file listing number of classes and sources
- example: 14
4
(i.e., 14 classes and 4 sources)

"1.txt": - input files giving source data for each class
"2.txt" - example: 1 3
"3.txt" 46 39 63 20
etc. 44 41 66 18
49 38 62 19
(i.e., class number 1; number of pixels in class:3; data is given for 4 sources and 3 pixels)

Outputs: a series of outputs which can be submitted as inputs to NN, ER, and ML programs (see below).

Evidential Reasoning Programs

INT256.C

Purpose: To interpolate and extrapolate "continuous" (i.e., non-thematic) training data. The program as compiled uses a bin size of 51.

Inputs: any name - list of data to be extrapolated (file specified by user at command line)
- example: 44
41
39
(i.e., each file is simply a list of numbers; all files end with *999*)

Outputs: "out.txt" - extrapolated and interpolated data; format same as input.

ER129FX.C (and ER129FXVA14.C - see "variations" below)

Purpose: To classify test data or image data. The "X" in *ER129FX.C* corresponds to a number identifying a particular variation (see below).

Inputs: "level_0.txt" - source data for test pixels or full image
"level_1.txt" - example: 46
"level_2.txt" 44
etc. (i.e., each file is simply a list of numbers for a particular source)

"c0_s0.txt" - training data for a particular class and source
"c0_s1.txt" - example: 48
"c1_s0.txt" 45
"c1_s1.txt" 46
etc. (i.e., each file is simply a list of numbers for a particular source and class combination; all files end with *999*)

Outputs: "out.img" - file of classifications
- example: 2
6
(i.e., the file is a simple list of integers corresponding to classes)

(continued on following page)

Variations: *ER129F.C* - 4 sources, 14 classes; *ER129F10.C* - 4 sources, 10 classes
ER129F9.C - 4 sources, 9 classes; *ER129F6.C* - 4 sources, 6 classes
ER129F7.C - 4 sources, 7 classes;
ER129F6V.C - 4S/6C, and verbose (used to verify ER functionality in Ch.5).
ER129FXVA14.C - *X* is #classes (6, 7, 9, 10, or 14), 4 sources, verbose, reads 10 sets of neural network output-node activations as input (these data are produced by,e.g., *FEED9E.C*)

Neural Network Programs

The two main elements of neural network executions are *N400X.C*, which trains a network, and *FEEDX.C* (or, more specifically, a particular variant of *FEEDX.C*; e.g., *FEED6.C*), which subsequently classifies data based on the weights and biases produced by *N400X.C*. Note that, while an "X" in a program name listed elsewhere in this appendix represents a particular version number, the "X" in *N400X.C* is part of the actual name of the program.

N400X.C

Purpose: To train a neural network based on training data. The weight and bias outputs of this program are inputs to the *FEEDX.C* series of programs.

Inputs:

"param.txt" - is a parameter file that defines key network attributes
- example (text in brackets not included):

```
2       (number of hidden layers)
4       (number of nodes in input layer)
7       (number of nodes in 1st hid layer)
7       (number of nodes in 2nd hid layer)
7       (number of nodes in output layer)
0.1     (learning parameter)
0.9     (momentum parameter)
0.0     (bias momentum parameter)
5000    (maximum number of iterations)
60      (acceptable tss error)
294     (number of training pixels in train.txt)
```

"train.txt" - lists training data
- example:

```
0.0343  0.03934  0.7743  0.2343 0
0.0319  0.04146  0.7317  0.2299 0
0.0387  0.03843  0.7433  0.2149 1
```

(i.e., file lists source data for two pixels in class 0 and one pixel in class 1; there are four sources; data must be normalized to the range 0-1; classes are labelled from 0).

Outputs:

"weight.txt" - a simple list of weight values; used as input to *FEEDX.C*

"bias.txt" - a simple list of bias values; used as input to *FEEDX.C*

"tss.txt" - an iteration-by-iteration record of tss error

Variations: *N401XJ2.C* - jitter = ±2; *N401XJ4.C* - jitter = ±4; *N401XJ5.C* - jitter = ±5

FEEDX.C

Purpose:	To classify test data or image data. The "X" in *FEEDX.C* corresponds to a number/letter designation corresponding to a particular variation (below).	
Inputs:	"weight.txt"	- a simple list of weight values produced by *N400X.C*
	"bias.txt"	- a simple list of bias values produced by *N400X.C*
	"param.txt"	- the same parameter file used by *N400X.C*
	"train0.txt" "train1.txt" etc.	- source data for test data or image data; sources labelled from 0; data are normalized to range 0-1 in same manner. as the training data used as input to *N400X.C*
Outputs:	"output.txt"	- file of classifications - example: 2 6 (i.e., file is a list of integers corresponding to classes, numbered from 0; a value of 1 was typically added to each number in this file, to make class numbers match those used in this document)
Variations:	*FEED6.C*	- Melville Island Field Area classifications (635208 pixels)
	FEED6_Q.C	- Cape Smith Belt Field Area classifications (853600 pixels)
	FEED9.C	- used for Melville Island B, C, D, and E Series (294 pixels)
	FEED9B.C	- used for Cape Smith Belt A Series (237 pixels)
	FEED9E.C	- used for Melv. I. (294 pix.), but also saves output activations to "active.txt" (e.g., for input to *ER129FXVA14.C*), normalized highest activation to "confid.txt", and normalized highest-minus-2nd-highest activations to "diff.txt".
	FEED9G.C	- as *FEED9E.C*, but used for Cape Smith Belt (237 pixels)

PARAL294.C

Purpose:	To generate a majority-vote consensus of 10 different neural network classifications.	
Inputs:	"1.txt" "2.txt" etc	- each of these 10 files is a file generated by FEEDX.C, renamed from "output.txt" (and, as noted above, with 1 typically added to all values) .
Outputs:	"out.img"	- file of classifications, in same format as "output.txt" above.
Variations:	*PARAL237.C* - as PARAL294.C, but made for 237 pixels instead of 294 *PARAFULL.C / PARAFULQ.C* - as above, but for 635208 / 853600 pixels	

APPENDIX D: Evidential Reasoning Source Code

```
(ER_129f7.C)
#include <stdio.h>
#include <math.h>

#define NUM_CLASSES 7
#define NUM_LEVELS 4
#define SPECTRUM 256
#define NUM_TEMP_RESULTS 237
#define NUM_REPS_OF_SECOND_LOOP_CALL 1    /* thus 294 pixels classified */
#define CLASSIFICATION_SUM_STAGE 2        /* 1 = old 2_3 (ie.lev1_2) orth sum */
                                          /* 100 represents a 1 level run     */

void set_main_variables_to_zero(
        float data[NUM_CLASSES][NUM_LEVELS][SPECTRUM],int *prin,
        float num_read[NUM_CLASSES][NUM_LEVELS],
        float frequency[NUM_CLASSES][NUM_LEVELS],
        float test[],float frame[],float sum[NUM_LEVELS][NUM_CLASSES],
        float frame_new[]);

void read_signature_data(float data[NUM_CLASSES][NUM_LEVELS][SPECTRUM],
        float num_read[NUM_CLASSES][NUM_LEVELS]);

void calculate_frequency_matrix(float freq[NUM_CLASSES][NUM_LEVELS],
        float data[NUM_CLASSES][NUM_LEVELS][SPECTRUM],
        float num_read[NUM_CLASSES][NUM_LEVELS],float test[],int prin);

void calculate_frame_of_discernment(float frame[],
        float frequency[NUM_CLASSES][NUM_LEVELS],int prin);

void calculate_orthogonal_sum_of_first_two_layers(
        float sum[NUM_LEVELS][NUM_CLASSES],
        float frequency[NUM_CLASSES][NUM_LEVELS],float frame[],int prin,
        float k[],float total[],float frame_new[]);

void calculate_orthogonal_sum_of_remaining_layers(int combo,
        float sum[NUM_LEVELS][NUM_CLASSES],
        float frequency[NUM_CLASSES][NUM_LEVELS],
        float frame[],int prin,float k[],float total[],float frame_new[]);

int classify(float sum[NUM_LEVELS][NUM_CLASSES],
        float frequency[NUM_CLASSES][NUM_LEVELS]);

void write_results(int temp[]);

void info();


main()
{
  FILE *fp_level[NUM_LEVELS];   /* file pointers for reading input data layers */
  char *ch;                     /* pointer for changing level file names for reading */
  char level_file[12];          /* string for reading level files */
  float num_read[NUM_CLASSES][NUM_LEVELS];     /* number of values in each class/source input file */
  float data[NUM_CLASSES][NUM_LEVELS][SPECTRUM]; /* records frequency of occurrence for 0-SPECTRUM */
  float test[NUM_LEVELS];                   /* test pixel for set of sources*/
  float frequency[NUM_CLASSES][NUM_LEVELS]; /* frequency of occurrence for each class/source */
  float frame[NUM_LEVELS];                  /* frame of discernment for each source */
  float sum[NUM_LEVELS][NUM_CLASSES];       /* orthogonal summation variable */
  float k[NUM_LEVELS-1];                    /* 'K' variable for s1_s2 */
  float frame_new[NUM_LEVELS-1];            /* new frame of discernment after s1_s2 */
  float total[NUM_LEVELS-1];                /* a sum value used in orth.sum. calculations */
  int prin;                                 /* print variable... if = 1 then verbose */
  int mainloop;                             /* counter for the main loop */
  int temporary[NUM_TEMP_RESULTS];          /* temp values put here until sent to hdrive */
  int combo;                                /* value corresponding to 1_2,2_3,3 etc orth sums */
```

```
  int n;                          /* number read in from file */
  int lev;                        /* loop variable for cycling through level reading loops */
  int classification_sum_stage; /* for checking 100 value (1 level case) */
  long int second_loop;           /* number of times 2nd loop is performed */
  long int a,b,c;                 /* used as loop variables */

  info();

  set_main_variables_to_zero(data,&prin,num_read,frequency,test,frame,
        sum,frame_new);
  prin=1;
  read_signature_data(data,num_read);

  printf("\nOpening level_X.txt files... \n");
  strcpy(level_file,"level_X.txt");
  for(lev=0;lev<NUM_LEVELS;lev++)  {
    ch=&level_file[6];
    *ch=(lev+48);                 /* NOTE: this technique will not allow >9 levels */
    fp_level[lev]=fopen(level_file,"r");
    if(fp_level[lev]==NULL)  {
      printf("\nFile %s cannot be opened or does not exist!\n",level_file);
      exit();
    }
    printf("Opened level_file: %s\n",level_file);
  }
  printf("\nEach '*' below represents %d pixels classified.\n",NUM_TEMP_RESULTS);
  printf("\nPROCESSING...\n");  /* **** main loop begins below **** */

  for(mainloop=0;mainloop<NUM_REPS_OF_SECOND_LOOP_CALL;mainloop++)  {
    for(second_loop=0;second_loop<NUM_TEMP_RESULTS;second_loop++)  {
      if(prin==1) printf("\n********** second_loop=%ld *********\n",second_loop);
      for(lev=0;lev<NUM_LEVELS;lev++)  {
        printf("\nNow reading source data for a pixel...");

        fscanf(fp_level[lev],"%f",&test[lev]);  /* read test level data */
        if(test[lev]==(-1)) test[lev]=360;      /* convert if aspect data */
        printf("\ntest[%d]=%f",lev,test[lev]);
      }
      printf("\n");

      calculate_frequency_matrix(frequency,data,num_read,test,prin);

      calculate_frame_of_discernment(frame,frequency,prin);

      calculate_orthogonal_sum_of_first_two_layers(sum,frequency,frame,prin,
                k,total,frame_new);

      for(combo=1;combo<(NUM_LEVELS-1);combo++)  {
        calculate_orthogonal_sum_of_remaining_layers(combo,sum,frequency,
          frame,prin,k,total,frame_new);
      }
      temporary[second_loop]=classify(sum,frequency);
    }
    write_results(temporary);

    if(classification_sum_stage==100)  {    /* slows down Pentium write  */
      printf("\nmainloop=%d second_loop=%ld\n",mainloop,second_loop);
    }
  }                                         /* **** end of mainloop **** */
  info();

  printf("Done.");
}                                           /* **** end of function main() */


void set_main_variables_to_zero(
        float data[NUM_CLASSES][NUM_LEVELS][SPECTRUM],int *prin,
        float num_read[NUM_CLASSES][NUM_LEVELS],
```

```
        float frequency[NUM_CLASSES][NUM_LEVELS],
        float test[],float frame[],float sum[NUM_LEVELS][NUM_CLASSES],
        float *frame1_2)
{
  int loop1,loop2,loop3;

  for(loop1=0;loop1<NUM_CLASSES;loop1++)  {
    for(loop2=0;loop2<NUM_LEVELS;loop2++)  {
      for(loop3=0;loop3<SPECTRUM;loop3++)  {
        data[loop1][loop2][loop3]=0;
      }
      num_read[loop1][loop2]=0;
      frequency[loop1][loop2]=0;
      sum[loop2][loop1]=0;
      test[loop2]=0;
      frame[loop2]=0;
    }
    *prin=0;
  }
  *frame1_2=0;
}


void read_signature_data(float data[NUM_CLASSES][NUM_LEVELS][SPECTRUM],
        float num_read[NUM_CLASSES][NUM_LEVELS])
{
  FILE *fp;
  int loop1,loop2;
  long int loop3;
  int number;
  char signature_file[12];
  char *character;

  printf("\n");
  printf("Reading data files for %d classes and %d sources\n\n",
        NUM_CLASSES,NUM_LEVELS);

  for(loop1=0;loop1<(NUM_CLASSES);loop1++)  {
    for(loop2=0;loop2<(NUM_LEVELS);loop2++)  {/* below assumes #sources<10 */
      if(loop1<10)  {
        strcpy(signature_file,"cX_sX.txt");
        character=&signature_file[1];
        *character=(loop1+48);
        character=&signature_file[4];
        *character=(loop2+48);

        printf("Opening signature file: %s\n",signature_file);

        fp=fopen(signature_file,"r");
        if(fp==NULL)  {
          printf("\nFile %s cannot be opened or does not exist!\n",
                  signature_file);
          exit();
        }
        for(loop3=0;loop3>(-5);loop3++)  {
          fscanf(fp,"%d",&number);
          if(number==999) break;
          data[loop1][loop2][number]=data[loop1][loop2][number]+1;
        }
        num_read[loop1][loop2]=loop3;
        printf("num_read for loop1=%d loop2=%d is %f \n",loop1,loop2,num_read[loop1][loop2]);
        fclose(fp);
        printf("Just read class %d source %d \n",loop1,loop2);
      }
      if(loop1>9)  {                    /* this assumes not >19 classes */
        strcpy(signature_file,"c1X_sX.txt");
        character=&signature_file[2];
        *character=(loop1-10+48);
```

```
        character=&signature_file[5];
        *character=(loop2+48);

        printf("Opening signature file: %s\n",signature_file);

        fp=fopen(signature_file,"r");
        if(fp==NULL)  {
          printf("\nFile %s cannot be opened or does not exist!\n",
                  signature_file);
          exit();
        }
        for(loop3=0;loop3>(-5);loop3++)  {
          fscanf(fp,"%d",&number);
          if(number==999) break;
          data[loop1][loop2][number]=data[loop1][loop2][number]+1;
        }
        num_read[loop1][loop2]=loop3;
        printf("num_read for loop1=%d loop2=%d is %f \n",loop1,loop2,num_read[loop1][loop2]);
        fclose(fp);
        printf("Just read class %d source %d \n",loop1,loop2);
      }
    }
  }
}


void calculate_frequency_matrix(float freq[NUM_CLASSES][NUM_LEVELS],
        float data[NUM_CLASSES][NUM_LEVELS][SPECTRUM],
        float num_read[NUM_CLASSES][NUM_LEVELS],float test[],int prin)
{
  int a,b;
  int dummy1;
  float dummy2; /* these 3 dummy variables added to keep ccu compiler happy */
  float dummy3;

  for(a=0;a<NUM_CLASSES;a++)  {
    for(b=0;b<NUM_LEVELS;b++)  {
      dummy1=test[b];
      dummy2=data[a][b][dummy1];
      dummy3=num_read[a][b];
      freq[a][b]=dummy2/dummy3;
      if(prin==1)  {
        printf("frequency for a=%ld b=%ld is %f\n",a,b,freq[a][b]);
      }
    }
  }
}


void calculate_frame_of_discernment(float frame[],
        float frequency[NUM_CLASSES][NUM_LEVELS],int prin)
{
  int a,b;
  float sum_of_frequencies;

  for(b=0;b<NUM_LEVELS;b++)  {
    frame[b]=1;
    for(a=0;a<NUM_CLASSES;a++)  {
      frame[b]=frame[b]-frequency[a][b];
    }
    if(frame[b]<0)  {
      printf("HEY!  frame[b]<0!... = %f\n",frame[b]);
      frame[b]=0;
      sum_of_frequencies=0;
      for(a=0;a<NUM_CLASSES;a++)  {
        sum_of_frequencies=sum_of_frequencies+frequency[a][b];
      }
      if(prin==1)  {
```

```
        printf("Sum of frequencies: %f\n", sum_of_frequencies);
        printf("Frequencies normalized to 1.0: ");
      }
      for(a=0;a<NUM_CLASSES;a++)  {
        frequency[a][b]=frequency[a][b]/sum_of_frequencies;

        if(prin==1)  {
          printf(" %f ",frequency[a][b]);
        }
      }
    }
    if(prin==1)  {
      printf("\nframe [ %ld ] = %f \n",b,frame[b]);
    }
  }
}


void calculate_orthogonal_sum_of_first_two_layers(
        float sum[NUM_LEVELS][NUM_CLASSES],
        float frequency[NUM_CLASSES][NUM_LEVELS],float frame[],int prin,
        float k[],float total[],float frame_new[])
{
  int a,b;

  for(a=0;a<NUM_CLASSES;a++)  {
    sum[0][a]=frequency[a][0]*frequency[a][1] + frame[0]*frequency[a][1]
                        + frame[1]*frequency[a][0];
    if(prin==1)  {
    printf("sum[0][%ld] = %f \n",a,sum[0][a]);
    }
  }
  k[0] = 0;
  for(a=0;a<NUM_CLASSES;a++)  {
    for(b=0;b<NUM_CLASSES;b++)  {
      k[0]=k[0]+frequency[a][0]*frequency[b][1];
    }
  }
  for(a=0;a<NUM_CLASSES;a++)  {
    k[0]=k[0]-frequency[a][0]*frequency[a][1];
  }
  k[0]=1-k[0];

  if(prin==1)  {
    printf("k[0] is = %f \n",k[0]);
  }
  for(a=0;a<NUM_CLASSES;a++)  {
    sum[0][a]=sum[0][a] / k[0];
    if(prin==1)  {
      printf("new sum[0][%ld] = %f \n",a,sum[0][a]);
    }
  }
  frame_new[0] = 1;
  total[0] = 0;
  for(a=0;a<NUM_CLASSES;a++)  {
    total[0]=total[0]+sum[0][a];
  }
  frame_new[0]=frame_new[0]-total[0];
   if(prin==1)  printf("frame_new[0] = %f; if this value is <0, then all will be normalized.\n",
frame_new[0]);
  if(total[0]>1)  {
    if(prin==1) printf("\nA renormalization is being performed since the above value is < 0.\n");
    for(a=0;a<NUM_CLASSES;a++)  {
      sum[0][a]=sum[0][a]/total[0];    /* this renormalization is redundant */
    }
    frame_new[0]=0;
    total[0]=1;
  }
```

```
  if(prin==1)  {
    printf("frame_new[0] = %f \n",frame_new[0]);
  }
}


void calculate_orthogonal_sum_of_remaining_layers(int combo,
        float sum[NUM_LEVELS][NUM_CLASSES],
        float frequency[NUM_CLASSES][NUM_LEVELS],
        float frame[],int prin,float k[],float total[],float frame_new[])
{
  int a,b;

  for(a=0;a<NUM_CLASSES;a++)  {
    sum[combo][a]=sum[combo-1][a]*frequency[a][combo+1] +
        frame_new[combo-1]*frequency[a][combo+1]
        + frame[combo+1]*sum[combo-1][a];
    if(prin==1)  {
      printf("Sum of products %fx%f, %fx%f, %fx%f: sum[%d][%d]=%f\n",
        sum[combo-1][a], frequency[a][combo+1], frame_new[combo-1], frequency[a][combo+1],
        frame[combo+1], sum[combo-1][a], combo,a,sum[combo][a]);
    }
  }
  k[combo]=0;
  for(a=0;a<NUM_CLASSES;a++)  {
    for(b=0;b<NUM_CLASSES;b++)  {
    k[combo]=k[combo]+sum[combo-1][a]*frequency[b][combo+1];
    }
  }
  for(a=0;a<NUM_CLASSES;a++)  {
    k[combo]=k[combo]-sum[combo-1][a]*frequency[a][combo+1];
  }
  k[combo]=1-k[combo];
  if(prin==1)  {
    printf("k[%d] is = %f \n",combo,k[combo]);
  }
  for(a=0;a<NUM_CLASSES;a++)  {
    sum[combo][a]=sum[combo][a] / k[combo];
    if(prin==1)  {
      printf("new sum[ %d ][ %ld ] = %f \n",combo,a,sum[combo][a]);
    }
  }
  frame_new[combo] = 1;
  total[combo] = 0;
  for(a=0;a<NUM_CLASSES;a++)  {
    total[combo]=total[combo]+sum[combo][a];
  }
  frame_new[combo]=frame_new[combo]-total[combo];
  if(prin==1)  printf("frame_new[%d] = %f; if this value is <0, then will be
                        normalized.\n",combo,frame_new[combo]);
  if(total[combo]>1)  {
    if(prin==1) printf("\nA renormalization is being performed since the above value is < 0.\n");
    for(a=0;a<NUM_CLASSES;a++)  {
      sum[combo][a]=sum[combo][a]/total[combo];
    }
    frame_new[combo]=0;
    total[combo]=1;
  }
  if(prin==1)  {
    printf("frame_new[%d] = %f \n",combo,frame_new[combo]);
  }
}


int classify(float sum[NUM_LEVELS][NUM_CLASSES],
        float frequency[NUM_CLASSES][NUM_LEVELS])
{
  int highest;              /* variable to indicate predicted class */
```

```
  int a;
  int classification_sum_stage=CLASSIFICATION_SUM_STAGE;
  float max_sumX_X;

  highest=NUM_CLASSES;      /* anything not assigned is given max class + 1   */
  max_sumX_X = 0;
  for(a=0;a<NUM_CLASSES;a++)  {
    if(classification_sum_stage==100)  {
      if(frequency[a][0]>max_sumX_X)  {
        max_sumX_X = frequency[a][0];
        highest = a;
      }
    }
    else  {
      printf("sum[CLASSIFICATION_SUM_STAGE][a]=%f\n",sum[CLASSIFICATION_SUM_STAGE][a]);
      if(sum[CLASSIFICATION_SUM_STAGE][a]>max_sumX_X)  {
        printf("The value given above is the highest yet.\n");
        max_sumX_X = sum[CLASSIFICATION_SUM_STAGE][a];
        highest = a;
      }
    }
  }
  printf("The class with the greatest evidence is: %d\n\n",highest);
  return(highest);
}


void write_results(int temp[])
{
  FILE *out;
  int loop;

  printf("*");
  out=fopen("out.img","a");
  for(loop=0;loop<NUM_TEMP_RESULTS;loop++)  {
    fprintf(out,"%d",temp[loop]);
    fprintf(out,"\n");
  }
  fclose(out);
}


void info()
{
  printf("\n\nEVIDENTIAL REASONING PROGRAM Version 3.0\n");
  printf("(C) Leverington 1999\n");
  printf("Compiled : "__DATE__"  "__TIME__"\n");
}
```

APPENDIX E: Evidential Reasoning Source Code (Consensus Version)

(er129f10va14.c)

```
/* the code below was used for consensus of 10 sets of neural network activations (i.e., output
activations were used as measures of evidence). The code is identical to that of the main evidential
reasoning code, except for the file-reading and initial-evidence-calculation routines. The file-
reading routines should be replaced by tighter code, but are fully functional as they are. */

#include <stdio.h>
#include <math.h>

#define NUM_CLASSES 10
#define NUM_LEVELS 10
#define SPECTRUM 256
#define NUM_TEMP_RESULTS 294
#define NUM_REPS_OF_SECOND_LOOP_CALL 1
#define CLASSIFICATION_SUM_STAGE 2

void set_main_variables_to_zero(
        float data[NUM_CLASSES][NUM_LEVELS][SPECTRUM],int *prin,
        float num_read[NUM_CLASSES][NUM_LEVELS],
        float frequency[NUM_CLASSES][NUM_LEVELS],
        float test[],float frame[],float sum[NUM_LEVELS][NUM_CLASSES],
        float frame_new[]);

void calculate_frame_of_discernment(float frame[],
        float frequency[NUM_CLASSES][NUM_LEVELS],int prin);

void calculate_orthogonal_sum_of_first_two_layers(
        float sum[NUM_LEVELS][NUM_CLASSES],
        float frequency[NUM_CLASSES][NUM_LEVELS],float frame[],int prin,
        float k[],float total[],float frame_new[]);

void calculate_orthogonal_sum_of_remaining_layers(int combo,
        float sum[NUM_LEVELS][NUM_CLASSES],
        float frequency[NUM_CLASSES][NUM_LEVELS],
        float frame[],int prin,float k[],float total[],float frame_new[]);

int classify(float sum[NUM_LEVELS][NUM_CLASSES],
        float frequency[NUM_CLASSES][NUM_LEVELS]);

void write_results(int temp[]);

void info();


main()
{
  FILE *fp_level[NUM_LEVELS];   /* file pointers for reading input data layers */

  FILE *fp_nn0, *fp_nn1, *fp_nn2, *fp_nn3, *fp_nn4, *fp_nn5, *fp_nn6, *fp_nn7, *fp_nn8, *fp_nn9;
                              /* file pointers for reading neural network activations */

  char *ch;                   /* pointer for changing level file names for reading */
  char level_file[12];        /* string for reading level files */
  float num_read[NUM_CLASSES][NUM_LEVELS];       /* number of values in each class/source input file
*/
  float data[NUM_CLASSES][NUM_LEVELS][SPECTRUM]; /* records frequency of occurrence for 0-SPECTRUM */
  float test[NUM_LEVELS];                  /* test pixel for set of sources*/
  float frequency[NUM_CLASSES][NUM_LEVELS]; /* frequency of occurrence for each class/source */
  float frame[NUM_LEVELS];                 /* frame of discernment for each source */
  float sum[NUM_LEVELS][NUM_CLASSES];      /* orthogonal summation variable */
  float k[NUM_LEVELS-1];                   /* 'K' variable for s1_s2 */
  float frame_new[NUM_LEVELS-1];           /* new frame of discernment after s1_s2 */
  float total[NUM_LEVELS-1];               /* a sum value used in orth.sum. calculations */
  int prin;                                /* print variable... if = 1 then verbose */
```

```
int mainloop;                              /* counter for the main loop */
int temporary[NUM_TEMP_RESULTS];           /* temp values put here until sent to hdrive */
int combo;                                 /* value corresponding to 1_2,2_3,3 etc orth sums */
int cl;                          /* class variable for looping while reading NN values */
int n;                           /* number read in from file */
int lev;                         /* loop variable for cycling through level reading loops */
int classification_sum_stage; /* for checking 100 value (1 level case) */
long int second_loop;            /* number of times 2nd loop is performed */
long int a,b,c;                  /* used as loop variables */

info();

set_main_variables_to_zero(data,&prin,num_read,frequency,test,frame,
      sum,frame_new);
prin=1;

fp_nn0=fopen("nn0.txt","r"); /* opening NN files, so that can read consecutive sets of #'s below */
if(fp_nn0==NULL) {
  printf("\nFile nn0.txt cannot be opened or does not exist in the active directory.\n\nHalt.\n\n");
  exit(1);
}
fp_nn1=fopen("nn1.txt","r"); /* THERE WILL ALWAYS BE 10 NN FILES OPENED */
if(fp_nn1==NULL) {
  printf("\nFile nn1.txt cannot be opened or does not exist in the active directory.\n\nHalt.\n\n");
  exit(1);
}
fp_nn2=fopen("nn2.txt","r");
if(fp_nn2==NULL) {
  printf("\nFile nn2.txt cannot be opened or does not exist in the active directory.\n\nHalt.\n\n");
  exit(1);
}
fp_nn3=fopen("nn3.txt","r");
if(fp_nn3==NULL) {
  printf("\nFile nn3.txt cannot be opened or does not exist in the active directory.\n\nHalt.\n\n");
  exit(1);
}
fp_nn4=fopen("nn4.txt","r");
if(fp_nn4==NULL) {
  printf("\nFile nn4.txt cannot be opened or does not exist in the active directory.\n\nHalt.\n\n");
  exit(1);
}
fp_nn5=fopen("nn5.txt","r");
if(fp_nn5==NULL) {
  printf("\nFile nn5.txt cannot be opened or does not exist in the active directory.\n\nHalt.\n\n");
  exit(1);
}
fp_nn6=fopen("nn6.txt","r");
if(fp_nn6==NULL) {
  printf("\nFile nn6.txt cannot be opened or does not exist in the active directory.\n\nHalt.\n\n");
  exit(1);
}
fp_nn7=fopen("nn7.txt","r");
if(fp_nn7==NULL) {
  printf("\nFile nn7.txt cannot be opened or does not exist in the active directory.\n\nHalt.\n\n");
  exit(1);
}
fp_nn8=fopen("nn8.txt","r");
if(fp_nn8==NULL) {
  printf("\nFile nn8.txt cannot be opened or does not exist in the active directory.\n\nHalt.\n\n");
  exit(1);
}
fp_nn9=fopen("nn9.txt","r");
if(fp_nn9==NULL) {
  printf("\nFile nn9.txt cannot be opened or does not exist in the active directory.\n\nHalt.\n\n");
  exit(1);
}

printf("\nEach '*' below represents %d pixels classified.\n",NUM_TEMP_RESULTS);
```

```
printf("\nPROCESSING...\n");  /* **** main loop begins below **** */

for(mainloop=0;mainloop<NUM_REPS_OF_SECOND_LOOP_CALL;mainloop++)  {
  for(second_loop=0;second_loop<NUM_TEMP_RESULTS;second_loop++)  {
    if(prin==1) printf("\n********** second_loop=%ld *********\n",second_loop);
     printf("\nNow reading 10 sets of NN activation data corresponding to a particular test
                              pixel...\n\n");
    for(cl=0;cl<NUM_CLASSES;cl++)  {
      fscanf(fp_nn0, "%f", &frequency[cl][0]);   /* read class activations for NN job 0 */
      printf("Just read the value for class %d and 'source' 0\n", cl);
    }
    for(cl=0;cl<NUM_CLASSES;cl++)  {
      fscanf(fp_nn1, "%f", &frequency[cl][1]);   /* read class activations for NN job 1 */
    }
    for(cl=0;cl<NUM_CLASSES;cl++)  {
      fscanf(fp_nn2, "%f", &frequency[cl][2]);   /* read class activations for NN job 2 */
    }
    for(cl=0;cl<NUM_CLASSES;cl++)  {
      fscanf(fp_nn3, "%f", &frequency[cl][3]);   /* read class activations for NN job 3 */
    }
    for(cl=0;cl<NUM_CLASSES;cl++)  {
      fscanf(fp_nn4, "%f", &frequency[cl][4]);   /* read class activations for NN job 4 */
    }
    for(cl=0;cl<NUM_CLASSES;cl++)  {
      fscanf(fp_nn5, "%f", &frequency[cl][5]);   /* read class activations for NN job 5 */
    }
    for(cl=0;cl<NUM_CLASSES;cl++)  {
      fscanf(fp_nn6, "%f", &frequency[cl][6]);   /* read class activations for NN job 6 */
    }
    for(cl=0;cl<NUM_CLASSES;cl++)  {
      fscanf(fp_nn7, "%f", &frequency[cl][7]);   /* read class activations for NN job 7 */
    }
    for(cl=0;cl<NUM_CLASSES;cl++)  {
      fscanf(fp_nn8, "%f", &frequency[cl][8]);   /* read class activations for NN job 8 */
    }
    for(cl=0;cl<NUM_CLASSES;cl++)  {
      fscanf(fp_nn9, "%f", &frequency[cl][9]);   /* read class activations for NN job 9 */
    }
     printf("\nActivation data has now been read.  Orthogonal summation of 'evidence' follows:\n\n");


    calculate_frame_of_discernment(frame,frequency,prin);

    calculate_orthogonal_sum_of_first_two_layers(sum,frequency,frame,prin,
              k,total,frame_new);

    for(combo=1;combo<(NUM_LEVELS-1);combo++)  {
      calculate_orthogonal_sum_of_remaining_layers(combo,sum,frequency,
        frame,prin,k,total,frame_new);
    }
    temporary[second_loop]=classify(sum,frequency);
  }
  write_results(temporary);

  if(classification_sum_stage==100)  {    /* slows down Pentium write  */
    printf("\nmainloop=%d second_loop=%ld\n",mainloop,second_loop);
  }
}                                         /* **** end of mainloop **** */
fclose(fp_nn0);
fclose(fp_nn1);
fclose(fp_nn2);
fclose(fp_nn3);
fclose(fp_nn4);
fclose(fp_nn5);
fclose(fp_nn6);
fclose(fp_nn7);
fclose(fp_nn8);
fclose(fp_nn9);
```

```
  info();

  printf("Done.");
}                                          /* **** end of function main() */


void set_main_variables_to_zero(
        float data[NUM_CLASSES][NUM_LEVELS][SPECTRUM],int *prin,
        float num_read[NUM_CLASSES][NUM_LEVELS],
        float frequency[NUM_CLASSES][NUM_LEVELS],
        float test[],float frame[],float sum[NUM_LEVELS][NUM_CLASSES],
        float *frame1_2)
{
  int loop1,loop2,loop3;

  for(loop1=0;loop1<NUM_CLASSES;loop1++)  {
    for(loop2=0;loop2<NUM_LEVELS;loop2++)  {
      for(loop3=0;loop3<SPECTRUM;loop3++)  {
        data[loop1][loop2][loop3]=0;
      }
      num_read[loop1][loop2]=0;
      frequency[loop1][loop2]=0;
      sum[loop2][loop1]=0;
      test[loop2]=0;
      frame[loop2]=0;
    }
    *prin=0;
  }
  *frame1_2=0;
}


void calculate_frame_of_discernment(float frame[],
        float frequency[NUM_CLASSES][NUM_LEVELS],int prin)
{
  int a,b;
  float sum_of_frequencies;

  for(b=0;b<NUM_LEVELS;b++)  {
    frame[b]=1;
    for(a=0;a<NUM_CLASSES;a++)  {
      frame[b]=frame[b]-frequency[a][b];
    }
    if(frame[b]<0)  {
      printf("HEY!  frame[b]<0!... = %f\n",frame[b]);
      frame[b]=0;
      sum_of_frequencies=0;
      for(a=0;a<NUM_CLASSES;a++)  {
        sum_of_frequencies=sum_of_frequencies+frequency[a][b];
      }
      if(prin==1)  {
        printf("Sum of frequencies: %f\n", sum_of_frequencies);
        printf("Frequencies normalized to 1.0: ");
      }
      for(a=0;a<NUM_CLASSES;a++)  {
        frequency[a][b]=frequency[a][b]/sum_of_frequencies;
        if(prin==1)  {
          printf(" %f ",frequency[a][b]);
        }
      }
    }
    if(prin==1)  {
      printf("\nframe [ %ld ] = %f \n",b,frame[b]);
    }
  }
}
```

```
void calculate_orthogonal_sum_of_first_two_layers(
        float sum[NUM_LEVELS][NUM_CLASSES],
        float frequency[NUM_CLASSES][NUM_LEVELS],float frame[],int prin,
        float k[],float total[],float frame_new[])
{
  int a,b;

  for(a=0;a<NUM_CLASSES;a++)  {
    sum[0][a]=frequency[a][0]*frequency[a][1] + frame[0]*frequency[a][1]
                        + frame[1]*frequency[a][0];
    if(prin==1)  {
    printf("sum[0][%ld] = %f \n",a,sum[0][a]);
    }
  }
  k[0] = 0;
  for(a=0;a<NUM_CLASSES;a++)  {
    for(b=0;b<NUM_CLASSES;b++)  {
      k[0]=k[0]+frequency[a][0]*frequency[b][1];
    }
  }
  for(a=0;a<NUM_CLASSES;a++)  {
    k[0]=k[0]-frequency[a][0]*frequency[a][1];
  }
  k[0]=1-k[0];

  if(prin==1)  {
    printf("k[0] is = %f \n",k[0]);
  }
  for(a=0;a<NUM_CLASSES;a++)  {
    sum[0][a]=sum[0][a] / k[0];
    if(prin==1)  {
      printf("new sum[0][%ld] = %f \n",a,sum[0][a]);
    }
  }
  frame_new[0] = 1;
  total[0] = 0;
  for(a=0;a<NUM_CLASSES;a++)  {
    total[0]=total[0]+sum[0][a];
  }
  frame_new[0]=frame_new[0]-total[0];
 if(prin==1)  printf("frame_new[0] = %f; if this value is <0, then all will be normalized.\n",
        frame_new[0]);
  if(total[0]>1)  {
     if(prin==1) printf("\nA renormalization appears to be necessary since the above value is < 0.
        \nWill set frame to zero, since everything should have already been renormalized above.\n");
    frame_new[0]=0;
    total[0]=1;
  }
  if(prin==1)  {
    printf("frame_new[0] = %f \n",frame_new[0]);
  }
}


void calculate_orthogonal_sum_of_remaining_layers(int combo,
        float sum[NUM_LEVELS][NUM_CLASSES],
        float frequency[NUM_CLASSES][NUM_LEVELS],
        float frame[],int prin,float k[],float total[],float frame_new[])
{
  int a,b;

  for(a=0;a<NUM_CLASSES;a++)  {
    sum[combo][a]=sum[combo-1][a]*frequency[a][combo+1] +
        frame_new[combo-1]*frequency[a][combo+1]
        + frame[combo+1]*sum[combo-1][a];
    if(prin==1)  {
      printf("Sum of products %fx%f, %fx%f, %fx%f: sum[%d][%d]=%f\n",
        sum[combo-1][a], frequency[a][combo+1], frame_new[combo-1], frequency[a][combo+1],
```

```
        frame[combo+1], sum[combo-1][a], combo,a,sum[combo][a]);
      }
    }
    k[combo]=0;
    for(a=0;a<NUM_CLASSES;a++)  {
      for(b=0;b<NUM_CLASSES;b++)  {
      k[combo]=k[combo]+sum[combo-1][a]*frequency[b][combo+1];
      }
    }
    for(a=0;a<NUM_CLASSES;a++)  {
      k[combo]=k[combo]-sum[combo-1][a]*frequency[a][combo+1];
    }
    k[combo]=1-k[combo];
    if(prin==1)  {
      printf("k[%d] is = %f \n",combo,k[combo]);
    }
    for(a=0;a<NUM_CLASSES;a++)  {
      sum[combo][a]=sum[combo][a] / k[combo];
      if(prin==1)  {
        printf("new sum[ %d ][ %ld ] = %f \n",combo,a,sum[combo][a]);
      }
    }
    frame_new[combo] = 1;
    total[combo] = 0;
    for(a=0;a<NUM_CLASSES;a++)  {
      total[combo]=total[combo]+sum[combo][a];
    }
    frame_new[combo]=frame_new[combo]-total[combo];
    if(prin==1)  printf("frame_new[%d] = %f; if this value is <0, then will be
          normalized.\n",combo,frame_new[combo]);
    if(total[combo]>1)  {
      if(prin==1) printf("\nA renormalization is being performed since the above value is < 0.\n");
      for(a=0;a<NUM_CLASSES;a++)  {          /* renormalization */
        sum[combo][a]=sum[combo][a]/total[combo];
      }
      frame_new[combo]=0;
      total[combo]=1;
    }
    if(prin==1)  {
      printf("frame_new[%d] = %f \n",combo,frame_new[combo]);
    }
  }


int classify(float sum[NUM_LEVELS][NUM_CLASSES],
        float frequency[NUM_CLASSES][NUM_LEVELS])
{
  int highest;              /* variable to indicate predicted class */
  int a;
  int classification_sum_stage=CLASSIFICATION_SUM_STAGE;
  float max_sumX_X;

  highest=NUM_CLASSES;      /* anything not assigned is given max class + 1   */
  max_sumX_X = 0;
  for(a=0;a<NUM_CLASSES;a++)  {
    if(classification_sum_stage==100)  {  /* check to see if only one level   */
      if(frequency[a][0]>max_sumX_X)  {   /* 0 since only consider level 0    */
        max_sumX_X = frequency[a][0];
        highest = a;
      }
    }
    else  {                             /* else look at orth sums (>1 level) */
      printf("sum[CLASSIFICATION_SUM_STAGE][a]=%f\n",sum[CLASSIFICATION_SUM_STAGE][a]);
      if(sum[CLASSIFICATION_SUM_STAGE][a]>max_sumX_X)  {
        printf("The value given above is the highest yet.\n");
        max_sumX_X = sum[CLASSIFICATION_SUM_STAGE][a];
        highest = a;
      }
```

```
    }
  }
  printf("The class with the greatest evidence is: %d\n\n",highest);
  return(highest);
}


void write_results(int temp[])
{
  FILE *out;
  int loop;

  printf("*");
  out=fopen("out.img","a");
  for(loop=0;loop<NUM_TEMP_RESULTS;loop++)  {
    fprintf(out,"%d",temp[loop]);
    fprintf(out,"\n");
  }
  fclose(out);
}


void info()
{
  printf("\n\nEVIDENTIAL REASONING PROGRAM Version 3.0\n");
  printf("(C) Leverington 1999\n");
  printf("Compiled : "__DATE__"  "__TIME__"\n");
}
```

APPENDIX F: Neural Network Source Code (Learning Module)

(N400X.C)

```
#include <stdio.h>
#include <math.h>
#include <stdlib.h>

#define MAX_NUM_LAYERS 10
#define MAX_NUM_WEIGHTS 800    /* ie max # weights for whole network  */
#define MAX_NUM_NODES 200
#define MAX_NUM_TRAINING_CASES 590  /* max value (is set in param.txt */
#define MAX_NUM_SOURCES_PLUS_ONE 7  /* change when necessary          */

#define PRINT 0

void clear_screen();

void intro();

void check_for_old_files();

void read_parameter_file(int *num_hidden_layers,int num_nodes[MAX_NUM_LAYERS],
                                double *epsilon, double *momentum_w,
                                double *momentum_b,
                                double *number_of_iterations,
                                int *num_training_cases,
                                double *desired_tss);

void print_parameter_values(int num_hidden_layers,
                                int num_nodes[MAX_NUM_LAYERS],
                                double epsilon, double momentum_w,
                                double momentum_b,
                                double number_of_iterations,
                                int num_training_cases,
                                double desired_tss);

int calculate_number_weights(int num_hidden_layers,
                                int num_nodes[MAX_NUM_LAYERS]);

void set_initial_weights(double weight[MAX_NUM_WEIGHTS],int num_weights,
                                double bias[MAX_NUM_NODES],
                                double previous_weight_change[MAX_NUM_WEIGHTS],
                                double previous_bias_change[MAX_NUM_NODES]);

void read_whole_training_file(double
        training_database[MAX_NUM_TRAINING_CASES][MAX_NUM_SOURCES_PLUS_ONE],
                                int num_training_cases,
                                int num_nodes[MAX_NUM_LAYERS]);

void print_whole_training_file(double
        training_database[MAX_NUM_TRAINING_CASES][MAX_NUM_SOURCES_PLUS_ONE],
                                int num_training_cases,
                                int num_nodes[MAX_NUM_LAYERS]);

void feedforward(int num_nodes[MAX_NUM_LAYERS],int num_hidden_layers,
                                double weight[MAX_NUM_WEIGHTS],
                                double bias[MAX_NUM_NODES],
                                double activation[MAX_NUM_NODES]);

double factor1(int layer, int num_nodes[MAX_NUM_LAYERS]);

double factor2(int layer, int num_nodes[MAX_NUM_LAYERS]);

double factor3(int layer, int num_nodes[MAX_NUM_LAYERS]);
```

```
void backpropagation(int num_nodes[MAX_NUM_LAYERS],int num_hidden_layers,
                double weight[MAX_NUM_WEIGHTS],
                double activation[MAX_NUM_NODES],double epsilon,
                double train_class, double delta[MAX_NUM_NODES],
                double bias[MAX_NUM_NODES],
                double *pixel_total_sum_of_squares,double momentum_w,
                double momentum_b,
                double previous_weight_change[MAX_NUM_WEIGHTS],
                double previous_bias_change[MAX_NUM_NODES]);

main()
{
  double number_of_iterations;
  int num_training_cases;
  int total_num_nodes;
  int num_hidden_layers;
  int num_nodes[MAX_NUM_LAYERS];        /* ie to store #nodes for ea layer */
  int num_weights;                      /* ie total #weights               */
  int found;                          /* used in random selection of patterns */
  int current_pattern;                /* used in random selection of patterns */
  int already_used[MAX_NUM_TRAINING_CASES]; /* used in rand sel of patt's  */
  double epsilon;                       /* ie learning rate parameter      */
  double momentum_w;                    /* momentum for non-bias weights   */
  double momentum_b;                    /* momentum for bias weights only  */
  double weight[MAX_NUM_WEIGHTS];       /* ie actual value of each weight  */
  double previous_weight_change[MAX_NUM_WEIGHTS];  /* for use re: momentum */
  double previous_bias_change[MAX_NUM_NODES];      /* for use re: momentum */
  double bias[MAX_NUM_NODES];
  double activation[MAX_NUM_NODES];     /* ie total #nodes in network      */
  double delta[MAX_NUM_NODES];          /* ie a delta value for each node  */
  double iteration;
  double desired_tss;     /* ie tss that causes 'early' exit from main loop */
  double it;                            /* ie needed for graphing purposes     */
  int training_case;                    /* ie number of training case          */
  double train_class;                   /* ie desired class label (node #)     */
  double iteration_total_sum_of_squares;  /* an error measure over a     */
                                          /* single iteration            */
  double pixel_total_sum_of_squares;      /* an error measure over a     */
                                          /* single pixel's case within  */
                                          /* an iteration                */
  double training_database[MAX_NUM_TRAINING_CASES][MAX_NUM_SOURCES_PLUS_ONE];
  FILE *fp_weights;                   /* for writing calculated weights to   */
  FILE *fp_tss;                       /* for writing interation tss          */

  int x;
  int p;  /* simply used to cycle through already_used, to set to 0 */

  clear_screen();
  intro();
  check_for_old_files();
  read_parameter_file(&num_hidden_layers,num_nodes,&epsilon,&momentum_w,
                &momentum_b,
                &number_of_iterations,&num_training_cases,&desired_tss);
  print_parameter_values(num_hidden_layers,num_nodes,epsilon,momentum_w,
                momentum_b,
                number_of_iterations,num_training_cases,desired_tss);

  num_weights=calculate_number_weights(num_hidden_layers,num_nodes);
  printf("\n\ntotal number of weights: %d",num_weights);
  if(num_weights>MAX_NUM_WEIGHTS) {
    printf("\nNumber of weights req'd exceeds max number allowed");
    exit(1);
  }
  set_initial_weights(weight,num_weights,bias,previous_weight_change,
        previous_bias_change);

  printf("\n\nweights set...\n\n");
```

```
read_whole_training_file(training_database,num_training_cases,
                                        num_nodes);
print_whole_training_file(training_database,num_training_cases,
                                        num_nodes);

/* now, loop here to cycle through all training cases; for each case,
go through feedforward and backpropagation procedures, modifying weights;
keep in mind that program must change output class value into proper output
values, such that desired output class = 0.9, and other nodes = 0.1 */

iteration_total_sum_of_squares=0;

/* ********** ITERATIONS BEGIN HERE ********** */

for(iteration=0.0;iteration<number_of_iterations;iteration++)  {

  /* DATA OUTPUT FOR EACH ITERATION PERFORMED HERE */
  printf("\niteration:%lf ",iteration);
  printf("tss:%lf ",iteration_total_sum_of_squares);
  printf("avgnode:%lf     working...",sqrt(iteration_total_sum_of_squares/
              (num_training_cases*num_nodes[num_hidden_layers+1])));
  it=iteration;/* get double version of iteration, so can divide below */
  /* DATA OUTPUT FOR EACH ITERATION STOPS HERE */

  fp_tss=fopen("tss.txt","a");
  fprintf(fp_tss,"\n%lf  %lf",iteration,iteration_total_sum_of_squares);
  fclose(fp_tss);

  if((iteration>500.0)&&(iteration_total_sum_of_squares<desired_tss)) break;
  /* above will stop training early, if error 'low enough'and iter>500 */
  iteration_total_sum_of_squares=0;

  for(p=0;p<num_training_cases;p++)  {   /* re-set already_used */
    already_used[p]=0;
  }

  /* now, cycle through a full iteration of training cases, each one
  being randomly selected (but all cases are used in a given iteration) */

  /* NOTE: throughout this code, I use the terms training 'case' and
  training 'pattern' interchangeably (although note also that the
  variable training_case below cycles through a total number of
  training cases equal to num_trainin_cases, while the variable
  current_pattern is the actual active randomly-selected case #)  */

  for(training_case=0;training_case<num_training_cases;training_case++)  {

    /* now, randomly pick a training pattern that has not been selected
    before (in this particular iteration); the code immediately below
    is inefficient, and should be replaced with a better routine. */
    found=0;
    while(found==0)  {
      current_pattern=rand() / (RAND_MAX / num_training_cases);
      /* printf("Current potential case selection: %d\n",current_pattern); */
      if(already_used[current_pattern]==0)  {
        already_used[current_pattern]=already_used[current_pattern]+1;
        found=1;
        /* printf("\nPattern: %d chosen and available.",current_pattern); */
      }
    }

    /* now that a training pattern has been selected, run through
    network, etc. */

    for(x=0;x<num_nodes[0];x++)  {
      activation[x]=training_database[current_pattern][x];
      /* printf("\nActivation is... %lf",activation[x]); */
    }
```

```
      /* now, all input values for a given case are in activation...
      must proceed with feedforward...then read desired output values... */

      feedforward(num_nodes, num_hidden_layers, weight, bias, activation);

      /* now, all activations associated with each node - including output
      nodes - have been calculated... must now change weights according to
      error in output nodes */

      train_class=training_database[current_pattern][num_nodes[0]];
      /*
      printf("\nthe class to which this training case belongs is %lf",
                training_database[current_pattern][num_nodes[0]]);

      */
      if(PRINT==1) printf(" desired class label: %lf\n\n",train_class);
      pixel_total_sum_of_squares=0;
      backpropagation(num_nodes, num_hidden_layers, weight, activation,
                epsilon, train_class,delta, bias,
                &pixel_total_sum_of_squares,momentum_w,
                momentum_b, previous_weight_change,
                previous_bias_change);
      iteration_total_sum_of_squares=iteration_total_sum_of_squares+
                pixel_total_sum_of_squares;
    }
  }
  printf("\nNOW WRITING WEIGHT VALUES TO WEIGHT.TXT\n");
  fp_weights=fopen("weight.txt","a");
  for(x=0;x<num_weights;x++)  {
    if(PRINT==1) printf("\nweight[%d]=%.12lf",x,weight[x]);
    fprintf(fp_weights,"%.12lf\n",weight[x]);
  }
  fclose(fp_weights);

  total_num_nodes=0;
  printf("\nNOW WRITING BIAS VALUES TO BIAS.TXT\n");
  fp_weights=fopen("bias.txt","a");
  for(x=0;x<(num_hidden_layers+2);x++)  {
    total_num_nodes=total_num_nodes+num_nodes[x];
  }
  printf("\ntotal_num_nodes=%d",total_num_nodes);
  for(x=0;x<total_num_nodes;x++)  {
    if(PRINT==1) printf("\nbias[%d]=%.12lf",x,bias[x]);
    fprintf(fp_weights,"%.12lf\n",bias[x]);
  }
  fclose(fp_weights);

  printf("\nDone: Press any key to exit...\n");

}

void clear_screen()
{
  int x;
  for(x=0;x<30;x++)  {
    printf("\n");
  }
}

void intro()
{
  printf("\n\nNEURAL NETWORK PROGRAM      Version 5.0 (Unix)\n");
  printf("(C) Leverington 1999\n");
  printf("Compiled : "__DATE__"  "__TIME__"\n\n\n");
}

void check_for_old_files()
```

```
{
  FILE *fp_check;
  fp_check=fopen("weight.txt","r");
  if(fp_check!=NULL)  {
    printf("\nAbort: an old version of weight.txt has been detected.");
    printf("\nRemove this file from the active directory.");
    exit(1);
  }
  fclose(fp_check);
  fp_check=fopen("bias.txt","r");
  if(fp_check!=NULL)  {
    printf("\nAbort: an old version of bias.txt has been detected.");
    printf("\nRemove this file from the active directory.");
    exit(1);
  }
  fclose(fp_check);
  fp_check=fopen("tss.txt","r");
  if(fp_check!=NULL)  {
    printf("\nAbort: an old version of tss.txt has been detected.");
    printf("\nRemove this file from the active directory.");
    exit(1);
  }
  fclose(fp_check);
}

void read_parameter_file(int *num_hidden_layers,int num_nodes[MAX_NUM_LAYERS],
                                double *epsilon, double *momentum_w,
                                double *momentum_b,
                                double *number_of_iterations,
                                int *num_training_cases,
                                double *desired_tss)
{
  FILE *fp_parameters;
  int x;
  int num_hidden_lay;
  double epsil;          /* next 5 variables: temporary holders of data */
  double moment_w;       /* momentum for non-bias weights  */
  double moment_b;       /* momentum for bias weights only */
  double num_of_it;
  double des_tss;
  int num_tr_cases;

  fp_parameters=fopen("param.txt","r");
  if(fp_parameters==NULL)  {
    printf("\nFile param.txt cannot be opened or does not exist.\n");
    exit(1);
  }
  fscanf(fp_parameters,"%d",&num_hidden_lay);      /* ie #hidden layers   */
  for(x=0;x<(num_hidden_lay+2);x++)  {
    fscanf(fp_parameters,"%d",&num_nodes[x]);      /* ie #nodes per layer */
  }
  fscanf(fp_parameters,"%lf",&epsil);
  fscanf(fp_parameters,"%lf",&moment_w);
  fscanf(fp_parameters,"%lf",&moment_b);
  fscanf(fp_parameters,"%lf",&num_of_it);
  fscanf(fp_parameters,"%lf",&des_tss);
  fscanf(fp_parameters,"%d",&num_tr_cases);
  fclose(fp_parameters);

  printf("\nFile param.txt successfully opened and values have been read");

  /* now, the interim variables have been 'filled'... must transfer these
     values to the memory locations of the respective variables of main() */

  *num_hidden_layers=num_hidden_lay;
  *epsilon=epsil;
  *momentum_w=moment_w;
  *momentum_b=moment_b;
```

```
  *number_of_iterations=num_of_it;
  *desired_tss=des_tss;
  *num_training_cases=num_tr_cases;
}

void print_parameter_values(int num_hidden_layers,
                            int num_nodes[MAX_NUM_LAYERS],
                            double epsilon, double momentum_w,
                            double momentum_b,
                            double number_of_iterations,
                            int num_training_cases,
                            double desired_tss)
{
  int x;

  printf("\n\nnumber of hidden layers: %d",num_hidden_layers);
  for(x=0;x<(num_hidden_layers+2);x++)  {
    printf("\nnumber of nodes for layer %d: %d",x,num_nodes[x]);
  }
  printf("\nepsilon:  %lf",epsilon);
  printf("\nmomentum_w: %lf",momentum_w);
  printf("\nmomentum_b: %lf",momentum_b);
  printf("\nnumber of iterations: %lf",number_of_iterations);
  printf("\ndesired tss: %lf",desired_tss);
  printf("\nnumber of training cases: %d",num_training_cases);

  if(num_training_cases>MAX_NUM_TRAINING_CASES)  {
    printf("\nAbort: num_training_cases (%d) > MAX_NUM_TRAINING_CASES (%d)",
                        num_training_cases, MAX_NUM_TRAINING_CASES);
    exit(1);
  }
  if((num_nodes[0]+1)>MAX_NUM_SOURCES_PLUS_ONE)  {
    printf("\nAbort: num_nodes[0] (%d) > MAX_NUM_SOURCES_PLUS_ONE (%d)",
                        num_nodes[0],MAX_NUM_SOURCES_PLUS_ONE);
    exit(1);
  }
}

int calculate_number_weights(int num_hidden_layers,
                                        int num_nodes[MAX_NUM_LAYERS])
{
  int x;
  int total=0;

  for(x=0;x<(num_hidden_layers+1);x++)  {
    total=total+num_nodes[x]*num_nodes[x+1];
  }
  return (total);
}

void set_initial_weights(double weight[MAX_NUM_WEIGHTS],int num_weights,
                            double bias[MAX_NUM_NODES],
                            double previous_weight_change[MAX_NUM_WEIGHTS],
                            double previous_bias_change[MAX_NUM_NODES])
{
  int x;
  double now;

  srand(time(&now) % 37);
  for(x=0;x<num_weights;x++)  {
    previous_weight_change[x]=0;   /* not a weight, but setting all to 0 */
    weight[x]=((rand()*0.00001)-(rand()*0.00001))*1.6;   /* ~0.5 to (-0.5) */
    if(PRINT==1) printf("\nweight[%d]=%lf",x,weight[x]);
  }
  for(x=0;x<MAX_NUM_NODES;x++)  { /* for all possible #biases - change later */
    bias[x]=((rand()*0.00001)-(rand()*0.00001))*1.6;
    previous_bias_change[x]=0;
  }
```

```
}

void read_whole_training_file(double
        training_database[MAX_NUM_TRAINING_CASES][MAX_NUM_SOURCES_PLUS_ONE],
                        int num_training_cases,
                        int num_nodes[MAX_NUM_LAYERS])
{
  int x;
  int y;

  FILE *fp_train;

  fp_train=fopen("train.txt","r");
  if(fp_train==NULL)  {
    printf("\nFile train.txt cannot be opened or does not exist.\n");

    exit(1);
  }
  for(x=0;x<num_training_cases;x++)  {
    for(y=0;y<(num_nodes[0]+1);y++)  {
      if(PRINT==1) printf("\n%d",y);
      fscanf(fp_train,"%lf",&training_database[x][y]);
    }
  }
  fclose(fp_train);
}

void print_whole_training_file(double
        training_database[MAX_NUM_TRAINING_CASES][MAX_NUM_SOURCES_PLUS_ONE],
                        int num_training_cases,
                        int num_nodes[MAX_NUM_LAYERS])
{
  int x;
  int y;

  for(x=0;x<num_training_cases;x++)  {
    printf("\n");
    for(y=0;y<(num_nodes[0]+1);y++)  {
      printf("%lf ",training_database[x][y]);
    }
  }
}

void feedforward(int num_nodes[MAX_NUM_LAYERS],int num_hidden_layers,
                double weight[MAX_NUM_WEIGHTS], double bias[MAX_NUM_NODES],
                double activation[MAX_NUM_NODES])
{
  int layer;
  int in_node;     /* ie the node _to which_ all values are being sent */
  int out_node;    /* ie the nodes _from which_ values are coming in   */
  int dummy1;      /* dummy variables to avoid using doubles in arrays  */
  int dummy2;
  double sum;
  double factor_1;
  double factor_2;
  double factor_3;
  double factor_4;

  for(layer=1;layer<(num_hidden_layers+2);layer++)  {
    for(in_node=0;in_node<num_nodes[layer];in_node++)  {
      sum=0;
      for(out_node=0;out_node<num_nodes[layer-1];out_node++)  {
        factor_1=factor1(layer,num_nodes);
        factor_2=factor2(layer,num_nodes);
        factor_3=factor3(layer,num_nodes);
        factor_4=num_nodes[layer-1]*in_node;
        if(PRINT==1) printf("\nfactors 1,2,3,4 = %lf %lf %lf %lf\n",factor_1,factor_2,
                                factor_3, factor_4);
```

```
        dummy1=out_node+factor_2;
        dummy2=factor_3+factor_4+out_node;
        sum=sum+activation[dummy1]*weight[dummy2];
        /*
        if(PRINT==1)  {
          printf("\nactivation[%lf]=%lf",out_node+factor_2,
                                        activation[out_node+factor_2]);
          printf("\nweight[%lf]=%lf",factor_3+factor_4+out_node,
                                        weight[factor_3+factor_4+out_node]);
          printf("\nin_node=%d, out_node=%d, sum=%lf",in_node, out_node,sum);
        }
        */
      }
      dummy1=in_node+factor_1;
      sum=sum+bias[dummy1];
      /*
      if(PRINT==1)  {
        printf("\nadded bias=%lf",bias[in_node+factor_1]);
        printf("\ntotal sum=%lf",sum);
      }
      */
      dummy1=in_node+factor_1;
      activation[dummy1]=1/(1+exp(-sum));
      /*
      if(PRINT==1) printf("\nactivation of node[%lf]=%lf\n\n\n",in_node+factor_1,
                                  activation[in_node+factor_1]);

      */
    }
  }
}

double factor1(int layer, int num_nodes[MAX_NUM_LAYERS])
{
  int x;
  double factor_1=0;

  for(x=0;x<layer;x++)  {
    factor_1=factor_1+num_nodes[x];
  }
  /* printf("\nfactor_1=%lf",factor_1); */
  return factor_1;
}

double factor2(int layer, int num_nodes[MAX_NUM_LAYERS])
{
  int x;
  double factor_2=0;

  for(x=0;x<(layer-1);x++)  {
    factor_2=factor_2+num_nodes[x];
  }
  /* printf("\nfactor_2=%lf",factor_2);     */
  return factor_2;
}

double factor3(int layer, int num_nodes[MAX_NUM_LAYERS])
{
  int x;
  double factor_3=0;

  for(x=1;x<layer;x++)  {
    factor_3=factor_3+num_nodes[x-1]*num_nodes[x];
  }
  /* printf("\nfactor_3=%lf",factor_3);     */
  return factor_3;
}
```

```
void backpropagation(int num_nodes[MAX_NUM_LAYERS],int num_hidden_layers,
                double weight[MAX_NUM_WEIGHTS],
                double activation[MAX_NUM_NODES],double epsilon,
                double train_class, double delta[MAX_NUM_NODES],
                double bias[MAX_NUM_NODES],
                double *pixel_total_sum_of_squares, double momentum_w,
                double momentum_b,
                double previous_weight_change[MAX_NUM_WEIGHTS],
                double previous_bias_change[MAX_NUM_NODES])
{
  int x,z;
  int num_nodes_before_output_layer=0;
  int layer;
  int node;
  int total_num_nodes;
  int dummy1;   /* dummy variables to prevent doubles being used in arrays */
  int dummy2;
  int dummy3;
  double sum;
  double factor_1;
  double factor_2;
  double factor_3;
  double factor_4;
  int in_node;
  int out_node;
  double tss;      /* ie 'total sum of squares', an error measure */

  if(PRINT==1) printf("\n\n** STARTING BACKPROPAGATION FUNCTION **\n\n");

  /* set up desired values of all output cells, based on train_class value,
  which is the desired class label */

  /* determine delta values for all output nodes */
  for(x=0;x<(num_hidden_layers+1);x++)  {
    num_nodes_before_output_layer=num_nodes_before_output_layer+num_nodes[x];
  }
  /*  printf("\nNODE ERRORS =");     */
  tss=0;
  for(x=0;x<num_nodes[num_hidden_layers+1];x++)  {
    if(x==train_class)  {
      delta[num_nodes_before_output_layer+x]=
                        (0.9-(activation[num_nodes_before_output_layer+x]))*
                        activation[num_nodes_before_output_layer+x]*(1-
                        activation[num_nodes_before_output_layer+x]);
      /* printf(" %lf ",0.9-(activation[num_nodes_before_output_layer+x])); */
      tss=tss+(0.9-activation[num_nodes_before_output_layer+x])*
              (0.9-activation[num_nodes_before_output_layer+x]);
      if(PRINT==1)  {
        printf("\nDelta[%d]=%lf",num_nodes_before_output_layer+x,
                        delta[num_nodes_before_output_layer+x]);
        printf("\nActivation[%d]=%lf",num_nodes_before_output_layer+x,
                        activation[num_nodes_before_output_layer+x]);
        printf("\nerror=0.9-activation=%lf\n",
                        0.9-activation[num_nodes_before_output_layer+x]);
      }
    }
    else  {
      delta[num_nodes_before_output_layer+x]=
                        (0.1-(activation[num_nodes_before_output_layer+x]))*
                        activation[num_nodes_before_output_layer+x]*(1-
                        activation[num_nodes_before_output_layer+x]);
      /*  printf(" %lf ",0.1-(activation[num_nodes_before_output_layer+x])); */
      tss=tss+(0.1-activation[num_nodes_before_output_layer+x])*
              (0.1-activation[num_nodes_before_output_layer+x]);
      if(PRINT==1)  {
        printf("\nDelta[%d]=%lf",num_nodes_before_output_layer+x,
                        delta[num_nodes_before_output_layer+x]);
        printf("\nActivation[%d]=%lf",num_nodes_before_output_layer+x,
```

```
                        activation[num_nodes_before_output_layer+x]);
        printf("\nerror=0.1-activation=%lf\n",
                        0.1-activation[num_nodes_before_output_layer+x]);
      }
    }
  }
  /* printf("\n");  */
  *pixel_total_sum_of_squares=tss;          /* give value of tss (which is  */
                                            /* total sum of squares for     */
                                            /* current pixel case) to the   */
                                            /* pixel_total_sum_of_squares   */
                                            /* variable, which will transfer*/
                                            /* value to main(), where added */
                                            /* to iteration's tss           */


  /* now, propagate delta values back from the output nodes... */

  total_num_nodes=num_nodes_before_output_layer+
                        num_nodes[num_hidden_layers+1];
  if(PRINT==1) printf("\n** total number of nodes in network is: %d",
                                                    total_num_nodes);
  for(layer=(num_hidden_layers);layer>0;layer=layer-1)  {
    /* note that the middle term was changed to >0 from >-1 ... */
    if(PRINT==1) printf("\nNow Backpropagating at Layer %d",layer);
    for(node=0;node<num_nodes[layer];node++)  {
      sum=0;                    /* ie sum of products of weights * delta's */
      for(z=0;z<num_nodes[layer+1];z++)  {     /* z is nodes in next layer */
        factor_1=factor1((layer+1), num_nodes);
        factor_2=factor2((layer+1), num_nodes);
        factor_3=factor3((layer+1), num_nodes);
        factor_4=num_nodes[layer]*z;/* changed to layer, instead of layer+1*/
                                    /* change back??? */
        if(PRINT==1) printf("\nFactors 1,2,3,4: %lf %lf %lf %lf",factor_1,
                                                factor_2, factor_3,factor_4);

        dummy1=factor_3+factor_4+node;
        dummy2=factor_1+z;
        sum=sum+weight[dummy1]*delta[dummy2];

      }
      dummy1=factor_2+node;
      delta[dummy1]=(activation[dummy1]*(1-
                                activation[dummy1])*sum);
      /* above calculates delta for each node except those in output layer */
    }
  }
    /* Now have deltas for each and every node in network */
    /* Now must calculate change in each weight, and implement this change */
    /* Change in weight = delta for "to-node" * activation for "from-node"
                                * epsilon */

  for(layer=1;layer<(num_hidden_layers+2);layer++) {
                /* note: changed to +2 above, but was +1... change back? */
    for(in_node=0; in_node<num_nodes[layer];in_node++)  {
      for(out_node=0; out_node<num_nodes[layer-1];out_node++)  {
        factor_1=factor1(layer,num_nodes);
        factor_2=factor2(layer,num_nodes);
        factor_3=factor3(layer,num_nodes);
        factor_4=num_nodes[layer-1]*in_node;

        dummy1=factor_3+factor_4+out_node;
        dummy2=factor_1+in_node;
        dummy3=factor_2+out_node;
        weight[dummy1]=weight[dummy1]+
                        (epsilon*delta[dummy2]*
                        activation[dummy3])+(momentum_w*
                        previous_weight_change[dummy1]);
```

```
        previous_weight_change[dummy1]=
                        (epsilon*delta[dummy2]*
                        activation[dummy3])+(momentum_w*
                        previous_weight_change[dummy1]);
                        /* the above statement sets 'previous_weight_change'
                        for the next time that the weight is changed       */
      }
    }
  }

  for(x=num_nodes[0];x<total_num_nodes;x++)  { /* run thru relevant        */
                                               /* (ie non-input) biases    */
    bias[x]=bias[x]+delta[x]*epsilon+momentum_b*previous_bias_change[x];
                                              /* activation of all bias=1 */
    previous_bias_change[x]=delta[x]*epsilon+momentum_b*previous_bias_change[x];
  }
}
```

APPENDIX G: Neural Network Source Code (Classification Module)

(FEED9.C)

```
#include <stdio.h>
#include <math.h>
#include <conio.h>

#define MAX_NUM_LAYERS 50
#define MAX_NUM_WEIGHTS 5000        /* ie max # weights for whole network  */
#define MAX_NUM_NODES 1000
#define MAX_NUM_ITERATIONS 1        /* THIS IS NOW IRRELEVANT - CHANGE TO 1 OR DELETE */
#define NUM_TRAINING_CASES 294      /* # PIXELS IN IMAGE OR TEST DATABASE */
#define PRINT 0

/*        NOTE: THE CODE MUST BE RE-COMPILED IF ANY OF                  */
/*        THE FOLLOWING VARIABLES CHANGES:                              */
/*        1) # PIXELS IN IMAGERY TO BE CLASSIFIED                       */
/*                  (REQUIRES NUM_TRAINING_CASES TO BE CHANGED          */
/*        2) # SOURCES USED (REQUIRES CHANGE IN FILE-READING ROUTINE    */
/*                  (WHICH MEANS APPROX LINES 94,150,170,214).          */

/*       Note that, because the classification module's code is
         derived directly from that of the training module, the
         overall organizaton of the code is the same, and there are
          small segments of code (vestiges of the training module)
         that do not perform any useful function here.                 */

void clear_screen();

void intro();

void check_for_old_files();

void read_parameter_file(int *num_hidden_layers,int num_nodes[MAX_NUM_LAYERS],
                                double *epsilon, double *momentum);

void print_parameter_values(int num_hidden_layers,
                                int num_nodes[MAX_NUM_LAYERS],
                                double epsilon, double momentum);

int calculate_number_weights(int num_hidden_layers,
                                int num_nodes[MAX_NUM_LAYERS]);

void read_initial_weights(double weight[MAX_NUM_WEIGHTS],int num_weights,
                                double bias[MAX_NUM_NODES],
                                int num_hidden_layers,
                                int num_nodes[MAX_NUM_LAYERS]);

void feedforward(int num_nodes[MAX_NUM_LAYERS],int num_hidden_layers,
                                double weight[MAX_NUM_WEIGHTS],
                                double bias[MAX_NUM_NODES],
                                double activation[MAX_NUM_NODES]);

double factor1(int layer, int num_nodes[MAX_NUM_LAYERS]);

double factor2(int layer, int num_nodes[MAX_NUM_LAYERS]);

double factor3(int layer, int num_nodes[MAX_NUM_LAYERS]);


main()
{
  int num_hidden_layers;
  int num_nodes[MAX_NUM_LAYERS];    /* ie to store #nodes for each layer   */
  int num_weights;                  /* ie total #weights                   */
  int last_layer;                   /* ie the layer # for output layer     */
```

```
double epsilon;                    /* ie learning rate parameter          */
double momentum;
double weight[MAX_NUM_WEIGHTS];    /* ie actual value of each weight      */
double bias[MAX_NUM_NODES];
double activation[MAX_NUM_NODES]; /* ie total #nodes in network          */
double delta[MAX_NUM_NODES];       /* ie a delta value for each node      */
int iteration;
long int training_case;             /* ie number of training case          */
double train_class;                 /* ie desired class label (node #)     */
double maximum;
int max;

FILE *fp_train0;                   /* source 0 imagery   */
FILE *fp_train1;                   /* source 1 imagery   */
FILE *fp_train2;                   /* source 2 imagery   */
FILE *fp_train3;                   /* source 3 imagery   */
/* FILE *fp_train4; */             /* source 4 imagery   */
/* FILE *fp_train5; */             /* source 5 imagery   */

FILE *fp_output;                   /* classified imagery */
FILE *fp_weights;                  /* for writing calculated weights to */

int x;

clear_screen();
intro();
check_for_old_files();
read_parameter_file(&num_hidden_layers,num_nodes,&epsilon,&momentum);
print_parameter_values(num_hidden_layers,num_nodes,epsilon,momentum);

num_weights=calculate_number_weights(num_hidden_layers,num_nodes);
printf("\n\ntotal number of weights: %d",num_weights);
if(num_weights>MAX_NUM_WEIGHTS) exit();

printf("\npress any key to continue...");
getch();

read_initial_weights(weight,num_weights,bias,num_hidden_layers,
                     num_nodes);

printf("\n\nweights+biases read... press any key to continue...\n\n");
getch();

for(iteration=0;iteration<MAX_NUM_ITERATIONS;iteration++)  {
  printf("\n\n************ITERATION %d**********************\n",iteration);

  fp_train0=fopen("train0.txt","r");
  if(fp_train0==NULL)  {
    printf("\nFile train0.txt cannot be opened or does not exist.\n");
    exit(1);
  }
  fp_train1=fopen("train1.txt","r");
  if(fp_train1==NULL)  {
    printf("\nFile train1.txt cannot be opened or does not exist.\n");
    exit(1);
  }
  fp_train2=fopen("train2.txt","r");
  if(fp_train2==NULL)  {
    printf("\nFile train2.txt cannot be opened or does not exist.\n");
    exit(1);
  }
  fp_train3=fopen("train3.txt","r");
  if(fp_train3==NULL)  {
    printf("\nFile train3.txt cannot be opened or does not exist.\n");
    exit(1);
  }
  /*  THIS VERSION IS COMPILED FOR 4 SOURCES (0,1,2,3)
  fp_train4=fopen("train4.txt","r");
```

```
    if(fp_train4==NULL)  {
      printf("\nFile train4.txt cannot be opened or does not exist.\n");
      exit(1);
    }
    fp_train5=fopen("train5.txt","r");
    if(fp_train5==NULL)  {
      printf("\nFile train5.txt cannot be opened or does not exist.\n");
      exit(1);
    }
    */
    for(training_case=0;training_case<NUM_TRAINING_CASES;training_case++)  {

      if(PRINT==1) printf("\n%d",x);

      fscanf(fp_train0,"%lf",&activation[0]);
      fscanf(fp_train1,"%lf",&activation[1]);
      fscanf(fp_train2,"%lf",&activation[2]);
      fscanf(fp_train3,"%lf",&activation[3]);
      /*
      fscanf(fp_train4,"%lf",&activation[4]);
      fscanf(fp_train5,"%lf",&activation[5]);
      */
      /*
      printf("\nactivations are... 0:%lf\n",activation[0]);
      printf("\nactivations are... 1:%lf\n",activation[1]);
      printf("\nactivations are... 2:%lf\n",activation[2]);
      printf("\nactivations are... 3:%lf\n",activation[3]);
      printf("\nactivations are... 4:%lf\n",activation[4]);
      printf("\nactivations are... 5:%lf\n",activation[5]);
      */
      /* now, all input nodes for a given case are in memory...
      must proceed with feedforward                                    */

      feedforward(num_nodes, num_hidden_layers, weight, bias, activation);

      /* now, all activations associated with each node - including output
      nodes - have been calculated...                                  */

      maximum=0;                          /* i.e.: re: activation    */
      max=999;                            /* a 'dummy' value         */
      last_layer=num_hidden_layers+1;     /* layer # of output layer */
      fp_output=fopen("output.txt","a");
      for(x=0;x<num_nodes[last_layer];x++)  {
        /* printf("\nactivation[%d]: %lf",x,activation[x+36]);  */
        if(activation[x+factor1(last_layer,num_nodes)]>maximum)  {
          maximum=activation[x+factor1(last_layer,num_nodes)];
          max=x;
        }
      }
      fprintf(fp_output,"%d\n", max);
      /* printf("\nPixel classified as: %d",max); */
      fclose(fp_output);
    }
  }
  printf("\n\nFeedforward Module done... output is in output.txt\n\n");
  printf("Press any key to exit...\n\n");
  getch();
  fclose(fp_train0);
  fclose(fp_train1);
  fclose(fp_train2);
  fclose(fp_train3);
  /*
  fclose(fp_train4);
  fclose(fp_train5);
  */
}

void clear_screen()
```

```
{
  int x;
  for(x=0;x<30;x++)  {
    printf("\n");
  }
}

void intro()
{
  printf("\n\nNEURAL NETWORK PROGRAM: Feedforward Module  Version 3.0\n");
  printf("(C) Leverington 1999\n");
  printf("Compiled : "__DATE__"  "__TIME__"\n");
  printf("\nThis code has been compiled for use in 4-source");
  printf("\nclassifications, with #pixels in each image = %d.\n\n\n",
                NUM_TRAINING_CASES);
}

void check_for_old_files()
{
  FILE *fp_check;

  fp_check=fopen("output.txt","r");
  if(fp_check!=NULL)  {
    printf("Abort: an old copy of output.txt has been found.");
    exit(1);
  }
}

void read_parameter_file(int *num_hidden_layers,int num_nodes[MAX_NUM_LAYERS],
                                 double *epsilon, double *momentum)
{
  FILE *fp_parameters;
  int x;
  int num_hidden_lay;
  double epsil;
  double moment;

  fp_parameters=fopen("param.txt","r");
  if(fp_parameters==NULL)  {
    printf("File param.txt cannot be opened or does not exist.\n");
    exit(1);
  }
  fscanf(fp_parameters,"%d",&num_hidden_lay);       /* ie #hidden layers   */
  for(x=0;x<(num_hidden_lay+2);x++)  {
    fscanf(fp_parameters,"%d",&num_nodes[x]);       /* ie #nodes per layer */
  }
  fscanf(fp_parameters,"%lf",&epsil);                /* not necessary now   */
  fscanf(fp_parameters,"%lf",&moment);
  fclose(fp_parameters);

  printf("File param.txt successfully opened and values have been read");

  /* now, the interim variables have been 'filled'... must transfer these
     values to the memory locations of the respective variables of main() */

  *num_hidden_layers=num_hidden_lay;
  *epsilon=epsil;
  *momentum=moment;
}

void print_parameter_values(int num_hidden_layers,
                                 int num_nodes[MAX_NUM_LAYERS],
                                 double epsilon, double momentum)
{
  int x;

  printf("\n\nnumber of hidden layers: %d",num_hidden_layers);
  for(x=0;x<(num_hidden_layers+2);x++)  {
```

```
    printf("\nnumber of nodes for layer %d: %d",x,num_nodes[x]);
  }
  printf("\nepsilon:  %lf",epsilon);
  printf("\nmomentum: %lf",momentum);
}


int calculate_number_weights(int num_hidden_layers,
                                        int num_nodes[MAX_NUM_LAYERS])
{
  int x;
  int total=0;

  for(x=0;x<(num_hidden_layers+1);x++)  {
    total=total+num_nodes[x]*num_nodes[x+1];
  }
  return (total);
}


void read_initial_weights(double weight[MAX_NUM_WEIGHTS],int num_weights,
                                  double bias[MAX_NUM_NODES],
                                  int num_hidden_layers,
                                  int num_nodes[MAX_NUM_LAYERS])
{
  int x;
  int total_num_nodes;

  FILE *fp_w;
  FILE *fp_b;

  fp_w=fopen("weight.txt","r");
  if(fp_w==NULL)  {
    printf("File weight.txt cannot be opened or does not exist.\n");
    exit(1);
  }
  for(x=0;x<num_weights;x++)  {
    fscanf(fp_w,"%lf",&weight[x]);
    printf("\nweight[%d]=%lf",x,weight[x]);
  }
  fclose(fp_w);

  total_num_nodes=0;
  for(x=0;x<(num_hidden_layers+2);x++)  {   /* determine #nodes = #biases */
    total_num_nodes=total_num_nodes+num_nodes[x];
  }
  printf("\nThe total number of nodes in the network is %d",total_num_nodes);
  printf("\nPress any key to continue.");
  getch();
  fp_b=fopen("bias.txt","r");
  if(fp_b==NULL)  {
    printf("File bias.txt cannot be opened or does not exist.\n");
    exit(1);
  }
  for(x=0;x<total_num_nodes;x++)  {
    fscanf(fp_b,"%lf",&bias[x]);
    printf("\nbias[%d]=%lf",x,bias[x]);
  }
  fclose(fp_b);
}

void feedforward(int num_nodes[MAX_NUM_LAYERS],int num_hidden_layers,
                 double weight[MAX_NUM_WEIGHTS], double bias[MAX_NUM_NODES],
                 double activation[MAX_NUM_NODES])
{
  int layer;
  int in_node;     /* ie the node _to which_ all values are being sent */
```

```
  int out_node;    /* ie the nodes _from which_ values are coming in   */
  double sum;
  double factor_1;
  double factor_2;
  double factor_3;
  double factor_4;

  for(layer=1;layer<(num_hidden_layers+2);layer++)  {
    for(in_node=0;in_node<num_nodes[layer];in_node++)  {
      sum=0;
      for(out_node=0;out_node<num_nodes[layer-1];out_node++)  {
        factor_1=factor1(layer,num_nodes);
        factor_2=factor2(layer,num_nodes);
        factor_3=factor3(layer,num_nodes);
        factor_4=num_nodes[layer-1]*in_node;
        if(PRINT==1) printf("\nfactors 1,2,3,4 = %lf %lf %lf %lf\n",factor_1,factor_2,
                                  factor_3, factor_4);
        sum=sum+activation[out_node+factor_2]*weight[factor_3+factor_4+
                                  out_node];
        if(PRINT==1)  {
          printf("\nactivation[%lf]=%lf",out_node+factor_2,
                                  activation[out_node+factor_2]);
          printf("\nweight[%lf]=%lf",factor_3+factor_4+out_node,
                                  weight[factor_3+factor_4+out_node]);
          printf("\nin_node=%d, out_node=%d, sum=%lf",in_node, out_node,sum);
        }
      }
      sum=sum+bias[in_node+factor_1];
      if(PRINT==1)  {
        printf("\nadded bias=%lf",bias[in_node+factor_1]);
        printf("\ntotal sum=%lf",sum);
      }
      activation[in_node+factor_1]=1/(1+exp(-sum));
      if(PRINT==1) printf("\nactivation of node[%lf]=%lf\n\n\n",in_node+factor_1,
                                  activation[in_node+factor_1]);
      if(PRINT==1) getch();
    }
  }
}

double factor1(int layer, int num_nodes[MAX_NUM_LAYERS])
{
  int x;
  double factor_1=0;

  for(x=0;x<layer;x++)  {
    factor_1=factor_1+num_nodes[x];
  }
  /* printf("\nfactor_1=%lf",factor_1); */
  return factor_1;
}

double factor2(int layer, int num_nodes[MAX_NUM_LAYERS])
{
  int x;
  double factor_2=0;

  for(x=0;x<(layer-1);x++)  {
    factor_2=factor_2+num_nodes[x];
  }
  /* printf("\nfactor_2=%lf",factor_2);     */
  return factor_2;
}

double factor3(int layer, int num_nodes[MAX_NUM_LAYERS])
{
  int x;
  double factor_3=0;
```

```
  for(x=1;x<layer;x++)  {
    factor_3=factor_3+num_nodes[x-1]*num_nodes[x];
  }
  /* printf("\nfactor_3=%lf",factor_3);      */
  return factor_3;
}
```